THE EARTH-MOON SYSTEM AS A DYNAMICAL LABORATORY

EDITED BY: Elisa Maria Alessi, Josep Masdemont and Alessandro Rossi
PUBLISHED IN: Frontiers in Astronomy and Space Sciences and
Frontiers in Applied Mathematics and Statistics

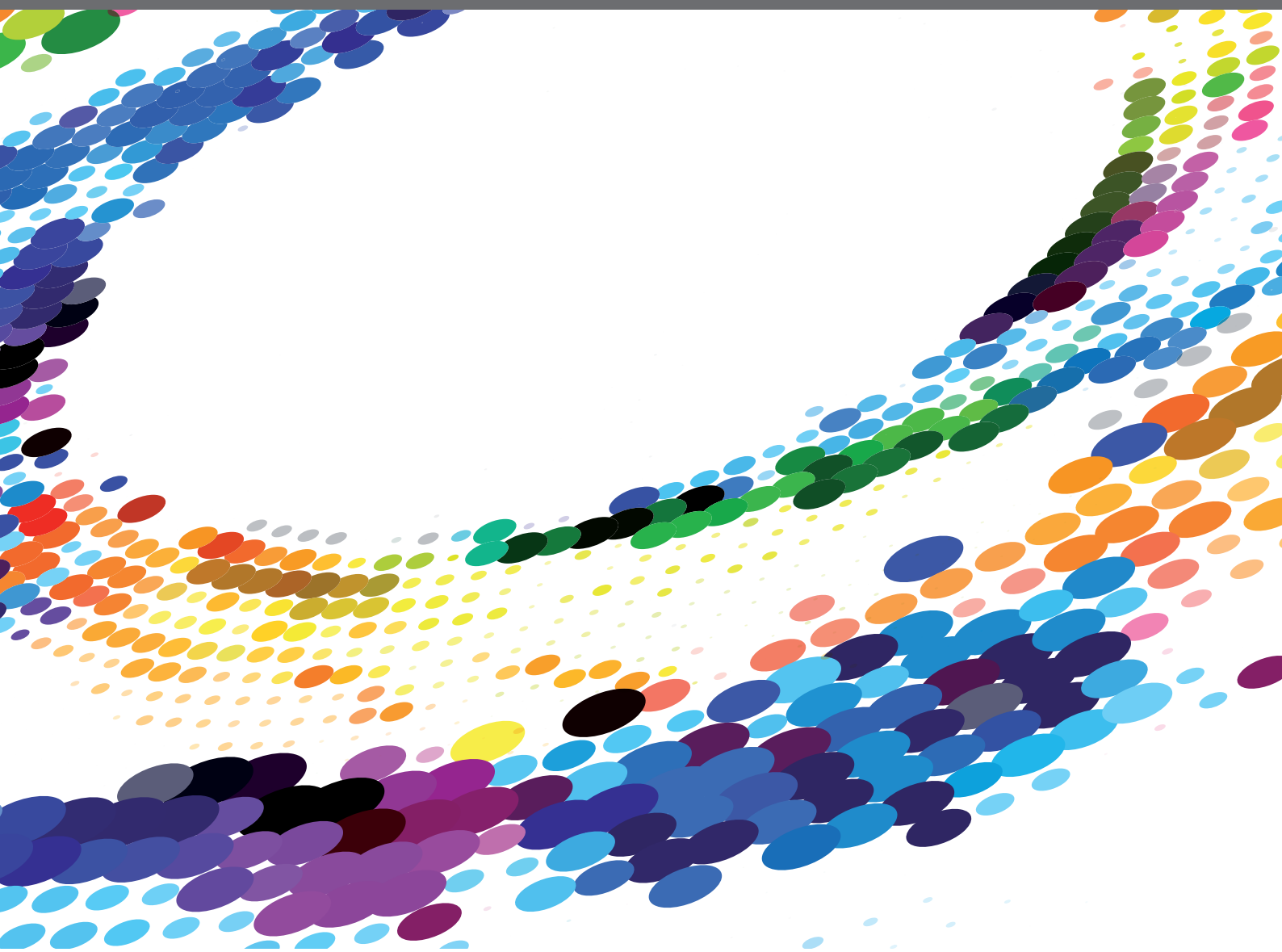

frontiers Research Topics

frontiers

ISSN 1664-8714
ISBN 978-2-88963-044-8
DOI 10.3389/978-2-88963-044-8

About Frontiers

Frontiers is more than just an open-access publisher of scholarly articles: it is a pioneering approach to the world of academia, radically improving the way scholarly research is managed. The grand vision of Frontiers is a world where all people have an equal opportunity to seek, share and generate knowledge. Frontiers provides immediate and permanent online open access to all its publications, but this alone is not enough to realize our grand goals.

Frontiers Journal Series

The Frontiers Journal Series is a multi-tier and interdisciplinary set of open-access, online journals, promising a paradigm shift from the current review, selection and dissemination processes in academic publishing. All Frontiers journals are driven by researchers for researchers; therefore, they constitute a service to the scholarly community. At the same time, the Frontiers Journal Series operates on a revolutionary invention, the tiered publishing system, initially addressing specific communities of scholars, and gradually climbing up to broader public understanding, thus serving the interests of the lay society, too.

Dedication to Quality

Each Frontiers article is a landmark of the highest quality, thanks to genuinely collaborative interactions between authors and review editors, who include some of the world's best academicians. Research must be certified by peers before entering a stream of knowledge that may eventually reach the public - and shape society; therefore, Frontiers only applies the most rigorous and unbiased reviews.
Frontiers revolutionizes research publishing by freely delivering the most outstanding research, evaluated with no bias from both the academic and social point of view. By applying the most advanced information technologies, Frontiers is catapulting scholarly publishing into a new generation.

What are Frontiers Research Topics?

Frontiers Research Topics are very popular trademarks of the Frontiers Journals Series: they are collections of at least ten articles, all centered on a particular subject. With their unique mix of varied contributions from Original Research to Review Articles, Frontiers Research Topics unify the most influential researchers, the latest key findings and historical advances in a hot research area! Find out more on how to host your own Frontiers Research Topic or contribute to one as an author by contacting the Frontiers Editorial Office: researchtopics@frontiersin.org

THE EARTH-MOON SYSTEM AS A DYNAMICAL LABORATORY

Topic Editors:
Elisa Maria Alessi, Istituto di Fisica Applicata Nello Carrara (CNR), Italy
Josep Masdemont, Universitat Politècnica de Catalunya & IEEC, Spain
Alessandro Rossi, Istituto di Fisica Applicata Nello Carrara (CNR), Italy

Image credit: NASA
caption: the full Moon from the International Space Station

The Earth-Moon neighborhood is the scene of a large variety of applications that concern asteroids, lunar exploration and space debris in Earth orbit. In particular, recent efforts by the scientific community have focused on the possibility of extending the human operations beyond the radiation belts; of exploiting in-situ resources, either on the lunar surface or on asteroids retrieved to the vicinity of the Earth; and of mitigating the space debris concern by taking advantage of the lunar perturbation.

The characteristic dynamics in the cislunar space represents an opportunity for the mission designer, but also a challenge in terms of theoretical understanding and operational control. This Research Topic covers the Earth-Moon dynamics in its complexity and allure, considering the most relevant aspects for both natural and artificial objects, in order to get a new comprehension of the dynamics at stake along with the operational procedures that can handle it.

Citation: Alessi, E. M., Masdemont, J., Rossi, A., eds. (2019). The Earth-Moon System as a Dynamical Laboratory. Lausanne: Frontiers Media.
doi: 10.3389/978-2-88963-044-8

Table of Contents

04 ***Editorial: The Earth–Moon System as a Dynamical Laboratory***
Elisa Maria Alessi, Josep Masdemont and Alessandro Rossi

06 ***Earth's Minimoons: Opportunities for Science and Technology***
Robert Jedicke, Bryce T. Bolin, William F. Bottke, Monique Chyba, Grigori Fedorets, Mikael Granvik, Lynne Jones and Hodei Urrutxua

25 ***Trajectory Design for Asteroid Retrieval Missions: A Short Review***
Joan-Pau Sánchez, Rita Neves and Hodei Urrutxua

31 ***Orbit Design for LUMIO: The Lunar Meteoroid Impacts Observer***
Ana M. Cipriano, Diogene A. Dei Tos and Francesco Topputo

54 ***Enhancing Station-Keeping Control With the Use of Extended State Observers***
James D. Biggs, Helen C. Henninger and Aman Narula

63 ***Rendezvous Strategies in the Vicinity of Earth-Moon Lagrangian Points***
Stephanie Lizy-Destrez, Laurent Beauregard, Emmanuel Blazquez, Antonino Campolo, Sara Manglativi and Victor Quet

82 ***Homo- and Heteroclinic Connections in the Planar Solar-Sail Earth-Moon Three-Body Problem***
Jeannette Heiligers

99 ***Drift and its Mediation in Terrestrial Orbits***
Jérôme Daquin, Ioannis Gkolias and Aaron J. Rosengren

113 ***Long-Term Evolution of Highly-Elliptical Orbits: Luni-Solar Perturbation Effects for Stability and Re-entry***
Camilla Colombo

135 ***Periodic Orbits Close to That of the Moon in Hill's Problem***
Giovanni B. Valsecchi

141 ***Two Periodic Models for the Earth-Moon System***
Marc Jorba-Cuscó, Ariadna Farrés and Àngel Jorba

frontiers in Astronomy and Space Sciences

EDITORIAL
published: 12 June 2019
doi: 10.3389/fspas.2019.00043

Editorial: The Earth–Moon System As a Dynamical Laboratory

Elisa Maria Alessi[1]*, *Josep Masdemont*[2] and *Alessandro Rossi*[1]

[1] Istituto di Fisica Applicata "Nello Carrara," Consiglio Nazionale delle Ricerche, Sesto Fiorentino, Italy, [2] Department of Mathematics, Universitat Politècnica de Catalunya & IEEC, Barcelona, Spain

Keywords: cislunar dynamics, Earth–Moon system, libration point orbits, mini-moons, lunar perturbation, asteroid retrieval, Earth–Moon–Sun

Editorial on the Research Topic

The Earth-Moon System as a Dynamical Laboratory

The aim of this collection is to address the dynamical challenges related to the cislunar space. The Earth–Moon environment can be considered as a laboratory of dynamics, characterized by very peculiar features. On the one hand, we can notice the high ratio between the mass of the Earth and the mass of the Moon, the lunar orbit itself, the proximity to the Sun and the chaotic behavior of the dynamics associated with small bodies (artificial and non). On the other hand, crucial experiments are taking place in the cislunar place. First, it is well-known that there exists a concrete effort to explore the lunar surface with both uncrewed and crewed missions, and to operate a Lunar Gateway. Second, the understanding of the minor bodies population in the solar system cannot overlook a deep knowledge of the minor bodies orbiting in the Earth–Moon system, paying attention in particular to the objects of a few-meters diameter size, whose characterization is still missing. Third, the gravitational attraction of the Moon exhibits a demonstrated influence on high altitude Earth' satellites, which can be crucial in the perspective of limiting the growth of artificial space debris in the long term.

All these aspects are covered within this Research Topic, which includes 1 review, 1 mini review, 1 methods, and 7 original research papers, and it is the result of the collective commitment brought by international experts in celestial mechanics and astrodynamics (both authors and referees). It is worth noticing that they come from different background—mathematics, physics, aerospace engineering- and different generations. The articles of the issue focus on theoretical and numerical developments, but also on the practical use of the given models and tools. In practice, this reflects into the design of space missions but also in the understanding of the motion of natural bodies and their possible exploitation. Moreover, many of the mathematical and operational concepts presented in the Research Topic can be extended to different planet-moon systems.

To study the motion of either a spacecraft or a natural body (in both cases assumed with a negligible mass), the authors consider as a baseline dynamical model either the Circular Restricted Three-Body Problem (CR3BP) (in Biggs et al., Cipriano et al., Lizy-Destrez et al., Jedicke et al., and Sánchez et al.) or the classical theory of perturbations applied to the Kepler problem, assuming as perturbations the Earth's oblateness and the lunar perturbations (in Colombo and Daquin et al.). The role of the Sun is accounted in Biggs et al. and Heiligers in terms of solar radiation pressure (SRP) and in Daquin et al. and Jorba-Cuscó et al. in terms of gravitational perturbation. In Valsecchi, the Hill's model is applied to find orbital solutions for the motion of the Moon itself.

Natural bodies play a central role in the reviews by Jedicke et al. and Sánchez et al. Jedicke et al. focus the analysis on the population of asteroids of a few-meter diameter size, which are temporary-captured in the Earth–Moon system. The authors address the aspects concerning the dynamical definition of these configurations, along with

Edited by:
Sergei M. Kopeikin, University of Missouri, United States

Reviewed by:
Leonid Zotov, National Research University Higher School of Economics, Russia

***Correspondence:**
Elisa Maria Alessi
em.alessi@ifac.cnr.it

Specialty section:
This article was submitted to Fundamental Astronomy, a section of the journal Frontiers in Astronomy and Space Sciences

Received: *09 May 2019*
Accepted: *21 May 2019*
Published: *12 June 2019*

Citation:
Alessi EM, Masdemont J and Rossi A (2019) Editorial: The Earth–Moon System As a Dynamical Laboratory. Front. Astron. Space Sci. 6:43. doi: 10.3389/fspas.2019.00043

the possible mechanism of capture. Moreover, they explain the challenges associated with the observation of this minor body population, describing also their possible technological and commercial exploitation. This analysis is complemented by the review provided by Sánchez et al., who present the main trajectory designs envisaged so far to retrieve an asteroid either to the Earth–Moon system or to the Sun–Earth system.

The dynamics of artificial objects in the context of the CR3BP is tackled by Cipriano et al., Biggs et al., Lizy-Destrez et al., and Heiligers. Cipriano et al. present the LUMIO (LUnar Meteoroid Impact Observer) mission, which was selected for consideration for future implementation by the European Space Agency under the SysNova Competition entitled "Lunar CubeSats for Exploration." The concept is particularly interesting because it addresses the trajectory design of a Libration Point Orbit (LPO) mission in the Earth–Moon system, but also because it aims at the observation of impacts of meteoroids on the lunar farside, by detecting their impact flashes, and thus complementing the ground-based measures. LPO missions in the Earth–Moon systems are the focus also of the work by Biggs et al. and Lizy-Destrez et al. Biggs et al. show how an Extended State Observer can be used to estimate the SRP perturbation on a halo orbit, together with the possible injection errors. The main purpose is to improve the station-keeping control. Lizy-Destrez et al. face the rendez-vous problem in the CR3BP, which is a fundamental topic for the establishment and the operability of a Lunar Gateway. Finally, Heiligers shows how to compute homoclinic and heteroclinic connections between planar Lyapunov orbits in the CR3BP embedded with a constant SRP acceleration. Such dynamical corridors, opened by an *ad hoc* usage of solar sails, represent new natural transport mechanisms that can be considered in the cislunar space.

Daquin et al. and Colombo are concerned with the long-term effect of the lunisolar gravitational perturbation on Medium Earth Orbits and Highly Elliptical Orbits (HEO), respectively. While Daquin et al. concentrate on the role of chaos and its quantification, Colombo shows how to model accurately the lunisolar perturbations on HEO, and how to exploit effectively the corresponding dynamical maps for real missions.

In the last two articles, Valsecchi and Jorba-Cuscó et al., different dynamical models to work in the Earth–Moon system are proposed. Valsecchi shows the existence of periodic solutions in the Hill's problem, that respect the periodicity of the Saros. He also provides a comparison of the solutions with the NASA Jet Propulsion Laboratory ephemerides of the Moon, obtaining good consistency. A possible extension of this work is to have a simple realistic model where the three gravitational attractions—Sun, Earth, Moon—are considered, and that can be used to more accurately define the dynamical behavior of a small body orbiting in the cislunar space. With an analogous purpose, Jorba-Cuscó et al. analyze the Bicircular Problem and the Quasi-Bicircular Problem and their applicability in the neighborhood of the collinear and triangular points of the original CR3BP.

In conclusion, the Earth–Moon system is the paradigm of how a proper modeling of the dynamics and its understanding leads to an effective exploitation of the environment for scientific purposes. The various methods and applications presented in the Research Topic also show that a key role is played by the synergy that should be found among applied mathematics, space engineering, and planetary science.

AUTHOR CONTRIBUTIONS

All the authors contributed to the editorial and have critically reviewed and approved it.

Conflict of Interest Statement: The authors declare that the research was conducted in the absence of any commercial or financial relationships that could be construed as a potential conflict of interest.

frontiers in Astronomy and Space Sciences

REVIEW
published: 24 May 2018
doi: 10.3389/fspas.2018.00013

Earth's Minimoons: Opportunities for Science and Technology

Robert Jedicke[1], Bryce T. Bolin[2], William F. Bottke[3], Monique Chyba[4], Grigori Fedorets[5], Mikael Granvik[5,6], Lynne Jones[2] and Hodei Urrutxua[7]*

[1] Institute for Astronomy, University of Hawai'i at Mānoa, Honolulu, HI, United States, [2] Department of Astronomy, University of Washington, Seattle, WA, United States, [3] Southwest Research Institute, Boulder, CO, United States, [4] Department of Mathematics, University of Hawai'i at Mānoa, Honolulu, HI, United States, [5] Department of Physics, University of Helsinki, Helsinki, Finland, [6] Department of Computer Science, Electrical and Space Engineering, Luleå University of Technology, Kiruna, Sweden, [7] Universidad Rey Juan Carlos, Madrid, Spain

Twelve years ago the Catalina Sky Survey discovered Earth's first known natural geocentric object other than the Moon, a few-meter diameter asteroid designated 2006 RH_{120}. Despite significant improvements in ground-based telescope and detector technology in the past decade the asteroid surveys have not discovered another temporarily-captured orbiter (TCO; colloquially known as minimoons) but the all-sky fireball system operated in the Czech Republic as part of the European Fireball Network detected a bright natural meteor that was almost certainly in a geocentric orbit before it struck Earth's atmosphere. Within a few years the Large Synoptic Survey Telescope (LSST) will either begin to regularly detect TCOs or force a re-analysis of the creation and dynamical evolution of small asteroids in the inner solar system. The first studies of the provenance, properties, and dynamics of Earth's minimoons suggested that there should be a steady state population with about one 1- to 2-m diameter captured objects at any time, with the number of captured meteoroids increasing exponentially for smaller sizes. That model was then improved and extended to include the population of temporarily-captured flybys (TCFs), objects that fail to make an entire revolution around Earth while energetically bound to the Earth-Moon system. Several different techniques for discovering TCOs have been considered but their small diameters, proximity, and rapid motion make them challenging targets for existing ground-based optical, meteor, and radar surveys. However, the LSST's tremendous light gathering power and short exposure times could allow it to detect and discover many minimoons. We expect that if the TCO population is confirmed, and new objects are frequently discovered, they can provide new opportunities for (1) studying the dynamics of the Earth-Moon system, (2) testing models of the production and dynamical evolution of small asteroids from the asteroid belt, (3) rapid and frequent low delta-v missions to multiple minimoons, and (4) evaluating *in-situ* resource utilization techniques on asteroidal material. Here we review the past decade of minimoon studies in preparation for capitalizing on the scientific and commercial opportunities of TCOs in the first decade of LSST operations.

Keywords: minimoon, asteroid, NEO, ISRU, dynamics

OPEN ACCESS

Edited by:
Elisa Maria Alessi, Consiglio Nazionale Delle Ricerche (CNR), Italy

Reviewed by:
Davide Farnocchia, Jet Propulsion Laboratory, United States
Thomas Marshall Eubanks, Asteroid Initiatives, United States
Gerard Gomez, Universitat de Barcelona, Spain

****Correspondence:***
Robert Jedicke
jedicke@hawaii.edu

Specialty section:
This article was submitted to Fundamental Astronomy, a section of the journal Frontiers in Astronomy and Space Sciences

Received: *28 February 2018*
Accepted: *30 April 2018*
Published: *24 May 2018*

Citation:
Jedicke R, Bolin BT, Bottke WF, Chyba M, Fedorets G, Granvik M, Jones L and Urrutxua H (2018) Earth's Minimoons: Opportunities for Science and Technology. Front. Astron. Space Sci. 5:13. doi: 10.3389/fspas.2018.00013

1. MINIMOON INTRODUCTION

For more than four billion years the Earth has been accompanied by the ∼3,500 km diameter Moon, its only permanent natural satellite. Our outsized satellite places the Earth at the top of the list of the eight planets in the Solar System in terms of the primary-to-satellite mass ratio despite the fact that the Moon is only about 1% of Earth's mass. This work reviews the history, properties, and future potential of natural objects that are *temporarily* gravitationally bound within the Earth-Moon system (EMS). We refer to them as either temporarily captured objects (TCO) or temporarily captured flybys (TCF) depending on whether they make at least one revolution around Earth (the definition will be refined in section 3). As an homage to the Moon and Austin Powers[1] we usually refer to TCOs and TCFs as "minimoons" though, to be more precise based on their relative diameters, they may more accurately be considered micromoons.

The most basic definition of whether two objects are gravitationally bound to one another requires that the sum of their relative kinetic and potential energy must be less than zero. i.e.,

$$\epsilon = \frac{E_T}{m} = \frac{c_3}{2} = \frac{1}{2}v^2 - \frac{\mu}{r} < 0 \qquad (1)$$

where ϵ is an object's specific orbital energy, the total energy (E_T) per unit mass (m) of the smaller object, c_3 is its "characteristic energy," v and r are the relative speed and distance between the objects, and $\mu = GM$ is the standard gravitational parameter where G is the gravitational constant and M is the mass of the primary. This definition breaks down when there are more than two objects (i.e., in all real situations) and in our Solar System "temporary capture" usually also requires a limit on the separation between the objects of less than 3 Hill radii (e.g., Kary and Dones, 1996; Granvik et al., 2012). Minimoons are temporarily captured natural satellites of Earth in the sense that they have $\epsilon < 0$ with respect to Earth *and* are within 3 Hill radii (**Figure 1**).

The existence of minimoons was long regarded as impossible or, at best, unlikely, because several long-running asteroid surveys had not identified any natural geocentric objects in many years of operation. We think this is most likely due to these objects typically being too small, too faint, and moving too rapidly to be efficiently detected, but there is also likely a psychological bias against their discovery that still remains. Since it is "well known" that Earth has no other natural satellites any geocentric object must be artificial even if it was identified on an unusual distant orbit. In this work we will show that this bias is unwarranted, minimoons have been discovered and will be discovered in even greater numbers in the near future as highly capable astronomical surveys begin their operations.

2. MINIMOON DISCOVERIES

The Catalina Sky Survey (Larson et al., 1998) has been in operation for about 20 years and has discovered many near-Earth objects (NEO; objects with perihelia $q < 1.3$ au) and comets but in September 2006 they discovered the first verified minimoon[2], now known as 2006 RH_{120} (Kwiatkowski et al., 2009). While its geocentric orbit was established soon after discovery there was some controversy over its nature as an artificial or natural object. Several launch vehicle booster stages have achieved sufficient speed for them to escape the gravitational bonds of the EMS (e.g., Jorgensen et al., 2003) only to be subsequently recaptured in the system after a few decades. Subsequent astrometric observations of 2006 RH_{120} established its provenance as a natural object because the perturbations to its trajectory caused by solar radiation pressure[3] were inconsistent with it being artificial

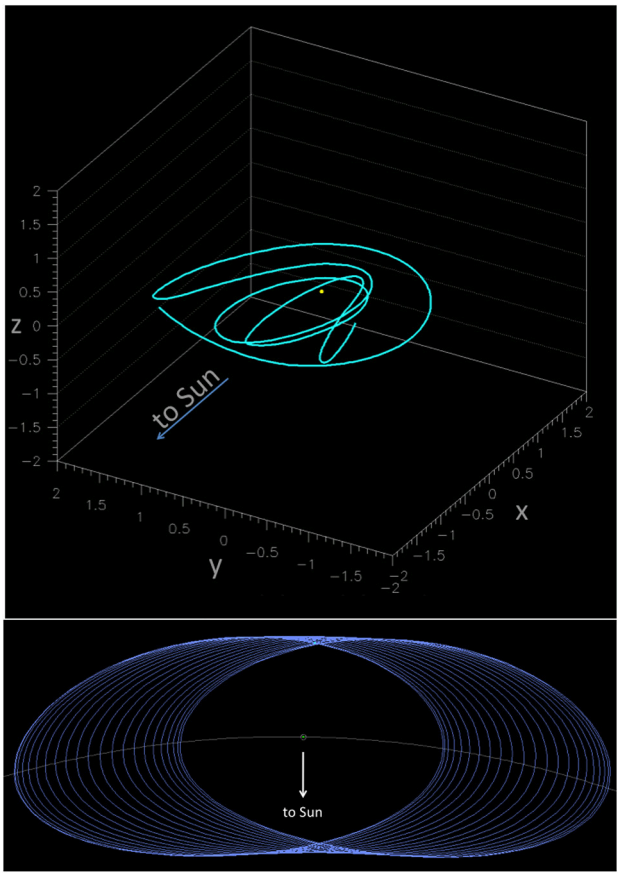

FIGURE 1 | Minimoons (temporarily captured objects, TCOs) are gravitationally bound to the Earth-Moon system while quasi-satellites (section 4) are not. **(Top)** Trajectory of the minimoon 2006 RH_{120} during its capture in the Earth-Moon system in 2006–2007. The Earth is represented by the yellow dot located at the origin of the J2000.0 mean equator and equinox reference system. **(Bottom)** Trajectory of Earth's quasi-satellite 2016 HO_3 shown in blue as projected onto the heliocentric ecliptic $x - y$ plane in the synodic frame. Earth is represented by the green dot in the center and the Moon's orbit is represented by the small white circle. Earth's orbit is shown as as the white arc from left to right and the direction to the Sun is to the bottom [credit: Paul Chodas (NASA/JPL); Chodas, 2016].

[1] A fictional secret agent played by the Canadian comedian Mike Myers.

[2] MPEC 2008-D12; https://www.minorplanetcenter.net/mpec/K08/K08D12.html

[3] https://echo.jpl.nasa.gov/asteroids/6R10DB9/6R10DB9_planning.html

(Kwiatkowski et al., 2009). Later radar observations established that it is a few meters in diameter (Benner et al., 2015). 2006 RH_{120} remained bound in the Earth-Moon system for about a year during which it made about four revolutions around the geocenter (**Figure 1**). Its pre-capture orbit had a semi-major axis of $(a, e, i) \sim (0.95\,\text{au}, 0.05, 0.6^\circ)$ so its aphelion was near Earth's orbit while its post-capture orbit has a perihelion close to 1 au with $(a, e, i) \sim (1.03\,\text{au}, 0.03, 0.6^\circ)$ (Granvik et al., 2012). We will show below that 2006 RH_{120}'s dynamical properties make it a poster child for minimoon behavior while asteroids close to its few-meter diameter should be captured with decadal frequency.

While 2006 RH_{120} is undoubtedly the first verified minimoon discovered while in its TCO phase there are other significant minimoon observations. The first was "The Extraordinary Meteoric Display" on 9 February 1913 that was observed from Saskatchewan to Bermuda (**Figure 2**) and was described and analyzed by Chant (1913a,b). Historical researchers have even identified sightings of the event off the coast of Brazil (Olson and Hutcheon, 2013)! The meteor display included dozens, and perhaps hundreds, of fragments that moved *slowly* across the sky in "perfect formation." They were not the typical shooting star that last for only a fraction of second—the entire procession lasted more than 3 min! Witnesses reported that the meteors caused a "rumbling noise" and houses to shake along the path. Chant's detailed analysis of eyewitness reports concluded that the object's speed with respect to Earth's surface was between 8 km s^{-1} and 16 km s^{-1} while Earth's escape speed or, equivalently, the speed at which an object with zero relative speed at infinity would strike Earth, is about 11.2 km s^{-1}. He thus concluded that the meteoroid "had been traveling through space, probably in an orbit about the Sun, and that on coming near the Earth they were promptly captured by it and caused to move about it as a satellite." A few years later Denning (1916) concluded that "the large meteors" that passed over Northern America in 1913 must have been temporary Earth satellites because they traveled 2,600 miles in the atmosphere suggesting that the orbits were "concentric, or nearly concentric, with the Earth's surface." Given that this event pre-dates the launch of any artificial objects it must have been a natural object and a minimoon by our definition.

Clark et al. (2016) suggest that a meteor observed on 2014 January 13 in the Czech Republic with an all-sky digital camera system that is part of the European Fireball Network has an $\sim$ 95% probability of having been on a geocentric orbit before impact. Complementary spectroscopic data prove that it must have been a natural object. Detailed modeling of the object's atmospheric deceleration and fragmentation suggest that its pre-entry mass must have been about 5 kg with a diameter of $\sim$ 15 cm. It entered Earth's atmosphere at just over 11.0 km s^{-1}, consistent with having a $v_\infty = 0$ with respect to Earth as expected for geocentric objects, and their backward dynamical integrations suggest that it was a minimoon for at least 48 days and perhaps for more than 5 years. Clark et al. (2016) concluded that the predicted rate of minimoon meteors was far higher than the observed rate based on this object but we have confirmed that their estimated rate did not account for the vastly different detection efficiency of minimoon meteors compared to heliocentric meteors. Meteor luminous efficiency, the fraction of a meteor's kinetic energy that is converted into visible light, is proportional to the 4th or 5th power of the impact speed so the apparent brightness of a meteor with a heliocentric origin $v \sim 20$ km s^{-1}; (Brown et al., 2013) will be 16× to 32× brighter than a minimoon meteor of the same initial mass.

3. MINIMOON DYNAMICS

Heppenheimer and Porco (1977) defined "capture" as "the process whereby a body undergoes transition from heliocentric orbit to a planetocentric orbit." Therefore, the three-body problem (3BP) is the natural framework to study the capture mechanisms for which the invariant manifolds of the orbits around the collinear Lagrange points are known to play a significant role. The capture definition entails that the body should remain gravitationally bound to the planet but, in a purely gravitational three-body scenario, captures can only be temporary (Huang and Innanen, 1983; Tanikawa, 1983).

The three-body problem has no general analytical solution and is often simplified to the case in which two massive bodies are in circular orbits revolving around their center of mass while the third body is massless and moving in their gravitational potential. In this circular restricted 3BP (CR3BP) the dynamical system has an integral of motion that yields an invariant parameter known as the Jacobi constant, C. It is related to the total energy of the particle in the synodic frame (the co-rotating frame with origin at the barycenter and the line between the two primary objects fixed) and its constancy imposes a dynamical constraint between the position and velocity of a particle.

For a given value of the Jacobi constant space is divided into *forbidden* and *allowable* regions (Hill regions) that are separated by "zero-velocity" surfaces (Szebehely, 1967). These surfaces are defined in the synodic frame where they are invariant and symmetrical with respect to the $x - y$ plane in the CR3BP. The surfaces' intersection with the $x - y$ plane yields the zero-velocity curves (**Figure 3**). C_1 and C_2 are the values of the Jacobi constant on the zero-velocity surface at the L_1 and L_2 libration points, respectively. For the Sun-Earth-asteroid system (but without loss of generality), when $C < C_1$ there are three disjointed Hill regions where the asteroid can reside: (1) in close proximity to Earth; (2) in the vicinity of the Sun; and (3) in the exterior domain that extends to infinity. None of these regions are connected, so an asteroid that resides in the Hill region surrounding Earth is gravitationally trapped and cannot escape into heliocentric orbit and vice versa. When $C = C_1$ the Hill regions around the Sun and Earth connect at L_1, and for $C_1 < C < C_2$ a pathway exists around L_1 that allows an asteroid to transition from heliocentric to geocentric orbit. Equivalently, when $C > C_2$ another gateway opens at L_2, connecting the exterior Hill region and enabling distant asteroids to transition to geocentric orbit. Hence, in the CR3BP framework it is impossible to effect a *permanent* capture because when the Jacobi constant is such that transfers from heliocentric to geocentric orbits are allowed there is no way to prevent the asteroid from returning into heliocentric orbit. The capture and escape trajectories are both governed by manifold dynamics, so once asteroids reach the vicinity of L_1 or L_2 the

FIGURE 2 | On 9 February 1913 "The [Toronto] Globe [newspaper] office was flooded with reports of 'a meteoric performance of stupendous dimensions"' (Semeniuk, 2013). Toronto artist Gustav Hahn witnessed the minimoon fireball procession of 1913 and later painted it [University of Toronto Archives (A2008-0023) Copyright Natalie McMinn]. The first meteor photograph was obtained in 1885 (Weber, 2005) but eyewitness accounts and paintings were acceptable forms of observational evidence in the early twentieth century.

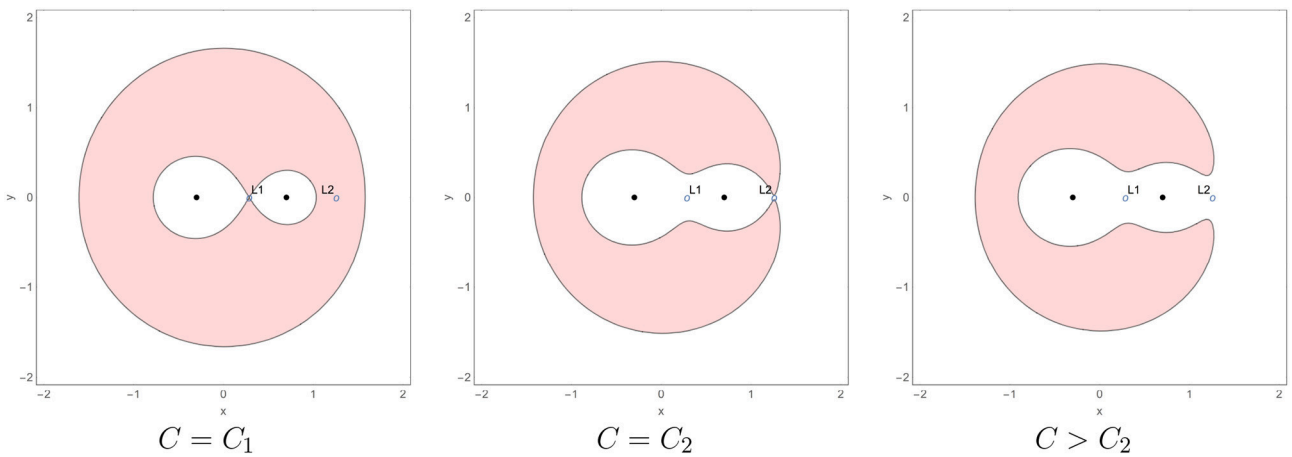

FIGURE 3 | Schematic view of the zero-velocity curves in the synodic frame for three different values of the Jacobi constant. The red shading illustrates regions where it is impossible for an object with the given value of the Jacobi constant to be located. The positions of the primary bodies are indicated by the filled black circles on the $y = 0$ line while L_1 and L_2 are labeled and illustrated as unfilled circles.

invariant manifolds of libration orbits are able to attract and pull them into the region around the planet following a stable manifold where they remain temporarily captured until they escape following an unstable manifold (Carusi and Valsecchi, 1981; Koon et al., 2001). Note, however, that the duration of the temporary capture can be arbitrarily long.

The eccentricity of the Earth's orbit can be accounted for within the framework of the elliptic restricted three-body

problem (ER3BP). An immediate consequence is that the Jacobi constant ceases to be an invariant quantity of the system (i.e., it is no longer constant) and Hill regions, as well as zero-velocity surfaces, are not invariant either; instead, they become periodic, time-dependent functions. As the Earth revolves around the Sun, the instantaneous Jacobi constant modulates and the Lagrange points shift inwards and outwards. Accordingly, at every value of Earth's true anomaly a different set of *pulsating* zero-velocity surfaces exist with shapes and dimensions that vary in time. Hence, it might happen that the capture paths through L_1 and L_2 always remain closed or open, or open and close periodically every orbital revolution, depending on the geometrical layout and instantaneous value of the Jacobi constant. As a consequence, the eccentricity of planetary orbits is insufficient to provide a feasible capture mechanism on its own. Even if Earth's orbital eccentricity might enable the transition into geocentric orbit of asteroids that could not otherwise have transitioned within the CR3BP (Makó and Szenkovits, 2004), there is no instrument to prevent them from returning into the heliocentric domain; the very same pathways will periodically reopen, thus enabling the asteroid's eventual escape. Therefore, in the gravitational three-body problem no dynamical mechanism exists that enables permanent capture. Doing so requires dissipative mechanisms that produce an irreversible change in the value of the Jacobi constant so that an asteroid may enter geocentric orbit through an open gateway which later closes before the asteroid can escape. Such dissipative mechanisms can only appear through the action of non-gravitational forces (e.g., Pollack et al., 1979; Astakhov et al., 2003), or the introduction of other perturbing bodies (e.g., other Solar System bodies, Nesvorný et al., 2007).

The Earth's case is more complex due to the subtle dynamical implications of the Moon so that a reliable study of the temporary capture of Earth's minimoons needs to be addressed within the framework of the Sun-Earth-Moon-Asteroid four-body problem.

Despite the evidence of the "Chant Procession," the minimoon 2006 RH_{120}, and the well known properties of temporary captures of comets and asteroids by the Jovian planets (e.g., Carusi and Valsecchi, 1981; Vieira-Neto and Winter, 2001; Ohtsuka et al., 2008), the first estimate of the number and properties of the EMS's steady-state minimoon population was performed by Granvik et al. (2012). They generated a synthetic population of NEOs that are the minimoon "source" population—the set of objects that may be captured in the EMS—according to what was at that time the best estimate of the NEO orbit distribution (Bottke et al., 2002), and then used an N-body integrator to simulate their dynamical evolution and determine the fraction that would be captured in the EMS. They included the gravitational effects of the Sun, Moon, Earth, and the seven other planets and found that about 0.00001% of all NEOs are captured as minimoons (TCOs) per year (i.e., 10^{-7} of the NEO population per year). This may seem like an insignificant fraction but there are estimated to be on the order of 10^9 NEOs larger than 1 m diameter (e.g., Brown et al., 2013; Schunová-Lilly et al., 2017), implying that a population of small minimoons is possible. In their careful accounting of the capture probabilities Granvik et al. (2012) calculated that there are likely one or two minimoons $\gtrsim$ 1 m diameter in the EMS at any time and that there should also be a $\sim 10\times$ larger population of temporarily captured flybys (TCF). The average minimoon spends about 9 months in our system during which it makes almost 3 revolutions around Earth.

Fedorets et al. (2017) improved upon the earlier work of Granvik et al. (2012) in a number of ways, notably by using an improved NEO model (Granvik et al., 2016) and a more careful accounting of the NEO orbital element distribution as $e \rightarrow 0$ and $i \rightarrow 0^\circ$. The improved NEO model has a higher resolution in the orbital element distribution that was enabled by the use of much higher statistics and smaller time steps in the underlying dynamical integrations, and a significantly more careful analysis of the orbital element distribution of the main belt NEO "sources" (the main belt is the source of the NEOs just as the NEOs are, in turn, the minimoon source population). Even with the higher resolution in the NEO orbital element distribution they found that it is still important to implement a more sophisticated treatment of the distribution of orbital elements *within* the bins at the smallest inclinations and eccentricities; i.e., the Granvik et al. (2016) NEO model specifies the number of objects in the bins that contain $e = 0$ and $i = 0^\circ$ but phase-space arguments suggest that the number distributions near zero should go as $n(e) \propto e^3$ and $n(i) \propto i^3$ (Harris et al., 2016). Since Earth-like minimoon pre-capture orbits are highly favored (**Figure 4**) their improved treatment of the distribution caused a reduction of about $2\times$ in the predicted steady-state TCO population. The reduction in the predicted TCO population was somewhat offset by a similarly more careful treatment of the TCF population. Some of these objects may be bound to Earth for $>$ 200 d, they are more abundant than TCOs because of the reduced criteria for number of revolutions around Earth, and they have a slightly higher rate of impacting Earth during their capture. Summarizing all their improvements, they found that the temporary natural satellite population (TCO+TCF) is smaller by $\sim$ 10% compared to Granvik et al. (2012)'s estimate.

Urrutxua and Bombardelli (2017) subsequently refined the TCO and TCF definitions originally proposed by Granvik et al. (2012). They suggested that since temporary captures around Earth are best studied in a Sun-Earth synodic frame the number of revolutions should be counted by recording the angle swept by the ecliptic projection of the geocentric trajectory in the synodic frame. Accordingly, temporarily captured objects can be classified as TCOs when they complete at least one full revolution around Earth or as TCFs if they fail to complete a full revolution under this definition.

If TCOs followed circular orbits around Earth then there would be a linear correlation between capture duration and revolutions with a different slope for each geocentric distance (**Figure 6**). The spread in the capture duration is thus linked to each TCO's average geocentric distance. Although Granvik et al. (2012)'s minimoon sub-classification criteria is conceptually sound, unanticipated complications arise in practice. For instance, the synthetic minimoon in the left panel of **Figure 5** completes several "loops" during a temporary capture spanning 11 months though it only counts 0.93 revolutions about Earth and would be classified as a TCF according to Granvik et al. (2012)'s definition. Similarly, the synthetic minimoon in the right panel of **Figure 5** is bound within the EMS for barely a

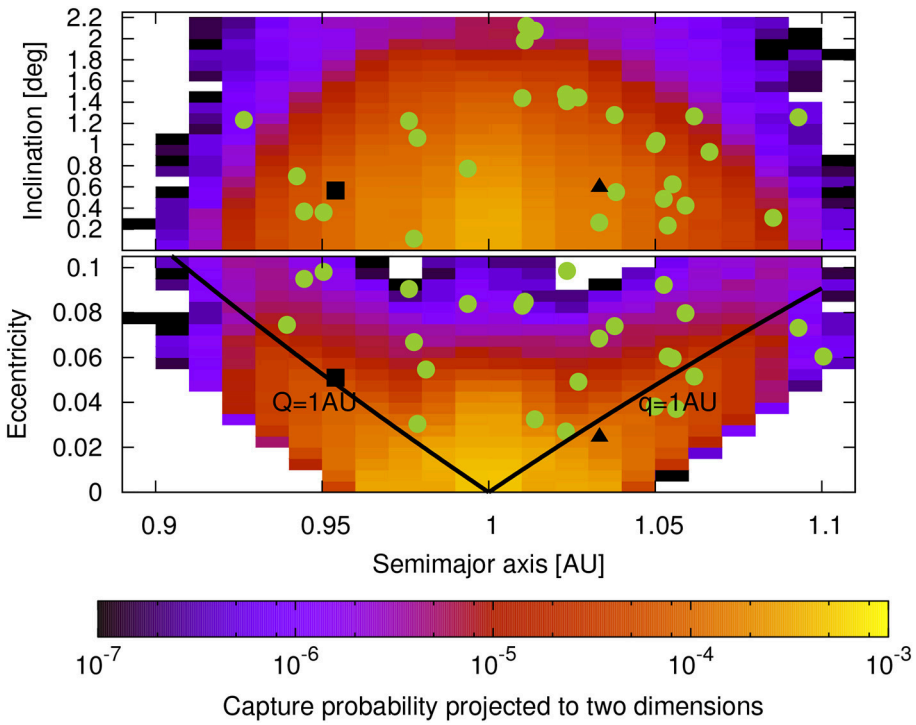

FIGURE 4 | Combined TCO and TCF capture probability in heliocentric orbital element (a,e,i) space (adapted from Fedorets et al., 2017). Green circles represent orbital elements of known NEOs as of 4 November 2014. Solid black lines correspond to $q = 1au$ and $Q = 1au$, perihelion and aphelion at Earth's orbit respectively. The black square represents the orbital elements of 2006 RH_{120} at capture and the black triangle represents its current orbital elements.

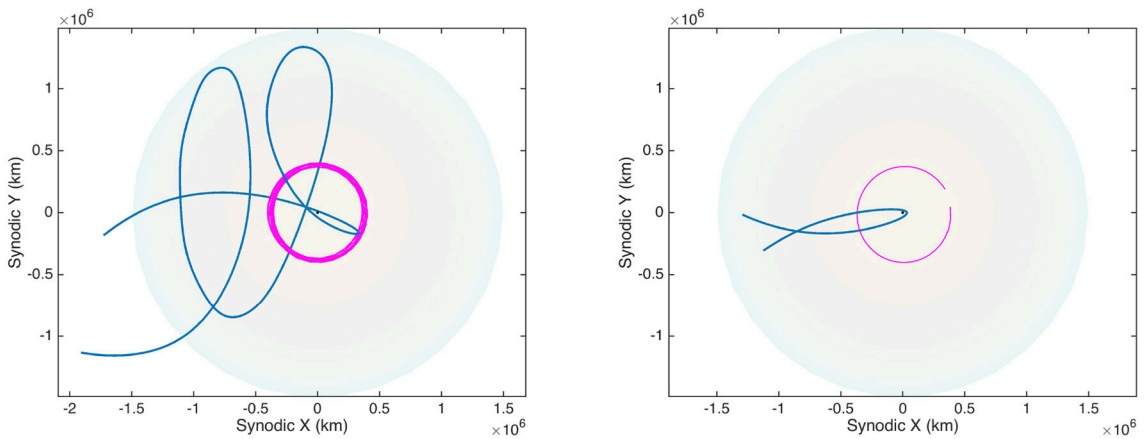

FIGURE 5 | Adapted from Urrutxua and Bombardelli (2017). **(Left)** Geocentric synodic trajectory of a TCF that becomes a TCO under the new definition of Urrutxua and Bombardelli (2017). **(Right)** A TCF that is misclassified as a TCO under the classical definition. The shaded area is the Hill sphere and the magenta curves depict the Moon's trajectory.

month while describing a short arc around Earth, yet the ecliptic projection of the trajectory happens to make more than one revolution so the object would be considered a TCO by Granvik et al. (2012). These examples are contrary to common sense that would suggest that the TCF would be better classified as a TCO, while the TCO should be a TCF, i.e., they appear to be misclassified. Examples of misclassified synthetic temporary captures are common, which indicated that the minimoon categorization algorithm required revision.

To address these issues Urrutxua and Bombardelli (2017) proposed the simple yet effective idea of counting the revolutions based on the intrinsic curvature of the synodic trajectory which is better suited to the three-dimensional non-elliptical nature of a minimoon's trajectory. It also decouples the definition from

a geocentric reference and tracks the actual trajectory and the traversed arclength so it is more tightly linked to the dynamics and yields a stronger correlation between the capture duration and the number of completed revolutions (**Figure 6**). The revised definition correctly reclassifies short-lived TCOs as TCFs, and long-lived TCOs with a previously small revolution count now have an appropriately higher number of revolutions. Thus, the "banding" in **Figure 6** (left) is caused by TCOs whose synodic trajectories projected on the ecliptic describe loops that do not sum to the revolutions count under the classical definition (e.g., left panel in **Figure 5**).

Urrutxua and Bombardelli (2017) also propose a classification scheme for TCO sub-types (**Figure 6**). Type I TCOs cross the Hill sphere and are separated into retrograde and prograde orbits which reveals that, for an equal number of revolutions, prograde TCOs typically have shorter capture durations than retrograde ones i.e., the average geocentric distance during capture tends to be smaller for prograde TCOs. Type II TCOs remain outside the Hill sphere and are long duration captures at any revolution count.

As described above, TCOs and TCFs are typically "captured" (**Figure 7**), i.e., the moment their geocentric orbital energy becomes negative (Equation 1), when they are near the Earth-Sun L_1 or L_2 points (Granvik et al., 2012). Their geocentric inclinations favor retrograde orbits in a 2:1 ratio, typical of irregular satellites and, perhaps surprisingly, the Moon has little to do with the capture process. Granvik et al. (2012) established that the Moon is not important by running integrations with and without the Moon (but incorporating the Moon's mass into Earth) and found essentially identical capture rates from the NEO population. The only significant difference was their finding that the Moon is a harsh mistress—it causes TCO and TCF orbits to evolve to Earth-impacting trajectories while none of them impacted Earth without the Moon's influence. There is no dynamical mechanism to shield Earth from minimoon impacts without the Moon but $\sim$ 1% of minimoons strike Earth with the Moon in the simulation while $\lesssim$ 0.02% of minimoons strike Earth without the Moon at the 90% confidence level.

Minimoon captures may begin over a wide range of geocentric distances (**Figure 7**) and, as noted above, TCOs may or may not cross the Hill sphere at all during their temporary capture. There is a strong symmetry in the incoming TCO distribution at the time of capture far from the Hill sphere but by the time they cross it the symmetry is lost and they are evenly distributed over the Hill sphere's surface. This suggests that the Hill sphere is not an appropriate reference surface for the study of temporary captures (Urrutxua and Bombardelli, 2017).

Granvik et al. (2012)'s prediction that some minimoons can strike Earth provides a means of testing the minimoon theory because they calculated that about 0.1% of all Earth impactors are TCOs. TCO meteors have a distinctive signature in that their atmospheric impact speed is $\sim 11.18 \pm 0.02\, km\, s^{-1}$—essentially Earth's escape velocity or, equivalently, the speed at which an object would strike Earth if it started at infinity with zero speed with respect to Earth. Heliocentric meteors have $v_\infty > 0$ and therefore must impact with speeds >11.19 km s^{-1}. They have an average impact speed of $\sim$20 km s^{-1} (e.g., Taylor, 1995; Hunt et al., 2004) but can range in speed anywhere from 11.19 km s^{-1} to 72 km s^{-1}. The problem is that meteor luminous efficiency (and the radar echo as well) is a very steep function of the impact speed, so detecting a slow-moving meteor requires that the object be particularly large to be detected. Thus, Clark et al. (2016)'s detection of a meteor with an origin on a geocentric orbit confirms Granvik et al. (2012)'s prediction that such objects exist but can not be used to test the minimoon population's size-frequency distribution without a detailed understanding of the detection biases.

Conversely, Hills and Goda (1997) calculated the probability that an Earth-atmosphere-grazing meteoroid could be captured into a geocentric orbit due to the loss of kinetic energy during its atmospheric passage. They suggested that the cross section for orbital capture is about 1/1,000th that of objects striking Earth which implies that the time scale for atmospheric capture of a 1 m diameter object is a few decades—much longer than the capture time scale calculated by Granvik et al. (2012) and Fedorets et al. (2017). Furthermore, objects that are captured by atmospheric drag must dive back into the atmosphere on every subsequent orbit, thereby rapidly dissipating kinetic energy until they fall to Earth as slow meteors. Given their infrequent capture and short residence times we expect that this mechanism can not be a major minimoon source.

A sub-set of the minimoon population is the particularly long-lived orbits associated with the Earth-Moon L_4 and L_5 Trojan regions (e.g., Marzari and Scholl, 2013; Hou et al., 2015). These objects are deep within Earth's Hill sphere and can have lifetimes even up to a million years (Hou et al., 2015) if they have small inclinations and eccentricities, and decameter-scale objects would even be stable under the influence of the Yarkovsky effect (Marzari and Scholl, 2013). The problem is that even though minimoons in the E-M Trojan population have very long dynamical lifetimes they are not long compared to the age of the solar system. Thus, any E-M Trojan minimoon population must be transient but capturing NEOs into this sub-population is even less likely than the less restrictive captures described by Granvik et al. (2012) and Fedorets et al. (2017). Furthermore, there has never been a discovery of an Earth-Moon Trojan in the decades of operations of modern NEO surveys or in targeted surveys (Valdes and Freitas, 1983). We were unable to identify any limits on the size of population in the existing literature even though the requirements to do so are modest by contemporary asteroid survey standards (Hou et al., 2015). One possible issue is that their typical apparent rate of motion would be about the same speed as the Moon's, $\sim$ 12 deg day^{-1}, which is quite fast and would cause trailing of the detected asteroids on the image plane during typical exposures. We expect that the LSST (Ivezic et al., 2008; Schwamb et al., 2018) will either detect the first E-M Trojans or set a tight upper limit on their size-frequency distribution.

A missing component from minimoon population modeling is an accurate incorporation of the Yarkovsky and YORP effects, thermal radiation forces and torques that cause small objects to undergo semimajor axis drift and spin vector modifications, respectively, as a function of their spin, orbit, and material properties (e.g., Bottke et al., 2006). These tiny thermal forces are

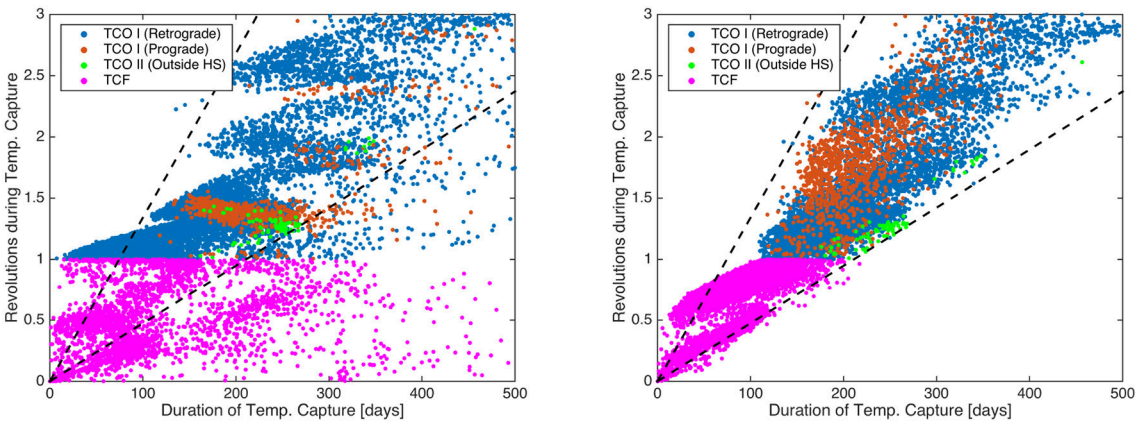

FIGURE 6 | Adapted from Urrutxua and Bombardelli (2017). **(Left)** TCO revolutions vs. capture duration for the definition and synthetic minimoon population of Granvik et al. (2012). **(Right)** The same population but using the definitions and method of revolution counting of Urrutxua and Bombardelli (2017). Type I TCOs, both retrograde (blue) and prograde (orange), enter Earth's Hill sphere. Type II TCOs (green) remain outside the Hill sphere during their entire capture phase. TCFs (magenta) make less than one revolution around Earth (but the method for counting revolutions is different in the two panels). Dashed lines correspond to circular orbits at geocentric distances of 0.5 and 1 Hill radii.

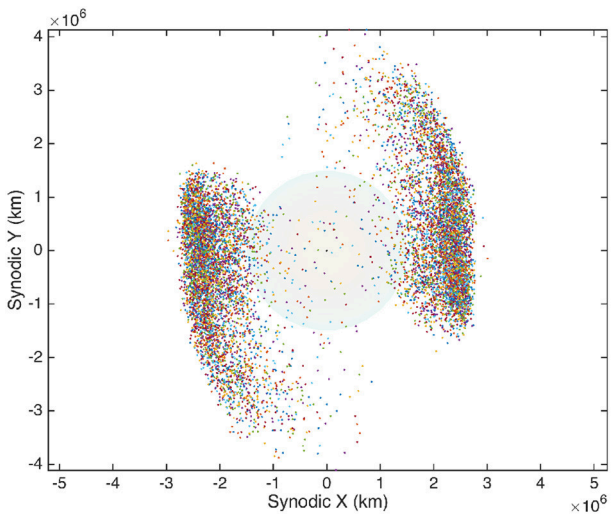

FIGURE 7 | Adapted from Urrutxua and Bombardelli (2017). TCO capture location in the synodic frame at the moment that their energy becomes negative with respect to the Earth-Moon barycenter. The Earth is located at the origin, the Sun is far off to the left, and the shaded gray circle represents Earth's Hill sphere. There is no significance to the colors of the dots.

partly responsible for allowing many of these bodies to escape the main asteroid belt in the first place. At present, it is unclear how the inclusion of Yarkovsky thermal drift forces into our models would modify the minimoon capture rate near Earth but we suspect it would not be by very much because the change in semimajor axis produced by the Yarkovsky effect is probably on the order of $0.001 - 0.01\,\mathrm{au\,Myr^{-1}}$, very small when one considers that their source NEO population is strongly affected by planetary close encounters. It is probable that for every proto-minimoon moved onto a trajectory where capture was possible via the Yarkovsky effect, another would be moved off such a trajectory. Ultimately, though, new models are needed to fully evaluate their importance.

The heliocentric orbits after capture remain "capturable" during subsequent Earth encounters (**Figure 4** and Granvik et al., 2012). This implies that artificial objects launched from Earth that escape the EMS to a heliocentric orbit can be captured during subsequent EMS encounters; e.g., a recently discovered object and candidate minimoon, 2018 AV_2, was initially predicted to have had an earlier capture in the late 1980s but follow-up astrometry later showed that a capture did not happen and that the object is likely artificial. (It is nearly impossible to distinguish between minimoons and artificial objects based only on their orbital elements and dynamics but section 5 describes how they can be differentiated using their response to radiative forces to measure their area-to-mass ratio.)

Finally, Earth is not the only world with minimoons. The most commonly known "minimoons" in the Solar System are associated with Jupiter whose Hill sphere is much larger than Earth's. Jupiter-family comets that evolve onto low-eccentricity, low-inclination heliocentric orbits similar to that of Jupiter can be captured in the Jupiter system via its L_1 or L_2 Lagrange points; i.e., they form in the exactly the same way as described above for Earth's minimoons. The most famous example was comet Shoemaker-Levy 9 that was likely captured around 1929 (Chodas and Yeomans, 1996) and orbited within Jupiter's Hill sphere until it passed within Jupiter's Roche limit. This deep encounter disrupted the comet and created the famous "string of pearls" that later returned to strike Jupiter in 1994. Other known comets have minimoon orbits with Jupiter (e.g., Comet 147P/Kushida-Muramatsu; Ohtsuka et al., 2008) but the steady state population has yet to be quantified with the latest dynamical models. Note that the orbits of Jupiter minimoons are different from Jupiter's irregular satellites, a population that exists on stable orbits with semimajor axes between 0.1 and 0.5 Jupiter Hill radii.

The irregular satellites were likely captured during a time of giant planet instability and migration that took place 4–4.5 Gyr ago (e.g., Nesvorný et al., 2007, 2014).

4. MINIMOON SOURCE POPULATION

The minimoon source population, the set of objects from which minimoons are drawn, are Earth's co-orbital asteroids (Morais and Morbidelli, 2002), objects that are in a 1:1 mean-motion resonance with Earth like 2010 TK_7 (Connors et al., 2011), or at least those objects very close to the 1:1 mean-motion resonance, (Granvik et al., 2012; de la Fuente Marcos and de la Fuente Marcos, 2013; Fedorets et al., 2017). Thus, understanding the dynamics and population of co-orbitals is important to our understanding of the minimoon population as well. The small population of known co-orbitals are all transient objects and therefore must not be primordial, having originated within the inner solar system, perhaps as impact ejecta from Venus, Earth, the Moon, or Mars, or, more likely, were delivered to the inner solar system from the main belt (e.g., Granvik et al., 2017).

An interesting sub-class of asteroids that are tangentially related to minimoons are "quasi-satellites" (e.g., Sidorenko et al., 2014; Chodas, 2016; de la Fuente Marcos and de la Fuente Marcos, 2016). Unlike geocentric minimoon orbits, quasi-satellites are heliocentric but their specific orbit elements while in the 1:1 mean-motion resonance cause them to appear to be in a distant retrograde orbit around Earth *from Earth's perspective* (**Figure 1**). This type of orbit can be dynamically stable because they never approach too close to any massive object and have been proposed for astrophysical and asteroid survey spacecraft missions because they provide inter-planetary-scale observations of Earth but at relatively constant geocentric distances (e.g., Cyr et al., 2000; Stramacchia et al., 2016; Perozzi et al., 2017).

Like minimoons, quasi-satellites are not just dynamical mathematical curiosities—several examples are known to exist including asteroids (164207), (277810), 2013 LX_{28}, 2014 OL_{339}, and 2016 HO_3 (Chodas, 2016; de la Fuente Marcos and de la Fuente Marcos, 2016). Both minimoons and quasi-satellites are drawn from the same NEO population and should have similar taxonomic distributions. However, the dynamical lifetimes of quasi-satellites can be orders of magnitude longer than for minimoons so it is to be expected that there should be more quasi-satellites and that the population should include larger bodies. The largest object that may be in the steady-state population at any time is directly related to the population lifetime; e.g., the largest minimoon in the steady-state population at any time is likely $\sim$ 1 m diameter. Thus, given their long lifetimes , it is not surprising that quasi-satellites like 2016 HO_3 exist with an absolute magnitude $H \sim 24.2$ corresponding to a diameter of $\sim$50 m.

There are less than half the expected number of NEOs with semi-major axes within half a Hill radius of Earth's orbit (**Figure 8**). We expect that this is an observational selection effect because NEOs in or near Earth's 1:1 mean-motion resonance have extremely long synodic periods (**Figure 8**). The closer the NEO is to the 1:1 mean-motion resonance the longer its synodic period, making it much more difficult to discover. Modern asteroid surveys have only been in operation for a couple decades so they have only an $\sim$ 2% chance of detecting an NEO with a 1,000 yr synodic period. Thus, the discovery of Earth's co-orbitals, and objects in the minimoon source population, simply requires a long period of time or more aggressive space-based observation platforms.

Finally, like minimoons, quasi-satellites are often touted as promising spacecraft mission targets because they are in not-too-deep space and always at relatively constant geocentric distances. They are larger and easier to find than minimoons but require higher Δv and longer communication times and, since they are on orbits essentially identical to the minimoons' NEO source population, they will have the same taxonomic distribution as minimoons.

5. MINIMOON CURRENT STATUS AND FUTURE PROSPECTS

The major problem with the minimoon hypothesis is the small number of known objects that have ever been minimoons (section 2). On the other hand, there have been numerous cases of objects that were TCOs or TCFs that later turned out to be artificial objects. It would seem that the tremendous success of the current generation of NEO surveys at finding different classes of objects throughout the solar system ranging from a nearby and fast interstellar object (e.g., Meech et al., 2017) to distant and slow scattered disk objects (e.g., Chen et al., 2016) should translate into more minimoon discoveries. To assist in identifying geocentric objects the JPL Scout system[4] (Farnocchia et al., 2016) includes a geocentric orbit "score" to indicate whether an object may be bound in the EMS and it has been successful at properly recognizing artificial geocentric objects, particularly those with large semi-major axis. So why haven't the surveys found more minimoons?

The explanation is simply that most minimoons are very difficult to detect. Fedorets et al. (2017) calculated that the largest object in the steady-state population is likely only about 80 cm in diameter and the most probable distance is about 4 lunar distances or 0.01 au (a function of the orbit distribution and because the objects spend much more time at apogee than perigee). At that distance a 1 m diameter ($H \sim 32.75$) object at opposition has an apparent magnitude of $V \sim 22.7$—one magnitude fainter than the Pan-STARRS1 limiting magnitude for detecting main belt asteroids in its most efficient wide-band filter (Denneau et al., 2013). Since minimoons will typically be moving much faster than main belt asteroids ($\sim 3\,\mathrm{deg\,day^{-1}}$ vs. $\sim 0.25\,\mathrm{deg\,day^{-1}}$) they will be more difficult to detect because their images will be trailed by more than the system's typical point-spread function. When minimoons are closer they are brighter but also moving much faster, conditions under which the matched-filter algorithm[5] applied to high-speed, low-noise cameras should excel (e.g., Gural et al., 2005; Shao et al., 2014;

[4] https://cneos.jpl.nasa.gov/scout/intro.html

[5] The matched filter algorithm is also known as the "shift-and-stack" algorithm or "synthetic tracking" or "digital tracking."

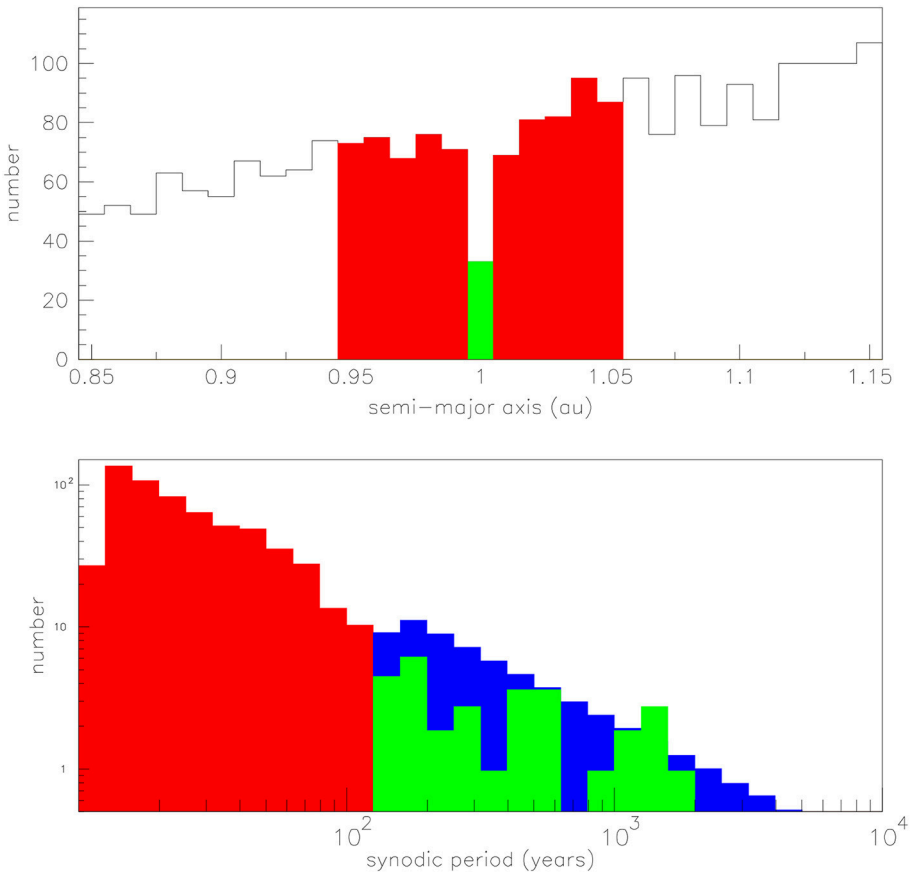

FIGURE 8 | (Top) The distribution of known NEO semi-major axes near 1*au* as of 2018 Feb 25 (from astorb: ftp://cdsarc.u-strasbg.fr/pub/cats/B/astorb/astorb.html). The green bins are for objects with semi-major axes very close to Earth's with $0.995au < a < 1.005$ au, in or close to the 1:1 mean-motion resonance. The red bins correspond to NEOs just outside that range with 0.945 au $< a <$ 0.995 au and 1.005 au $< a <$ 1.055 au. **(Bottom)** The distribution of synodic periods color coded to the same objects in the top panel. The blue histogram is the expected distribution of synodic periods if NEOs are distributed evenly in the range [0.995 au, 1.005 au] based on an extrapolation from the range [0.845 au, 1.155 au].

Heinze et al., 2015). The problem is that these cameras are still only available in small formats (i.e., small field-of-view). Thus, the discovery of the next minimoon with the current survey systems will likely be of the serendipitous capture of a few meter diameter object like 2006 RH_{120}, an event that occurs on the order of once a decade (Fedorets et al., 2017).

Even though minimoons and minimoon-like objects are difficult to detect the asteroid surveys do identify objects on a geocentric orbit. Most are quickly associated with known artificial satellites but there are currently a few dozen unidentified geocentric objects[6]. Rapid follow-up on these objects is typically problematic because they are faint and have high apparent rates of motion. As described above, these objects are usually dismissed as being artificial and this is probably true of almost all of them and especially so for the lower eccentricity, small revolution period objects. However, the most likely minimoon geocentric orbits (**Figure 9**) overlap some of the longer period unidentified objects with high eccentricity. Thus, while we agree that it is likely that most of the unidentified objects are artificial it should not be assumed that they are necessarily so.

Bolin et al. (2014) performed an extensive analysis of existing capabilities for detecting minimoons and came to the same conclusion—contemporary asteroid survey systems are only capable of serendipitous detections of the largest minimoons on decadal time scales. They also explored options for fortuitous minimoon discoveries with existing space-based surveys such as NEOWISE (e.g., Mainzer et al., 2011) and with all-sky meteor surveys such as CAMS (Jenniskens et al., 2011), CAMO (Weryk et al., 2013), and ASGARD (Brown et al., 2010) and, again, arrived at the conclusion that minimoon discoveries must be rare. They suggested that targeted observations with a two-station (bi-modal) radar system would have a high probability of detecting a $>$ 10 cm diameter minimoon in about 40 h of operation but they note that their estimates are optimistic and that the effort may not justify the expense. Their conclusion was that LSST could detect many minimoons and that a targeted multi-night survey with Hyper Suprime-Cam (HSC; Takada, 2010) on the Subaru telescope on Maunakea had a small chance of detecting

[6]https://www.projectpluto.com/pluto/mpecs/pseudo.htm

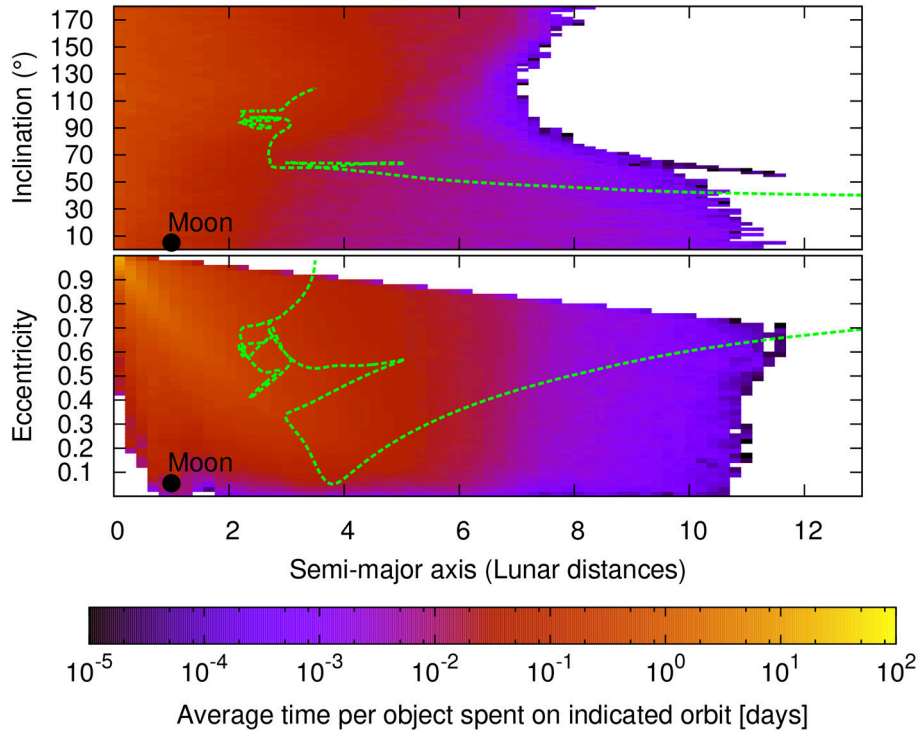

FIGURE 9 | Figure 10A from Fedorets et al. (2017). The residence time for synthetic minimoons as a function of their geocentric orbital elements. i.e., the amount of time that minimoons spend on orbits with a given (a, e, i) combination. The green dashed line is the trajectory of 2006 RH_{120} through this representation of the orbital element phase space.

a minimoon and would certainly be able to set a limit on the population statistics.

Jedicke et al. (2017) then obtained five nights of targeted minimoon surveying with HSC on Subaru under excellent conditions in an observing cadence specifically designed to identify geocentric objects over the course of a single night. They acquired about 5 images of the same near-opposition fields spaced roughly evenly over about 4–6 h in a field-of-regard of about 1,000 deg^2 (i.e., the total survey area). They predict that they have about a 10% chance of discovering a minimoon but the data analysis is still in progress. Even without discovering a minimoon the data will allow the calculation of the first controlled upper limit on the minimoon population.

The LSST's advantages for minimoon discovery include its 8.4 m diameter primary mirror that will achieve a limiting magnitude of $V \sim 24.5$ in 30 s exposures over a 9.6deg2 field-of-view. LSST is currently under construction on Cerro Pachón, Chile and is scheduled to commence operations in 2022 (e.g., Ivezic et al., 2008). Fedorets et al. (2015)'s simulated LSST survey was based on a current implementation of the expected survey pattern, weather, and performance characteristics to assess its performance for detecting minimoons. The Fedorets et al. (2017) synthetic population of TCOs and TCFs was run through the LSST survey simulator and the output was then passed through their moving object processing system (MOPS) to emulate their baseline 10-year's of operations. They found that LSST could discover many minimoons (**Figure 10**) and should efficiently and single-handedly discover[7] essentially *all* the larger members of the population (if they can link detections of the same minimoon acquired on different nights).

There remain at least a few difficulties with establishing the reality of new minimoons: (1) overcoming a prejudice against their existence, (2) obtaining evidence that they have a natural provenance, and (3) establishing that they are not "merely" lunar fragments ejected from the Moon's surface during an impact event.

The first issue will eventually be resolved when so many minimoons have been discovered that it is impossible to maintain a prejudice against them or when a serious flaw is discovered in the dynamical models that predict their existence.

Resolving the second issue is a key input to the first but establishing the natural provenance of a tiny, fast moving, transient object is difficult (see the discussion on 2018 AV_2 at the end of section 3). Apart from *in-situ* observations, the options for establishing a candidate as natural include obtaining spectra or colors, radar observations, or measuring its area-to-mass ratio (AMR) based on the magnitude of the effect of solar radiation pressure on its trajectory. Obtaining sufficiently high signal-to-noise ratio (SNR) spectra of small, faint, fast objects is

[7]We use the word "discover" here to mean that LSST can detect the same minimoon multiple times in a single night *and* in at least three nights to determine its orbit.

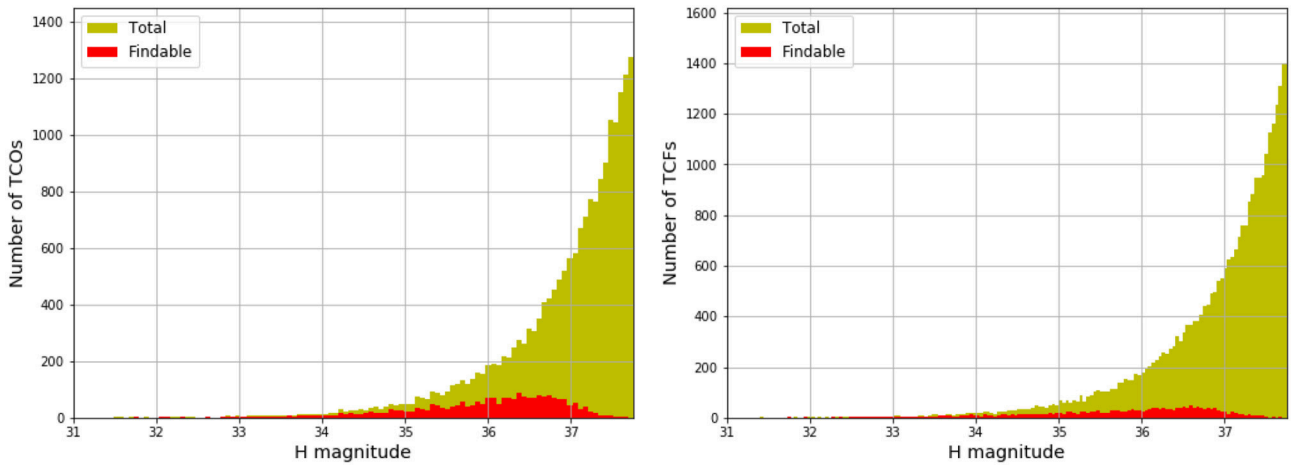

FIGURE 10 | Adapted from Fedorets et al. (2015). Estimated number of TCOs **(Left)** and TCFs **(Right)** in the minimoon population (yellow) and which could be discovered in 10 years of LSST operations (red) as a function of absolute magnitude (H). A 1 m diameter object has $H \sim 33$ and a 10 cm diameter minimoon has $H \sim 38$.

TABLE 1 | Area-to-Mass ratios (AMR) for select artificial satellites, the Moon, and small asteroids.

Object	Type	AMR ($\times 10^{-4} m^2 kg^{-1}$)	References
Lageos 1 & 2	Artificial	7	Beutler et al., 2006
Starlette	Artificial	10	Beutler et al., 2006
GPS (Block II)	Artificial	200	Beutler et al., 2006
2006 RH_{120}	Natural	11	ProjectPluto[8]
2009 BD	Natural	2.97 ± 0.33	Micheli et al., 2012
2011 MD	Natural	7.9 ± 7.4	Mommert et al., 2014
2012 LA	Natural	3.35 ± 0.28	Micheli et al., 2013
2012 TC_4	Natural	1.0 ± 0.4	JPL Small-Body Database[9]
2015 TC_{25}	Natural	$6 - 7$	Farnocchia et al., 2017
Moon	Natural	0.0000013	Beutler et al., 2006

notoriously difficult and even low resolution color photometry could require large telescopes and a disproportionate amount of observing time. Radar observations can quickly establish an object's nature as the radar albedo easily differentiates between a natural rocky surface and the highly reflective surface of an artificial object, but there are few radar observatories in the world and it is not always possible to obtain radar observations of tiny, nearby objects that have very short round-trip times to the candidate; i.e., minimoons are so close, and the reflected signal returns so fast, that they require bi-static observations in which one system transmits and the other receives. Thus, perhaps the most straightforward manner of identifying natural objects is the AMR. Artificial objects such as empty spacecraft booster stages or defunct satellites tend to have high AMRs while the few known small asteroids with measured AMRs are much smaller (**Table 1**). The typical minimoon candidate is so small that astrometric measurements over just a few month's time, comparable to the average minimoon's capture phase, have been sufficient to measure AMRs of similarly sized objects (**Table 1**).

Having established that a minimoon is natural there still remains a "concern" that it could be fragment of lunar ejecta launched into geocentric or heliocentric orbit by the impact of a large asteroid on the Moon's surface. We do not consider this issue to be of concern for many reasons.

First, the scientific and practical utility of a large piece of lunar ejecta is high; e.g., for developing *in-situ* resource utilization technology and techniques. A single 1 m diameter lunar minimoon would have a mass of over 1,000 kg (assuming 50% porosity and $5,000\,kg\,m^{-3}$) while the six Apollo missions returned a total of about 382 kg or lunar material[10] and the combined mass of all known lunar meteorites[11] is about 65 kg. While their is a tremendous scientific value associated with knowing the origin of the Apollo lunar samples it is also clear that lunar meteorites are important to our understanding of the Moon with 529 refereed journal papers listed on ADS[12] including the words "lunar" and "meteorite" in the title. We imagine that a verified lunar minimoon would have implications for the lunar cratering rate, impact ejecta models, dynamics in the EMS, measurement of Yarkovsky and YORP on small objects, etc. From an ISRU and human mission perspective it matters not whether a minimoon has a lunar or other origin as these objects provide small, low Δv, cis-lunar candidates for testing system operations.

Second, Granvik et al. (2016)'s dynamical simulations of orbital evolution of objects from the main belt into the NEO population show that there *are* dynamical pathways to the Earth-orbit-like heliocentric orbits necessary for capture in the EMS

[8]https://www.projectpluto.com/pluto/mpecs/6r1.htm
[9]https://ssd.jpl.nasa.gov/sbdb.cgi?sstr=2012tc4
[10]https://curator.jsc.nasa.gov/lunar/
[11]https://curator.jsc.nasa.gov/antmet/lmc/lunar_meteorites.cfm
[12]http://adsabs.harvard.edu/, The SAO/NASA Astrophysics Data System.

(i.e., orbits with $a \sim 1$ au, $e \sim 0$, and $i \sim 0°$). Using that model, Fedorets et al. (2017) calculated that in the steady state there should be 3.5 ± 1.4 NEOs with $H < 25$ on "capturable" orbits so there must be many more objects on those kinds of orbits at smaller sizes. We stress that the NEO model already accounts for dynamical scattering of the NEOs by the EMS and should be considered the best possible model of the minimoon source population that is currently available. (One possible issue is the impact of Yarkovsky on the evolution of the smallest NEOs as discussed earlier.)

Third, let's assume a large impact on the Moon took place, and that ejecta from this event delivered a large number of small objects from the Moon's surface to orbits within the Earth-Moon system. Dynamical models suggest many will quickly impact Earth, the Moon, or will escape to heliocentric space. For the latter, many may return at later times as impactors and potential minimoons. In this scenario, the impact capable of creating numerous meter-sized minimoons well after the event took place should also produce many lunar meteorites. Accordingly, we would predict that the petrology of many lunar meteorites should indicate they came from the same region while the cosmic ray exposure (CRE) ages of many lunar meteorites should have similar ages but neither prediction is supported by lunar meteorite studies. Warren (1994) studied the delivery of lunar meteorites and argued that their formation craters are likely to have been both small and scattered across the Moon. The CRE ages of lunar meteorites are consistent with this formation scenario as most of their ages are short (< 1 Myr) with only a small fraction between $2 - 10$ Myr (Eugster et al., 2006). There is little evidence for a group of lunar meteorites having similar ages. Note that the largest young impact crater on the Moon, the 22 km diameter Giordano Bruno crater, formed about 4 Myr ago yet there is no obvious indication that ejecta from this impact event is present in the lunar meteorite record. Accordingly, we are skeptical that lunar ejecta is a good source of present-day minimoons.

6. MINIMOON SCIENCE OPPORTUNITIES

Minimoons will provide interesting science opportunities as a consequence of their small sizes and their relatively long capture duration. Although similarly sized non-captured objects are much more numerous they are typically observable for a much shorter period of time during their Earth fly-by. No meter-scale objects have ever been recovered during a subsequent apparition and hence their observability is limited to the discovery apparition. The minimoons' longer observation window allows for more detailed follow-up observations. In addition, the orbital uncertainty for minimoons becomes negligible within a few days and therefore allows for detailed follow-up to be carried out earlier than for non-captured objects (**Figure 12** and Granvik et al., 2013).

The interior structure of meter-scale meteoroids is largely uncharted territory that could be tested with minimoons (it is arguable that the interior structure of asteroids of any size is largely unknown). There is essentially no data to constrain models that range from "sandcastles" held together by cohesive forces (Sánchez and Scheeres, 2014) to solid, monolithic structures. Measured rotation rates are inconclusive because even small internal cohesive forces allow for faster rotation rates than would otherwise be possible for a non-rigid body. An asteroid's density provides some information to constrain its interior characteristics because we can assume that most of the material is "rocky" so a measured density less than rock implies that the interior contain voids (e.g., Carry, 2012). Asteroid volumes are typically based on photometry and/or radar data while mass estimation requires that it gravitationally perturbs a less massive test body such as a spacecraft or another much smaller asteroid (e.g., Siltala and Granvik, 2017, and references therein). Neither of these techniques is suitable for measuring a minimoon's mass but a minimoon's AMR (described above) can provide useful constraints on mass and density (e.g., Micheli et al., 2012, 2013; Mommert et al., 2014). The AMR can provide a measure of an object's bulk density when combined with an estimate of its size and shape derived from lightcurve measurements. Minimoons, that spend months in Earth orbit, are particularly suited to AMR estimation since measuring the AMR requires that the object is small and tracked for a long period of time.

While remote minimoon measurements can be useful for answering some scientific questions we think it is clear that the most important science opportunities derive from *in-situ* minimoon measurements. A small spacecraft mission could determine the shape and structure of a meteoroid, its regolith properties, and obtain high-resolution surface images in many wavelengths that can be compared to remote measurements of much larger asteroids. Returning a minimoon to Earth will be difficult but minimoons could provide a tremendous amount of pristine asteroid material from many different asteroids. Remember that meter-scale meteoroids deliver meteorites but only the strongest material survives passage through Earth's atmosphere, and impact and weathering on Earth's surface. Minimoons provide an intact, pre-contact meteoroid in its entirety, with all the fragile components in their original context.

7. MINIMOON MISSION OPPORTUNITIES

After the discovery of 2006 RH_{120} and the realization that there is likely a steady-state population of similar objects, Earth's minimoons have entered the game as candidates for future space missions. They have been delivered for free to cis-lunar space by the solar system's gravitational dynamics and are now available in *our own backyard* under favorable energetic conditions which make them ideal targets. Given their small size, Earth proximity, and their accessibility to long-term capture orbits, minimoons could enable affordable robotic and crewed missions using existing technology, as well as retrieval of substantially larger amounts of material compared to traditional sample return missions. Also, scaled versions of hazardous asteroid mitigation techniques could be tested at a fraction of the cost of current proposals. For all these reasons, minimoons stand out as compelling candidates for asteroid retrieval missions.

From a technological and commercial perspective they provide an ideal opportunity for: (1) the development and testing of planetary defense technologies (e.g., deflecting an asteroid); (2) validating and improving close-proximity guidance, navigation, and control algorithms, (3) testing close-proximity

FIGURE 11 | Artist's illustration of asteroid ISRU showing astronauts at an asteroid as well as other mining and transportation vehicles operating in space (image credit: TransAstra Corporation & Anthony Longman).

procedures and protocols for safe operation of crewed missions around asteroids, and (4) establishing the feasibility of asteroid mining technologies for future commercial applications, all in an environment where the round-trip light-time delay is a few seconds. This short list illustrates that minimoons have far-reaching non-science implications for different stakeholders.

Many studies have suggested that a substantial amount of asteroidal resources can be accessed at an energy cost lower than that required to access resources from the Moon's surface (e.g., Sanchez and McInnes, 2011, 2013; Jedicke et al., 2018). Very simply, the lower the required Δv for a spacecraft to return from mining an asteroid, the lower the cost of the mission and, more importantly, the higher the profit. Known NEOs are accessible with much lower Δv than main belt asteroids (e.g., Elvis et al., 2011; García Yárnoz et al., 2013a; Taylor et al., 2018) and the population of yet-to-be-discovered small NEOs on Earth-like orbits offers the possibility of many more commercially profitable asteroid missions (Jedicke et al., 2018).

These ideas has been around for a while in the realm of speculative science and science-fiction literature and have recently started to gain popularity in the public and private aerospace community. The renewed interest has led to the development of new trajectory designs, and asteroid retrieval and mining concepts (e.g., **Figure 11**; Brophy and Muirhead, 2013; Strange et al., 2013; Graps et al., 2016; Jedicke et al., 2018). Some of these technologies involve the artificial deflection of an asteroid's trajectory to shepherd it into cis-lunar space; i.e., the creation of human-assisted natural minimoons (García Yárnoz et al., 2013b; Chen, 2016). In these scenarios, the selection of target asteroids is usually driven by minimizing a mission's Δv (cost). Naturally captured minimoons provide an excellent, easily-accessible testbed for developing those technologies (Granvik et al., 2013).

Baoyin et al. (2010) proposed capturing asteroids passing close to Earth by providing them with the necessary Δv so that zero-velocity surfaces would close within the framework of the CR3BP (i.e., creating minimoons) and their best (known) target asteroid, 2009 BD, only requires a $\Delta v \sim 410$ m s^{-1}. Hasnain et al. (2012) then studied the total Δv required to transport an asteroid into Earth's sphere of influence including capture, concluding that a $\Delta v = 700$ m s^{-1} for 2007 CB_{27} was the best opportunity for a known asteroid. A lunar flyby can be used to provide some of the required Δv for capture in the EMS as shown by Gong and Li (2015) who obtained a long duration capture with a $\Delta v = 49$ m s^{-1} for asteroid 2008 UA_{202}. It is important to note that all these studies were limited to *known* objects—the number of objects increases dramatically at smaller sizes for which the known population is only a small fraction of the total population. Thus, in the future, there will undoubtedly be many more objects available at even lower Δv, especially if space-based missions are designed specifically to identify these targets.

In a search for novel minimoon capture-enhancement strategies, NASA developed an innovative mission concept to deliver asteroid 2008 HU_4 into a stable "distant retrograde orbit" (DRO) around the Moon (i.e., a minimoon on a geocentric orbit such that it becomes a quasi-satellite of the Moon in the EMS), with an estimated $\Delta v \sim 170$ m s^{-1} (Brophy et al., 2012). DROs are stable solutions of the three-body problem that can be used whenever an object is required to remain in the neighborhood of a celestial body without being gravitationally bound (e.g., Perozzi et al., 2017).

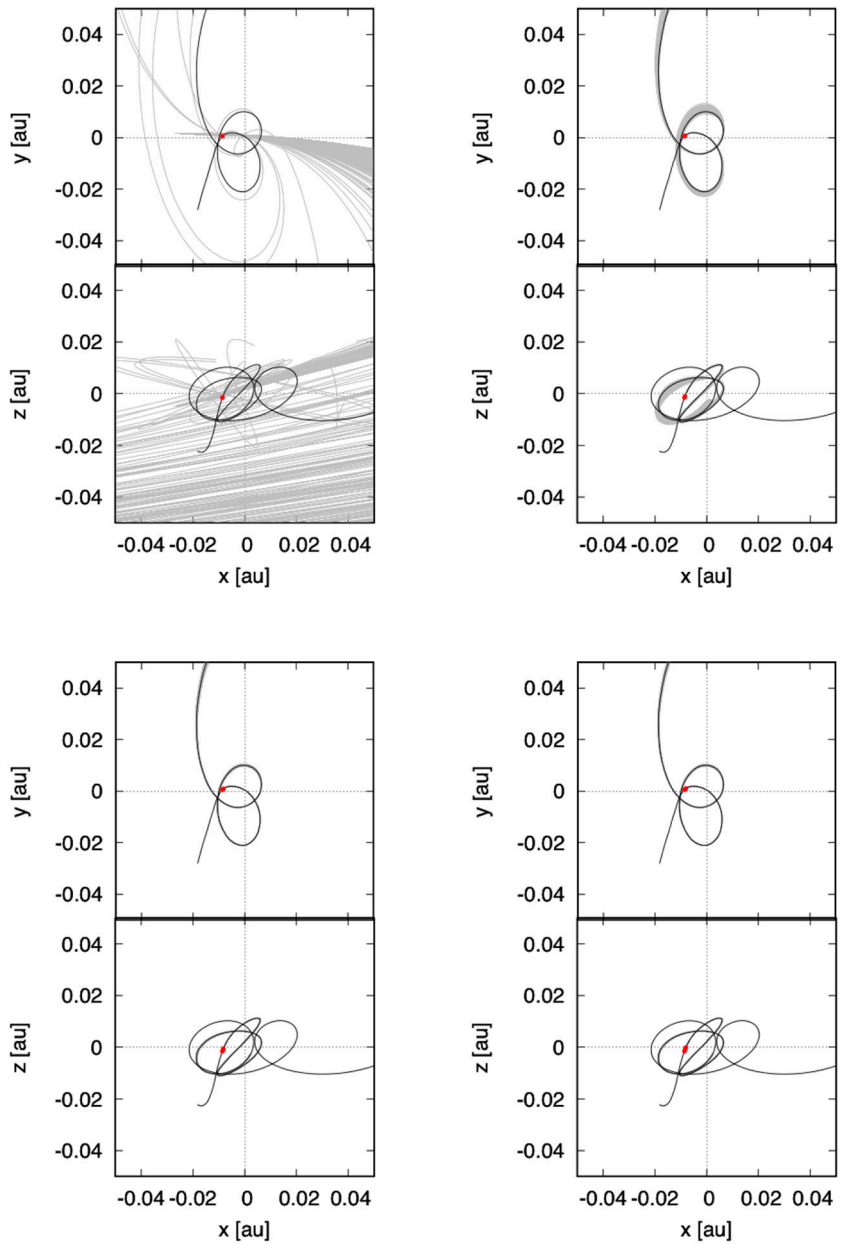

FIGURE 12 | Adapted from Granvik et al. (2013). The evolution of the orbital uncertainty for a synthetic minimoon as a function of increasing observational timespan and number of observations; **(Top left)** 3 detections in 1 h, **(Top right)** 6 detections in 25 h, **(Bottom left)** 9 detections in 49 h, and **(Bottom right)** 12 detections in 73 h. The black line shows the true orbit in the *XY* and *XZ* planes in an ecliptic coordinate system that is co-rotating with the Sun so that the Earth is always in the center (0, 0, 0) and the Sun is always at about (1, 0, 0). The gray shaded area shows the extent of all acceptable orbits and the red dots mark the locations of the synthetic minimoon at the observation dates. All orbits were extended 500 days into the future starting from the date of the first observation.

Another interesting strategy was proposed by García Yárnoz et al. (2013a), who utilized the CR3BP invariant manifold dynamics to identify low energy asteroid retrieval transfers. In particular, they coined the term "Easily Retrievable Objects" to refer to the subclass of NEOs that can be gravitationally captured in bound periodic orbits around the Earth-Sun L_1 and L_2 points. Interestingly, the lowest Δv object was 2006 RH_{120}, the first minimoon, that is now on a heliocentric orbit, at an astounding ~ 50 m s^{-1}.

The utility of minimoons as spacecraft targets may be limited by the length of time they remain captured (average capture durations of about 9 months; Granvik et al., 2012; Fedorets et al., 2017) but there are at least two ways to overcome this limitation: (1) artificially extend the capture duration or (2) have rendezvous spacecraft emplaced and "hibernating" in a high geocentric orbit for serendipitous missions of opportunity once a desirable minimoon is discovered. Normal spacecraft-asteroid rendezvous mission time frames for proposal, development, launch, and

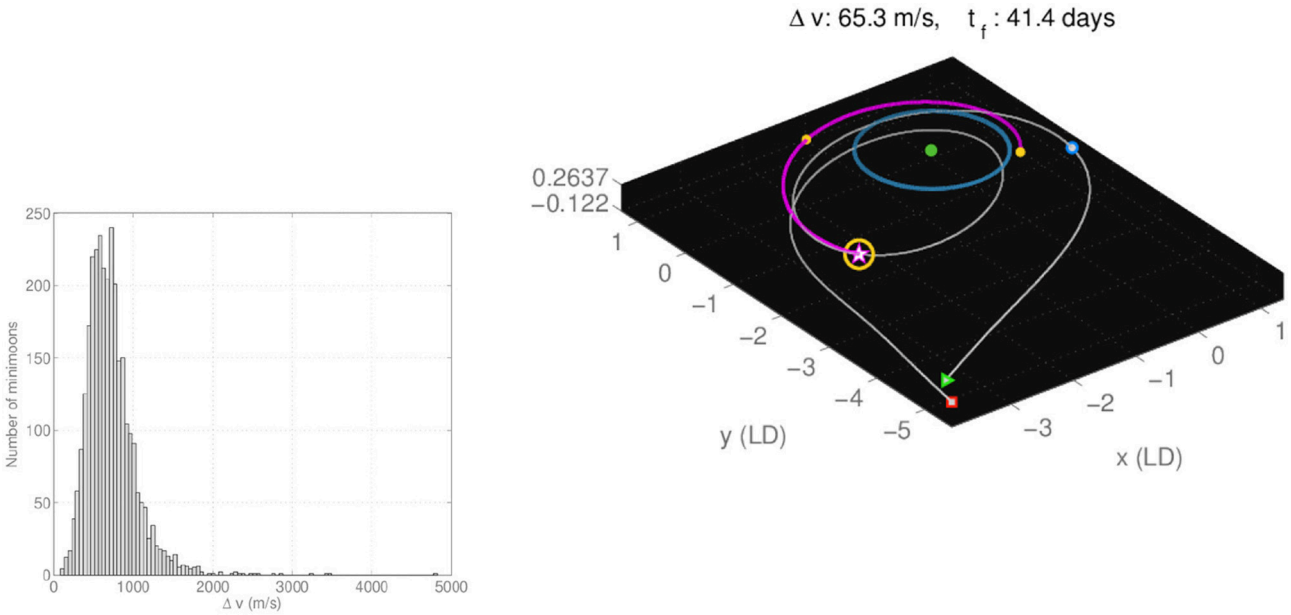

FIGURE 13 | Adapted from Brelsford et al. (2016). **(Left)** Δv distribution to 3,000 synthetic TCOs (Granvik et al., 2012) from an Earth-Moon L_2 halo orbit. **(Right)** The lowest Δv transfer from the distribution at left at 88 m s^{-1}. The Moon's orbit is shown as the blue ellipse around the green Earth. The thin gray path is the orbit of the TCO starting from its capture point (green triangle) to its escape point (red square). The blue circle on the TCO orbit marks where the TCO is when the spacecraft departs from its halo orbit, and the yellow star represents the rendezvous location. The magenta path is the spacecraft's trajectory and its three burn maneuvers are marked as yellow dots (including the final rendezvous burn).

operations are much longer than typical minimoon lifetimes and have not been considered to-date in the literature.

With the first vision in mind, Urrutxua et al. (2015) found that artificially extending a minimoon's capture duration could be accomplished in many cases at strikingly low Δvs. They found that a $\Delta v \sim 44$ m s^{-1} (with slow deflection techniques) during 2006 RH_{120}'s minimoon phase in 2006–2007 could have extended its capture duration to over 5.5 years from its nominal 9 month's time in cis-lunar space. In the unlikely scenario that the artificial deflection can begin *before* the temporary capture phase the authors concluded that by starting $\sim$ 316 d before perigee a total $\Delta v \sim 32$ m s^{-1} would have sufficed to extend the capture for an additional 5 years. It might be argued that 2006 RH_{120} was an unusual minimoon, so the authors extended their study to nine randomly selected virtual minimoons provided by Granvik et al. (2012) and found that some of their captures could be extended for decades at Δvs of just 9 m s^{-1}. They also suggested that temporary captures could be artificially induced for asteroids that would otherwise not be captured at all and in-so-doing produce captures that last for decades with a small to moderate early deflection. Of course, the challenge resides in identifying candidate asteroids with sufficient time to enable an asteroid retrieval mission to be planned and dispatched in a timely manner.

Several other studies suggest that capturing NEOs as minimoons is possible with small Δv. Tan et al. (2017) investigated opportunities using momentum exchange between an asteroid pair to capture one of the asteroids as the pair is directed close to one of the Sun–Earth L_1 or L_2 points. They proposed the ambitious concept of first creating the asteroid pair by engineering a capture or impact during the fly-by of a small asteroid by a large one. While their work shows that the process is possible, they note there remain "significant practical challenges." The same three authors also examined less complicated "direct capture" mechanisms whereby the orbit of a heliocentric NEO is modified with a small Δv to induce capture in the EMS (Tan et al., 2017). This scenario is essentially enhancing the natural minimoon capture process to capture specific NEOs onto long-lived geocentric orbits. Similarly, Bao et al. (2015) studied the use of lunar and Earth gravity assists (LGA and EGA) in maneuvering NEOs into becoming minimoons. They found that NEOs moving at <1.8 km s^{-1} with respect to Earth within Earth's Hill sphere could be captured using LGA and even higher speed objects could be captured using combinations of LGAs and EGAs. The known NEO with the smallest capture $\Delta v \sim 76$ km s^{-1} is 2000 SG_{344} but there are many, many more unknown NEOs that could be captured using these techniques.

The second technique to overcome the limitation of the short-duration minimoon captures is to maintain a spacecraft in a "hibernating" orbit awaiting the arrival and discovery of a suitably interesting minimoon. This idea may seem untenable at this time but will become practical once LSST begins discovering many minimoons per month (section 5). Unlike distant asteroids, minimoon orbits can be rapidly and accurately determined (**Figure 12**) to enable this opportunity and could even allow for multiple minimoon missions with the same spacecraft.

With this technique in mind, minimoon rendezvous missions have been studied using indirect (minimization) methods within the circular restricted four-body problem (CR4BP; Sun, Earth, Moon, spacecraft) with the Sun acting as a perturbation on the Earth-Moon-spacecraft CR3BP (Brelsford et al., 2016). Using a random sample of 3,000 TCOs from Granvik et al. (2012) they showed that rendezvous trajectories could be designed for all of them with a median Δv just under 680 m s^{-1} (**Figure 13**) with most of the transfer durations, the time from EM L_2 departure to minimoon rendezvous, requiring less than 3 months. The mean $\Delta v = 725$ m s^{-1} is about 7% higher than the median due to a tail of high Δv transfers but the minimum Δv is only 88 m s^{-1} with a transfer time of 41 d (**Figure 13**). Even more intriguing, in a future where the LSST is discovering all the large minimoon captures on a regular basis, we can envision multiple successive minimoon rendezvous missions with transfers directly between the minimoons. As a first step to modeling this possibility Brelsford et al. (2016) examined round trip mission opportunities for TCO 2006 RH_{120} because, in a worst case scenario, multiple minimoon missions could simply be back-to-back missions from the EM L_2 hibernating halo orbit (they assumed a z-excursion of 5,000 km in the halo orbit). The round trip is composed of a transfer to bring the spacecraft to 2006 RH_{120}, followed by a rendezvous phase where the spacecraft travels with the asteroid, and finally a return transfer back to the hibernating orbit. The lowest round-trip Δv required only 901 m s^{-1} with a total duration of 630 d (173 d for the approach and 240 d for the return) including 217 d at the asteroid.

8. CONCLUSIONS

Earth's minimoons will provide an opportunity for low-Δv scientific exploration and commercial exploitation of small asteroids where most of the effort of bringing the objects to Earth has been accomplished by their slow dynamical evolution from the main belt. While naturally produced minimoons will be too small for commercially profitable enterprises they will be extremely useful for testing techniques in a cis-lunar environment before moving operations into distant heliocentric space. There are also opportunities of artificially enhancing the minimoon population by selectively maneuvering scientifically or commercially interesting asteroids onto geocentric capture trajectories from their heliocentric orbits.

The challenge in minimoon studies or capture is discovering them. Naturally produced minimoons are small, with the largest in the steady state population being perhaps only 1 m in diameter. Enhancing the minimoon capture rate requires detecting decameter-scale asteroids long before they enter Earth's Hill sphere.

The Large Synoptic Survey Telescope will be capable of detecting the largest natural minimoons and will also detect a substantial number of NEOs that could be artificially induced into becoming minimoons but the real future for mining asteroids awaits an affordable space-based detection system. Once those assets are in place they will unlock the exploration of the solar system with minimoons being the first stepping stones.

AUTHOR CONTRIBUTIONS

The author order is alphabetical after the first author. RJ coordinated the entire effort and wrote the majority of the text. BB provided insight into future prospects for minimoon discovery and assisted writing the text on the area-to-mass ratio. WB provided text on the dynamical aspects of minimoons including the Yarkovsky and lunar-origin material. MC provided material on simulating and minimizing minimoon mission Δv. GF provided details from his paper on the minimoon population and opportunities for minimoon discovery with LSST. MG provided details from his paper on the minimoon population and perspective on the science and mission opportunities. LJ provided her expertise and results of LSST minimoon discovery capabilities. HU contributed the second largest amount to the paper with significant text regarding minimoon dynamics.

FUNDING

WB's participation was supported by NASA's SSERVI program Institute for the Science of Exploration Targets (ISET) through institute grant number NNA14AB03A. RJ was partly supported by WB. MC was partially supported by award # 359510 from the Simons Foundation. MG is partially funded by grant #299543 from the Academy of Finland. HU wishes to acknowledge funding from grant ESP2017-87271-P (MINECO/AEI/FEDER, UE). GF was supported in part by a grant from the Emil Aaltonen foundation.

ACKNOWLEDGMENTS

RJ thanks Giovanni Valsecchi (INAF & IAPS, Rome, Italy) and Marco Micheli (ESA SSA-NEO Coordination Centre, Frascati, Italy) for their insight and support in both dynamical and observational aspects of minimoons. We thank three reviewers and the editors for helpful suggestions to improve the review in many ways.

REFERENCES

Astakhov, S. A., Burbanks, A. D., Wiggins, S., and Farrelly, D. (2003). Chaos-assisted capture of irregular moons. *Nature* 423, 264–267. doi: 10.1038/nature01622

Bao, C., Yang, H., Barsbold, B., and Baoyin, H. (2015). Capturing near-earth asteroids into bounded earth orbits using gravity assist. *Astrophys. Space Sci.* 360:61. doi: 10.1007/s10509-015-2581-3

Baoyin, H.-X., Chen, Y., and Li, J.-F. (2010). Capturing near earth objects. *Res. Astron. Astrophys.* 10:587. doi: 10.1088/1674-4527/10/6/008

Benner, L. A. M., Busch, M. W., Giorgini, J. D., Taylor, P. A., and Margot, J.-L. (2015). *Radar Observations of Near-Earth and Main-Belt Asteroids*. Tucson: University of Arizona Press.

Beutler, G., Mervart, L., and Verdun, A. (2006). *Methods of Celestial Mechanics: Volume II: Application to Planetary System, Geodynamics and Satellite Geodesy*. Astronomy and Astrophysics Library. Berlin; Heidelberg: Springer.

Bolin, B., Jedicke, R., Granvik, M., Brown, P., Howell, E., Nolan, M. C., et al. (2014). Detecting Earth's temporarily-captured natural satellites-Minimoons. *Icarus* 241, 280–297. doi: 10.1016/j.icarus.2014.05.026

Bottke, W. F., Morbidelli, A., Jedicke, R., Petit, J.-M., Levison, H. F., Michel, P., et al. (2002). Debiased orbital and absolute magnitude distribution of the near-earth objects. *Icarus* 156, 399–433. doi: 10.1006/icar.2001.6788

Bottke, W. F. Jr., Vokrouhlický, D., Rubincam, D. P., and Nesvorný, D. (2006). The yarkovsky and yorp effects: implications for asteroid dynamics. *Ann. Rev. Earth Planet. Sci.* 34, 157–191. doi: 10.1146/annurev.earth.34.031405.125154

Brelsford, S., Chyba, M., Haberkorn, T., and Patterson, G. (2016). Rendezvous missions to temporarily captured near Earth asteroids. *Planet. Space Sci.* 123, 4–15. doi: 10.1016/j.pss.2015.12.013

Brophy, J., Culick, F., Friedman, L., Allen, C., Baughman, D., Bellerose, J., et al. (2012). *Asteroid Retrieval Feasibility Study*. Technical report, Keck Institute for Space Studies, California Institute of Technology, Jet Propulsion Laboratory.

Brophy, J. R., and Muirhead, B. (2013). *Asteroidnear-Earth Asteroid Retrieval Mission (Arm) Study*. Technical report, Keck Institute for Space Studies, California Institute of Technology, Jet Propulsion Laboratory.

Brown, P. G., Assink, J. D., Astiz, L., Blaauw, R., Boslough, M. B., Borovička, J., et al. (2013). A 500-kiloton airburst over Chelyabinsk and an enhanced hazard from small impactors. *Nature* 503, 238–241. doi: 10.1038/nature12741

Brown, P. G., Weryk, R., Kohut, S., Edwards, W. N., and Krzemenski, Z. (2010). Development of an all-sky video meteor network in southern ontario, canada: the asgard system. *J. IMO* 38, 25–30.

Carry, B. (2012). Density of asteroids. *Planet. Space Sci.* 73, 98–118.

Carusi, A., and Valsecchi, G. B. (1981). Temporary satellite captures of comets by jupiter. *Astron. Astrophys.* 94, 226–228.

Chant, C. A. (1913a). An extraordinary meteoric display. *J. RAS Can.* 7:145.

Chant, C. A. (1913b). Further information regarding the meteoric display of february 9 1913. *J. RAS Can.* 7:438.

Chen, H. (2016). "Analysis and design of asteroid retrieval missions using luni-solar gravity assists," in *41st COSPAR Scientific Assembly, (*COSPAR Meeting*)*.

Chen, Y.-T., Lin, H. W., Holman, M. J., Payne, M. J., Fraser, W. C., Lacerda, P., et al. (2016). Discovery of a new retrograde trans-neptunian object: hint of a common orbital plane for low semimajor axis, high-inclination TNOs and centaurs. *Astrophys. J. Lett.* 827:L24. doi: 10.3847/2041-8205/827/2/L24

Chodas, P. (2016). "The orbit and future motion of earth quasi-satellite 2016 HO3," in *AAS/Division for Planetary Sciences Meeting Abstracts #48* (Pasadena, CA: AAS/Division for Planetary Sciences Meeting Abstracts, 311.04).

Chodas, P. W., and Yeomans, D. K. (1996). "The orbital motion and impact circumstances of Comet Shoemaker-Levy 9," in *IAU Colloq. 156: The Collision of Comet Shoemaker-Levy 9 and Jupiter*, eds K. S. Noll, H. A. Weaver, and P. D. Feldman (Baltimore, MD), 1–30.

Clark, D. L., Spurný, P., Wiegert, P., Brown, P., Borovička, J., Tagliaferri, E., et al. (2016). Impact detections of temporarily captured natural satellites. *Astron. J.* 151:135. doi: 10.3847/0004-6256/151/6/135

Connors, M., Wiegert, P., and Veillet, C. (2011). Earth's Trojan asteroid. *Nature* 475, 481–483. doi: 10.1038/nature10233

Cyr, O. C. S., Mesarch, M. A., Maldonado, H. M., Folta, D. C., Harper, A. D., Davila, J. M., et al. (2000). Space weather diamond: a four spacecraft monitoring system. *J. Atmospher. Solar Terrest. Phys.* 62, 1251–1255. doi: 10.1016/S1364-6826(00)00069-9

de la Fuente Marcos, C., and de la Fuente Marcos, R. (2013). A resonant family of dynamically cold small bodies in the near-Earth asteroid belt. *Month. Notices RAS* 434, L1–L5. doi: 10.1093/mnrasl/slt062

de la Fuente Marcos, C., and de la Fuente Marcos, R. (2016). Asteroid (469219) 2016 HO_3, the smallest and closest Earth quasi-satellite. *Month. Notices RAS* 462, 3441–3456. doi: 10.1093/mnras/stw1972

Denneau, L., Jedicke, R., Grav, T., Granvik, M., Kubica, J., Milani, A., et al. (2013). The pan-STARRS moving object processing system. *Publ. ASP* 125, 357–395. doi: 10.1086/670337

Denning, W. F. (1916). The remarkable meteors of february 9, 1913. *Nature* 97:181. doi: 10.1038/097181b0

Elvis, M., McDowell, J., Hoffman, J. A., and Binzel, R. P. (2011). Ultra-low delta-v objects and the human exploration of asteroids. *Planet. Space Sci.* 59, 1408–1412. doi: 10.1016/j.pss.2011.05.006

Eugster, O., Herzog, G. F., Marti, K., and Caffee, M. W. (2006). *Irradiation Records, Cosmic-Ray Exposure Ages, and Transfer Times of Meteorites*. Tucson: University of Arizona Press.

Farnocchia, D., Chesley, S. R., and Chamberlin, A. B. (2016). "Scout: orbit analysis and hazard assessment for NEOCP objects," in *AAS/Division for Planetary Sciences Meeting Abstracts #48,* (Pasadena, CA: AAS/Division for Planetary Sciences Meeting Abstracts, 305.03).

Farnocchia, D., Tholen, D. J., Micheli, M., Ryan, W., Rivera-Valentin, E. G., Taylor, P. A., et al. (2017). "Mass estimate and close approaches of near-Earth asteroid 2015 TC25," in *AAS/Division for Planetary Sciences Meeting Abstracts #49,* (Provo, UT: AAS/Division for Planetary Sciences Meeting Abstracts, 100.09).

Fedorets, G., Granvik, M., and Jedicke, R. (2017). Orbit and size distributions for asteroids temporarily captured by the Earth-Moon system. *Icarus* 285, 83–94. doi: 10.1016/j.icarus.2016.12.022

Fedorets, G., Granvik, M., Jones, L., and Jedicke, R. (2015). Discovering asteroids temporarily captured by the Earth with LSST. *IAU Gen. Assembly* 22:2257052.

García Yárnoz, D., Sanchez, J. P., and McInnes, C. R. (2013a). Easily retrievable objects among the NEO population. *Celest. Mech. Dyn. Astron.* 116, 367–388. doi: 10.1007/s10569-013-9495-6

García Yárnoz, D., Sanchez, J.-P., and McInnes, C. R. (2013b). *Opportunities for Asteroid Retrieval Missions*. Berlin; Heidelberg: Springer.

Gong, S., and Li, J. (2015). Asteroid capture using lunar flyby. *Adv. Space Res.* 56, 848–858. doi: 10.1016/j.asr.2015.05.020

Granvik, M., Jedicke, R., Bolin, B., Chyba, M., and Patterson, G. (2013). *Earth's Temporarily-Captured Natural Satellites - The First Step Towards Utilization of Asteroid Resources*. Berlin; Heidelberg: Springer.

Granvik, M., Morbidelli, A., Jedicke, R., Bolin, B., Bottke, W. F., Beshore, E., et al. (2016). Super-catastrophic disruption of asteroids at small perihelion distances. *Nature* 530, 303–306. doi: 10.1038/nature16934

Granvik, M., Morbidelli, A., Vokrouhlický, D., Bottke, W. F., Nesvorný, D., and Jedicke, R. (2017). Escape of asteroids from the main belt. *Astron. Astrophys.* 598:A52. doi: 10.1051/0004-6361/201629252

Granvik, M., Vaubaillon, J., and Jedicke, R. (2012). The population of natural Earth satellites. *Icarus* 218, 262–277. doi: 10.1016/j.icarus.2011.12.003

Graps, A. L., Blondel, P., Bonin, G., Britt, D., Centuori, S., Delbo, M., et al. (2016). ASIME 2016 white paper: in-space utilisation of asteroids: "answers to questions from the asteroid miners". ArXiv e-prints.

Gural, P. S., Larsen, J. A., and Gleason, A. E. (2005). Matched filter processing for asteroid detection. *Astron. J.* 130, 1951–1960. doi: 10.1086/444415

Harris, A. W., Morbidelli, A., and Granvik, M. (2016). "Life and death near zero: the distribution and evolution of NEA orbits of near-zero MOID, (e, i), and q," in *AAS/Division for Planetary Sciences Meeting Abstracts #48,* (Pasadena, CA: AAS/Division for Planetary Sciences Meeting Abstracts, 305.05).

Hasnain, Z., Lamb, C. A., and Ross, S. D. (2012). Capturing near-earth asteroids around earth. *Acta Astronaut.* 81, 523–531. doi: 10.1016/j.actaastro.2012.07.029

Heinze, A. N., Metchev, S., and Trollo, J. (2015). Digital tracking observations can discover asteroids 10 times fainter than conventional searches. *Astron. J.* 150:125. doi: 10.1088/0004-6256/150/4/125

Heppenheimer, T. A., and Porco, C. (1977). New contributions to the problem of capture. *Icarus* 30, 385–401. doi: 10.1016/0019-1035(77)90173-7

Hills, J. G., and Goda, M. P. (1997). Meteoroids captured into Earth orbit by grazing atmospheric encounters. *Planet. Space Sci.* 45, 595–602. doi: 10.1016/S0032-0633(97)00039-1

Hou, X. Y., Xin, X., Scheeres, D. J., and Wang, J. (2015). Stable motions around triangular libration points in the real Earth-Moon system. *Month. Notices RAS* 454, 4172–4181. doi: 10.1093/mnras/stv2216

Huang, T.-Y., and Innanen, K. A. (1983). The gravitational espace/capture of planetary satellite. *Astron. J.* 88, 1537–1548. doi: 10.1086/113444

Hunt, S., Oppenheim, M., Close, S., Brown, P., McKeen, F., and Minardi, M. (2004). Determination of the meteoroid velocity distribution at the earth using high-gain radar. *Icarus* 168, 34–42. doi: 10.1016/j.icarus.2003.08.006

Ivezic, Z., Axelrod, T., Brandt, W. N., Burke, D. L., Claver, C. F., Connolly, A., et al. (2008). Large synoptic survey telescope: from science drivers to reference design. *Serbian Astron. J.* 176, 1–13. doi: 10.2298/SAJ0876001I

Jedicke, R., Boe, B., Bolin, B. T., Bottke, W., Chyba, M., Denneau, L., et al. (2017). "Minimoon survey with subaru hyper suprime-cam," in *AAS/Division for Planetary Sciences Meeting Abstracts #49,* (Provo, UT: AAS/Division for Planetary Sciences Meeting Abstracts, 112.01).

Jedicke, R., Sercel, J., Gillis-Davis, J., Morenz, K. J., and Gertsch, L. (2018). Availability and delta-v requirements for delivering water extracted from near-Earth objects to cis-lunar space. *Planet. Space Sci.* doi: 10.1016/j.pss.2018.04.005. [Epub ahead of print].

Jenniskens, P., Gural, P. S., Dynneson, L., Grigsby, B. J., Newman, K. E., Borden, M., et al. (2011). CAMS: cameras for allsky meteor surveillance to establish minor meteor showers. *Icarus* 216, 40–61. doi: 10.1016/j.icarus.2011.08.012

Jorgensen, K., Rivkin, A., Binzel, R., Whitely, R., Hergenrother, C., Chodas, P., et al. (2003). "Observations of J002E3: possible discovery of an apollo rocket body," in *AAS/Division for Planetary Sciences Meeting Abstracts #35,* (Monterey, CA: Bulletin of the American Astronomical Society 981).

Kary, D. M., and Dones, L. (1996). Capture statistics of short-period comets: implications for comet D/Shoemaker-Levy 9. *Icarus* 121, 207–224. doi: 10.1006/icar.1996.0082

Koon, W. S., Lo, M. W., Marsden, J. E., and Ross, S. D. (2001). Resonance and capture of jupiter comets. *Celestial Mech. Dyn. Astron.* 81, 27–38. doi: 10.1023/A:1013398801813

Kwiatkowski, T., Kryszczyńska, A., Polińska, M., Buckley, D. A. H., O'Donoghue, D., Charles, P. A., et al. (2009). Photometry of 2006 RH_{120}: an asteroid temporary captured into a geocentric orbit. *Astron. Astrophys.* 495, 967–974. doi: 10.1051/0004-6361:200810965

Larson, S., Brownlee, J., Hergenrother, C., and Spahr, T. (1998). "The catalina sky survey for NEOs," in *Bulletin of the American Astronomical Society,* (Madison, WI: Bulletin of the American Astronomical Society, 1037).

Mainzer, A., Bauer, J., Grav, T., Masiero, J., Cutri, R. M., Dailey, J., et al. (2011). Preliminary results from NEOWISE: an enhancement to the wide-field infrared survey explorer for solar system science. *Astrophys. J.* 731:53. doi: 10.1088/0004-637X/731/1/53

Makó, Z., and Szenkovits, F. (2004). Capture in the circular and elliptic restricted three-body problem. *Celest. Mech. Dyn. Astron.* 90, 51–58. doi: 10.1007/s10569-004-5899-7

Marzari, F., and Scholl, H. (2013). Long term stability of Earth Trojans. *Celest. Mech. Dyn. Astron.* 117, 91–100. doi: 10.1007/s10569-013-9478-7

Meech, K. J., Weryk, R., Micheli, M., Kleyna, J. T., Hainaut, O. R., Jedicke, R., et al. (2017). A brief visit from a red and extremely elongated interstellar asteroid. *Nature* 552, 378–381. doi: 10.1038/nature25020

Micheli, M., Tholen, D. J., and Elliott, G. T. (2012). Detection of radiation pressure acting on 2009 BD. *Nature* 17, 446–452. doi: 10.1016/j.newast.2011.11.008

Micheli, M., Tholen, D. J., and Elliott, G. T. (2013). 2012 LA, an optimal astrometric target for radiation pressure detection. *Icarus* 226, 251–255. doi: 10.1016/j.icarus.2013.05.032

Mommert, M., Farnocchia, D., Hora, J. L., Chesley, S. R., Trilling, D. E., Chodas, P. W., et al. (2014). Physical properties of near-earth asteroid 2011 MD. *Astrophys. J. Lett.* 789:L22. doi: 10.1088/2041-8205/789/1/L22

Morais, M. H. M., and Morbidelli, A. (2002). The population of near-earth asteroids in coorbital motion with the earth. *Icarus* 160, 1–9. doi: 10.1006/icar.2002.6937

Nesvorný, D., Vokrouhlický, D., and Deienno, R. (2014). Capture of irregular satellites at jupiter. *Astrophys. J.* 784:22. doi: 10.1088/0004-637X/784/1/22

Nesvorný, D., Vokrouhlický, D., and Morbidelli, A. (2007). Capture of irregular satellites during planetary encounters. *Astron. J.* 133, 1962–1976. doi: 10.1086/512850

Ohtsuka, K., Ito, T., Yoshikawa, M., Asher, D. J., and Arakida, H. (2008). Quasi-hilda comet 147P/Kushida-Muramatsu. Another long temporary satellite capture by Jupiter. *Astron. Astrophys.* 489, 1355–1362. doi: 10.1051/0004-6361:200810321

Olson, D. W., and Hutcheon, S. (2013). The great meteor procession of 1913. *Sky Telesc.*

Perozzi, E., Ceccaroni, M., Valsecchi, G. B., and Rossi, A. (2017). Distant retrograde orbits and the asteroid hazard. *Eur. Phys. J. Plus* 132:367. doi: 10.1140/epjp/i2017-11644-0

Pollack, J. B., Burns, J. A., and Tauber, M. E. (1979). Gas drag in primordial circumplanetary envelopes - A mechanism for satellite capture. *Icarus* 37, 587–611. doi: 10.1016/0019-1035(79)90016-2

Sanchez, J. P., and McInnes, C. R. (2011). Asteroid resource map for near-earth space. *J. Spacecraft Rockets* 48, 153–165. doi: 10.2514/1.49851

Sanchez, J. P., and McInnes, C. R. (2013). "Available asteroid resources in the earth's neighbourhood," in *Asteroids: Prospective Energy and Material Resources*, Chap. 18 (Berlin; Heidelberg: Springer), 439–458.

Sánchez, P., and Scheeres, D. J. (2014). The strength of regolith and rubble pile asteroids. *Meteorit. Planet. Sci.* 49, 788–811. doi: 10.1111/maps.12293

Schunová-Lilly, E., Jedicke, R., Vereš, P., Denneau, L., and Wainscoat, R. J. (2017). The size-frequency distribution of H>13 NEOs and ARM target candidates detected by Pan-STARRS1. *Icarus* 284, 114–125. doi: 10.1016/j.icarus.2016.11.010

Schwamb, M. E., Jones, R. L., Chesley, S. R., Fitzsimmons, A., Fraser, W. C., Holman, M. J., et al. (2018). Large synoptic survey telescope solar system science roadmap. ArXiv e-prints.

Semeniuk, I. (2013). Scientists yearn to catch a moon. *Toronto Globe Mail.*

Shao, M., Nemati, B., Zhai, C., Turyshev, S. G., Sandhu, J., Hallinan, G., et al. (2014). Finding very small near-earth asteroids using synthetic tracking. *Astrophys. J.* 782:1. doi: 10.1088/0004-637X/782/1/1

Sidorenko, V. V., Neishtadt, A. I., Artemyev, A. V., and Zelenyi, L. M. (2014). Quasi-satellite orbits in the general context of dynamics in the 1:1 mean motion resonance: perturbative treatment. *Celest. Mech. Dyn. Astron.* 120, 131–162. doi: 10.1007/s10569-014-9565-4

Siltala, L., and Granvik, M. (2017). Asteroid mass estimation using Markov-chain Monte Carlo. *Icarus* 297, 149–159. doi: 10.1016/j.icarus.2017.06.028

Stramacchia, M., Colombo, C., and Bernelli-Zazzera, F. (2016). Distant Retrograde Orbits for space-based Near Earth Objects detection. *Adv. Space Res.* 58, 967–988. doi: 10.1016/j.asr.2016.05.053

Strange, N., Landau, D., McElrath, T., Lantoine, G., Lam, T., McGuire, M., et al. (2013). "Overview of mission design for NASA asteroid redirect robotic mission concept," in *33rd International Electric Propulsion Conference (IEPC2013), October 6-10, 2013, id.4436* (Washington, DC), 4436.

Szebehely, V. (1967). *Theory of Orbits*. New-York, NY: Academic Press.

Takada, M. (2010). "Subaru hyper suprime-cam project," in *American Institute of Physics Conference Series*, Vol. 1279, eds N. Kawai and S. Nagataki (Kashiwa), 120–127.

Tan, M., McInnes, C., and Ceriotti, M. (2017). Direct and indirect capture of near-Earth asteroids in the Earth-Moon system. *Celest. Mech. Dyn. Astron.* 129, 57–88. doi: 10.1007/s10569-017-9764-x

Tan, M., McInnes, C. R., and Ceriotti, M. (2017). Low-energy near-earth asteroid capture using momentum exchange strategies. *J. Guid. Cont. Dyn.* 41, 632–643. doi: 10.2514/1.G002957

Tanikawa, K. (1983). Impossibility of the capture of retrograde satellites in the restricted three-body problem. *Celest. Mech. Dyn. Astron.* 29, 367–402. doi: 10.1007/BF01228530

Taylor, A. D. (1995). The harvard radio meteor project meteor velocity distribution reappraised. *Icarus* 116, 154–158. doi: 10.1006/icar.1995.1117

Taylor, A., McDowell, J. C., and Elvis, M. (2018). A delta-V map of the known main belt asteroids. *Acta Astronaut.* 146, 73–82. doi: 10.1016/j.actaastro.2018.02.014

Urrutxua, H., and Bombardelli, C. (2017). "A look at the capture mechanisms of the "temporarily captured asteroids" of the earth," in *26th International Symposium on Space Flight Dynamics, number ISSFD-2017-074* (Matsuyama), 1–7.

Urrutxua, H., Scheeres, D. J., Bombardelli, C., Gonzalo, J. L., and Peláez, J. (2015). Temporarily captured asteroids as a pathway to affordable asteroid retrieval missions. *J. Guid. Cont. Dyn.* 38, 2132–2145. doi: 10.2514/1.G000885

Valdes, F., and Freitas, R. A. (1983). A search for objects near the earth-moon Lagrangian points. *Icarus* 53, 453–457. doi: 10.1016/0019-1035(83)90209-9

Vieira-Neto, E., and Winter, O. C. (2001). Time analysis for temporary gravitational capture: satellites of uranus. *Astron. J.* 122:440. doi: 10.1086/321101

Warren, P. H. (1994). Lunar and martian meteorite delivery services. *Icarus* 111, 338–363. doi: 10.1006/icar.1994.1149

Weber, M. (2005). Some apparatuses of meteor astronomy from the pre-electronic epoch. *WGN J. Int. Meteor Organ.* 33, 111–114.

Weryk, R. J., Campbell-Brown, M. D., Wiegert, P. A., Brown, P. G., Krzeminski, Z., and Musci, R. (2013). The Canadian automated meteor observatory (CAMO): system overview. *Icarus* 225, 614–622. doi: 10.1016/j.icarus.2013.04.025

Conflict of Interest Statement: The authors declare that the research was conducted in the absence of any commercial or financial relationships that could be construed as a potential conflict of interest.

frontiers in Applied Mathematics and Statistics

MINI REVIEW
published: 02 October 2018
doi: 10.3389/fams.2018.00044

Trajectory Design for Asteroid Retrieval Missions: A Short Review

Joan-Pau Sánchez[1]*, *Rita Neves*[1] and *Hodei Urrutxua*[2]

[1] Centre of Autonomous and Cyber-Physical Systems, School of Aerospace, Cranfield University, Bedfordhire, United Kingdom, [2] European Institute for Aviation Training and Accreditation, Universidad Rey Juan Carlos, Madrid, Spain

In simple terms, an asteroid retrieval mission envisages a spacecraft that rendezvous with an asteroid, lassos it and hauls it back to the Earth's neighborhood. Speculative engineering studies for such an ambitious mission concept appeared in scientific literature at the beginning of the space age. This early work employed a two-body dynamical framework to estimate the Δv costs entailed with hauling an entire asteroid back to Earth. The concept however has experienced a revival in recent years, stimulated by the inclusion of a plan to retrieve a small asteroid in NASA's 2014 budget. This later batch of work is well aware of technological limitations, and thus envisages a much more level-headed space system, capable of delivering only the most minimal change of linear momentum to the asteroid. As a consequence, the design of retrieval trajectories has evolved into strategies to take full advantage of low energy transfer opportunities, which must carefully account for the simultaneous gravitational interactions of the Sun, Earth, and Moon. The paper reviews the published literature up to date, and provides a short literature survey on the historical evolution of the concept. This literature survey is particularly focused on the design of asteroid retrieval trajectories, and thus the paper provides a comprehensive account of: the endgame strategies considered so far, the different dynamical models and the trajectory design methodologies.

Keywords: near-earth asteroids, asteroid capture, low-energy trajectories, low-thrust trajectories, ballistic capture

OPEN ACCESS

Edited by:
Elisa Maria Alessi, Consiglio Nazionale Delle Ricerche (CNR), Italy

Reviewed by:
John R. Brophy, Jet Propulsion Laboratory, United States
Enrico Stoll, Technische Universitat Braunschweig, Germany

***Correspondence:**
Joan-Pau Sánchez
jp.sanchez@cranfield.ac.uk

Specialty section:
This article was submitted to Dynamical Systems, a section of the journal Frontiers in Applied Mathematics and Statistics

Received: *28 February 2018*
Accepted: *11 September 2018*
Published: *02 October 2018*

Citation:
Sánchez J-P, Neves R and Urrutxua H (2018) Trajectory Design for Asteroid Retrieval Missions: A Short Review. Front. Appl. Math. Stat. 4:44. doi: 10.3389/fams.2018.00044

INTRODUCTION

Our Solar System is crisscrossed by millions of minor bodies, including asteroids and comets. Significant attention is devoted to these small and irregular objects, since they ultimately hold the key to understand the formation and evolution of our Solar System. NASA, ESA, JAXA, and recently the China National Space Administration (CNSA) have conceived and launched a series of missions to obtain data from such bodies; particularly, from near Earth asteroids (NEAs). Among all asteroids, NEAs have stepped into prominence because they are the easiest celestial bodies to reach from the Earth, while also representing a potential impact threat to our planet [1].

Furthermore, in recent years, the concept of utilization of in-space resources has also been receiving a renewed and notable support. In-space resources would clearly benefit science and exploration, since their utilization in space would enable otherwise unaffordable mission scenarios. An increasing number of scientists and engineers are now advocating for the necessary technologies to prospect, mine and utilize materials in space [2]. Asteroids present particularly appealing concentrations of potentially valuable resources, as well as a plethora of useful materials [3]; e.g., volatiles, such as water, may be found in carbonaceous chondrite asteroids, while metals,

semi-conductors and rare Earth elements are present in metal-rich asteroids or ordinary chondrites.

Amid these trends, asteroid retrieval or capture missions were proposed. This mission concept envisages a spacecraft that rendezvous with an asteroid, lassos it and hauls it back to the Earth's neighborhood, so that it can be more easily accessed. The mission has clear synergies with all three of the above aspects of asteroid missions: science, planetary defense and resource utilization.

The paradigm of in-space utilization of asteroid resources was conceived together with the pioneering of rocketry at the start of twentieth century [4]. Thus, with the beginning of the space race, rocketry futurists, such as Cole and Cox [5], began to envisage ambitious mission scenarios where asteroids would be moved from their original orbits by means of large nuclear propulsion systems, for subsequent extraction of their resources. However, a much more level-headed mission concept, and serious effort to develop it, was pursued more recently; within NASA's Asteroid Initiative. Announced in 2013, the Asteroid Initiative included, among other activities, the Asteroid Redirect Robotic Mission (ARRM), which initially[1] aimed at hauling an asteroid to a distant retrograde lunar orbit [6].

It is immediately clear that capturing an asteroid, whose mass may be several orders of magnitude larger than that of a typical interplanetary spacecraft ($\sim 10^3$ kg), will require an extremely powerful propulsion system and/or an extremely low-energy transfer. This short paper concerns with the latter topic: the body of literature studying trajectory opportunities to retrieve asteroids has seen a many-fold increase in the last few years. Hence, the objective of this paper is to compile a short literature review and state-of-the-art of the trajectory design methodologies for the retrieval of asteroids.

The paper is structured as follows: section Introduction provides a general background introduction and a statement of the aim of the paper. Section Trajectories to Move an Asteroid contains the main literature survey, which follows a rough chronological order, where exceptions to the strict chronology are allowed for the sake of clarity. Section Trajectories to Move an Asteroid's literature survey focuses only on published work that has tackled the problem of designing trajectories to retrieve asteroids. Section Concluding Remarks instead provides a non-comprehensive literature review of a limited number of issues that relate to the trajectory design for asteroid retrieval.

TRAJECTORIES TO MOVE AN ASTEROID

Conceptually, the trajectory design for asteroid retrieval missions can be sketched into two distinctive elements: the Earth delivery trajectory and the endgame orbit. The former accounts for the transfer and rendezvous trajectory with the target asteroid (outbound leg) and the Earth delivery trajectory to bring the asteroid into the planet's neighborhood (inbound leg). On the other hand, the endgame[2] orbit refers to the selection of the particular destination orbit where the captured asteroid is to be placed. The dynamical richness of the Earth-Moon system offers a variety of appealing endgame options; **Figure 1** shows a schematic view of the endgame options that have been considered so far in the literature. **Table 1** summarizes inbound leg delivery trajectories and endgame strategies as published by some of the literature reviewed in the following paragraphs.

The nineteenth century began with the discovery of asteroids, namely main belt objects, while it was not until the beginning of the twentieth century that NEAs were discovered. With only 50 known NEA by the late 70's [16], asteroids were already recognized as potential interplanetary stepping stones, prior to an eventual human mission to Mars [17], as well as potential targets for space resources [18].

Bender et al. [16] conducted the first comprehensive trajectory analysis for the retrieval of asteroids into Earth-bound orbits, i.e., with a characteristic energy (C_3) smaller than 0 km^2/s^2. In their work, round-trip trajectories are shown to be possible with Δv from 6 km/s, as computed in a patched conics approximation and including Earth, Moon, and Venus gravity assists. O'Leary et al. [19] argued that minimizing the Δv of the out-bound leg reduces the total wet mass of the retrieval spacecraft, since the in-bound Δv was assumed to be achieved with a mass driver system and considering asteroidal reaction mass (i.e., the propellant for the return trip was expected to be obtained from *in-situ* resources). Nevertheless, the conceived retrieval spacecraft was still a colossal space endeavor, requiring on-orbit assembly and a total of 50 Space Shuttle launches [19]. This was due to the fact that the early population of NEAs was entirely made up with very large objects, since these are much brighter and easier to detect.

By early 2000, the population of known asteroids had already increased sufficiently to allow a sensible statistical analysis [20, 21]. Thus, instead of focusing on known objects, Sanchez and McInnes [22] analyze the orbital region that is accessible given a limiting Δv threshold, and study the statistical number of asteroids that should be found considering a state-of-the-art asteroid probability density function [21]. Using a free-phase patched conics approximation, Sanchez and McInnes [22] hypothesize that there should be a 10-m diameter asteroid that could be retrieved with only 30 m/s Δv.

Even a 10-m diameter boulder, whose density may range anywhere from 1.3 to 5.3 g/cm^3 depending on composition and structure [23], is likely to be from 100s to 1000s of times heavier than the standard interplanetary spacecraft. Hence, propulsion systems with high exhaust velocity would appear to be the most suitable systems to haul large inert masses. This is identified in Brophy et al. [24], where a high-power solar electric propulsion mission is conceived to haul a 2-m notional boulder to rendezvous with the ISS. Similarly, Hasnain et al. [25] investigate the necessary thrust to haul a series of known low inclination asteroids into Earth-bound orbits, by means of implementing a

[1]The concept later evolved into a plan to haul a multi-ton boulder from the surface of a larger NEA, and was finally cancelled in 2017.

[2]Term borrowed from chess, meaning the closing stage of a game, in which only a few pieces are left on the board; it is also used figuratively to refer to the final stage of some action or process (*e.g.,* negotiation, dispute, contest, war, …).

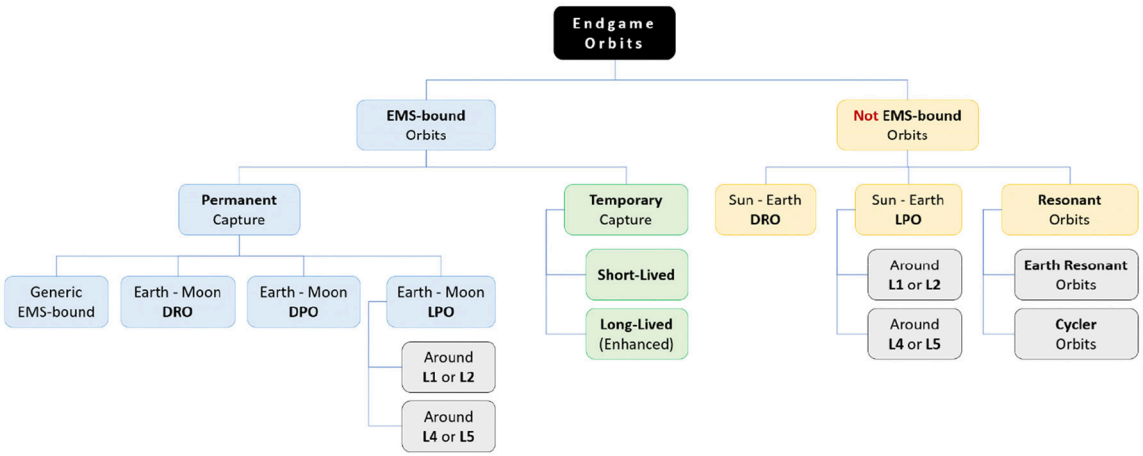

FIGURE 1 | Endgame options tree for asteroid retrieval missions. EMS, Earth-Moon System; DRO, Distant Retrograde Orbit; DPO, Distant Prograde Orbit; LPO, Libration Point Orbit.

TABLE 1 | Summary of asteroid retrieval missions found in the literature.

Bibliographic references	Target asteroid	V (m/s)	Endgame orbit	Comments
Baoyin et al. [7]	2009 BD	400	Generic EMS-bound	–
Brophy et al. [8]	2008 HU_4	170	Earth-Moon DRO (i.e., LDRO)	NASA's ARRM mission concept
García Yárnoz et al. [9]	2006 RH_{120}	58	Sun-Earth LPO	–
Strange et al. [10]	2008 LD	36	Resonant: Earth-Mars Cycler	–
Urrutxua et al. [11]	2006 RH_{120}	31	Enhanced Temporary Capture	Extended temp. capture of 5.5 year
Bao et al. [12]	2000 SG_{344}	79	Generic EMS-bound	Using lunar gravity assist
Gong and Li [13]	2008 UA_{202}	49	Generic EMS-bound	Capture duration of at least 10 year
Tan et al. [14]	2000 SG_{344}	40	Earth-Moon LPO	Optimal direct capture
Neves and Sánchez [15]	2012 TF_{79}	73	Sun-Earth LPO	–

Indicated Δv values account only for the retrieval transfer and capture phases (inbound-leg). To the knowledge of the authors, the table shows all published papers with explicit values of Δv for the inbound-leg, as of July 2018.

sub-optimal control law and a constant thrust assumption in a patched conics dynamical framework.

Earlier, Massonnet and Mayssignac [26] argue that asteroids that could be *easily* maneuvered, as of with a small Δv, must be energetically close to the Earth. Following a similar framework, Baoyin et al. [7] search for asteroids with an Earth close approach well within the sphere of influence of the Earth. The work then implements an impulsive Δv maneuver such that the zero velocity curves (ZVC) in the elliptical restricted three-body problem (ER3BP) close at both Sun-Earth L1 and L2 points. Such an approach would effectively capture an asteroid, and Baoyin et al. [7] identify one object, 2009 BD, which could have been captured with a Δv of 410 m/s during its close encounter in 2009.

Asteroids energetically close to the Earth are also nearly co-orbital, thus Bombardelli et al. [27] implement a sub-optimal low-thrust control law to modify the asteroid period in order to insert the body into a Quasi-Satellite Orbit (QSO) around the Earth (also known as Sun-Earth Distant Retrograde Orbits). On the other hand, both Massonnet and Mayssignac [26] and García Yárnoz et al. [9] focus instead on the endgame of capturing asteroids into Sun-Earth libration point orbits (LPOs).

García Yárnoz et al. [9] present a systematic approach to design impulsive retrieval transfers into the stable hyperbolic manifold of Sun-Earth LPOs in the Circular Restricted Three-Body Problem (CR3BP). Easily Retrievable Objects (EROs) are then identified as all those asteroids that can be captured with a total Δv maneuver of <500 m/s, and an initial list of 12 such objects is provided.

The original ARRM concept was proposed in 2011 after a feasibility study workshop at the Keck Institute of Space Studies [8]. In Landau et al. [28] a round-trip retrieval trajectory to asteroid 2008 HU4 is shown to be able to retrieve up to 1,300 tons of material (i.e., ∼7-m object). The retrieval spacecraft uses a high-power (∼40 kW) solar electric propulsion, has a wet mass of 18 tons, of which 5.5 tons are dry mass. The retrieval trajectories benefit from out-bound and in-bound lunar gravity assists to increase or decrease the Earth-relative orbital energy (i.e., C_3), as well as Earth-Earth leveraging transfers [29]. The endgame option is a lunar Distant Retrograde Orbit (LDRO), although options that are not Earth-bound are also discussed in Strange et al. [10].

It is thus widely agreed that a level-headed asteroid retrieval mission must use high-power electric propulsion and should target asteroids that are energetically close to the Earth. This implies that the design of *low-thrust, low-energy* trajectories must both: (1) solve the optimal control problem defined by a low-thrust trajectory; and (2) take into account dynamical models that carefully consider the simultaneous gravitational interaction of multiple bodies (i.e., Sun, Earth, and Moon). Lladó et al. [30] solve the optimal control problem for the low-thrust retrieval of 39 small asteroids. The transfer is computed in a two-body dynamical framework, however the targeted final state is that of the Sun-Earth L2 point as computed using JPL ephemeris model. Mingotti et al. [31] employ instead a CR3BP framework to solve the optimal control for the retrieval of the 12 EROs identified by García Yárnoz et al. [9]. Sánchez and García Yárnoz [32] present similar optimal control low-thrust solutions for 17 EROs. All [30–32] solve the optimal control problem using direct transcription methods, although their generation of necessary first guess solutions present a diverse range of techniques. He et al. [33] tackled the same optimal control problem in the restricted four-body dynamical framework (i.e., Sun, Earth, and Moon) within the context of a trajectory design competition, which proposed an asteroid retrieval mission as optimization challenge.

Granvik et al. [34] predict that one 3-m diameter asteroid should be on a temporarily captured orbit around the Earth every 10 years, due to a natural capture phenomenon that occurs in the dynamics of a multi-body system. Urrutxua et al. [11] studied how these temporary captures could be extended. In the specific case of 2006 RH120 (∼3-m diameter object), an asteroid which temporarily orbited the Earth for about 1 year in 2007, Urrutxua et al. [11] show how its stay could have been lengthened to 5 years with a Δv of only 32 m/s. Extending the temporary capture to a more permanent one is considered by Verrier and Mcinnes [35], who discuss a chaos-assisted capture mechanism associated with Kolmogorov–Arnold–Moser (KAM) orbits. Verrier and McInnes [35] demonstrate the process within the dynamical framework of the planar Hill problem. De Sousa-Silva and Terra [36] discuss a similar long-term capture within regions of effective stability near the triangular points L4 and L5 of the Earth-Moon system CR3BP.

Both Verrier and McInnes [35] and De Sousa-Silva and Terra [36] agree with Urrutxua et al. [11] on the fact that, in order for these highly sensitive capture trajectories to be applicable to real test cases, high-precision numerical ephemerides are indispensable. In particular, as discussed by both Granvik et al. [34] and Urrutxua et al. [11], the Moon plays a paramount role in the temporary capture of asteroids. This is also investigated by Gong and Li [13] who, in a planar restricted three-body framework, characterize the heliocentric orbit conditions that lead to a capture after a Moon fly-by. The process is also demonstrated in an ephemeris model (DE405) for a few test cases.

The active role of the Moon in the process of capturing an asteroid is also investigated by Mingotti et al. [31] and Tan et al. [14]. In these cases, however, the design strategy focuses on exploiting the stable hyperbolic manifold structures associated with periodic orbits in the Earth-Moon CR3BP. Tan et al. [14] target Earth-Moon LPOs, while Mingotti et al. [37] also consider LDRO and Lunar Distant Prograde Orbits (LDPO). In both cases, the intrinsic instability of these orbits is exploited by back-propagating a set of stable hyperbolic manifolds, which can be targeted by the asteroid-spacecraft system. While the generation of the stable hyperbolic manifold structures is performed in the CR3BP, the back-propagation and/or targeting are carried out in a restricted four-body problem considering Sun, Earth, and Moon.

Finally, the role of the Earth, not only as destination of retrieval trajectories, but also as leverage to reduce the final retrieval Δv is explored by Bao et al. [12] and Neves and Sánchez [15]. Bao et al. [12] explore the use of Earth-Earth leveraging transfers, as well as Moon fly-bys, to facilitate the capture of asteroids. The approach however is a relatively high-energy, in the sense that Lambert arcs and patched conic approximation are considered. Instead, Neves and Sánchez [15] present a methodology to benefit from Earth encounters that occur well outside the classic sphere of influence. The methodology allows exploiting the chaotic sensitivity of the multi-body problem, albeit at the cost of extremely long transfers.

One more exotic capture mechanism was recently described in Tan et al. [38]. As in previous scenarios, Tan et al. [38] also target stable hyperbolic invariant manifolds associated with Sun-Earth LPOs; however, in this case, the change of velocity needed to carry out the capture is produced by a linear momentum exchange. This is achieved by modifying the trajectory of a smaller asteroid so that this either impacts the targeted capture asteroid or performs a tethered fly-by.

In summary, it is noteworthy to highlight the diverse set of endgame orbits that have been considered in the literature (see **Figure 1**). Each endgame strategy implies a different set of methodologies to approach the design of the retrieval transfer. A substantial amount of work has not targeted a specific final capture orbit, but instead considered the energy conditions to enable permanent (or long-term stable) capture within the Earth's sphere of influence [7, 11–13, 25]. The other common approach has been to target a specific final orbit for the captured object; such as, Lunar Distant Retrograde Orbits (LDROs), as for NASA's ARRM concept [28, 31, 39], Sun-Earth LPOs [9, 26, 32, 40], or Earth-Moon LPOs [14, 31]. Additionally, Near Rectilinear Lunar Halo Orbits (NRHO) have recently been considered, as these have attracted attention as possible locations for a potential cis-lunar space station [41]. Note that the trajectory design techniques used to target many of the above final capture orbits benefit from their intrinsic instability; in the sense that one can construct the so-called stable hyperbolic invariant manifold structures associated to these orbits, which can be used for efficient targeting of the retrieval transfer. However, some of the proposed final orbits are instead linearly stable [35, 36], and do not have such a mathematical construct associated with them.

CONCLUDING REMARKS

The intrinsic stability or instability of the final capture orbit has been often quoted as a critical issue for the choice of an

appropriate location for the retrieved asteroid [8, 42]. Ideally, one would choose a stable orbit if this implies a well-behaved long term evolution of the uncontrolled trajectory. However, as shown by Roa and Handmer [43][3], a small deviation from a nominally stable LDRO may still trigger the escape from the Moon neighborhood. In contrast, station-keeping requirements for unstable orbits may be smaller than the standard station-keeping Δv budget for a geostationary satellite [44], as in the case of JWST [45]. Another important aspect which has not been yet fully explored is that of the navigability and controllability of the retrieval trajectory. Ceriotti and Sanchez [46] consider the impact of uncertainties in the insertion into the stable invariant manifolds associated with Sun-Earth LPOs. However, a full analysis considering navigation errors, uncertainties and maneuverability is still lacking.

The majority of the work has focused on the design of the in-bound retrieval trajectories. This should perhaps be expected, since the in-bound retrieval legs are key to the feasibility of the mission, especially regarding propulsion performance and propellant consumption. This is a clear consequence of the much larger mass that needs to be hauled on the way back, unless, of course, asteroidal reaction mass is considered [19, 47]. However, due to the long synodic period of easily retrievable objects, the out-bound trajectories need to be considered carefully indeed, to avoid a significant impact on the propulsion system and propellant consumption [48].

Note that the reviewed literature has only discussed the design of trajectories under the framework of gravitational forces. To the knowledge of the authors, no paper on trajectory design for asteroid retrieval missions has yet considered a non-gravitational acceleration, such as that caused by solar radiation pressure impinging on a solar sail [49]. Nevertheless, the benefit of a propulsion system requiring no reaction mass was identified early on within the wider literature on in-space resource utilization, (e.g., [50]). It must be noted however that the directionality of the thrust vector is heavily constrained for a solar sail [51], while the low thrust transfers discussed here assume a thrust vector that can be freely oriented.

Finally, from the discussion in section Trajectories to Move an Asteroid, the targeted population for low energy retrieval trajectories can be clearly identified as that of small asteroids in Earth-like orbits [9, 34]. As of July 2018, more than 18,000 NEAs have been discovered[4], from which about 3,500 are boulder-sized (<30 m diameter) and may potentially be candidates to be moved with near- to mid-term propulsion technology, akin to the ones reported in **Table 1**. While important uncertainties on the amount of boulder-size near-Earth asteroids yet exist [52, 53], this number is likely to be in the order of thousands of millions. Hence, the completeness level of the easily retrievable asteroid population is extremely low. New wide-field ground-based surveys, such as the Large Synoptic Survey Telescope, are likely to increase these levels by several orders of magnitude [54, 55].

AUTHOR CONTRIBUTIONS

All authors listed have made a substantial, direct and intellectual contribution to the work, and approved it for publication.

ACKNOWLEDGMENTS

RN would like to acknowledge the support of the Amelia Earhart Fellowship grant and the Coachmakers' Eric Beverley Bursary. HU wishes to acknowledge funding from grant ESP2017-87271-P (MINECO/AEI/FEDER, UE).

[3]Roa and Handmer [43] perturb a LDRO by adding a small Δv within the CR3BP framework.

[4]https://cneos.jpl.nasa.gov/stats/totals.html

REFERENCES

1. Alvarez LW, Alvarez W, Asaro F, Michel HV. Extraterrestrial cause for the cretaceous-tertiary extinction. *Science* (1980) **208**:1095–108. doi: 10.1126/science.208.4448.1095
2. Elvis M. Let's mine asteroids — for science and profit. *Nature* (2012) **485**:549. doi: 10.1038/485549a
3. Lewis JS, Hutson ML. Asteroidal resource opportunities suggested by meteorite data. In Lewis JS, Matthews MS, Guerrieri ML, editors. *Resources of Near-Earth Space*. Tucson, AZ: University of Arizona Press (1993). p. 523–42.
4. Tsiolkovsky KE. *The Exploration of Cosmic Space by Means of Reaction Devices*. Scientific Review (1903).
5. Cole DM, Cox DW. *Islands in Space: The Challenge of Planetoids* Philadelphia, PA: Chilton Books (1964).
6. Gates M, Muirhead B, Naasz B, Mcdonald M, Mazanek D, Stich S, et al. NASA's Asteroid Redirect Mission concept development summary. In: *2015 IEEE Aerospace Conference*. Big Sky, MT (2015). p. 1–13.
7. Baoyin H-X, Chen Y, Li J-F. Capturing near earth objects. *Res Astron Astrophys.* (2010) **10**:587–98. doi: 10.1088/1674-4527/10/6/008
8. Brophy J, Culick F, Friedman L, Allen C, Baughman D, Bellerose J, et al. *Asteroid Retrieval Feasibility Study*. Pasadena, CA: Keck Institute for Space Studies, Califonia Institute of Technology, Jet Propulsion Laboratory (2012).
9. García Yárnoz D, Sanchez JP, Mcinnes CR. Easily retrievable objects among the NEO population. *Celest Mech Dynam Astron.* (2013) **116**: 367–88. doi: 10.1007/s10569-013-9495-6
10. Strange NJ, Landau D, Longuski J, Chodas, P. Identification of retrievable asteroids with the tisserand criterion. In: *AIAA/AAS Astrodynamics Specialist Conference*. San Diego, CA: American Institute of Aeronautics and Astronautics (2014).
11. Urrutxua H, Scheeres DJ, Bombardelli C, Gonzalo JL, Peláez J. Temporarily captured asteroids as a pathway to affordable asteroid retrieval missions. *J Guid Control Dyn.* (2015) **38**:2132–45. doi: 10.2514/1.G000885
12. Bao C, Yang H, Barsbold B, Baoyin H. Capturing near-Earth asteroids into bounded Earth orbits using gravity assist. *Astrophys Space Sci.* (2015) **360**:61. doi: 10.1007/s10509-015-2581-3
13. Gong S, Li J. Asteroid capture using lunar flyby. *Adv Space Res.* (2015) **56**:848–58. doi: 10.1016/j.asr.2015.05.020
14. Tan M, Mcinnes C, Ceriotti M. Direct and indirect capture of near-Earth asteroids in the Earth–Moon system. *Celest Mech Dynam Astron.* (2017) **129**:57–88. doi: 10.1007/s10569-017-9764-x
15. Neves R, Sánchez JP. Multi-fidelity design of low-thrust resonant captures for near-earth asteroids. *J Guid Control Dyn.* (2018). [Epub ahead of print].
16. Bender DF, Dunbar SR, Ross DJ. Round-trip missions to low-delta-V asteroids and implications for material retrieval. *NASA Special Publ.* (1979) 161–72.

17. Niehoff JC. Round-trip mission requirements for asteroids 1976 AA and 1973 EC. *Icarus* (1977) **31**:430–8. doi: 10.1016/0019-1035(77)90146-4
18. O'neill GK. Space resources and settlements. In: Billingham J, Gilbreath W, O'leary B, editors. *1977 Summer Study*. Washington, DC: NASA (1979).
19. O'leary B, Gaffey MJ, Ross DJ, Salkeld R. Retrieval of asteroidal materials. In: Billingham J, Gilbreath W, O'Leary B, editors. *Space Resources and Settlements*. Washington, DC: NASA (1979).
20. D'abramo G, Harris AW, Boattini A, Werner SC, Harris AW, Valsecchi GB. A simple probabilistic model to estimate the population of near-earth asteroids. *Icarus* (2001). **153**:214–7. doi: 10.1006/icar.2001.6650
21. Bottke WF, Morbidelli A, Jedicke R, Petit J-M, Levison HF, Michel P, et al. Debiased orbital and absolute magnitude distribution of the near-earth objects. *Icarus* (2002) **156**:399–433. doi: 10.1006/icar.2001.6788
22. Sanchez JP, Mcinnes CR. Asteroid resource map for near-earth space. *J Spacec Rockets* (2011) **48**:153–65. doi: 10.2514/1.49851
23. Chesley SR, Chodas PW, Milani A, Yeomans DK. Quantifying the risk posed by potential earth impacts. *Icarus* (2002) **159**:423–32. doi: 10.1006/icar.2002.6910
24. Brophy JR, Gershman R, Landau D, Polk J, Porter C, Yeomans D, et al. Asteroid return mission feasibility study. In: *47th AIAA/ASME/SAE/ASEE Joint Propulsion Conference and Exhibit 2011* (2011).
25. Hasnain Z, Lamb C, Ross SD. Capturing near-earth asteroids around earth. *Acta Astron.* (2012) **81**:523–31. doi: 10.1016/j.actaastro.2012.07.029
26. Massonnet D, Mayssignac B. A captured asteroid: our david's stone for shielding earth and providing the cheapest extraterrestrial material. *Acta Astron.* (2006) **59**:77–83. doi: 10.1016/j.actaastro.2006.02.030
27. Bombardelli C, Urrutxua H, Peláez J. Earth delivery of a small NEO with an ion beam shepherd. In: McAdams JV, McKinley DP, Berry MM, Jenkins KL, editors. *Advances in the Astronautical Sciences*. Vol. 143. Charleston, SC: Univelt, Inc. (2012). p. 371–8.
28. Landau D, Dankanich J, Strange N, Bellerose J, Llanos P, Tantardini M. Trajectories to Nab a NEA (Near-Earth Asteroid). In: *AAS/AIAA 23rd Space Flight Mechanics Meeting*. Kauai: American Astronautical Society (2013).
29. Sims JA, Longuski JM, Staugler AJ. Vinf leveraging for interplanetary missions: multiple-revolution orbit techniques. *J Guid Control Dyn.* (1997) **20**:409–15. doi: 10.2514/2.4064
30. Lladó N, Ren Y, Masdemont JJ, Gómez G. Capturing small asteroids into a Sun–Earth Lagrangian point. *Acta Astron.* (2014) **95**:176–88. doi: 10.1016/j.actaastro.2013.11.007
31. Mingotti G, Sánchez JP, Mcinnes CR. Combined low-thrust propulsion and invariant manifold trajectories to capture NEOs in the Sun–Earth circular restricted three-body problem. *Celest Mech Dyn Astron.* (2014) **120**:309–36. doi: 10.1007/s10569-014-9589-9
32. Sánchez JP, García Yárnoz D. Asteroid retrieval missions enabled by invariant manifold dynamics. *Acta Astron.* (2016) **127**:667–77. doi: 10.1016/j.actaastro.2016.05.034
33. He S, Zhu Z, Peng C, Ma J, Zhu X, Gao Y. Optimal design of near-Earth asteroid sample-return trajectories in the Sun–Earth–Moon system. *Acta Mech Sin.* (2016) **32**:753–70. doi: 10.1007/s10409-015-0527-1
34. Granvik M, Vaubaillon J, Jedicke R. The population of natural Earth satellites. *Icarus* (2012) **218**:262–77. doi: 10.1016/j.icarus.2011.12.003
35. Verrier PE, Mcinnes CR. Low-energy capture of asteroids onto kolmogorov–arnold–moser tori. *J Guid Control Dyn.* (2014) **38**:330–5. doi: 10.2514/1.G000797
36. De Sousa-Silva PA, Terra, MO. Long term capture of asteroids for resources and scientific exploitation using hyperbolic objects in the solar system. In: *Proceedings of the International Astronautical Congress, IAC*. Jerusalem (2015). p. 5410–9.
37. Mingotti G, Sánchez JP, Mcinnes C. Low energy, low-thrust capture of near earth objects in the Sun-Earth and Earth-Moon restricted three-body systems. In: *AIAA/AAS Astrodynamics Specialist Conference*. San Diego, CA: American Institute of Aeronautics and Astronautics (2014).
38. Tan M, Mcinnes CR, Ceriotti M. Low-energy near-earth asteroid capture using momentum exchange strategies. *J Guid Control Dyn.* (2018) **41**:632–43. doi: 10.2514/1.G002957
39. Strange N, Landau D, Mcelrath T, Lantoine G, Lam T. Overview of mission design for NASA Asteroid Redirect Robotic Mission concept. In: *33rd International Electric Propulsion Conference (IEPC2013)*. Washington, DC: NASA. Jet Propulsion Laboratory (2013).
40. Sanchez JP, García Yárnoz D, Alessi EM, Mcinnes CR. Gravitational capture opportunities for asteroid retrieval missions. In: *63nd International Astronautical Congress*. Naples: International Astronautical Federation (2012).
41. Strange N, Brophy J, Alibay F, Mcguire M.L, Muirhead B, Hack K.J. High power solar electric propulsion and the Asteroid Redirect Robotic Mission (ARRM). In: *2017 IEEE Aerospace Conference* (2017). p. 1–10.
42. Muirhead BK, Brophy JR. Asteroid redirect robotic mission feasibility study. In: *Aerospace Conference, 2014 IEEE*. Big Sky, MT (2014). p. 1–14.
43. Roa J, Handmer CJ. Quantifying hazards: asteroid disruption in lunar distant retrograde orbits. *arXiv preprint arXiv:1505.03800* (2015).
44. Simó C, Gómez G, Llibre J, Martínez R, Rodríguez J. On the optimal station keeping control of halo orbits. *Acta Astronautica* (1987) **15**:391–7. doi: 10.1016/0094-5765(87)90175-5
45. Dichmann DJ, Alberding CM, Yu WH. Stationkeeping Monte Carlo simulation for the James Webb space telescope. In: *International Symposium on Space Flight Dynamics 2014*. Laurel, MD (2014).
46. Ceriotti M, Sanchez JP. Control of asteroid retrieval trajectories to libration point orbits. *Acta Astron.* (2016) **126**:342–53. doi: 10.1016/j.actaastro.2016.03.037
47. Pearson J. *Asteroid Retrieval by Rotary Rocket*. Pasadena, CA: AIAA Paper (1980).
48. Englander JA, Cardiff EH. Asteroid retrieval via direct launch and solar electric propulsion. In: Wilson RS, Zanetti R, Mackison DL, Abdelkhalik O, editors. *Advances in the Astronautical Sciences*. Vol. 152. Santa Fe, NM: Univelt, Inc. (2014). p. 1137–1153.
49. Mcinnes C. *Solar Sailing: Technology, Dynamics and Mission Applications*. London: Springer (2004).
50. Drexler KE. High performance solar sails and related reflecting devices. In: *4th Conference on Space Manufacturing Facilities Princeton University*. Princeton, NJ: American Institute of Aeronautics and Astronautics (1979).
51. Dachwald B, Seboldt W. Multiple near-Earth asteroid rendezvous and sample return using first generation solar sailcraft. *Acta Astron.* (2005) **57**:864–75. doi: 10.1016/j.actaastro.2005.04.012
52. Fedorets G, Granvik M, Jedicke R. Orbit and size distributions for asteroids temporarily captured by the Earth-Moon system. *Icarus* (2017) **285**:83–94. doi: 10.1016/j.icarus.2016.12.022
53. Granvik M, Morbidelli A, Jedicke R, Bolin B, Bottke WF, Beshore E, et al. Debiased orbit and absolute-magnitude distributions for near-Earth objects. *Icarus* (2018) **312**:181–207. doi: 10.1016/j.icarus.2018.04.018
54. Fedorets G, Granvik M, Jones L, Jedicke R. *Discovering asteroids temporarily captured by the Earth with LSST*. Honolulu, HI: IAU General Assembly (2015).
55. Jones RL, Jurić M, Ivezić Ž. Asteroid discovery and characterization with the large synoptic survey telescope. *Proc Int Astron Union* (2015) **10**:282–92. doi: 10.1017/S1743921315008510

Conflict of Interest Statement: The authors declare that the research was conducted in the absence of any commercial or financial relationships that could be construed as a potential conflict of interest.

frontiers in Astronomy and Space Sciences

ORIGINAL RESEARCH
published: 19 September 2018
doi: 10.3389/fspas.2018.00029

Orbit Design for LUMIO: The Lunar Meteoroid Impacts Observer

Ana M. Cipriano[1], *Diogene A. Dei Tos*[2] *and Francesco Topputo*[2]*

[1] Astrodynamics and Space Missions, Delft University of Technology, Delft, Netherlands, [2] Department of Aerospace Science and Technology, Politecnico di Milano, Milan, Italy

The Lunar Meteoroid Impacts Observer, or LUMIO, is a space mission concept awarded winner of ESA's SysNova Competition "Lunar CubeSats for Exploration," and as such it is now under consideration for future implementation by the Agency. The space segment foresees a 12U CubeSat, placed at Earth–Moon L_2, equipped with an optical instrument, the LUMIO-Cam, which is able to spot the flashes produced by impacts of meteoroids with the lunar surface. In this paper, the work undertaken to design the baseline orbit of LUMIO is documented. The methodology is thoroughly described, both in qualitative and quantitative terms, in support to the mission analysis trade-off activities. The baseline solution is presented with evidence to support the orbit design.

Keywords: LUMIO, orbit design, lagrange point, lunar meteoroid, impact flash

OPEN ACCESS

Edited by:
Elisa Maria Alessi, Consiglio Nazionale Delle Ricerche (CNR), Italy

Reviewed by:
Jose Luis Ortiz, Consejo Superior de Investigaciones Científicas (CSIC), Spain
David Charles Folta, Goddard Space Flight Center, United States

***Correspondence:**
Francesco Topputo
francesco.topputo@polimi.it

Specialty section:
This article was submitted to Fundamental Astronomy, a section of the journal Frontiers in Astronomy and Space Sciences

Received: *13 April 2018*
Accepted: *10 August 2018*
Published: *19 September 2018*

Citation:
Cipriano AM, Dei Tos DA and Topputo F (2018) Orbit Design for LUMIO: The Lunar Meteoroid Impacts Observer. Front. Astron. Space Sci. 5:29. doi: 10.3389/fspas.2018.00029

1. INTRODUCTION

1.1. Scientific Relevance

Near-Earth Objects (NEOs) are asteroids or comets with a perihelion of <1.3 astronomical units (AU), whose orbits encounter the Earth neighborhood. In the Minor Planet Center database[1], the vast majority of NEOs are classified as Near-Earth Asteroids (NEAs), while only a small fraction are classified as Near-Earth Comets (NECs). Both types of minor bodies (NEAs and NECs) are remnant debris of the solar system formation and contain clues that can contribute to the understanding of the composition of planets. The relatively easier accessibility of NEOs, when compared to deep-space asteroids, represents a valuable opportunity to improve the understanding of the solar system at an affordable cost.

Impacts due to Near-Earth Objects could cause a devastating humanitarian crisis and potentially the extinction of the human race. While the probability of such an event is low, the outcome is so catastrophic that it is imperative to invest resources to mitigate them. The largest impact event recorded in history is attributed to a NEO impact, is know as the Tunguska event and occurred in 1908. According to Brown et al. (2013), an event like this could occur every 100 years. The second largest airburst event recorded occurred in 2013 in the Russian city of Chelyabinsk, causing damages over a 120 km radius and at least 374 injured (Popova et al., 2013). Telescopic surveys detect NEOs whose size ranges from slightly larger than 1 km down to tens of meters (Koschny and McAuliffe, 2009), but there are few direct methods for monitoring the sub-meter meteoroid population. Serendipitous monitoring of atmospheric explosions due to airbursts of large meteoroids are also being undertaken.

Meteoroids are small Sun-orbiting fragments of asteroids and comets, whose sizes range from micrometers to meters and masses from 10^{-15} to 10^{4} kg (Ceplecha et al., 1998). Their formation

[1] https://www.minorplanetcenter.net/. Last retrieved on May 2018.

is a consequence of asteroids colliding with each other or with other bodies, comets releasing dust particles when close to the Sun, and minor bodies shattering into individual fragments. Meteoroids are hardly detectable even with dedicated surveys. However, they may be observed indirectly when an impact occurs with a planetary or moon solid surface. An impact represents in fact a unique opportunity to understand and update the models describing the spatial distribution of NEOs in the solar system, which is critical for a number of reasons. The development of reliable models for the small meteoroid impact flux is required for the sustainable design of space assets: if the models fail to predict the correct flux of meteoroids that may potentially impact a spacecraft, the result could be either an over-conservative or an ineffective shielding, affecting the overall mission performance. The study of micrometeoroids, whose size ranges from 10 μm to 2 mm (Rubin and Grossman, 2010), is also of interest for space weather phenomena: the development of reliable models in the micrometeoroid size range can help deepening the understanding of the change of airless bodies optical properties. Finally, vast amounts of meteoroids and micrometeoroids continuously enter the Earth–Moon system and consequently become a potential threat which has caused, in particular, a substantial change in the lunar surface and its properties (Oberst et al., 2012). As such, the ability to accurately and timely predicting these impacts by relying on accurate meteoroid models becomes a fundamental asset.

1.2. Lunar Meteoroid Impacts

Estimations of the larger-than-1-kg meteoroid flux at the Moon varies across the literature. The model in Brown et al. (2002) estimates 1290 impacts per year, while the one in Ortiz et al. (2006) estimates approximately 4000 impacts per year (Gudkova et al., 2011). More recent studies suggest that the meteoroid impact flux at the Moon is approximately $6 \times 10^{-10}/\mathrm{m}^2/\mathrm{year}$, for meteoroids larger than 30 g (Suggs et al., 2014). Assuming a lunar collecting area equal to its surface area, 3.8×10^{13} m^2, this gives a larger-than-30-grams meteoroid flux of approximately 23,000 impacts per year. Part of the discrepancies across literature is due to the current lack of knowledge regarding meteoroid impact physics, such as the luminous efficiency of an impactor (see section 2.2.2), and a non-uniformity on how lunar meteoroid impacts data is processed (Ortiz et al., 2015; Suggs et al., 2017). As such, more experimental data on lunar meteoroid impacts is still required.

There are also speculations on the possible asymmetries of the spatial distribution of impacts across the lunar surface (Oberst et al., 2012; Suggs et al., 2014). In Oberst et al. (2012), it is theorized that the Moon nearside has approximately 0.1% more impacts than the lunar farside, due to the Earth gravity field; the equatorial flux is 10–20% larger than that at polar regions, due to the higher number of large meteoroids in low orbital inclinations; and the lunar leading side (apex) encounters between 37 and 80% more impactors than the lunar trailing side (antapex), due the Moon synchronous rotation. Full-disk observations of the Moon are necessary to definitively confirm or rule out these characteristics.

Monitoring the Moon surface for meteoroid impacts allows covering a significantly larger area than the traditional methods that monitor portions of the Earth atmosphere (Ortiz et al., 2006). In a lunar meteoroid impact, the kinetic energy of the impactor is partitioned into (1) the generation of a seismic wave, (2) the excavation of a crater, (3) the ejection of particles, and (4) the emission of radiation. Any of these phenomena can be observed to detect lunar meteoroid impacts. The main characteristics of each observation method are summarized in the form of a graphical trade-off in **Table 1**. The detection of lunar impact flashes is the most advantageous method since it yields an independent detection of meteoroid impacts, provides the most complete information about the impactor, and allows for the monitoring of a large Moon surface area. Remote observation of light flashes is thus baselined for the detection of lunar meteoroid impacts.

1.3. Lunar Meteoroid Impact Flashes

Light flashes at the Moon are typically observed by detecting a local spike of the luminous energy in the visible spectrum when pointing a telescope at the lunar nightside. The background noise is mainly composed by the Earthshine (Earth reflected light on the Moon surface) in the visible spectrum, and by thermal emissions of the Moon surface in the infrared spectrum (Bouley et al., 2012). Measurements with high signal-to-noise ratios can be obtained through observations of the lunar nightside (Bellot Rubio et al., 2000). The detected luminous energy spike is quantified using the apparent magnitude of the light flash.

Lunar impact flashes detected from Earth-based observations have apparent magnitude between +5 and +10.5 (Oberst et al., 2012), which correspond to very faint signals. Also, Earth-based observations of lunar impact flashes are restricted to periods when the lunar nearside illumination is 10–50% (Ortiz et al., 2006; Suggs et al., 2008). The upper limit restriction is due to the dayside of the Moon glaring the telescope field of view (FOV). The lower limit restriction of 10% corresponds to the New Moon phase. During this phase, the observations should be made when the Moon presents itself at low elevations in the sky (morning or evening), but the observation periods are too short to be useful (Suggs et al., 2008; Oberst et al., 2012).

The first unambiguous lunar meteoroid impact flashes were detected during 1999's Leonid meteoroid showers and were reported in Ortiz et al. (2000). The first redundant detection of sporadic impacts was only reported 6 years later in Ortiz et al. (2006). These events gave origin to several monitoring programs. In 2006, a lunar meteoroid impact flashes observation programme was initiated at NASA Marshall Space Flight Center (Suggs et al., 2008). This facility is able to monitor 4.5×10^6 km^2 of the lunar surface, approximately 10 nights per month, subject to weather conditions. Approximately half of the impact flashes observations occur between the Last Quarter and New Moon (0.5–0.1 illumination fraction) and the other half between New Moon and First Quarter (0.1–0.5 illumination fraction). The former monitoring period occurs in the morning (waning phase) and the latter occurs in the evening (waxing phase), covering the nearside part of the eastern and western lunar hemisphere, respectively. 126 high-quality flashes were reported in Suggs et al.

TABLE 1 | Trade-off analysis of methods for the lunar meteoroid impacts observation.

Observation	Type of method	Moon surface covered (%)	Meteoroid impacts detection	Meteoroid information obtained
Seismic waves	*In-situ*	red ~ 1.3%	red Not possible independently	red None independently
Craters	Remote sensing	green ~ 100%	yellow Formation of new craters; if independently, with time-consuming process	yellow Position of impact and crater size
Particles	*In-situ*	red ~ 0%	green Burst of particles; independent detection	yellow Position and time of impact
Radiation	Remote sensing	yellow up to 50%	green Observation of light flashes; independent detection	green Position and time of impact; kinetic energy (mass and/or velocity)

green Good features; yellow Fair features; red Poor features.

(2014), for 266.88 h of monitoring, over a 5 years period. The magnitude range detected is between +10.42 and +5.07, which is estimated to correspond to an impactor kinetic energy range between 6.7×10^{-7} and 9.2×10^{-4} kton TNT, taking into account the correction factor of 4 suggested in Ortiz et al. (2015). The corresponding impact velocities range from 24 km/s to 70 km/s.

The most recent monitoring program, NELIOTA, was initiated on February 2017 in Greece under ESA fundings. As of November 2017, 16 validated impacts have been detected over 35 h of observations. NELIOTA aims to detect flashes as faint as +12 apparent visual magnitude (Bonanos et al., 2015) and is the first allowing the determination of the impact flash blackbody temperature by observing both in the visible and infrared spectrum. Monitoring the Moon for impact flashes inherently imposes several restrictions that can be avoided if the same investigation were conducted with space-based assets, such as LUMIO.

1.4. The LUMIO Mission

Observing lunar impacts with space-based assets yields a number of benefits over ground-based ones:

- **No atmosphere**. Ground-based observations are biased by the atmosphere that reduces the light flash intensity depending upon present conditions, which change in time. This requires frequent recalibration of the telescope. Inherent benefits of the absence of atmosphere in space-based observations are 2-fold: (1) there is no need of recalibrating the instrument, and (2) fainter flashes can be detected.
- **No weather**. Ground-based observations require good weather conditions, the lack of which may significantly reduce the observation time within the available window. There is no such constraint in space-based observations.
- **No day/night**. Ground-based observations may only be performed during Earth night, significantly reducing the observation period within the available window. There is no such limitation when space-based observations are performed.
- **Full disk**. Ground-based observations are performed in the first and third quarter, when nearside illumination is 10–50%. Full-disk observations during New Moon are not possible because of low elevation of the Moon and daylight. Space-based observations of the lunar farside can capture the whole lunar full-disk at once, thus considerably increasing the monitored area.
- **All longitudes**. Ground-based observations happening during the first and third quarter prevent resolving the meteoroid flux across the central meridian. There is no such restriction in space-based, full-disk observations.

Moreover, observing the lunar farside with space-based assets yields further benefits, i.e.,

- **No Earthshine**. By definition, there is no Earthshine when observing the lunar farside. This potentially yields a lower background noise, thus enabling the detection of fainter signals, not resolvable from ground.
- **Complementarity**. Space-based observations of the lunar farside complement ground-based ones
  - *In space*. The two opposite faces of the Moon are monitored when the Moon is in different locations along its orbit;
  - *In time*. Space-based observations are performed in periods when ground-based ones are not possible, and vice-versa.

High-quality scientific products can be achieved with *space-based observations of the lunar farside*. These may complement those achievable with ground-based ones to perform a comprehensive survey of the meteoroid flux in the Earth–Moon system. All of the above considerations drove the formulation of the LUMIO mission statement:

LUMIO is a CubeSat mission orbiting in the Earth–Moon region that shall observe, quantify, and characterize meteoroid impacts on the lunar farside by detecting their impact flashes, complementing Earth-based observations of the lunar nearside, to provide global information on the lunar meteoroid environment and contribute to Lunar Situational Awareness.

LUMIO mission is conceived to address the following issues.

- **Science Question**. What are the spatial and temporal characteristics of meteoroids impacting the lunar surface?
- **Science Goal**. Advance the understanding of how meteoroids evolve in the cislunar space by observing the flashes produced by their impacts with the lunar surface.

- **Science Objective**. Characterize the flux of meteoroids impacting the lunar surface.

The mission utilizes a 12U form-factor CubeSat which carries the LUMIO-Cam, an optical instrument capable of detecting light flashes in the visible spectrum to continuously monitor and process the data. The mission implements a novel orbit design and latest CubeSat technologies to serve as a pioneer in demonstrating how CubeSats can become a viable tool for deep space science and exploration.

The selection of the operative orbit is detailed throughout the rest of the paper, which is organized as follows. In section 2 the methodology is given, including the criteria defined and the models developed to support the trade-off. In section 3, the trade-off process is detailed by following a hierarchical structure ranging from qualitative to quantitative arguments. Potential operative orbits are presented in section 3.3.4, and final remarks are drawn in section 4.

2. METHODOLOGY

The methodology used for LUMIO orbit design relies on the following approach (refer to **Figure 1**):

1. Evaluation criteria are defined, based on requirements and mission objectives.
2. The relevant orbit types for lunar remote sensing are identified.
3. A *preliminary trade-off* scans orbit families, accounting for their main characteristics and eliminating clearly non-feasible options. The orbit families encompass two-body Keplerian orbits and several three-body libration point orbits (LPOs). *Candidate orbits* are the output of the preliminary trade-off.
4. A *coverage analysis* is performed for the candidate orbits. The physics of the impact is modeled together with the space environment, the local orbital geometry, and the payload characteristics. The model is then validated against a known dataset. *Ad-hoc* simulations engage the scientific goal of maximizing the number of observable impacts with the need to have lunar full-disk visibility for autonomous optical navigation (Topputo et al., 2017). Non-feasible candidate orbits, according to these criteria, are eliminated and the remaining *feasible orbits* move on to the next orbital trade-off level.
5. A *detailed trade-off* quantifies and compares station-keeping and transfer costs for each feasible orbit. Evaluation criteria related to Δv budget are first determined by optimizing the transfer trajectory and station-keeping costs and later applied to select LUMIO *operative orbit*.

2.1. Evaluation Criteria for LUMIO Orbits

The evaluation criteria are divided into *acceptance criteria* and *selection criteria*. The former are defined based on the science and mission requirements (Topputo et al., 2017). The latter are defined based on orbital performance parameters and allow the selection of optimal orbits, from a set of candidate orbits that meet the acceptance criteria. The acceptance criteria are defined as follows:

EC.A.01 The operational orbit shall allow the detection of meteoroids in the equivalent kinetic energy range at Earth of 10^{-6} to 10^{-1} kton TNT.
EC.A.02 The operational orbit shall allow the detection of at least 240 meteoroid impacts during the mission lifetime.
EC.A.03 The operational orbit shall allow the detection of at least 2 meteoroid impacts in the equivalent kinetic energy range at Earth of 10^{-4} to 10^{-1} kton TNT.
EC.A.04 The operational orbit shall allow the detection of at least 100 meteoroid impacts in the equivalent kinetic energy range at Earth of 10^{-6} to 10^{-4} kton TNT.
EC.A.05 The operational orbit shall allow monitoring of the lunar farside at night.
EC.A.06 The operational orbit shall support a minimum mission lifetime of 1 year, with a maximum total Δv budget of 200 m/s.
EC.A.07 The operational orbit shall be accessible from the departure orbit, with a maximum total Δv budget of 200 m/s.

Evaluation criterion EC.A.01 defines a kinetic energy range to be observed, which is mainly a function of orbit altitude (see section 2.2.2). On the other hand, evaluation criteria EC.A.02–04 are mainly a function of cumulative observation time in the mentioned kinetic energy ranges. In EC.A.02, the approximate number of meteoroid impact flashes used by Suggs et al. (2014) to estimate the lunar impact flux in this range has been considered reasonable for an acceptance criteria. Evaluation criteria EC.A.05 is directly related to the mission requirement of detecting impact flashes on the lunar farside and the need to monitor it at night follows from the fact that impact flashes can only be detected under very low illumination conditions. Finally, in EC.A.06 and EC.A.07, a total Δv budget of 200 m/s is considered based on the constraint on the maximum mass of 24 kg for LUMIO. The allocated Δv budget is deemed reasonable for a CubeSat, in order to support a minimum mission lifetime of 1 year and deployment from a Lunar Orbiter, which would release LUMIO in a given injection orbit around the Moon (see section 3.3).

The selection criteria defined are the following:

EC.S.01 The total number of meteoroids detected during the mission lifetime shall be maximized.
EC.S.02 The total Δv budget shall be minimized.
EC.S.03 The duration spent in observing the lunar full-disk shall be maximized.

The selection criteria are defined in view of mission objectives. As such, in order to determine a good orbit to improve current Earth-based lunar impact flashes observation, the selection criteria are defined in view of the performance of the orbit. EC.S.01 is chosen because one of the main goals of lunar impact flashes monitoring is to improve the current solar system meteoroid models, and a larger number of observations can contribute toward this goal. Moreover, selecting the orbit with the minimum Δv budget can also contribute toward the same goal. This is because the station-keeping Δv could be increased, allowing for a larger mission lifetime and, so, the possibility of detecting more meteoroid impact flashes. Finally, in order

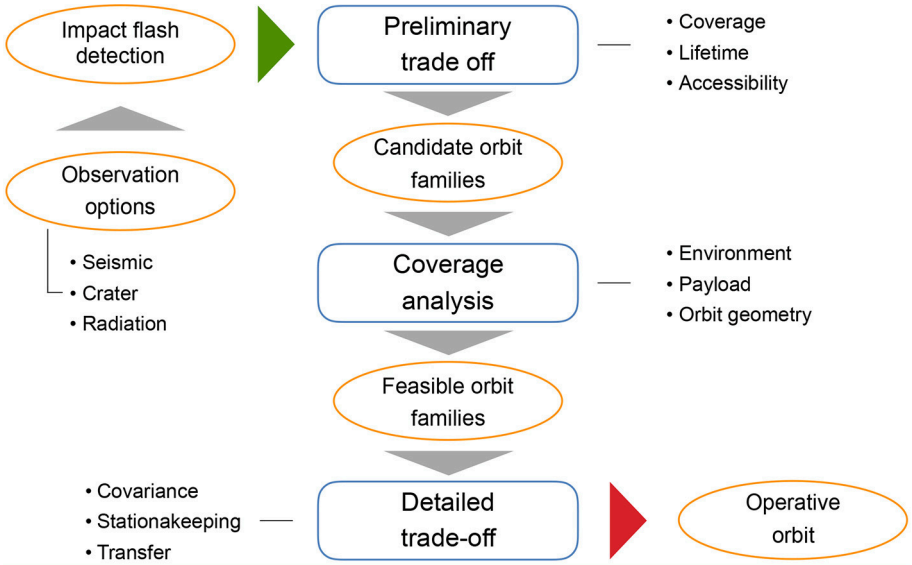

FIGURE 1 | Trade-off scheme for the selection of LUMIO operative orbit.

to perform reliable optical navigation using the lunar full-disk, EC.S.03 is defined to ensure navigation images can be acquired whenever necessary (Franzese et al., 2018). Furthermore, EC.S.03 also allows for a more uniform coverage of the lunar farside, which can contribute to the understanding of lunar meteoroid impact flux asymmetries.

2.2. Models

2.2.1. Orbital Geometry in Near-Lunar Space

Three different classes of orbits are considered: Keplerian; perturbed Keplerian, and libration point orbits. Only orbits that allow a periodic or repetitive motion with respect to the Moon surface are considered as lunar remote sensing orbits. Orbits whose range to the lunar surface exceeds one third of the Earth–Moon distance ($\approx$ 100,000 km) are excluded from the analysis. The considered Keplerian orbits are low lunar orbits (LLO) and elliptical lunar orbits (ELO). LLO have a constant low altitude, h, with respect to the Moon surface and a short period (roughly 2 h for the $h = 100$ km case). For $h > 100$ km, Earth gravitational field affects the satellite motion in such a way that the orbit can no longer be considered as only under the influence of the lunar gravity field (Abad et al., 2009; Carvalho et al., 2010). ELO typically have low perilune altitude and relatively large apolune altitude. Therefore, the spacecraft-to-Moon distance varies significantly in one orbital revolution, along with the coverage periods of certain lunar regions.

The considered perturbed Keplerian orbits are frozen orbits (FO) and Sun-synchronous orbits (SSO). FO are orbits whose orbital elements are stationary, due to reduced or null secular and long-period perturbations. They usually exist only for certain combinations of a (semi-major axis), e (eccentricity), i (inclination), and ω (argument of perilune). The latter is typically fixed at 90 or 270 degrees, meaning that the periapsis of the orbit remains directly above the north or south pole of the central body in case of polar orbits. Hence, the satellite altitude remains constant over each latitude, making coverage patterns repetitive. Two different types of lunar frozen orbits are considered. The first takes only into account perturbations by the zonal terms of the lunar nonspherical gravity field, i.e., J_n-terms, and has low altitudes, i.e., $h \leq 100$ km. The second takes also into account perturbations of the Earth gravity field, and has higher altitudes ($h > 100$ km). On the other hand, SSO are orbits whose line of nodes rotates to freeze the orbital plane orientation relative to the Sun, i.e., the orbital plane rotates at ≈ 0.9856 deg/day as the Earth–Moon system revolves about the Sun. **Table 2** summarizes the main characteristics of Keplerian and perturbed Keplerian orbits.

When compared with selenocentric Keplerian orbits, libration point orbits are typically more easily accessible from Earth, have more favorable thermal environments, few or no lunar eclipses, and infrequent Earth shadowing/occultation (Pergola and Alessi, 2012; Whitley and Martinez, 2016). However, they are mostly associated to large instability indicators. The definition of stability index S used in the present work is that of Folta et al. (2015):

$$S = \frac{1}{2}\left(|\nu| + \frac{1}{|\nu|}\right), \tag{1}$$

where ν denotes the (reciprocal) pair of eigenvalues associated with the stable/unstable subspace of the orbit. With this definition, $S > 1$ indicates instability of the orbit, and $S \leq 1$ indicates stability. A large stability index is usually associated with large station-keeping costs, but lower transfer costs (Grebow, 2006). Five types of three-body periodic orbits have been considered for orbital design: Lyapunov orbits (LYO), halo orbits (HO), Lyapunov vertical orbits (VO), distant retrograde

orbits (DRO), and low prograde orbits (LoPO). **Table 3** summarizes the main characteristics of the LPO, also presented in **Figure 2**.

LYO circulate $L_{1,2}$ in the circular restricted three-body problem (CRTBP) xy plane and are typically characterized by the amplitude along the x axis (A_x). Their orbital periods in the Earth–Moon system range from approximately 15–30 days and their stability index is relatively high ($S \sim 300$). HO circulate $L_{1,2}$ with a three-dimensional motion. The frequency of their out-of-plane motion matches the in-plane motion and only exist for a specific set of A_y (Farquhar and Kamel, 1973). Halo orbits at the Earth–Moon $L_{1,2}$ become almost rectilinear when close to the Moon (Breakwell and Brown, 1979), generating the family of near-rectilinear halo orbits (NRHO), whose stability index is smaller than that of the nominal halos. NRHO are not considered in this work. VO circulate $L_{1,2}$ in eight-shaped trajectories, crossing the x axis twice in one orbital period (Folta et al., 2015). Their orbital periods in the Earth–Moon system range from approximately 10–20 days and their stability index is in between that of halo and Lyapunov orbits ($S \sim 200$). Given their shape, these orbits can be used to monitor both lunar poles in one orbital revolution. DRO circulate the smaller primary (e.g., the Moon) in a retrograde motion (Hénon, 1970). These orbits have no apparent size limit, so they can even encompass both L_1 and L_2 (Ming and Shijie, 2009). LoPO circulate also the smaller primary, but in a prograde motion (Hénon, 1970). Their orbital periods range from approximately 2–14 days and their stability index vary significantly with size. LoPO may be used to cover more extensively the nearside of the Moon.

TABLE 2 | Characteristics of Keplerian and perturbed Keplerian lunar remote sensing orbits.

Orbit	h (km)	e	i (deg)	ω (deg)	P (h)	Coverage characteristics
LLO	< 100[a,b]	0	$[0, 180]$	–	< 2	Constant altitude
ELO	$< 10,000$[c] (apoapsis altitude)	< 0.74 (crash)	$[0, 180]$	$[0, 360]$	< 27 ($e = 0.1$; $h_a = 10000$ km)	Variable altitude; possible to cover more extensively certain regions
FO	< 100[a] (only Moon zonal harmonics)	$[0, 0.1]$[a,d]	$[0, 63] \cup [73, 86.5]$*[,a,d]	90 or 270±3[a]	< 2 ($e = 0.01$; $h_a = 100$ km)[a]	Possibly variable altitude, but constant over each latitude[b]
	$[100, 9000]$[a,e] (Moon zonal harmonics and Earth)	$[0, 0.7]$[†] ($h = 3700$ km)	0 or $[40, 70]$[a]	90 or 270[a]	< 24 ($e = 0.6$; $h_a = 9,000$ km)[e]	
SSO	< 100[b] (only Moon's J_2 and C_{22})	< 0.05 (crash)	$[125, 170]$	$[0, 360]$	< 2	Approximately constant altitude and illumination angles

The information within brackets denotes the conditions corresponding to interval limits.
[a]*Abad et al. (2009);* [b]*Carvalho et al. (2009);* [c]*Whitley and Martinez (2016);* [d]*Elipe and Lara (2003);* [e]*Ely and Lieb (2006).*
**Symmetric intervals with respect to* 90 *deg also exist (Park and Junkins, 1994).*
[†]*Smaller interval for lower altitudes (Abad et al., 2009).*

TABLE 3 | Characteristics of libration point lunar remote sensing orbits.

Orbit	Geometry	h (10^3 km)	P (days)	S*	Coverage characteristics	Earth Visibility
LYO	2D	$[40, 78]$[a] ($A_x = 20,000$ km, $P = 15.5$ days)	L_1:$[12, 32]$ L_2:$[14, 36]$[b]	L_1:350 L_2:300[b]	Lunar nearside or farside and possibly lunar apex and antapex[c]	Occultation can occur
DRO	2D	$[20, 50] \cup [60, 80]$[d] (Initial distance to the Moon)	$[4, 16]$[d] (resonant state: $T_{Moon}/T \in [1.6, 6]$)	1[b]	Lunar nearside and farside	Occultation can occur
LoPO	2D	$[38, 50]$[e] (Maximum range in X-axis)	$[2, 14]$[b]	4[b]	Lunar nearside covered more extensively	Occultation can occur
HO	3D	L_1:$[20, 65]$ L_2:$[10, 75]$[f] (Maximum distance)	L_1 :$[7, 13]$ L_2 :$[4, 15]$[f]	L_1:175 L_2:100	Lunar nearside or farside and possibly north or south pole	Always visible
VO	3D	L_1:$[50, 60]$ L_2:$[50, 65]$[f] (Maximum distance)	L_1:$[10, 18]$ L_2:$[14, 18]$[b,f]	L_1:250 L_2:200[b]	Lunar nearside or farside and both poles	Occultation can occur

[a]*Bernelli Zazzera et al. (2004);* [b]*Folta et al. (2015);* [c]*Doedel et al. (2007);* [d]*Turner (2016);* [e]*Guzzetti et al. (2016);* [f]*Grebow (2006).*
**Average over orbit family.*

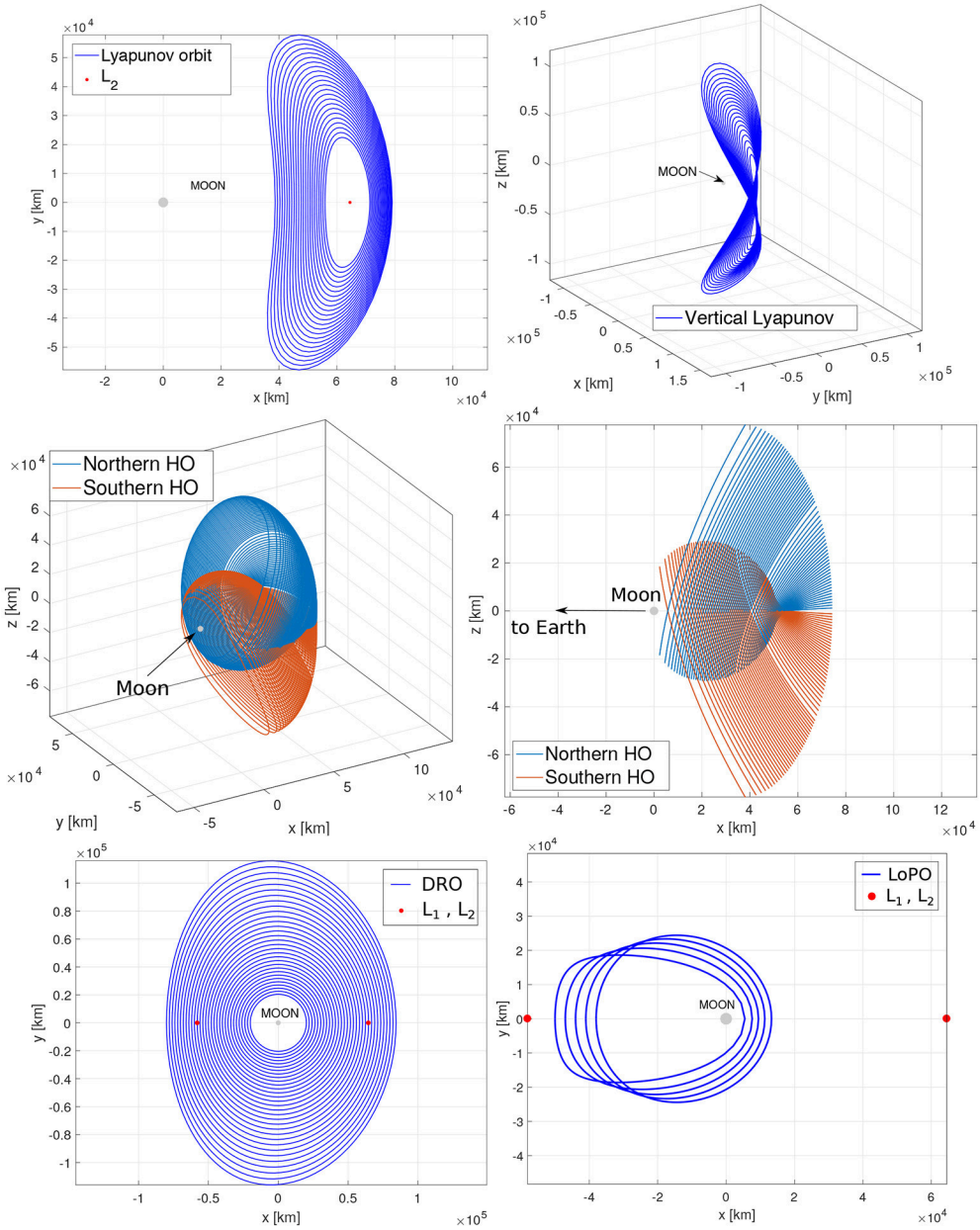

FIGURE 2 | Libration point orbit families, represented in the Moon-centered CRTBP reference frame.

2.2.2. Environment Model

In support to the coverage analysis, a meteoroid environment model is needed capable of 1) estimating the kinetic energy of the impactor from the light flash intensity detectable by the payload and of 2) representing the lunar impact time and space flux with accuracy. This model is then used to predict the number of meteoroid impacts that can be observed from a given orbit. Two different methods are used to estimate the detectable kinetic energy. These are referred to as the luminous efficiency method and the blackbody method. The first assumes a directly proportional relation between light emitted in the visible spectrum and the impactor kinetic energy. The second assumes that the impact flash emits radiation as a blackbody and the emitting surface scales with the size of the impact crater.

The luminous efficiency method used consists of the following steps.

1. Estimation of received energy flux (J/m^2) in the visible spectrum (Raab, 2002),

$$E_R = \frac{s_{\text{impact}}}{\tau A_{\text{lens}}} \frac{\overline{E_\gamma}}{\overline{\text{qe}}}, \tag{2}$$

where s_{impact} is a number in the range of signals detectable by one pixel of the camera, in e^-/pixel (see section 2.2.3 for more details), $\overline{\text{qe}}$ and $\overline{E_\gamma}$ are the mean quantum efficiency and mean photon energy over the sensor observation spectrum, respectively, A_{lens} is the area of the optic lens, and τ is a constant that accounts for lens transmissivity, transparency, and the light spreading across multiple pixels.

2. Estimation of the total emitted energy in the visible spectrum (Bellot Rubio et al., 2000),

$$E_V = 2\pi d^2 E_R, \tag{3}$$

where d is the distance between the payload sensor and the impact flash and radiation is assumed to be emitted into 2π steradians, as done in Suggs et al. (2014).

3. Estimation of the meteoroid kinetic energy (Bellot Rubio et al., 2000),

$$\text{KE} = \frac{E_V}{\eta}, \tag{4}$$

where η is the luminous efficiency in the visible spectrum.

The luminous efficiency is assumed to be in the range $\eta \in [5, 50] \times 10^{-4}$ (Bouley et al., 2012) and its nominal value is assumed to be $\eta = 20 \times 10^{-4}$ (Ortiz et al., 2015).

The blackbody method used consists of the following steps.

1. Estimation of the flux of electrons (e^-/m^2) generated in the sensor (Raab, 2002),

$$e_R = \frac{s_{\text{impact}}}{\tau A_{\text{lens}}}. \tag{5}$$

2. Estimation of the total flux of photons emitted in the visible spectrum, converted to an electron flux (Bouley et al., 2012),

$$e_T = \Delta t \int_{\lambda_1}^{\lambda_2} L(\lambda, T_F) \frac{\text{qe}(\lambda)}{E_\gamma(\lambda)} \, \text{d}\lambda, \tag{6}$$

with

$$L(\lambda, T_F) := \pi \frac{2hc^2}{\lambda^5 \left[\exp\left(\frac{hc}{\lambda k T_F} \right) - 1 \right]} \quad \text{and} \quad E_\gamma(\lambda) := \frac{h\,c}{\lambda}, \tag{7}$$

where Δt is the assumed duration of the impact, $\lambda \in [\lambda_1, \lambda_2]$ is the observed wavelength, and T_F is the assumed (constant) blackbody temperature of the flash. $L(\lambda, T_F)$ is Plank's law in $W/m^2/nm$ and $E_\gamma(\lambda)$ is the energy of a photon (γ).

3. Estimation of the emitting surface area, i.e., the effective area of the impact flash (Bouley et al., 2012):

$$S = 2\pi d^2 \frac{e_R}{e_T}. \tag{8}$$

4. Estimation of the impact's crater diameter,

$$D = \frac{2\sqrt{S/\pi}}{n_{\text{crater}}}, \tag{9}$$

where n_{crater} is the ratio between the diameter of the impact flash and respective crater (Bouley et al., 2012). Assuming that the impact is only detected by one pixel, D should be smaller than the ground sampling distance (GSD).

5. Estimation of the meteoroid kinetic energy, from Gault's crater law (Bouley et al., 2012; Madiedo et al., 2015),

$$\text{KE} = \left(\frac{D}{0.25 \rho_p^{0.167} \rho_t^{-0.5} g^{-0.165} (\sin\theta_i)^{1/3}} \right)^{1/0.29}, \tag{10}$$

where ρ_p and ρ_t are the projectile and target densities, g is the gravitational acceleration at the Moon, and θ_i is the impact angle with respect to the horizontal.

The nominal parameters assume $\Delta t = 10$ ms, which is the lower bound of the impact flashes detected on Earth (Bouley et al., 2012), $T_F = 2{,}700$ K, which is within the interval mentioned in Suggs et al. (2017), $n_{\text{crater}} = 1$, which is the minimum ratio assumed in Bouley et al. (2012), $\rho_p = 2000$ kg/m^3; $\rho_t = 3000$ kg/m^3 and $\theta_i = 45$ deg (Bouley et al., 2012). It should be noted that Δt, T_M, and n_{crater} are assumed as constants and not a function of the impactor kinetic energy, as no relation is known yet.

In both methods, for (perturbed) Keplerian orbits the distance between the impact flash and payload is assumed equal to the satellite altitude, i.e., the impact is assumed to occur at nadir. However, such assumption significantly affects the libration point orbits results. The number of impacts detectable closer to the edge of the payload FOV area is found to be approximately 90% lower than the number of impacts detectable at nadir. As such, the impacts are conservatively assumed to occur at the midpoint between nadir and the edge of the FOV-area.

The meteoroid impact flux model used in this work is that of Brown et al. (2002):

$$\log_{10}[f_E(\geq \text{KE}_E)] = 0.5677 - 0.9 \log_{10}(\text{KE}_E), \tag{11}$$

where f_E is the cumulative number of meteoroid impacts with Earth, per year, for kinetic energies equal or $>\text{KE}_E$. However, the meteoroid impact flux at the Moon is smaller than the meteoroid impact flux at Earth given by Equation 11, due to (1) the smaller surface area and (2) the weaker gravity field. As such, in order to scale down the flux at Earth to a meteoroid flux at the Moon, the Moon–Earth surface area ratio and a gravitational correction term for the Earth are taken into account. The gravitational correction term for the Moon is considered negligible (Bouley et al., 2012). The implemented gravitational correction considers both a larger effective target area of Earth and a larger impactor velocity relative to the Earth when compared to true physical values. The gravitational correction factors applied are (Suggs et al., 2014)

$$f_{\text{area}} = f_{\text{KE}} := A_{\text{eff}}/A_{\text{phy}} = 1 + v_{esc}^2/v^2, \tag{12}$$

where A_{eff} is the effective cross sectional area of the target body, A_{phy} is the physical cross sectional area of the target body, v_{esc} is the escape velocity at the target body, and v is the

impactor velocity, relative to the target body, before gravitational correction. Assuming $v_{esc} = 11$ km/s (Suggs et al., 2014) and $v = 17$ km/s (Bouley et al., 2012), the gravitational correction factors are $f_{\text{area}} = f_{\text{KE}} = 1.42$. The cumulative yearly meteoroid impact flux at the Moon is then:

$$f_M(\geq \text{KE}_M) = \frac{f_E(f_{\text{KE}}\text{KE}_M)}{f_{\text{area}}}\frac{R_M^2}{R_E^2}, \tag{13}$$

where KE_M is the impactor kinetic energy at the Moon and R_M and R_E are the radii of the Moon and Earth, respectively. For a given instrument FOV, the estimated impact rate detectable (impacts/year), as a function of time, is computed:

$$f_{\text{impacts}}(t) = \frac{1}{2}\frac{\text{FOV}_{\text{eff}}(t)}{4\pi R_M^2}\left[f_M(\geq \text{KE}_{\min}(t)) - f_M(\geq \text{KE}_{\max}(t))\right], \tag{14}$$

where $\text{FOV}_{\text{eff}}(t)$ is the observable nonilluminated Moon surface area, and $\text{KE}_{\min}(t)$, $\text{KE}_{\max}(t)$ are the minimum and maximum kinetic energy detectable, estimated using Equations (4–10). Equation 14 also includes a factor of 50% reduction of meteoroid impacts detectable to take into account possible occultations by lunar mountains (Koschny and McAuliffe, 2009). It should be noted that, using Brown's flux in this fashion, it is inherently assumed that the impact flux of meteoroids is uniform across the lunar surface and is evenly distributed throughout the year.

This meteoroid environment model is validated with data from the NELIOTA program: a telescope with 1.2 m diameter, capable of performing observations in the R-band ($\lambda \in [520, 796]$ nm). Since 16 impacts in 35 h observation time had been detected by November 2017, it is assumed that the program typically detects 0.46 impacts per hour. The visual magnitudes ranged from +11 to +6. Assuming that these values correspond to the limiting capacity of the detector, it is possible to estimate the minimum and maximum signal received at the detector. Then, it is possible to apply both kinetic energy estimation methods and predict the total number of impacts detectable from Earth ($d = 384,401$ km). For that purpose, the FOV-area of the telescope has been assumed as 1/3 of the entire (dark) Moon disk. Using the luminous efficiency method, a rate of between 0.35 and 0.12 impacts per hour is determined, assuming $\Delta t \in [10, 33]$ ms. Using the blackbody method, a rate of 0.13 impacts per hour is estimated. As such, the results obtained with both methods used in this work are the same order of magnitude as the detected in the NELIOTA program.

2.2.3. Payload Model

In order to determine if the signal of an impact flash is detectable by LUMIO's CCD sensor, the concept of signal-to-noise ratio (SNR) is used. Given the signal of the impact (s_{impact}) and the Poisson noise associated with all signals (σ), the SNR is defined as:

$$\text{SNR} = \frac{s_{\text{impact}}}{\sigma}, \tag{15}$$

where s_{impact} is measured in electrons generated in the CCD, per pixel (e^-/pixel), and σ is measured in electrons root-mean-square (rms). The Poisson noise of a signal is defined as $\sigma_i = \sqrt{s_i}$ and the total Poisson noise is given by

$$\sigma = \sqrt{\sum_i \sigma_i^2}. \tag{16}$$

The CCD sensor also has the possibility of amplifying the incoming signals by a gain factor G, at the expense of an excess-noise factor (ENF). When computing the SNR, all signals generated in the detector before the multiplication register must be multiplied by G and the corresponding noises by ENF, as follows:

$$\text{SNR} = \frac{\text{G}\, s_{\text{impact}}}{\sqrt{\text{ENF}^2\,\text{G}\,(s_{\text{impact}} + s_M + s_C + s_{DC}) + \sigma_{RON}^2 + \sigma_{OCN}^2 + \sigma_{QN}^2}}, \tag{17}$$

where $\sigma_i^2 = \text{G}\, s_i$, for the first four noise sources considered, which correspond to the incoming signals. In Equation (17), the noise sources that are taken into account are:

- σ_{impact}, the noise associated with the impact flash signal itself.
- σ_M, the Moon surface background noise, estimated at

$$\sigma_M^2 = \text{G}s_M = \text{G}\, e_{RM}\, A_{\text{lens}}\, \tau, \tag{18}$$

  where e_{RM} is the flux of photons received, due to the Moon background light emission, converted to an electron flux Bouley et al. (2012),

$$e_{RM} = \frac{S_{\text{Moon}} t_{\text{exp}}}{2\pi h^2}\int_{\lambda_1}^{\lambda_2} L(\lambda, T_M)\frac{\text{qe}(\lambda)}{E_\gamma(\lambda)}\,\text{d}\lambda, \tag{19}$$

  and h is the satellite's altitude, $T_M \approx 150$ K is the assumed (constant) blackbody temperature of the Moon, t_{exp} is the exposure time of the sensor and S_{Moon} is the emitting surface of the Moon, which is assumed equal to the Moon surface area observed by one pixel at nadir.
- σ_C, the cosmic background noise, estimated as follows (Raab, 2002),

$$\sigma_C^2 = \text{G}\, s_C = \text{G}\, p_{R_C}\, A_{\text{lens}}\, \tau\, \overline{\text{qe}}, \tag{20}$$

  where p_{R_C} is the flux of photons received at the sensor,

$$p_{R_C} = 2748\, t_{\text{exp}}\, A_{\text{IFOV}}, \tag{21}$$

  and it is assumed that the cosmic background noise corresponds to visual magnitude $m_V = +18$, so, 2748 γ/s/m^2 per square arc second are received by the sensor (Raab, 2002). A_{IFOV} is the sensor instantaneous FOV in square arc seconds.
- σ_{DC}, the CCD internal noise, known as Dark-Current, estimated as follows:

$$\sigma_{DC}^2 = \text{G}\, s_{DC} = \text{G}\,\text{DC}\, t_{\text{exp}}, \tag{22}$$

  where DC is the number of electrons generated in the sensor per second and per pixel, at a certain temperature.
- σ_{RON}, the CCD Read-Out Noise, given in **Table 4**.

TABLE 4 | LUMIO-Cam parameters, including those of the chosen detector (Teledyne e2V CCD201-20*).

Parameter	Acronym/ Symbol	Value	Units
Exposure time	t_{exp}	66	ms
Field of view	FOV	6 × 6	deg × deg
Observation spectrum	$[\lambda_1, \lambda_2]$	400–900	nm
Optics aperture	$d_{\varnothing}$	55	mm
Optics focal length	d_{FL}	127	mm
Optics lens reduction factor	τ	53.55†	%
Detector frame	N_{pixels}	1024 × 1024	pixels×pixels
Detector pixel size	d_{pixel}	13 × 13	μm × μm
Detector capacity	$\text{cap}_{(G)}$	8×10^4 (no gain) 73×10^4 (with gain)	electrons/pixel
Detector dark-current	DC	260 (at 20 deg C)	electrons/s/pixel
Detector read-out noise	σ_{RON}	43	electrons
Detector gain	G	2	–
Detector excess noise factor	ENF	$\sqrt{2}$	–
Detector Off-chip noise	off_n	20×10^{-9}	volt/$\sqrt{Hz}$
Detector output amplifier Responsivity	OAR	1.4×10^{-6}	electrons/volt
A/D bit number	N_{bits}	14	bits

*Datasheet accessed on July 23, 2017.
† Takes into account transmissivity, transparency and the light spreading across multiple pixels.

- σ_{OCN}, the CCD Off-Chip Noise, estimated as

$$\sigma_{OCN} = \frac{\text{off}_n}{\text{OAR}} \sqrt{\frac{\pi\, N_{\text{pixels}}}{t_{\text{exp}}}}, \tag{23}$$

  where off_n denotes the off-chip noise, OAR denotes the Output Amplifier Responsivity of the detector and N_{pixels} denotes the total number of pixels of the sensor.
- σ_{QN}, the A/D converter's noise, known as Quantisation Noise, estimated as

$$\sigma_{QN} = \frac{0.7\, \text{cap}_G}{2^{N_{\text{bits}}} \sqrt{12}}, \tag{24}$$

  where cap_G is the multiplication register capacity (detector with gain) and N_{bits} is the A/D converter number of bits.

Assuming that the impact flash can be detected for $\text{SNR} \geq \text{SNR}_{\text{min}}$, the determination of the minimum signal detectable was made by solving Equation (17) for $s_{\text{impact}} = s_{\text{min}}$, as

$$s_{\text{min}} = \frac{(\text{SNR}_{\text{min}}\, \text{ENF})^2 + \sqrt{(\text{SNR}_{\text{min}}\, \text{ENF})^4 + 4\text{Noise}\, \text{SNR}_{\text{min}}^2}}{2\text{G}}, \tag{25}$$

with

$$\text{Noise} := \text{ENF}^2(\sigma_M^2 + \sigma_C^2 + \sigma_{DC}^2) + \sigma_{RON}^2 + \sigma_{OCN}^2 + \sigma_{QN}^2. \tag{26}$$

On the other hand, the maximum impact flash signal detectable is given by the capacity of the detector (cap), given in **Table 4**. Given the payload characteristics presented in **Table 4** and considering that a signal is detectable for $\text{SNR}_{\text{min}} = 5$, the range of signals detectable by the CCD is given by $s = [s_{\text{min}}, s_{\text{max}}] = [292, 80000]$ e^-/pixel. These values apply for all altitudes, as $\sigma_M(\text{d})$ is found to be negligible with respect to other noise sources, and are then used to estimate the minimum and maximum kinetic energy detectable by the payload, using the methods presented in section 2.2.2.

3. LUMIO OPERATIVE ORBIT TRADE-OFF

3.1. Preliminary Analysis

The main characteristics of the candidate orbit types presented in section 2 are assessed and compared in order to eliminate non-feasible options by means of criteria EC.A.05-07 and EC.S.01-02 (see section 2.1). Results are presented in **Tables 5**, **6** for the (perturtbed) Keplerian and three-body orbits, respectively. The first column of the tables indicate the orbit family. The remaining five columns indicate the compatibility of the orbit family with criteria EC.A.05-07 and EC.S.01-02.

All orbital families presented in section 2, with the exception of L_1-circulating LYO, halos, and VO, have orbits which allow the monitoring of the lunar farside at night (EC.A.05), at least once per synodic month.

Selection criteria EC.S.01 requires the maximization of the total number of impacts detected, for which detailed modeling is required. However, it is possible to directly relate this criterion with the total lunar nightside observation time, per synodic month. This is easier to estimate than the total number of meteoroid detections. Recurring to orbital dynamics, it is thus used to assess preliminary performance with respect to EC.S.01. L_2-circulating orbits (i.e., LYO, halos, and vertical orbits) observe mostly the lunar farside and opposite lunar phases than an observer on Earth. As such, assuming that <50% illumination is required for impact flashes detection, these orbits can only observe 50% of the time the lunar nightside, per synodic month. Selenocentric orbits can observe both the lunar nearside and farside. However, for a resonant DRO, the sequence of lunar phases observed by the spacecraft can be very similar to those of L_2 orbits. It is conservatevely estimated a lunar nightside observation time of approximately 50%, per synodic month. An analogous reasoning is made for the remaining selenocentric orbits.

The orbital lifetime (EC.A.06) is dominated by the satellite duration before crashing on the Moon or escaping without means of recovery. It is only defined for (perturbed) Keplerian orbits. Since a mission lifetime larger than 1 year is required, this characteristic can be useful in assessing if that requirement is met. Nonetheless, if the natural lifetime of an orbit is smaller than 1 year, it is its maintenance Δv that determines the compliance with EC.A.06. LLO typically have an orbital lifetime smaller than 200 days, the exception being inclinations for which the orbit is frozen (Ramanan and Adimurthy, 2005). SSO orbital lifetime is rouglhy 300 days. On the other hand, the lifetime of ELO varies from 140 days, for $e = 0.45$, to 1,000 days, for $e = 0.01$ (Prado,

TABLE 5 | Trade-off of (perturbed) Keplerian orbits.

Orbit Type	Farside monitoring at night	Nightside observation time per synodic month (%)	Lifetime (days)	Total Δv budget (EC.S.02)	
				Maintenance Δv (m/s per year)	Accessibility from departure orbit
	EC.A.05	EC.S.01	EC.A.06	EC.A.06	EC.A.07
LLO	blue	green	red	yellow	red
	Possible	< 50	$[16, 160]^a$	$> 50^b$	Low — High
		(best case scenario)	($i < 90$ deg, $h = 100$ km orbit, NSG: $n = 100$)	($i \in [0{\cdot}360]$ deg, $h = 100$ km)	(> 150 m/s, from circular $h = 500$ km to $h = 100$ km)
ELO	blue	red	yellow	red	blue
	Possible	$[8, 92]$	$[140; 1,000]^c$	$> [120, 300]^b$	Low — Medium
		(function of line of nodes angle with Sun direction; $h_a = 10,000$ km, $i = 0$ deg and $e = 0.74$)	(function of decreasing e, from 0.45 to 0; $a = 7,000$ km)	($i = 0$ deg, $e = [0.1, 0.73]$, $a \approx 7,000$ km)	(> 72 m/s, from circular to elliptic; or > 4 m/s, between elliptic)
FO	blue	green	green	green	yellow
	Possible	If circular: < 50	$> 1000^d$	0^b	Low — Medium
		(best case scenario: low-altitude)	($e = 0$, $i = 78$ deg, $h = 100$ km)	($i = 40$ deg, $e = 0.6$, $880 \times 8,800$ km)	(≈ 140 m/s, from circular $h = 500$ km to $h = 1,000$ km)
SSO	blue	green	yellow	yellow	red
	Possible	< 50	$\approx 300^a$	$> 50^b$	High
			($i = 100$ deg, $h = 100$ km)	($i \in [0, 360]$ deg, $h = 100$ km)	(> 890 m/s, from $i = 90$ to $i = 125$ deg, at circular $h = 100$ km)

[a] *Ramanan and Adimurthy (2005)*; [b] *Whitley and Martinez (2016)*; [c] *Prado (2003)*; [d] *Elipe and Lara (2003)*.
green Exceeds requirements; blue Meets requirements; yellow Correctable deficiencies; red Unacceptable.
Accessibility Δv: Low → < 200 m/s; Medium → [200, 600] m/s; High → > 600 m/s.

TABLE 6 | Trade-off of CRTBP orbits.

Orbit Type	Farside monitoring at night	Nightside observation time per synodic month (%)	Total Δv budget (EC.S.02)	
			Maintenance Δv (m/s per year)	Accessibility from departure orbit
	EC.A.05	EC.S.01	EC.A.06	EC.A.07
LYO	blue	green	blue	red
	Possible if L_2 orbit	< 50	$[15; 18]^a$	Medium – High
		(small orbit)	(L_2 orbit)	(Plane change maneuver required)
HO	blue	green	blue	green
	Possible if L_2 orbit	< 50	$[0; 55]^a$	Low
		(Not too close to the Moon)	(L_2 orbit, smaller for orbits closer to the Moon)	(< 140 m/s, departing from elliptic selenocentric orbit)
VO	blue	green	yellow	yellow
	Possible if L_2 orbit	< 50	$\sim 88^b$	Low – Medium
		(small orbit)	(L_2 orbit, not optimized)	(< 300 m/s from elliptic selenocentric orbit)
DRO	blue	green	green	red
	Possible	< 50	$[3, 5]^a$	Medium – High
		(resonant state)	(large orbit)	(Plane change maneuver required)
LoPO	blue	green	yellow	red
	Possible	< 50	Unknown	Medium – High
		(resonant state)		(Plane change maneuver required)

[a] *Folta et al. (2015)*; [b] *Grebow (2006)*.
green Exceeds requirements; blue Meets requirements; yellow Correctable deficiencies; red Unacceptable.
Accessibility Δv: Low → < 200 m/s; Medium → [200, 600] m/s; High → > 600 m/s.

2003). A lifetime larger than 1 year is only possible for a low-eccentricity orbit of $e < 0.15$. Lastly, FO have been estimated to last more than 3 years (Elipe and Lara, 2003).

However, it is mainly the maintenance Δv that dictates compliance with EC.A.06, the exception being frozen orbits that have orbital lifetimes larger than 1 year and, theoretically, do not need intervention (Whitley and Martinez, 2016). There are some ELO and SSO with low eccentricities which also have longer-than-1-year orbital lifetimes, but their coverage characteristics quickly degenerate with time. For highly elliptic ELO, the station-keeping Δv can be larger than 300 m/s, while for SSO and LLO ($h = 100$ km) it may overcome 50 m/s per year (Whitley and Martinez, 2016). For low-eccentricity orbits, an estimation is done at 120 m/s per year. The maintenance Δv budget for most of the CRTBP orbits has been taken from (Folta et al., 2015). These were computed with a long-term strategy of 12 orbital revolutions as nominal guidance, including random errors in position, velocity and impulsive correction maneuvers, for an average of 500 trials. VO require 88 m/s station-keeping (S/K) Δv per year (Grebow, 2006). No information regarding LoPO maintenance is available.

The accessibility from the departure orbit (EC.A.07) is measured in terms of the Δv spent for the transfer to the operational orbit. For Keplerian orbits, the optimal transfer Δv can easily be estimated resorting the orbital dynamics knowledge of the two-body dynamics. For three-body orbits, the optimal transfer Δv needs to be computed numerically, e.g., using optimization methods. As such, in this preliminary trade-off, only optimal transfers between Keplerian orbits are computed. For three-body orbits, representative values found in literature are assumed.

The amount of propellant spent in reaching the operational orbit and maintaining it are two quantities that should be assessed together, given that there is only a limit for their sum: the total Δv budget (EC.S.02). This should be <200 m/s to comply with EC.A.06-07 and should be the smallest possible to comply with EC.S.02.

As a result of the preliminary trade-off analysis, summarized in **Tables 5**, **6**, we consider (1) Circular frozen orbits with $h \in [100, 1,000]$ km and $i \in [50, 90]$ degrees (which is chosen to reduce plane change cost); (2) L_2-circulating halo orbits; and (3) L_2-circulating vertical orbits. The trade-off is conducted assuming that the Lunar Orbiter would deploy LUMIO either in a 500 km-altitude circular parking orbit or a 200 by 15,000 km lunar parking orbit. The inclination of this orbit is assumed to be between 50 and 90 degrees.

These orbits have been modeled in order to perform the following coverage analysis. Preliminary lunar frozen orbits have been found by numerically minimizing the amplitude of the osculating eccentricity, taking into account third body perturbations from Earth and the lunar non-spherical gravity model GL0660B (Konopliv et al., 2013), up to degree and order 7. The initial conditions for Halo and Vertical orbits have been found in the CRTBP, using a time-varying targeting scheme. All orbits have been propagated for one synodic month.

3.2. Coverage Analysis

The evaluation criteria related to lunar meteoroid impacts are applied, and a meteoroid impact flashes coverage analysis is performed. The coverage analysis is characterized by the interaction between three modules:

1. **FOV-area module**. The surface area that an instrument can observe (FOV-area), at one instant or extended period of time, defines the coverage of the central body. The FOV-area of LUMIO is computed considering the instrument working principles, the LUMIO-Cam characteristics, and the actual curvature of the central body. The payload FOV and the S/C position are the two main inputs of this module. Furthermore, is is assumed that the S/C points toward nadir.
2. **Lunar nightside monitoring module**. The effective FOV-area is defined as the fraction of the FOV-area that it is not illuminated by the Sun. Since lunar impact flashes can only be detected on the lunar nightside, this module allows the determination of the lunar portion in which meteoroids flashes may be actually detected. The main input is the Sun–Moon–spacecraft angle (β), which determines the illumination conditions of the FOV-area, such that

$$\mathrm{FOV}_{\mathrm{eff}}(t) = \begin{cases} f_{\mathrm{dark}}\,\mathrm{FOV}_{\mathrm{area}}, & \text{if} \quad \beta(t) \geq 90 \text{ deg}, \\ 0, & \text{if} \quad \beta(t) < 90 \text{ deg}, \end{cases} \tag{27}$$

   where $f_{\mathrm{dark}}(t) = \beta(t)/180$ is the percentile dark lunar portion, with $\beta \in [0, 180]$ deg. In Equation (27), the effective FOV-area is zero when $f_{\mathrm{dark}} < 0.5$, thus no observations can be performed in this range.
3. **Meteoroid environment module**. Given the range of signals detectable by the payload at each instant and an altitude profile, this module can independently determine the range of kinetic energies detectable by LUMIO (see section 2), for each candidate orbit. Given also the effective FOV-area, the total number of meteoroids detected in the kinetic energy range $[\mathrm{KE}_{\mathrm{min}}, \mathrm{KE}_{\mathrm{max}}]$, over the mission lifetime, is determined through (1) Estimation of the impact flux (indicator of impacts per year) visible in the satellite effective FOV-area, as function of time (Equation 14); (2) Estimation of the average impact flux visible in the satellite effective FOV-area, during one synodic month by means of an integral function; and (3) Estimation of the total number of meteoroids detected over the mission lifetime (1 year).

3.2.1. Coverage Trade-Off

Figures 3A,B show the minimum and maximum kinetic energy detectable by the LUMIO-Cam from a frozen orbit, for the luminous efficiency and blackbody methods. Only the inclinations which allow the maximum number of detections, per semi-major axis, are presented for brevity, but the results shown are representative of all inclinations. With both methods, $\mathrm{KE}_{\mathrm{min}}$ and $\mathrm{KE}_{\mathrm{max}}$ increase with altitude, but they considerably disagree in the kinetic energy ranges detectable for frozen orbits. The luminous efficiency method estimates that $\mathrm{KE}_{\mathrm{min}} \in [10^{-13}, 10^{-9}]$ kton TNT and $\mathrm{KE}_{\mathrm{max}} \in [10^{-10}, 10^{-7}]$ kton TNT, while the blackbody method estimates that $\mathrm{KE}_{\mathrm{min}} \in [10^{-18}, 10^{-12}]$ kton TNT and $\mathrm{KE}_{\mathrm{max}} \in [10^{-12}, 10^{-8}]$ kton TNT.

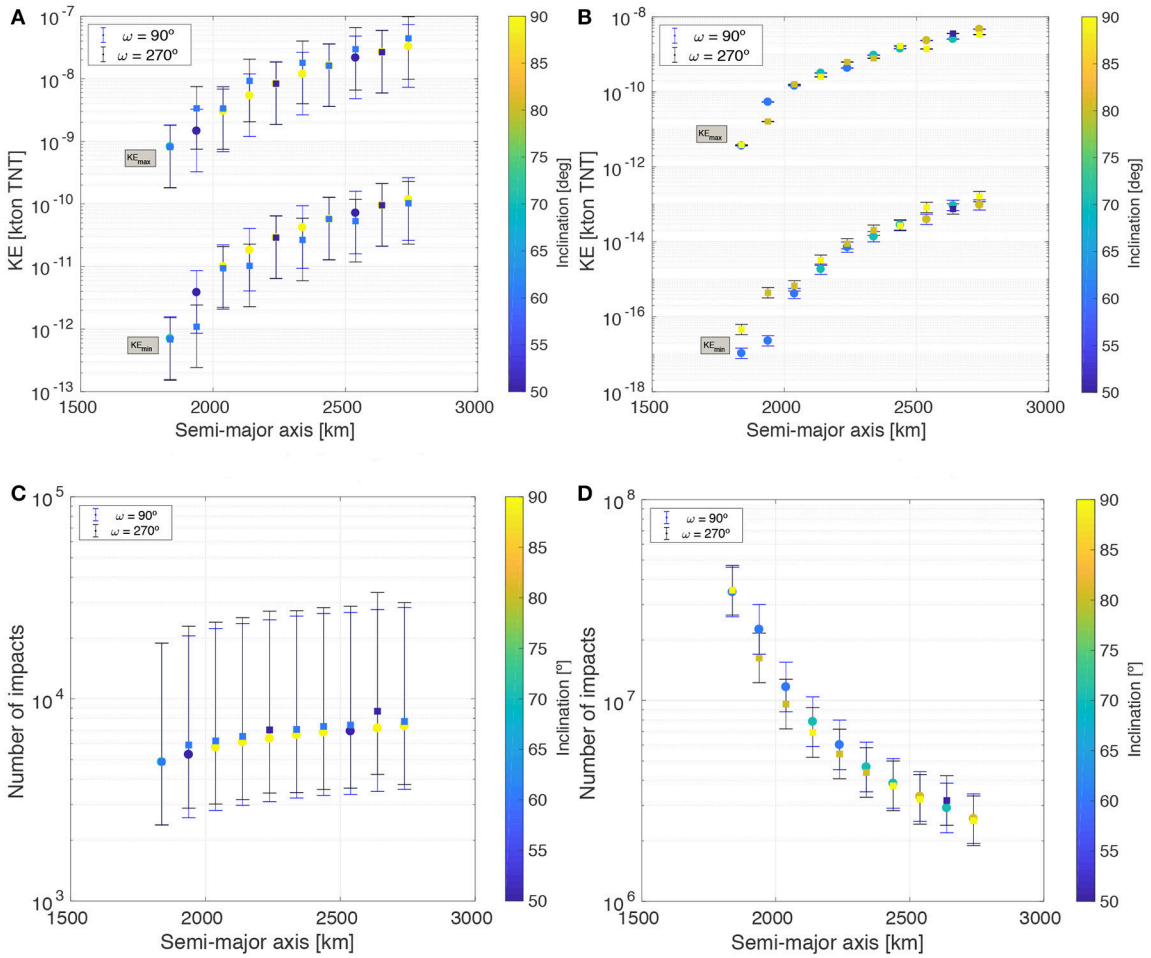

FIGURE 3 | Estimation of detectable kinetic energy range and meteoroid impacts for frozen orbits. **(A)** Luminous efficiency method. **(B)** Blackbody method. **(C)** Detected meteoroids (LE). **(D)** Detected meteoroids (BB).

Figures 3C,D show the corresponding total number of meteoroid detections during the mission lifetime, where the luminous efficiency method predicts more meteoroid detections for increasing altitude, while the blackbody method predicts the opposite trend. This is because, using the luminous efficiency method the number of impacts detectable is actually proportional to $h^{0.2}$ and with the blackbody method the number of impacts detectable is proportional to $h^{-1.1}$, given that, for low altitudes, the FOV-area is proportional to h^2 (see section 2.2.2). Furthermore, due to the disagreement in the estimation of KE_{min}, the luminous efficiency method predicts the detection of much less meteoroids than the blackbody method. The former estimates between 4 and 9 thousands meteoroid detections during the mission lifetime for a frozen orbit, while the later estimates roughly between 2×10^6 and 2×10^8 meteoroids during the same period. Given the LUMIO-Cam optical properties, the estimation made by the luminous efficiency method is more in alignment with the one presented in Oberst et al. (2011). On the other hand, the blackbody method overestimates the number of impacts detectable from a frozen orbit by at least two orders of magnitude.

Figures 4A,B show the minimum and maximum kinetic energy detectable by the LUMIO-Cam for the candidate three-body orbits and for the two kinetic energy estimation methods applied. The black lines represent the kinetic energy requirements as per EC.A.03-04. Being these energies defined at Earth, they are scaled trough the Earth gravitational correction factor (section 2.2.2) to obtain 7×10^{-7} and 7×10^{-2} kton TNT at the Moon. The methods disagree with respect to the estimated kinetic energy range, especially regarding KE_{max}. The blackbody method predicts a wider kinetic energy range, with smaller KE_{min} and larger KE_{max}.

The difference between the two methods, for three-body orbits, when it comes to the number of meteoroid detections, is not as prominent as for frozen orbits. **Figures 4C,D** show the corresponding total number of meteoroid detections during the mission lifetime. As can be seen in this figure, for halos and vertical orbits, the number of impacts estimated by both

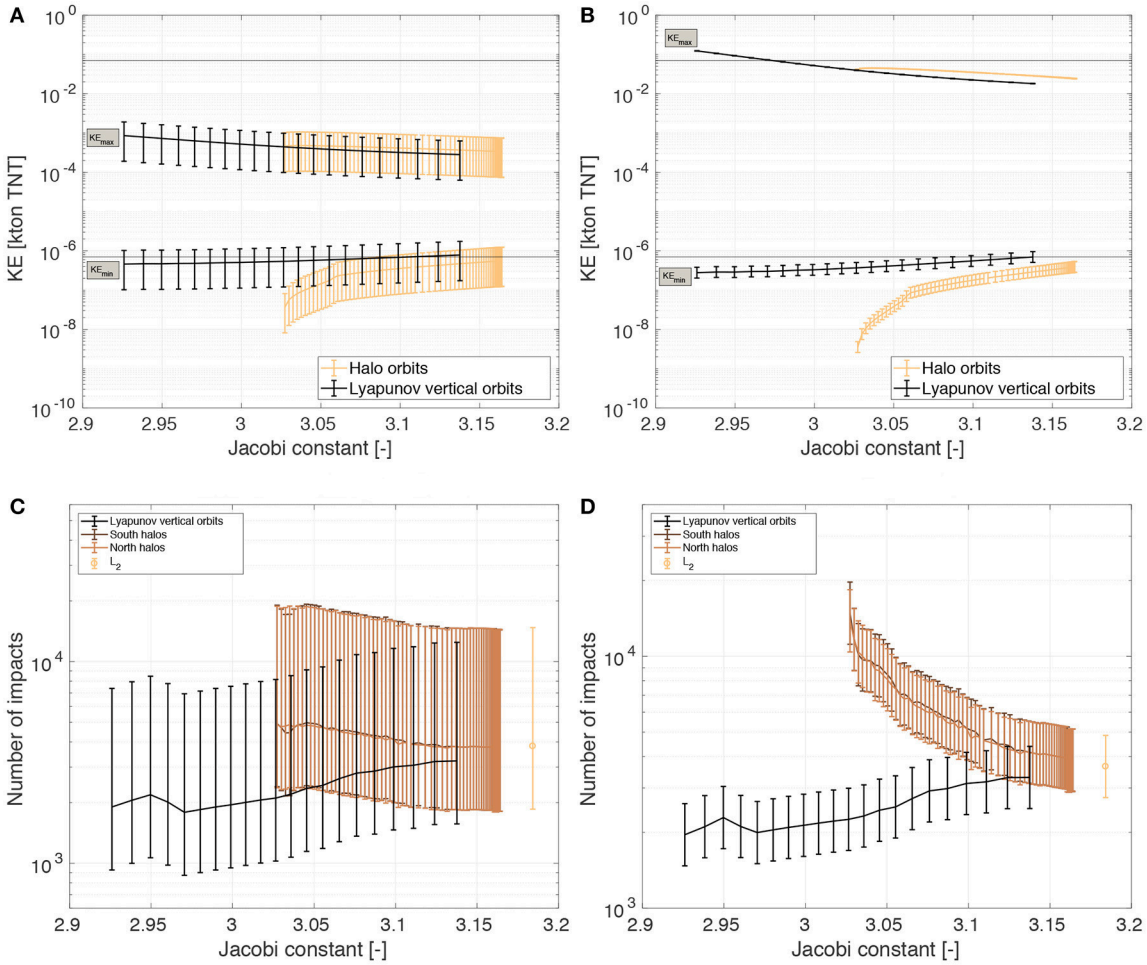

FIGURE 4 | Estimation of detectable kinetic energy range and meteoroid impacts for the considered three-body orbits over the mission lifetime. Black lines represent the kinetic energy limits as set in the requirements (corrected for the Moon). **(A)** Luminous efficiency method. **(B)** Blackbody method. **(C)** Detectable meteoroids (LE). **(D)** Detectable meteoroids (BB).

methods is in the same order of magnitude (between 10^3 and 10^4). This is because, for higher altitudes, the methods are in agreement with respect to KE_{min}, parameter which drives the number of meteoroid detections. The total number of detections estimated for a satellite permanently at the Earth–Moon L_2 is also presented, for comparison. The results at L_2 represent a limit case for L_2-circulating candidate orbits.

The error bars shown here for the luminous efficiency method are associated with the luminous efficiency uncertainty, while the errors bars shown for the blackbody method are a 1σ error related to the magnitude measured by the CCD sensor (Raab, 2002). The blackbody method results show smaller error bars than the luminous efficiency results, but it inherently has more assumptions than the luminous efficiency method and the possible errors associated with those assumptions are not represented in the results shown here.

The results presented here do not account for scattered light from the Moon dayside, consequent detector blooming, and impact flash detection redundancy. In fact, scattered light and blooming may potentially hinder the detection of impact flashes and influence the minimum detected kinetic energy estimation the most, as opposed to the maximum detected kinetic energy. Impact flash detection redundancy can be dealt with in two ways: (1) by slightly defocussing the LUMIO-Cam, in order to avoid false positives; or (2) by adding a second detector to the camera. In both cases, the minimum kinetic energy estimation is also affected. However, to compensate for the loss of signal, the camera sensitivity can be increased with gains $G > 2$. These issues affect neither the assessment of orbit types made in this work nor the validity of the coverage trade-off that follows. These issues will be taken into account in future mission design phases.

The coverage trade-off accounts for evaluation criteria EC.A.01-04. **Table 7** displays the orbit trade-off for the results of both luminous efficiency method and blackbody methods, as

TABLE 7 | First orbit trade-off, given the results of both luminous efficiency method and blackbody method.

Orbit	Allows observations in $KE \in 10^{-[6,1]}$ kton TNT	$N_{impacts} \geq 240$	$N_{impacts} \geq 2$ for $KE \in 10^{-[4,1]}$ kton TNT	$N_{impacts} \geq 100$ for $KE \in 10^{-[6,4]}$ kton TNT
	EC.A.01	EC.A.02	EC.A.03	EC.A.04
FO	red None	green All assessed	red None	red None
(NR)HO	blue All assessed	green All assessed	green All assessed	green All assessed
VO	blue All assessed	green All assessed	green All assessed	green All assessed

green Exceeds requirements; blue Meets requirements; yellow Correctable deficiencies; red Unacceptable.

the two sets of results obtained lead to identical conclusions on orbits feasibility. Both methods exclude frozen orbits (1 out of 4 acceptance criteria related to meteoroid impacts met), while both halo and vertical orbits meet all acceptance criteria. The halo family has the additional advantage of allowing a constant visibility of the spacecraft from Earth and a quasi-resonance 2:1 with the synodic period.

3.3. Detailed Analysis

It has been shown that remotely detecting flashes is the only technically and economically viable option for a CubeSat to monitor meteoroid impacts on the lunar surface. When considering the conclusions of the preliminary trade-off (section 3.1), the coverage trade-off (section 3.2), the mission type flight heritage, and solar eclipse occurrences, the Earth–Moon L_2 halo family is baselined for LUMIO mission. The vertical Lyapunov orbit family is selected as back-up plan and it is not detailed in this paper.

The LUMIO mission is divided in 4 well defined phases (refer to **Figure 5**),

1. Parking:
   (a) Starts when the lunar orbiter deploys LUMIO on the prescribed selenocentric elliptic parking orbit (orbital elements of the parking orbit are shown in **Table 8**);
   (b) Ends when LUMIO performs the Stable Manifold Injection Maneuver (SMIM);
   (c) Lasts 14 days.
2. Transfer:
   (a) Starts when LUMIO completes the SMIM;
   (b) Ends when LUMIO performs the Halo Injection Maneuver (HIM);
   (c) Lasts 14 days.
3. Operative:
   (a) Starts when LUMIO completes the HIM;
   (b) The primary mission modes during the operative phase are *Science Mode* and *Navigation and Engineering Mode* (or Nav&Eng), that alternate between every other orbit;
   (c) Ends after 1 year of operations.
4. End of Life (EoL):
   (a) Starts with de-commission of all (sub)systems;
   (b) Ends when the EoL maneuver is correctly performed for safe disposal of the spacecraft.

3.3.1. Earth–Moon L_2 Halos in High-Fidelity Model

A set of quasi-periodic halo orbits (sometimes referred here as quasi-halos or quasi-halo orbits) about Earth–Moon L_2 are found by employing the methodology described in Dei Tos and Topputo (2017a). Fourteen quasi-halo orbits are computed in the high-fidelity roto-pulsating restricted n-body problem (RPRnBP) and saved as SPICE[2] kernels (see Dei Tos and Topputo, 2017a for more details on frames and models). The initial feeds to compute the quasi-halo samples are Earth–Moon three-body halos at 14 different Jacobi constants, ranging from $C_j = 3.04$ to $C_j = 3.1613263$. The latter value corresponds to the one assumed for the very first iteration of the activities. All orbits are computed starting from 2020 August 30 00:00:00.000 TDB. Although quasi-halos, shown in **Figure 6**, are computed for a fixed initial epoch, the persistence of libration point orbits in the solar system ephemeris model allows wide freedom in the refinement algorithm also for mission starting at different epochs (Dei Tos and Topputo, 2017b).

Quasi-halo orbits of **Figure 6** are all possible LUMIO operative orbits. As the orbit becomes more energetic (or as its CRTBP Jacobi constant decreases), the quasi-halo exhibits a wider range of motion both in terms of a) Moon range and of b) geometrical flight envelope about the corresponding CRTBP trajectory. The latter trend is disadvantageous when a hard pointing constraint must be respected (e.g., Moon full disk on optical instrument). On the other hand, the lunar distance places a constraint on the minimum FOV for the optical instrument on board LUMIO to be able to resolve the Moon full disk at any location along the quasi-halo, compatibly with evaluation criteria EC.S.03. Bar charts in **Figure 7** show the ranges from the lunar surface to the quasi-halo samples. For given values of

[2]SPICE is NASA's Observation Geometry and Information System for Space Science Missions (Acton Jr, 1996; Acton Jr et al., 2018). The toolkit is freely available through the NASA NAIF website http://naif.jpl.nasa.gov/naif/. Last downloaded on February 7, 2018.

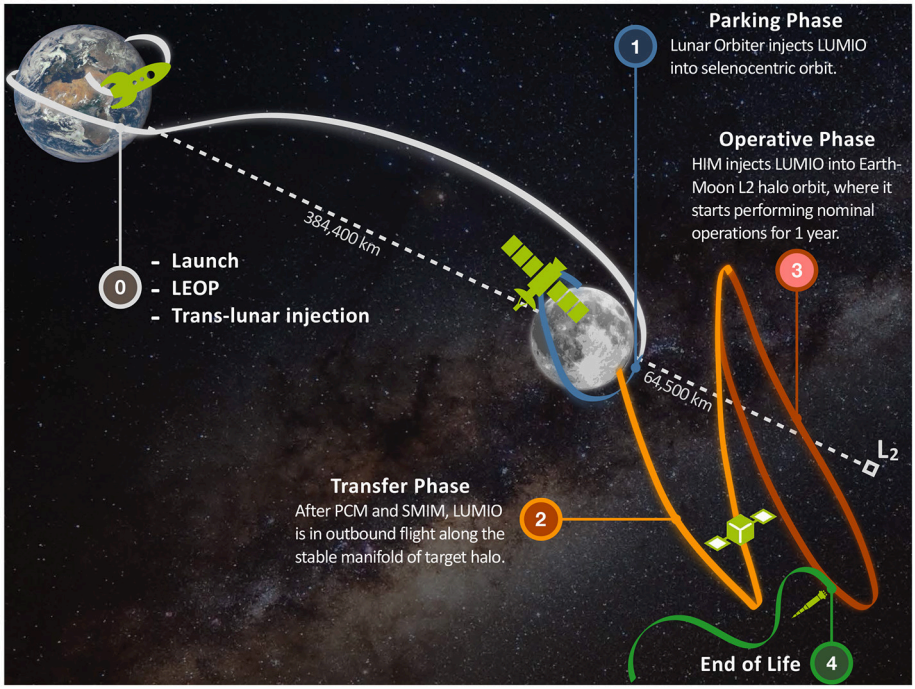

FIGURE 5 | Outline of LUMIO mission phases.

TABLE 8 | Main parameters for the transfer phase.

Parameter	h_p	h_a	i	Ω	ω	ϑ	T	t_{po}	t_{sm}
Value	200	14964.2	78.1	30.0	301.2	≈ 0	22.42551	0.7406	7.5397
Units	[km]	[km]	[deg]	[deg]	[deg]	[deg]	[hours]	[adim]	[adim]

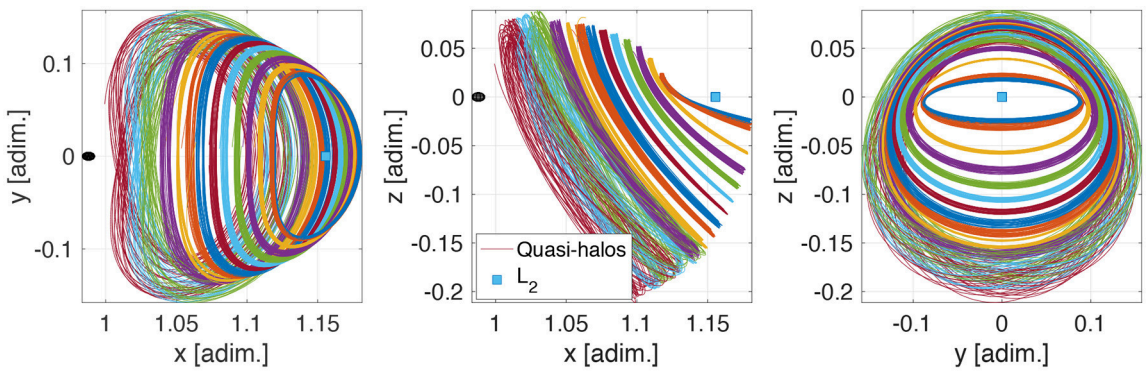

FIGURE 6 | Projection of Earth–Moon L_2 quasi-halos in the roto-pulsating frame. (adim. stands for nondimensional variable).

the camera FOV, simple trigonometric calculations provide the minimum distance above which the Moon disk is entirely seen by the instrument. The wider the FOV, the closer LUMIO can get to the Moon still being able to see its full disk. The horizontal dashed lines in **Figure 7** indicate this distance for different values of FOV in degrees.

3.3.2. Orbital Transfer

The transfer phase of LUMIO is done entirely in the CRTBP. Free transport mechanisms are leveraged to reach a target halo. Specifically, intersection in the configuration space is sought between the halo stable manifolds and the selenocentric injection orbit in which LUMIO is deployed by the lunar orbiter. Since

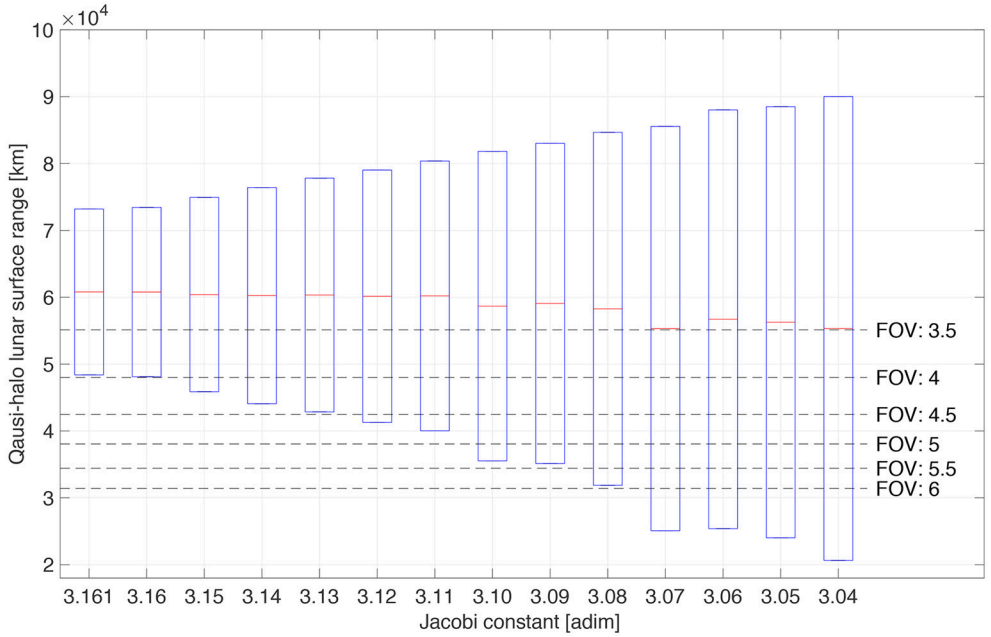

FIGURE 7 | Bars for quasi-halos ranges from lunar surface.

the sought intersection occurs only in configuration space, a maneuver is necessary for orbital continuity. This maneuver places the spacecraft on the stable manifold of the target halo and is thus called stable manifold injection maneuver (SMIM), $\Delta \boldsymbol{v}_{\text{SMIM}}$. The transfer phase starts when the SMIM is executed, and ends after the halo injection maneuver (HIM), $\Delta \boldsymbol{v}_{\text{HIM}}$, inserts the S/C into the target halo orbit. The aim of the transfer design analysis is to find the parameters of the injection orbit and the stable manifold that lead to a minimum $\Delta \boldsymbol{v}_{\text{SMIM}}$ at the intersection. The optimization problem is stated and solved with a NLP method.

It is convenient to briefly recall the methodology used to numerically compute the invariant manifolds in the CRTBP. This approach relies on finding a linear approximation of the manifold in the neighborhood of an orbit. An algorithm is implemented that scans the stable manifold space by varying the time along the originating halo, t_{po}, and the time along the stable manifold, t_{sm}. Once t_{po} and t_{sm} are specified, the stable manifold is completely determined (Topputo, 2016). t_{po} uniquely specifies a state along the halo, $\boldsymbol{x}(t_{\text{po}})$. At $\boldsymbol{x}(t_{\text{po}})$, the invariant manifolds are locally spanned by the stable and unstable eigenvectors of $M(t_{\text{po}})$, the monodromy matrix associated to $\boldsymbol{x}(t_{\text{po}})$. The initial conditions used to compute the stable manifold are $\boldsymbol{x}_{s_0} = \boldsymbol{x}(t_{\text{po}}) \pm \varepsilon \boldsymbol{v}_s$, where $\boldsymbol{v}_s$ is the stable eigenvector of $M(t_{\text{po}})$ and ε is a small displacement perturbing in the stable direction, whereas the $\pm$ discriminates which of the two branches of the manifold has to be generated. As for ε, it should be small enough to preserve the local validity of the linear approximation, but also large enough to prevent from long integration times needed to compute the manifold. In this work, $\varepsilon = 10^{-6}$ has been used, consistently with the arguments in Gómez et al. (1993). t_{sm} is the duration $\boldsymbol{x}_s$ is flown in backward time. The stable manifold state yields:

$$\boldsymbol{x}_s = \boldsymbol{\varphi}(\boldsymbol{x}_{s_0}, 0; -t_{\text{sm}}), \tag{28}$$

where $\boldsymbol{\varphi}$ is the flow of the CRTBP from $\boldsymbol{x}_{s_0}$ to $-t_{\text{sm}}$. An outline of the transfer design logic is shown in Algorithm 1. The problem of transfer design with an optimal impulsive maneuver can be formally stated as a constrained minimization:

$$\min_{\boldsymbol{y}} J(\boldsymbol{y}) \quad s.t. \quad \begin{cases} \boldsymbol{c}_{eq} &= \boldsymbol{0}, \\ \boldsymbol{c} &\leq \boldsymbol{0}, \end{cases} \tag{29}$$

where

$$\boldsymbol{y} = (h_p, h_a, i, \Omega, \omega, \theta, t_{\text{po}}, t_{\text{sm}}), \qquad J(\boldsymbol{y}) = \|\Delta \boldsymbol{v}_{\text{SMIM}}\|, \tag{30}$$

$$\boldsymbol{c}_{eq} = \begin{pmatrix} \boldsymbol{r}_t - \boldsymbol{r}_s \\ h_p - 200 \end{pmatrix}, \qquad \boldsymbol{c} = \begin{pmatrix} 500 - h_a \\ h_a - 15,000 \end{pmatrix}; \tag{31}$$

where $\boldsymbol{r}_t$ is the position along the injection orbit, and $\boldsymbol{r}_s$ is the position along the stable manifold according to Equation (28). The minimization is solved with an *active-set* algorithm. Algorithm 1 is applied to all halos in the Jacobi energy range detailed above. Note that if the inclination of the injection orbit is found to be outside of the admissible range ($[50, 90]$ deg), a plane chance maneuver (PCM) is added. The transfer parameters to quasi-halo generated by $C_j = 3.09$ are shown in **Table 8**. As expected, the SMIM occurs at the periselene of the injection orbit ($\theta \approx 0$).

3.3.3. Station-Keeping

In many cases, it is not strictly necessary for the spacecraft to move precisely along the nominal trajectory to accomplish

Algorithm 1 Transfer design.

procedure INITIALIZATION
  Set the CRTBP as default dynamical model
  Select C_j of target halo orbit
  Select manifold branch flying toward the Moon (i.e., left branch for L_2 LPOs)
end procedure
procedure MANIFOLD SCAN FOR INITIAL GUESS GENERATION
  Set bounds for the time along the target halo, $t_{\text{po}} \in [0, T]$
  Set maximum time along the stable manifold, $t_{\text{sm}}^{(\max)}$
  Discretize t_{po} by $\mathrm{d}t_{\text{po}}$ to get n_t discrete values
  Initialize vector $\boldsymbol{\tau} \in \mathbb{R}^{n_t \times 3}$
  for $t_{\text{po}} = 0 \rightarrow T$ by $\mathrm{d}t_{\text{po}}$ with index k **do**
    Get stable manifold state, $\boldsymbol{x}_s$, for current t_{po} and $t_{\text{sm}}^{(\max)}$ ▷ See Equation (28)
    Find t_{sm} at which altitude, h_p, is closest to 200 km
    Store $(t_{\text{po}}, t_{\text{sm}}, h_p)$ in the k-th row of vector $\boldsymbol{\tau}$
  end for
end procedure
procedure TRANSFER MANEUVER
  Initialize vector $\boldsymbol{\Gamma} \in \mathbb{R}^{n_t \times 16}$
  loop in $\boldsymbol{\tau}$ with index j
    repeat
      Randomly initialize injection orbit elements in $\boldsymbol{e} = (h_a, i, \Omega, \omega, \theta)$
      Solve for $\Delta\boldsymbol{v}_{\text{SMIM}}$ using $\boldsymbol{e}$ and j-th row of $\boldsymbol{\tau}$ as first guess ▷ Equation (29)
    until convergence is attained
    if $i^{(\text{opt})} \notin [50, 90]$ deg **then**
      Select nearest target inclination of parking orbit, i_{pk} ▷ See section 3.1
      Schedule plane rotation around apoaxis by $\Delta i = |i_{pk} - i^{(\text{opt})}|$
      Compute plane rotation maneuver at apoaxis, $\Delta\boldsymbol{v}_{\text{pc}}$
      Compute updated Ω_{pk} and ω_{pk} of parking orbit
    else
      Set $\Delta\boldsymbol{v}_{pc} = \boldsymbol{0}$
      Set parking orbits elements equal to transition orbit elements
    end if
    Store optimization results, $(\Delta\boldsymbol{v}_{\text{SMIM}}, \Delta\boldsymbol{v}_{\text{pc}}, \boldsymbol{y}^{(\text{opt})}, \Omega_{pk}, \omega_{pk})$, in $\boldsymbol{\Gamma}$ j-th row
  end loop
end procedure

mission objectives. Indeed, once the nominal orbit is determined, it is desired to maintain the spacecraft within some region (e.g., torus- or box-shaped) about the reference path. Non-modeled perturbations and errors will cause the spacecraft to drift from the nominal path, and the unstable nature of the libration point orbits will further amplify the deviation. Assuming discrete and impulsive corrections, the station-keeping problem consists in finding the required corrective maneuvers in terms of magnitude, direction, and timing of each Δv. In optimal station-keeping problems, the total Δv budget is minimized.

In light of the limited Δv capability, fuel consumption for station-keeping (S/K) around the operative orbits will be a critical factor for mission sustainability. Taking advantage of the generated orbits as reference trajectories, a computationally efficient Monte-Carlo routine is devised for estimation of the cost of each S/K maneuver. An effort is directed toward the development of a station-keeping strategy that can be used to maintain CubeSats near such nominal LPOs.

The S/K cost is estimated by employing the *target points method* (TPM) first introduced in Dwivedi (1975), then adapted to the problem of LPOs by Howell and Pernicka (1993), and finally used for JAXA's EQUULEUS mission analysis (Oguri et al., 2017). A massive Monte-Carlo simulation is performed with 10,000 samples, considering the impact of the injection, tracking, and maneuver execution processes on the nominal orbit determined in the presence of solar radiation pressure and gravity of the main solar system celestial bodies (i.e., Sun, 8 planets, the Moon, and Pluto). To precisely simulate a realistic trajectory,

1. The initial conditions of the quasi-halos are altered to account for orbit insertion error.
2. Tracking windows are considered in which orbit determination (OD) campaigns modify the actual knowledge of the spacecraft state by means of optical measurements and non-linear filtering. Because of various uncertainties in the OD process, the spacecraft position and velocity are never

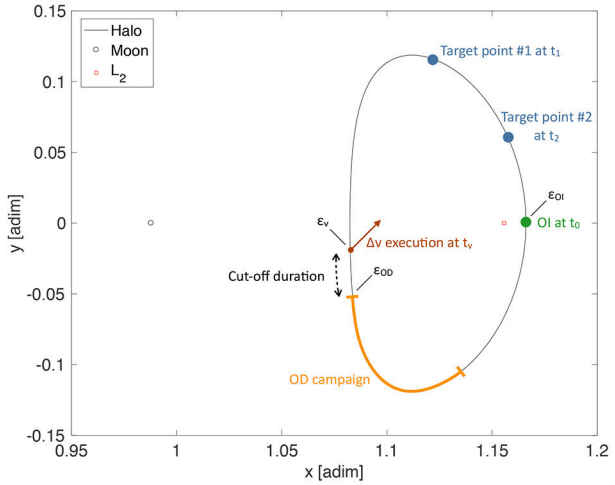

FIGURE 8 | Overview of S/K simulation process and target points method.

Algorithm 2 Cost estimation for of station-keeping along a reference quasi-halo.

function DVSK(t_0, t_f, Φ, Δt_v, Δt_c, Δt_i, σ^2_{OI}, σ^2_{OD}, σ^2_{EX}, Q, R)
  $t \leftarrow t_0$
  Generate six-dimensional OI error, $\boldsymbol{\varepsilon}_{OI} \sim \mathcal{N}(0, \sigma^2_{OI})$
  OI: $\delta \boldsymbol{x}_{\text{true}} \leftarrow \boldsymbol{\varepsilon}_{OI}$
  while $t \leq t_f$ & $\delta \boldsymbol{x}_{\text{true}} \leq 10,000$ km **do**
    $t_v \leftarrow t + \Delta t_v$
    $t_c \leftarrow t_v - \Delta t_c$
    $t_i \leftarrow t + \Delta t_i$
    $\delta \boldsymbol{x}_{\text{true}} \leftarrow \Phi(t, t_c)\delta \boldsymbol{x}_{\text{true}}$
    Generate six-dimensional OD error, $\boldsymbol{\varepsilon}_{OD} \sim \mathcal{N}(0, \sigma^2_{OD})$
    OD: $\delta \boldsymbol{x}_c \leftarrow \delta \boldsymbol{x}_{\text{true}} + \boldsymbol{\varepsilon}_{OD}$, where $\delta \boldsymbol{x}_c = [\delta \boldsymbol{r}_c; \delta \boldsymbol{v}_c]$
    Maneuver planning: $\Delta \boldsymbol{v}_{S/K} = A \sum_{i=1}^{N_{pt}} (\alpha_i \delta \boldsymbol{r}_c + \beta_i \delta \boldsymbol{v}_c)$ ▷ See Equation (34)
    $\delta \boldsymbol{x}_{\text{true}} \leftarrow \Phi(t_c, t_v)\delta \boldsymbol{x}_c$
    Generate three-dimensional maneuver execution error, $\boldsymbol{\varepsilon}_{EX} \sim \mathcal{N}(0, \sigma^2_{EX})$
    $\Delta \boldsymbol{v} \leftarrow \Delta \boldsymbol{v} + \Delta \boldsymbol{v} \circ \boldsymbol{\varepsilon}_v$ ▷ Here, $\circ$ represents the Hadamard product
    Maneuver execution: $\delta \boldsymbol{x}_{\text{true}} \leftarrow \delta \boldsymbol{x}_{\text{true}} + [0_{3\times 1}; \Delta \boldsymbol{v}]$
    $t \leftarrow t_v$
  end while
end function

exactly known. To simulate tracking errors, the six S/C states are altered at the end of each OD campaign.

3. At various times along the trajectory, the S/K strategy will determine that a maneuver is required, and its magnitude and direction will be computed. To model the inaccuracy of maneuvers actual implementation, each $\Delta \boldsymbol{v}_{S/K}$ component is randomly altered.

The orbit injection, $\boldsymbol{\varepsilon}_{OI}$, orbit determination, $\boldsymbol{\varepsilon}_{OD}$, and the maneuver execution, $\boldsymbol{\varepsilon}_{EX}$, errors are all modeled and generated with zero-mean Gaussian distributions, i.e., $\boldsymbol{\varepsilon}_{OI} \sim \mathcal{N}(0, \sigma^2_{OI})$, $\boldsymbol{\varepsilon}_{OD} \sim \mathcal{N}(0, \sigma^2_{OD})$, $\boldsymbol{\varepsilon}_{EX} \sim \mathcal{N}(0, \sigma^2_{v})$, where σ^2_{OI}, σ^2_{OD}, σ^2_{EX} are the covariances of the orbit insertion, orbit determination, and maneuver execution uncertainties, respectively.

TABLE 9 | Standard deviations.

Standard deviation	LUMIO	Units
$\sigma_{OI_x}, \sigma_{OI_y}, \sigma_{OI_z}$	10, 10, 10	[km]
$\sigma_{OI_u}, \sigma_{OI_v}, \sigma_{OI_w}$	10, 10, 10	[cm/s]
$\sigma_{OD_x}, \sigma_{OD_y}, \sigma_{OD_z}$	10, 10, 10	[km]
$\sigma_{OD_u}, \sigma_{OD_v}, \sigma_{OD_w}$	10, 10, 10	[cm/s]
$\sigma_{EX_u}, \sigma_{EX_v}, \sigma_{EX_w}$	2, 2, 2	[%]

The station-keeping maneuvers are conducted at specific selected epochs during the mission. That is, maneuver timings are parameters of the S/K strategy, rather than variables. Referring to **Figure 8**, every OD campaign is always terminated Δt_c time units before the maneuver execution. Δt_c is termed cut-off duration and it is necessary to compute, schedule, and prepare the maneuver. The S/K maneuver planning is assumed to use N_{pt} downstream points, i.e., the target points, as reference states to compute the maneuver magnitude and direction. In **Figure 8**, there are two target points, $N_{pt} = 2$, and one S/K maneuver per halo orbit. The algorithm for the detailed station-keeping cost analysis is shown in Algorithm 2.

The TPM provides optimal $\Delta \boldsymbol{v}_{S/K}$ computed as solution of a LQR problem that minimizes a weighted sum of the maneuvers cost and the position deviation from a reference trajectory at N_{pt} downstream control points. The cost function reads

$$J_{S/K} = \Delta \boldsymbol{v}^T_{S/K} Q \Delta \boldsymbol{v}_{S/K} + \sum_{i=1}^{N_{pt}} \boldsymbol{d}_i^T R_i \boldsymbol{d}_i, \tag{32}$$

where $\Delta \boldsymbol{v}_{S/K}$ is the station-keeping maneuver, Q the cost weight matrix, $\boldsymbol{d}_i$ the predicted position deviation from the reference trajectory at the i-th target point, and R_i the weighing matrix of the deviation at the i-th target point. The position deviation is predicted by means of the state transition matrix of the reference trajectory, Φ:

$$\boldsymbol{d}_i = \Phi_{rr}(t_c, t_i)\delta \boldsymbol{r}_c + \Phi_{rv}(t_c, t_i)\delta \boldsymbol{v}_c + \Phi_{rv}(t_v, t_i)\Delta \boldsymbol{v}_{S/K}. \tag{33}$$

In Equation (33), Φ_{rr} and Φ_{rv} are 3-by-3 matrices that map deviation of position and velocity, respectively, to a position deviation at a subsequent epoch, t_c is the cut-off epoch, t_v is the maneuver execution epoch, and t_i the epoch of the i-th target point. The solution of the minimization problem yields the analytic expression for the optimal station-keeping maneuver:

$$\Delta \boldsymbol{v}_{S/K} = A \sum_{i=1}^{N_{pt}} (\alpha_i \delta \boldsymbol{r}_c + \beta_i \delta \boldsymbol{v}_c);$$
$$A = -\left[\left(Q^T + Q\right) + \sum_{i=1}^{N_{pt}} \Phi_{rv}^T(t_v, t_i) \left(R_i^T + R_i\right) \Phi_{rv}(t_v, t_i) \right]^{-1},$$
$$\alpha_i = \Phi_{rv}^T(t_v, t_i) \left(R_i^T + R_i\right) \Phi_{rr}(t_c, t_i),$$
$$\beta_i = \Phi_{rv}^T(t_v, t_i) \left(R_i^T + R_i\right) \Phi_{rv}(t_c, t_i). \tag{34}$$

Table 9 reports the standard deviations of orbit insertion, navigation, and maneuver execution errors for the S/K analysis. The values of **Table 9** are in well accordane with existing applications (Folta et al., 2014). More important, simulations have shown the standard deviations of **Table 9** can be achieved with the autonomous optical navigation algorithm on-board LUMIO (Franzese et al., 2018). All parameters for the correct functioning of Algorithm 2 have been fine-tuned with extensive simulation campaigns. The parameters fine-tuned values of the S/K algorithm are shown in **Table 10**. The cut-off duration of 12 h is at the same time sufficiently short to prevent the spacecraft state knowledge from growing excessively, and long enough to schedule maneuver execution operations on-board LUMIO. The target points are located at 35 and 42 days after orbit insertion and any subsequent S/K maneuvers. This ensures approximately 1 month of operations in case of maneuver execution failure. Finally, having the eigenspectrum of Q a larger magnitude than that R_i means the optimization weighs the deviation with respect to reference position more than the $\Delta \boldsymbol{v}_{S/K}$ cost.

TABLE 10 | Standard deviations.

Parameter	Value	Units
Δt_c	12	[h]
Δt_1	35	[days]
Δt_2	42	[days]
Q	$I_{3\times3} \cdot 10^{-1}$	[-]
R_1	$I_{3\times3} \cdot 10^{-2}$	[-]
R_2	$I_{3\times3} \cdot 10^{-2}$	[-]

Figure 9 shows the strategy employed for station-keeping maneuvers timing. For clarity, just 70 days of operations are shown and the quasi-halo orbital period is assumed to be fixed and equal to 14 days. The first quasi-halo orbit is entirely dedicated to recover any orbit insertion (OI) errors by means of two maneuvers, 1 and 7 days after OI, respectively. In the orbits after that, nominal operations occur, i.e., there is a series of Nav&Eng and Science orbits. Three S/K maneuvers are placed within the Nav&Eng orbit: the first at the entry point, the second in the middle (i.e., 7 days after the entry), and the third at the end of the Nav&Eng orbit. This maneuvers frequency configuration allows for pristine Science orbit operations, albeit it increases the cost when compared to a more spread and regular distribution of S/K maneuvers.

Station-keeping cost is computed for 1 year of life cycle for each of the quasi-halos considered. To obtain reliable station-keeping cost estimation results, a massive Monte-Carlo simulation of 10,000 cases is performed with respect to each reference orbit generated. Each Monte-Carlo run employs Algorithm 2 to compute S/K cost for a realization of $\boldsymbol{\varepsilon}_{OI}$, $\boldsymbol{\varepsilon}_{OD}$, and $\boldsymbol{\varepsilon}_{EX}$. **Table 11** displays the 1-year S/K cost with 1σ, 2σ, and 3σ confidence. The Monte-Carlo data is fitted by

TABLE 11 | Confidence for the 1-year station-keeping cost.

C_j [adim]	S/K cost [m/s]		
	1σ	2σ	3σ
3.16132363	75.5	137.9	196.5
3.16	72.4	131.6	186.9
3.15	53.4	92.7	128.4
3.14	40.1	66.4	89.7
3.13	29.2	45.4	59.2
3.12	22.0	31.6	39.1
3.11	17.8	23.8	28.5
3.10	13.3	16.9	19.6
3.09	18.3	23.9	28.1
3.08	11.0	13.9	15.6
3.07	8.8	10.2	11.2
3.06	8.5	9.9	10.9
3.05	7.6	8.6	9.3
3.04	7.2	7.9	8.4

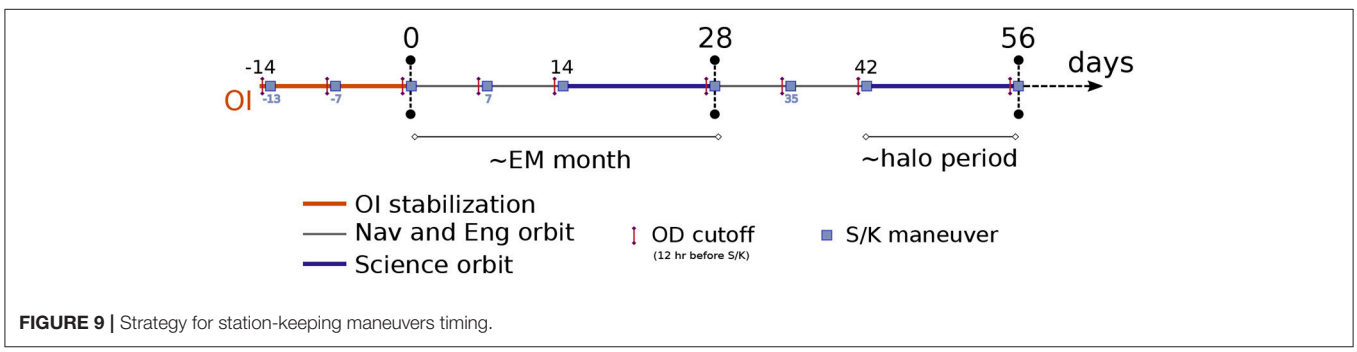

FIGURE 9 | Strategy for station-keeping maneuvers timing.

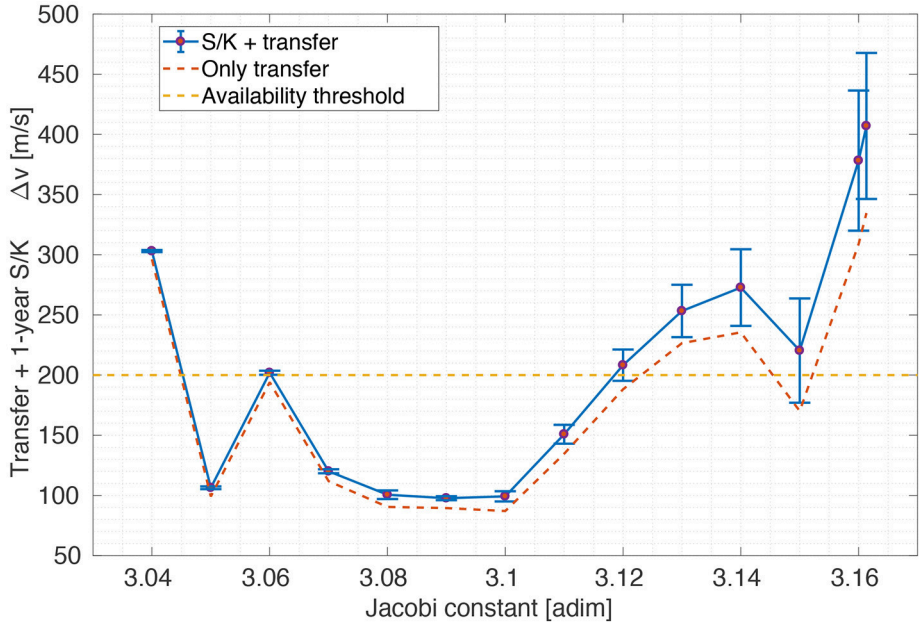

FIGURE 10 | Total transfer cost for different halos.

means of an Inverse Gaussian distribution. As expected, the S/K cost increases for smaller (i.e., higher Jacobi constant) quasi-halos. This trend reflects the stability (eigenspectrum of monodromy matrix) properties of halo orbits. That is, a larger halo is generally less unstable and thus cheaper to maintain.

Preliminary observations have been made on alternative station-keeping strategies: an i) Orbit continuation approach and the ii) Floquet unstable modes cancellation method (FM). Although the FM appears as the least expensive in terms of station-keeping total budget (Folta et al., 2014), the TPM is able to give a wider latitude on the selection of the S/K maneuver epoch and phasing, favoring LUMIO orbital geometry and ConOps. Indeed, the FM tends to place S/K maneuvers when the halo unstable component exceeds a defined threshold, regardless of the Phase LUMIO is flying. A further analysis on how to adapt the Floquet modes approach to the LUMIO case may still reduce the station-keeping costs presented in this work. In addition, the $\Delta \boldsymbol{v}_{S/K}$ calculation may be overly constrained since the LQR strategy requires the use of target locations and fine-tuning of weight matrices. A different optimization may also reduce the S/K costs presented here.

3.3.4. Detailed Trade-Off

Figure 10 shows the total transfer cost for different halos. The cost includes S/K, SMIM, and plane change maneuvers. It is conjectured the reason why the transfer cost has a clearcut minimum area is 2- fold. (1) For high energy levels (i.e., low Jacobi constant), the stable manifold configuration space does not get close enough to the Moon to permit intersection with the selenocentric transition orbit. At the other end of the spectrum, (2) for high Jacobi constant values, the stable manifolds cross the lunar region sufficiently close to provide patching opportunities with a selenocentric transition orbit, but the speed mismatch is comparatively large. i.e., the outbound stable manifold is much faster than the S/C at periselene.

TABLE 12 | Mission Δv budgets for LUMIO operative orbit.

Maneuver	Deterministic	Cost [m/s]		
		1σ	2σ	3σ
PCM	0	–	–	–
Injecton orbit S/K	–	8	8	8
SMIM	89.47	–	–	–
TCM1	–	28.6	53.0	73.1
TCM2	–	6.5	15.0	24.8
HIM	0.5	–	–	–
1-year S/K	–	18.3	23.9	28.1
Disposal	3	–	–	–
TOTAL		154.4	192.9	227.0

Quasi-halo generated from $C_j = 3.09$ is the designated LUMIO operative orbit. The selection of LUMIO operative orbit is based on results of **Figure 10**. Indeed, the quasi-halo is located at the center of a minimum plateau for total transfer cost which provide both a) Optimality of maneuvers cost, and b) Robustness against errors in the actual energy level of the injected stable manifold.

The selected operative orbit for the LUMIO mission is the most suitable only according to the specified evaluation and acceptance criteria. The selection may change if additional

criteria and requirements are investigated in a further step of the mission.

Mission Δv budgets for each maneuver and phase are reported in **Table 12** with both deterministic and confidence values. The total 1σ-cost is 154.4 m/s, which is also in line with a 12U CubeSat volume and mass budgets and with acceptance criteria EC.A.06–07. Note that ESA "Margin philosophy for science assessment studies" (Ref. SRE-PA/2011.097/, item MAT-DV-14) states that stochastic maneuvers shall be calculated based on the 3σ confidence interval with no additional margins (SRE-PA and D-TEC staff, 2012). The choice to consider a 1σ confidence interval on stochastic maneuvers for LUMIO is motivated by the inherently higher risk of a low-cost mission. Nonetheless, the overall stochastic Δv computed based on a 95.32% confidence level of a combination of all stochastic maneuvers is smaller than linear sum by 19%. With this approach, the 3σ Δv budget sums up to 191.3 m/s (195.5 m/s with margins on SMIM, HIM, and disposal maneuver), which is still within the bounds for mission feasibility, according to EC.A.06-07.

4. CONCLUSION

The primary science goal of LUMIO mission is to observe meteoroid impact flashes on the lunar farside in order to study the characteristics of meteoroids and to improve the meteoroid models of the solar system. This might lead to a further study of the sources of these meteoroids, such as asteroids in the near-Earth environment and comets. The LUMIO mission complements ground-based observations with remote space-based observations, so improving the lunar situational awareness.

A number of potential orbit families have been considered as candidate operative orbits for LUMIO, namely Keplerian, perturbed-Keplerian, and three-body orbits. An orthodox trade-off logic has been followed with hierarchical structure. An initial pruning has been made based on the way qualitative indicators delivered against acceptance and selection criteria. A second-level trade-off has been performed by coupling the developed models for the environment, impact flash, payload, and astrodynamics. The capability of the payload to resolve the impact flash in each of the candidate orbits as well as to satisfy the mission requirements has been assessed. As a result, L_2 halo orbits have been selected. Within the third-level trade-off, a fully quantitative analysis has been conducted by considering the accessibility and station-keeping costs with a high-fidelity concept of operations. Eventually, the LUMIO operative orbit has been baselined.

AUTHOR CONTRIBUTIONS

All authors listed have made a substantial, direct and intellectual contribution to the work, and approved it for publication.

FUNDING

The work described in this paper has been funded by the European Space Agency through Contract No. 4000120225/17/NL/GLC/as.

ACKNOWLEDGMENTS

The work described in this paper is a spin-off of a bigger project, namely the LUMIO Phase 0 design. For this reason the authors are grateful to the rest of LUMIO Team: M. Massari, J. Biggs, S. Ceccherini, K. Mani, V. Franzese, A. Cervone, P. Sundaramoorthy, S. Mestry, S. Speretta, A. Ivanov, D. Labate, A. Jochemsen, Q. Leroy, R. Furfaro, K. Jacquinot, as well as to the Technical Officers at ESA: Roger Walker and Johan Vennekens. The authors are also grateful to Detlef Koschny and Chrysa Avdellidou from ESA NEO Segment for their valuable inputs.

REFERENCES

Abad, A., Elipe, A., and Tresaco, E. (2009). Analytical model to find frozen orbits for a lunar orbiter. *J. Guid. Control Dyn.* 32, 888–898. doi: 10.2514/1.38350

Acton Jr, C. (1996). Ancillary data services of nasa's navigation and ancillary information facility. *Planet. Space Sci.* 44, 65–70. doi: 10.1016/0032-0633(95)00107-7

Acton Jr, C., Bachman, N., Semenov, B., and Wright, E. (2018). A look towards the future in the handling of space science mission geometry. *Planet. Space Sci.* 150, 9–12. doi: 10.1016/j.pss.2017.02.013

Bellot Rubio, L. R., Ortiz, J. L., and Sada, P. V. (2000). Luminous efficiency in hypervelocity impacts from the 1999 lunar leonids. *Astrophys. J. Lett.* 542, L65–L68. doi: 10.1086/312914

Bernelli Zazzera, F., F. Topputo, F., and Massari, M. (2004). *Assessment of Mission Design Including Utilization of Libration Points and Weak Stability Boundaries*. Technical report, Ariadna Study, ESA Contract No. 18147/04/NL/MV.

Bonanos, A., Xilouris, M., Boumis, P., Bellas-Velidis, I., Maroussis, A., Dapergolas, A., et al. (2015). NELIOTA: ESA's new NEO lunar impact monitoring project with the 1.2 m telescope at the National Observatory of Athens. *Proc. Int. Astron. Union* 10, 327–329. doi: 10.1017/S1743921315006973

Bouley, S., Baratoux, D., Vaubaillon, J., Mocquet, A., Le Feuvre, M., Colas, F., et al. (2012). Power and duration of impact flashes on the moon: implication for the cause of radiation. *Icarus* 218, 115–124. doi: 10.1016/j.icarus.2011.11.028

Breakwell, J., and Brown, J. (1979). The halo family of 3-dimensional periodic orbits in the earth–moon restricted 3-body problem. *Celestial Mech.* 20, 389–404. doi: 10.1007/BF01230405

Brown, P. G., Assink, J. D., Astiz, L., Blaauw, R., Boslough, M. B., Borovička, J., et al. (2013). A 500-kiloton airburst over Chelyabinsk and an enhanced hazard from small impactors. *Nature* 503, 238–241. doi: 10.1038/nature12741

Brown, P. G., Spalding, R. E., ReVelle, D. O., Tagliaferri, E., and Worden, S. P. (2002). The flux of small near-Earth objects colliding with the Earth. *Nature* 420, 294–296. doi: 10.1038/nature01238

Carvalho, J. P. D. S., De Moraes, R. V., and Prado, A. F. B. A. (2009). Nonsphericity of the moon and near sun-synchronous polar lunar orbits. *Math. Probl. Eng.* 2009:740460. doi: 10.1155/2009/740460

Carvalho, J. P. D. S., Vilhena de Moraes, R. V., and Prado, A. F. B. A. (2010). Some orbital characteristics of lunar artificial satellites. *Celestial Mech. Dyn. Astron.* 108, 371–388. doi: 10.1007/s10569-010-9310-6

Ceplecha, Z., Borovička, J., Elford, W. G., ReVelle, D. O., Hawkes, R. L., Porubčan, V., et al. (1998). Meteor Phenomena and Bodies. *Space Sci. Rev.* 84, 327–471. doi: 10.1023/A:1005069928850

Dei Tos, D. A., and Topputo, F. (2017a). On the advantages of exploiting the hierarchical structure of astrodynamical models. *Acta Astronaut.* 136, 236–247. doi: 10.1016/j.actaastro.2017.02.025

Dei Tos, D. A., and Topputo, F. (2017b). Trajectory refinement of three-body orbits in the real solar system model. *Adv. Space Res.* 59, 2117–2132. doi: 10.1016/j.asr.2017.01.039

Doedel, E., Romanov, V., Paffenroth, R., Keller, H., Dichmann, D., Galán-Vioque, J., et al. (2007). Elemental periodic orbits associated with the libration points in the circular restricted 3-body problem. *Int. J. Bifurcat. Chaos* 17, 2625–2677. doi: 10.1142/S0218127407018671

Dwivedi, N. P. (1975). Deterministic optimal maneuver strategy for multi-target missions. *J. Optimization Theory Appl.* 17, 133–153. doi: 10.1007/BF00933919

Elipe, A., and Lara, M. (2003). Frozen orbits about the moon. *J. Guid. Control Dyn.* 26, 238–243. doi: 10.2514/2.5064

Ely, T., and Lieb, E. (2006). Constellations of elliptical inclined lunar orbits providing polar and global coverage. *J. Astronaut. Sci.* 54, 53–67. doi: 10.1007/BF03256476

Farquhar, R. and Kamel, A. (1973). Quasi-periodic orbits about the translunar libration point. *Celestial Mech.* 7, 458–473. doi: 10.1007/BF01227511

Folta, D. C., Bosanac, N., Guzzetti, D., and Howell, K. C. (2015). An earth–moon system trajectory design reference catalog. *Acta Astronaut.* 110, 341–353. doi: 10.1016/j.actaastro.2014.07.037

Folta, D. C., Pavlak, T. A., Haapala, A. F., Howell, K. C., and Woodard, M. A. (2014). Earth–moon libration point orbit stationkeeping: Theory, modeling, and operations. *Acta Astronaut.* 94, 421–433. doi: 10.1016/j.actaastro.2013.01.022

Franzese, V., Di Lizia, P., and Topputo, F. (2018). "Autonomous optical navigation for lumio mission," in *2018 Space Flight Mechanics Meeting, AIAA SciTech Forum* (Kissimmee, FL: American Institute of Aeronautics and Astronautics), 1–11. doi: 10.2514/6.2018-1977

Gómez, G., Jorba, A., Masdemont, J., and Simó, C. (1993). Study of the transfer from the earth to a halo orbit around the equilibrium point l1. *Celestial Mech. Dyn. Astron.* 56, 541–562. doi: 10.1007/BF00696185

Grebow, D. (2006). *Generating Periodic Orbits in the Circular Restricted Three-Body Problem with Applications to Lunar South Pole Coverage*. Master of Science in Aeronautics and Astronautics Thesis, Purdue University.

Gudkova, T. V., Lognonné, P. H., and Gagnepain-Beyneix, J. (2011). Large impacts detected by the Apollo seismometers: impactor mass and source cutoff frequency estimations. *Icarus*, 211, 1049–1065. doi: 10.1016/j.icarus.2010.10.028

Guzzetti, D., Bosanac, N., Haapala, A. F., Howell, K. C., and Folta, D. C. (2016). Rapid trajectory design in the earth–moon ephemeris system via an interactive catalog of periodic and quasi-periodic orbits. *Acta Astronaut.* 126, 439–455. doi: 10.1016/j.actaastro.2016.06.029

Hénon, M. (1970). Numerical exploration of the restricted problem. *Astron. Astrophys.* 9, 24–36.

Howell, K. C., and Pernicka, H. J. (1993). Stationkeeping method for libration point trajectories. *J. Guid. Control Dyn.* 16, 151–151. doi: 10.2514/3.11440

Konopliv, A. S., Park, R. S., Yuan, D. N., Asmar, S. W., Watkins, M. M., Williams, J. G., et al. (2013). The JPL lunar gravity field to spherical harmonic degree 660 from the GRAIL Primary Mission. *J. Geophys. Res. Planets* 118, 1415–1434. doi: 10.1002/jgre.20097

Koschny, D., and McAuliffe, J. (2009). Estimating the number of impact flashes visible on the Moon from an orbiting camera. *Meteorit. Planet. Sci.* 44, 1871–1875. doi: 10.1111/j.1945-5100.2009.tb01996.x

Madiedo, J. M., Ortiz, J. L., Organero, F., Ana-Hernández, L., Fonsenca, F., Morales, N., et al. (2015). Analysis of Moon impact flashes detected during the 2012 and 2013 Perseids. *Astron. Astrophys.* 577:A118. doi: 10.1051/0004-6361/201525656

Ming, X., and Shijie, X. (2009). Exploration of distant retrograde orbits around moon. *Acta Astronaut.* 65, 853–860. doi: 10.1016/j.actaastro.2009.03.026

Oberst, J., Christou, A., Suggs, R. M., Moser, D. E., Daubar, I. J., McEwen, A. S., et al. (2012). The present-day flux of large meteoroids on the lunar surface–a synthesis of models and observational techniques. *Planet. Space Sci.* 74, 179–193. doi: 10.1016/j.pss.2012.10.005

Oberst, J., Flohrer, J., Elgner, S., Maue, T., Margonis, A., Schrdter, R., et al. (2011). The smart panoramic optical sensor head (sposh)a camera for observations of transient luminous events on planetary night sides. *Planet. Space Sci.* 59, 1–9. doi: 10.1016/j.pss.2010.09.016

Oguri, K., Kakihara, K., Campagnola, S., Ozaki, N., Ohima, K., Yamaguchi, T., et al. (2017). "Equuleus mission analysys: design of the science orbit phase," in *26th International Symposium on Space Flight Dynamics* (Ehime), 1–7.

Ortiz, J. L., Aceituno, F. J., Quesada, J. A., Aceituno, J., Fernández, M., Santos-Sanz, P., et al. (2006). Detection of sporadic impact flashes on the Moon: Implications for the luminous efficiency of hypervelocity impacts and derived terrestrial impact rates. *Icarus* 184, 319–326. doi: 10.1016/j.icarus.2006.05.002

Ortiz, J. L., Madiedo, J. M., Morales, N., Santos-Sanz, P., and Aceituno, F. J. (2015). Lunar impact flashes from geminids: analysis of luminous efficiencies and the flux of large meteoroids on earth. *Mon. Not. R. Astron. Soc.* 454, 344–352. doi: 10.1093/mnras/stv1921

Ortiz, J. L., Sada, P. V., Bellot Rubio, L. R., Aceituno, F. J., Aceituno, J., Gutierrez, P. J., et al. (2000). Optical detection of meteoroidal impacts on the Moon. *Nature* 405, 921. doi: 10.1038/35016015

Park, S. Y., and Junkins, J. L. (1994). "Orbital mission analysis for a lunar mapping satellite," in *AAS/AIAA Astrodynamics Specialist Conference* (Scottsdale, AZ), 93–98. doi: 10.2514/6.1994-3717

Pergola, P., and Alessi, E. M. (2012). Libration point orbit characterization in the earth–moon system. *Mon. Not. R. Astron. Soc.* 426, 1212–1222. doi: 10.1111/j.1365-2966.2012.21585.x

Popova, O. P., Jenniskens, P., Emel'yanenko, V., Kartashova, A., Biryukov, E., Khaibrakhmanov, S., et al. (2013). Chelyabinsk airburst, damage assessment, meteorite recovery, and characterization. *Science* 342, 1069–1073. doi: 10.1126/science.1242642

Prado, A. F. B. A. (2003). Third-body perturbation in orbits around natural satellites. *J. Guid. Control Dyn.* 26, 33–40. doi: 10.2514/2.5042

Raab, H. (2002). "Detecting and measuring faint point sources with a CCD," in *Proceedings of Meeting on Asteroids and Comets in Europe (MACE)* (Visnjam), 1–12.

Ramanan, R., and Adimurthy, V. (2005). An analysis of near-circular lunar mapping orbits. *J. Earth Syst. Sci.* 114, 619–626. doi: 10.1007/BF02715946

Rubin, A. E., and Grossman, J. N. (2010). Meteorite and meteoroid: new comprehensive definitions. *Meteorit. Planet. Sci.* 45, 114–122. doi: 10.1111/j.1945-5100.2009.01009.x

SRE-PA and D-TEC staff (2012). *Margin Philosophy for Science Assessment Studies*. Technical Report, ESA, Document Reference SRE-PA/2011.097, Issue 1, Revision 3.

Suggs, R. M., Cooke, W. J., Suggs, R. J., Swift, W. R., and Hollon, N. (2008). The NASA lunar impact monitoring program. *Earth Moon Planets* 102, 293–298. doi: 10.1007/s11038-007-9184-0

Suggs, R. M., Ehlert, S. R., and Moser, D. E. (2017). A comparison of radiometric calibration techniques for lunar impact flashes. *Planet. Space Sci.* 143, 225–229. doi: 10.1016/j.pss.2017.04.016

Suggs, R. M., Moser, D. E., Cooke, W. J., and Suggs, R. J. (2014). The flux of kilogram-sized meteoroids from lunar impact monitoring. *Icarus* 238(Suppl. C), 23–36. doi: 10.1016/j.icarus.2014.04.032

Topputo, F. (2016). Fast numerical approximation of invariant manifolds in the circular restricted three-body problem. *Commun. Nonlin. Sci. Numerical Simul.* 32(Suppl. C), 89–98. doi: 10.1016/j.cnsns.2015.08.004

Topputo, F., Massari, M., Biggs, J. D., Dei Tos, D. A., Ceccherini, S., Mani, K., et al. (2017). *Lunar Cubesats for Exploration. Lumio: Lunar Meteoroid Impacts Observer*. Technical Report, ESA Contract No. 4000120225/17/NL/GLC/as.

Turner, G. (2016). Results of long-duration simulation of distant retrograde orbits. *Aerospace* 3, 37. doi: 10.3390/aerospace3040037

Whitley, R., and Martinez, R. (2016). "Options for Staging Orbits in Cislunar Space," in *IEEE Aerospace Conference Proceedings* (Big Sky, MT), 1–9. doi: 10.1109/AERO.2016.7500635

Conflict of Interest Statement: The authors declare that the research was conducted in the absence of any commercial or financial relationships that could be construed as a potential conflict of interest.

frontiers in Applied Mathematics and Statistics

METHODS
published: 28 June 2018
doi: 10.3389/fams.2018.00024

Enhancing Station-Keeping Control With the Use of Extended State Observers

James D. Biggs, Helen C. Henninger and Aman Narula*

Aerospace Science and Technology, Politecnico di Milano, Milan, Italy

Recently there has been a resurgence of interest in missions to the moon and a major challenge of such missions is to provide a continuous communication between the Earth and the Moon's far side. Orbits around the L_2 Earth-Moon Lagrange point have been a topic of interest in this field due to their potential for constant communication with both the Earth and the Moon, however the Lagrange point orbits are innately unstable and so station-keeping control is required to maintain them. Station-keeping problems are highly nonlinear and a traditional approach to control design is first to linearize the nonlinear system. However, this first-order approximation introduces errors if there are large injection errors. This paper demonstrates how a simple Extended State Observer (ESO) can be used to improve the convergence time of spacecraft to the reference orbit given with large injection errors. Additionally, solar radiation pressure (SRP) a dominant disturbance in deep-space, can lead to inefficient station-keeping if it is not taken into account in the reference orbit design. New reference orbits can be designed that exploit the SRP perturbation but this assumes that it is known apriori. Here we show how an ESO could provide an in-orbit measurement of the SRP which could be used to modify the reference trajectory to a more fuel efficient one. Finally, it is shown how an ESO can be used to estimate, not only the disturbance, but simultaneously the velocity of the spacecraft meaning that only the position of the spacecraft is required.

Keywords: station-keeping control, lagrange points, linear quadratic regulator, extended-state observer, active disturbance rejection control

OPEN ACCESS

Edited by:
Josep Masdemont, Universitat Politecnica de Catalunya, Spain

Reviewed by:
Saleh Mobayen, University of Zanjan, Iran
Yilun Shang, Tongji University, China

****Correspondence:***
James D. Biggs
jamesdouglas.biggs@polimi.it

Specialty section:
This article was submitted to Dynamical Systems, a section of the journal Frontiers in Applied Mathematics and Statistics

Received: *28 February 2018*
Accepted: *08 June 2018*
Published: *28 June 2018*

Citation:
Biggs JD, Henninger HC and Narula A (2018) Enhancing Station-Keeping Control With the Use of Extended State Observers. Front. Appl. Math. Stat. 4:24. doi: 10.3389/fams.2018.00024

1. INTRODUCTION

Deep-space station-keeping exploits the natural dynamics of the solar system to design fuel-efficient reference trajectories [1–5]. Natural orbits, such as Libration Point Orbits (LPOs) in the circular restricted three body problem (CRTBP) have been used to design reference orbits in real missions such as ISEE-3, Wind, SOHO, ACE, Genesis, DSCVER and Lisa pathfinder which exploit LPO in the vicinity of the Earth-Sun Libration point L_1, while the spacecraft ARMETIS and Chang'e 5-T1 exploit LPOs in the vicinity of the Earth-Moon Libration point orbits (see [3] and references therein). More recently LPOs in the vicinity of L_2 have been identified as the ideal position for a 12 U CubeSat mission for the purpose of observing meteroid impact with the Moon [6]. In Shirobokov et al. [3] it is pointed out that only investigations including precise models of the dynamics of the spacecraft are of relevance to station-keeping design particularly in the Earth-Moon system. Moreover, if the reference is designed in a low-fidelity model then the station-keeping cost in a high-fidelity model will require greater cost. Furthermore, although high-fidelity models such as

SPICE [7] are available to design fuel-efficient spacecraft the precise nature of the SRP acting on the spacecraft in deep space is uncertain (for example through degradation of a solar sails reflective surface in the space environment [8, 9]).

Solar Radiation Pressure (SRP) should also be taken into account in order to design fuel-efficient orbits and it can also be used to obtain observational advantages [10–15]. However, the design of these SRP perturbed reference orbits requires that the force exerted on the solar sail is accurately known. In this paper it is shown that by using an extended state observer (ESO) the SRP can be measured on-board from the knowledge of the position of the spacecraft and therefore adjustments to the reference orbit could be made during the mission. Indeed, it could be possible that once an accurate measure of the SRP is obtained on-board that a differential corrector could be used to refine the reference orbit to one that requires less station-keeping control. In other words with a known SRP a natural reference trajectory can be constructed that incorporates realistic perturbations.

The second major aspect of mission planning on LPO is to design an efficient station-keeping control since these orbits are inherently unstable. Deep-space station-keeping is made more complicated by initial orbit injection errors, uncertain dynamics such as SRP and sensor faults. There are a plethora of different strategies for station-keeping on LPOs; those which exploit the underlying dynamics of the CRTBP, mainly by Floquet theory and those which apply classical control techniques such as the linear quadratic regulator (LQR)[4, 13–15], nonlinear regulation [16], disturbance accommodating control [17] and sliding mode control [18] amongst others (see [3] for a review of current methods). In this paper we focus on coupling a simple proportional feedback-control with an ESO and demonstrate the potential benefits to station-keeping on LPOs. Moreover, it is shown to improve convergence in the presence of large injection errors, measure the SRP on-board while simultaneously measuring the spacecraft's velocity (only knowledge of the spacecraft position is required). Although the focus here is on complimenting a simple proportional controller with an ESO in-the-loop it could potentially improve a wide range of existing controls [4, 13, 14, 16–18].

The use of ESOs in station-keeping design was first demonstrated in Zhu et al. [19] whereby the reference orbit was designed using a linearization in the vicinity of an LPO in the CRTBP and then the control to track this was implemented in a high-fidelity model including eccentricity and SRP. These perturbations were considered to be unknown and the ESO was used to measure the entire disturbance which was then compensated for in the control. It was shown to improve the tracking error with respect to an LQR controller while maintaing the ΔV requirement. In Narula and Biggs [20] it was shown that an ESO could be used to estimate the extent of a fault in an actuator and then the control input adjusted to compensate for this fault. In this paper we demonstrate how including an ESO can improve convergence time of a proportional controller and show that the closed-loop system yields a tunable linear response. It is also shown that it is possible to perform low-thrust station-keeping in the Earth-Moon system in the presence of SRP with only knowledge of the position of the spacecraft making the control robust to failures of velocity sensors.

The paper is presented as follows: In section 2 the station-keeping problem is formulated including the equations of motion in the circular-restricted three-body problem (CR3BP) in the Earth-Moon- Spacecraft system with SRP and the reference trajectory. In section 3 we construct a Linear active uncertainty measurement control that couples a proportional controller with a linear ESO and then with a nonlinear ESO. This section demonstrates the use of each control in terms of improving convergence, SRP and velocity measurements. Simulations are given to demonstrate the effectiveness of the controller.

2. PROBLEM FORMULATION

From Gómez et al. [5], we consider the CR3BP equations in the synodic frame, centered at the Earth-Moon barycenter and rotating with the angular speed of the Moon. We denote by (x, y, z) the coordinates of the spacecraft in this frame, while we denote by $(\widehat{X}, \widehat{Y}, \widehat{Z})$ the inertial frame, a Cartesian frame centered at the Earth with fixed axes. The coordinates used are non-dimensionalized; i.e., the sum of the masses, the distance between the primaries, and the gravitational parameter all equal one and these values are normalized by a three-body parameter μ, which is defined as the ratio of the smaller primary's mass to the sum of the mass of the two primaries,

$$\mu = \frac{m_2}{m_1 + m_2} \tag{1}$$

where m_1 and m_2 are the masses of the Earth and the Moon respectively. With the distance between the two primaries equal to one, the distances between the barycenter and the primary and barycenter and the secondary are equal to $-\mu$ and $1 - \mu$, respectively where $\mu = 0.01215$. To this CR3BP we add the control $\boldsymbol{u} = [u_x, u_y, u_z]$. We also add the solar radiation pressure (SRP), the disturbance force vector $\boldsymbol{a}_S = [a_S^x \quad a_S^y \quad a_S^z]^T$ arising from the incoming solar photons perpendicular to the surface of the large spacecraft, in the direction $\boldsymbol{n}$. Thus the spacecraft dynamics are given by

$$\begin{aligned} \ddot{x} - 2\dot{y} - x + \frac{(1-\mu)(x+\mu)}{d^3} - \frac{\mu(x-(1-\mu))}{r^3} &= u_x + a_S^x \\ \ddot{y} + 2\dot{x} - y + \frac{(1-\mu)y}{d^3} - \frac{\mu y}{r^3} &= u_y + a_S^y \\ \ddot{z} + \frac{(1-\mu)z}{d^3} - \frac{\mu z}{r^3} &= u_z + a_S^z \end{aligned} \tag{2}$$

where

$$\begin{aligned} d^2 &= (x+\mu)^2 + y^2 + z^2, \\ r^2 &= (x-(1+\mu))^2 + y^2 + z^2 \end{aligned} \tag{3}$$

Assuming that the solar radiation pressure is constant in magnitude throughout the Earth-Moon system, the SRP $\boldsymbol{a}_S$ can be written as:

$$\boldsymbol{a}_S = a_0(\boldsymbol{S}\cdot\boldsymbol{n})^2\boldsymbol{n} \tag{4}$$

where $\boldsymbol{S}$ is the vector direction of the Sun-line

$$\boldsymbol{S} = [\cos(\Omega_S t), -\sin(\Omega_S t), 0]^\top \tag{5}$$

with $\Omega_S = 0.9252$ the angular rate of the Sun line in the non-dimensional variables, and a_0 is the SRP acceleration in non-dimensional units. The characteristic acceleration is the acceleration generated by the spacecraft when it faces the Sun at Earth's distance. Note that this parameter is difficult to measure and is not known with certainty. The right-hand side of (2) possesses a constant of integration known as the Jacobi Constant J_c.

$$\begin{aligned} J_c &= x^2+y^2+2\frac{1-\mu}{r_1}+2\frac{\mu}{r_2}-(\dot{x}^2+\dot{y}^2+\dot{z}^2)\\ &= 2U-(\dot{x}^2+\dot{y}^2+\dot{z}^2)\end{aligned}$$

where U is the modified potential energy function

$$U = \frac{1}{2}(x^2+y^2)+\frac{(1-\mu)}{d}+\frac{\mu}{r} \tag{6}$$

which can be expressed in the simple form [5]

$$\begin{cases}\ddot{x} &= \frac{\partial U}{\partial x}+2\dot{y}+u_x+a_S^x\\ \ddot{y} &= \frac{\partial U}{\partial y}-2\dot{x}+u_y+a_S^y\\ \ddot{z} &= \frac{\partial U}{\partial z}+u_z+a_S^z\end{cases} \tag{7}$$

which can be expressed in the form

$$\begin{aligned}\dot{\boldsymbol{x}}_1 &= \boldsymbol{x}_2\\ \dot{\boldsymbol{x}}_2 &= f(\boldsymbol{x}_1,\boldsymbol{x}_2)+\boldsymbol{u}+\boldsymbol{a}_S\end{aligned} \tag{8}$$

where the position $\boldsymbol{x}_1 = [x,y,z]$ and the velocity $\boldsymbol{x}_2 = [\dot{x},\dot{y},\dot{z}]$ and $\boldsymbol{x} = [x,y,z,\dot{x},\dot{y},\dot{z}]$, $\boldsymbol{a}_S = [a_S^x, a_S^y, a_S^z]$ is the uncertain SRP that is required to be estimated. The initial conditions have been taken from Gómez et al. [5] and modified to increase the precision using a differential corrector to yield LPOs when SRP is not included in the model. We briefly analyze these orbits to choose the one with the maximum coverage of the lunar surface. The choice of orbit is based on the percentage time in contact with Moon and ground station on Earth. Since the Chandrayan-I mission and LCROSS by NASA has pointed out many important crater locations on the far side of the moon, the decision is based on the orbit coverage of the important craters of moon. By evaluating the percentage time of coverage time for each of the orbit candidates (shown in **Table 1**). It can be seen that best performing orbit is the halo orbit, and so for the purpose of providing continuous communications to a lunar ground station as well as continuous connection with stations with Earth, a halo orbit is chosen as the candidate reference orbit in this paper.

TABLE 1 | Percentage coverage of each orbit.

Zone of coverage	Vertical Lyupanov (%)	Planar Lyupanov (%)	Halo orbit (%)
Tsiolkovsky crater	65.75	44.81	75.21
SPA-1 crater	53.34	47.06	90.86
Schrödinger center	27.70	56.78	97.82
Shakaleton crater	23.65	57.35	88.36

It can be seen that best performing orbit is the halo orbit, and so for the purpose of providing continuous communications to a lunar ground station as well as continuous connection with stations with Earth, a halo orbit with the following initial conditions is chosen as the candidate reference orbit in this paper:

$$\begin{bmatrix}x_0\\ y_0\\ z_0\\ \dot{x}_o\\ \dot{y}_0\\ \dot{z}_0\end{bmatrix} = \begin{bmatrix}1.12424283994529\\ 0\\ 0.187435048916681\\ 0\\ -0.223784191244108\\ 0\end{bmatrix} \tag{9}$$

The general problem is then to design a feedback control such that the magnitude of the error state converges to zero as $t\to\infty$ in the presence of potentially large injection errors, SRP and only position measurements.

3. A GENERAL ACTIVE UNCERTAINTY MEASUREMENT CONTROL (AUMC)

The general AUMC is based on the original idea of the active disturbance rejection control (ADRC) proposed in Han [21]. ADRC is used to measure the unknown disturbances within the system and to cancel the estimated disturbance in the control at each sampling period. In this paper we refer to the coupling of a proportional controller and an ESO as AUMC as the ESO is used to measure (depending on its form) the SRP disturbance while taking into account the higher-order terms in the linearization and velocity measurement. In this section we introduce a general AUMC which combines a proportional-type controller coupled with an ESO of the form:

$$\boldsymbol{u} = -K\delta\boldsymbol{x}-\hat{\boldsymbol{x}}_3 \tag{10}$$

where $\delta\boldsymbol{x} = \boldsymbol{x}-\boldsymbol{x}_{ref}$, K is a gain matrix that can be tuned experimentally or computed using LQR [20] by removing the unknown dynamics from the equation of motion. The current state of the spacecraft $\boldsymbol{x}$ is assumed to be measurable and $\hat{\boldsymbol{x}}_3$ is the output of the following ESO:

$$\begin{aligned}\dot{\hat{\boldsymbol{x}}}_1 &= \hat{\boldsymbol{x}}_2+\beta_1(\boldsymbol{x}_1-\hat{\boldsymbol{x}}_1)\\ \dot{\hat{\boldsymbol{x}}}_2 &= \hat{\boldsymbol{x}}_3+\boldsymbol{g}(\boldsymbol{x})+\boldsymbol{u}+\beta_2(\boldsymbol{x}_1-\hat{\boldsymbol{x}}_1)\\ \dot{\hat{\boldsymbol{x}}}_3 &= \beta_3(\boldsymbol{x}_1-\hat{\boldsymbol{x}}_1)\end{aligned} \tag{11}$$

where $\hat{\boldsymbol{x}}_1$ is the estimate of $\boldsymbol{x}_1$ (or $\delta\boldsymbol{x}_1$ if the linearization of $f(\boldsymbol{x}_1, \boldsymbol{x}_2)$ is used), $\hat{\boldsymbol{x}}_2$ is the estimate of $\boldsymbol{x}_2$ (or $\delta\boldsymbol{x}_2$ in the linear case) and $\hat{\boldsymbol{x}}_3$ is the estimate of

$$h = f(\boldsymbol{x}_1, \boldsymbol{x}_2) - g(\boldsymbol{x}_1, \boldsymbol{x}_2) + \boldsymbol{a}_S \tag{12}$$

where $g(\boldsymbol{x})$ is a prescribed function that is defined by the control engineer depending on the control objectives, for example, it can be set to be the known nonlinear or linearized dynamics or simply set to zero. To initialize the estimator we set $\hat{\boldsymbol{x}}_1(0) = \boldsymbol{x}_1(0)$ and $\hat{\boldsymbol{x}}_2(0) = \boldsymbol{x}_2(0)$ (or $\hat{\boldsymbol{x}}_1(0) = \delta\boldsymbol{x}_1(0)$ and $\hat{\boldsymbol{x}}_2(0) = \delta\boldsymbol{x}_2(0)$ if the linearized dynamics are being used for control design) as these values are known and assumed to be given by the sensors, while $\hat{\boldsymbol{x}}_3(0) = 0$ as this is an uncertain quantity. Note that this control requires the input of both the position and the velocity (or position and velocity errors in the linear case) of the spacecraft $\boldsymbol{x}_1, \boldsymbol{x}_2$ which will require both reference or optical sensors as well as an inertial measurement unit. In the case that there is a fault in the velocity measurement sensor the control law (10) can be adapted to:

$$\boldsymbol{u} = -K_1\delta\boldsymbol{x}_1 - K_2\delta\hat{\boldsymbol{x}}_2 - \hat{\boldsymbol{x}}_3 \tag{13}$$

where $\delta\boldsymbol{x}_1 = \boldsymbol{x}_1 - \boldsymbol{x}_1^{ref}$ and $\delta\hat{\boldsymbol{x}}_2 = \hat{\boldsymbol{x}}_2 - \hat{\boldsymbol{x}}_2^{ref}$ where $\hat{\boldsymbol{x}}_2$ and $\hat{\boldsymbol{x}}_3$ are outputs of the ESO:

$$\begin{aligned}
\dot{\hat{\boldsymbol{x}}}_1 &= \hat{\boldsymbol{x}}_2 + \beta_1(\boldsymbol{x}_1 - \hat{\boldsymbol{x}}_1)\\
\dot{\hat{\boldsymbol{x}}}_2 &= \hat{\boldsymbol{x}}_3 + \boldsymbol{g}(\boldsymbol{x}_1, \hat{\boldsymbol{x}}_2) + \boldsymbol{u} + \beta_2(\boldsymbol{x}_1 - \hat{\boldsymbol{x}}_1)\\
\dot{\hat{\boldsymbol{x}}}_3 &= \beta_3(\boldsymbol{x}_1 - \hat{\boldsymbol{x}}_1)
\end{aligned} \tag{14}$$

Defining the unknown derivative of $h = \boldsymbol{x}_3$ as $\dot{\boldsymbol{x}}_3 = \boldsymbol{\phi}$ and the error to be $\boldsymbol{e}_i = \boldsymbol{x}_i - \hat{\boldsymbol{x}}_i$ for $i = 1, 2$ and $\boldsymbol{e}_3 = h - \hat{\boldsymbol{x}}_3$ then the error dynamics of the ESO can be defined as:

$$\begin{aligned}
\dot{\boldsymbol{e}}_1 &= \boldsymbol{e}_2 - \beta_1\boldsymbol{e}_1\\
\dot{\boldsymbol{e}}_2 &= \boldsymbol{e}_3 - \beta_2\boldsymbol{e}_1\\
\dot{\boldsymbol{e}}_3 &= \phi - \beta_3\boldsymbol{e}_1.
\end{aligned} \tag{15}$$

We adopt the general tuning method for second order active disturbance rejection controls described in Xing et al. [22] where $\beta_1 = 3\omega_0, \beta_2 = 3\omega_0^2, \beta_3 = \omega_0^3$ where ω_0 is denoted as the observer band-width and k is an additional tuning parameter reducing the tuning to only one parameter. Then writing $\boldsymbol{e}_2/\omega_0 = \boldsymbol{f}_2$ and $\boldsymbol{e}_3/\omega_0^2 = \boldsymbol{f}_3$ we have

$$\begin{aligned}
\dot{\boldsymbol{e}}_1 &= \boldsymbol{f}_2\omega_0 - 3\omega_0\boldsymbol{e}_1\\
\dot{\boldsymbol{f}}_2 &= \boldsymbol{f}_3\omega_0 - 3\omega_0\boldsymbol{e}_1\\
\dot{\boldsymbol{f}}_3 &= \phi/\omega_0^2 - \omega_0\boldsymbol{e}_1.
\end{aligned} \tag{16}$$

then adapting the proof in Bai et al. [23] to the higher-dimensional problem here and defining $\varepsilon = [\boldsymbol{e}_1 \quad \boldsymbol{f}_2 \quad \boldsymbol{f}_3]^T$ we write

$$\begin{aligned}
\dot{\varepsilon} &= \omega_0 A\varepsilon + B\frac{\phi}{\omega_0^2}\\
A &= \begin{bmatrix} -3I_{3\times3} & I_{3\times3} & 0_{3\times3}\\ -3I_{3\times3} & 0_{3\times3} & I_{3\times3}\\ -I_{3\times3} & 0_{3\times3} & 0_{3\times3}\end{bmatrix}, B = \begin{bmatrix} 0_{3\times3}\\ 0_{3\times3}\\ I_{3\times3}\end{bmatrix}
\end{aligned} \tag{17}$$

defining $\tilde{\varepsilon}_i = [e_{1i} \quad f_{2i} \quad f_{3i}]^T$ where $\boldsymbol{e}_1 = [e_{11} \quad e_{12} \quad e_{13}]^T$, $\boldsymbol{f}_2 = [f_{21} \quad f_{22} \quad f_{23}]^T$ and $\boldsymbol{f}_3 = [f_{31} \quad f_{32} \quad f_{33}]^T$ we can re-write the expression as

$$\begin{aligned}
\tfrac{d\tilde{\varepsilon}_i}{dt} &= \tilde{A}\tilde{\varepsilon}_i + \tilde{B}\tfrac{\phi_i}{\omega_0^2}\\
\tilde{A} &= \begin{bmatrix} -3\omega_0 & \omega_0 & 0\\ -3\omega_0 & 0 & \omega_0\\ -\omega_0 & 0 & 0\end{bmatrix}, \tilde{B} = \begin{bmatrix} 0\\ 0\\ 1\end{bmatrix}
\end{aligned} \tag{18}$$

which has the solution

$$\tilde{\varepsilon}_i(t) = \exp(\tilde{A}t)\tilde{\varepsilon}_i(0) + \int_0^t \exp[\tilde{A}(t-\tau)]\tilde{B}\frac{\phi_i}{\omega_0^2}d\tau \tag{19}$$

it follows that

$$\left\|\tilde{\varepsilon}_i(t)\right\| \leq \left\|\exp(\tilde{A}t)\tilde{\varepsilon}_i(0)\right\| + \left\|\int_0^t \exp[\tilde{A}(t-\tau)]\tilde{B}\frac{\phi_i}{\omega_0^2}d\tau\right\| \tag{20}$$

where $\|\cdot\|$ is the Euclidean Norm then

$$\left\|\tilde{\varepsilon}_i(t)\right\| \leq \left\|\exp(\tilde{A}t)\tilde{\varepsilon}_i(0)\right\| + \frac{\left\|\tilde{B}\phi_i\right\|}{\omega_0^2}\left\|\int_0^t \exp[\tilde{A}(t-\tau)]d\tau\right\|_F \tag{21}$$

where $\|\cdot\|_F$ is the Frobenius Norm of a matrix then assuming the disturbance is bounded such that $\|\phi_i\| < \partial$ then

$$\left\|\tilde{\varepsilon}_i(t)\right\| \leq \left\|\exp(\tilde{A}t)\tilde{\varepsilon}_i(0)\right\| + \frac{\partial}{\omega_0^2}\left\|-\tilde{A}^{-1}[I - \exp(\tilde{A}t)]\right\|_F \tag{22}$$

Then noting that the eigenvalues of $\tilde{A}$ are $\lambda = -\omega_0, -\omega_0, -\omega_0$ then $\exp(\tilde{A}t) \to 0_{3\times3}$ as $t \to \infty$ such that in the limit

$$\left\|\tilde{\varepsilon}_i(t)\right\| \leq \frac{\partial}{\omega_0^2}\left\|-\tilde{A}^{-1}\right\|_F \tag{23}$$

then

$$\left\|\tilde{\varepsilon}_i(t)\right\| \leq \frac{\sqrt{21}\partial}{\omega_0^3} \tag{24}$$

This implies that $\hat{\boldsymbol{x}}_3 \to h$ as $t \to \infty$ to within some small bounded error which can be decreased with an increase in the gain ω_0. Furthermore, as $\hat{\boldsymbol{x}}_2 \to \boldsymbol{x}_2$ then $\boldsymbol{g}(\boldsymbol{x}_1, \hat{\boldsymbol{x}}_2) \to \boldsymbol{g}(\boldsymbol{x})$. Therefore given the position (and velocity if it is available)as an input then the estimated output of the ESO $\hat{\boldsymbol{x}}_2$ converges to the velocity vector $\boldsymbol{x}_2$ within an error bound defined by $\left\|\hat{\boldsymbol{x}}_2 - \boldsymbol{x}_2\right\| \leq \frac{\sqrt{21}\partial}{\omega_0^2}$ and $\hat{\boldsymbol{x}}_3$ converges to the uncertain dynamics $\boldsymbol{x}_3 = h$ within an error bound defined by $\left\|\hat{\boldsymbol{x}}_3 - \boldsymbol{x}_3\right\| \leq \frac{\sqrt{21}\partial}{\omega_0^2}$. Therefore, for a high-gain ($\omega_0 \to \infty$) we can assume that the error of the ESO is negligible.

3.1. Linear AUMC for Improved Convergence With Orbit Injection-Errors

Low-thrust propulsion station-keeping often linearizes the nonlinear equations about the reference trajectory, in this case a halo orbit, and applies linear control theory such as an optimal

Linear control as LQR. Defining the error state $\delta\boldsymbol{x} = \boldsymbol{x} - \boldsymbol{x}_{ref}$, where $\boldsymbol{x}(t) = [x, y, z, \dot{x}, \dot{y}, \dot{z}]^T$ and $\boldsymbol{x}_{ref}$ is the reference halo we can write (7) in the form:

$$\frac{d(\delta\boldsymbol{x})}{dt} = \boldsymbol{A}(t)\delta\boldsymbol{x} + \boldsymbol{u} + \boldsymbol{a}_s + \mathcal{O}(\delta\boldsymbol{x}_2^2) \tag{25}$$

where where $\boldsymbol{A}(t)$ is given by

$$\boldsymbol{A}(t) = \begin{bmatrix} \boldsymbol{0}_{3X3} & \boldsymbol{I}_{3X3} \\ \boldsymbol{U}_{ij} & 2\boldsymbol{\Omega} \end{bmatrix} \tag{26}$$

for

$$\boldsymbol{\Omega} = \begin{bmatrix} 0 & 0 & 1 \\ -1 & 0 & 0 \\ 0 & 0 & 0 \end{bmatrix} \tag{27}$$

and $\boldsymbol{U}_{ij}$ is the Jacobian of U, where each term is defined as

$$\begin{aligned}
U_{xx} &= 1 - \frac{1-\mu}{d^3} - \frac{\mu}{r^3} + 3\frac{(1-\mu)(x+\mu)^2}{d^5} + 3\frac{\mu(x-1+\mu)^2}{r^5} \\
U_{yy} &= 1 - \frac{1-\mu}{d^3} - \frac{\mu}{r^3} + 3\frac{(1-\mu)y^2}{d^5} + 3\frac{\mu y^2}{r^5} \\
U_{zz} &= \frac{1-\mu}{d^3} - \frac{\mu}{r^3} + 3\frac{(1-\mu)z^2}{d^5} + 3\frac{\mu z^2}{r^5} \\
U_{xy} &= 3\frac{(1-\mu)(x+\mu)y}{d^5} + 3\frac{\mu(x-1+\mu)y}{r^5} = U_{yx} \\
U_{xz} &= 3\frac{(1-\mu)(x+\mu)z}{d^5} + 3\frac{\mu(x-1+\mu)z}{r^5} = U_{zx} \\
U_{yz} &= 3\frac{(1-\mu)yz}{d^5} + 3\frac{\mu yz}{r^5} = U_{zy}
\end{aligned} \tag{28}$$

which can be expressed in terms of the position and velocity, writing $\boldsymbol{x}_1 = [\delta x, \delta y, \delta z]$, $\boldsymbol{x}_2 = [\delta\dot{x}, \delta\dot{y}, \delta\dot{z}]$, where

$$\begin{aligned}
\dot{\boldsymbol{x}}_1 &= \boldsymbol{x}_2 \\
\dot{\boldsymbol{x}}_2 &= \boldsymbol{C}(t)\delta\boldsymbol{x} + \mathcal{O}(\delta\boldsymbol{x}_2^2) + \boldsymbol{u} + \boldsymbol{a}_s
\end{aligned} \tag{29}$$

where $\boldsymbol{C}(t)$ is the 6×3 matrix $\boldsymbol{C}(t) = \begin{bmatrix} \boldsymbol{U}_{ij} & 2\boldsymbol{\Omega} \end{bmatrix}$. Note that using the ESO (14) with $\delta\boldsymbol{x}$ from (25) as the input and setting $f(\boldsymbol{x}_1, \boldsymbol{x}_2) = g(\boldsymbol{x}_1, \boldsymbol{x}_2) = \boldsymbol{C}(t)\delta\boldsymbol{x}$ then $\hat{\boldsymbol{x}}_3 \to h$ as $t \to \infty$ where $h = \mathcal{O}(\delta\boldsymbol{x}_2^2) + \boldsymbol{a}_s$, with the linear control taking the form

$$\boldsymbol{u} = -K\delta\boldsymbol{x} - \hat{\boldsymbol{x}}_3 \tag{30}$$

where $\hat{\boldsymbol{x}}_3$ is the output of the following Linear ESO:

$$\begin{aligned}
\dot{\hat{\boldsymbol{x}}}_1 &= \hat{\boldsymbol{x}}_2 + \beta_1(\boldsymbol{x}_1 - \hat{\boldsymbol{x}}_1) \\
\dot{\hat{\boldsymbol{x}}}_2 &= \hat{\boldsymbol{x}}_3 + \boldsymbol{C}(t)\delta\boldsymbol{x} + \boldsymbol{u} + \beta_2(\boldsymbol{x}_1 - \hat{\boldsymbol{x}}_1) \\
\dot{\hat{\boldsymbol{x}}}_3 &= \beta_3(\boldsymbol{x}_1 - \hat{\boldsymbol{x}}_1)
\end{aligned} \tag{31}$$

as $t \to \infty$ the closed-loop dynamics of (25) become:

$$\begin{aligned}
\dot{\boldsymbol{x}}_1 &= \boldsymbol{x}_2 \\
\dot{\boldsymbol{x}}_2 &\approx (C(t) - K)\delta\boldsymbol{x}
\end{aligned} \tag{32}$$

which can be expressed as $\delta\dot{\boldsymbol{x}} \approx A(K, t)\delta\boldsymbol{x}$ then the gain matrix K can be chosen such that $A(K, t)$ is point-wise negative definite and the convergence of the system has a linear response even in the presence of unknown higher-order nonlinear terms and SRP. Typically for large injection errors without an ESO a simple proportional controller would render the closed-loop dynamics nonlinear. Thus, using an ESO to compliment a linear controller can provide the guarantee of a global linear response. The performance of the linear AUMC which yields a linear response is compared to the nonlinear closed-loop response of the LQR in the following subsection.

3.1.1. Simulations

The velocity increments ΔV and the position errors of the spacecraft are important performance metrics to assess the station-keeping strategies. However, when comparing these performance metrics between LQR and AUMC there is only a small improvement when using an ESO. However, simulations show that there is an improvement in the convergence time when considering large injection-errors to within a bounded region of the reference orbit of 20 km and 0.05 m/s . In the simulations this is demonstrated for an initial injection error of $\delta X = 100$ Km, $\delta V = 1$ m/s. The observer is tuned with $\omega_0 = 100$. In this simulation

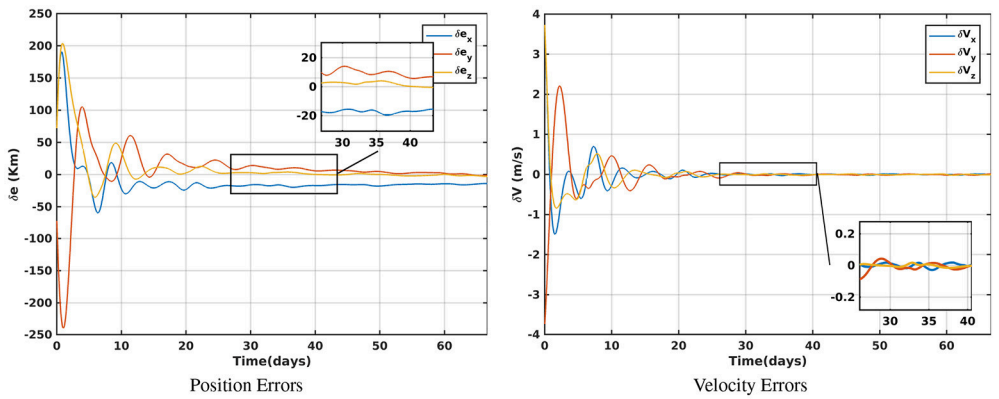

FIGURE 1 | Errors in the position and velocity: LQR.

we assume the SRP is negligible. Recall that in the case of a Linear ESO the inputs are $\delta \boldsymbol{x}$

Figure 1 highlights the results of halo orbits position and velocity errors encountered due to the presence of injection error of 100 Km for the LQR control. Similar results can be seen for the control AUMC in **Figure 2**.

It takes around 17.027 days to converge to a steady state error within 20 km compared to 27.117 days for LQR which is about of 37.2% decrease in convergence time while the error is just decreased by 4.2%.

It can be seen from **Figure 3** that the control effort over time for the AUMC and the LQR is similar in magnitude and nature and therefore the ΔV is approximately the same.

Note that an additional possibility for the design of a linear ESO is to set $g(\boldsymbol{x}_1, \boldsymbol{x}_2) = 0$. In this case $h = C(t)\boldsymbol{x} + \boldsymbol{a}_S$ and therefore as $t \to \infty$ the output of ESO $\hat{\boldsymbol{x}}_3 \to C(t)\boldsymbol{x} + \boldsymbol{a}_S$. Then as $t \to \infty$ the closed-loop linear system becomes:

$$\begin{aligned} \dot{\boldsymbol{x}}_1 &= \boldsymbol{x}_2 \\ \dot{\boldsymbol{x}}_2 &= -K\delta \boldsymbol{x} \end{aligned} \tag{33}$$

Therefore, K can be chosen such that the system is asymptotically stable. In this case the closed-loop system exhibits a linear response independently. This type of control is also useful as it requires only the position of the spacecraft with respect to the reference trajectory and does not require the dynamics of the problem to be stored on-board.

3.2. Nonlinear AUMC for Velocity and SRP Estimation

In this section we consider using the control with an ESO where $g(\boldsymbol{x}_1, \boldsymbol{x}_2) = f(\boldsymbol{x}_1, \hat{\boldsymbol{x}}_2)$ is described by the full-nonlinear function. In contrast to the linear ESO whose input is $\delta \boldsymbol{x}$ the input to the nonlinear ESO is the absolute position of the spacecraft $\boldsymbol{x}_1$. In this case $h = \boldsymbol{a}_S$ and therefore as $t \to \infty$ the output of ESO $\hat{\boldsymbol{x}}_3 \to \boldsymbol{a}_S$. Therefore, while stabilizing the spacecraft on a Halo orbit it is possible to measure the SRP $\boldsymbol{a}_S$ and given that the Sun-direction can be obtained from a Sun sensor and the position of the spacecraft is known then the uncertain coefficient a_0 can be obtained. As $\hat{\boldsymbol{x}}_2 \to \boldsymbol{x}_2$ as $t \to \infty$ then $f(\boldsymbol{x}_1, \hat{\boldsymbol{x}}_2) \to f(\boldsymbol{x}_1, \boldsymbol{x}_2)$. In this case as $t \to \infty$ the closed-loop dynamics are:

$$\begin{aligned} \dot{\boldsymbol{x}}_1 &= \boldsymbol{x}_2 \\ \dot{\boldsymbol{x}}_2 &= f(\boldsymbol{x}_1, \boldsymbol{x}_2) - K_1\delta \boldsymbol{x}_1 - K_2\delta \boldsymbol{x}_2 \end{aligned} \tag{34}$$

although the closed-loop dynamics is independent of the SRP a linear response can only be guaranteed if $f(\boldsymbol{x}_1, \boldsymbol{x}_2) \approx C(t)\delta \boldsymbol{x}$. For the nonlinear stability to be guaranteed we can augment the control (35) to include a sliding-mode component and setting $K_1 = kK_2$ with $kK_1\boldsymbol{x}_i = K_2\boldsymbol{x}_i = k_1\boldsymbol{x}_i$ where k_1 is a scalar then

$$\boldsymbol{u} = -k_1 S - \hat{\boldsymbol{x}}_3 - k_3 \mathrm{sgn} S \tag{35}$$

where S defines the sliding surface $S = k\delta \boldsymbol{x}_1 + \delta \boldsymbol{x}_2$ that this is assuming that the estimator accurately measures the velocity.

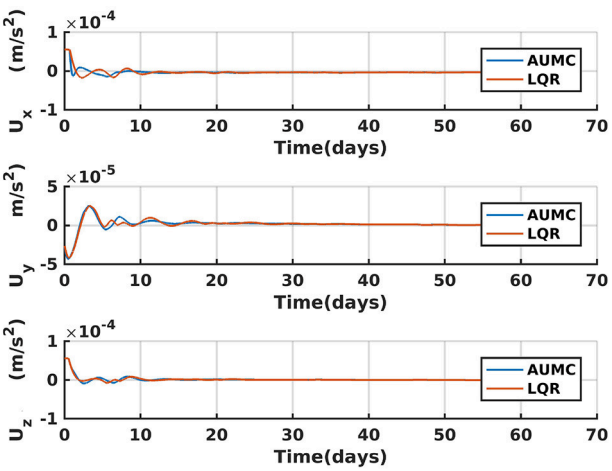

FIGURE 3 | Control effort of LQR and AUMC.

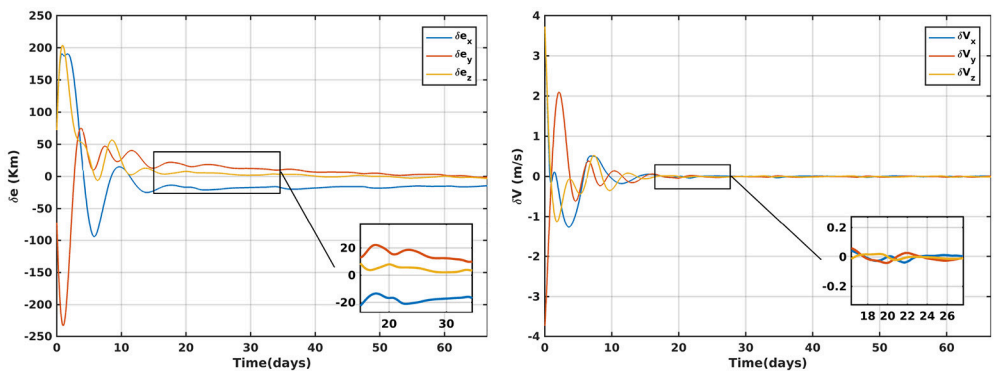

FIGURE 2 | Errors in the position and velocity: AUMC.

Then considering the Lyapunov function:

$$V = \frac{1}{2} S^T S \tag{36}$$

differentiating this with respect to time and substituting in (35) yields

$$\begin{aligned} \dot{V} &= S^T \dot{S} = S^T (k\delta\dot{\boldsymbol{x}}_1 + \delta\dot{\boldsymbol{x}}_2) \\ &= S^T (k\delta\boldsymbol{x}_2 + \boldsymbol{C}(t)\delta\boldsymbol{x} + \mathcal{O}(\delta\boldsymbol{x}_2^2) - k_1 S - k_3 \mathrm{sgn} S) \\ &= -k_1 S^T S - k_3 S^T \mathrm{sgn} S + S^T (k\delta\boldsymbol{x}_2 + \boldsymbol{C}(t)\delta\boldsymbol{x} + \mathcal{O}(\delta\boldsymbol{x}_2^2)) \\ &\leq -k_1 S^T S - k_3 |S| + |S| \left| k\delta\boldsymbol{x}_2 + \boldsymbol{C}(t)\delta\boldsymbol{x} + \mathcal{O}(\delta\boldsymbol{x}_2^2) \right| \end{aligned} \tag{37}$$

Therefore, we have asymptotic stability if $k_3 > \left| k\delta\boldsymbol{x}_2 + \boldsymbol{C}(t)\delta\boldsymbol{x} + \mathcal{O}(\delta\boldsymbol{x}_2^2) \right|$.

3.2.1. Simulations

In the following simulations we assume that a single side of the spacecraft and its solar panels (or a solar sail surface) is controlled to point continuously toward the Sun such that is $\boldsymbol{S} = \boldsymbol{n}$ in (4). In addition for the purpose of demonstration we choose a large value for the SRP acceleration in non-dimensional units to be $a_0 = 0.0798$ or $0.215 \mathrm{mms}^{-2}$ which is a typical value considered for the characteristic acceleration of the Sunjammer Solar sail [11]. However, we consider here that this value is uncertain and must be accurately estimated on-board. The nonlinear ESO is able to accurately measure the characteristic acceleration using only inputs of the position of the spacecraft. **Figure 4** shows that the estimator converges to the correct value of a_0 after approximately 0.6 days. The simulation is carried out with an initial position error magnitude of 120 km. Recall that this simulation includes injection errors, large characteristic acceleration due to SRP and only position knowledge. The demonstrated simulations here only include the disturbance rejection and proportional part of the controller so that they are more readily comparable to the linear case.

Figure 5 illustrates the estimated velocity in the x-direction which shows good tracking performance after an initial transient of approximately 2 days while an additional improvement in the estimation error can be seen after around 10 days.

Figure 6 shows the tracking error over time and **Figure 7** shows the corresponding control. The tracking error is within the range of 50 km although this can be improved by increasing the magnitude of the gain matrix K but at the expense of an increase in the control magnitude. The important point here is that station-keeping is achieved without knowledge of the velocity. It is not possible to obtain good tracking performance without velocity measurements or an estimate of the velocity provided by ESO.

The simulations demonstrate that a nonlinear ESO can be useful for estimating the uncertain disturbances such as SRP in deep-space. Such information would be useful to modify the reference orbit to obtain more fuel-efficient station-keeping. Moreover, although high-fidelity solar system models are available SRP is still uncertain and an ESO provides a simple mechanism for estimating it. Furthermore, the ESO provides robustness to velocity sensor failure. In particular, without velocity information a proportional controller will perform very poorly and the tracking error can be unacceptably large. Using an ESO the tracking performance and corresponding control effort is improved significantly.

4. CONCLUSION

The dynamics of a spacecraft in a Lagrange point orbit are highly nonlinear and are affected by uncertain forces of solar radiation pressure. In this paper, we construct active uncertainty measurement controls for station-keeping that can guarantee asymptotic stability in the presence of orbit injection errors and SRP. The SRP acceleration parameter is estimated by the observer while station-keeping. This could be useful as accurate measures of the disturbances would allow a more accurate dynamical model of the spacecraft's orbit and the reference trajectory could be updated to a more efficient one during the mission. In addition, it is shown that station-keeping and

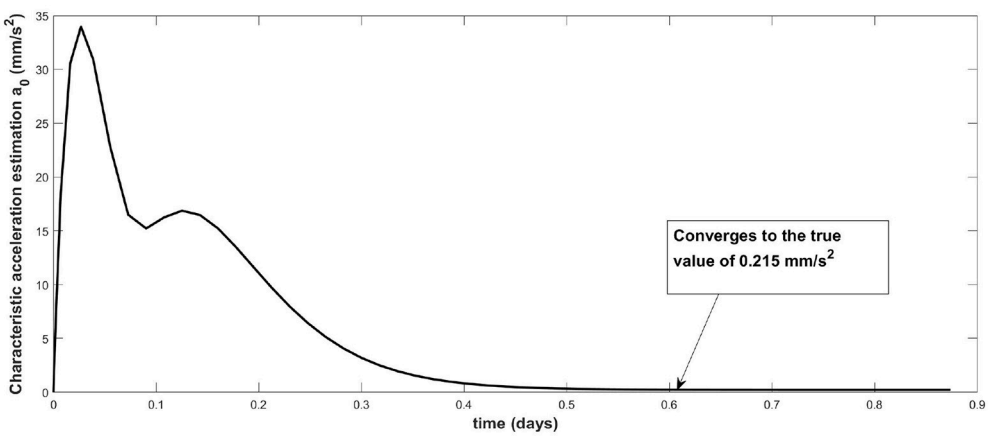

FIGURE 4 | Plot of the output estimation of the ESO of the characteristic acceleration a_0 related to the SRP disturbance.

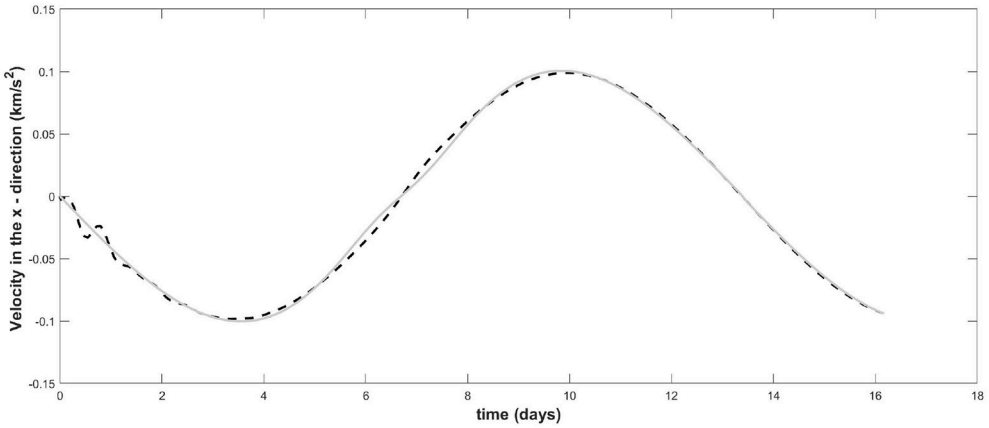

FIGURE 5 | The ESO estimation of the velocity in the x-direction: The real velocity is in gray and the dashed line is the estimated velocity.

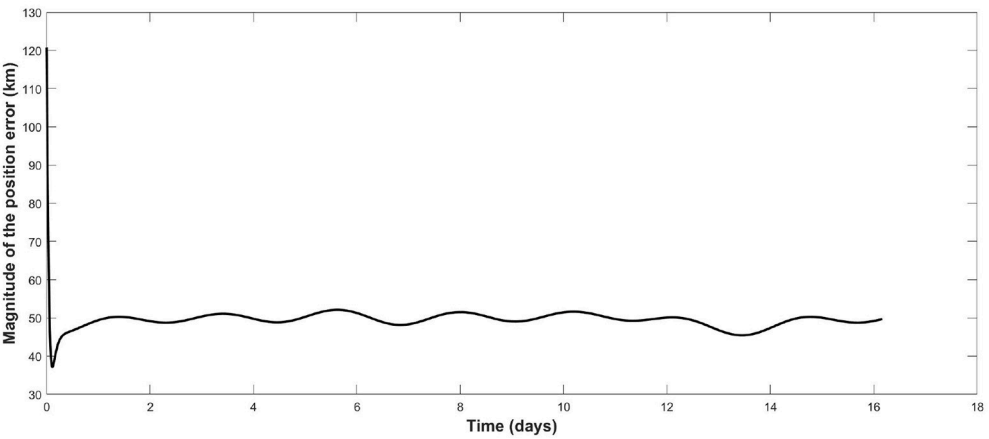

FIGURE 6 | Tracking position error over time.

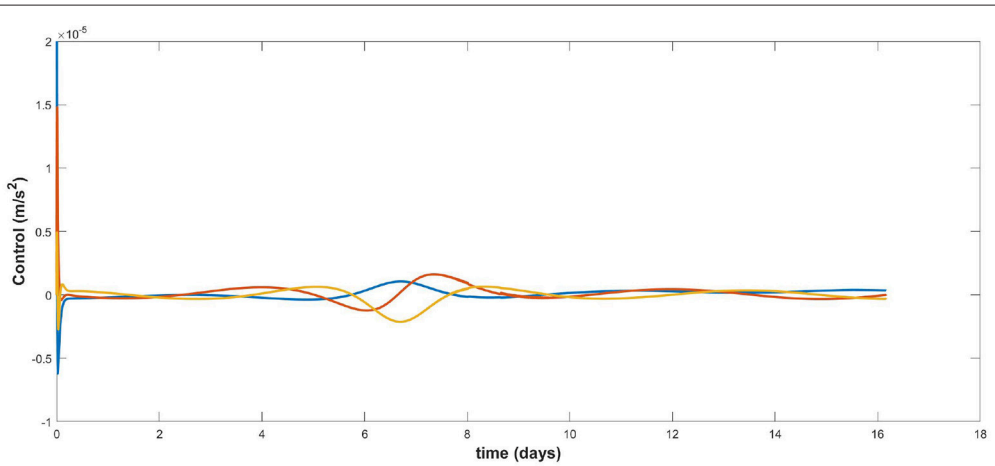

FIGURE 7 | Control signal over time.

disturbance measurements can be undertaken simultaneously using only the position knowledge of the spacecraft. This could be useful in the event that velocity sensors experience failure. This paper has demonstrated the potential uses of coupling a simple ESO with a proportional control to form an AUMC. However, there is scope for potential improvement in performance by replacing the proportional controller with other higher-performance controllers, such as sliding mode controllers, while replacing the simple ESO with nonlinear observers with the potential for greater accuracy and faster convergence. Future work could also include coupling the ESO that measures the solar radiation pressure with an on-board differential corrector so that when an accurate measure of the disturbance is obtained the reference orbit can be updated to a more natural one of the true dynamical model. In addition while we show here that the ESO can be used to measure the SRP with only knowledge of the position of the spacecraft it could be possible to use an extension of this approach to estimate highly-inhomogeneous gravity fields when orbiting asteroids or Moons. Furthermore, the mathematical demonstration of stability and the linear response of the closed-loop system in this paper relies on the assumption that the estimation error of the ESO is negligible. Future work could develop stability proofs and control laws that do not include this assumption.

AUTHOR CONTRIBUTIONS

AN undertook extensive simulations of the comparison of LQR control and the control with an extended state observer. HH assisted in developing the mathematical proofs and writing of the paper. JB described the general extended state observer with proof of convergence and its use for improving convergence and obtaining the solar radiation pressure.

REFERENCES

1. Howell KC. Three dimensional, periodic, 'halo'orbits. *Celest Mech.* (1984) **32**:53. doi: 10.1007/BF01358403
2. Farquhar R. *The Utilization of Halo Orbits in Advanced Lunar Operation*. Greenbelt, MD: NASA TN D-6365, GSFC (1971).
3. Shirobokov M, Trofimov S, Ovchinniko M. Survey of station-keeping techniques for libration point orbits. *J Guid Control Dyn.* (2017) **40**:1085–105. doi: 10.2514/1.G001850
4. Wie B. *Space Vehicle Dynamics and Control*, Chap. 2. AIAA Education Series. Reston, VA: AIAA (2008).
5. Gómez G, Llibre J, Martínez R, Simó C. *Dynamics and Misson Design Near Libration Points. Vol II Fundamentals: The Case of Colinear Libration Points*. Singapore: World Scientific (2001).
6. Topputo F, Massari M, Biggs JD, Di Lizia P, Mani K, Dei Tos D, et al. *LUMIO: Lunar Meteroid Impacts Observer*. ESA contract number: 4000120225/17/NL/GLC/ac, Technical Report (2017).
7. Acton C Jr, Bachman N, Semenov B, Wright E. A look towards the future in the handling of space science mission geometry. *Planet Space Sci.* (2018) **150**:9–12. doi: 10.1016/j.pss.2017.02.013
8. Dachwald B, Macdonald M, McInnes CR, Mengali G, Quarta AA. Impact of optical degradation on solar sail mission performance. *J Spacecraft Rock.* (2007) **44**:740–9. doi: 10.2514/1.21432
9. Spencer H, Carroll KA. Real solar sails are not ideal, and yes it matters. In: Macdonald M, editor. *Advances in Solar Sailing, Springer Praxis Books*. Berlin; Heidelberg: Springer (2014). p. 921–40.
10. McKay R, Macdonald M, Biggs J, McInnes C. Survey of highly non-keplerian orbits with low-thrust propulsion. *J Guid Control Dyn.* (2011) **34**:645–66. doi: 10.2514/1.52133
11. Heiligers J, Hiddink S, Noomen R, McInnes CR. Solar sail Lyapunov and halo orbits in the Earth-Moon three-body problem. *Acta Astronaut.* (2015) **116**:25–35. doi: 10.1016/j.actaastro.2015.05.034
12. Heiligers J, Ceriotti M, McInnes CR, Biggs JD. Design of optimal earth pole-sitter transfers using low-thrust propulsion. *Acta Astronaut.* (2012) **79**:253–68. doi: 10.1016/j.actaastro.2012.04.025
13. Biggs JD, McInnes CR. Solar sail formation flying for deep-space remote sensing. *J Spacecraft Rock.* (2009) **46**:670–8. doi: 10.2514/1.42404
14. Biggs JD, McInnes CR, Waters T. Control of solar sail periodic orbits in the elliptic three-body problem. *J Guid Control Dyn.* (2009) **32**:318–20. doi: 10.2514/1.38362
15. Biggs JD, McInnes CR. Passive orbit control for space-based geo-engineering. *J Guid Control Dyn.* (2010) **33**:1017–20. doi: 10.2514/1.46054
16. Di Giamberardino P, Monaco S. On halo orbits spacecraft stabilization. *Acta Astronaut.* (1996) **38**:903–25. doi: 10.1016/S0094-5765(96)00082-3
17. Cielaszyk D, Wie B. New approach to halo orbit determination and control. *J Guid Control Dyn.* (1996) **19**:266–73. doi: 10.2514/3.21614
18. Lian Y, Gómez G, Masdemont J, Tang G. Station-keeping of real Earth-Moon libration point orbits using discrete-time sliding mode control. *Commun Nonlin Sci Numer Simulat.* (2014) **19**:3792–807. doi: 10.1016/j.cnsns.2014.03.026
19. Zhu M, Karimi H, Zhang H, Gao Q, Wang Y. Active disturbance rejection station-keeping control of unstable orbits around collinear libration points. *Math Prob Eng.* (2014) **2014**:410989. doi: 10.1155/2014/410989
20. Narula A, Biggs JD. Fault-tolerant station-keeping on libration point orbits. *J Guid Control Dyn.* (2018) **41**:879–87. doi: 10.2514/1.G003115
21. Han J. From PID to active disturbance rejection control. *IEEE Trans Indust Electr.* (2009) **56**:900–6. doi: 10.1109/TIE.2008.2011621
22. Xing C, Donghai L, Zhiqiang G, Chuanfeng W. Tuning method for second-order active disturbance rejection control. In: *Proceedings of the 30th Chinese Control Conference 22–24 July*. Yantai (2011).
23. Bai Y, Biggs JD, Bernelli-Zazzera F, Cui N. Adaptive attitude tracking with active uncertainty rejection. *J Guid Control Dyn.* (2018) **41**:550–8. doi: 10.2514/1.G002391

Conflict of Interest Statement: The authors declare that the research was conducted in the absence of any commercial or financial relationships that could be construed as a potential conflict of interest.

frontiers in Astronomy and Space Sciences

ORIGINAL RESEARCH
published: 22 January 2019
doi: 10.3389/fspas.2018.00045

Rendezvous Strategies in the Vicinity of Earth-Moon Lagrangian Points

Stephanie Lizy-Destrez[1]*, *Laurent Beauregard*[1], *Emmanuel Blazquez*[1], *Antonino Campolo*[1,2], *Sara Manglativi*[1,2] and *Victor Quet*[1]

[1] ISAE-SUPAERO, Toulouse, France, [2] Dipartimento di Scienze e Tecnologie Aerospaziali (DAER), Politecnico di Milano, Milan, Italy

In the context of Human Spaceflight exploration mission scenario, with the Lunar Orbital Platform- Gateway (LOP-G) orbiting about Earth-Moon Lagrangian Point (EML), Rendezvous and Docking (RVD) operational activities are mandatory and critical for the deployment and utilization of the LOP-G (station assembly, crew rotations, cargo delivery, lunar sample return). There is extensive experience with RVD in the two-body problem: in Low Earth Orbit (LEO) to various space stations, or around quasi-circular Low Lunar Orbits (LLO), the latter by Apollo by means of manual RVD. However, the RVD problem in non-Keplerian environments has rarely been addressed and no RVD has been performed to this date in the vicinity of Lagrangian points (LP) where Keplerian dynamics are no longer applicable. Dynamics in such regions are more complex, but multi-body dynamics also come with strong advantages that need to be further researched by the work proposed here. The aim of this paper is to present methods and results of investigations conducted to first set up strategies for far and close rendezvous between a target (the LOP-G, for example) and a chaser (cargo, crew vehicle, ascent and descent vehicle, station modules, etc.) depending on target and chaser orbit. Semi-analytical tools have been developed to compute and model families of orbits about the Lagrangian points in the Circular Restricted Three Body Problem (CR3BP) like NRHO, DRO, Lyapunov, Halo and Lissajous orbits. As far as close rendezvous is concerned, implementation of different linear and non-linear models used to describe cis-lunar relative motion will be discussed and compared, in particular for NRHO and DRO.

Keywords: rendezvous, trajectory, CR3BP, Earth-Moon system, Lagrangian points, relative motion

OPEN ACCESS

Edited by:
Elisa Maria Alessi,
Italian National Research Council, Italy

Reviewed by:
Francesco Topputo,
Politecnico di Milano, Italy
Fabio Ferrari,
NASA Jet Propulsion Laboratory (JPL), United States
Maksim Shirobokov,
Keldysh Institute of Applied Mathematics (RAS), Russia

***Correspondence:**
Stephanie Lizy-Destrez
stephanie.lizy-destrez@isae-supaero.fr

Specialty section:
This article was submitted to Fundamental Astronomy, a section of the journal Frontiers in Astronomy and Space Sciences

Received: *26 February 2018*
Accepted: *05 December 2018*
Published: *22 January 2019*

Citation:
Lizy-Destrez S, Beauregard L, Blazquez E, Campolo A, Manglativi S and Quet V (2019) Rendezvous Strategies in the Vicinity of Earth-Moon Lagrangian Points. Front. Astron. Space Sci. 5:45. doi: 10.3389/fspas.2018.00045

INTRODUCTION

On the road to a solar system human exploration, the International Space Exploration Coordination Group (ISEGC) (ISECG, 2018) has identified several mission scenarios beyond Low Earth Orbit (LEO) as significant landmarks. In particular, it envisions to develop and operate with the collaboration of all main international space agencies a Lunar Orbital Platform—Gateway (LOP-G) as an outpost, located about one of the Earth-Moon Lagrangian points. This station will be used as a strategic platform and a logistic hub for human missions in cis-lunar space, including lunar surface and even beyond (Mars or asteroids destinations). Moreover, innovative technologies could be tested onboard, taking benefit from a unique environment. At this time, such an option is likely to rely on the NASA/ESA Orion MPCV (Multi-Purpose Crew Vehicle) and a heavy launcher, like the Space Launch System (SLS). Thus, Rendezvous and Docking (RVD) operational activities become mandatory and critical for the deployment and utilization of the

LOP-G (like station assembly, crew rotations, cargo delivery, or lunar sample return). As the next space station will be a gateway for future exploration missions, various rendezvous missions may be performed, including logistics flight and crew transportation missions from the Low Earth Orbit (LEO), Geostationary (GEO) or LLO (Lunar Low Orbit), so as to reach NRHO (Near Rectilinear Halo Orbit), DRO (Distant Retrograde Orbit) or Halo Orbits. As the capacity to rendezvous in the vicinity of Earth-Moon Lagrangian Points is by nature necessary, its analysis becomes fundamental.

Despite a very extensive experience with RVD in the two-body problem (in Low Earth Orbit to various space stations, or around quasi circular Low Lunar Orbits, the latter by Apollo by means of manual RVD), the RVD problem in non-Keplerian environment has rarely been addressed and no RVD has yet been performed to this date in the vicinity of Lagrangian points where Keplerian dynamics are no longer applicable. As a consequence, researches presented in this paper contribute to a better understanding of potential mission scenarios to rendezvous in the vicinity of Earth-Moon Lagrangian Points.

This paper aims to study the rendezvous trajectories in the vicinity of the Earth-Moon Lagrangian points, EML1 or EML2. The Circular Restricted Three–Body Problem (CR3BP) has been highlighted among more complex models so as to describe the non-linear dynamics in this area. In the selected scenario, the target's orbit is assumed to belong to Halo orbits, NRHO or DRO families, with a fixed attitude. The chaser is supposed to be equipped with chemical propulsion. Considering only impulsive maneuvers, their effect is instantaneous and chaser's motion is ballistic between maneuvers. This paper addresses the feasibility of a rendezvous based on trajectories benefiting from natural dynamics and limiting fuel consumption. Once the feasibility has been demonstrated, an optimization process will be carried out in order to minimize rendezvous operations' duration and the consumption. This optimal scenario can be then used as a first guess to develop refined trajectories with intermediate maneuvers so as to correct the effects of orbit estimation's errors, of maneuvers inaccuracies and perturbations (gravitational influence of the other celestial bodies like the Sun, the Sun radiation pressure, etc.). In this paper, those effects are neglected.

After transfer from LEO, lunar surface or other distant locations (Mars, asteroids, etc.) and before docking activities, the rendezvous is decomposed in two main stages. On the one hand, far rendezvous and close rendezvous are analyzed independently from the theoretical point of view. On the other hand, for application purposes, a unique scenario will be presented for NRHO, with proposed extensions to other families of orbits, and in particular when the chaser and the target's orbit are of a different type. Moreover, when close rendezvous is concerned, the objective is to extend classical methods proven in the two-body problem to the three-body problem. The first contribution of this paper is to propose a far rendezvous strategy with the use of invariant structures extended by Lambert arcs to minimize the cost of the mission. A second contribution lies in the use of a non-linear model to describe the relative motion during close rendezvous stage. The third contribution corresponds to a preliminary safety analysis in case of a failure of the propulsion sub-system (either in direction or in magnitude).

After a summary of the bibliographical context and a description of the theoretical background, this paper will propose strategies for far and close rendezvous between a target and a chaser depending on both vehicles' initial orbits. In the case of the far rendezvous, a strategy in three maneuvers is presented, with the main objective of using the invariant structures derived from the natural dynamics in the vicinity of the Lagrange point. In the case of the close rendezvous, the algorithm used to compute the trajectory of the chaser to the target is detailed in two steps: a first guess, where the relative motion between the chaser and the target is linearized, then a more precise computation of the trajectory arcs with a non-linearized relative motion. The last paragraph depicts two specific scenarios where the chaser and the target are in orbits (from the same family) around the EML2. The selected examples mainly concern the Halo and NRHO orbits. They are chaining the far rendezvous and the close rendezvous, before analyzing the safety aspects.

HISTORICAL OVERVIEW OF THE BIBLIOGRAPHICAL CONTEXT

A growing interest of the space scientific community for trajectories toward, around and from Lagrangian points has been registered in recent years. In particular, the three-body problem (Szebehely, 1967) is one of the most studied models not only in celestial mechanics, but also in mathematics. For the early first solar system exploration missions (like Voyager), a patched conics model was satisfactory to compute the trajectory. As interplanetary missions became more demanding (as far as fuel consumption or accuracy are concerned), this strategy connecting several two body-problems was applied as a first design approximation. Thus, other strategies (like three body-problem and more) can be preferred. Moreover, some science space missions take advantage of particular properties of the Lagrangian points. In recent decades, many theoretical studies have demonstrated the benefits of highly non-linear dynamics to space exploration missions.

When looking at the set of studies performed in the field of Lunar Libration Points, one stumbles upon the fathers and main advocates of utilization concepts for these points repeatedly. Lagrangian points are defined as equilibrium points in the rotating referential of the studied system. R. Farquhar published the first papers on the utilization of co-linear EMLs in the late sixties and early seventies, including the application for communication relay satellites (Farquhar, 1967), inhabited space stations in a Halo orbit around EML2 (Farquhar, 1972) and moreover, on the utility of Lagrangian Points (LPs) for human solar system exploration (Farquhar et al., 2004)

Beyond the study of utilization of the Lagrangian Points location, the interest in these models focuses on the emergence of invariant structures, such as periodic or quasi-periodic orbits (Farquhar, 1973; Richardson, 1980; Howell, 1984) and their related stable and unstable manifolds (Gómez et al., 2001, 2004; Koon et al., 2001). These invariant structures make it possible first

to design staging orbits in the vicinity of the Lagrangian points, then to establish low-energy trajectories for transfer between the Earth, the Moon and the Lagrangian points. This paved the way for mission's concepts taking benefit of these invariant structures so as to minimize fuel consumption through various strategies like Indirect transfer (Alessi et al., 2010), Weak Stability Boundary (Belbruno and Carrico, 2000; Belbruno, 2002) or Lunar flyby (Mingtao and Zheng, 2010), for Earth-to-EML2 (Parker and Anderson, 2013) or Earth-to-Moon tranfers (Mingotti et al., 2012).

Despite this vast literature on orbits about the Lagrangian points and transfers in the cis-lunar realm, the scientific community has, at the moment, very few relevant researches on rendezvous trajectories in non-keplerian dynamics. Actually, a large amount of publications from 1950s to today dealing with rendezvous can be found. But the typical rendezvous problem considers that both vehicles are in orbit about a massive celestial body (Earth, Moon, Mars…) and lies only in the two-body problem. Even though rendezvous is a critical phase, it has rarely been studied in the context of the non-keplerian dynamics except by Gerding (1971) in 1971, Jones and Bishop (1994) in 1993 and 1994 and by Canalias (Canalias and Masdemont, 2006) in 2006. Nevertheless, a recent emergence of some sparse publications can be observed since 1993, with a growing interest after 2015 that can be explained by the studies related to LOP-G and Orion missions (Davis et al., 2017; Williams et al., 2017). Two main periods can be noticed: first scenario with the target on Halo orbit around EML2, second scenario with the target on NRHO or a DRO around EML1/2. During the first period, Mand (2014) expressed linearized relative motion of the chaser compared to the target on a Halo orbit around the EML2 within an ephemeris model. Afterwards Ueda and Murakami (Murakami et al., 2015; Ueda and Murakami, 2015) presented a global scenario with a departure from LEO, a transfer in cis-lunar realm, a lunar flyby, an insertion on the target's Halo orbit around EML2, close rendezvous and proximity operations, within ephemeris model for transfer and CR3BP in the vicinity of EML2. This scenario is limited to a unique case with a given Halo orbit of the target, with a fixed attitude and only one insertion point for the chaser (best compromise between fuel consumption and time of flight). Meanwhile, Lizy-Destrez (2015) proposed a different strategy with three burns, relying on invariant structures in the CR3BP to transfer the chaser from a Halo parking orbit to the target's parking orbit. This approach is detailed in section Far Rendezvous Strategy. A parametric analysis was conducted to evaluate the impact of the chaser's departure location, of the position of the intermediate maneuver and of the insertion location on the target's Halo orbit on the rendezvous performances (duration, time of flight). Colagrossi (Colagrossi et al., 2016) extended the theme to rendezvous with very large infrastructures, including coupling effects between orbital and attitude motion. A second period took place after recent publications from NASA (Whitley and Martinez, 2016; Davis et al., 2017; Williams et al., 2017), that confirmed the attractiveness of less classical families of orbits, like DRO and NRHO. In 2015, Murakami (Murakami and Yamanaka, 2015) introduced transfer trajectories from LEO to DRO with three-impulsive maneuvers, one of which is a lunar flyby. In 2017, Ueda (Ueda et al., 2017) evaluates the guidance performance of a linearized relative motion on Halo orbits, a NRHO or a DRO. In 2017, Campolo (Campolo et al., 2017) presented a general close approach rendezvous strategy designed to ensure safety throughout during all rendezvous stages in the NRHO about EML2 case.

Thanks to this analysis of the bibliographic context, it can be observed that the theme of the transfer trajectories in the Earth-Moon system has been largely covered, that the theme of the rendezvous strategies is booming and that the theme of the safety begins slowly.

THEORETICAL PROBLEM OVERVIEW

The mathematical model selected here to represent the dynamical environment is the Circular Restricted Three-Body Problem, as it produces quick and efficiently quantitative results for transfers between primaries and libration orbits. As this model has been deeply detailed in many publications, this paper mainly refers to Parker and Chua (2012), which proposes a complete synthesis.

Circular Restricted Three-Body Problem

The 3-body problem consists in the prediction of the motion of a particle of mass m under the gravitational influence of two massive bodies with respective masses (m_1 and m_2), with $m << m_2 < m_1$. The three bodies are assumed to be isolated, that is to say that no other effect has to be taken into account. Considering that the particle is massless, the problem is said to be "Restricted." The model becomes the Circular Restricted Three-Body Problem (CR3BP) when the primaries are supposed to be on circular orbits about their common center of mass. The equations of motion of the particle are described in the rotating reference synodic frame, centered on O, the center of mass of the system M_1-M_2 and with the x-axis directed from M_1 (the larger primary) to M_2 (the smaller primary) and the y-axis in the plane of the

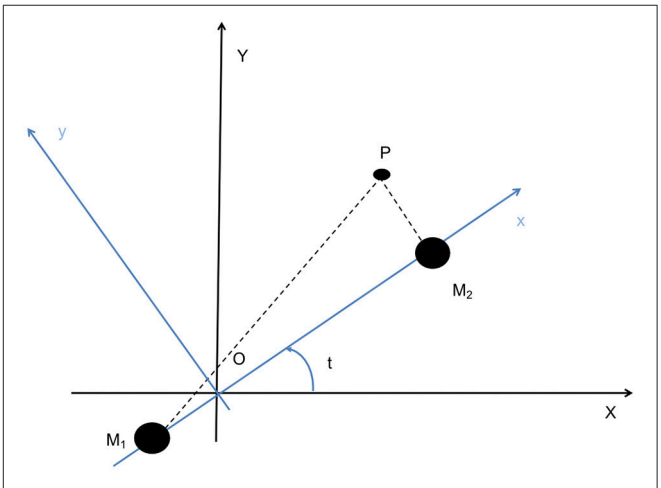

FIGURE 1 | Inertial and synodic reference frames.

primaries' motion (see **Figure 1**), the z-axis completes the right hand system.

Masses, distances and time are normalized respectively with the sum of the primaries' masses, the distance between them and their angular velocity around their barycenter. The unit of time is taken such that the period of the orbits of the primaries is 2π. The universal constant of gravitation, G, becomes then $G = 1$. The only remaining parameter in the system of equations is the mass parameter, μ, defined as $\mu = \frac{m_2}{m_1+m_2}$ where $\mu \in \left[0, \frac{1}{2}\right]$.

When the position vector of the particle is given by $\mathbf{r} = (x, y, z)$, its equations of motion in the CR3BP (Koon et al., 2001), using Newton's law are:

$$\begin{cases} \ddot{x} - 2\dot{y} = \frac{\partial U}{\partial x} \\ \ddot{y} + 2\dot{x} = \frac{\partial U}{\partial y} \\ \ddot{z} = \frac{\partial U}{\partial z} \end{cases} \quad (1)$$

where the effective potential, $\bar{U}$, is given by:

$$\bar{U}(x, y, z) = \frac{x^2 + y^2}{2} + \frac{1-\mu}{r_1} + \frac{\mu}{r_2} + \frac{\mu(1-\mu)}{2} \quad (2)$$

where $r_1 = \sqrt{(x+\mu)^2 + y^2 + z^2}$ and $r_2 = \sqrt{(x-1+\mu)^2 + y^2 + z^2}$ are the distances from the particle to M_1 and M_2 primaries.

The dot ($\dot{}$) denotes the time first derivative (velocity) and the double dot ($\ddot{}$) denotes the time second derivative (acceleration). The state of the particle is given by: $X = (x, y, z, \dot{x}, \dot{y}, \dot{z})$. The equations of motion (1) can be written as:

$$\dot{X} = f(X) \quad (3)$$

From the equation of motion (3), let's denote, Φ , the flow map of the system, mapping the position of the particle from its initial location at time, t_0 to its location at time, t, with under initial conditions X_0: $\Phi(t, t_0, X_0) : X(t_0) \rightarrow X(t) \, \forall t \geq t_0$ with $\Phi(t_0, t_0, X(t_0)) = X_0$.

Lagrangian Points and Families of Orbits in the CR3BP

The system (1) has five equilibrium points, referred to as Libration or Lagrangian points, L_i, $i = 1 \ldots 5$ or EML_i in the Earth-Moon system. The collinear points L_1, L_2, and L_3 are on the line connecting the two primaries, while L_4 and L_5 are equilateral points. In this paper, the distance from L_i, to the smallest primary, is named γ_i (Szebehely, 1967). According to the literature (Szebehely, 1967; Farquhar, 1972, 1973; Whitley and Martinez, 2016), several families of orbits around them exist, usually designated as: Lissajous orbits, Horizontal Lyapunov orbits, Vertical Lyapunov orbits, Halo orbits (including Near Rectilinear Halo Orbits) or Distant Retrograde Orbits. This paper mainly focuses on Halo orbits, which are three-dimensional and periodic with the same in- and out-of-plane oscillation and

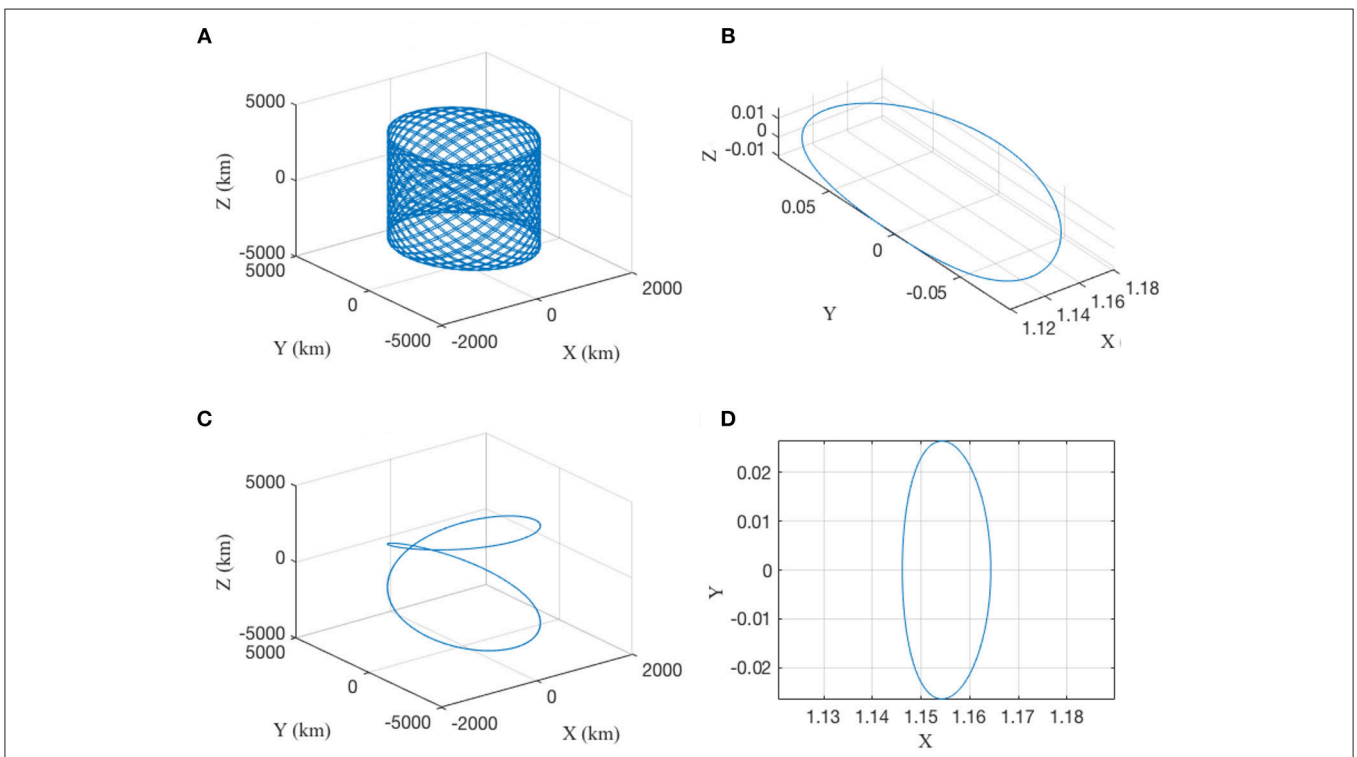

FIGURE 2 | Examples of periodic orbits around EML2. **(A)** Lissajous trajectory with Ay = Az = 3,500 km, **(B)** Halo trajectory Az = 5,000 km, **(C)** Eight shape Lissajous trajectory with Ay = Az = 3,500 km and **(D)** Horizontal Lyapunov trajectory with Ay = 3,500 km.

NRHO, which are particular case of Halo orbits, with a close passage over a lunar pole. Moving inside the family toward the Moon, the Halo orbits become more and more rectilinear as the lunar gravitational influence becomes highly predominant. Some studied cases refer to Horizontal Lyapunov orbits, which lays in the orbital plane of the primaries (xy-plane), to Vertical Lyapunov (or eight-shaped) orbits, which are three-dimensional, almost vertical and periodic orbits. Some scenarios are also applied on DRO, which are very stable solutions, encircling the Moon in a clockwise way in the Earth-Moon rotating frame.

Figure 2 depicts some examples of periodic orbits about EML2, obtained from an expansion of the linearized equations of motions in the CR3BP with Legendre polynomials, as a first guess for the Lindstedt-Poincaré method (Parker and Chua, 2012). Plots on **Figure 2** correspond to (A) Lissajous trajectory with $A_y = A_z = 3{,}500$ km, (B) Halo trajectory $A_z = 5{,}000$ km, (C) Eight shape Lissajous trajectory with $A_y = A_z = 3{,}500$ km and (D) Horizontal Lyapunov trajectory with $A_y = 3{,}500$ km.

From (Canalias, 2007), the system (1) of equations of motion of the particle can be linearized in the vicinity of the studied Lagrangian point with the Legendre polynomial. Under those conditions, the solutions of the linearized system can be expressed as:

$$\begin{cases} x = A_1 e^{\lambda t} + A_2 e^{-\lambda t} + A_x \cos(\omega_p t + \phi) \\ y = cA_1 e^{\lambda t} - cA_2 e^{-\lambda t} + \kappa A_x \sin(\omega_p t + \phi) \\ z = A_z \cos(\omega_v t + \psi) \end{cases} \quad (4)$$

where A_1, A_2, A_x, A_z, ϕ, and ψ depend on the initial condition $(\pm\lambda, \pm i\omega_p, \pm i\omega_v,)$ are the eigenvalues of the characteristic equation of the system (1) and c, κ depend exclusively on the mass parameter μ and the Libration point that is studied (in our case EML2). Solutions with A_1 and A_2 equal to zero correspond to periodic orbits, with an amplitude A_x and a phase φ in xy-plane and an amplitude A_z and a phase ψ in z direction.

A differential correction scheme is deployed to compute the orbits, with a high order analytical approximation as first guess (Howell, 1984). The method used for the first guess depends on the orbit family studied.

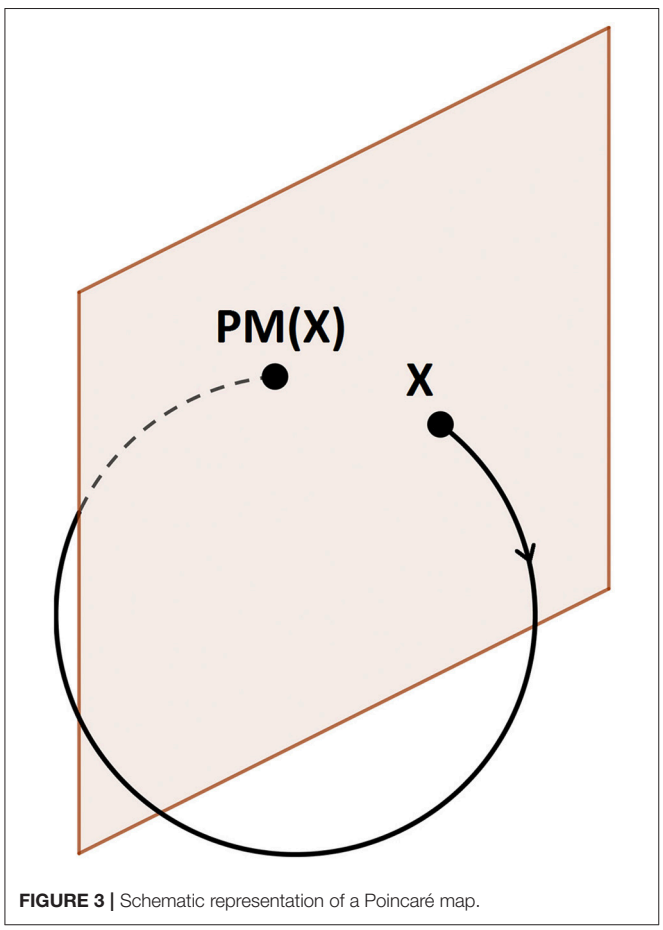

FIGURE 3 | Schematic representation of a Poincaré map.

Invariant Manifolds

The concept of unstable and stable manifold is exploited to determine transfers from the orbits about the primaries to the vicinity of the Lagrangian points as well as periodic solutions.

For a given orbit, the stable (resp. unstable) invariant manifold is defined as the sub-space of the 6-dimensional phase space consisting of all vectors whose future (resp. past) positions converge to the periodic orbit. The corresponding trajectories in the vicinity of the orbit are often called asymptotic orbits since they slowly converge to or diverge from the orbit. As the equations of motion are Hamiltonian, the system has an energy integral of motion. Its expression is given by

$$E(x, y, z, \dot{x}, \dot{y}, \dot{z}) = \frac{1}{2}\left(\dot{x}^2 + \dot{y}^2 + \dot{z}^2\right) + \bar{U}(x, y, z) \quad (5)$$

From the expression of the solutions of the linearized system of Equations (4), it can be concluded that a small variation of the trajectory can put the spacecraft on the unstable manifold A_1 and correspond to the hyperbolic amplitudes of the solution, with A_1 for the unstable component and A_2 for the stable one. This concept is then used to compute trajectories that converge toward the orbit around the Lagrangian point (stable manifold) and departs from the orbit (unstable manifold). Actually, the stable manifold will converge to the desired orbit, while the unstable manifold will exit the region of the Lagrangian point.

The invariant manifolds are often referred as "tubes" since they exhibit tube-like shapes when projected onto the 3-dimensional position space.

For any given state $\boldsymbol{X} = (x, y, z, \dot{x}, \dot{y}, \dot{z})$, on the aforementioned given periodic orbit, the invariant stable (resp. unstable) manifold can be computed thank to a linear approximation, while considering a small perturbation ε applied to X which becomes $\boldsymbol{X_s}$ (resp. $\boldsymbol{X_u}$) and propagating the equations of motion backward (resp. forward) from $\boldsymbol{X_s}$ (resp. $\boldsymbol{X_u}$), with:

- For the stable manifold W_s: $\boldsymbol{X_s} = \boldsymbol{X} \pm \varepsilon \mathbf{v_s}$
- For the unstable manifold W_u: $\boldsymbol{X_u} = \boldsymbol{X} \pm \varepsilon \mathbf{v_u}$

where v^s and v^u are eigenvectors associated to the real eigenvalues of the monodromy matrix of the closed trajectory. v^u corresponds to the eigenvalue > 1 and v^s to the eigenvalue smaller than one.

As the small perturbation, ε, can be positive or negative, two stable (resp. unstable) manifolds can be obtained, which are denominated, respectively interior and exterior. The manifold is generated from a starting point, selected at a distance d_M in the stable or unstable direction provided by the eigenvector. For this study, d_M is set to 50 km (Gómez et al., 2001).

In order to decide when to stop the propagation of the manifold branches, a Poincaré map (recorded as P_{Σ_p}) is used. Considering $\Phi(t, t_0, X(t_0))$, the trajectory representing one solution of the system with X_0 as initial conditions and Σ_p, a hypersurface, the Poincaré map, P_{Σ_p}, is defined as the set of points of the trajectory, $\Phi(t, t_0, X(t_0))$ when it intersects the hypersurface, Σ_p with:

$$P_{\Sigma_p} = \left\{ \boldsymbol{X} = \left(x, y, z, \dot{x}, \dot{y}, \dot{z}\right) / \boldsymbol{X} \in \Sigma_p \text{ and } \dot{\boldsymbol{X}} = f(\boldsymbol{X}) \right\} \quad (6)$$

Figure 3 provides a schematic representation of the use of a Poincaré Map.

Manifolds Connection

Given an initial orbit and a final orbit, denoted by ψ_i and ψ_f, respectively. Intersections between the unstable manifold $W^u(\psi_i)$ of the initial orbit and the stable manifold $W^s(\psi_f)$ of the final orbit is defined as the set

$$X_p \subset W^u(\psi_i) \cap W^s(\psi_f) = \left\{ \begin{pmatrix} x_u \\ y_u \\ z_u \\ \dot{x}_u \\ \dot{y}_u \\ \dot{z}_u \end{pmatrix} \in W^u(\psi_i), \begin{pmatrix} x_s \\ y_s \\ z_s \\ \dot{x}_s \\ \dot{y}_s \\ \dot{z}_s \end{pmatrix} \in W^s(\psi_f) \middle| \begin{array}{ll} x_u^i = x_s^j & \dot{x}_u^i = \dot{x}_s^j \\ y_u^i = y_s^j & \dot{y}_u^i = \dot{y}_s^j \\ z_u^i = z_s^j & \dot{z}_u^i = \dot{z}_s^j \end{array} \right\} \quad (7)$$

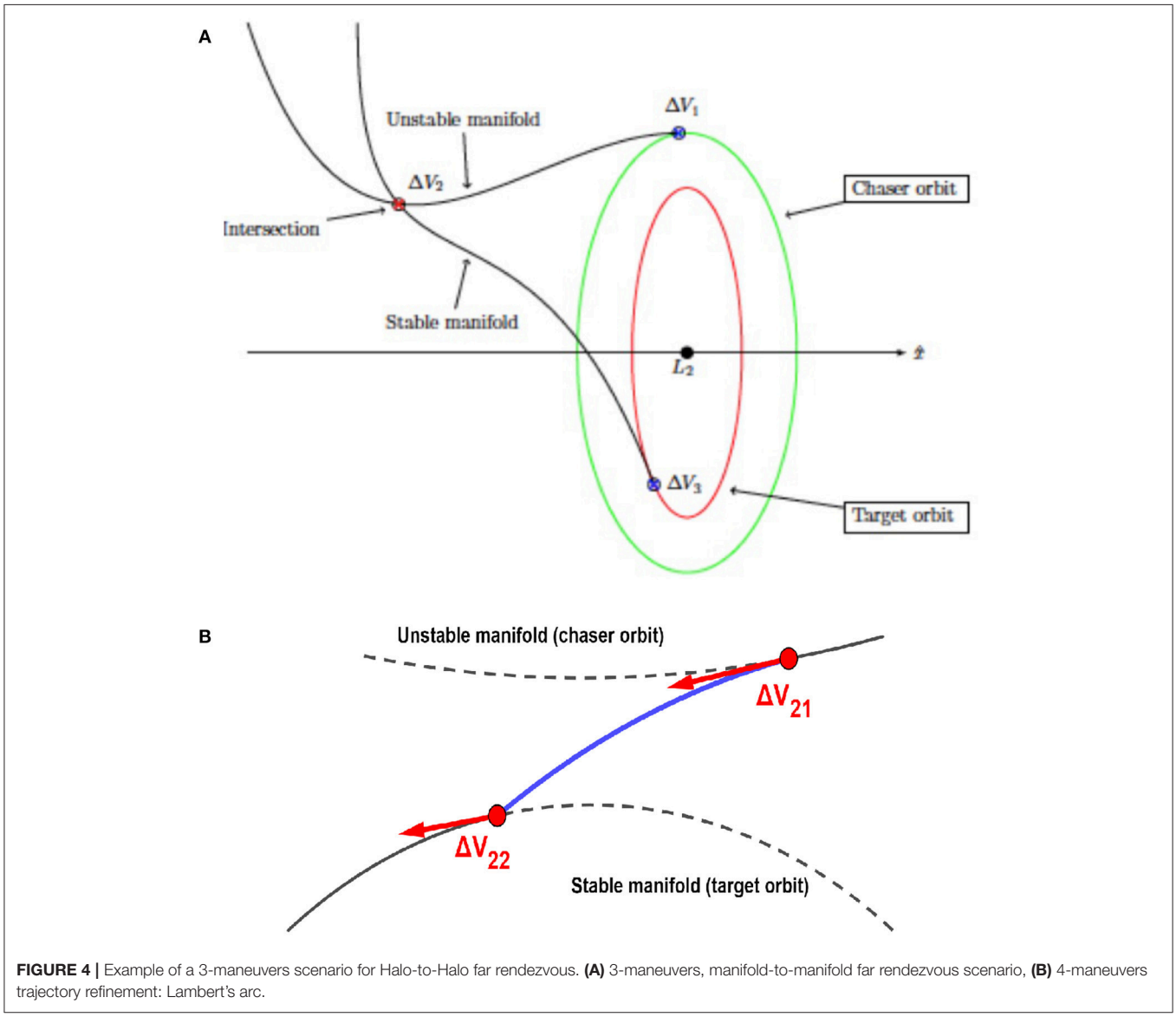

FIGURE 4 | Example of a 3-maneuvers scenario for Halo-to-Halo far rendezvous. **(A)** 3-maneuvers, manifold-to-manifold far rendezvous scenario, **(B)** 4-maneuvers trajectory refinement: Lambert's arc.

Intersections in 6-D space of the manifolds are called free intersections and provide an asymptotic path from one periodic solution to another one (Parker and Chua, 2012). However, such connections require stringent conditions on the initial and final orbits, for example, they must be of the same energy level (5). For the purpose of this study, only physical intersections (x,y,z) between the manifolds will be sought for. While intersections can happen at any point of space, the search space will be restricted on a Poincaré map to reduce the computational burden.

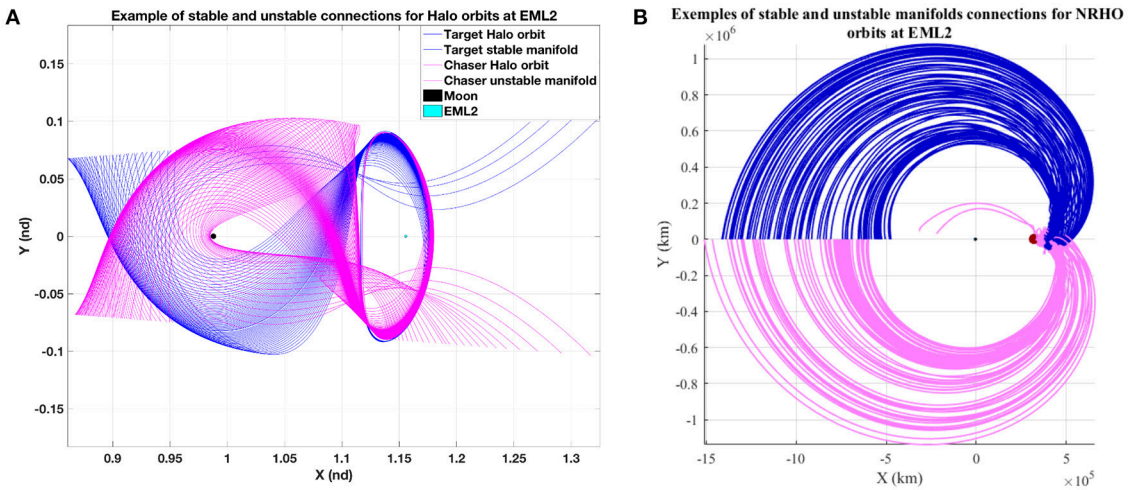

FIGURE 5 | Example of stable and unstable manifolds connections for EML2 Halo orbits and NRHO. **(A)** stable and unstable manifolds originated from Halo Southern orbits (with $A_z^C = 8{,}000$ km in purple and $A_z^T = 10{,}000$ km in blue) **(B)** stable and unstable manifolds originated from Northern NRHO (with $A_z^C = 70{,}000$ km and $A_z^T = 74{,}960$ km).

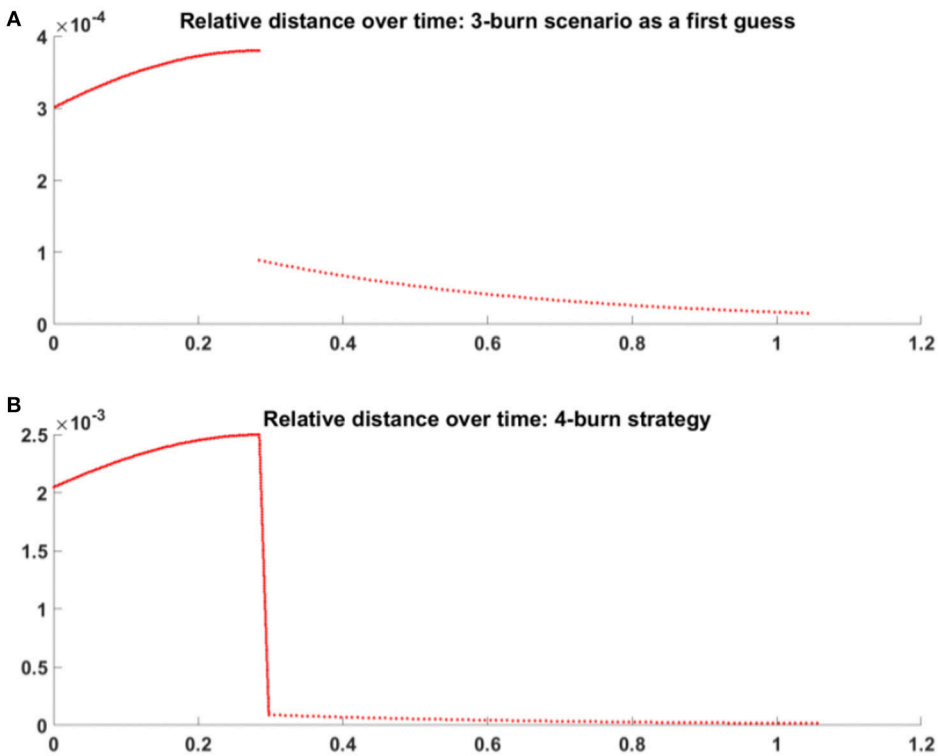

FIGURE 6 | Example of Halo-to-Halo far rendezvous, $A_z^C = 7{,}800$ km, $A_z^T = 8{,}000$ km, θ_i^C=330, θ_f^T=80, φ_{PM}=4.46. **(A)** Relative distance between chaser and target over time, 3-burn strategy as a first guess, adimensional units, **(B)** Relative distance between chaser and target over time, 4-burn continuation, adimensional units.

RENDEZVOUS

This paper focuses on rendezvous problematic in the vicinity of EML2, as it constitutes one of the most critical sets of operations during a Human spaceflight mission scenario.

Rendezvous Concepts Definition

Houbolt (1960) defines the rendezvous as:

> "*The problem of rendezvous in space, involving, for example, the ascent of a satellite or space ferry as to make a soft contact with another satellite or space station already in orbit.*"

The space vehicle that is already in orbit is commonly called the target, while the one that is arriving, is named the chaser. Rendezvous then consists in all maneuvers and trajectories performed by both vehicles to get nearer and nearer before contact. The different phases and maneuvers of a typical rendezvous mission from launch to docking have been extensively studied from the Apollo missions to the International Space Station (ISS) resupply missions. They are mostly named: *launch, transfer, orbital injection, phasing, and proximity maneuvers* (including homing, closing and final approach). Rendezvous can be followed by either docking or berthing, depending on the nature of the chaser. Rendezvous operations considered in this study will start from the departure of the chaser from its parking orbit to the injection maneuver onto the target orbit in the vicinity of the Lagrangian point. As an extension of successful rendezvous operations performed in Low Earth Orbit, it is possible to identify three successive phases in a rendezvous scenario: transfer phase, far rendezvous and close rendezvous.

Far Rendezvous Strategy

Two different scenarios can be identified depending on the chaser injection. The chaser can either travel on its transfer trajectory from the Earth to the target orbit or can be injected on a parking orbit about the Lagrangian point. It is not necessary that the chaser's parking orbit belong to the same families as target's orbit. In the second case, the chaser will wait there until far approach operational activities start. Considering the launch and transfer uncertainties inherent to the first scenario, the paper focuses on scenarios including the use of a parking orbit. Four phases are considered: parking orbit, far approach, insertion on the target's orbit and close rendezvous operations. Both chaser and target are assumed to be traveling on two different closed orbits about the L2 libration point, which admit stable and unstable manifolds.

The far approach strategy proposed in this paper takes advantage of the natural dynamics of the system and follows two steps. A 3-maneuver scenario is considered first. The chaser performs a first maneuver (Δv_1) to leave its parking orbit and to travel on the unstable manifold. It will then perform a second maneuver (Δv_2) to leave the unstable manifold so as to reach the stable manifold of the target orbit. Finally, arriving near the target, it will perform a third maneuver (Δv_3) to leave the manifold and enter the target parking orbit. As mentioned previously, finding exact intersections between manifolds is difficult and resource-consuming, a distance gap between the stable and unstable manifold at the intersection exists in this scenario. The second and final step is to use the 3-burns trajectory as a first guess for a 4-burns trajectory design with a lambert arc connecting the extremities of both manifolds. **Figure 4** presents an example of the methodology used in this work for a Halo-to-Halo rendezvous about EML2 (target and chaser amplitudes $A_z^T = 30,000$ km and $A_z^C = 8,000$ km, respectively). On the upper hand (A), the 3-maneuvers strategy is presented, while on the lower hand (B), the connection between the manifolds is depicted for the 4-maneuvers refinement: the two burns (Δv_{21}) and (Δv_{22}) replace the single burn (Δv_2) of the 3-maneuvers scenario.

3-Maneuvers Scenario

The total Δv for the 3-maneuvers scenario is, as defined previously:

$$\Delta v = \Delta v_1 + \Delta v_2 + \Delta v_3 \tag{8}$$

The main challenge of this study case is to find the right location and best moment to perform the intermediate maneuver (Δv_2), to compute a trajectory that resembles a free connection. This leads to finding a compromise between the time of flight (duration of the transfer) and the cost (quantified by the total Δv).

Assuming that the chaser leaves its parking orbit at time, t_1, reaches the intersection between both manifolds at time, t_2, and is inserted in the target parking orbit at time, t_3, the rendezvous trajectory of the chaser is split into three arcs:

- From t_1 to t_2, the chaser travels on the unstable manifold of the chaser parking orbit, W_u^C, after the first maneuver (Δv_1)
- At t_2 the second burn (Δv_2), the chaser leaves W_u^C, and gets into the stable manifold of the target parking orbit, W_S^T.
- From t_2 to t_3, the chaser travels on W_S^T before the last maneuver (Δv_3).

As mentioned previously, only physical intersections between manifolds in the (x,y,z) subspace are sought. The resulting gap in the velocity subspace will provide the intermediate required burn, (Δv_2). Writing $\left(x_u^C, y_u^C, z_u^C\right)$ the position vector on the unstable manifold issued from the chaser parking orbit and $\left(x_s^T, y_s^T, z_s^T\right)$ the position vector on the stable manifold issued from the target parking orbit, the rendezvous problem can be stated as:

- $t \in [t_1; t_2[$, $\frac{d\Phi(t,t_1,X_0^C)}{dt} = f\left(\Phi(t,t_1,X_0^C)\right.$with $\Phi(t_1,t_1,X_0^C) = X_0^C$
- at t= t_2,

$$\begin{cases} x_u^C(t_2) = x_s^T(t_2) = x_2 \\ y_u^C(t_2) = y_s^T(t_2) = y_2 \\ z_u^C(t_2) = z_s^T(t_2) = z_2 \end{cases} \tag{9}$$

- $\forall t \in [t_2; t_3]$, $\frac{d\Phi(t,t_3,X_0^T)}{dt} = f\left(\Phi(t,t_3,X_0^T)\right.$ with $\Phi(t_3,t_3,X_0^T) = X_0^T$

Solving the problem is equivalent to finding the three unknown variables, (t_1, t_2, t_3) that satisfy system (9). This is equivalent to

finding three others variables $\left(\theta_i^C, \theta_f^T, \varphi_{PM}\right)$, where θ_i^C defines the angular parameter of the chaser on its parking orbit at time t_1 (defined as an angular fraction of the period of the orbit), θ_f^T defines as well the angular parameter of the chaser on the target orbit at time t_3. With this parameterization, the NRHO aposelene corresponds to $\theta = \pi$, while the periselene corresponds to $\theta = 0$. φ_{PM} is the angle defining the Poincaré map, used to determine the location of spatial intersections of the two manifolds. The manifold propagation stops at its spatial intersection with the plane defined, by the angle φ_{PM}.

Figure 5 depicts examples of possible connections between stable (blue) and unstable (purple) manifolds for part (A) with EML2 Southern Halo orbit (with for the chaser, in purple $A_z^C = 8{,}000$ km and $A_z^T = 10{,}000$ km) and for part (B), with EML2 northern NRHO (with for the chaser, in purple $A_z^C = 70{,}000$ km and $A_z^T = 74{,}960$ km). φ_{PM} is set equal to 2° for Halo orbits and 3° for NRHO.

The selected Poincaré map is a plane perpendicular to the xy-plane, forming an angle φ_{PM} with the x-axis from EMLi, where i = 1 or 2 depending on the considered Lagrangian point. As a summary:

- θ_i^C is determined by $\left(x_u^C,\ y_u^C,\ z_u^C\right)$ at $t = t_1$,
- θ_f^T is determined by $\left(x_s^T,\ y_s^T,\ z_s^T\right)$ at $t = t_3$,
- $\begin{cases} x_2 = \sqrt{x_2^2 + y_2^2} \times cos\left(\varphi_{PM}\right) \\ y_2 = \sqrt{x_2^2 + y_2^2} \times sin\left(\varphi_{PM}\right) \end{cases}$

As the problem cannot be solved analytically, the following numerical methodology is applied:

- Generating the target orbit and the chaser parking orbit.
- Propagating the stable manifold, $W_s^T\left(\theta^T\right)$ issued from each angular location θ^T on the target orbit until the Poincaré map, PM .
- Propagating the unstable manifold, $W_u^C\left(\theta^C\right)$, from each angular location θ^C on the chaser parking orbit until the Poincaré map, PM.
- Computing for each pair $\left(W_s^T\left(\theta^T\right), W_u^C\left(\theta^C\right)\right)$, the distance gap, ΔX, and the velocity gap, Δv_2.

The integration of the equations of motion must be performed using a numerical solver. This work relies on Runge-Kutta propagators, ODE45 (or even ODE113), implemented in Matlab. The solver implies that all components (time and state) have been discretized. As a consequence, the concept of exact intersection in the spatial sub-space is replaced by the minimization of the distance between the positions on both manifolds at the Poincaré map location.

To select the best $\left(\theta_i^C,\ \theta_f^T,\ \varphi_{PM}\right)$ candidate, the following optimization process has been applied, so as to:

- Find a compromise between cost (total $\Delta \mathbf{V}$) and duration (time of flight, ΔT).
- Ensure feasibility (distance gap, $\Delta \mathbf{X}$), that is to say, to define numerically the acceptable distance between the two manifolds at the intersection.

The problem to be optimized is:

$$\begin{aligned} &\min \mathrm{J} = \|\Delta \mathbf{V_2}\| \\ &\textit{subject to } \|\Delta \boldsymbol{X}\| \leq d \end{aligned} \tag{10}$$

$\|.\|$ denotes the quadratic norm: $\|\Delta X\|$ refers to the gap in position between the position of the chaser on the unstable manifold and the position of the chaser on the stable manifold, at the intersection, $\|\Delta V_2\|$ refers to the gap in velocity between the position of the chaser on the unstable manifold and the velocity of the chaser on the stable manifold, at the intersection and $d = 50$ km is the maximum distance allowed between the two spacecrafts at the Poincaré section.

4-Maneuvers Trajectory Refinement

Results from the 3-maneuvers strategy are used as an initial guess, feeding a local optimization process based on the variation the time of flight in both the unstable and stable manifold. The connection between the manifolds is not considered as a simple discontinuity in the state space anymore but is "patched" by means of a Lambert's arc computed in the CR3BP. In this scenario, the PM intersection constraint at the manifold end points is relaxed.

The cost function of the new optimization problem, using the terminology presented in the introduction of section Far Rendezvous Strategy, is:

$$\mathrm{J} = \|\Delta \mathbf{V_{21}}\| + \|\Delta \mathbf{V_{22}}\| \tag{11}$$

The outputs of this process are the new positions of the end points of both manifolds, the total $\|\Delta V\|$ and the time of flight required to perform the transfer between both manifolds. An entire continuous trajectory can then be built, for the chaser to rendezvous the target, starting from its parking orbit, passing by an unstable manifold, Lambert arc and stable manifold and finishing on the target parking orbit. The far rendezvous strategy now includes an additional trajectory arc that connects properly the unstable and stable manifolds.

Figure 6 provides an example of the procedure detailed in this section. The study case is between two Halo orbits of the Southern family about EML2, with an elongation of 8,000 km for the target orbit and 7,800 km for the chaser parking orbit The chaser transfer trajectory from its parking orbit to the chaser orbit is plotted in bold dark blue solid line. The chaser initial angular location is $\theta_i^C = 330$ and the target final location is $\theta_f^T = 80$. Performances are obtained for $\varphi_{PM} = 4.46$. **Figure 6A** shows the result of the 3-burn strategy as an initial guess, and **Figure 6B** showcases the continuation of the solution and relaxation of the ToF constraint. The total velocity increment in that particular case is 0.374 $.s^{-1}$ km with a Lambert's time of flight of ~ 1.39 h.

Close Rendezvous Strategy

The main goal of the close rendezvous phase is to conduct gradually the chaser from its insertion location closer to the target so as to allow berthing or docking operations. This time, unlike for the far rendezvous phase, chaser and target are

traveling on the same trajectory, but with a gap in position. For safety considerations, the close rendezvous trajectory is split into several legs, delimited by hold points (HP), as security checkpoints. In this phase, maneuvers are considered impulsive, performed instantaneously at the HPs and the motion on the arcs is ballistic. The proposed strategy is based firstly on the selection of breakpoints, then on the calculation of the arc-by-arc trajectory from the equations of motion. Finally, safety aspects are discussed. Actually, trajectory design must take into account an assortment of random errors acquired while in orbit, such as the initial condition dispersions or inaccurate thrust velocities. Free drift motion may occur if the thrusters of the chaser cease to operate. This phenomenon has been simulated while assuming dispersion on maneuver. Safety analyses must verify that the selected trajectory of the chaser will not enter the safety region, in case of a missed maneuver, so as to avoid collision with the target in case of failure.

Hold-on Points Determination

In close rendezvous scenarii, the HP are significant locations on chaser's trajectories where to perform maneuvers after security checks (missions parameters, chaser health status), as the chaser is not permitted to approach freely the target. In case of failure, braking may become impossible and the failure could jeopardize the mission. The chaser must thus follow a precise path, meeting all the hold points. Similarly to Mand (2014), two geometrical strategies are proposed to define their positions: line-of-sight corridor (LoS-C) and line-of-sight glide (LoS-G). With them, the chaser is always approaching the target along its docking port direction within the field of view of its rendezvous sensors modeled by a cone. The target attitude is not taken into account, as its attitude is assumed to be perfect. The implemented strategies are:

- LoS-C, characterized by three angles: two trigger angles (α, β) and an offset angle, φ as $\phi < \alpha$ and $\phi < \beta$. Each time the chaser's trajectory (assumed to be locally rectilinear) intersects one side of the cone, a maneuver is performed to reorient the chaser inside the field of view. Hold points are then located at this intersection.
- LoS-G, characterized by two angles: one trigger angle α and one offset angle ϕ as $\phi < \alpha$. Within LoS-G, the chaser does not cross the line of sight as in LoS-C, but remains on the same side of the cone.

Figure 7 represents both strategies, with a definition of the angles, in the LVLH (Local-Vertical/Local-Horizontal) reference frame, defined in section Clohessy-Wiltshire Equations.

The process outputs the number of required hold points. In addition to HP, two safety regions are defined around the target, as an extension of concepts developed in Keplerian dynamic (mainly in LEO). They are identified as two spheres: the Approach Sphere (AS) and the Keep Out Sphere (KOS), both centered on the target.

Trajectory Arcs Computation

Dealing with close rendezvous means an analytic description of the relative motion of the chaser according to the target, referring

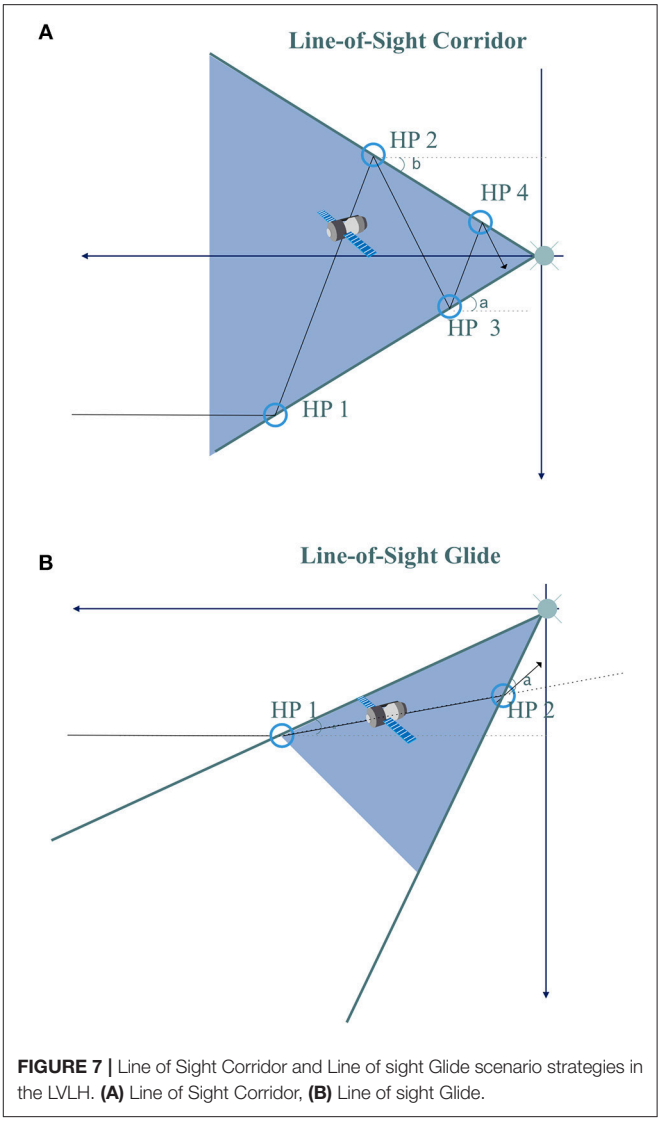

FIGURE 7 | Line of Sight Corridor and Line of sight Glide scenario strategies in the LVLH. **(A)** Line of Sight Corridor, **(B)** Line of sight Glide.

to two relative reference frames and one inertial frame, presented on **Figure 8**.

In blue, the Earth-Moon synodic reference frame is a rotating frame centered on the center of gravity of Earth-Moon system, with Moon and Earth fixed on the x-axis. The z-axis is orthogonal to the plane of motion of the celestial bodies. The y-axis completes the right-hand rule. In black, the Moon-Centered inertial (MCI) frame is defined such that the origin is at the center of the Moon. An Earth-Centered inertial (ECI) reference frame could also have been selected. x-axis and y-axis are selected so as to overlap at initial conditions. In red, the LVLH reference frame is presented.

The equations of motion of both vehicles and their relative motions are described in the CR3BP in (Mand, 2014) and (Campolo et al., 2017). Their expression leads to a complete set of non-dimensional non-linear relative equations. As the distance between chaser and target is very low compared to the

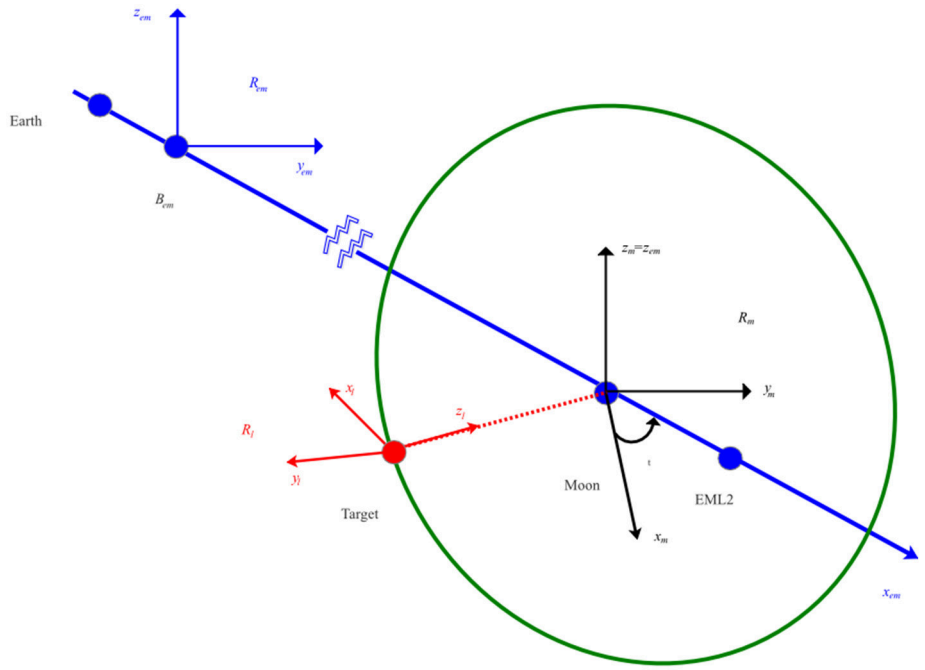

FIGURE 8 | Reference frames definition for close rendezvous.

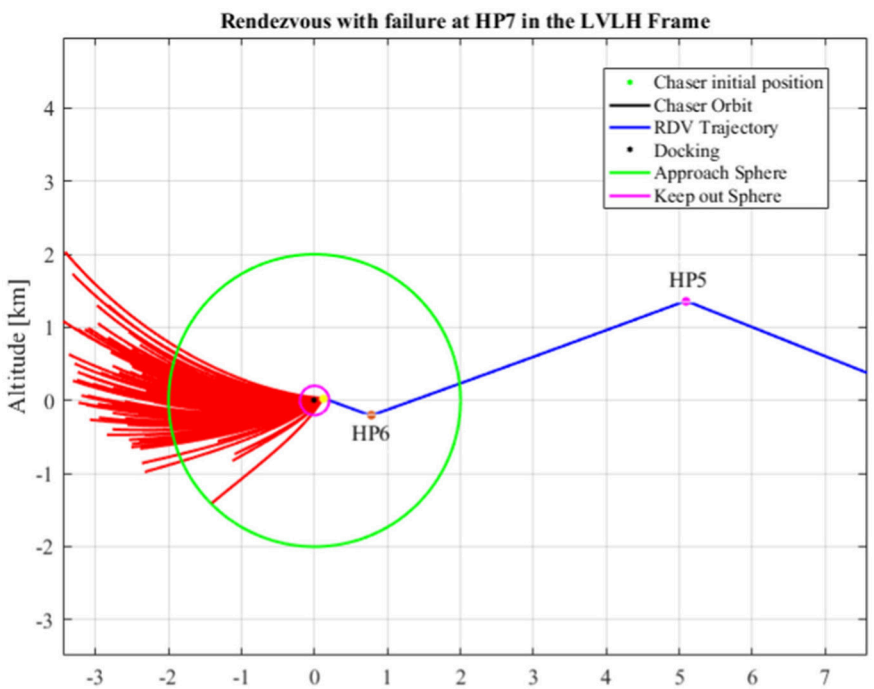

FIGURE 9 | Close Rendezvous with failure at HP n°7 in the LVLH for Halo-to-Halo case.

dimensions of the system (for example, distance between the two primaries), the expression of the relative motion can be linearized to simplify the problem, as a first approximation.

The expression of the simplified equations of the relative motion will all be presented in a state-space form as $\dot{X}_r = A_i X_r$ where i denominates the selected simplified method. Three

models are compared: Linearized Relative (LR), Clohessy—Wiltshire (C–W), and Straight-Line (SL).

Since the matrix A is time-dependent, the trick consists in dividing each transfer in smaller arcs, where A can be considered as constant. The approach to compute the trajectory arc between two HP corresponds to solving arc-by-arc small Lambert problems. It lies in finding a trajectory between an initial and final position given a specific time of flight, (ΔT). For each arc, the time of flight is fixed and the HP provide initial and final points.

The algorithm is divided into two steps:

- Linear targeting: computation of the maneuver Δv_{HPi_linear} first guess
- Shooting method: computation of final Δv_{HPi} to be performed by the chaser with Δv_{HPi_linear} as a first guess. The shooting algorithm cycles with a full non-linear relative model in CR3BP until the final position error is considered acceptable.

For certain families of orbits (above all for NRHO), the accuracy of linear models depends on the orbital regions where the computation is performed. As a consequence, the first section compares the three methods to estimate the error introduced by the three relative linear models with respect to the non-linear model and consequently, to assess their ability to accurately model the dynamics during close rendezvous operations. For each arc of the trajectory, an approximation of the solution of the system is computed numerically with the three previously linearized methods. The linear method that presents the lowest error in terms of final position (distance from the target) is then selected to perform the second step. This two-steps algorithm is an iterative process to compute the entire close rendezvous trajectory of the chaser.

Non-linear relative equations

The non-dimensional non-linear relative equations of motion written in the synodic reference frame can be obtained by the difference of the absolute equations of motion (2) of the chaser and the target, respectively, in the CR3BP:

$$\begin{cases} \ddot{x}_r - 2\dot{y}_r - x_r = (1-\mu)\left[\frac{x^T+\mu}{\|r_1^T\|^3} - \frac{x^T+x_r+\mu}{\|r_1^T+\rho\|^3}\right] \\ \qquad\qquad +\mu\left[\frac{x^T+\mu-1}{\|r_2^T\|^3} - \frac{x^T+x_r+\mu-1}{\|r_2^T+\rho\|^3}\right] \\ \ddot{y}_r + 2\dot{x}_r - y_r = (1-\mu)\left[\frac{y^T}{\|r_1^T\|^3} - \frac{y^T+y_r}{\|r_1^T+\rho\|^3}\right] \\ \qquad\qquad +\mu\left[\frac{y^T}{\|r_2^T\|^3} - \frac{y^T+y_r}{\|r_2^T+\rho\|^3}\right] \\ \ddot{z}_r = (1-\mu)\left[\frac{z^T}{\|r_1^T\|^3} - \frac{z^T+z_r}{\|r_1^T+\rho\|^3}\right] + \mu\left[\frac{z^T}{\|r_2^T\|^3} - \frac{z^T+z_r}{\|r_2^T+\rho\|^3}\right] \end{cases} \quad (12)$$

where the relative state is $\boldsymbol{X_r} = \boldsymbol{X^C} - \boldsymbol{X^T} = \left(x_r, y_r, z_r, \dot{x}_r, \dot{y}_r, \dot{z}_r\right)$, the absolute state of the target is given by $\boldsymbol{X^T} = \left(x^T, y^T, z^T, \dot{y^T}, \dot{z^T}\right)$, the absolute state of the chaser is given by $\boldsymbol{X^C} = \left(x^C, y^C, z^C, \dot{x^C}, \dot{y^C}, \dot{z^C}\right)$. The position vector of the target to M_1 is $\boldsymbol{r_1^T} = \left(x^T + \mu, y^T, z^T\right)$, the position of the target to M_2 is $\boldsymbol{r_2^T} = \left(x^T + \mu - 1, y^T, z^T\right)$ and the relative position is $\rho = \left(x_r, y_r, z_r\right)$.

The absolute distances of the target from M_1 and M_2 are respectively:

$$\begin{cases} r_1^T = \sqrt{\left(x^T+\mu\right)^2 + y^{T2} + z^{T2}} \\ r_2^T = \sqrt{\left(x^T+\mu-1\right)^2 + y^{T2} + z^{T2}} \end{cases}$$

Linearized relative equations

The Linearized Relative equations can be adapted from formation flight studies (Luquette, 2006), while linearizing the dynamics about the target as a reference vehicle, taking into account a canonical CR3BP synodic frame. From (12), assuming that $\|\rho\| \ll r_1^T$, $\|\rho\| \ll r_2^T$ and applying a second order Taylor expansion $(1+\varepsilon)^{-3} \approx 1 - 3\varepsilon + o(\varepsilon)$ to linearize relative equations of motion in the synodical frame:

$$\dot{\boldsymbol{X}}_{\boldsymbol{r}} = \begin{bmatrix} 0_3 & I_3 \\ \Xi - nn & -2n_1 \end{bmatrix} \boldsymbol{X_r} = A_{LR}\boldsymbol{X_r} \quad (13)$$

where $\Xi = -\left(\frac{1-\mu}{r_1^{T3}} + \frac{\mu}{r_2^{T3}}\right) I_3 + \frac{3(1-\mu)}{r_1^{T5}}\left[\mathbf{r_1^T r_1^{Tt}}\right] + \frac{3\mu}{r_2^{T5}}\left[\boldsymbol{r_2^T r_2^{Tt}}\right]$

with $\boldsymbol{r_1^{Tt}}$ the transpose vector of $\boldsymbol{r_1^T}$ and $\boldsymbol{r_2^{Tt}}$ the transpose vector of $\boldsymbol{r_2^T}$, $I_3 = \begin{pmatrix} 1 & 0 & 0 \\ 0 & 1 & 0 \\ 0 & 0 & 1 \end{pmatrix}$,

$$0_3 = \begin{pmatrix} 0 & 0 & 0 \\ 0 & 0 & 0 \\ 0 & 0 & 0 \end{pmatrix}, nn = \begin{pmatrix} -1 & 0 & 0 \\ 0 & -1 & 0 \\ 0 & 0 & 0 \end{pmatrix} \text{ and } n_1 = \begin{pmatrix} 0 & -1 & 0 \\ 1 & 0 & 0 \\ 0 & 0 & 0 \end{pmatrix}.$$

Clohessy—wiltshire equations

The Clohessy-Wiltshire equations (Clohessy and Wiltshire, 1960) describe relative motion in a 2-Body environment. This model assumes only one primary mass, the target's orbit is circular and that the relative distance between target and chaser is small with respect to target-attractor distance. These assumptions are not usually valid in the CR3BP, and can only be applied locally to generate a first guess. The model is given in the local-vertical/local-horizontal (LVLH) reference frame of the primary M_2, centered on the center of gravity of the target. The x-axis points along the direction of the velocity of the target. The z-axis points the direction from the target to M_2. The y-axis is mutually perpendicular to the x- and z-axes so as to form a right-handed coordinate frame. An example of LVLH is given in red on **Figure 8** for motion description of an NRHO in cis-lunar space. The Earth-Moon synodical reference frame R_{em} is represented in blue, while, the Moon-Centered Inertial (MCI) frame R_m is in black.

The C-W equations, written in the LVLH reference frame are:

$$\begin{cases} \ddot{x}_r - 2n\dot{z}_r = 0 \\ \ddot{y}_r + n^2 y_r = 0 \\ \ddot{z}_r + 2n\dot{x}_r - 3n^2 z_r = 0 \end{cases} \quad (14)$$

Where n represents the mean angular motion of the M_2-centered keplerian circular orbit with a radius of r_2^T and is given by $n = \sqrt{\frac{\mu}{r_2^{T^3}}}$.

The C-W equations can also be written in state-space representation:

$$\dot{\boldsymbol{X}_r} = \begin{bmatrix} 0_3 & I_3 \\ \Omega & -2n \times n_2 \end{bmatrix} \boldsymbol{X_r} = A_{CW} \boldsymbol{X_r} \tag{15}$$

where $\Omega = \begin{pmatrix} 0 & 0 & 0 \\ 0 & -n^2 & 0 \\ 0 & 0 & 3n \end{pmatrix}$ and $n_2 = \begin{pmatrix} 0 & 0 & 1 \\ 0 & 0 & 0 \\ -1 & 0 & 0 \end{pmatrix}$.

Straight line equations

In the Straight-Line approach, the velocity vector of the chaser points to the target at time, t_i, after a maneuver $\mathbf{\Delta v}_i$, disregarding any gravitational effect. The expression of $\mathbf{\Delta v}_i$ in the LVLH reference frame is, during the period of time $\Delta t_i = t_{i+1} - t_i$

$$\Delta \boldsymbol{v_i} = \frac{1}{\Delta t} \times (\boldsymbol{r_{i+1}} - \boldsymbol{r_i}) - \boldsymbol{v_i} \tag{16}$$

Where $\mathbf{r}_i$ and $\mathbf{v}_i$ indicate the initial position and velocity at time, t_i, and r_{i+1} the final position at time, t_{i+1}. The state-space representation of the system is:

$$\dot{\boldsymbol{X}_r} = \begin{bmatrix} 0 & I_3 \\ 0 & 0 \end{bmatrix} \boldsymbol{X_r} = A_{SL} \boldsymbol{X_r} \tag{17}$$

STUDIED CASES

The objective of this paragraph is to assess the feasibility of the proposed strategies for far and close rendezvous, then to study the safety aspects of an end-to-end scenario. The output is the entire trajectory of the chaser from its parking orbit to the target orbit, in a three-steps process (far and close rendezvous and safety analysis). Guaranteeing the safety aspects requires going through an intermediate orbit, which is the final objective of the far rendezvous and the starting point of close rendezvous. Two study cases have been selected to illustrate the proposed strategies, in order to be consistent with the results of the historical study of the bibliography. They both lie in the Earth-Moon system, modeled by the CR3BP. Chaser parking orbit and target parking orbit belong to the same family. The first part of **Table 1** summarizes

TABLE 1 | Study cases input parameters.

	Parameter	Symbol	Units	Value	
Earth-Moon system parameters		Gravitational constant	G	$km^3.kg^{-1}.s^{-2}$	$6.67428.\ 10^{-11}$
	Earth mass	m_1	kg	$5.97219.\ 10^{+24}$	
	Moon mass	m_2	kg	$0.07346.\ 10^{+24}$	
	Earth-Moon mass ratio	μ	–	0.012150581623434	
Scenario step		**Parameter**	**Units**	**Halo**	**NRHO**
End-to-end scenario inputs	Parking	A_z^C	km	7000	70000
		m^C	–	Northern	Northern
		A_z^T	km	9000	75000
		m^T	–	Northern	Northern
	Far rendezvous	d_M	km	50	50
		θ^I	°	2	2
		θ^C	°	−2	−2
		A_z^I	km	8980	74960
		m^I	–	Northern	Northern
		φ_{PM}	°	0	0
		W_u^C direction	–	Interior	Interior
		W_s^I direction	–	Exterior	Exterior
	Close rendezvous	θ^T	°	0	0
		duration	h	10	10
		Line-of-Sight	–	corridor	corridor
		α	°	15	15
		β	°	15	15
	Safety	r_{KOS}	m	200	200
		r_{AS}	m	2000	2000
		Error in magnitude (3σ)	%	1	1
		Error in pointing (3σ)	mrad	1	1
		Number of Monte Carlo simulations	–	100	100

the parameters of the Earth-Moon system. The name of a study case is composed by:

"NAME_of_chaser_parking_orbit-to-NAME_of_target_orbit."

For example, HALO-to-HALO means that the chaser parking orbit is a Halo orbit and the target orbit is a Halo orbit. The considered study cases are: Halo-to-Halo and NRHO-to-NRHO.

At the end of this chapter, further conducted analyses are presented: a systematic analysis for far rendezvous (paragraph 5.4) within different orbit families and a close rendezvous on a DRO (paragraph 5.4 and section 5.5).

Scenario Algorithm

The final angular location, θ^T, of the chaser on the target orbit being fixed, the corresponding scenario is divided into four steps:

- **Parking orbit:** the chaser parking orbit at the beginning of the scenario is defined by its maximal elongation A_z^C and its family $m^C \in \{1; 3\}$. The target orbit is also defined by its maximal elongation A_z^T and its family $m^T \in \{1; 3\}$.
- **Far rendezvous strategy:** at this stage, the chaser leaves its parking orbit and targets an angular location θ^I, on the intermediate orbit, defined by its maximal elongation A_z^I and its family $m^I \in \{1; 3\}$. θ^I is forced to be equal to θ^T. An optimization process is run to identify the best θ^C to minimize criterion (10). The outputs are: θ^C, TOF and v, where TOF is the time of flight, necessary for the chaser to travel from θ^C to θ^I.
- **Close rendezvous strategy:** the chaser then approaches the target situated at θ^T on the target orbit defined by $\left(A_z^T, m^T\right)$ from its intermediate angular location θ^I on the intermediate orbit defined by $\left(A_z^I, m^I\right)$. The outputs are the number of HP (n_{HP}), the position of the HP and the total velocity v_{close}.
- **Safety analysis:** A failure is injected at the selected HP with dispersion of velocity in magnitude and in direction. A Monte Carlo process models the influence of random dispersion on the trajectory. Chaser trajectory is propagated for a time of 24h starting with new conditions of velocity. The output is a label that indicates if there is a risk of collision. Lessons learnt from ISS resupply cargo missions lead to defining two spheres centered on the target identified as the safety regions: the Approach Sphere (AS) with radius r_{AS} and the Keep out Sphere (KOS) with radius r_{KOS}. The values of r_{AS} and r_{KOS} are selected from operational missions like the European cargo ATV (Automated Transfer Vehicle) and the Japanese HTV (H-1 Transfer Vehicle).

TABLE 2 | Study cases results.

	Scenario step	Parameter	Units	Halo	NRHO
End-to-end scenario outputs	Far rendezvous	Δv_1	km/s	0.0182	0.0046
		Δv_2	km/s	0.1772	1.2606
		Δv_3	km/s	0.0018	0.0045
		Δv_{far}	km/s	0.2134	1.2697
		ΔT	h	05h00	02h26
	Close rendezvous	n_{HP}	–	7	6
		Δv_{close}	km/s	0.0168	0.0018

Scenario Input Parameters and Results

The second part of **Table 1** presents input parameters for the two study cases. Selected values for (α, β) correspond to actual navigation sensor field-of-view equal to 30°, which imposes a relative distance of 20 km (resp. 40 km) between the intermediate Halo (resp. NRHO) orbit and the target Halo (resp. NRHO) orbit. "W_u^C direction" represents the chosen direction to propagate the unstable manifold issued from chaser parking orbit, while "W_s^I direction" corresponds to the propagation direction for the stable manifold that converges to the intermediate orbit. Direction can take two values: "interior" or "exterior" for interior realm or exterior realm. Proposed variation ranges for θ^C and φ_M come from preliminary exploratory analyses. Chaser and target angular locations are computed with respect to EML2 (resp. the center of the Moon) for Halo case (resp. for NRHO case). The angle reference is set on the Earth-Moon axis in the synodic frame. The angle value grows clockwise: 0° is on the side of the Earth. The angle φ_M is also measured from the same reference axis and origin, but anti-clockwise.

For the studied scenario, the selected angular location for rendezvous is ($\theta^T = 0$). In the case of the close rendezvous on a NRHO, it corresponds to the periselene. Consequentially, it is an interesting location for ISRU (*In-Situ* Resource Utilization) or Moon sample return missions. Preliminary analyses conducted in this orbital zone have shown that the LR method appears less reliable than C-W or SL. Performances were thus obtained, by computing the difference in position, at the HP, between the arc generated by the linearized model and the Lambert's arc. Result can mainly be explained by the particularity of the observed zone. On the one hand, as LR equations are designed in the CR3BP problem, their validity is quite limited when the Moon influence is very predominant . On the other hand, the CW model evaluated under a Two-Body problem is the most suitable method in the periselene zone. As a consequence, it is recommended to select the LR model only for very large Halo orbits or in aposelenic zones. The selected initial angular location of the chaser on its parking orbit is ($\theta^C = -2$), since the chaser and target must be in a same proximity area. The location of the PM, φ_{PM}, is set equal to 0° to minimize the transfer distance.

For close rendezvous, the chaser starts its trajectory on the intermediate orbit defined by $\left(A_z^I, m^I\right)$, at angular location θ^I. The algorithm computes the number of HPs, their location, the maneuver to be performed at each HP and the arc of trajectory between two of them, so as to comply with a maximal duration of 10 h and following the LoS-C strategy. Results highly depend on the location on orbit where the rendezvous will take place.

Table 2 provides syntheses of main results computed for the entire RDV scenario in both study cases, for far and close rendezvous. Results obtained for far rendezvous in the Halo study case are very encouraging, with a total duration about

5 h and a total cost about 0.21 km/s. In the NRHO case, the duration is even more affordable with about 2h26, but with the cost > 1.27 km/s. The selection of the rendezvous location at periselene can explain these performances. Actually, in this zone, the gravitational influence of the Moon cannot be neglected. The out-of-plane component of the maneuver between both trajectories is thus very expensive. Those results are coherent with the ones presented in (Campolo et al. (2017), recommending to perform close rendezvous at the aposelene.

Those far rendezvous simulations support the use of invariant structures for low-cost transfer from the chaser parking orbit to the target, extended with a Lambert arc at the connection. Parametric analysis on the angular location of both vehicles could then be conducted to propose best scenarios compliant with operational constraints of ground segments.

For close rendezvous, with a fixed duration of 10 h, computed cost is affordable, for both scenarios. At this stage, the most important criteria are the safety performances, because of the highly non-linear dynamics. Actually, the proposed far rendezvous strategy tries to take advantage to reduce fuel consumption. On the contrary, safety analysis seeks to prevent collision when the chaser motion becomes ballistic, after a failure. For both study cases, one injects a failure at each HP. The chaser trajectory is then propagated during 24 h, taking into account the dispersion (1% in magnitude (3σ) and an error of 1 mrad in pointing direction (3σ). In the particular Halo-to-Halo case, it results that when the failure takes place between HP n°1 and HP n°4, there is no risk of collision between the chaser and the target, as the chaser doesn't not get into the AS. When the failure occurs at HP n°5 or HP n°6, the chaser trajectory with dispersion may enter the AS but not the KOS. Finally, when the failure happens beyond the 6th HP, the chaser enters the KOS and thus, there is a risk of collision. **Figure 9** presents the dispersion (in red) of the chaser trajectory when a failure is injected at HP n°7 in the Halo-to-Halo study case. The green circle represents the AS, while the purple one is the KOS. In the NRHO-to-NRHO study case, there is no risk of collision from the first HP to the third one. When there is a failure at HP n°4, the chaser enters the AS, but not the KOS. If the failure occurs at HP n°5 or HP n°6, the collision is certain. **Figure 10** presents the dispersion of the chaser trajectory when a failure is injected at HP n°7 (in red) in the NRHO-to-NRHO study case. This safety analysis emphasizes the necessity for an accurate definition of safety areas as AS or KOS. Inside these zones, the HP should not only be maneuver locations, but also safety check-points, where decision are made with Go/No-Go to continue close rendezvous approach, depending on the vehicle heath status.

Two additional studies were conducted to analyze the impact of orbits from different families and close rendezvous on a DRO orbit and are presented in the two next sections.

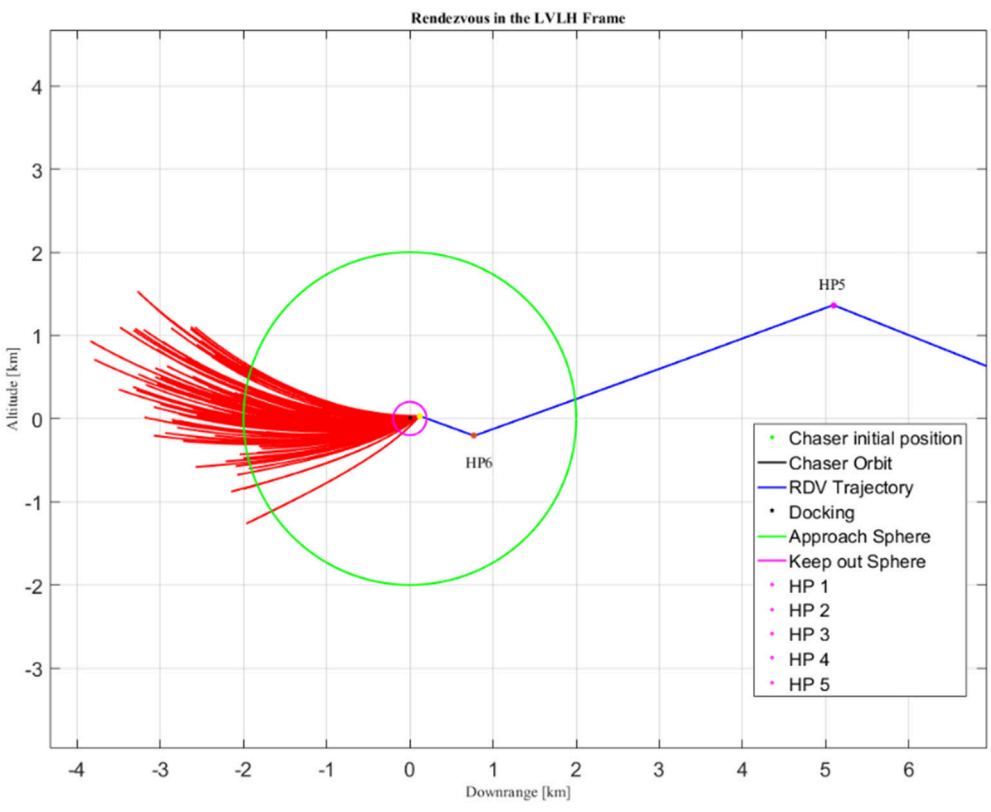

FIGURE 10 | Close Rendezvous with failure at HP n°7 in the LVLH for NRHO-to-NRHO case.

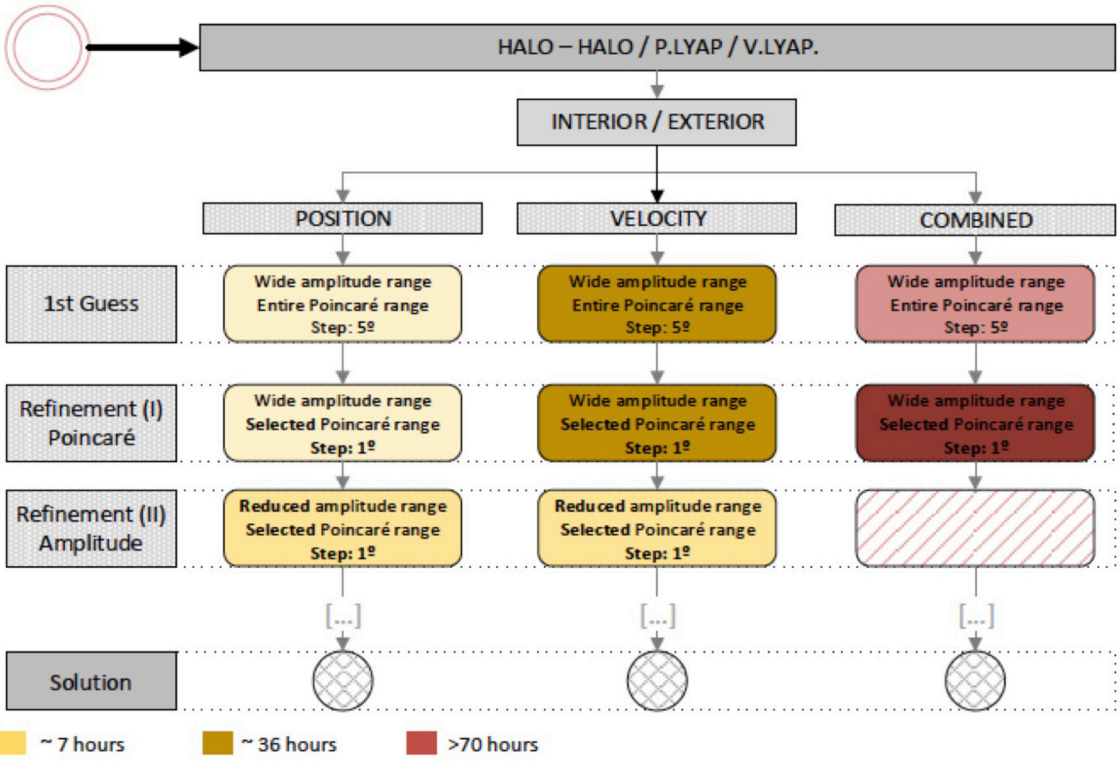

FIGURE 11 | Far rendezvous systematic algorithm.

Exploration n°1: Far Rendezvous Systematic Analysis

Actually, some exploration missions (vehicle coming back from Mars, Asteroids, or the Moon) can include parking orbit issued from other periodic families so as to take into account the inclination. The far rendezvous proposed strategy has been applied extensively to three rendezvous scenarios, so as to compare their performance cost (Δv_{far}), duration (ΔT), and feasibility (ΔX), in the Earth-Moon system, to extend the preceding studies cases to others libration periodic orbits families. It is assumed that the target is on a Halo orbit with a maximal elongation, A_z^T. The chaser parking orbit can be a Halo orbit, a Horizontal Lyapunov orbit or Vertical Lyapunov orbit. For each type of chaser parking orbit, performances are computed with interior or exterior manifolds. A wide simulation campaign was run based on an inclusive Matlab-based tool whose algorithm is presented on **Figure 11**. For each category of simulation, a first set was run so as to refine the range of variation of the parameters: amplitude of the chaser parking orbit A_z^C and angular location of the intermediate maneuver (φ_{PM}) at the Poincaré map. This first step was followed by two successive sets so as to further refine the results. The preliminary scenarios present a 5° step in φ_{PM}while the refined ones present a 1° step.

Figure 12 presents the best results obtained for three scenarios (Halo-to-Halo, Halo-to-Planar Lyapunov and Halo-to-Vertical Lyapunov) with interior and exterior directions, $\varphi_{PM} \epsilon\ [0:1:5]$ in deg., A_z^T fixed equal to 8,000 km, $A_z^C \epsilon\ [8,000:500:9,000]$ in km, $\left(\theta^C, \theta^T\right) \epsilon\ [0:1:5] \times [0:1:5]$ in deg. On this figure, the plot depicts the duration "Rendezvous time" in days and the cost "Total delta v" in km/s for three scenarios (Halo-to-Halo in red, Halo-to-Planar Lyapunov in blue and Halo-to-Vertical Lyapunov in green), for interior (+) and exterior (o) manifolds at three different value of A_z^T ($A_z^T = 8,000$ km in solid line, in $A_z^T = 8,500$ km in dot line and $A_z^T = 9,000$ km in dashed line). The plot makes it easy to infer the variation of cost and duration required as the parking orbit changes. Best results are obtained for Halo-to-Halo rendezvous with a $A_z^T = 8,500$ km on interior manifold with a $\Delta v_{far} = 0.83$ m / s and a $\Delta T = 2{,}47$ days. Being only initial guesses, these results do not take into account the Lambert arc to connect the manifolds. The doubly iterative process, proposed in this paper, can improve them. From this graph, it can be observed that obtained performances belong to four distinct groups, depending on the type of chaser parking orbit and type of manifold. It can obviously be deduced that cost increases largely from Halo to Planar Lyapunov and Vertical Lyapunov, for both interior and exterior manifolds. This confirms initial intuition that the best option is a Halo-to-Halo rendezvous, which can help for decision-making during mission design phase.

However, this study remained within the context of periodic orbits. It could be interesting to further investigate Lissajous and other quasi-periodic orbits, but it would require a different approach in term of procedures, that could be part of future research work.

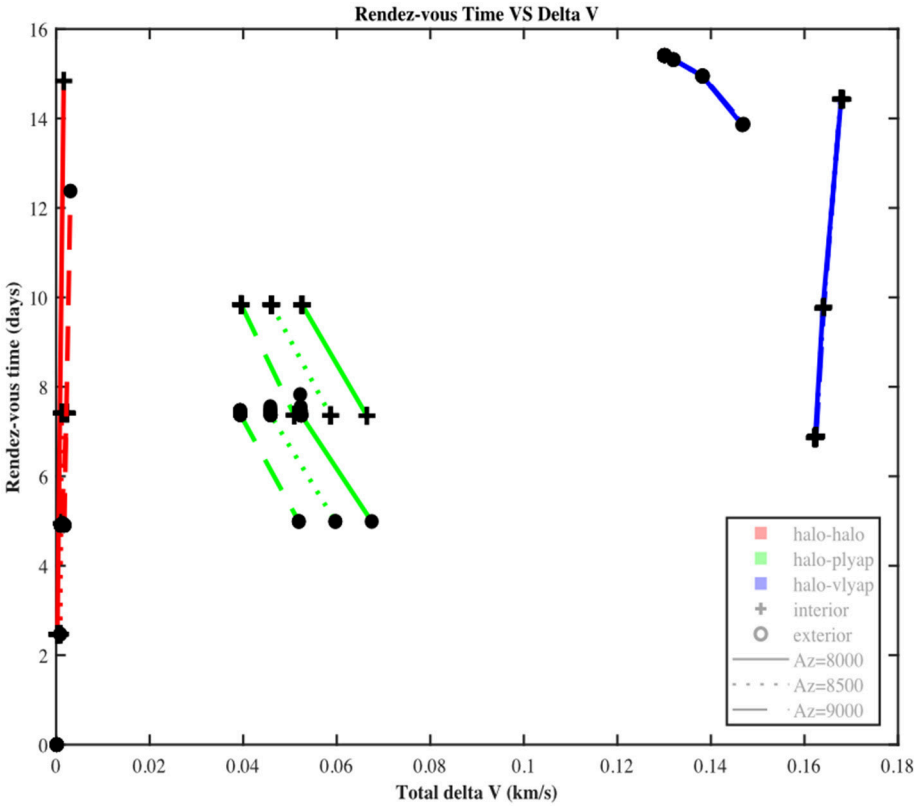

FIGURE 12 | Far Rendezvous duration vs. delta-v for the three scenarios.

Exploration n°2: Close Rendezvous on a DRO

First planed mission for Orion will take place on a DRO (Whitley and Martinez, 2016). **Figure 13** presents on the left the 14 first orbits computed from Henon (1969) data and on the right the enlarged family obtained by the continuation process.

As a consequence, it seems relevant to envisage rendezvous on this kind of orbit. Lunar DRO cannot be related to invariant structure such as stable or unstable manifolds (Ueda et al., 2017). The proposed strategy for far rendezvous cannot be applied. This exploratory analysis therefore focuses on the close rendezvous, applying a simplified algorithm compared to the one presented in 5.1. with only three steps: parking orbit (the chaser parking orbit defined by its maximal elongation A_z^C and target orbit defined by its maximal elongation A_z^T), close rendezvous strategy (the chaser approaches the target situated at θ^T on the target orbit from its initial location θ^C on its parking orbit defined by A_z^C) and safety analysis (with Monte Carlo simulations to model failure occurrence).

In this analysis, the rendezvous is assumed to take place on DRO at $\theta^T = 180$, on the target orbit defined by $A_z^T = 70,000$ km. The chaser initial conditions are: $A_z^C = 69,930$ km and $\theta^C = 178$. The reference angle is the x-axis (i.e., the Earth-Moon axis in the synodic reference frame), and the origin is the center of the Moon. Angles are measured clockwise. The Line-of-Sight corridor strategy is applied with a cone with a half top angle of ±15. The same parameters as Halo and NRHO study cases are taken into account for safety analysis. The AS is a sphere with a radius, r_{AS}, equal to 2km, and the KOS with a radius, r_{KOS}, equal to 200 m. Both spheres are centered on the target position. 100 simulations are run to model an error of 1% in magnitude (3σ) and an error of 1 mrad in pointing direction (3σ).

As far as the accuracy obtained along the chaser trajectory arcs is concerned, the differences in position, at the HP obtained by the three linearized model and the Lambert's arc are compared. From this simulation campaign, it appears that, in the particular case of close rendezvous on a DRO, the LR algorithm is far more precise, than C-W and SL, with even a wider validity domain. In fact only C-W can lead to better performance when the rendezvous occurs on a DRO with an elongation $A_z^T < 50,000$ km. However, the length of the elongation is not the only influencing parameter. The angular location of the final point for the rendezvous on the DRO plays a major role.

Coupled analyses for close rendezvous and safety aspects are then conducted. As a result, seven HP are obtained, with a $v_{close} = 8,92$ m/s, within 10 h and LOS-C strategy. When a failure occurs at HP n°1 to HP n°4, there is no risk of collision as the chaser trajectory does not intersect neither AS, nor KOS. For a failure injected at HP n°5, the rendezvous is still safe as the chaser enters the AS, but not the KOS. From HP n°6 and HP n°7, the chaser trajectory becomes dangerous for the target as the chaser enters the KOS after the failure injection.

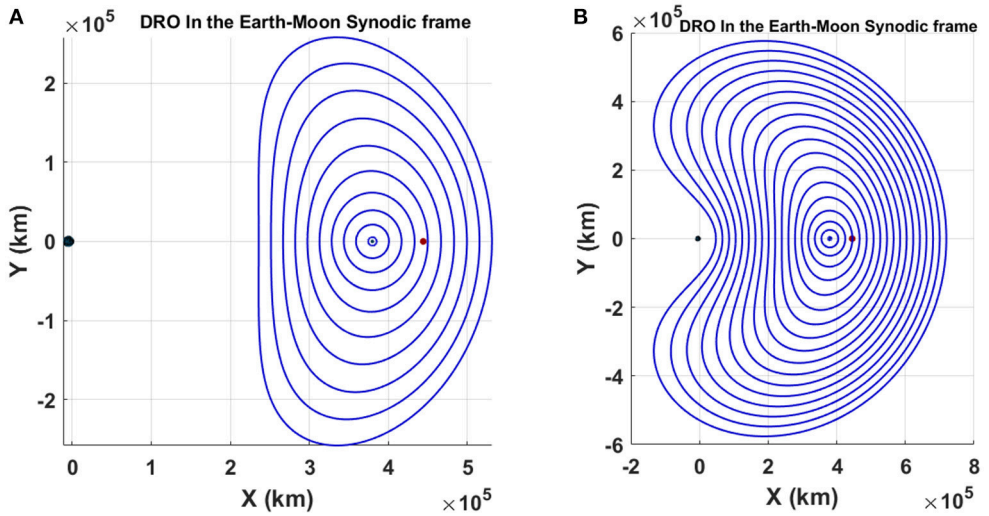

FIGURE 13 | DRO family in the Earth-Moon synodic frame. **(A)** 14 first DRO in the Earth-Moon synodic frame, **(B)** Enlarged DRO family obtained with the continuation process.

It can be concluded that the proposed strategy for close rendezvous on a DRO is applicable. Close rendezvous and safety analyses performed at DRO lead to results similar to the ones obtained for Halo orbits and NRHO. Further research will be necessary to propose a generic strategy, including an innovative far rendezvous strategy.

PERSPECTIVES AND CONCLUSION

In a context of growing interest of the international space community to design Human spaceflight missions to Earth-Moon Lagrangian point, the strategy for rendezvous in the vicinity of the Moon becomes an actual challenge. This paper studies a scarcely explored field of astrodynamics, dealing with relative motion in highly non-linear dynamics. The intrinsic complexity of the three-body problem demands a departure from the standards of relative motion in the two-body problem, while still ensuring a smooth transition between far rendezvous and close proximity operations. This paper has first summarized the bibliographical context and a description of the theoretical background for rendezvous strategy in the vicinity of Lagrangian point in the CR3BP. Then, it has discussed strategies for far and close rendezvous. As far as far rendezvous was concerned, a three-maneuvers strategy based on natural connection between manifolds of the target orbit and the chaser orbit was presented. Then a close rendezvous strategy was described, composed of two main steps to obtain the chaser's approach trajectory arcs: a first guess computed from the best-adapted linearized model, then a second iteration with a non-linear model as a solution of the Lambert's problem. Afterwards, safety aspects were discussed, adapted from lessons learned from cargo missions to resupply the ISS. Finally, two studies cases were introduced to illustrate the end-to-end scenario from parking orbit to close rendezvous, with safety criteria. Complementary analyses were presented to explore different rendezvous scenario when the chaser and target orbits belong to different periodic solution family and to study close rendezvous on a DRO.

Studies cases and exploratory analyses have shown that, for a given mission stating target and chaser initial conditions, an end-to-end scenario can be established, based on two-steps scenario, chaining sequentially far rendezvous and close rendezvous. The scenario will be unique for each given mission. The methodology will recommend locations for maneuvers (angular location for far rendezvous and HP number and position for close rendezvous). This study also highlighted the sensitivity of the close rendezvous performance to the performance of navigation sensors. Finally, it also emphasized the definition of safety zones such as the Approach Sphere and the Keep-Out Sphere, which should be standardized for better collaboration in international programs such as the future Lunar Orbital Platform-Gateway.

Complementary studies could be conducted so as to compare this methodology to other ones. A first option could be to elaborate a systematic process to find spatial intersections between the manifolds, without using Poincaré map. A second option could be based on a direct Lambert arc between chaser and target parking orbits, without the utilization of stable and unstable manifolds. To go even further the exploratory systematic analysis should be completed with planar (like DRO) and quasi-periodic solutions. The close rendezvous strategy is almost mature. It would now be interesting to see the possibilities of embedding it in flight software, taking into account the actual characteristics of flight equipment.

AUTHOR CONTRIBUTIONS

SL-D proposed strategies for far rendezvous, perform the corresponding analyses, supervised the research over several years. AC performed close rendezvous strategies analyses. VQ performed safety analyses for close rendezvous. LB and EB contributed to far rendezvous strategies, in particular

to 4-maneuvers strategy. SM performed analyses for close rendezvous on NRO.

ACKNOWLEDGMENTS

The authors would like to thank all the students involved in the different research projects that permitted to write this paper as a synthesis: Jean-Baptiste Bouvier, Adrien Brunel, Loic Cousin Raul Delgado Cuevas, Mani Vinayak Gopalan-Singamani, Rashika Jain, Bastien Le Bihan, Marc Morales, Nathanael Tepakbong-Tematio, Alejandro José Valverde, William Zanga. This research was entirely funded by ISAE-SUPAERO.

REFERENCES

Alessi, E. M., Gomez, G., and Masdemont, J. (2010). Two-manoeuvres transfers between LEOs and Lissajous orbits in the Earth-Moon system. *Adv. Space Res.* 45, 1276–1291. doi: 10.1016/j.asr.2009.12.010

Belbruno, E. A. (2002). Analytic estimation of weak stability boundaries and low energy transfers. *Contem. Math.* 292, 17–45. doi: 10.1007/s10569-006-9053-6

Belbruno, E. A., and Carrico, J. P. (2000). "Calculation of weak stability boundary ballistic lunar transfer trajectories," in *AIAA/AAS Astrodynamics Specialist Conference* Denver, CO.

Campolo,. A., Manglaviti, S., Le Bihan, B., and Lizy-Destrez, S. (2017). "Safety analysis for near rectilinear orbit close approach rendezvous in the circular restricted three-body problem," in *IAC-17-F1.2.3, IP,20,x37564* (Adelaide, SA), 25–29.

Canalias, E. (2007). *Contributions to Libration Mission Design Using Hyperbolic Invariant Manifolds*. Valencia: Universitat Politecnica de Catalunya.

Canalias, E., and Masdemont, J. J. (2006). *Rendezvous in Lissajous Orbits using the Effective Phases Plane*. Available online at: arc.aiaa.org

Clohessy, W., and Wiltshire, R. (1960). Terminal guidance system for satellite Rendezvous. *J. Aerospace Sci.* 27, 653–658.

Colagrossi, A., Lavagna, M., and Rafano Carna, S. F. (2016). "Dynamical analysis of rendezvous and docking with very large infrastructures in non-keplerian orbits," in *6th International Conference on Astrodynamics Tools and Techniques* (Darmstadt).

Davis, D. C., Bhatt, S., Howell, K., Jang, J.-W., Whitley, R., Clark, F., et al. (2017). "Orbit maintenance and navigation of human spacecraft at cislunar near rectilinear halo orbits," in *27th AAS/AIAA Space Flight Mechanics Meeting* (San Antonio, TX; United States), 5–9.

Farquhar, R. (1967). Lunar communications with libration-point satellites. *J. Spacecraft Rockets.* 4, 1383–1384.

Farquhar, R. (1973). Quasi-periodic orbits about the translunar libration point. *Celestial Mech.* 7, 458–473.

Farquhar, R. W. (1972). A Halo-Orbit Lunar Station. *Astronautics Aeronautics*, 59–63.

Farquhar, R. W., Dunham, D. W., Guo, Y., McAdams, J. V. (2004). Utilization of libration points for human exploration in the Sun–Earth–Moon system and beyond. *Acta Astron.* 55, 687–700. doi: 10.1016/j.actaastro.2004.05.021

Gerding, R. B. (1971). Rendezvous equations in the vicinity of the second libration point. *J. Spacecraft Rockets* 8, 292–294. doi: 10.2514/3.30263

Gómez, G., W. S., Koon, M., Lo, J. E., Marsden, J., Masdemont., and Ross, S. D (2004). Connecting orbits and invariant manifolds in the spatial three-body proble. *Nonlinearity* 17, 1571–1606. doi: 10.1088/0951-7715/17/5/002

Gómez, G., W. S., Koon, M., Lo, J. E., Marsden, J., Masdemont., and Ross, S. D. (2001). "Invariant Manifolds, The Spatial Three-body Problem and Space Mission Design," in *Advances in Astronautical Science* (San Diego, CA: American Astronautical Society), 3–22.

Henon, M. (1969). Numerical exploration of the restricted problem. *Astron. Astrophys.* 1, 223–238

Houbolt, J. C. (1960). *Considerations of the Rendezvous Problems for Space Vehicles*. New York, NY: SAE international. doi: 10.4271/600268

Howell, K. (1984). Three-dimensionnal, periodic, 'Halo' orbits. *Celestial Mech.* 32, 53–71.

ISECG (2018). *Global Exploration Roadmap*.

Jones, B. L., and Bishop, R. H. (1994). Rendezvous targeting and navigation for a translunar Halo orbit. *J. Guidance Control Dynam.* 17, 1109–1114.

Koon, W. S., Lo, M. W., Marsden, J. E., and Ross, S. D. (2001). Low energy transfer to the Moon. *Celestial Mech. Dynam. Astron.* 81, 63–73. doi: 10.1023/A:1013359120468

Lizy-Destrez,. S. (2015). "Rendezvous optimization with an inhabited space station at EML2," in *Proceedings of 25th International Symposium on Space Flight Dynamics ISSFD 2015* (Munich).

Luquette, R. J. (2006). *Nonlinear Control Design Techniques for Precision Formation Flying at Lagrange Points*, Ph.D. thesis, University of Maryland.

Mand, K. (2014). *Rendezvous and Proximity Operations at the Earth-Moon L2 Lagrange Point: Navigation Analysis for Preliminary Trajectory Design.* MSc Thesis, Rice University, Houston, TX.

Mingotti, G., Topputo, F., and Bernelli-Zazzera, F. (2012). Efficient invariant manifold,low-thrust planar trajectories to the Moon. *Commun. Nonlinear Sci. Numer. Simul.* 17, 817–831. doi: 10.1016/j.cnsns.2011.06.033

Mingtao, L., and Zheng, J. (2010). Impulsive lunar halo transfers using the stable manifolds and lunar flybys. *Acta Astron.*66, 1481–1492. doi: 10.1016/j.actaastro.2009.11.014

Murakami, N., and Yamanaka, K. (2015). "Trajectory design for rendezvous in lunar distant retrograde orbit," in *Japan Aerospace Exploration Agency.* Big Sky, MT

Murakami, N.,Ueda, S., Ikenaga, T., Maeda, M., Yamamoto, T., Ikeda, H., et al. (2015). "Practical rendezvous scenario for transportation missions to cis-lunar station in earth-moon L2 Halo orbit," in *Proceedings of 25th International Symposium on Space Flight Dynamics ISSFD 2015* (Munich).

Parker, J. S., and Anderson, R. L. (2013). *Low Energy Lunar Trajectory Design.* New York, NY: Jet Propulsion Laboratory

Parker, T. S., and Chua, L. (2012). *Practical Numerical Algorithms for Chaotic Systems*, Berlin: Springer-Verlag

Richardson, D. L. (1980). Analytic construction of periodic orbits about the collinear points. *Celestial Mech.* 22, 241–253.

Szebehely, V. (1967). *Theory of Orbits: The Restricted Problem of Three Bodies*. New York, NY: Academic Press Inc.

Ueda, S., and Murakami, N. (2015). "Optimim guidance strategy for rendezvous mission in Earth-Moon L2 Halo orbit," in *Proceedings of 25th International Symposium on Space Flight Dynamics ISSFD 2015* (Munich).

Ueda, S., Murakami, N., and Ikenaga, T. (2017). "A study on rendezvous trajectory design utilizing invariant manifolds of cislunar periodic orbits," in *AIAA 2017-1729, AIAA SciTech* (Grapevine, TX), 9–13.

Whitley, R., and Martinez, R. (2016). "Options for staging orbits in cis-lunar space," in *2016 IEEE Aerospace Conference* (Big Sky, MT).

Williams, J., Lee, D. E., Whitley, R. J., Bokelmann, K. A., Davis, D. C., Christopher, F. (2017). Berry targeting cislunar near rectilinear halo orbits for human space exploration (Preprint). *AAS* 17–267.

Conflict of Interest Statement: The authors declare that the research was conducted in the absence of any commercial or financial relationships that could be construed as a potential conflict of interest.

The reviewer FT declared a past supervisory role with one of the authors AC and a shared affiliation, with no collaboration, with the author SM to the handling editor at the time of review.

frontiers in Applied Mathematics and Statistics

ORIGINAL RESEARCH
published: 10 October 2018
doi: 10.3389/fams.2018.00042

Homo- and Heteroclinic Connections in the Planar Solar-Sail Earth-Moon Three-Body Problem

*Jeannette Heiligers**

Astrodynamics and Space Missions Section, Department of Space Engineering, Faculty of Aerospace Engineering, Delft University of Technology, Delft, Netherlands

This paper explores the existence of homo- and heteroclinic connections between solar-sail periodic orbits in the planar Earth-Moon circular restricted three-body problem. The existence of such connections has been demonstrated to great extent for the planar and spatial classical (no-solar sail) three-body problem, but remains unexplored for the inclusion of a solar-sail induced acceleration. Similar to the search for homo- and heteroclinic connections in the classical case, this paper uses the tools and techniques of dynamical systems theory, in particular trajectories along the unstable and stable manifolds, to generate these connections. However, due to the time dependency introduced by the solar-sail induced acceleration, common methods and techniques to find homo- and heteroclinic connections (e.g., using the Jacobi constant and applying spatial Poincaré sections) do not necessarily apply. The aim of this paper is therefore to gain an understanding of the extent to which these tools do apply, define new tools (e.g., solar-sail assisted manifolds, temporal Poincaré sections, and a genetic algorithm approach), and ultimately find the sought for homo- and heteroclinic connections. As a starting point of such an investigation, this paper focuses on the planar case, in particular on the search for homo- and heteroclinic connections between three specific solar-sail Lyapunov orbits (two at the L_1 point and one at the L_2 point) that all exist for the same near-term solar-sail technology. The results of the paper show that, by using a simple solar-sail steering law, where a piece-wise constant sail attitude is applied in the unstable and stable solar-sail manifold trajectories, homo- and heteroclinic connections exist for these three solar-sail Lyapunov orbits. The remaining errors on the position and velocity at linkage of the stable and unstable manifold trajectories are <10 km and <1 m/s. Future studies can apply the tools and techniques developed in this paper to extend the search for homo- and heteroclinic connections to other solar-sail Lyapunov orbits in the Earth-Moon system (e.g., for different solar-sail technology), to other planar solar-sail periodic orbits, and ultimately also to the spatial, three-dimensional case.

Keywords: solar sailing, circular restricted three-body problem, homoclinic connections, heteroclinic connections, transfer trajectories, Lyapunov orbits, libration point orbits

OPEN ACCESS

Edited by:
Elisa Maria Alessi, Consiglio Nazionale Delle Ricerche (CNR), Italy

Reviewed by:
Esther Barrabes, University of Girona, Spain
Ariadna Farres, Goddard Space Flight Center, United States

***Correspondence:**
Jeannette Heiligers
m.j.heiligers@tudelft.nl

Specialty section:
This article was submitted to Dynamical Systems, a section of the journal Frontiers in Applied Mathematics and Statistics

Received: *07 May 2018*
Accepted: *22 August 2018*
Published: *10 October 2018*

Citation:
Heiligers J (2018) Homo- and Heteroclinic Connections in the Planar Solar-Sail Earth-Moon Three-Body Problem. Front. Appl. Math. Stat. 4:42. doi: 10.3389/fams.2018.00042

INTRODUCTION

In recent years, the L_1 and L_2 libration points of the Earth-Moon system have drawn renewed interest as they hold potential to support future human space exploration activities. Such support may come in the form of landing missions [1, 2], lunar far-side communication capabilities [3, 4], or as a gateway to more distant interplanetary destinations [1, 5, 6]. The natural motion around the libration points has been studied in great detail [7–9] and several families of (quasi-)periodic orbits around the libration points have been identified, e.g., Lissajous [10], Lyapunov [11], and halo [12] orbits, with more families in, for example, Kazantzis [13, 14]. Though of immense importance, the fact that the spacecraft dynamics in these works are fully governed by gravitational accelerations only leaves little flexibility. Recent work by the author and her collaborators [15] has therefore explored an extension of the families of libration point orbits by complementing the dynamics with a solar-sail induced acceleration.

Solar sailing is a flight-proven form of in-space propulsion that makes use of an extremely thin, mirror-like membrane to reflect solar photons. The momentum exchange between the photons and the membrane induces a force, and therefore an acceleration, on the spacecraft which can be used for spacecraft orbit and trajectory design [16]. As a propellant-less form of propulsion, it holds great mission enabling potential [17] with applications in advanced space weather warning [18, 19], multi-asteroid rendezvous [20, 21], geomagnetic tail monitoring [22], and polar observation [23, 24]. With a range of successful solar-sail technology demonstration missions to date [25–27] and more such missions planned for the near future [28, 29], the application of solar sailing as main propulsion system on a science mission is in reach.

The addition of a solar-sail induced acceleration to the classical Earth-Moon three-body dynamics yields families of solar-sail planar and vertical Lyapunov, halo, and distant retrograde orbits [15, 30] and allows new orbit families to arise with potential applications for high-latitude observation of the Earth and Moon [4]. In particular, the work in Heiligers et al. [4] shows that a constellation of two sailcrafts in so-called clover-shaped orbits can achieve near-continuous coverage of the Earth's North Pole. If motion to the mirrored counterpart of this constellation can be achieved, a single solar-sail mission may enable high-temporal resolution observations of both the North and South Poles, thereby significantly increasing the mission's scientific return. To date only one mission, the ARTEMIS mission, has exploited such motion between libration point orbits when it transferred between Lissajous orbits at the Earth-Moon L_1 and L_2 points [31, 32].

The objective of this paper is to start the investigation of maneuver-free motion between solar-sail periodic orbits in the Earth-Moon system, where "maneuver-free" refers to no induced acceleration other than from the solar sail. Both homoclinic and heteroclinic motion will be investigated. In the classical system, the design and application of homo- and heteroclinic connections has already been researched extensively [33–38] with extensions to higher-fidelity dynamics in Haapala and Howell [38] and optimal control approaches for the inclusion of a variable specific impulse system or to connect periodic orbits in different three-body systems in Stuart et al. [39] and Heiligers et al. [40]. In the classical sense, homo- and heteroclinic connections are established by exploiting the instability of the libration point orbits and exploring motion along their associated invariant manifolds. By identifying connections on suitable spatial Poincaré sections of trajectories that depart from one orbit along the unstable manifold and arrive on another orbit along the stable manifold, such transfers can be established. A similar approach is adopted here, however connections between trajectories along the *solar-sail assisted* stable and unstable manifolds are sought after in order to achieve homo- and heteroclinic connections between solar-sail periodic orbits in the Earth-Moon system. Here, solar-sail assisted manifolds are the invariant manifolds of the solar-sail periodic orbit where the same sail-steering law is adopted along the manifolds as in the solar-sail periodic orbits. The dynamics are thus consistent throughout the solar-sail periodic orbit and its invariant manifolds.

Though the approach may be similar, the search for connections in the solar-sail three-body problem is more complex due to the (periodic) time dependency that the solar-sail induced acceleration introduces into the dynamics. This prevents, for example, the use of "spatial" Poincaré sections. The effect of this time dependency needs to be understood, appropriate search methods need to be established, and the actual existence of homo- and heteroclinic connections needs to be verified. This paper will go through each of these individual steps. As a first investigation into the problem, the paper will limit itself to planar motion, in particular to homo- and heteroclinic connections between solar-sail Lyapunov orbits, with the idea to define a framework that can be extended in future work to other planar solar-sail periodic orbits in the Earth-Moon system as well as to the spatial, three-dimensional case.

To set up such a framework, the rest of this paper is organized as follows. First, the dynamical framework is introduced in the section "Dynamical Framework". The three solar-sail Lyapunov orbits that will act as test cases in this paper will be discussed in the section "Solar-sail Lyapunov Orbits" with a description of their associated solar-sail assisted invariant manifolds in the section "Solar-sail Assisted Invariant Manifolds". The section "Problem Definition" will continue with the problem definition and a discussion on the applicability of tools traditionally used for the search of homo- and heteroclinic connections in the classical three-body problem (spatial Poincaré section and the Jacobi constant). The conclusion of that section leads to an exploration of new tools (temporal Poincaré section and a figure of merit) in the section "Exploration Methodology". In the sections "Homoclinic Connections" and "Heteroclinic Connections" these tools will be further extended to generate homoclinic and heteroclinic connections through grid searches and a genetic algorithm. The paper ends with the conclusions.

DYNAMICAL FRAMEWORK

The dynamical framework employed in this paper is that of the Earth-Moon circular restricted three-body problem (CR3BP) [41], complemented with the acceleration generated by the solar sail. Note that the perturbative acceleration due to the gravitational attraction of the Sun is not included in the dynamics: for reasonable solar-sail technology, this perturbative acceleration is much smaller than the solar-sail induced acceleration throughout much of the Earth-Moon system. The assumptions in the classical (no-solar sail) CR3BP are that the motion of a mass m is governed by the gravitational attraction of two larger masses m_1 and m_2; that the gravitational effect of mass m on masses m_1 and m_2 is negligible; and that m_1 and m_2 move in circular co-planar orbits about their barycenter. When complementing the classical CR3BP with a solar sail, the motion of m is no longer governed by gravitational accelerations only, but also by the acceleration generated by the sail. In this paper, m is thus the sailcraft, whereas m_1 and m_2 represent the Earth and Moon, respectively. It is convenient to define the motion of the sailcraft in a synodic frame of reference, $R\left(x,y,z\right)$, which has its origin at the Earth-Moon barycenter, the x axis pointing from the Earth to the Moon, the z axis perpendicular to the Earth-Moon orbital plane, and the y axis completing the right-handed reference frame, see **Figure 1**. With respect to inertial space, this frame rotates at an angular rate ω around the z axis: $\boldsymbol{\omega} = \omega\hat{\mathbf{z}}$. Furthermore, a set of canonical units is used, where the sum of m_1 and m_2, the distance between m_1 and m_2, and $1/\omega$ are taken as the units of mass, length, and time, respectively. Finally, the mass ratio $\mu = m_2/\left(m_1 + m_2\right) = 0.01215$ is defined. Then, the dimensionless masses of the Earth and Moon become $1-\mu$ and μ , respectively, and their location along the x axis of frame $R\left(x,y,z\right)$ are $-\mu$ and $1-\mu$, respectively. In frame $R\left(x,y,z\right)$, the equations of motion of the sailcraft are given as [16]

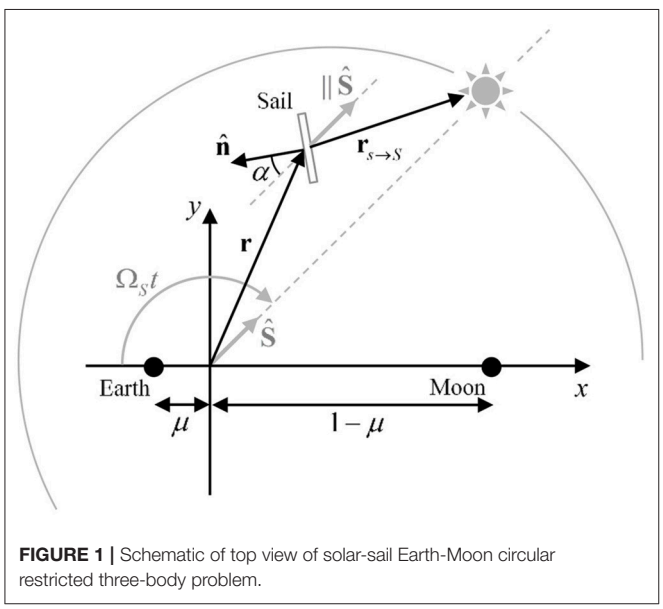

FIGURE 1 | Schematic of top view of solar-sail Earth-Moon circular restricted three-body problem.

$$\ddot{\mathbf{r}} + 2\boldsymbol{\omega} \times \dot{\mathbf{r}} + \nabla U = \mathbf{a}_s\left(t\right). \tag{1}$$

The left-hand side of Equation (1) represents the classical CR3BP, whereas the right-hand side adds the solar-sail induced acceleration. In Equation (1), $\mathbf{r}$ is the sailcraft position vector, which, combined with the sailcraft velocity vector, gives its state vector, $\mathbf{x} = \left[\mathbf{r}\ \dot{\mathbf{r}}\right]^T$; U is the effective potential from which the gravitational and centripetal accelerations can be computed

$$U = -\tfrac{1}{2}\left(x^2 + y^2\right) - \left(\left[1-\mu\right]/r_1 + \mu/r_2\right), \tag{2}$$

where $r_1 = \left\|\mathbf{r} + \left[\mu\ 0\ 0\right]^T\right\|$ and $r_2 = \left\|\mathbf{r} - \left[1-\mu\ 0\ 0\right]^T\right\|$. Finally, in Equation (1), $\mathbf{a}_s\left(t\right)$ is the solar-sail induced acceleration vector.

To define the solar-sail induced acceleration vector, the motion of the Sun in frame $R\left(x,y,z\right)$ is assumed to be in the Earth-Moon plane, i.e., in the $\left(x,y\right)$ plane, thereby neglecting the small, 5° inclination difference between the ecliptic and Earth-Moon orbital planes. Furthermore, the Sun orbits the Earth-Moon system in a clockwise direction at a dimensionless rate of $\Omega_S = 0.9252$ with a dimensionless period of $P_S = 2\pi/\Omega_S$, which will be referred to as the synodic period throughout the paper. The position vector of the Sun is then given through

$$\mathbf{r}_S = r_S\hat{\mathbf{S}} = r_S\begin{bmatrix} -\cos\left(\Omega_S t\right) \\ \sin\left(\Omega_S t\right) \\ 0 \end{bmatrix}. \tag{3}$$

In Equation (3), the Sun is assumed to be on the negative x axis at time $t = 0$. In this work, a constant value for the magnitude of the Sun's position vector r_S of 1 astronomical unit (au) is assumed. Furthermore, because the magnitude of the sailcraft's position vector is much smaller than that of the Sun, i.e., $\|\mathbf{r}\| << r_S$, the sail-Sun distance is also assumed to be equal to 1 au, i.e., $\|\mathbf{r}_{s\to S}\| = r_S$, see **Figure 1**. The result of this assumption is a constant solar radiation pressure throughout the Earth-Moon system. To further define the solar-sail induced acceleration vector, an ideal solar-sail model is adopted where the sail is assumed to be a perfect reflector, resulting in pure specular reflection of the impinging solar photons [16]. For realistic sails, optical imperfections and wrinkles will cause diffuse reflection, absorption, and thermal emission of the solar photons [16], but for the preliminary analysis considered in this paper, these effects are neglected. Under the assumption of specular reflection, the solar-sail induced acceleration vector acts perpendicular to the solar-sail membrane and can be defined as [15, 42]

$$\mathbf{a}_s\left(t\right) = a_{0,EM}\cos^2\left(\alpha\right)\hat{\mathbf{n}} \tag{4}$$

with $a_{0,EM}$ the dimensionless characteristic solar-sail acceleration, $-90^o \leq \alpha \leq 90^o$ the solar-sail pitch angle, see **Figure 1**, and $\hat{\mathbf{n}}$ the unit vector normal to the solar-sail

membrane. The latter can be defined through the pitch angle, α, and a rotation around the z axis of angle $-\Omega_S t$

$$\hat{\mathbf{n}} = R_z\left(-\Omega_S t\right)\begin{bmatrix}\cos\alpha\\ \sin\alpha\\ 0\end{bmatrix}. \tag{5}$$

Finally, the characteristic solar-sail acceleration, $a_{0,EM}$, is the acceleration generated by the solar sail at 1 au when $\alpha = 0$, i.e., when the sail is oriented perpendicular to the direction of sunlight and the unit vectors $\hat{\mathbf{n}}$ and $\hat{\mathbf{S}}$ are aligned, but opposite, i.e., $\hat{\mathbf{n}} = -\hat{\mathbf{S}}$. Near-term values for this dimensionless characteristic solar-sail acceleration are in the order of $a_{0,EM} = 0.1$, which equates to a dimensional value of 0.2698 mm/s^2 [15, 18].

SOLAR-SAIL LYAPUNOV ORBITS

As mentioned in the introduction, previous work by the author and her collaborators [15] has extended the families of classical Lyapunov orbits to families of solar-sail Lyapunov orbits. These orbits are generated by first selecting classical Lyapunov orbits with a period that coincides with the period of the Sun around the Earth-Moon system, i.e., the synodic period. Subsequently, a continuation is started on the solar-sail characteristic acceleration $a_{0,EM}$ and for each increment in $a_{0,EM}$ a differential correction scheme is applied to find a periodic solar-sail Lyapunov orbit. This procedure results in a family of solar-sail Lyapunov orbits parameterized by $a_{0,EM}$. Different families can be generated for different steering laws and by choosing either of the two y axis crossings of the initial classical orbit as the starting point for the orbit propagation, i.e., either the initial condition on the left- or right-hand side of the libration point. This choice of starting point, hereafter referred to as the Sun-sail phasing, results in a different phasing of the solar sail and the Sun over time and therefore in different solar-sail Lyapunov orbit families.

The orbits selected for this study are shown in **Figure 2A** (**Figure 2B** will be discussed in the section "Problem Definition"). The figure shows three orbits, designated by the numbers 1–3, which all have a period equal to one synodic period, P_S, and they exist for $a_{0,EM} = 0.1$ and a zero-pitch angle steering law, i.e., $\alpha = 0$ and thus $\hat{\mathbf{n}} = -\hat{\mathbf{S}}$. Orbits 1 and 2 exist around the L_1 point, whereas orbit 3 exists around the L_2 point. Finally, the initial condition of orbit 1 lies on the left-hand side of L_1, while the initial conditions of orbits 2 and 3 lie on the right-hand side of either L_1 or L_2. Note that many other solar-sail Lyapunov orbits could have been selected [15], e.g., for different steering laws, different dimensionless characteristic solar-sail accelerations, and so on. However, the three orbits in **Figure 2A** are considered sufficient for the purpose of the current investigation: they consider a realistic value for the characteristic solar-sail acceleration, consider orbits about both the L_1 and L_2 points, incorporate both types of Sun-sail phasing, and use a simple steering law. Finally, by limiting the number of orbits to three, the number of connections to be investigated, see **Table 1**, also remains limited to a workable number of six. Note that the numerical designation of the transfers introduced in **Table 1** will be used throughout this paper. While transfers 1–3 represent homoclinic connections, transfers 4–6 consider heteroclinic connections, where transfers 4 and 5 connect orbits around the L_1 point with orbits around the L_2 point, while transfer 6 connects the two different orbits at the L_1 point. The latter allows a change in the Sun-sail phasing between the orbits. Note that the reverses of transfers 4–6 (e.g., from L_2 to L_1) are not considered.

SOLAR-SAIL ASSISTED INVARIANT MANIFOLDS

The stability analysis carried out in Heiligers et al. [15] showed that all three orbits in **Figure 2A** are highly unstable, implying the existence of stable and unstable invariant manifolds [9, 43]. Trajectories along these manifolds can be obtained by propagating the dynamics in Equation (1) from a state-vector along the stable and unstable eigenvectors of the linearized system around the periodic orbit, i.e., the reference trajectory, $\mathbf{r}_0$. Replacing $\mathbf{r} \rightarrow \mathbf{r}_0 + \delta\mathbf{r}$ in Equation (1) gives the following linearized system

$$\delta\dot{\mathbf{x}} = \mathbf{A}\delta\mathbf{x} \tag{6}$$

and

$$\mathbf{A} = \begin{bmatrix}\mathbf{0} & \mathbf{I}\\ -\frac{\partial \nabla U}{\partial \mathbf{r}}\big|_{\mathbf{r}_0} & \mathbf{\Omega}\end{bmatrix}, \mathbf{\Omega} = \begin{bmatrix}0 & 2 & 0\\ -2 & 0 & 0\\ 0 & 0 & 0\end{bmatrix}. \tag{7}$$

Note that the solar-sail induced acceleration does not appear in the linearized system as it is not a function of the Cartesian position coordinates. This is a direct result of the assumption that $\|\mathbf{r}_{s\rightarrow S}\| = r_S$ and therefore that the solar radiation pressure is constant throughout the Earth-Moon system. For a system of the form $\delta\dot{\mathbf{x}} = \mathbf{A}\delta\mathbf{x}$, the state-vector at time t after the initial time t_0 can be obtained through the state transition matrix (STM), $\mathbf{\Phi}(t; t_0)$, as

$$\delta\mathbf{x}(t) = \mathbf{\Phi}(t; t_0)\,\delta\mathbf{x}(t_0), \tag{8}$$

where the STM can be obtained by simultaneously propagating the equations of motion in Equation (1) and

$$\dot{\mathbf{\Phi}}(t; t_0) = \mathbf{A}\mathbf{\Phi}(t; t_0). \tag{9}$$

The STM evaluated after one full orbit, i.e., at time $t = t_0 + P_S$, is called the monodromy matrix. Its six eigenvalues, λ_i with $i = 1, 2, ..., 6$, appear in reciprocal pairs and define the linear stability properties of the orbit. An orbit is stable if all six eigenvalues lie on the unit circle. If the norm of any of the eigenvalues is larger than one, $\|\lambda_i\| > 1$, the orbit is unstable, with larger norm values indicating greater instability. The largest eigenvalues, $\lambda_{\max} = \max(\lambda_i)$, for orbits 1–3 in **Figure 2A** are 7.09410×10^5, 11.08556×10^5, and 8.12799×10^5, respectively, indicating that these orbits are indeed highly unstable. The unstable invariant manifold is defined as the set of trajectories that the spacecraft

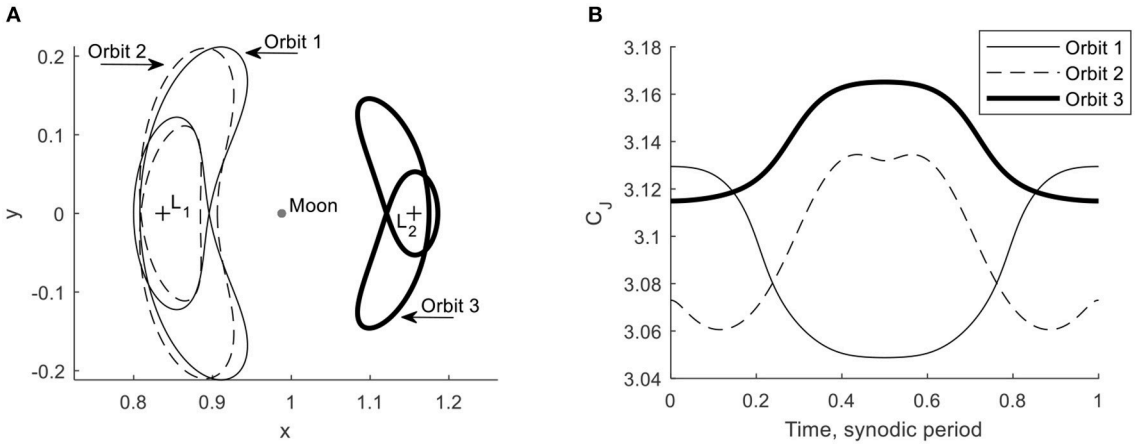

FIGURE 2 | Selected solar-sail Lyapunov orbits. **(A)** Orbits. **(B)** Jacobi constant value along the orbits.

TABLE 1 | Homo- and heteroclinic connections to be investigated.

Transfer number	Homo- or heteroclinic	Starting orbit	Final orbit
1	Homoclinic	1	1
2	Homoclinic	2	2
3	Homoclinic	3	3
4	Heteroclinic	1	3
5	Heteroclinic	2	3
6	Heteroclinic	1	2

takes if it is perturbed anywhere along the orbit in the direction of the local eigenvector associated with this largest eigenvalue, $\mathbf{w}_0^U$ [9, 43]. Similarly, the stable invariant manifold contains all trajectories that a spacecraft takes backwards in time after a perturbation in the direction of the local eigenvector associated with the eigenvalue $1/\lambda_{\max}, \mathbf{w}_0^S$ [9, 43]. This manifold contains the trajectories that asymptotically wind onto the periodic orbit. The local stable and unstable eigenvectors along the orbit at any time t, $\mathbf{w}^U(t)$ and $\mathbf{w}^S(t)$, can efficiently be obtained after a single, full-orbit propagation of the STM through

$$\mathbf{w}^U(t) = \mathbf{\Phi}(t, t_0)\,\mathbf{w}_0^U \tag{10}$$

$$\mathbf{w}^S(t) = \mathbf{\Phi}(t, t_0)\,\mathbf{w}_0^S. \tag{11}$$

Initial conditions along the local unstable and stable invariant manifolds, $\mathbf{x}_{M,0}^U$ and $\mathbf{x}_{M,0}^S$, are obtained by perturbing any state vector along the periodic orbit, $\mathbf{x}\left(t_{M,0}\right)$, by a magnitude ε along the unstable and stable eigenvectors as

$$\mathbf{x}_{M,0}^U\left(t_{M,0}\right) = \mathbf{x}\left(t_{M,0}\right) \pm \varepsilon \frac{\mathbf{w}^U\left(t_{M,0}\right)}{\left\|\mathbf{w}^U\left(t_{M,0}\right)\right\|} \tag{12}$$

$$\mathbf{x}_{M,0}^S\left(t_{M,0}\right) = \mathbf{x}\left(t_{M,0}\right) \pm \varepsilon \frac{\mathbf{w}^S\left(t_{M,0}\right)}{\left\|\mathbf{w}^S\left(t_{M,0}\right)\right\|}. \tag{13}$$

The actual trajectories along the unstable invariant manifolds can be obtained by forward propagating the initial condition in Equation (12) in the dynamics of Equation (1), whereas the actual trajectories along the stable invariant manifolds can be obtained by backward propagating the initial conditions in Equation (13) in the dynamics of Equation (1). Note that the dynamics in Equation (1) include the solar-sail induced acceleration. The propagation thus leads to solar-sail assisted manifold trajectories where the same sail steering law is applied as in the orbits themselves, i.e., $\hat{\mathbf{n}} = -\hat{\mathbf{S}}$. This steering law will be used throughout the paper unless explicitly mentioned otherwise (from the section "Non-zero Pitch Angles" onwards). The plus-minus signs in Equations (12) and (13) represent the two branches of the invariant manifolds that either move toward the smaller body (the interior manifold) or away from the smaller body (the exterior manifold). In this work, only the interior manifolds will be exploited for both the homoclinic and heteroclinic connections. Finally, in this work a value for the perturbation magnitude in Equations (12) and (13) of $\varepsilon = 10^{-6}$ (0.38 km) is used.

The resulting solar-sail assisted manifolds for orbit 1 appear in **Figure 3.** This figure has been generated by propagating 50 trajectories along each manifold (unstable/stable and interior/exterior) for an integration time of 1.2 P_S and by truncating the trajectories when their distance to the Moon becomes smaller than twice the lunar radius to prevent operational difficulties. The red trajectories follow the unstable manifold, whereas the green trajectories follow the stable manifold. The figure shows that the symmetry, which is inherent in the classical CR3BP, is preserved in the solar-sail CR3BP due to the periodicity and symmetry of the solar-sail induced acceleration. Therefore, the interior and exterior unstable and stable manifolds are mirrored in the (x, z) plane. More specifically, mirrored trajectories can be found for initial conditions $\mathbf{x}_{M,0}^U\left(t_{M,0}\right)$ and $\mathbf{x}_{M,0}^S\left(P_S - t_{M,0}\right)$ along the solar-sail Lyapunov orbits.

PROBLEM DEFINITION

For the rest of the paper, it is useful to specify a set of conventions, see **Figure 4**. This will allow to properly define the initial and final conditions of the unstable and stable manifold trajectories as

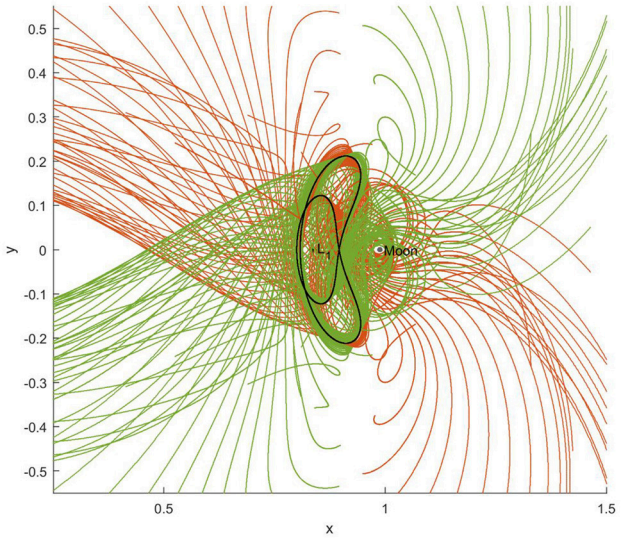

FIGURE 3 | Trajectories along the solar-sail assisted stable (green) and unstable (red) manifolds of orbit 1.

well as the time of linkage between these trajectories. The initial conditions of the (un)stable manifold trajectories are defined as discretized coordinates along the periodic orbits, while their final conditions and the time of linkage are defined through the integration time along the manifolds. Note that, throughout this and the following sections, a subscript M relates to variables associated with the manifold trajectories, while the omission of the subscript M refers to variables associated with the solar-sail periodic orbits.

First of all, the initial time in the starting and final solar-sail Lyapunov orbits are designated by $t_0^U = 0$ and t_0^S, respectively, see **Figure 4**. The initial time in the final orbit, t_0^S, occurs an integer number of synodic periods after t_0^U, i.e., $t_0^S = nP_S$ to allow time for the homo- or heteroclinic transfers to take place. Note that $t_0^S = nP_S$ can be seen as the earliest arrival time in the final orbit. The value chosen for n will determine how much time is allowed for the transfer and may take on different values for different cases throughout the paper to achieve the best results.

The orbits are discretized into N_M number of equally spaced points in time from where different manifold trajectories are assumed to start. The actual node numbers are denoted by i_M^U and i_M^S for the unstable and stable manifold trajectories, respectively, with i_M^U and i_M^S from 1 to N_M, see again **Figure 4**. Note that the first and last nodes coincide, i.e., $i_M^U = 1$ and $i_M^U = N_M$ as well as $i_M^S = 1$ and $i_M^S = N_M$, in order to demonstrate some periodic features throughout the paper. The time between discretization nodes is given by $\Delta t = P_S/(N_M - 1)$. The time at each of the discretization nodes is the initial time of the manifold trajectory and is given by $t_{M,0}^U = t_0^U + \left(i_M^U - 1\right)\Delta t$ for the starting orbit and $t_{M,0}^S = t_0^S + \left(i_M^S - 1\right)\Delta t$ for the final orbit. The state vector at the start of the unstable and stable manifold trajectories are denoted as $\mathbf{x}_{M,0}^U$ and $\mathbf{x}_{M,0}^S$. These are propagated over an integration time of t_{int}^U and t_{int}^S up to the final times $t_{M,f}^U$ and $t_{M,f}^S$ so that $t_{\text{int}}^U = t_{M,f}^U - t_{M,0}^U$ and $t_{\text{int}}^S = t_{M,f}^S - t_{M,0}^S$. The state vectors at the end of the propagation are denoted as

$$\mathbf{x}_{M,f}^U = \left[\mathbf{r}_{M,f}^U \ \mathbf{v}_{M,f}^U\right]^T = \left[x_{M,f}^U \ y_{M,f}^U \ \dot{x}_{M,f}^U \ \dot{y}_{M,f}^U\right]^T \text{ and}$$
$$\mathbf{x}_{M,f}^S = \left[\mathbf{r}_{M,f}^S \ \mathbf{v}_{M,f}^S\right]^T = \left[x_{M,f}^S \ y_{M,f}^S \ \dot{x}_{M,f}^S \ \dot{y}_{M,f}^S\right]^T.$$

For a connection, the state vectors at the end of the unstable and stable manifold trajectories should match, i.e., $\mathbf{x}_{M,f}^U = \mathbf{x}_{M,f}^S$, which occurs at the linking time, t_{link}. This implies that the following four constraints need to be satisfied

$$\begin{aligned} x_{M,f}^U &= x_{M,f}^S \\ y_{M,f}^U &= y_{M,f}^S \\ \dot{x}_{M,f}^U &= \dot{x}_{M,f}^S \\ \dot{y}_{M,f}^U &= \dot{y}_{M,f}^S. \end{aligned} \tag{14}$$

For the *classical* (no-solar sail) case, two of these constraints can easily be satisfied by choosing a suitable Poincaré section, e.g., by propagating both the unstable and stable manifold trajectories up to $x_{M,f}^U = x_{M,f}^S = 1 - \mu$, thereby inherently satisfying the first constraint in Equation (14). In addition, by choosing the starting and final orbits such that they have the same Jacobi constant value (which is inherently the case for a *classical* homoclinic connection), the compliance of another constraint, e.g., the third constraint in Equation (14), can be ensured. This leaves only the compliance of two constraints to be evaluated, which can be found visually by plotting the values for $\left(y_{M,f}^U, \dot{y}_{M,f}^U\right)$ and $\left(y_{M,f}^S, \dot{y}_{M,f}^S\right)$ at the Poincaré section.

When adding the time-dependent solar-sail induced acceleration to the dynamics, an additional constraint needs to be satisfied: the ends of the stable and unstable trajectories not only need to match in the spatial domain, but also in time

$$t_{link} = t_{M,f}^U = t_{M,f}^S. \tag{15}$$

The consequence of this time constraint is that it impedes the use of "spatial" Poincaré sections as the time of arrival at the Poincaré section will be different for each trajectory. Instead, Poincaré sections "in time" will have to be used, where all trajectories are not propagated up to, for example, a prescribed x coordinate, but up to a specific integration time.

The time-dependent solar-sail induced acceleration also impedes the use of the Jacobi constant to automatically satisfy one of the constraints in Equation (14). The Jacobi constant is defined as [41]

$$C_J = 2\left(\frac{1-\mu}{r_1} + \frac{\mu}{r_2}\right) + \left(x^2 + y^2\right) - \left(\dot{x}^2 + \dot{y}^2 + \dot{z}^2\right). \tag{16}$$

First of all, for heteroclinic connections between solar-sail periodic orbits in the Earth-Moon system (like the solar-sail

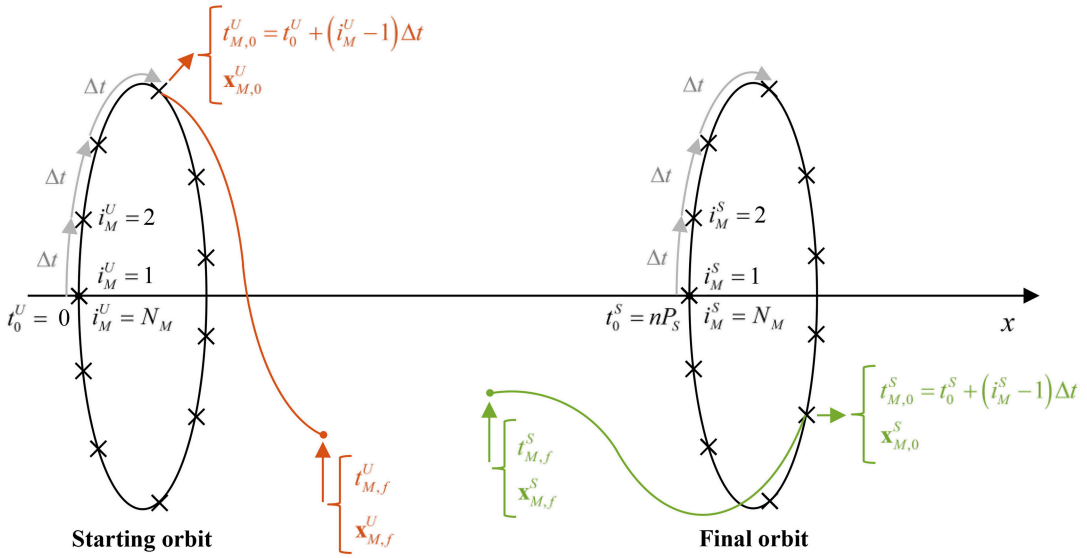

FIGURE 4 | Schematic of conventions. Note that, for a homoclinic connection the starting and final orbits are the same orbit.

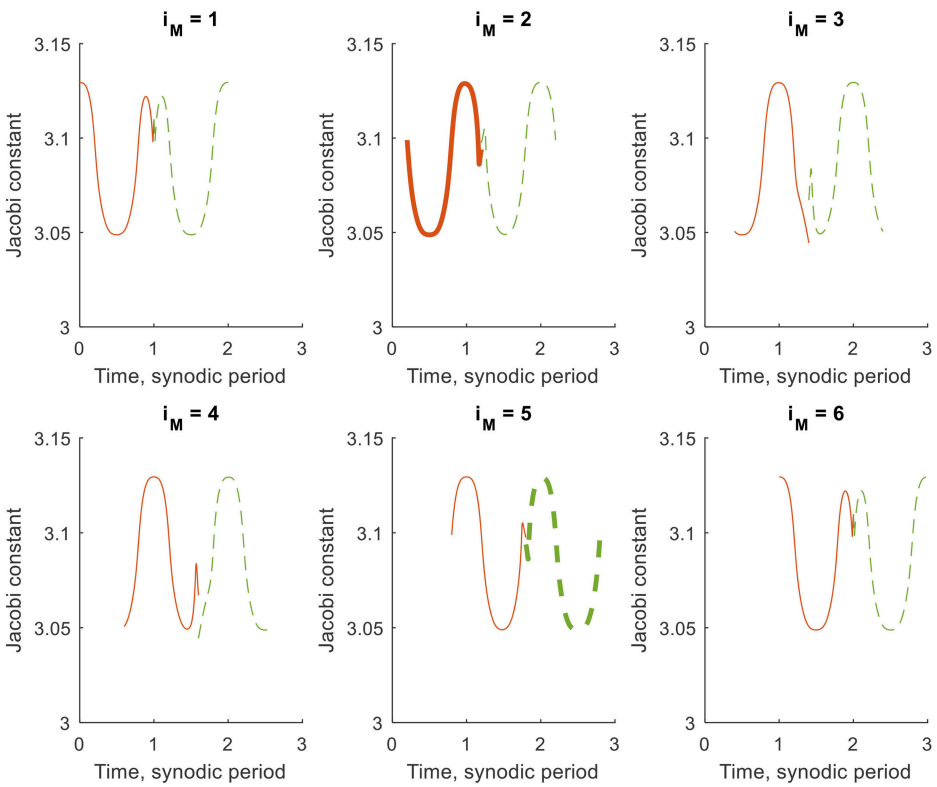

FIGURE 5 | Jacobi constant along six trajectories along the stable (red, solid) and unstable (green, dashed) manifolds of orbit 1, where $i_M = i^U_M = i^S_M$.

Lyapunov orbits considered in this paper), it will be difficult, if not impossible, to find two orbits with the same value for C_J, as the main orbit selection criterion will be that both orbits exist for the same sail technology, i.e., for the same value for $a_{0,EM}$. Furthermore, due to the time dependent solar-sail induced acceleration, the value for C_J is not constant along the orbits, see **Figure 2B**. Though not constant, its value is periodic and could therefore potentially provide a means to reduce the number of

constraints. However, as soon as the manifold trajectories are being propagated from their initial condition, the periodicity in the value for C_J is lost, see **Figure 5.**

Figure 5 provides the C_J-value along the stable and unstable manifolds of orbit 1 for $N_M = 6$ (six trajectories per manifold), $n = 2$ (the earliest arrival time in the final orbit is two synodic periods after the initial time of the starting orbit), and $t^U_{\text{int}} = t^S_{\text{int}} = P_S$ (the manifold trajectories are propagated for one synodic period). By selecting the parameter values as such, the time constraint in Equation (15) is automatically satisfied for $i^U_M = i^S_M$. However, the different plots in **Figure 5** show a difference in C_J-value at the end of the stable and unstable manifold trajectories for $i^U_M = i^S_M$. Only for $i^U_M = N_M + 1 - i^S_M$ does the symmetry in the dynamical system guarantee the same C_J-value after an integer number of synodic periods, see for example the thick lines for $i^U_M = 2$ and $i^S_M = 5$ in **Figure 5**. However, for this combination of manifold trajectories, the time constraint is not satisfied, i.e., while a link in C_J-value exists, the trajectories do not link in time. It can therefore be concluded that the Jacobi constant does not provide any benefit in the search for either homoclinic or heteroclinic connections between solar-sail Lyapunov orbits in the Earth-Moon system.

EXPLORATION METHODOLOGY

The previous section has demonstrated that methods, conventionally used to find homo- or heteroclinic connections between Lyapunov orbits in the classical Earth-Moon system, do not apply for the inclusion of a solar-sail induced acceleration. Connections can therefore not simply be obtained from a visual inspection of two-dimensional spatial Poincaré sections. This section will explore a different methodology, where the time constraint in Equation (15) is satisfied by suitable choices of "temporal" Poincaré sections (either by defining a fixed propagation time, see the section "Fixed Propagation Time", or a fixed linkage time, see the section "Fixed Linkage Time"). Furthermore, the coordinate constraints in Equation (14) are assessed by defining the following figure of merit (or objective):

$$J = w\Delta r + \Delta v, \tag{17}$$

with w a weight and

$$\Delta r = \left\| \mathbf{r}^U_{M,f} - \mathbf{r}^S_{M,f} \right\|, \Delta v = \left\| \mathbf{v}^U_{M,f} - \mathbf{v}^S_{M,f} \right\|. \tag{18}$$

The objective in Equation (17) is thus a weighted sum of the error in dimensionless position and dimensionless velocity between the ends of the unstable and stable manifold trajectories. In this work, a value for the weight of $w = 5$ is selected. This value is based on trial runs as well as the fact that an error in velocity is of slightly less importance than an error in position as it can be physically overcome, e.g., in worst case, by an additional propulsion source.

For brevity, the applicability of the proposed tools will be explored for homoclinic connections only, i.e., for transfers 1–3, and will be shown to provide a good framework. However, more flexibility in both the temporal "positioning" of the Poincaré section as well as other design parameters such as the solar-sail steering law is required to fully satisfy the constraints in Equations (14) and (15). This will be further explored for the homo- and heteroclinic connections separately in the sections "Homoclinic Connections" and "Heteroclinic Connections", respectively.

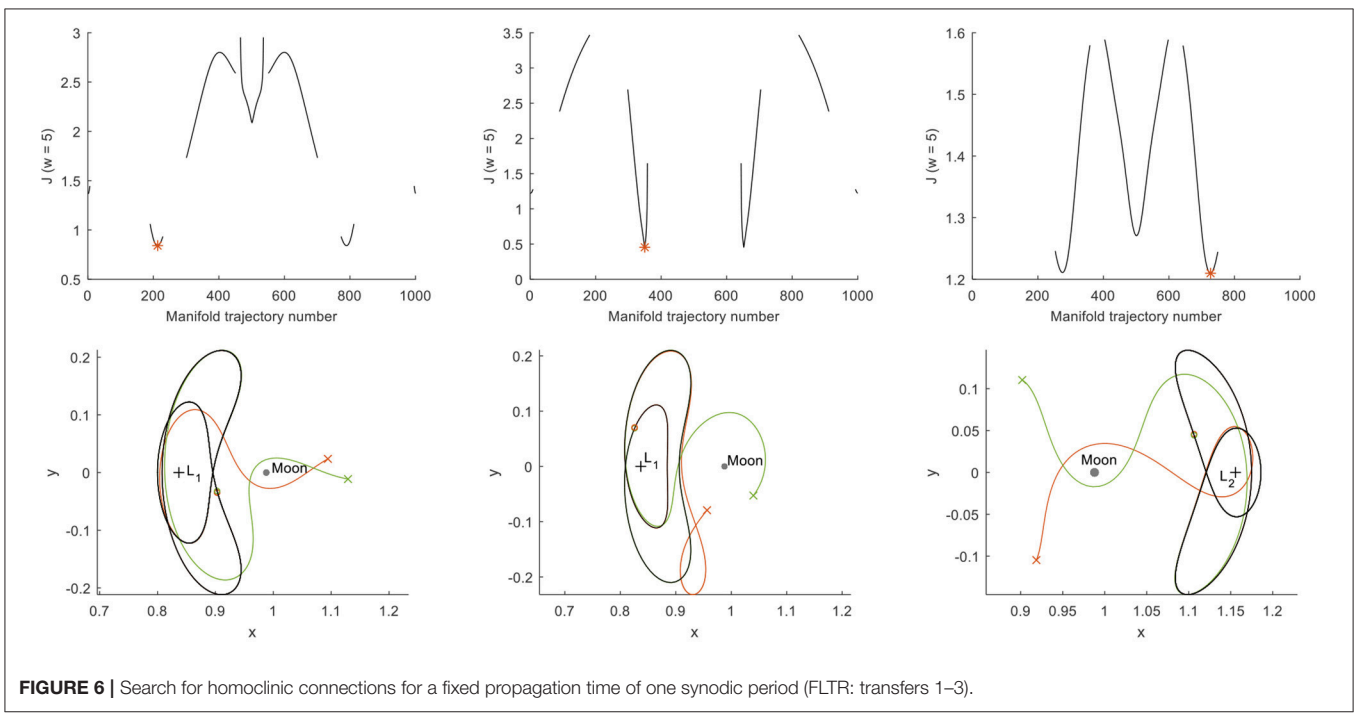

FIGURE 6 | Search for homoclinic connections for a fixed propagation time of one synodic period (FLTR: transfers 1–3).

Fixed Propagation Time

In the section "Problem Definition", a propagation time of one synodic period was used to generate the results in **Figure 5**, in which case the time constraint in Equation (15) is satisfied *only* for connections between trajectories where $i_M^U = i_M^S$. This can be generalized to a propagation time of any integer number of synodic periods, i.e., $t_{\text{int}}^U = t_{\text{int}}^S = n_{\text{int}} P_S$. Then, the total transfer time becomes $2n_{\text{int}}$ and thus $n = 2n_{\text{int}}$, i.e., $t_{M,0}^U \in [0, P_S]$ and $t_{M,0}^S \in [2n_{\text{int}}P_S, (2n_{\text{int}}+1)\,P_S]$.

The results for $n_{\text{int}} = 1$ and $N_M = 1{,}000$ appear in **Figure 6** and in the first data column of **Table 2** (heading "Fixed propagation time"). Note that the other columns in **Table 2** will be discussed in the following sections where more advanced approaches in the search for homoclinic connections will be explored. The figures in the top row of **Figure 6** provide for transfers 1–3 the objective value for the different manifold trajectory numbers, i.e., for different values for $i_M^U = i_M^S$. Gaps in these results appear due to the early truncation of trajectories that approach the Moon at less than twice the lunar radius. The figures clearly show the symmetry in the dynamics, i.e., the results in terms of objective value are the same for $i_M^U = i_M^S$ and $N_M + 1 - i_M^U = N_M + 1 - i_M^S$. The computational effort for generating these results could thus be reduced by only considering $i_M^U = i_M^S = 1, 2, ..., \frac{1}{2}N_M$. The red star indicates one of two minima in the objective value with further numerical values on the departure, link and arrival times ($t_{M,0}^U$, t_{link}, and $t_{M,0}^S$, all in synodic period units) in **Table 2**. These different epochs are all one synodic period apart due to the fixed propagation time. The figures in the bottom row of **Figure 6** show the actual unstable (red) and stable (green) manifold trajectories corresponding to that minimum objective value, where circles and crosses mark the start and end of the manifold trajectories. Due to the condition $i_M^U = i_M^S$, the circles overlap. For true homoclinic connections, the crosses should also overlap. This is clearly not the case for the results in **Figure 6.** In fact, **Table 2** shows that the errors on the position are between 18,000 and 83,000 km and that the errors on the velocity are in the range 17–606 m/s. Note that longer integration times have been considered, e.g., $n_{\text{int}} = 2$, but that this did not lead to improvements in the objective value.

Fixed Linkage Time

To loosen the requirement that only connections for $i_M^U = i_M^S$ can be explored, this section moves away from a fixed propagation time of an integer number of synodic periods and instead propagates the initial conditions $\mathbf{x}_{M,0}^U$ and $\mathbf{x}_{M,0}^S$ forward and backward up to a specific linkage time, t_{link}. Consequently, $t_{M,f}^U = t_{M,f}^S = t_{link}$ and Equation (15) is automatically satisfied. The results can then be presented as temporal Poincaré sections at the linkage time, see the figures on the left-hand side of **Figure 7**. In this figure, the red and green dots represent the position

TABLE 2 | Objective value, dimensional errors on position and velocity, and further details for transfers 1–3 for different approaches in the search for homoclinic connections.

Transfer		Fixed propagation time	Fixed linkage time	Grid search: free linkage time	Grid search: non-zero pitch angles	Genetic algorithm
1	J	0.8414	0.2226	0.0836	0.0262	5.111×10^{-7}
	Δr, *km*	18962.9	2554.9	113.3	609.6	4.7×10^{-3}
	Δv, *m/s*	605.6	192.9	83.6	18.6	4.6×10^{-4}
	$t_{M,0}^U$, *synodic period*	0.212	0.563	0.999	0.83	0.641
	t_{link}, *synodic period*	1.212	2	1.906	2.048	1.791
	$t_{M,0}^S$, *synodic period*	2.212	3.385	3.020	3.16	3.308
	α^U, *deg*	0	0	0	63	40.2
	α^S, *deg*	0	0	0	−63	−27.8
2	J	0.4552	0.1146	0.0734	0.0165	2.199×10^{-4}
	Δr, *km*	33705.5	592.8	1361.4	1141.1	0.8
	Δv, *m/s*	17.1	108.8	56.7	1.7	0.2
	$t_{M,0}^U$, *synodic period*	0.349	0.523	0.636	0.84	0.836
	t_{link}, *synodic period*	1.349	2	2.142	2.046	1.950
	$t_{M,0}^S$, *synodic period*	2.349	3.478	3.479	3.17	3.153
	α^U, *deg*	0	0	0	46	48.2
	α^S, *deg*	0	0	0	−46	−43.9
3	J	1.2099	0.0366	0.0098	0.0350	2.609×10^{-4}
	Δr, *km*	82925.4	530.4	424.1	900.2	0.6
	Δv, *m/s*	133.6	30.2	4.4	23.7	0.3
	$t_{M,0}^U$, *synodic period*	0.726	0.571	0.573	0.47	0.480
	t_{link}, *synodic period*	1.726	1.5	1.504	1.456	1.483
	$t_{M,0}^S$, *synodic period*	2.726	2.429	2.432	2.53	2.540
	α^U, *deg*	0	0	0	15	13.9
	α^S, *deg*	0	0	0	−15	−15.6

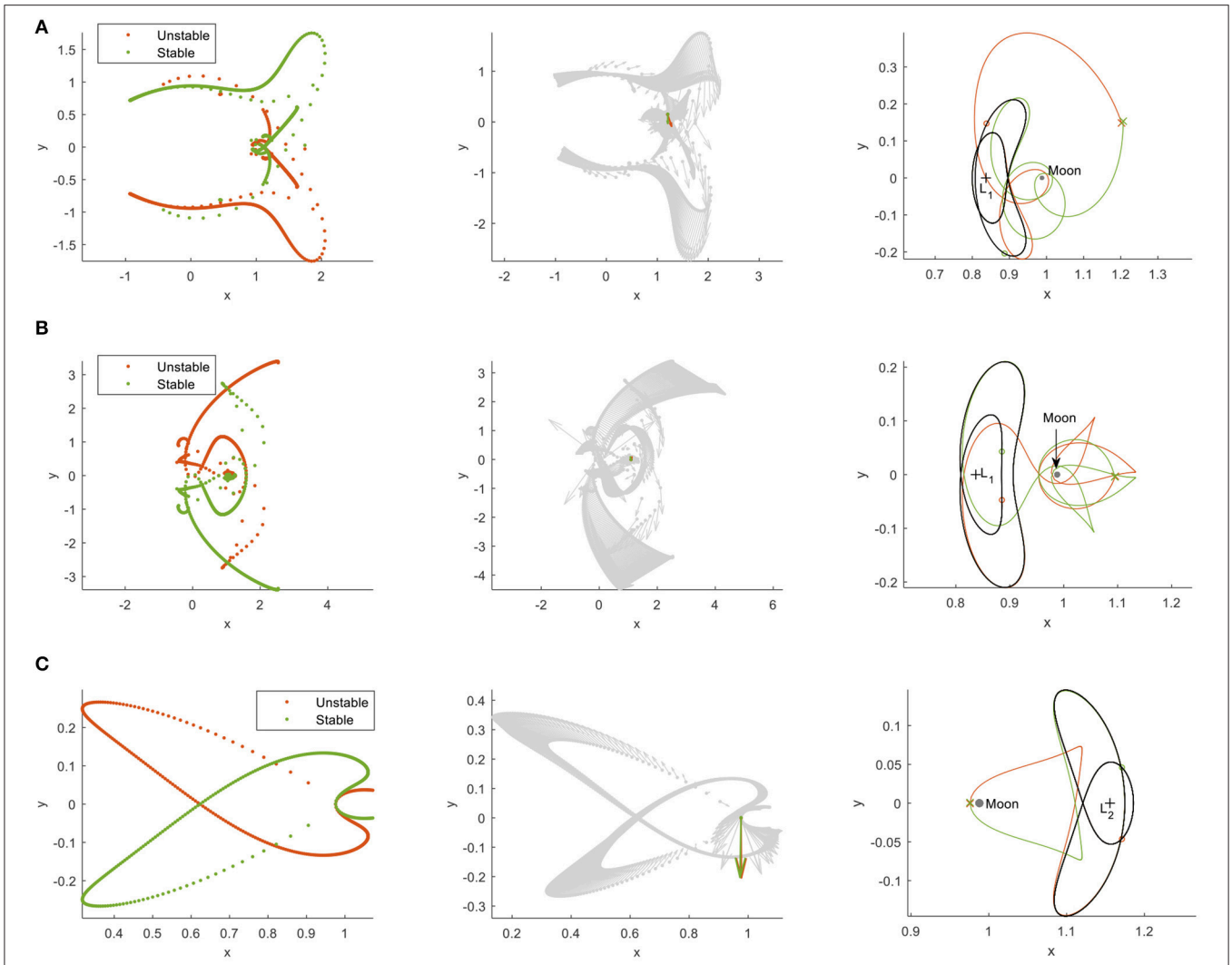

FIGURE 7 | Search for homoclinic connections for a fixed linkage time. **(A)** Transfer 1. **(B)** Transfer 2. **(C)** Transfer 3.

coordinates at the end of the unstable and stable manifold trajectories, respectively, for transfers 1–3. For transfers 1 and 2, these Poincaré sections are generated for $n = 3$ (i.e., $t^U_{M,0} \in [0, P_S]$ and $t^S_{M,0} \in [3P_S, 4P_S]$), while for transfer 3 better results were obtained for $n = 2$ (i.e., $t^U_{M,0} \in [0, P_S]$ and $t^S_{M,0} \in [2P_S, 3P_S]$). Furthermore, the linkage time is defined halfway, i.e., $t_{link} = \frac{1}{2}(n+1)\,P_S$, $N_M = 1{,}000$ and trajectories that approach the Moon by less than twice the lunar radius are again discarded.

The symmetry in the dynamics is once again clear from these figures (allowing the computational effort to be halved) and some connections *in position* can be observed, i.e., where the red and green dots overlap. Information on the velocity at the end of each trajectory can be included in the temporal Poincaré sections by using the "glyph representation" introduced by Haapala and Howell [38]. This glyph representation is shown in the figures in the middle column of **Figure 7** where an arrow indicates a scaled version of the velocity vector at the end of the unstable and stable manifold trajectories, i.e., $\mathbf{v}^U_{M,f}$ and $\mathbf{v}^S_{M,f}$. If a green and red dot overlap and the accompanying velocity arrows are of the same magnitude and point in the same direction, a homoclinic connection is established. The best connection, i.e., the combination of unstable and stable manifold trajectories with the smallest objective value in Equation (17), is highlighted in color in the figures in the middle column of **Figure 7**, while all other velocity vectors are marked in gray. The corresponding trajectories appear on the right-hand side of **Figure 7**. Comparing these trajectories with those in **Figure 6** shows the improvement that a fixed linkage time can establish over a fixed propagation time. Actual numerical values on the objective value and errors in position and velocity are provided in the second data column of **Table 2** (heading "Fixed linkage time"), which shows a reduction in the objective by a factor 3.7–33.1 and a reduction in the position error of 1–2 orders of magnitude.

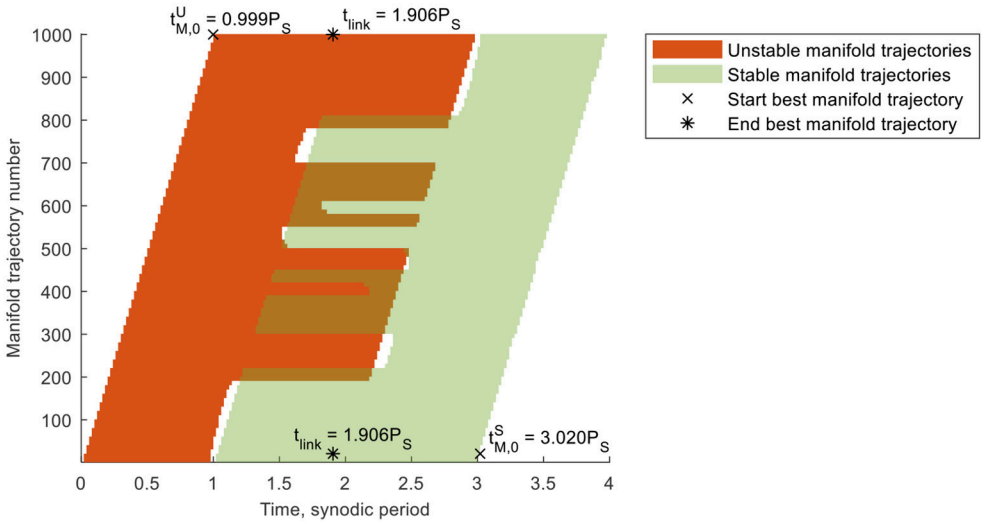

FIGURE 8 | Trajectory times per manifold trajectory number for transfer 1 including the departure, link, and arrival epochs for the best stable and unstable manifold trajectories.

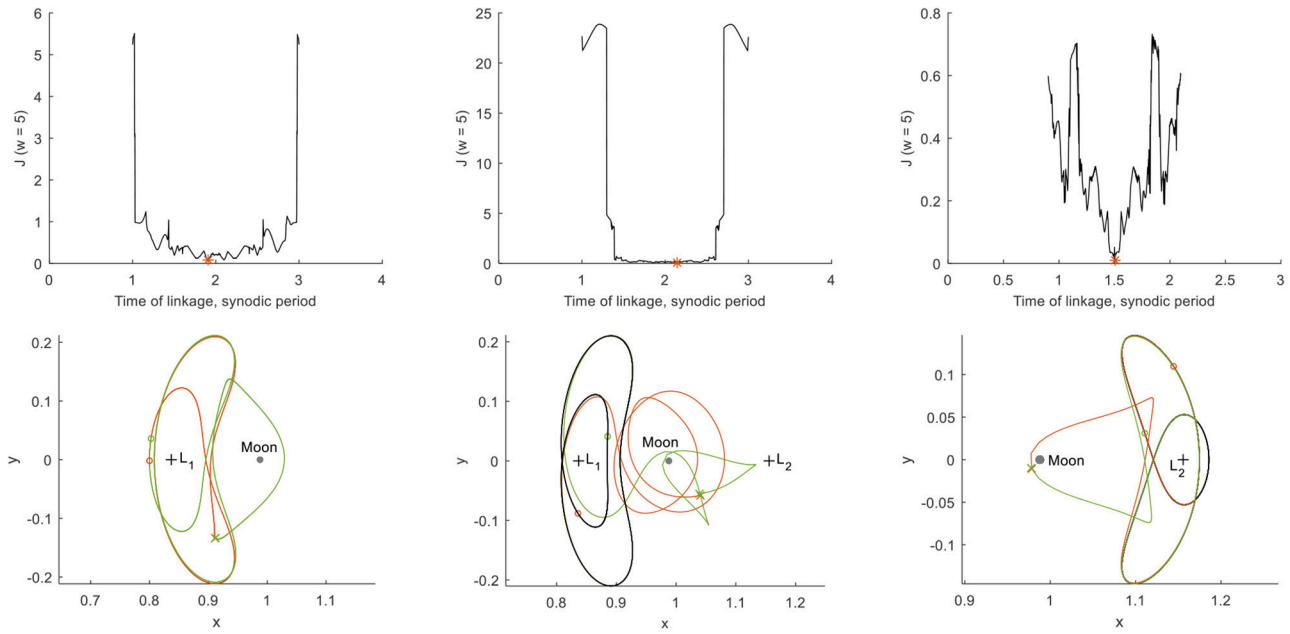

FIGURE 9 | Search for homoclinic connections for a free linkage time (FLTR: transfers 1–3).

This section has shown the usability of temporal Poincaré sections and the figure of merit in Equation (17) for the search of homoclinic connections. However, the highly constrained definition of the temporal Poincaré section as well as other design parameters such as the solar-sail steering law, cause the absolute values for the linkage errors to be too large in order to consider these transfers as true homoclinic connections. The subsequent sections will therefore introduce more flexibility into the design of the homo- and heteroclinic connections in the sections "Homoclinic Connections" and "Heteroclinic Connections", respectively.

HOMOCLINIC CONNECTIONS

Building on the results found for homoclinic connections in the previous section, this section introduces more flexibility into the design of the homoclinic connections by allowing the linkage time to be freely selected and by adopting non-zero solar-sail

pitch laws. To find the optimal linkage time and sail-steering law, two approaches are adopted: a simple grid search in the section "Grid Search" and a genetic algorithm approach in the section "Genetic Algorithm".

Grid Search

This section will explore the use of grid searches to improve the quality of the homoclinic connections by choosing a free linkage time, see the section "Free Linkage Time", and non-zero solar-sail pitch angles, see the section "Non-zero Pitch Angles".

Free Linkage Time

To explore the idea of a free linkage time, the following grid-search approach is adopted:

- $N_M = 1{,}000$ trajectories are propagated along the unstable and stable manifolds for two synodic periods, i.e., $t^U_{\text{int}} = t^S_{\text{int}} = 2P_s$.
- As in the previous section, $n = 3$ for transfers 1 and 2, while $n = 2$ for transfer 3. This means that the initial conditions of the trajectories along the unstable and stable manifolds are bound to the domains $t^U_{M,0} \in [0, P_S]$ and $t^S_{M,0} \in [2P_S, 3P_S]$ $(n = 2)$ and $t^S_{M,0} \in [3P_S, 4P_S]$ $(n = 3)$.
- A minimum transfer time of $0.9P_S$ is enforced to ensure that the trajectories will sufficiently move away from the solar-sail Lyapunov orbits. The final conditions of the trajectories along the unstable and stable manifolds are then confined to the domains $t^U_{M,f} \in [0.9P_S, 3P_S]$ and $t^S_{M,f} \in [0, 2.1P_S]$ $(n = 2)$ and $t^S_{M,f} \in [P_S, 3.1P_S]$ $(n = 3)$. There thus exists an overlap in linkage time in the domain $t_{link} \in [0.9P_S, 2.1P_S]$ $(n = 2)$ and $t_{link} \in [P_S, 3P_S]$ $(n = 3)$.
- Each propagated trajectory is interpolated at $n_{nodes} = 1{,}000$ equally spaced nodes in time.

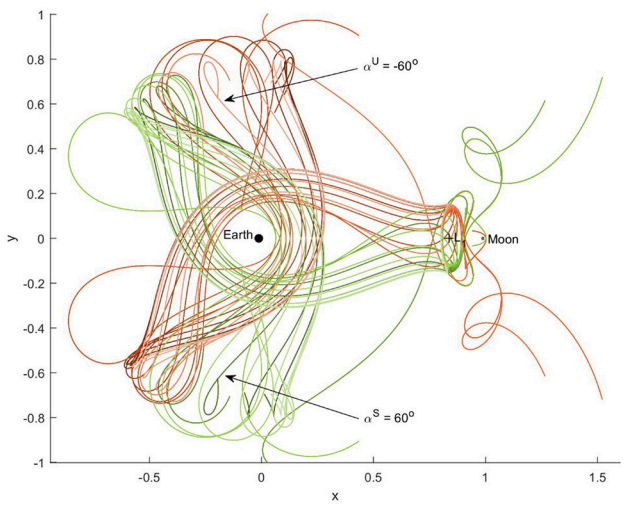

FIGURE 10 | Effect of non-zero pitch angle on the unstable (red) and stable (green) manifold trajectories of orbit 1 for $i^U_M = i^S_M = 1$, i.e., at $t^U_{M,0} = t^S_{M,0} = 0$, and for pitch angles between $-90°$ (dark color) and $90°$ (light color) with a step size of $10°$.

- The position and velocity coordinates at those nodes are stored in four individual matrices (one for each of the two position and two velocity coordinates) of size $\left[N_M, \frac{1}{2}(n+1)\, n_{nodes}\right]$. The rows of these matrices represent the trajectory numbers, whereas the columns represent the time at the nodes. This is further demonstrated in **Figure 8** for transfer 1, where the horizontal and vertical axes can be interpreted as the columns and rows of the matrices, respectively, and the colored surfaces indicate which elements of the matrices are filled. Note that the gaps in **Figure 8** are introduced by an early truncation of the trajectories because of a close lunar approach.
- After filling up the four individual matrices, for each potential linkage time [i.e., for each column between $t_{link} \in [0.9P_S, 2.1P_S]$ $(n = 2)$ or $t_{link} \in [P_S, 3P_S]$ $(n = 3)$], the errors in position and velocity for each combination of rows of the matrices for the stable and unstable manifolds are computed.
- Finally, the absolute minimum objective value for the best linkage time is extracted and the corresponding unstable and stable manifold trajectories are further evaluated.

The results for transfers 1–3 appear in **Figure 9**. The figures in the top row of **Figure 9** show the smallest objective value at each possible linkage time and the red star indicates the absolute minimum. The corresponding trajectories appear in the bottom row of **Figure 9** with numerical values for the objective, errors in position and velocity, and departure, link and arrival epochs in the third data column of **Table 2** (heading "Grid search: free linkage time"). For transfer 1, the epochs are also illustrated in **Figure 8**. From **Table 2** it can be concluded that a free linkage time further reduces the objective value by a factor 2.7–8.9, bringing the errors on the position and velocity at linkage down to less than the lunar radius (<1,738 km) and <100 m/s, respectively. For transfer 3, the result is very close to that for a fixed linkage time: the departure and arrival conditions along the solar-sail Lyapunov orbit and linkage time are only slightly changed. The result is a near-homoclinic connection with $\Delta r = 424.1$ km and $\Delta v = 4.4$ m/s.

Non-zero Pitch Angles

Up to this point, the attitude of the solar sail in the stable and unstable manifold trajectories has been assumed equal to that of the solar-sail Lyapunov orbits, i.e., $\alpha = 0$ and thus $\hat{\mathbf{n}} = -\hat{\mathbf{S}}$. This section investigates if further improvements on the objective value can be achieved by orienting the sail at a constant, but non-zero, pitch angle along the stable and unstable manifold trajectories. Note that, when considering non-zero pitch angles, the terms "invariant manifolds" or "manifold trajectories" no longer really apply, but that, for consistency, this paper will continue to use these terms.

By changing the sail's orientation with respect to the incoming solar radiation through the pitch angle, see **Figure 1**, the solar-sail induced acceleration changes as per Equation (4). **Figure 10** demonstrates the effect of a non-zero pitch angle along the manifold trajectories of orbit 1. To generate **Figure 10**, the initial conditions at $i^U_M = i^S_M = 1$, i.e., $\mathbf{x}^U_{M,0}(0)$ and $\mathbf{x}^S_{M,0}(0)$, are

forward and backward propagated for different pitch angles in the unstable, α^U, and stable, α^S, manifold trajectories. In particular, a range in α^U and α^S of $[-90^o, 90^o]$ is considered with a step size of 10^o. Note that pitch angles larger than 70^o may not always fall within mission constraints [29], but that the full theoretical range in pitch angles is considered in this paper for illustrative purposes. Also note that using different pitch angles in the stable and unstable manifold trajectories requires an instantaneous attitude change at linkage, but that this may be smoothed in future work by employing optimal control algorithms. However, this is considered beyond the scope of the current investigation.

Figure 10 shows that, by pitching the sail away from $\alpha^U = \alpha^S = 0$, a wealth of new trajectories arises. Note that the sign in Equations (12) and (13) is chosen such that the interior manifold results for $\alpha^U = \alpha^S = 0$ and that non-zero pitch angles subsequently cause the manifold trajectories to divert away from the Moon and move toward the Earth. The figure furthermore shows that the symmetry as explained in the section "Solar-sail Assisted Invariant Manifolds" is maintained for $\mathbf{x}^U_{M,0}(t_{M,0})$ and $\mathbf{x}^S_{M,0}(P_S - t_{M,0})$ as long as $\alpha^U = -\alpha^S$, see the trajectories indicated with $\alpha^U = -60^\circ$ and $\alpha^S = 60^\circ$ in **Figure 10**.

To assess the improvement in the objective value for non-zero pitch angles, the approach detailed in the section "Free linkage Time" is expanded by a loop around that approach to evaluate the minimum objective value for a mesh in α^U of $\alpha^U \in [-90^\circ, 90^\circ]$ with a step size of 1°. The pitch angle in the stable manifold trajectories is constrained to $\alpha^S = -\alpha^U$ The only difference with respect to the approach in the section "Free linkage Time" is a reduction in the number of manifolds trajectories to $N_M = 100$ to counter the increase in computational time introduced by the loop over α^U. The trajectories that yield the smallest objective value for transfers 1–3 appear in the top row of **Figure 11** with numerical values in the fourth data column of **Table 2** (heading "Grid search: non-zero pitch angles"). From **Table 2** it can be concluded that the best trajectories abide by, or are close to, the condition of $\mathbf{x}^U_{M,0}(t_{M,0})$ and $\mathbf{x}^S_{M,0}(P_S - t_{M,0})$ (i.e., the sum of $t^U_{M,0}$ and $t^S_{M,0}$ is equal to an integer number of synodic periods) and thus exploit the symmetry in the system. This is also clear from the position of the circle markers in **Figure 11**. As such, for transfers 1 and 2 a further reduction in the objective value of a factor 3.2–4.4 is achieved to position and velocity errors that start to resemble true homoclinic connections. However, the reduction in the number of manifold trajectories from $N_M = 1000$ in the previous section to $N_M = 100$ in the current investigation leads to an increase in the objective value for transfer 3.

Genetic Algorithm

The use of a grid search inherently limits the search space to discrete steps in the departure/arrival locations along the solar-sail Lyapunov orbits ($t^U_{M,0}$ and $t^S_{M,0}$), the linkage time, t_{link}, and the pitch angles in the unstable and stable manifold trajectories (α^U and α^S). To efficiently explore the design space in between these discrete steps, this section investigates the use of a genetic algorithm. In particular, the Matlab® function *ga.m* is used to find the values for the design parameters, $\mathbf{p}_{GA}$, that minimize the objective in Equation (17). The parameters are the previously used design variables $t^U_{M,0}$, $t^S_{M,0}$, α^U, α^S, and t_{link}, and bounds on

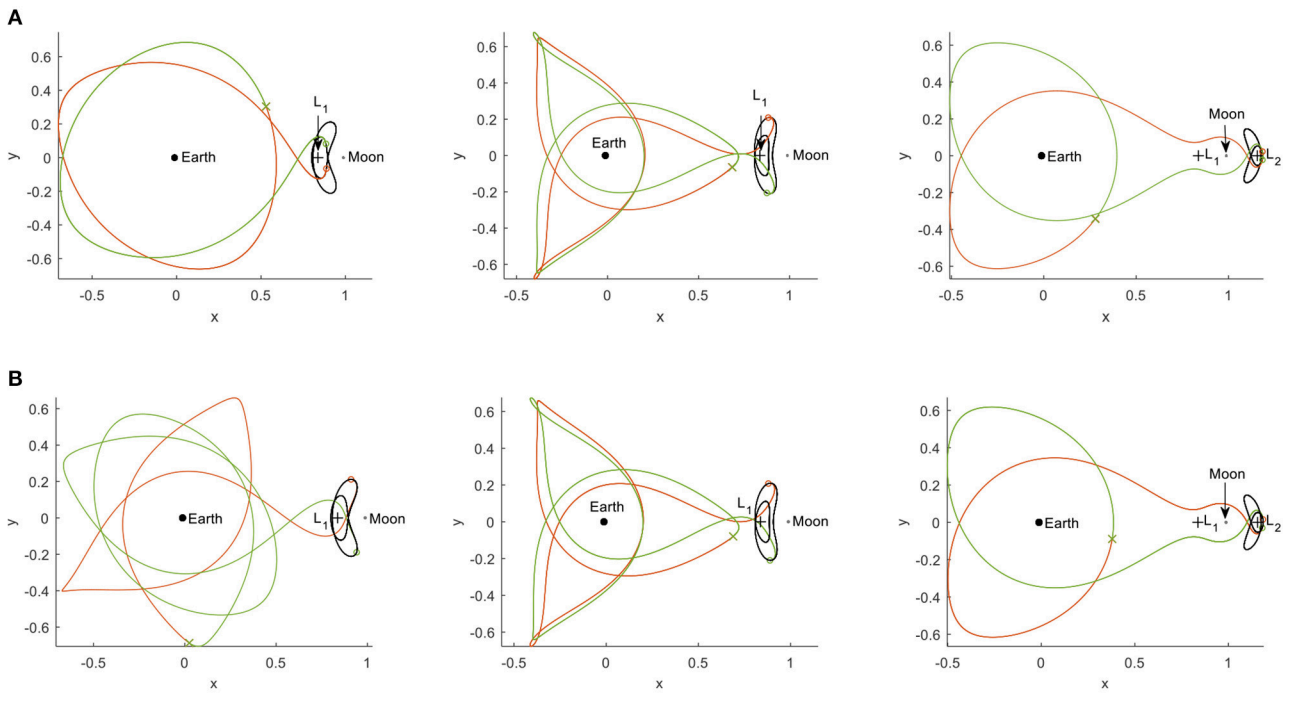

FIGURE 11 | Best homoclinic connections (FLTR: transfers 1–3). **(A)** For opposite-sign pitch angles. **(B)** For genetic algorithm approach.

these parameters are defined as

$$\begin{bmatrix} 0 \\ 2P_S \\ 0 \\ -90^o \\ -90^o \end{bmatrix} \leq \mathbf{p}_{GA} = \begin{bmatrix} t^U_{M,0} \\ t^S_{M,0} \\ t_{link} \\ \alpha^U \\ \alpha^S \end{bmatrix} \leq \begin{bmatrix} P_S \\ 4P_S \\ 4P_S \\ 90^o \\ 90^o \end{bmatrix}. \tag{19}$$

Furthermore, the following linear constraints are imposed to ensure that departure, linkage and arrival occur sequentially

$$t^U_{M,0} + \xi \leq t_{link} \leq t^S_{M,0} - \xi. \tag{20}$$

In Equation (20), ξ represents the previously introduced minimum transfer time to ensure that the trajectories move sufficiently away from the solar-sail Lyapunov orbits

$$\xi = 0.9P_S. \tag{21}$$

The genetic algorithm is initiated for a population of 1,000 individuals, is run for 100 generations and for five different seeds of the random generator to account for the inherent randomness of the genetic algorithm approach. For ease of implementation, the *ga.m* function is used with its default settings. The results appear in the bottom row of **Figure 11** and in the last column of **Table 2**. Especially the last column of **Table 2** shows that the continuous, instead of discrete, design space for the design parameters enables a reduction in the objective value of several orders of magnitude, with resulting errors in the position and velocity of <1 km and <1 m/s. This proves the feasibility of homoclinic connections between solar-sail Lyapunov orbits as well as the applicability of temporal Poincaré sections, the figure of merit in Equation (17), and the genetic algorithm approach for finding these connections.

HETEROCLINIC CONNECTIONS

This section follows the same approach as in the section "Homoclinic Connections" to find heteroclinic connections between the different solar-sail Lyapunov orbits, see trajectories 4–6 in **Table 1**. However, while that section first considered zero-pitch angles in the stable and unstable manifold trajectories, followed by opposite-sign pitch angles, the section "Grid Search"

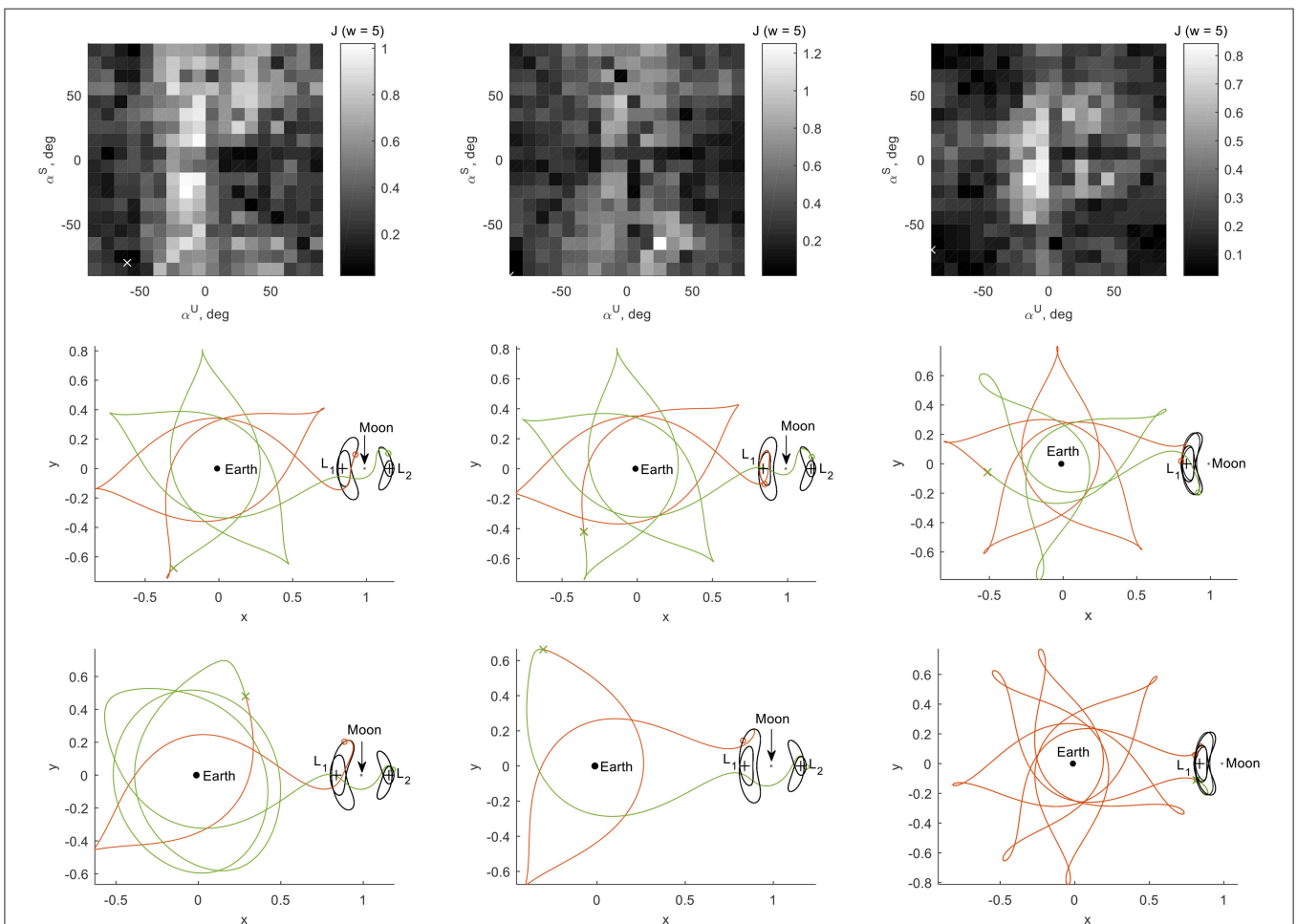

FIGURE 12 | Best heteroclinic connections (FLTR: transfers 4–6) for grid search in pitch angles (top and middle row) and for genetic algorithm approach (bottom row).

TABLE 3 | Objective value, dimensional errors on position and velocity, and further details for transfers 4–6 for different approaches in the search for heteroclinic connections.

Transfer		Grid search: non-zero pitch angles	Genetic algorithm
4	J	0.0203	6.8450×10^{-4}
	Δr, *km*	535.0	4.8
	Δv, *m/s*	13.6	0.6
	$t^U_{M,0}$, *synodic period*	0.76	0.613
	t_{link}, *synodic period*	2.188	1.389
	$t^S_{M,0}$, *synodic period*	3.93	3.454
	α^U, *deg*	−60	36.0
	α^S, *deg*	−80	−32.2
5	J	0.0124	5.9987×10^{-4}
	Δr, *km*	934.2	9.8
	Δv, *m/s*	0.2	0.5
	$t^U_{M,0}$, *synodic period*	0.62	0.766
	t_{link}, *synodic period*	2.058	1.676
	$t^S_{M,0}$, *synodic period*	3.95	2.5072
	α^U, *deg*	−90	34.5
	α^S, *deg*	−90	−9.6
6	J	0.0248	2.0332×10^{-4}
	Δr, *km*	1524.5	3.6
	Δv, *m/s*	5.1	0.2
	$t^U_{M,0}$, *synodic period*	0.01	0.034
	t_{link}, *synodic period*	1.758	2.989
	$t^S_{M,0}$, *synodic period*	3.11	3.257
	α^U, *deg*	−90	−80.6
	α^S, *deg*	−70	−25.3

below will immediately merge those approaches based on the improvements that non-zero pitch angles provided. The section "Grid Search" will even expand the search space on the usable pitch angles. Subsequently, in the section "Genetic Algorithm" the genetic algorithm approach will be applied to the search for heteroclinic connections.

Grid Search

To consider a wide range of pitch angle values in both the stable and unstable manifold trajectories, this section takes an approach similar to the one described in the section "Non-zero Pitch Angles". However, that section constrained the pitch angle in the stable manifold trajectory to $\alpha^S = -\alpha^U$ to exploit the symmetry in the system. Because this symmetry is lost for heteroclinic connections, this section allows α^S to take on any value within a predefined mesh. For this, an extra loop is created around the approach in the section "Non-zero Pitch Angles", where now the inner- and outer loops consider meshes in the pitch angles of $\alpha^U \in [-90°, 90°]$ and $\alpha^S \in [-90°, 90°]$. Note that the only differences with the methodology for the grid search for homoclinic connections are that no minimum transfer time is defined, that $n = 3$ for all transfers, and that, to limit the increase in computation cost introduced by the additional loop, the step size in α^U and α^S is increased to 10°.

For each combination of α^U and α^S, the unstable and stable manifold trajectories that yield the smallest objective value for transfers 4–6 appear in the top row of **Figure 12**. From this figure the lack in symmetry for the heteroclinic connections is indeed clear. The best result, i.e., the combinations of α^U and α^S that lead to the absolute minimum objective value are indicated by a white cross. Further details on these trajectories are shown in the middle row of **Figure 12** with numerical details in the first data column of **Table 3** (heading "Grid search: non-zero pitch angles"). The remaining results in these tables will be discussed in the section "Genetic Algorithm" below. Despite the lack in symmetry, the objective values in **Table 3** hint at the possibility for heteroclinic connections with errors on the position and velocity that are of similar magnitude as for the "opposite-sign pitch angles"-approach in the section "Non-zero Pitch Angles". Finally, from the data in **Table 3** it is interesting to note that very large pitch angles provide the best results. Since very large pitch angles create very small solar-sail induced accelerations, the current approach appears to provide the best heteroclinic connections by exploiting the (near-)classical dynamics.

Genetic Algorithm

The second, and final, step in the search for heteroclinic connections is near-identical to the approach previously described for homomclinic connections: a genetic algorithm is taken at hand to explore the design space in between the discrete steps of the meshes used in the previous section for the design parameters $t^U_{M,0}$, $t^S_{M,0}$, t_{link}, α^U, and α^S. The set-up of the algorithm is that as described in the search for homoclinic connections, only the margin on the minimum transfer time in the unstable and stable manifold trajectories is significantly loosened, i.e., $\xi = 0.01 P_S$ for use in Equation (20).

The results appear in the bottom row of **Figure 12** with numerical details in the last column of **Table 3**. With errors in the position and velocity of <10 km and <1 m/s, also the feasibility of heteroclinic connections between solar-sail Lyapunov orbits and the suitability of the proposed tools has been demonstrated. While for the grid searches in the previous section the best pitch angles were of rather large values, the genetic algorithm approach shows that much smaller angles (and therefore significant solar-sail induced accelerations) are required to establish these connections.

CONCLUSIONS

This paper has established an understanding of, and a framework for, the computation of homo- and heteroclinic connections between planar solar-sail Lyapunov orbits in the Earth-Moon three-body problem. These connections have been found by linking the unstable and stable solar-sail assisted invariant manifolds associated to the orbits. Since the solar-sail induced acceleration introduces a time dependency into the dynamics, the use of traditional techniques (Jacobi constant and spatial Poincaré sections) were proven to be of no benefit in the search for these connections. Instead, connections have been found by introducing temporal Poincaré sections, defining a suitable

figure of merit to assess the quality of the connections, and using grid searches on the departure, arrival and linkage times as well as on constant, non-zero solar-sail pitch angles in the unstable and stable manifold trajectories. While these methods allowed to find homo- and heteroclinic connections with errors on the position and velocity at linkage of $<$1,525 km and $<$25 m/s, true connections were only found when exploring the design space in between the discrete mesh of the grid search. For this a genetic algorithm approach has been successfully applied, reducing the errors down to $<$10 km and $<$1 m/s. With that, this paper has proven the feasibility of homo- and heteroclinic connections between solar-sail Lyapunov orbits for a simple solar-sail steering strategy in the form of a piece-wise constant sail attitude. These results and the framework defined in this paper form only the start of a much larger investigation into homo- and heteroclinic connections between other planar solar-sail periodic orbits in the Earth-Moon system as well as into the extension to the spatial, three-dimensional case.

AUTHOR CONTRIBUTIONS

JH: idea conception, problem formulation, method development, method implementation, data generation, data analysis, result interpretation, and manuscript writing.

REFERENCES

1. Ross S, Lo M. The lunar L1 gateway - portal to the stars and beyond. In: *AIAA Space 2001 Conference and Exposition, American Institute of Aeronautics and Astronautics* (2001).
2. Parker JS. *Establishing a Network of Lunar Landers via Low-Energy Transfers (AAS 14-472)*. Sante Fe, NM: AAS/AIAA Space Flight Mechanics Meeting (2014).
3. Farquhar R. Lunar communications with libration-point satellites. *J Spacecraft Rockets* (1967) **4**:1383–4. doi: 10.2514/3.29095
4. Heiligers J, Parker JS, Macdonald M. Novel solar-sail mission concept for high-latitude earth and lunar observation. *J Guidance Control Dyn.* (2018) **41**:G002919. doi: 10.2514/1.G002919
5. Olson J, Craig D, Maliga K, Mullins C, Hay J, Graham R, et al. *Voyages: Charting the Course for Sustainable Human Exploration*. Hampton, VA: NASA Langley Reesearch Center (2011).
6. Vergaaij M, Heiligers J. Time-optimal solar sail heteroclinic connections for an earth-mars cycler. *68th International Astronautical Congress*. Adelaide (2017).
7. Szebehely V. *Theory of Orbits*: *The Restricted Problem of Three Bodies*. New York, NY: Elsevier (1967).
8. Howell KC. Families of orbits in the vicinity of the collinear libration points. *J Astronaut Sci.* (2001) **49**:107–25. doi: 10.2514/6.1998-4465
9. Koon WS, Lo MW, Marsden JE, Ross SD. *Dynamical Systems, the Three-Body Problem and Space Mission Design*. New York, NY: Springer (2006).
10. Howell KC, Pernicka HJ. Numerical determination of lissajous trajectories in the restricted three-body problem. *Celes Mech.* (1988) **41**:107–24.
11. Hénon M. Numerical exploration of the restricted problem. V. Hill's case periodic orbits and their stability. *Astron Astrophys.* (1969) **1**:223–38.
12. Howell KC. Three-dimensional, periodic, 'Halo' orbits. *Celes Mech Dynamic Astron.* (1983) **32**:53–71.
13. Kazantzis PG. Numerical determination of families of three-dimensional double-symmetric periodic orbits in the restricted three-body problem. I. *Astrophys Space Sci.* (1979) **65**:493–513.
14. Kazantzis PG. Numerical determination of families of three-dimensional double-symmetric periodic orbits in the restricted three-body problem. II. *Astrophys Space Sci.* (1980) **69**:353–68.
15. Heiligers J, Macdonald M, Parker JS. Extension of earth-moon libration point orbits with solar sail propulsion. *Astrophys Space Sci.* (2016) **361**:241. doi: 10.1007/s10509-016-2783-3
16. McInnes CR. *Solar Sailing: Technology, Dynamics and Mission Applications*. Berlin: Springer-Verlag (1999). doi: 10.1007/978-1-4471-3992-8
17. Macdonald M, McInnes C. Solar sail science mission applications and advancement. *Adv Space Res.* (2011) **48**:1702–16. doi: 10.1016/j.asr.2011.03.018
18. Heiligers J, Diedrich B, Derbes B, McInnes CR. Sunjammer: preliminary end-to-end mission design. In: *2014 AIAA/AAS Astrodynamics Specialist Conference*. San Diego, CA (2014).
19. McInnes C, Bothmer V, Dachwald B, Geppert UME, Heiligers J, Spietz A, et al. Gossamer roadmap technology reference study for a sub-L1 space weather mission. In: Macdonald M, editor. *Advances in Solar Sailing*. Berlin: Springer (2014). p. 227–42.
20. Dachwald B, Boehnhardt H, Broj U, Geppert URME, Grundmann J-T, Reinhard W, et al. Gossamer roadmap technology reference study for a multiple NEO rendezvous mission. In: Macdonald M, editor. *Advances in Solar Sailing*. Berlin: Springer (2014) 211–226.
21. Peloni A, Ceriotti M, Dachwald B. Solar-sail trajectory design for a multiple near-earth-asteroid rendezvous mission. *J Guidance Control Dyn.* (2016) **39**:2712–24. doi: 10.2514/1.G000470
22. Macdonald M, Hughes C, McInnes L, Falkner AP, Atzei A. GeoSail: an elegant solar sail demonstration mission. *J Spacecraft Rockets* (2007) **44**:784–96. doi: 10.2514/1.22867
23. Waters TJ, McInnes CR. Periodic orbits above the ecliptic in the solar-sail restricted three-body problem. *J Guidance Control Dyn.* (2007) **30**:687–93. doi: 10.2514/1.26232
24. Walmsley M, Heiligers J, Ceriotti M, McInnes C. Optimal trajectories for planetary pole-sitter missions. *J Guidance Control Dyn.* (2016) **39**:2461–8. doi: 10.2514/1.G000465
25. JAXA. *Press Releases: Small Solar Power Sail Demonstrator 'IKAROS' Confirmation of Photon Acceleration* (2010). Available online at: http://www.jaxa.jp/press/2010/07/20100709_ikaros_e.html (Accessed 9 July 2010).
26. Johnson L, Whorton M, Heaton A, Pinson R, Laue G, Adams C. NanoSail-D: a solar sail demonstration mission. *Acta Astronaut.* (2011) **68**:571–5. doi: 10.1016/j.actaastro.2010.02.008
27. Biddy C, Svitek T. LightSail-1 solar sail design and qualification. In: *Proceedings of the 41st Aerospace Mechanisms Symposium*. Pasadena, CA: Jet Propulsion Laboratory (2012). p. 451–63.
28. McNutt L, Johnson L., Clardy D, Castillo-Rogez J, Frick A, Jones L. Near-earth asteroid scout. In: *AIAA SPACE 2014 Conference and Exposition*. San Diego, CA: American Institute of Aeronautics and Astronautics (2014).
29. Heaton A, Ahmad N, Miller K. Near earth asteroid scout solar sail thrust and torque model (17055). In: *4th International Symposium on Solar Sailing*. Kyoto: Japan Space Forum (2017).
30. Jorba-Cuscó M, Farrés A, Jorba À. Periodic and quasi-periodic motion for a solar sail in the earth-moon system. In: *67th International Astronautical Congress*. Guadalajara (2016).
31. Angelopoulos V. The THEMIS mission. *Space Sci Rev.* (2008) **141**:5. doi: 10.1007/s11214-008-9336-1
32. Broschart SB, Chung MJ, Hatch SJ, Ma JH, Sweetser TH, Angelopoulos SS, et al. Preliminary trajectory design for the ARTEMIS Lunar Mission (AAS 09-382). In: *Space Flight Mechanics Meeting*. Savannah, GA (2009).
33. Gómez G, Masdemont JJ. Some zero cost transfers between libration point orbits. *Adv Astronaut Sci.* (2000) **105**:1199–215.
34. Koon WS, LoMW, Marsden JE, Ross SD. Heteroclinic connections between periodic orbits and resonance transitions in celestial mechanics. *Chaos* (2000) **10**:427–69. doi: 10.1063/1.166509
35. Gómez G, Koon WS, Lo MW, Marsden JE, Masdemont J, Ross SD. Connecting orbits and invariant manifolds in the spatial restricted three-body problem. *Nonlinearity* (2004) **17**:1571–606. doi: 10.1088/0951-7715/17/5/002

36. Canalias E, Josep JM. Homoclinic and heteroclinic transfer trajectories between planar Lyapunov orbits in the sun-earth and earth-moon systems. *Discrete Continuous Dyn Syst A* (2005) **14**:261–79. doi: 10.3934/dcds.2006.14.261
37. Barrabés E, Mondelo JM, Ollé M. Numerical continuation of families of homoclinic connections of periodic orbits in the RTBP. *Nonlinearity* (2009) **22**:2901. doi: 10.1088/0951-7715/22/12/006
38. Haapala AF, Howell KC. A framework for constructing transfers linking periodic libration point orbits in the spatial circular restricted three-body problem. *Int J Bifurcation Chaos* (2016) **26**:1630013-1630011. doi: 10.1142/S0218127416300135
39. Stuart J, Ozimek M, Howell K. Optimal, low-thrust, path-constrained transfers between libration point orbits using invariant manifolds. In: *AIAA/AAS Astrodynamics Specialist Conference*. Toronto, ON: American Institute of Aeronautics and Astronautics (2010).
40. Heiligers J, Mingotti G, McInnes CR. Optimal solar sail transfers between halo orbits of different sun-planet systems. *Adv Space Res.* (2015) **55**:1405–21. doi: 10.1016/j.asr.2014.11.033
41. Battin RH. *An Introduction to the Mathematics and Methods of Astrodynamics, Rev ed*. Reston, VA: American Institute of Aeronautics and Astronautics, Inc. (1999). doi: 10.2514/4.861543
42. McInnes CR. Solar sail trajectories at the lunar L2 lagrange point. *J Spacecraft Rockets* (1993) **30**:782–4. doi: 10.2514/3.26393
43. Parker JS, Anderson RL. *Low-Energy Lunar Trajectory Design*. Pasadena, CA: Jet Propulsion Laboratory (2013).

Conflict of Interest Statement: The author declares that the research was conducted in the absence of any commercial or financial relationships that could be construed as a potential conflict of interest.

frontiers in Applied Mathematics and Statistics

ORIGINAL RESEARCH
published: 21 August 2018
doi: 10.3389/fams.2018.00035

Drift and Its Mediation in Terrestrial Orbits

Jérôme Daquin[1,2,3]*, *Ioannis Gkolias*[4] *and Aaron J. Rosengren*[5]

[1] Department of Mathematics "Tullio Levi-Civita", University of Padova, Padua, Italy, [2] School of Science, RMIT University, Melbourne, VIC, Australia, [3] Space Environment Research Centre (SERC) Limited, Mount Stromlo Observatory, Canberra, ACT, Australia, [4] Department of Aerospace Science and Technology, Politecnico di Milano, Milan, Italy, [5] Aerospace and Mechanical Engineering, University of Arizona, Tucson, AZ, United States

The slow deformation of terrestrial orbits in the medium range, subject to lunisolar resonances, is well approximated by a family of Hamiltonian flow with 2.5 degree-of-freedom. The action variables of the system may experience chaotic variations and large drift that we may quantify. Using variational chaos indicators, we compute high-resolution portraits of the action space. Such refined meshes allow to reveal the existence of tori and structures filling chaotic regions. Our elaborate computations allow us to isolate precise initial conditions near specific zones of interest and study their asymptotic behaviour in time. Borrowing classical techniques of phase-space visualization, we highlight how the drift is mediated by the complement of the numerically detected KAM tori.

Keywords: lunisolar secular resonance, Hamiltonian chaos, drift, terrestrial dynamics, Earth satellite

OPEN ACCESS

Edited by:
Elisa Maria Alessi,
Consiglio Nazionale Delle Ricerche (CNR), Italy

Reviewed by:
Slawomir Breiter,
Adam Mickiewicz University in Poznań, Poland
Martin Lara,
University of La Rioja, Spain

***Correspondence:**
Jérôme Daquin
daquin@math.unipd.it

Specialty section:
This article was submitted to Dynamical Systems, a section of the journal Frontiers in Applied Mathematics and Statistics

Received: *28 February 2018*
Accepted: *16 July 2018*
Published: *21 August 2018*

Citation:
Daquin J, Gkolias I and Rosengren AJ (2018) Drift and Its Mediation in Terrestrial Orbits. Front. Appl. Math. Stat. 4:35. doi: 10.3389/fams.2018.00035

1. INTRODUCTION

Various groups of scientists have become enchanted anew by the lunisolar resonances affecting the dynamics of terrestrial orbits. The study of them and the resurgence of their significance has not been visible since the notorious and colossal triptych of Breiter [1–3]. Later rebranded by Rossi [4] in the context of the *medium-Earth orbits* (MEOs), the study of their long-term dynamics, and in particular their eccentricity growths in the *elliptic domain* [5], represent current deep motivations for the community. In our opinion, the most complete and up-to-date panorama of the literature is excellently presented by Armellin and San-Juan [6]. The existence of such a condensation allows us to adopt here a rather direct style in this present contribution. We are particularly interested by questions related to the stability of orbits. Based on the divergence of nearby trajectories, the existence of a mixed phase space where there is a cohabitation of stable and chaotic components has been recently pictured [7–11] and partially explained applying Chirikov's resonances overlap criterion [12]. The Hamiltonian flow obtained under the simplest assumptions for the disturbing effects of the perturbers (i.e., a development restricted to its lowest order and averaged over fast variables), Moon and Sun, encapsulates all the details of the dynamics in which we are interested [7]. In particular, the Hamiltonian possesses 2 degrees-of-freedom (DOF) and depends periodically on the time t (see [11] for omitted details). We recall in the next section how the Hamiltonian

$$\mathcal{H}\colon D \times \mathbb{T}^2 \times \mathbb{T} \to \mathbb{R},\ (x, y, t) \mapsto \mathcal{H}(x, y, t) = h_0(x) + \varepsilon h_1(x, y, t) \tag{1.1}$$

with $h_1(x, y, t) = \sum_{m \in \mathcal{A} \subset \mathbb{Z}^3_\star} h_m(x) \cos(m \cdot (y, t) + \phi_m)$ is obtained. The form of Equation (1.1) is the standard form of a nearly-integrable problem written in action-angles variables. The non-linearity parameter ε belongs to a certain subinterval $\mathcal{I}$ of $\mathbb{R}_+$ and is function of the semi-major axis, which

is a first integral in the secular approximation. The functions $\{h_m\}_{m\in\mathcal{A}}$ are real valued functions of the sole action $x \in D \subset \mathbb{R}^2$ (and some constant physical parameters), the ϕ_m are phase terms. When ε sweeps $\mathcal{I}$, a transition from a globally ordered phase space to a mixed phase space is known to exist. It turns out that the presence of a chaotic regime for large values of ε, say for ε close to $\max\mathcal{I}$, corresponds to the range of semi-major axes where the navigation satellites are located. The occurrence of the two apparent antonyms, "how awkward it is"[1] and "how useful and fruitful it can be"[2], crystallizes assuredly the challenges, implications and beauty of the dynamical and engineering problems we face.

Gravitational problems are kaleidoscopes of pure and applied science. Our Solar System has been the source and receptacle of many theoretical and practical dynamical facets and aspects (KAM theory, hyperbolic dynamics, shadowing theory, numerical analysis, phase visualization techniques). Spaceflight dynamics is not excluded and has gained from this rich heritage [13–15]. We cannot take a definitive position on the space-debris mitigation via "chaos targeting" and transfers in phase space, nevertheless, let us underline that the concept embraces the continuous necessary exchanges between (technological and scientific) communities.

In this paper, we depart from former goals where the main impetus was the explanation of the mechanisms supporting the apparition of chaos. Instead, we focus rather on (i) the physical consequences in terms of transport in the phase space and (ii) on the visualization of these excursions *via* double sections in the action-like phase space. The techniques we used have been extensively employed in Dynamical Astronomy and overall in the context of the dynamics of quasi-integrable Hamiltonian systems and symplectic discrete maps (confer [16–20], just to name a few). To achieve our tasks, we provide a cartographic view of the prograde *and* retrograde region in section 3.2, based on a lighting-fast *ad-hoc* secular model that we recall in section 3.1. The fine resolutions of the meshes used to discretize the domains D allow for highly detailed views of the phase space. We then focus on the computation of diameters-like quantities to relate the degree of hyperbolicity (a local property) with a more practical transport-like index (a global property). Thanks to our resolved grids, precise initial conditions (ICs) can be extracted, which lie near specific structures of interest, in particular where large diameters are expected. Once obtained, we proceed to their asymptotic analysis (in time) using ensemble orbit propagation (section 4). We close with section 5 where we summarize our contributions and discuss an open problem that inspires our future efforts.

2. THE MODEL

We recall briefly, for the sake of completeness, under which hypotheses the 2.5-DOF Hamiltonian is obtained. After the presentation of the model, we present to the newcomers a few facets of the resonant aspects.

2.1. Derivation of the Hamiltonian Model

Numerical evidence has shown that, for the range of the treated perturbation $\mathcal{I}$ (recall $\mathcal{I} \simeq [2.2r_\oplus, 4.65r_\oplus]$), refinements of the gravitational potentials beyond the quadrupolar level are not necessary to capture details of the *global* dynamics we are interested in, even on long timescales [7]. It means that when the potentials of the Earth *and* those of the external bodies, Moon and Sun, are developed using Legendre expansions, terms with $l > 2$ are disregarded. By recognizing the timescales of the dynamics, further simplifications are even possible to get a more pertinent analytical model (and numerical as well; see also section 3.1). Based on the Lagrangian averaging principle [21–23], the potentials are averaged over the mean anomaly of the test particle ℓ and those of the third bodies[3], $\ell_\odot$ and $\ell_\leftmoon$.

For an oblate Earth, we recall the classical averaged potential

$$\mathcal{H}_{J_2}(G,H) = \alpha_{J_2}\left(G^{-3} - 3G^{-5}H^2\right) \tag{2.1}$$

expression, with $\alpha_{J_2} = J_2 r_\oplus^2 \mu_\oplus^4/4L^3 \in \mathbb{R}$. Here (G,H) denotes the second and third variables of the Delaunay actions (L,G,H), $\mu_\oplus$ denotes the (Earth's) gravitational parameter. The canonically conjugated vector of angles is classically denoted (ℓ,g,h). Omitting details that might be found in Celletti et al. [9, 11], the disturbing function of the Sun's attraction, $\mathcal{R}_\odot$, reads as

$$\begin{aligned}&\mathcal{R}_\odot(G,H,g,h)\\ &= \sum_{m=0}^{2}\sum_{p=0}^{2} \alpha_\odot \mathrm{s}_m F_{2,m,p}(i) F_{2,m,1}(i_\odot) H_{2,p,2p-2}(e) \cos\left(f_{m,p}(g,h)\right)\end{aligned} \tag{2.2}$$

with

$$f_{m,p} : \mathbb{T}^2 \to \mathbb{T},\ (g,h) \mapsto (2-2p)g + m(h - h_\odot). \tag{2.3}$$

The scalar $\alpha_\odot = \mu_\odot\left(\frac{a^2}{a_\odot^3}\right)(1-e_\odot^2)^{-3/2}$ has a constant magnitude of $\sim 3.96 \times 10^{-14}$ in the international system of units. The coefficients s_m are defined as $\mathrm{s}_m = K_m(2-m)!/(2+m)!$. The functions $F_{2,m,p}(\bullet)$ refers to Kaula's inclination function [24] and $H_{2,p,2p-2}(e)$ is related to the Hansen coefficients. For the disturbing function of the Moon, the following formula holds true

$$\begin{aligned}&\mathcal{R}_\leftmoon\,(G,H,g,h,h_\leftmoon\,) =\\ &\sum_{m=0}^{2}\sum_{p=0}^{2}\sum_{s=0}^{2} \alpha_\leftmoon\, \mathrm{m}_{m,s} F_{2,m,p}(i) F_{2,s,1}(i_\leftmoon\,) H_{2,p,2p-2}(e)\\ &\times\left(U_2^{m,-s}\cos\left(g_{m,p,s}(g,h)\right) + U_2^{m,s}\cos\left(h_{m,p,s}(g,h)\right)\right)\end{aligned} \tag{2.4}$$

[1] The Lyapunov times $\tau_{\mathcal{L}}$, which dynamically speaking constitute the barriers of predictability, are on the order of decades [7].

[2] There is a birth of a new ideology to remedy the space-debris problem, based on a "judicious" use of the instabilities to define re-entry orbits and navigate the phase space.

[3] In the following, we use the subscripts $\bullet_\oplus$, $\bullet_\leftmoon$, $\bullet_\odot$ to denote parameters referring to the Earth, Moon and Sun, respectively.

with

$$g_{m,p,s}:\mathbb{T}^2\to\mathbb{T},\,(g,h)\mapsto(2-2p)g+mh+sh_{\mathbb{C}}+s\frac{\pi}{2}-y_s\pi, \tag{2.5}$$

$$h_{m,p,s}:\mathbb{T}^2\to\mathbb{T},\,(g,h)\mapsto(2-2p)g+mh-sh_{\mathbb{C}}-s\frac{\pi}{2}-y_s\pi. \tag{2.6}$$

The expressions $U_2^{m,\pm s}$ are function of the obliquity of the eccliptic, and are present due to a rotation of the spherical harmonics needed in this mixed-reference frame formalism. Note that the size of the coefficient $\alpha_{\mathbb{C}}=\frac{\mu_{\mathbb{C}}}{2}\left(\frac{a^2}{a_{\mathbb{C}}^3}\right)(1-e_{\mathbb{C}}^2)^{-3/2}\sim 4.32\times10^{-14}$ is close to $\alpha_\odot$ (The ratio $\alpha_{\mathbb{C}}/\alpha_\odot\sim 1.09$). The coefficients $\mathrm{m}_{m,s}$ are defined as $\mathrm{m}_{m,s}=(-1)^{[m/2]}K_mK_s(2-s)!/(2+m)!$. It turns out that the time derivative of the angle $h_{\mathbb{C}}$ is well approximated by a constant frequency defining a period of 18.6 years. In other words, we consider the explicit time dependence of the lunar potential as linear. At this stage, it is recognizable and transparent that the Hamiltonian formed on the perturbations,

$$\mathcal{H}=\mathcal{H}_{J_2}(G,H)-\mathcal{R}_\odot(G,H,g,h)-\mathcal{R}_{\mathbb{C}}(G,H,g,h,t), \tag{2.7}$$

possesses 2 DOF and is periodically-time dependent (i.e., a 2.5-DOF problem). The explicit time dependence due only to the node of the Moon[4] plays a fundamental role in shaping the dynamics. The well-known distinctive feature with the case of 2 DOF is that, *a priori* (in absence of additional known first-integrals apart the energy function itself), the tori cannot act as practical barriers preventing transport in the phase space (for an N-DOF autonomous problem with $N\geq 3$, the codimension between the N-dimensional tori and the dimension of the phase space restricted to an energy surface $(2N-1)$ is at least 2). The Delaunay variable ℓ being a cyclic variable, its conjugate variable $L=\sqrt{\mu a}$ is a constant of motion. Let us introduce normalized new actions $\tilde{x}=x/\sqrt{\mu a}$. The reduced system is kept canonical as long as the new angles $\tilde{y}=\sqrt{\mu a}\cdot y$ are introduced and the physical-time multiplied by the same factor. It is clear that the new Hamiltonian has the same form as in Equation (2.7). The previous factor α_{J_2} absorbs now a contribution from L and we get the new $\alpha_{J_2}=J_2r_\oplus^2\mu^4/4L^6$. Factorizing the external perturbation by the greatest $\alpha_{\mathbb{C}}$, the Hamiltonian can be rewritten as

$$\begin{aligned}\mathcal{H}(\tilde{G},\tilde{H},\tilde{g},\tilde{h},\sqrt{\mu a}t)&=\underbrace{\alpha_{J_2}f_0(\tilde{G},\tilde{H})}_{h_0(\tilde{G},\tilde{H})}\\&+\alpha_{\mathbb{C}}\underbrace{\left(-\frac{\alpha_\odot}{\alpha_{\mathbb{C}}}\tilde{\mathcal{R}}_\odot(\tilde{G},\tilde{H},\tilde{g},\tilde{h})-\tilde{\mathcal{R}}_{\mathbb{C}}(\tilde{G},\tilde{H},\tilde{g},\tilde{h},\sqrt{\mu a}t)\right)}_{h_1(\tilde{G},\tilde{H},\tilde{g},\tilde{h},t)}.\end{aligned} \tag{2.8}$$

[4] We emphasize that the Hamiltonian depends on time just through the lunar contribution as we assumed that, over our timescale of interest, the rate of variation of the ascending node of the Sun is zero (see discussions in Celletti et al. [11]).

The hierarchy $\alpha_{\mathbb{C}}\ll\alpha_{J_2}$ enables us to write $\alpha_{\mathbb{C}}=\varepsilon\alpha_{J_2}$, $\varepsilon\ll 1$, and Equation (2.8) becomes

$$\mathcal{H}(\tilde{G},\tilde{H},\tilde{g},\tilde{h},\sqrt{\mu a}t)=h_0(\tilde{G},\tilde{H})+\varepsilon h_1(\tilde{G},\tilde{H},\tilde{g},\tilde{h},t). \tag{2.9}$$

Clearly $\mathcal{H}$ shares the form of the standard perturbed Hamiltonian system as announced in the introduction. The very useful information that we got from these manipulations is that the dimensionless perturbative parameter ε is proportional to the secular invariant semi-major axis,

$$\varepsilon(a)\equiv\frac{\alpha_{\mathbb{C}}}{\alpha_{J_2}}=\frac{2n_{\mathbb{C}}^2}{(1-e_{\mathbb{C}}^2)^{3/2}}\cdot\frac{1}{J_2n^2}\left(\frac{a}{r}\right)^2. \tag{2.10}$$

(The mean motions of the test particle and disturbing bodies are noted n and $n_{\mathbb{C}}$, respectively.) Note that this perturbing parameter is of the same nature as that introduced by Breiter [3], but we are treating herein the regime of the lunisolar *secular* (not *semi-secular*) resonances. The Hamiltonian model based on the quadrupolar level is physically relevant up to a semi-major axis close to $a_{\max}=6r_\oplus$ (beyond, octupolar refinements, $l=3$, are needed) corresponding to $\varepsilon(a_{\max})=0.8$. In the following, we will be interested in semi-major axes up to $a=29,600$ km, leading to $\epsilon=0.22$. From our numerical investigations, we noted that for $a=13,600$ km, the chaos is thin and confined to a few inclination-dependent-only resonances. These two constraints together define the subinterval $\mathcal{I}=[0.004,0.22]\subset\mathbb{R}_+$ of interest for ε. Adding quite "virtually" the point $\{0\}$ to this set, $\varepsilon\in\left(\{0\}\bigcup\mathcal{I}\right)$, we obtain when $\varepsilon=0$ an integrable dynamics with a linear flow on a torus. The actions are constant and determine the invariant tori. On these tori the dynamics consist of a rotation at constant speed characterized by the vector of constant frequencies (*the unperturbed frequency vector*) $\Omega(G,H)=(\varpi_g,\varpi_h)$ given by

$$\begin{cases}\varpi_g=\frac{1}{2}\kappa(5\cos^2 i-1)(1-e^2)^{-2},\\ \varpi_h=-\kappa\cos i(1-e^2)^{-2},\end{cases} \tag{2.11}$$

where $\kappa=\frac{3}{2}J_2nr_\oplus^2/a^2\in\mathbb{R}$ [24].

Let us be more precise regarding the definition of the interval $\mathcal{I}$ and the energy function considered. An important factor leading to the 2.5 DOF model lies in the omission of the *tesseral* contributions in the Hamiltonian (2.7). Tesseral resonances occur when the commensurability $\dot{M}/\dot{\theta}\sim q/p$ takes place. Given the upper and lower bounds of $\mathcal{I}$, the *main* tesseral resonances affecting the motion are given by the set of commensurabilities $\mathcal{T}=\{2:1,3:1,4:1\}$ (see e.g., [25, 26]). Near a tesseral resonance, the semi-major axis is no longer secularly invariant and, in fact, might experience (confined) chaotic variations near their corresponding resonant action value $L_\star^{p:q}$. Putting all of these together, a more precise definition of our interval of interest for the perturbing parameter ε is instead $\mathcal{I}'=\mathcal{I}\setminus\mathcal{I}_{\mathcal{T}}$ where $\mathcal{I}_{\mathcal{T}}=\bigcup_{p:q\in\mathcal{T}}[\varepsilon(L_\star^{p:q}-\delta_{p:q},\varepsilon(L_\star^{p:q})+\delta_{p:q}]$ where $\delta_{p:q}$ characterize the strength (width) of the resonance. The eventual local coupling of the tesseral contributions and the lunisolar

resonances on the evolutions of the actions (G, H), for perturbing values precisely within the tesseral resonant domain (*i.e.,* for $\varepsilon \in [\varepsilon(L_\star^{p:q} - \delta_{p:q}, \varepsilon(L_\star^{p:q}) + \delta_{p:q}])$, is not discussed in this contribution, but is the object of a further study (accordingly, tesseral contributions are disregarded in the energy function). Using estimations obtained in former works [25, 26], let us stress that the ratio of the measures $\mathrm{m}(\mathcal{I}')/\mathrm{m}(\mathcal{I}) \sim 0.99$ is very close to 1. Moreover, accurate low-altitude or very local studies could require additional refinements of the energy function (e.g., near the critical inclination, see [27]). Although our model is subject to these possible limitations, we should highlight that the considered dynamics are accurate enough to describe general MEO orbits, and from a mathematical point of view provide a simple testbed to investigate transport theories and capture the big picture.

We abused the vocabulary and treat the eccentricity e and inclination i as "actions," instead of using the veritable actions variables (G, H). This is rather to stick to classical notations [24]. Nevertheless, these variables are functionally independent and the "true" actions easily obtained as $e^2 = 1 - (G/L)^2$ and $\cos i = H/G$. Let us precise that, when dealing with the autonomous Hamiltonian by introducing an extra conjugated variables $(\Gamma, \gamma) \in \mathbb{R} \times \mathbb{T}$ for $\varepsilon \neq 0$, one couple of actions $x = (G, H)$ characterize an invariant torus of $\mathbb{T}^3$ since Γ does not enter into the equations of motion. In other words, we can consider the orbits in the reduced phase space defined by $\mathcal{X} = \left\{(G, H, g, h, \gamma), x = (G, H) \in D \subset \mathbb{R}^2, y = (g, h, \gamma) \in \mathbb{T}^3\right\}$. In section 3, we will offer views of the dynamics in action-action sections, meaning that within the space $\mathcal{X}$, we fix the angles to a specific vector to obtain the section $S = \left\{(G, H) \in D \subset \mathbb{R}^2 \,|\, (g, h, \gamma) = \nu_\star, \nu_\star \in \mathbb{T}^3\right\}$. Let us now discuss fundamental phenomenon for $\varepsilon \neq 0$.

2.2. Secular Lunisolar Resonances

A determinant feature in the long-term properties of nearly-integrable systems of the form $h(x, y) = h_0(x) + \epsilon h_1(x, y)$ is the presence of resonances[5] [30]. They arrive when a vector $k \in \mathbb{Z}_\star^n$ satisfy with the (unperturbed) frequency vector a commensurability condition over the rationals. The resonant condition reads $k \cdot \Omega(x) = 0$. For a fixed vector $k \in \mathbb{Z}_\star^n$, the sets (potentially empty) of the actions x such that $k \cdot \Omega(x) = 0$ form the *resonant manifolds*. The resonance under consideration is then characterized by an index, *the resonance order*, usually though the ℓ_1-norm of k, $\|k\|_1 = \sum_i |k_i|$. Under the quadrupolar assumption, the system (2.9) is prone to resonate with a maximal order of 6. Let us consider the frequency vector $\Omega(x) = (\varpi_g(x), \varpi_h(x), \varpi_{\mathbb{Q}})$, then, as already recognized by Ely [25], the resonant conditions read as

$$k_1\varpi_g(x) + k_2\varpi_h(x) + k_3\varpi_{\mathbb{Q}} = 0,\ k_1 \in \{-2, 0, 2\},\ k_2 \in [\![0, 2]\!],\ k_3 \in [\![-2, 2]\!],\ k \neq 0. \quad (2.12)$$

These algebraic equations admit non-trivial solutions that define the lunisolar resonant manifolds. The resonant manifolds are mirrored with respect to the resonance $(0, k, 0) \cdot \Omega(x) = k\varpi_h(x) = 0$. (However, as we will clearly illustrate it, the symmetry of the resonant manifolds does not imply a mirroring of the geography of the KAM tori and hyperbolic structures.) In Daquin et al. [7], the extent of the resonant zones have been estimated (in a subdomain of the prograde $0 < i \leq \pi/2$ domain) by reducing the Hamiltonian to the *first fundamental model* of resonance, a pendulum. This procedure involved the introduction of resonant coordinates through canonical transformations $\mathfrak{T}_k \in \mathrm{SL}(3, \mathbb{Q})$ leading to an intuitive physical interpretation of Chirikov's overlap as a driver of chaos. However, since the work of Celletti et al. [9], it has been observed that such a reduction does not always capture the features of the dynamics. In order to get a more refined and precise view of the extent of chaos, a superior way is instead to look at the destruction of KAM curves, e.g., using fast dynamical indicators.

3. PHASE-SPACE VIEWS

We revisit and complement the transition order/chaos in terrestrial orbits by scanning the dynamics under the rays of a first order variational chaos indicator. The motivation is twofold:

(1) The resolutions used in former studies are generally sufficient to detect and isolate chaotic components; yet, they are too coarse to detect the eventual presence of structures immersed within them. In addition, the dissection of the dynamics with a fine resolution makes possible the extraction of the chaotic skeleton with surgical precision[6]. This property will be used to study transport properties (*confer* section 4).
(2) Gkolias et al. [10] claimed that "*the retrograde orbits are not intrinsically more stable then their prograde counterparts.*" This diagnosis was established by scanning the region with an *averaged* FLI (over some angles) focusing on low eccentricity (up to $e = 0.1$). We feel necessary to investigate further this assertion beyond $e = 0.1$ without the averaged indicator (which naturally tends to smooth and absorb the details).

To overcome and constrain these two symptoms, we first briefly recall how we efficiently deal with the equations of motions, after which we present and discuss our highly-resolved phase-space views on a macroscale.

3.1. Numerical Treatment of the Equations of Motions

Ordinary and partial differential equations with disparate scales (spatial, temporal) are numerically challenging. The difficulty arrises from the fact that the inhomogeneities in the scale constrain parameters of the numerical methods employed (say, e.g., the size of the timestep, the discretisation of the mesh) to be small and highly resolved. In the present case, we deal with (highly) oscillatory ODEs. They are omnipresent in the

[5] In the "multiscale analysis" community, resonances are sometimes named "*slow hidden variables*," see e.g., [28, 29]. This semantic is pretty accurate as this is precisely what resonances are: resonances form "new slow variables" solely under specific combinations of the fast variables. Having this in mind, it is clear that in the presence of resonances the *direct averaging* may be crude ("naive" averaging) and conducts to a wrong dynamics.

[6] In a somehow different but connected context, Armellin and San-Juan [6] have shown that fine discretisations are also needed for optimizers to operate properly.

context of Newton's equations[7] and are ubiquitous in the context of Celestial Mechanics. To circumvent the problem, *effective models* and *model reductions* techniques are often employed. The core idea is to substitute to the original dynamics a more amenable, numerical and/or analytical, dynamical system [33–35]. One method of choice to design effective dynamics relies on the Lagrangian *averaging principle* [21–23, 36], which has a long-lasting tradition in Celestial Mechanics. This principle is usually used when the components of the equations themselves allow to recognize explicitly the time scales. When it is so, the fast dynamics is *integrated* into the slow variables to design an *averaged* approximation. In this setup, the new slow constituents somewhat incorporate the informations of the fast-dynamics and serve as a new input for the investigations. To deal efficiently with our problem at hand, we adopt here our own secular MILAN model, as presented by Gkolias et al. [10]. The MILAN model is based on the vectorial Milankovitch element and admits a minimal force model (consisting of the averaged J_2 contribution, to which is added the secular quadrupolar third-bodies perturbations). The MILAN formulation bears also net advantages compared to the numerical treatment of the Hamiltonian equations in forms of those given in section 2.1. First, the formulation is free of singularity and, secondly, the averaging is done in a closed form in the eccentricity. The external third-bodies potentials are both averaged over the fast variables of the problem, i.e., over the mean-anomaly of the test particle *and* the mean anomalies of the third bodies. This "doubly" averaged model allows the propagation of a test-particle over 10^6–10^7 orbital periods in a few seconds only. Such a performance is essential in investigating properties of the phase space for range of parameters. When invoking effective models, we always face the question of the relevance of the reduced model (how sound are the qualitative or quantitative informations derived from it). Gkolias et al. [10] established the testimony of this doubly-averaged model against a singly-averaged approach. By simulating the two dynamics on different domains of the action-action, action-angle and angle-angle spaces[8], we showed that dynamical features of interests were reproduced and in perfect agreement. Even if the simulation of the full dynamics (i.e., the original, non-reduced and "exact" dynamics) on such domains is still missing in the literature, recent reassuring numerical agreements have been presented by Armellin and San-Juan [6]. Namely, they presented nice agreements between their in-house doubly average model and the original non-averaged dynamics. All these together allow us to be confident enough on the numerical results presented hereafter.

3.2. Highly Resolved Phase-Space Views

We use the Fast Lyapunov Indicator (FLI), a first-order variational indicator initially introduced by Froeschlé et al. [37], to discriminate orbit stability. This scalpel has been used extensively over the past decade across different dynamical problems, ranging from Symplectic Maps studies to Dynamical Astronomy, including Astrodynamical practical problems [38–41]. The work of C. Froeschlé, M. Guzzo and E. Lega over the last decade provides a good overview of its possibilities and range of applications. When the dynamics under consideration is written in first order and autonomous form as $\dot{x} = f(x)$, $x \in \mathbb{R}^n$, the FLI is simply derived from the variational system in $\mathbb{R}^{2n}$,

$$\begin{cases} \dot{x} = f(x), \\ \dot{w} = \partial_x f(x)(w), \end{cases} \tag{3.1}$$

as

$$\mathrm{FLI}(x_0, w_0, \tau_{\mathrm{run}}) = \sup_{0 \le t \le \tau_{\mathrm{run}}} \log \left\| w(t) \right\|. \tag{3.2}$$

Contrarily to Lyapunov exponents, the FLIs (computed at some time τ_{run} for a specific set of initial conditions x_0, w_0) keep trace of the resonant nature of the orbits, while taking approximately the same value FLI $\sim \log(\tau_{\mathrm{run}})$ on KAM tori [38, 42]. By computing the FLIs on a discretised specific $2d$-section of ICs (e.g., related to the action-action, action-angle, or angle-angle planes) on a domain D, we can reveal the geography of the survival KAM tori and their complement hyperbolic set. The information given by the FLIs ("intensity") is then color-coded to obtain a *map of stability*. Note that sometimes, in order to get a sharper visualization, the FLIs that initially take variation in $\mathcal{J} \subset \mathbb{R}_+$ are restricted to a subinterval $\mathcal{K}$ of $\mathcal{J}$ (see e.g., [16, 19]). This rescaling is achieved by fixing the two following thresholds. The notion of chaoticity is based on the exponential evolution of the norm between two nearby orbits. Therefore, to reveal anomalies with respect to the linear trend (log-scale of an exponential growth), the criteria

$$\mathrm{FLI}(\tau_{\mathrm{run}}) \ge \log(\tau_{\mathrm{run}}^{\alpha}) = \alpha \log(\tau_{\mathrm{run}}),\ \alpha > 1, \tag{3.3}$$

can be used to derive a lower threshold for chaotic orbits (i.e., all FLIs larger than $\alpha \log(\tau_{\mathrm{run}})$ are assigned to $\alpha \log(\tau_{\mathrm{run}})$). Symmetrically, we obtain an upper threshold to judge regularity with the criteria

$$\mathrm{FLI}(\tau_{\mathrm{run}}) \le \log(\tau_{\mathrm{run}}/\beta),\ \beta > 1. \tag{3.4}$$

(And again, all the FLIs smaller than $\log(\tau_{\mathrm{run}}/\beta)$ are assigned to $\log(\tau_{\mathrm{run}}/\beta)$.) The **Figures 1**, **2** resume in many ways the transition from order to chaos in the prograde *and* retrograde region of terrestrial orbits. This original unscrewed fence views of the action-action phase space are very illuminative (and pedagogical) to visualize, with respect to the non-linear parameter $\varepsilon(a)$, the proliferation of chaos. Each map represents the result of $1,000 \times 500$ ICs propagated over a long timescale. Different simulation times τ_{run} have been used according to the perturbing parameter (the stronger is the perturbation, the shorter is the time required to get a sharp contrast of the dynamics). For the smallest perturbing parameter, $a = 18,600$ km, τ_{run} represents 30 lunar nodes, while for $a = 29,600$ km 16 lunar nodes are sufficient to get a sharp contrast (most probably those propagation times could be slightly shortened).

[7] They arrive also in Molecular Dynamics (see [31] and [32] for introductory papers and issues).

[8] In Gkolias et al. [10], we presented only sections in the angle-angle space but we have evidences of the agreement on complementary sections also for a range of different semi-major axes.

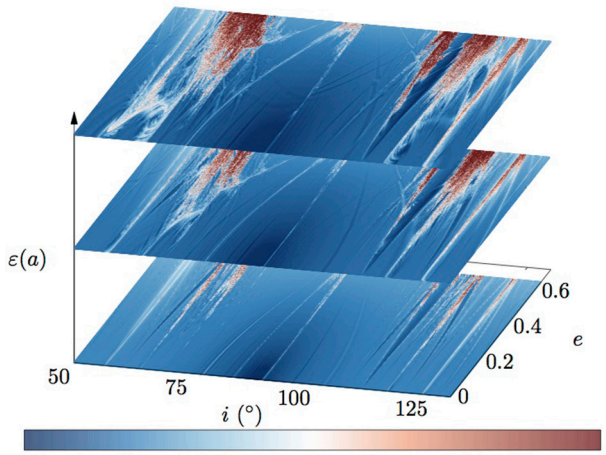

FIGURE 1 | A highly-resolved fence view of the stability of the prograde *and* retrograde regions obtained under the FLIs. The three slides depict the stability for a particular value of the non-linearity parameter $\varepsilon(a)$ which depends on the secularly invariant semi-major axis. KAM tori correspond to *white* to *light-red* color, stable resonant orbits appear in *blue* while *red* colors correspond to chaotic orbits. The values $\varepsilon(a)$ correspond to the three semi-major axis $\{18.6, 22.6, 24.6\} \times 10^3$ km (the z-scale is only symbolic, in particular the scale is not linear). This unscrewed view presents in a global, original and concise way the transition from order to chaos. See text for comments.

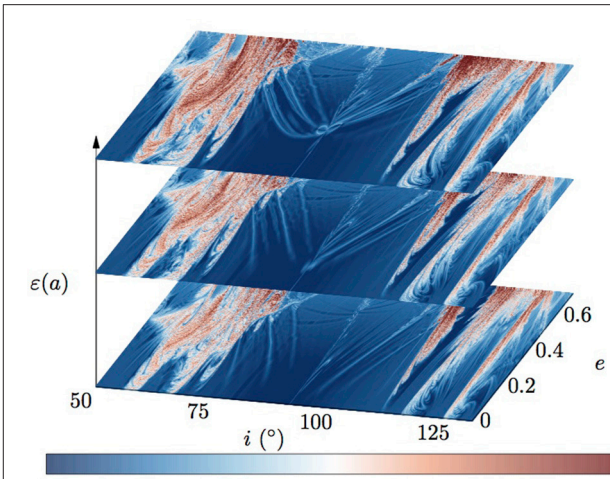

FIGURE 2 | The same as in **Figure 1** apart that the values $\varepsilon(a)$ correspond to the three semi-major axis $\{27.6, 28.6, 29.6\} \times 10^3$ km.

It represents about 7×10^5 and 1.8×10^5 test particle revolutions. The "actions" have been uniformly distributed along the rectangle $[50°, 130°] \times [0, e_{\max}]$, with $e_{\max}$ determined by the apogee-altitude condition $e_{\max} = 1 - (r_\oplus + \delta)/a$, $\delta = 120$ km. In all our maps, we have set the initial angles $y_0 \in \mathbb{T}^3$ to zero. Anticipating a bit the next section, we are here interested in the dynamical mechanisms leading to transport; in particular we have not discriminated *collisional orbits* as we did in earlier work. As it has already been discussed several times and pointed out in several contributions [7, 8, 10], the inclination dependent-only resonances widen and develop chaos when ε is increasing, letting less and less room for invariant KAM tori. Eventually for $a = 29,600$, there is a macroscopic chaotic component. At this macroscale, we even have the feeling of a *chaotic path-connected space* (i.e., for every two points in the hyperbolic set, there exists a hyperbolic path connecting them). This property is not exactly true as isolated chaotic islands do exist. Nevertheless, the volume of such isolated chaotic sea is rather small. Let us precise that, given the fact that we used different τ_{run}, the color palette has a symbolic meaning only. Also, in the same way, the z-scale which sets the different levels of the perturbing parameter $\varepsilon(a)$ is not a linear scale, and again, has only a schematic pictorial purpose.

For the two extreme perturbing parameters considered in this work, $\varepsilon(a)$ with $a = 18,600$ or $29,600$ km, we have superimposed for the newcomers the resonant manifolds obtained under the quadrupolar assumption (confer Equation 2.12). It is interesting to notice that, despite the symmetry of the resonant manifolds along the $(0, k, 0)$ resonance, the chaos is not mirrored at all in the retrograde region (see **Figure 3**). The coefficients of each harmonic, excepting the critical inclination, are dependent on the cosine of the inclination and hence the resonant topologies for prograde and retrograde orbits are necessarily different. A further striking illustration of this fact, on a microscale, is exemplified in **Figure 4**. Such fine resolutions allow to reveal incredible structures and details of the phase space. These two simulations clearly show us, at least for this realization of angles, that the retrograde region is more stable than its prograde counterpart. Applying the criteria given by Equation (3.3) with $\alpha = 1.1$, we found on that domain that the volume of chaotic orbits is 4 times larger than in its retrograde counterpart. We further quantified this question by applying various criteria on our former simulations. **Table 1** summarizes our results by giving the volume of chaotic orbits in the prograde vs. the retrograde region, for slightly different values of α on a macroscale. From our survey (which should be extended for completeness), the numerics tend to show that, for small to moderate values of the perturbing values of ε, the volume of chaotic orbits is roughly the same. However, for larger values of ε, the prograde region is more chaotic than its counterpart, the difference being now of several percent. (But again, we are aware of the dependence of our result against the choice of y_0. Further numerical investigations could constrain even more the result.) At a smaller scale, as already recognizable in **Figure 4**, the discrepancies may be largely more significant. It would be interesting to support or invalidate this phenomenology by characterizing (i) the widths of the resonances of the retrograde domain and (ii) by exploring their numerical widths as a function of the angles. Such an enterprise is yet to be performed.

4. DRIFT AND VISUALIZATION OF TRANSPORT

The computation of the FLIs provided a quantification of the degree of hyperbolicity and a discrimination of orbit stability. From a "practical" perspective, one might be more interested

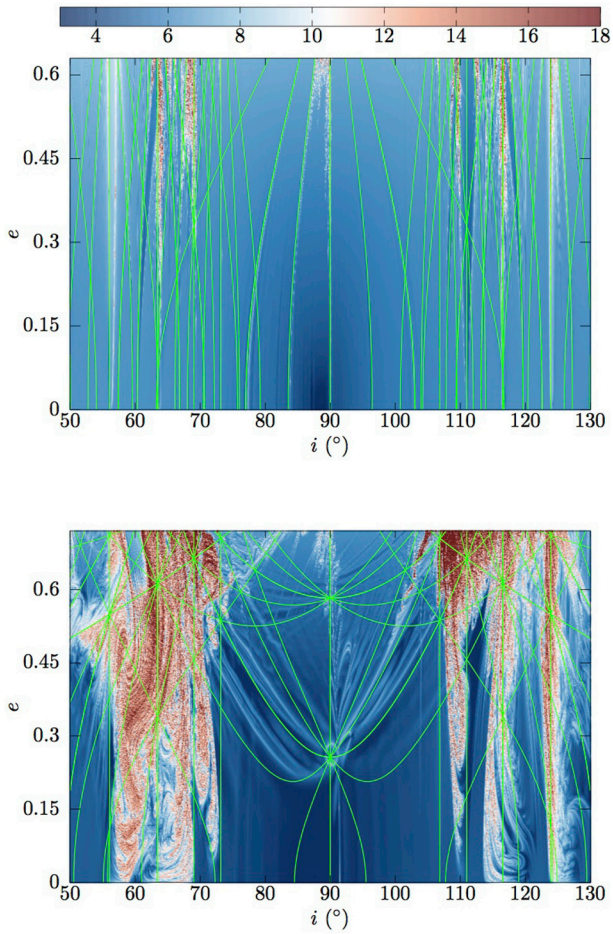

FIGURE 3 | Detailed views of the prograde *and* retrograde regions for the two-extreme values of the parameter ε considered in this work (**Top** $a = 18,600$ km, **Bottom** $a = 29,600$ km). The resonant manifolds defined by Equation (2.12) are superimposed on the FLIs. Despite the symmetry of the resonant manifolds, the chaos of the prograde region is not mirrored in the retrograde region.

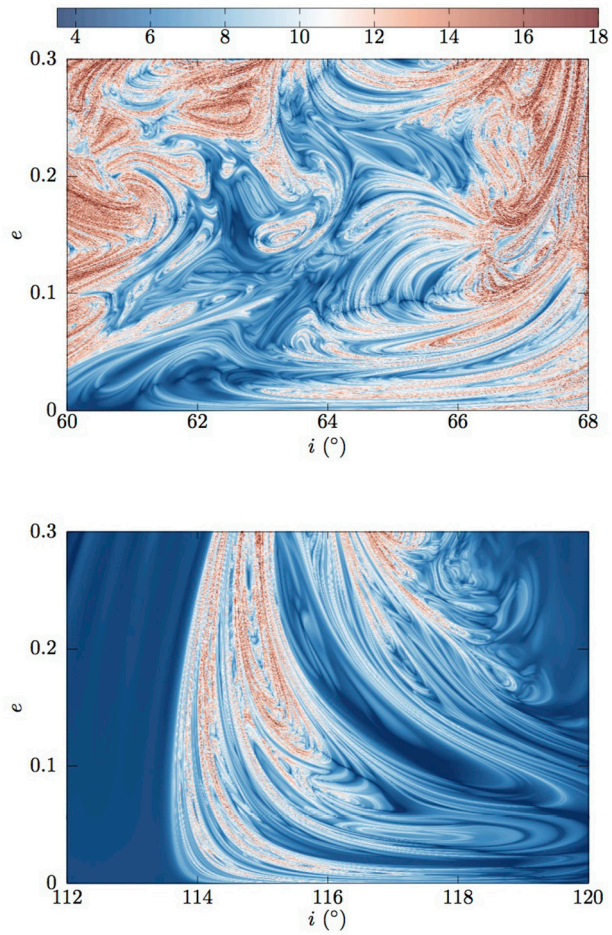

FIGURE 4 | Two detailed views of the phase space under the FLI analysis. 701 × 701 orbits have been propagated revealing the existence of very thin structures and KAM tori filling the chaotic regions. On this domain, the retrograde region contains 4 time less orbits satisfying the condition $\mathrm{FLI}(\tau_{\mathrm{run}}) \geq \alpha \log(\mathrm{run})$, $\alpha = 1.1$.

in drift estimation and visualization of transport to quantify changes of the unperturbed first integrals. This section is devoted to this task by investigating asymptotic properties of initial conditions close or immersed in hyperbolic structures. We base our approaches on individual propagations and on spatial ensemble averages.

4.1. Drift Estimation

There exist a tension between the local degree of hyperbolicity and the eventual large transport. In fact, the astronomical concept of *stable chaos* teaches us that positivity of a Lyapunov exponent does not necessarily implies large excursion in the phase space [43]. Large excursions in the phase space can be the signature of transport along the level curves of an integrable system. Nekoroshev's long-time stability theorem does not exclude the existence of chaotic variation. Finally, beyond a critical value, Chirikov's overlap criterion of resonances give rise to large connected chaotic domains, allowing possibly macroscopic transport [12].

The problem of chaotic transport (sometimes referred as *chaotic diffusion*) in nearly-integrable Hamiltonian systems and Dynamical Maps still occupy efforts of various dynamicists (see e.g., [40, 44, 45]). Given an orbit computed up to a final time τ_{run}, $\gamma(t) = \big\{\big(x(t), y(t)\big)\big\}_{0 \leq t \leq \tau_{\mathrm{run}}}$, we use the diameter along the action-variables to measure the drift of the unperturbed first-integrals. More precisely, given an action-like vector $x \in D \subset \mathbb{R}^n$, the diameter D of the orbit is defined as

$$\mathrm{D}(x_0, y_0, \tau_{\mathrm{run}}) = \max_{0 \leq t,s \leq \tau_{\mathrm{run}}} \big\| x(t) - x(s) \big\| . \tag{4.1}$$

For our computations we chose the ℓ_∞-norm and computed the drift along the normalized action variables, i.e., along $x = (\tilde{G}, \tilde{H})$ with $\tilde{G} = G/L$ and $\tilde{H} = H/L$ (we recall that in the secular

TABLE 1 | The estimation of the volume of chaotic orbits in the prograde *and* retrograde regions, for various perturbing parameters *and* on various domains.

Domain D	Size of a fixing $\varepsilon(a)$ [km]	Threshold α	Volume of chaotic orbits	
			$\mathcal{V}_\alpha^+$	$\mathcal{V}_\alpha^-$
$[0, 0.65] \times [0, \pi/2]$	18,600	1.1	0.009	0.009
		1.25	0.005	0.005
		1.3	0.004	0.005
$[0, 0.74] \times [0, \pi/2]$	24,600	1.1	0.05	0.05
		1.25	0.038	0.04
		1.3	0.035	0.038
$[0, 0.76] \times [0, \pi/2]$	27,600	1.1	0.18	0.12
		1.25	0.12	0.09
		1.3	0.1	0.08
$[0, 0.78] \times [0, \pi/2]$	29,600	1.1	0.22	0.14
		1.25	0.16	0.09
		1.3	0.14	0.08

The domain D refers to the definition of the domain in the prograde region, in the eccentricity-inclination action phase space. This domain is then mirrored in its retrograde counterpart to serve as a new domain to determine the volume of chaotic orbits in the retrograde region, $\mathcal{V}_\alpha^-$. The Equation (3.3) is used as a discrimination criteria. All results have been established with a fine mesh (all domains have been uniformly discretised with a grid consisting of at least 500 × 500 initial conditions). The prograde region appears to be slightly more chaotic than the retrograde counterpart on a macroscale the more we increase the perturbing parameter. Significant differences may also exist at smaller scales.

approximation, L is a constant parameter determined by the semi-major axis).

The results of the computation of the diameters, according to Equation (4.1) for two-extreme non-linearity parameters are shown in **Figure 5**. Comparing the results with the FLIs maps, we note that the relation between hyperbolicity and large transport is not that straightforward. For $a = 18,600$ km, we remark that regions with the larger FLIs do not necessarily correspond to regions where the transport is maximal. Conversely, the almost vertical resonant manifold emanating near $i \sim 56.1^\circ$ does not have the largest degree of hyperbolicity; yet it carries the largest transport index. Switching to $a = 29,600$ km, we note that the lowest diameter is already one order of magnitude larger than in the former case. The largest diameter is also significantly larger which confirm the known fact of the instabilities in the MEOs. We emphasize that the diameters have been computed on the same predefined grids of ICs used to estimate the FLIs (i.e., a highly-resolved grid of ICs). The emanating feeling of a resolution deterioration in the maps is once again a nice testimony of the sensitivity of variational indicators.

For large perturbing parameters, globally speaking, large hyperbolicity corresponds to large diameters. This fact has to be nuanced slightly near $e \sim 0.7$ and $i \sim 70^\circ$. Using an empirical criterion, we extracted from the maps the actions that satisfy the condition $\mathrm{FLI}(x, \tau_{\mathrm{run}}) \geq 1.2 \log(\tau_{\mathrm{run}})$ (i.e., chaotic orbits) as those satisfying $\mathrm{D}(x, \tau_{\mathrm{run}}) \geq 0.35$. The tracing orbits are shown in **Figure 6** and illustrate the link between large hyperbolicity and large diameters, and the necessity of finely resolved meshes (thin stable structures stripe the chaotic domains and can be detected with the diameters also).

Let us now comment on the diameter indicator that we used. Very often diameters-like quantities in terrestrial dynamics have been estimated using a more restrictive definition, namely a one-dimensional diameter of a specific observable f (see e.g., [41, 46]). This strategy reduces to nothing else than the amplitude estimation, equivalent to the estimation of $\Delta f = \max_t f(x) - \min_t f(x)$. For the MEO problem, the eccentricity diameter along the time is, rightly, tracked (as efforts are directed toward the perigee height and the need of re-entry solutions). However, when used as an empirical "measure of chaos," this diameter may be too loose. In fact, having in mind the geography of the resonant manifolds derived from the resonant condition in Equation (2.12) and the fact that two actions characterizes an invariant torus of $\mathbb{T}^3$, it is easy to "create" a quasi first-integral by choosing ICs near certain manifold. As an example, let us fix $a = 29,600$ km and consider a cluster of ICs in a small neighborhood of $\mathcal{V}(x_\star)$, where $x_\star = (e_\star, i_\star) = (0.616, 88^\circ)$. The time evolution (over 25 lunar periods) of the eccentricity and inclination for the whole cluster of orbits ($k = 200$ orbits) is displayed in **Figure 7**. The spatial averaged orbit is displayed and superimposed with a *bold red* line[9]. Clearly, the eccentricities of the whole cluster evolve in an apparent regular fashion. All the orbits incorporate similar dynamical informations, both on the quantitative and qualitative point of view. On the contrary, the inclination time-histories experience significant variations and a net sensitive dependence upon the ICs. From this example, easily generalisable, we easily infer why a one-dimensional diameter (based on the eccentricity) would fail in capturing these particularities. Pushing further the idea, we extended this approach on a grid of ICs near the point $x_\star$ by computing accordingly the diameters (and the FLIs). The obtained maps are presented in **Figure 8**. They confirm the rationale behind the intuition developed through the former example. Whilst the diameter based on both actions is in agreement with the FLI map, the method based on the one-diameter approach give an irrelevant and uniform signal.

Having presented a general way to quantify the drift, let us focus now on how the drift is mediated in the phase space.

4.2. Visualization of Transport

In the previous sections, we computed FLIs and diameters in various sections

$$\mathcal{S}(v) = \left\{(x, y) \in D \times \mathbb{T}^3 \,|\, y = v, v \in \mathbb{T}^3\right\} \tag{4.2}$$

with $D \subset \mathbb{R}^2$. By fixing $y = 0$, particular features in $\mathcal{S}(0)$ have been depicted. In order to visualize transport properties, and to show how its mediation is related to the detected hyperbolic web, we use projection and visualization techniques that have been extensively used over the past decade to study transport in

[9] Let us consider a cluster of size k, that we propagate up to time τ_{run}. We obtain k orbits $\gamma_k \in \left(\mathcal{C}[0, \tau_{\mathrm{run}}]\right)$. Le us denote by $x_j(i, t)$ the instantaneous value of the j-th component of the orbit γ_i at a specific epoch t. The spatial averaged orbit of the component j ($1 \leq j \leq n$), $\langle x_j \rangle$, is then defined through its components obtained at any time t by $\langle x_j(t) \rangle = \frac{1}{k} \sum_{i=1}^{k} x_j(i, t)$.

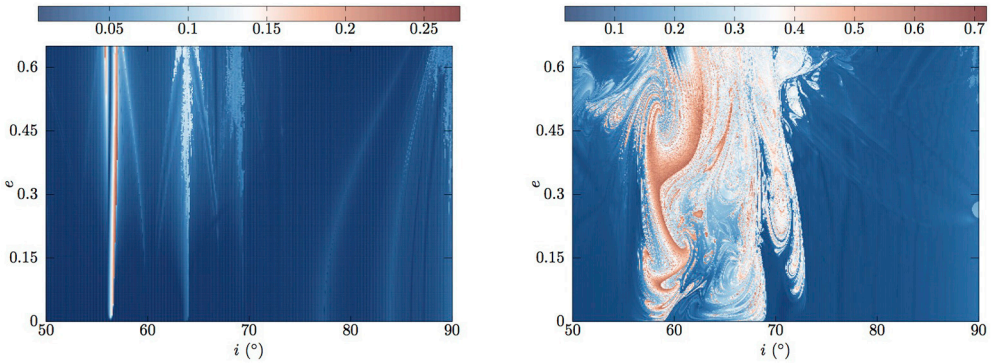

FIGURE 5 | Estimation of the diameters for the two perturbing parameters $\varepsilon(a)$ with $a = 18,600$ km and $a = 29,600$ km.

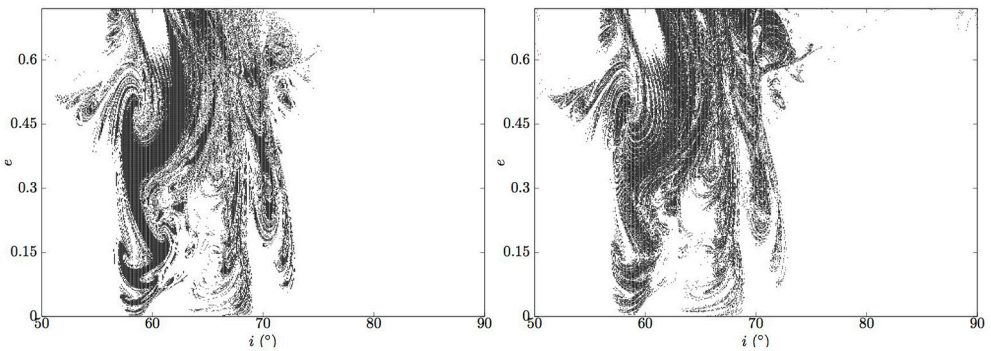

FIGURE 6 | Extraction of the ICs satisfying $\mathrm{D}(x, \tau_{\mathrm{run}}) \geq 0.35$ (left hand-side) and the chaotic ICs satisfying $\mathrm{FLI}(x, \tau_{\mathrm{run}}) \geq 1.2 \log(\tau_{\mathrm{run}})$.

nearly-integrable Hamiltonian system, symplectic Maps and in Dynamical Astronomy [16, 18, 19, 40, 42]. For a recent overview specifically around the FLIs and their applications, we advise the reader to consult [20] for a pedagogical introductory note. The methodology consists in the following. First, we compute the FLIs over a section $\mathcal{S}(\nu)$, say on $\mathcal{S}(0)$[10]. After this step, we are then able to recognize initial conditions close to hyperbolic borders or immersed within the chaotic sea. We then select one IC of interest in $\mathcal{S}(0)$. Let $x_\star \in \mathcal{S}(0)$ denotes this IC. Next, we define a small neighborhood $\mathcal{V}(x_\star)$ of k ICs of $x_\star$. In theory, it would be sufficient to deal with the sole numerical propagation up to τ_{run} of the orbit emanating from $x_\star$. However, the procedure is computationally facilitated by considering a cluster of k orbits. From these computed orbits $\gamma_k(t) \in \mathcal{C}\big([0, \tau_{\mathrm{run}}]\big)$, we keep trace only of the points that return *close enough* to the section $\mathcal{S}(\nu)$. For that purpose, we introduce the family of sections $\{\mathcal{S}_\delta(\nu)\}_\delta$ which are δ-close to $\mathcal{S}(\nu)$. These sections are defined as

$$\mathcal{S}_\delta(\nu) = \big\{(x, y) \in D \times \mathbb{T}^3 \mid \big\|y - \nu\big\| \leq \delta\big\},\ \delta \ll 1 \in \mathbb{R}_+. \quad (4.3)$$

When $\delta \to 0$, we recover the "exact" section $\mathcal{S}(\nu)$. The introduction of this family of section is essentially to circumvent numerical limitations. Firstly, we deal with a finite time τ_{run} (that we would like to keep "as small as possible" but "large enough" to extract dynamical mechanisms). Secondly, in practice we do not deal with an orbit $\gamma_k(t) \in \mathcal{C}\big([0, \tau_{\mathrm{run}}]\big)$, but with a discretised version of this orbit computed, say (to facilitate the exposition), at each multiple of the fixed step size Δt, $\{\gamma_k(t),\ t = i\Delta t\}_{i=0}^{n}$, $n\Delta t = \tau_{\mathrm{run}}$. All points of the orbits $\gamma_k(t) \in \mathcal{C}\big([0, \tau_{\mathrm{run}}]\big)$ that return during the simulation to a section of $\{\mathcal{S}_\delta(\nu)\}_\delta$ are identically projected into the exact section $\mathcal{S}(\nu)$, on which the FLIs are used as a background. By doing that, we are able to relate transport with the web detected by the FLIs. In our computation we dealt with the ℓ_∞-norm, δ is problem dependent and best determined by a calibration procedure[11]. Finally we worked with a cluster of size $k = 200$ initial conditions.

Figure 9 presents results in the range of "small" perturbation for two initial points of interest applying the methodology described previously. The clusters has been propagated up to a timescale of about 5.8×10^5 orbits revolution (25 lunar nodes).

[10] In this work we were interested in the action-action plane, but the approach can be extended to action-angle or angle-angle planes. For example, a angle-angle section can be defined as $\mathcal{T} = \big\{(x, y) \in D \times \mathbb{T}^3 \mid (y_1, y_2) \in B \subset \mathbb{T}^2, x \in D, y_3 = \nu_3\big\}$.

[11] To give an idea of the size of δ, the results presented in this manuscript have been obtained with $\delta = 0.08$ for the small range of ε, $\delta = 0.1$ for larger range. Different admissible δ just change the number of points on the section collected, but leave invariant the transport properties (angles are expressed in radians).

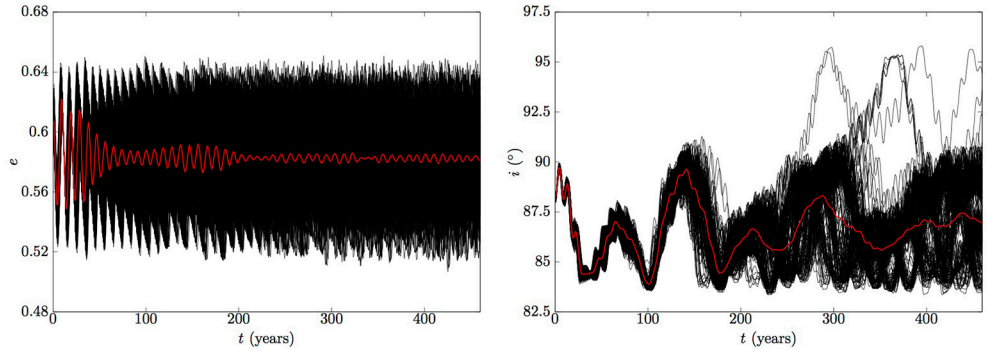

FIGURE 7 | Ensemble integration of a cluster of $k = 200$ orbits in a neighborhood $\mathcal{V}(x_\star)$ of $x_\star = (0.616, 88°)$. The ensemble averaged orbit of the considered observables are shown in *red*. The eccentricities do not experience a net sensitive dependence to the ICs, contrarily to the inclinations. From this example, it can be easily inferred that a diameter-measure based solely on the eccentricity (or equivalently on G) would fail to capture properties of the dynamics.

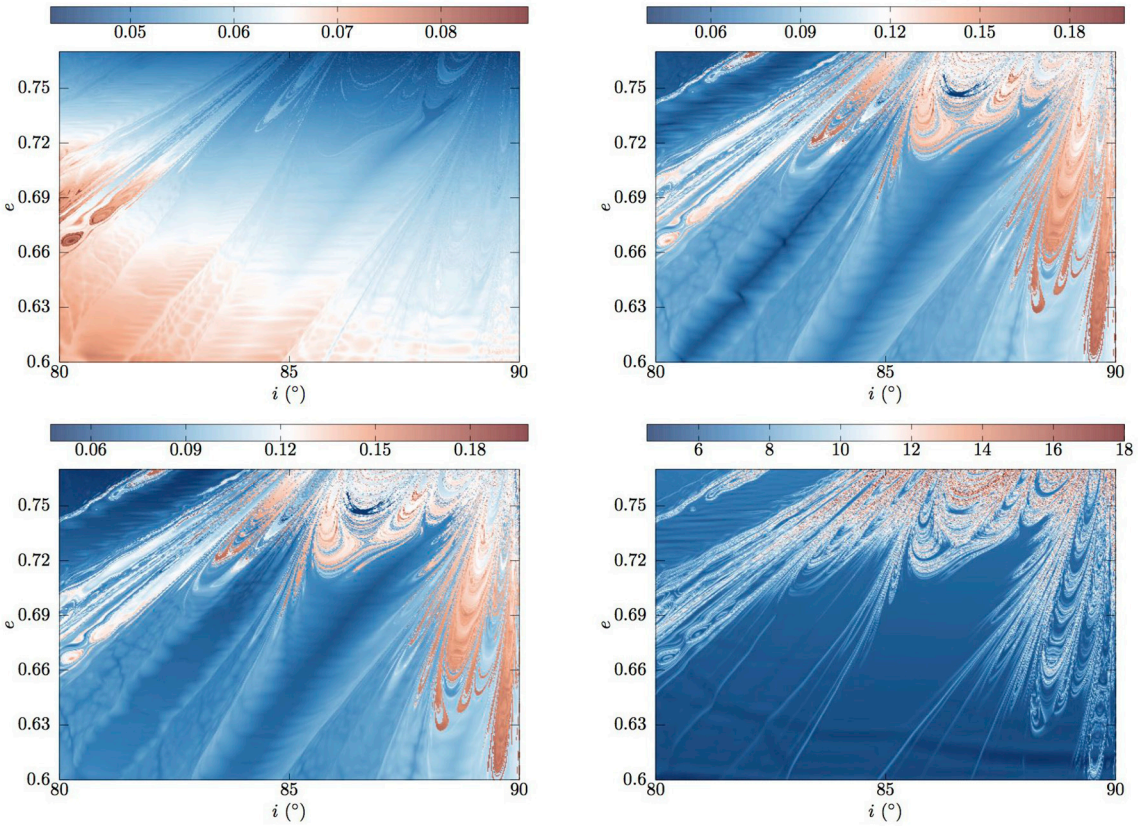

FIGURE 8 | The figures enable us to quantify how a one-dimensional diameter coefficient (here based on the action G, top left) may be inappropriate in some cases in capturing dynamical properties. *A contrario*, the two-dimensional diameter coefficient (bottom left) based on both actions, G and H, captures the subtleties of the dynamics and reconcile the results with the FLIs analysis.

The ICs serving a definition to the cluster are depicted in red. The points of the orbits that cross the double sections of the set $\{\mathcal{S}_\delta\}_\delta$ are depicted in *green*. (To facilitate the reading and interpretation of the figures, the FLIs background have been color coded with a light opacity-like filter. The points returning to the section are intentionally magnified.) The two clusters focus on thin manifold that still carry transport (see **Figure 5**). As the transport index is rather small, excursions are modest and rather confined. The returning points are guided by the thin hyperbolic skeleton detected by the FLI computation.

In **Figure 10**, we repeated the same experiment with a larger ε for 4 different scenarios. The approach enables us

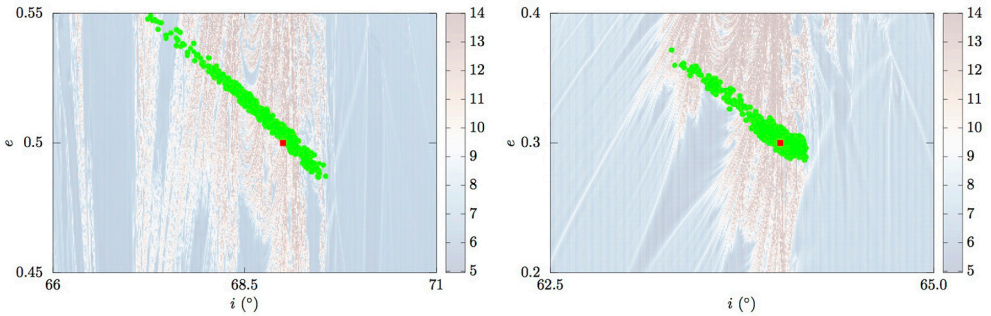

FIGURE 9 | Two diffusive scenarios illustrating transport scenarios along resonances in the regime of small perturbative parameters. The *red* spot indicates the initial condition where the ensemble of initial conditions are defined. Points of the orbits that return sufficiently close to the section (on which the FLIs appear as a background) are depicted with a *green* point. See text for comments.

to visualize and quantify the spread of the actions in the regime of strong chaos. The orbits of the clusters have been propagated on about $1.4 \times 2.8 \times 10^5$ orbits revolution. The spread of the orbits is well more appreciable and develops more drastically within the action-space. It covers a large portion of the connected chaotic domain. As it is observed for all scenarios, the change in inclination can be superior to 15°, with extremely large variations for the eccentricity (namely, the mechanism allows nearly circular orbits to become very eccentric).

It would be extremely interesting to extend the approaches and visualization of the diffusive properties by extending the dimension of the visualized space. Taking advantage of our model, we were able to extend the traditional stability maps in one more direction by stitching together *ad-hoc* others FLI sections. The results presented in **Figure 11** complement the global stability picture of the actions space by "unrolling" the dynamics according to one angle, here Ω. The resonant manifolds computed using Equation (2.12) are depicted in black in the "action-space." In the regime of small perturbation (left panel), a pendulum-like structure is clearly identifiable (minor structures can also be identified). By varying the size of the perturbation, a bifurcation-like phenomena occurred and the initially elliptic point becomes of a hyperbolic nature where collisional orbits develop. Such a systematic parametric methodology would allow, besides the quantification of chaos and the determination of the resonant regime (cf. [38]), the determination of precise perturbing parameters where such phenomena occur.

5. DISCUSSION AND CONCLUSIVE REMARKS

Dynamical chaos indicators as the FLI are valuable and formidable allies to gain knowledge on the dynamical system under investigation. Their systematic use over nearly the past two decades in transverse fields has brought its share of results. Applications toward terrestrial dynamics are still at their early stage but the current situation seems to evolve positively. In this contribution, we complemented and refined our past studies related to the long-term dynamics of terrestrial orbits in the range 2.91–4.64 Earth radii ($\varepsilon \in [0.02 : 0.22]$). We showed the complementarity and benefits of visualizing the global dynamics via sections, corroborated with the computation of the FLIs and practical action-diameter quantities. From our numerical experiments, we have seen that when the detected hyperbolic manifolds are very thin (but still carry large diameters), the transport occurs precisely along them. For higher values of the non-linearity parameter, resonances do overlap significantly and the transport is across a large domain of the chaotic sea. This mechanism allows nearly-circular orbits to become highly eccentric on a few lunar nodes only. In the later case of strong chaos, preferred directions for the transport are hard to establish. The FLIs allow to follow and delineate the routes of transport where the spread in the phase space take place. The natural complementary step that deserves serious attention concerns the nature of the transport, the computation of *diffusion-like coefficients* and its scaling with ε (Note that if in our actual set-up, we do have access only to a limited number of different order of magnitudes of ε. A theoretical possibility to extend its range is to artificially increase the semi-major axis - even if we know that physically the procedure is not that relevant as octupolar contributions should be incorporated). Let us comment and relate recent difficulties that we encountered in investigating these last points. Transport properties are generally characterized through the computations of moments of different order q,

$$M_q(\tau) = \left\langle |x(\tau) - \langle x(\tau) \rangle|^q \right\rangle. \tag{5.1}$$

Let us underline once more that when we deal with the dynamics numerically, we only have access to *finite time moments*. Usually, the second-order moment, i.e., the spread of the actions (the variance), is used to discriminate the case of diffusion we deal with. More precisely, under the explicit ansatz that

$$M_2(\tau) = \left\langle |x(\tau) - \langle x(\tau) \rangle|^2 \right\rangle \sim D_2 \tau^\nu, \tag{5.2}$$

the diffusion is called either *subdiffusive* ($\nu < 1$), *diffusive* ($\nu = 1$) or *superdiffusive* ($\nu > 1$). (The particular case of superdiffusive behavior with $\nu = 2$ is referred to *ballistic*

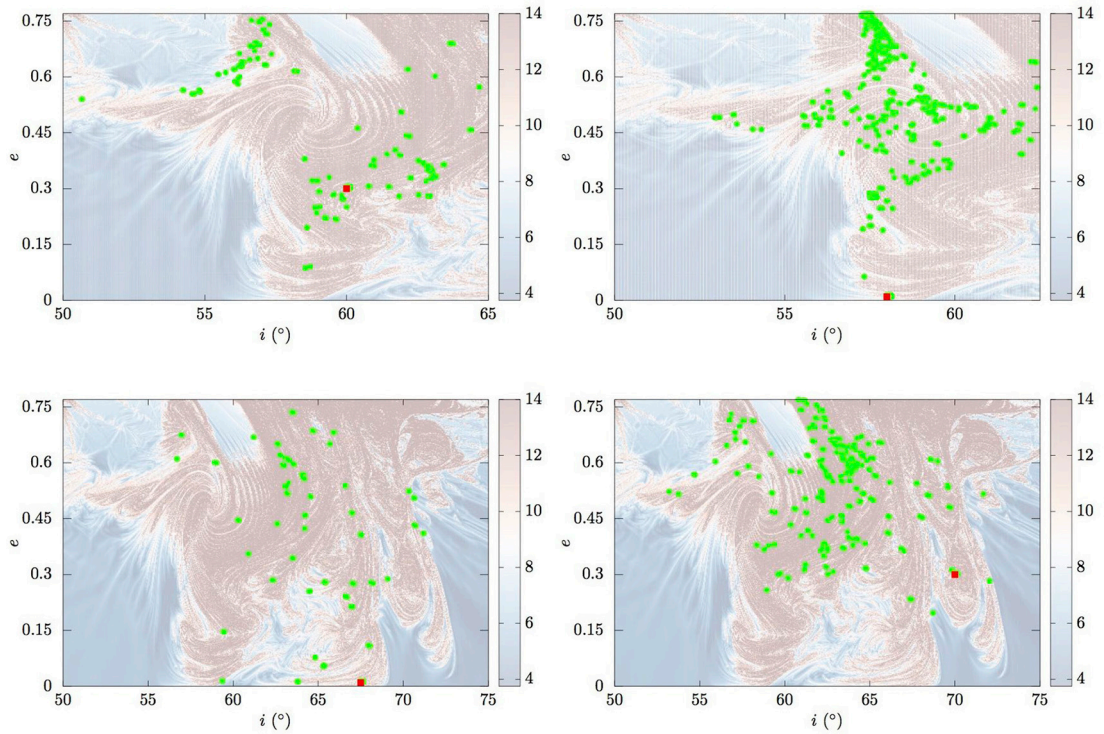

FIGURE 10 | Diffusive scenarios illustrating transport scenarios within the hyperbolic web in the regime of large perturbative parameters and strong resonances overlap. The *red* spots indicate the initial condition where the ensemble of initial conditions are defined. Points of the orbits that return sufficiently close to the section (on which the FLIs appear as a background) are depicted with a *green* point. See text for comments.

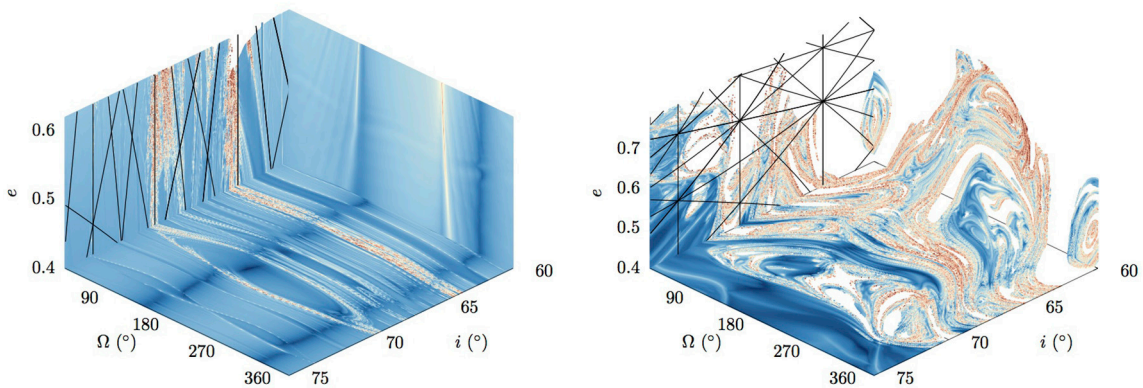

FIGURE 11 | These two FLI cubes, computed for $a = 18,600$ km **(Left)** and $a = 29,600$ km **(Right)** highlight a bifurcation phenomena. The resonant manifolds appear in black in the "action-action" space.

diffusion.) The real parameter D_2 is the estimated *diffusion coefficient*, and its sole determination can be sometimes tricky due to technical difficulties (see, e.g., Lega et al. [16] and further references in Cincotta et al. [45]). Anomalies to the strict diffusive case ($\nu = 1$), i.e., aberrations with respect to Gaussianity, might be the results of the existence of a mixed phase space (cohabitation of regular and chaotic components in the phase space) and correlation effects [47, 48]. Let us note that, to the best of our knowledge, the study of the correlation function $C(\tau)$ (even at least for the specific observable of interest, the eccentricity) and its possible decay which give us the scale of the *correlation time* τ_C (see discussions in [49, 50]) has never been undertaken for the MEO problem. (The exception is found in Wytrzyszczak et al. [51] where the autocorrelation function properties are used to discriminate regularity for geosynchronous objects.) Daquin et al. [52] claimed the normal character of the diffusion for the eccentricity observable in the regime of strong chaos. We redid some experiments along those lines apart that we used the spatial averaging ideology (and no longer the *temporal averaging*) assuming that all ICs of the

cluster are equivalent. We met difficulties to confirm our former conclusions and we stress here that they should be taken with a grain of salt. In fact, in our experiments, we noticed that such a conclusion depends *strongly* on the ansatz made on the evolution of the variance and the choice of the time-horizon investigated. Regarding the question related to the time-horizon, there might exist a transient time $\tau_{\text{tr.}}$ that should be constrained first. Indeed, in order to derive meaningful statistical conclusions, we have to ensure that $\tau \gg \tau_{\text{tr.}}$ (as a transient time seems to exist) and $\tau \gg \tau_C$. It is possible that, unfortunately, in our present setting, $\tau_{\text{tr.}} \sim \tau$, making conclusions hard to reach.

Constraining those difficulties are the directions being taken by our current research.

AUTHOR CONTRIBUTIONS

All authors listed have made a substantial, direct and intellectual contribution to the work, and approved it for publication.

ACKNOWLEDGMENTS

The present form of the manuscript owes a great deal to the reviewers. The authors greatly appreciated and acknowledge the discussions with Christos Efthymiopolous at the Perspectives in Hamiltonian dynamics conference held in Venice, June 18 − 22. JD is grateful to Bastian Märkisch of the SourceForge `gnuplot` forum for his precious advices in realizing **Figures 1**, **2** and thank Benoît Noyelles for his remarks. Numerical simulations were performed using HPC resources from the Institute for Celestial Mechanics and Computation of Ephemerides (IMCCE, Paris Observatory) and computing facilities from RMIT University. JD acknowledges the support of the Cooperative Research Centre for Space Environment Research Centre (SERC Limited) through the Australian Government's Cooperative Research Center Program and the support of the ERC project 677793 Stable and Chaotic Motions in the Planetary Problem (started on the 4th of June 2018). IG acknowledges the support of the ERC project 679086 Control for Orbit Manoeuvring through Perturbations for Application to Space Systems.

REFERENCES

1. Breiter S. Lunisolar apsidal resonances at low satellite orbits. *Celestial Mech Dyn Astron.* (1999) **74**:253–74.
2. Breiter S. Lunisolar resonances revisited. *Celestial Mech Dyn Astron.* (2001) **81**:81–91. doi: 10.1023/A:1013363221377
3. Breiter S. On the coupling of lunisolar resonances for Earth satellite orbits. *Celestial Mech Dyn Astron.* (2001) **80**:1–20. doi: 10.1023/A:1012284224340
4. Rossi A. Resonant dynamics of Medium Earth Orbits: space debris issues. *Celestial Mech Dyn Astron*. (2008) **100**:267–86. doi: 10.1007/s10569-008-9121-1
5. Bonnard B, Caillau J. Geodesic flow of the averaged controlled Kepler equation. *Forum Math.* (2009) **21**:797–814. doi: 10.1515/FORUM.2009.038
6. Armellin R, San-Juan JF. Optimal Earth's reentry disposal of the Galileo constellation. *Adv Space Res.* (2018) **61**:1097–120. doi: 10.1016/j.asr.2017.11.028
7. Daquin J, Rosengren A, Alessi EM, Deleflie F, Valsecchi G, Rossi A. The dynamical structure of the MEO region: long-term stability, chaos, and transport. *Celestial Mech Dyn Astron*. (2016) **124**:335–66. doi: 10.1137/070707245
8. Celletti A, Gales CB. A Study of the Lunisolar Secular Resonance $2\,\dot{\omega}+\dot{\Omega}=0$. *Front Astron Space Sci.* (2016) **3**:11 doi: 10.3389/fspas.2016.00011
9. Celletti A, Gales C, Pucacco G. Bifurcation of lunisolar secular resonances for space debris orbits. *SIAM J Appl Dyn Syst*. (2016) **15**:1352–83. doi: 10.1137/15M1042632
10. Gkolias I, Daquin J, Gachet F, Rosengren AJ. From order to chaos in Earth satellite orbits. *Astron J*. (2016) **152**:119. doi: 10.3847/0004-6256/152/5/119
11. Celletti A, Galeş C, Pucacco G, Rosengren AJ. Analytical development of the lunisolar disturbing function and the critical inclination secular resonance. *Celestial Mech Dyn Astron*. (2017) **127**:259–83. doi: 10.1007/s10569-016-9726-8
12. Chirikov B. A universal instability of many-dimensional oscillator systems. *Phys Rep*. (1979) **52**:263–379.
13. Bollt EM, Meiss JD. Targeting chaotic orbits to the Moon through recurrence. *Phys Lett A* (1995) **204**:373–8.
14. Koon WS, Lo MW, Marsden JE, Ross SD. Heteroclinic connections between periodic orbits and resonance transitions in celestial mechanics. *Chaos* (2000) **10**:427–69. doi: 10.1063/1.166509
15. Perozzi E, Ferraz-Mello S. *Space Manifold Dynamics.* New York, NY; Dordrecht; Heidelberg; London: Springer (2010). doi: 10.1007/978-1-4419-0348-8
16. Lega E, Guzzo M, Froeschlé C. Detection of Arnold diffusion in Hamiltonian systems. *Phys D Nonlinear Phen* (2003) **182**:179–87. doi: 10.1016/S0167-2789(03)00121-0
17. Todorović N, Lega E, Froeschlé C. Local and global diffusion in the Arnold web of a priori unstable systems. *Celestial Mech Dyn Astron*. (2008) **102**:13. doi: 10.1007/s10569-008-9152-7
18. Cincotta PM, Giordano CM. Chapter 6: Topics on diffusion in phase space of multidimensional Hamiltonian systems. In: Perlidze T, editor. *New Nonlinear Phenomena Research*. New York, NY: Nova Science Publishers (2008). p. 393–410.
19. Páez RI, Efthymiopoulos C. Trojan resonant dynamics, stability, and chaotic diffusion, for parameters relevant to exoplanetary systems. *Celestial Mech Dyn Astron*. (2015) **121**:139–70. doi: 10.1007/s10569-014-9591-2
20. Lega E, Guzzo M, Froeschlé C. Theory and applications of the fast Lyapunov Indicator (FLI) method. In: Skokos CH, Gottwald GA, Laskar J, editors. *Chaos Detection and Predictability*. Vol. 915. Springer (2016). p. 35–54.
21. Grebenikov E. Methods of averaging equations in celestial mechanics. *Soviet Astron*. (1965) **9**:146.
22. Mitropolsky IA. Averaging method in non-linear mechanics. *Int J Nonlinear Mech*. (1967) **2**:69–96.
23. Ghys É. Resonances and small divisors. In: Charpentier É, Lesne A, Nikolski NK, editors. *Kolmogorovs Heritage in Mathematics*. Springer Science & Business Media (2007). p. 187–213.
24. Kaula WM. *Theory of Satellite Geodesy: Applications of Satellites to Geodesy*. Waltham, MA: Blaisdell Publi. Co. (1966).
25. Ely TA. *Dynamics and Control of Artificial Satellite Orbits with Multiple Tesseral Resonances*. Ph.D. thesis. Purdue University (1996).
26. Celletti A, Galeş C. Dynamical investigation of minor resonances for space debris. *Celestial Mech Dyn Astron*. (2015) **123**:203–22. doi: 10.1007/s10569-015-9636-1
27. Lara M. Exploring sensitivity of orbital dynamics with respect to model truncation: the frozen orbits approach. In: Vasile M, Minisci E, Summerer L, McGinty P, editors. *Stardust Final Conference. Astrophysics and Space Science Proceedings,* Vol. 52. Cham: Springer (2018). p. 69–83.
28. Ariel G, Engquist B, Tsai R. Numerical multiscale methods for coupled oscillators. *Multiscale Model Simul*. (2009) **7**:1387–404. doi: 10.1137/070707245

29. Abdulle A, Weinan E, Engquist B, Vanden-Eijnden E. The heterogeneous multiscale method. *Acta Num*. (2012) **21**:1–87. doi: 10.1017/S09624929XXXXXXXX
30. Lochak P, Meunier C. *Multiphase Averaging for Classical Systems. With Applications to Adiabatic Theorems*. New York, NY: Springer-Verlag (1988).
31. Allen MP. Introduction to molecular dynamics simulation. In: N. Attig, K. Binder, H. Grubmüller, K. Kremer, editors, *Computational Soft Matter: From Synthetic Polymers to Proteins*, Vol. 23, Lecture Notes, NIC Series. Jürlich: John von Neumann Institute for Computing (2004). p. 1–28.
32. García-Archilla B, Sanz-Serna J, Skeel RD. Long-time step methods for oscillatory differential equations. *SIAM J Sci Comput*. (1998) **20**:930–63.
33. Givon D, Kupferman R, Stuart A. Extracting macroscopic dynamics: model problems and algorithms. *Nonlinearity* (2004) **17**:R55. doi: 10.1088/0951-7715/17/6/R01
34. Lesne A. Multi-scale approaches. In: Franxcoise JP, Naber G, Tsun TS, editors. *Encyclopedia of Mathematical Physics*. Elsevier (2006). p. 465–82.
35. Hartmann C. *Model Reduction in Classical Molecular Dynamics*. Ph.D. thesis. Free University Berlin (2007).
36. Pavliotis GI, Stuart AM. *Multiscale Methods: Averaging and Homogenization*. Heidelberg: Springer (2008).
37. Froeschlé C, Lega E, Gonczi R. Fast Lyapunov indicators. Application to asteroidal motion. Celestial Mechanics and Dynamical Astronomy. (1997) **67(1)**:41–62.
38. Froeschlé C, Guzzo M, Lega E. Graphical evolution of the Arnold web: from order to chaos. *Science* (2000) 289:2108–10. doi: 10.1126/science.289.5487.2108
39. Todorović N, Novaković B. Testing the FLI in the region of the Pallas asteroid family. *Mthly Notices R Astron Soc*. (2015) **451**:1637–48. doi: 10.1093/mnras/stv1003
40. Guillery N, Meiss JD. Diffusion and drift in volume-preserving maps. *Regular Chaot Dyn*. (2017) **22**:700–20. doi: 10.1134/S1560354717060089
41. Rosengren AJ, Daquin J, Tsiganis K, Alessi EM, Deleflie F, Rossi A, et al. Galileo disposal strategy: stability, chaos and predictability. *Mthly Notices R Astron Soc*. (2017) **464**:4063–76. doi: 10.1093/mnras/stw2459
42. Guzzo M, Lega E, Froeschlé C. On the numerical detection of the effective stability of chaotic motions in quasi-integrable systems. *Phys D Nonlinear Phen*. (2002) **163**:1–25. doi: 10.1016/S0167-2789(01)00383-9
43. Milani A, Nobili AM. An example of stable chaos in the Solar System. *Nature* (1992) **357**:569.
44. Lange S, Bäcker A, Ketzmerick R. What is the mechanism of power-law distributed Poincaré recurrences in higher-dimensional systems? *EPL* (2016) 116:30002. doi: 10.1209/0295-5075/116/30002
45. Cincotta P, Giordano C, Martí J, Beaugé C. On the chaotic diffusion in multidimensional Hamiltonian systems. *Celestial Mech Dyn Astron*. (2018) **130**:7. doi: 10.1007/s10569-017-9797-1
46. Alessi EM, Deleflie F, Rosengren A, Rossi A, Valsecchi G, Daquin J, et al. A numerical investigation on the eccentricity growth of GNSS disposal orbits. *Celestial Mech Dyn Astron*. (2016) **125**:71–90. doi: 10.1007/s10569-016-9673-4
47. Varvoglis H, Vozikis C, Barbanis B. Transport in perturbed integrable Hamiltonian systems and the fractality of phase space. In: Dvorak R, Henrard J, editors. *The Dynamical Behaviour of Our Planetary System*. Dordrecht: Springer (1997). p. 233–42.
48. Zaslavsky GM. Chaos, fractional kinetics, and anomalous transport. *Phys Rep*. (2002) **371**:461–580. doi: 10.1016/S0370-1573(02)00331-9
49. Wiggins S, Ottino J. Foundations of chaotic mixing. *Philos Trans R Soc Lond A* (2004) **362**:937–70. doi: 10.1098/rsta.2003.1356
50. Varvoglis H. Regular and chaotic motion in Hamiltonian systems. In: Dvorak R., Freistetter F, Kurths J, editors. *Chaos and Stability in Planetary Systems*. Lecture Notes in Physics, Vol 683. Berlin; Heidelberg: Springer (2004). p. 141–84.
51. Wytrzyszczak I, Breiter S, Borczyk W. Regular and chaotic motion of high altitude satellites. *Adv Space Res*. (2007) **40**:134–42. doi: 10.1016/j.asr.2006.11.020
52. Daquin J, Rosengren A, Tsiganis K. Diffusive chaos in navigation satellites orbits. In: Gwenn B, Christophe E, Xavier L, editors. *Chaos, Complexity and Transport: Proceedings of the CCT15, Conference on Chaos, Complexity and Transport 2015*. World Scientific (2017). p. 174–84.

Conflict of Interest Statement: The authors declare that the research was conducted in the absence of any commercial or financial relationships that could be construed as a potential conflict of interest.

frontiers in Astronomy and Space Sciences

ORIGINAL RESEARCH
published: 02 July 2019
doi: 10.3389/fspas.2019.00034

Long-Term Evolution of Highly-Elliptical Orbits: Luni-Solar Perturbation Effects for Stability and Re-entry

*Camilla Colombo**

Department of Aerospace Science and Technology, Politecnico di Milano, Milan, Italy

This paper investigates the long-term evolution of spacecraft in Highly Elliptical Orbits (HEOs). The single averaged disturbing potential due to luni-solar perturbations, zonal harmonics of the Earth gravity field is written in mean Keplerian elements. The double averaged potential is also derived in the Earth-centered equatorial system. Maps of long-term orbit evolution are constructed by measuring the maximum variation of the orbit eccentricity to identify conditions for quasi-frozen, long-lived libration orbits, or initial orbit conditions that naturally evolve toward re-entry in the Earth's atmosphere. The behavior of these long-term orbit maps is studied for increasing values of the initial orbit inclination and argument of the perigee with respect to the Moon's orbital plane. In addition, to allow meeting specific mission constraints, quasi-frozen orbits can be selected as graveyard orbits for the end-of-life of HEO missions, in the case re-entry option cannot be achieved due to propellant constraints. On the opposite side, unstable conditions can be exploited to target Earth re-entry at the end-of-mission.

Keywords: luni-solar perturbation, third body perturbation, highly elliptical orbit, orbit stability, frozen orbit, orbital perturbations, re-entry, mission end-of-life

OPEN ACCESS

Edited by:
Josep Masdemont, Universitat Politecnica de Catalunya, Spain

Reviewed by:
Eduard D. Kuznetsov, Ural Federal University, Russia
Catalin Bogdan Gales, Alexandru Ioan Cuza University, Romania
Todd Ely, NASA Jet Propulsion Laboratory (JPL), United States

***Correspondence:**
Camilla Colombo
camilla.colombo@polimi.it

Specialty section:
This article was submitted to Fundamental Astronomy, a section of the journal Frontiers in Astronomy and Space Sciences

Received: *06 August 2018*
Accepted: *18 April 2019*
Published: *02 July 2019*

Citation:
Colombo C (2019) Long-Term Evolution of Highly-Elliptical Orbits: Luni-Solar Perturbation Effects for Stability and Re-entry. Front. Astron. Space Sci. 6:34. doi: 10.3389/fspas.2019.00034

INTRODUCTION

Highly Elliptical Orbits (HEOs) about the Earth are often selected for astrophysics and astronomy missions, as well as for Earth missions, such as Molniya or Tundra orbits, as they offer vantage point for the observation of the Earth and the Universe (Draim et al., 2002). Moreover, elliptical Geostationary Transfer Orbits are commonly selected to inject spacecraft in geostationary orbit. HEOs guarantees spending most of the time at an altitude outside the Earth's radiation belt; therefore, long periods of uninterrupted scientific observation are possible. In addition, geo-synchronicity is opted to meet coverage requirements, enhanced at the apogee, and optimize the ground station down-link. If the inclination is properly selected, HEO can minimize the duration of the motion inside the eclipses.

This paper, whose preliminary version was presented at the 25th AAS/AIAA Space Flight Mechanics Meeting, in Williamsburg (VA) in January 2015 (Colombo, 2015), investigates the long-term evolution of spacecraft in HEOs through the exploitation and development of semi-analytical techniques. The dynamics of HEOs with high apogee altitude is mainly influenced by the effect of third body perturbations due to the Moon and the Sun, which induces long-term variations in the eccentricity and the inclination, corresponding to large fluctuations of the orbit perigee and the effect of the Earth's oblateness.

The semi-analytical technique based on averaging is an elegant approach to analyze the effect of orbit perturbations. It separates the constant, short periodic and long-periodic terms of the disturbing function. The short-term effect of perturbations is eliminated by averaging the variational equations, or the corresponding potential, over one orbit revolution of the small body. Indeed, averaging corresponds to filtering the higher frequencies of the motion (periodic over one orbit revolution), which typically have small amplitudes (Ely, 2014). The resulting system allows a deeper understanding of the dynamics (Shapiro, 1995; Krivov and Getino, 1997). Moreover, the use of the average dynamics reduces the computational time for numerical integration as the stiffness of the problem is reduced, while maintaining sufficient accuracy compatible with problem requirements also for long-term integrations.

The effect of third body is usually modeled as a series expansion of the potential with respect to the ratio between the orbit semi-major axis and the distance to the third body. In averaged development the potential is usually truncated to the second order. For example, Cook's formulation gives the secular and long-periodic perturbation due to luni-solar perturbation obtained through averaging over one orbit revolution of the satellite (Cook, 1962). It assumes circular orbit for the disturbing bodies and considers only the second term of a/a', where a and a' are, respectively, the spacecraft and the disturbing body semi-major axis about the Earth (Blitzer, 1970). However, it does consider the obliquity of the Sun and the Moon over the equator and the precession of the Moon plane due to the Earth's oblateness (in a period of 18.6 years with respect to the ecliptic). For orbits above Low Earth Orbits, considering only the second order is not enough to accurately estimate the effect of luni-solar perturbations. For example, Lara et al. (2012) focused on orbital configurations, such as the Global Navigation Satellite Systems, for which the second order effects of J_2 can be of the same order of magnitude as perturbations due to the P_2 up to P_5 terms in the Legendre polynomials expansion of the third-body's disturbing function. For this reason, some recursive formulations of the third body potential were developed (Cefola and Broucke, 1975; Laskar and Bou, 2010) also for recovering the short periodic effects (El'yasberg, 1967).

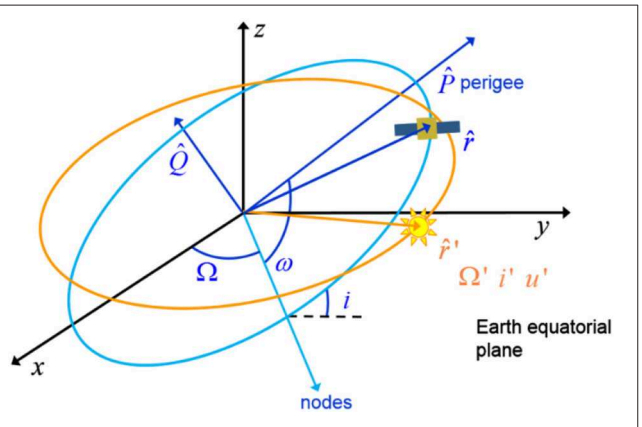

FIGURE 1 | Geometry of the third body with respect to the spacecraft and the central body.

In this paper, the single averaged disturbing potential due to luni-solar perturbations is developed in series of Taylor of the ratio between the orbit semi-major axis and the distance to the third body, following the approach by Kaufman and Dasenbrock (1972). The effect of other zonal harmonic of the Earth gravity field is also modeled up to order 6 considering also the J_2^2 term (Liu and Alford, 1980). As we want to focus here on the interaction between the terms of the Legendre polynomial of the luni-solar perturbation and the Earth's oblateness, the effect of solar radiation pressure and aerodynamics drag is neglected in this work. The perturbed dynamics is propagated in the Earth-centered equatorial frame by means of the single averaged variation (over the orbit revolution of the spacecraft) of the disturbing potential, implemented in the suite PlanODyn (Colombo, 2016). The long-term evolution of high elliptical orbits is characterized in the phase space of eccentricity, inclination and argument of the perigee with respect to the Earth-Moon plane. Maps of long-term evolution are constructed to assess the maximum and minimum eccentricity attained as function of the initial conditions. Through these maps, conditions for quasi-frozen, or long-lived libration orbits are identified. Recent projects funded by the European Space Agency on the design of disposal trajectories for Medium Earth Orbits (Rossi et al., 2015), Highly Elliptical Orbits and Libration Earth Orbits (Armellin et al., 2014; Colombo et al., 2014b) have demonstrated the possibility of exploiting orbit perturbations for designing of passive mitigation strategies for debris disposal. From the results of these projects, many work stemmed out proposing the use of maps for characterizing conditions for natural re-entry in low Earth orbit (Alessi et al., 2018), medium Earth orbit (Alessi et al., 2016; Daquin et al., 2016; Gkolias et al., 2016; Skoulidou et al., 2017), geostationary Transfer orbit (Srongprapa, 2015), geostationary orbit (Colombo and Gkolias, 2017; Gkolias and Colombo, 2017), and highly elliptical orbit (Colombo, 2015).

Third body perturbations show important effects on the long-term evolution of orbits within the Medium Earth orbit region and above. A relevant contribution to the understanding of high-altitude orbit dynamics was given by Kozai's (1962) analytical theory on secular perturbations of asteroid with high inclination and eccentricity. Assuming one perturbing body on a circular orbit, and considering the second term of the disturbing potential, an analytical solution was found, later named as Kozai-Lidov dynamics (Kozai, 1962; Lidov, 1962), which links the eccentricity of the orbit with the inclination, measured from the perturbing body plane, and the argument of the perigee. Their work was more recently extended to consider the slow variation due to the 4th term of the potential and highlighting shirking characteristics in the phase space (Katz et al., 2011; Naoz et al., 2013). Always in the line of long term analysis of the third body effect, El'yasberg (1967) derived the double averaged equations of the second term of the disturbing potential and Costa and Prado (2000) continued on the effort by El'yasberg by expanding the derivation of the double averaged potential up to order 8th. Their interest concerned the critical value of the inclination between

the perturbed and the perturbing body related to the stability of near-circular orbits. In other words for inclination higher than the critical values, circular orbits get very elliptic, while for lower values the orbit stays nearly circular. In El'yasberg (1967) and Costa and Prado (2000) the double averaging was performed using the orbital elements of the spacecraft as defined with respect to the third body plane. However, when considering both the third body effects of the Sun and the Moon, one has to assume that they orbit on the same plane; this reduce to consider that the 5.1° inclination of the Moon's plane over the ecliptic is equal to zero.

In this work, to guarantee the consistency with the single-averaged approach, we do not make this assumption. The double average variation is here obtained averaging on the fast variable describing the orbital motion of the perturbing body around the Earth as in El'yasberg (1967) and Costa and Prado (2000), but the different inclination of the perturbing bodies planes is retained. The double-averaged disturbing potential is derived in the Earth-centered equatorial reference system. The choice of this system has the advance of allowing the description of the perturbing effect of the Sun and the Moon, considering the actual ephemerides and their inclination with respect to the equator, and accommodating also the inclusion of the effect of the zonal harmonics of the Earth potential, which also affect the motion.

By using the single averaged and double averaged equations presented in this paper, the behavior of quasi-frozen solutions appearing for high inclinations orbits can be reproduced. The choice of representing the maps in terms of inclination and argument of the perigee with respect to the Moon plane is quite appropriate here as we want to study the effects on highly elliptical orbit for which the Moon third body perturbations is the most relevant effect. In addition, to allow meeting specific mission constraints, stable conditions for quasi-frozen orbits can be selected as graveyard orbits for the end-of-life of HEO missions, in the case re-entry option cannot be achieved due to propellant constraints, such as XMM-Newton, which is taken here as practical example. On the opposite side, unstable conditions can be exploited to target an Earth re-entry at the end-of-mission (Jenkin and McVey, 2008; Colombo et al., 2014a). This is the case of the end-of-life of INTEGRAL mission, requiring a small delta-v maneuvers for achieving a natural re-entry assisted by perturbations. In this paper, maps of stable and unstable HEOs are built, to be used as preliminary design tool for graveyard or frozen orbit design or natural re-entry trajectories

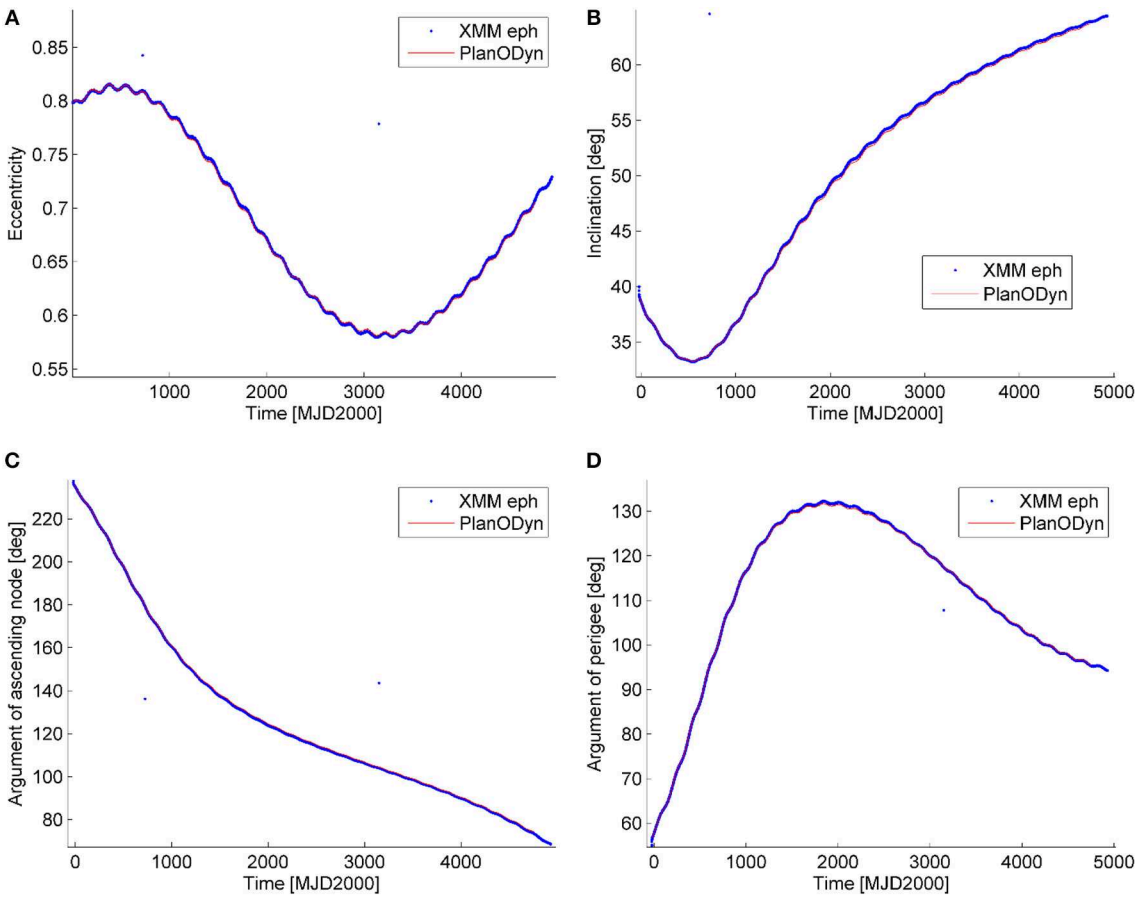

FIGURE 2 | XMM Newton's ephemerides: actual ephemerides in blue and propagation with PlanODyn in red. **(A)** Eccentricity, **(B)** inclination, **(C)** argument of the ascending node, and **(D)** argument of the perigee. The x-axis represents the time in Modified Julian Date since 2000 (Time origin at 12:00 year 2000).

at the end-of-life. Given the available delta-v on-board, the reachable space of orbital elements can also be identified as in the case of XMM-Newton mission.

LONG-TERM ORBIT EVOLUTION

Orbit Evolution With Single-Averaged Disturbing Potential

To analyze the long-term and secular effect of orbit perturbations, it is convenient to use an averaging approach. In the case the effect of perturbations is conservative, this can be described through a disturbing potential R. In this work we consider the perturbation to the two-body dynamics due to the zonal harmonics of the Earth gravity field, and the third-body perturbation of the Sun and the Moon as

$$R = R_{\text{zonal}} + R_{3-\text{Sun}} + R_{3-\text{Moon}}$$

The variation of the orbital elements is described through the planetary equations in the Lagrange form (Battin, 1999):

$$\begin{aligned}
\frac{da}{dt} &= \frac{2}{na}\frac{\partial R}{\partial M} \\
\frac{de}{dt} &= \frac{1}{na^2 e}\left(\left(1-e^2\right)\frac{\partial R}{\partial M} - \sqrt{1-e^2}\frac{\partial R}{\partial \omega}\right) \\
\frac{di}{dt} &= \frac{1}{na^2 \sin i\sqrt{1-e^2}}\left(\cos i\frac{\partial R}{\partial \omega} - \frac{\partial R}{\partial \Omega}\right) \\
\frac{d\Omega}{dt} &= \frac{1}{na^2 \sin i\sqrt{1-e^2}}\frac{\partial R}{\partial i} \\
\frac{d\omega}{dt} &= -\frac{1}{na^2 \sin i\sqrt{1-e^2}}\cos i\frac{\partial R}{\partial i} + \frac{\sqrt{1-e^2}}{na^2 e}\frac{\partial R}{\partial e} \\
\frac{dM}{dt} &= n - \frac{\left(1-e^2\right)}{na^2 e}\frac{\partial R}{\partial e} - \frac{2}{na}\frac{\partial R}{\partial a}
\end{aligned} \tag{1}$$

that can be written in condense form as

$$\frac{d\boldsymbol{\alpha}}{dt} = f\left(\boldsymbol{\alpha}, \frac{\partial R}{\partial \boldsymbol{\alpha}}\right) \tag{2}$$

where $\boldsymbol{\alpha}$ is here used as the condensed form of the Keplerian elements $\boldsymbol{\alpha} = \left[a\ e\ i\ \Omega\ \omega\ M\right]^T$, where a is the semi-major axis, e the eccentricity, i the inclination, Ω the right ascension of the ascending node, ω the argument of the perigee and M the mean anomaly. Through single averaging operation, the potential can be replaced by the orbit-averaged form of the disturbing function:

$$\bar{R} = \bar{R}_{\text{zonal}} + \bar{R}_{3-\text{Sun}} + \bar{R}_{3-\text{Moon}} \tag{3}$$

obtained under the assumption that the orbital elements are constant over one orbit revolution of the spacecraft around the central planet. Therefore, the variation of the mean elements is described by:

$$\frac{d\overline{\boldsymbol{\alpha}}}{dt} = g\left(\overline{\boldsymbol{\alpha}}, \frac{\partial \bar{R}}{\partial \boldsymbol{\alpha}}\right) \tag{4}$$

where now $\bar{\alpha}$ is the vector of the averaged orbital elements.

Luni-Solar Averaged Potential

For describing the effects of luni-solar third body perturbations, we follow the approach proposed by Kaufman and Dasenbrock (1972). Their approach is summarized in this section as is fundamental to give an insight into the orbital dynamics that is exploited in section Luni-Solar and Zonal Harmonics Maps. The disturbing potential due to the third body perturbation is (Murray and Dermott, 1999):

$$R\left(r, r'\right) = \mu'\left(\frac{1}{|\mathbf{r}-\mathbf{r}'|} - \frac{\mathbf{r}\cdot\mathbf{r}'}{r'^3}\right) \tag{5}$$

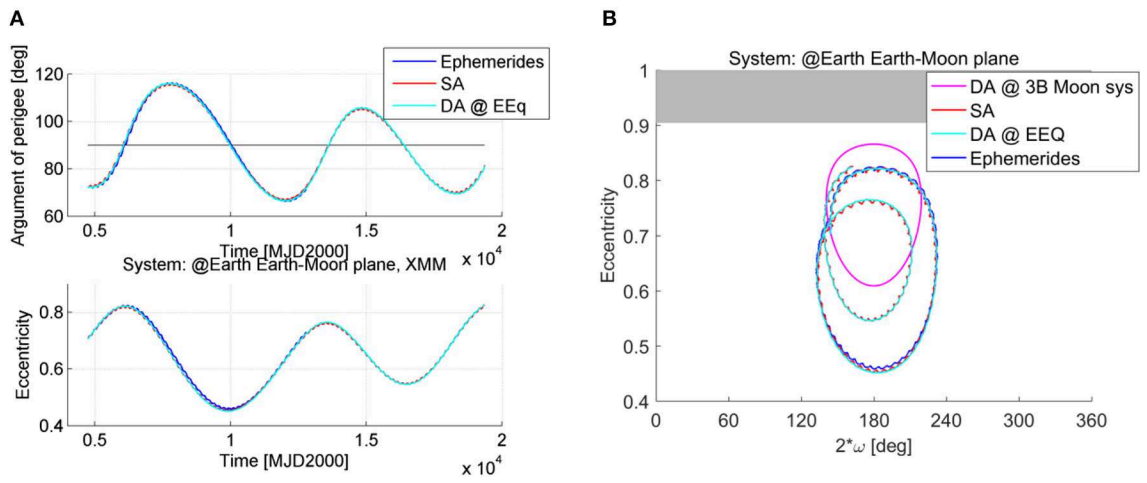

FIGURE 3 | Evolution of a high altitude orbit under the effect of luni-solar and zonal perturbations. **(A)** Comparison of the actual ephemerides (blue) with single averaged (red) and double averaged (cyan) dynamics. **(B)** Evolution in the eccentricity-2ω phase space, where the argument of the perigee is measured with respect to the Moon plane.

where μ' is the gravitational coefficient of the third body, $\mathbf{r}$ and $\mathbf{r}'$ are the position vectors of the satellite and the third body with respect to the central planet, respectively, as represented in **Figure 1**. Equation (5) can be expressed as function of the angle ψ between $\mathbf{r}$ and $\mathbf{r}'$ if the cosine rule is exploited in the first term of Equation (5) and the dot product in the second term is resolved (Murray and Dermott, 1999):

$$R\left(r,r'\right)=\frac{\mu'}{r'}\left(\left(1-2\frac{r}{r'}\cos\psi+\left(\frac{r}{r'}\right)^2\right)^{-1/2}-\frac{r}{r'}\cos\psi\right) \quad (6)$$

where

$$\cos\psi=\frac{\mathbf{r}\cdot\mathbf{r}'}{rr'}$$

Kaufman and Dasenbrock (1972) express the disturbing potential as function of the spacecraft's orbital elements, choosing as angular variable the eccentric anomaly E, the ratio between the orbit semi-major axis and the distance to the third body r':

$$\delta=\frac{a}{r'}$$

and the orientation of the orbit eccentricity vector with respect to the third body (Kaufman and Dasenbrock, 1972):

$$A=\hat{\mathbf{P}}\cdot\hat{\mathbf{r}}'$$
$$B=\hat{\mathbf{Q}}\cdot\hat{\mathbf{r}}'$$

where the eccentricity unit vector $\hat{\mathbf{P}}$, the semilatus rectum unit vector $\hat{\mathbf{Q}}$, and the unit vector to the third body $\hat{\mathbf{r}}'$ are expressed with respect to the equatorial inertial system, through the following composition of rotations (Kaufman and Dasenbrock, 1972; Lara et al., 2012):

$$\hat{\mathbf{P}}=\Re_3\left(\Omega\right)\Re_1\left(i\right)\Re_3\left(\omega\right)\cdot\left[1\ 0\ 0\right]^T$$

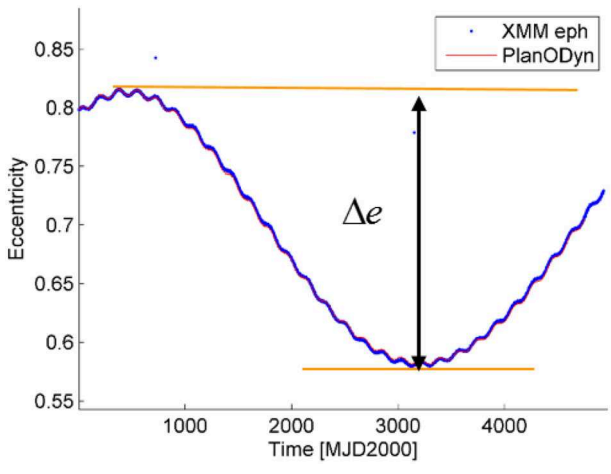

FIGURE 4 | XMM-Newton orbit evolution and minimum and maximum eccentricity attained during the motion evolution. Blue line: actual ephemerides, red line: propagation with PlanODyn.

$$\hat{\mathbf{R}}=\Re_3\left(\Omega\right)\Re_1\left(i\right)\Re_3\left(\omega+\pi/2\right)\cdot\left[1\ 0\ 0\right]^T$$
$$\hat{\mathbf{r}}'=\Re_3\left(\Omega'\right)\Re_1\left(i'\right)\Re_3\left(u'\right)\cdot\left[1\ 0\ 0\right]^T \quad (7)$$

where R_1 represents the rotation matrix around the x axis, R_2 the rotation matrix around y axis and R_3 the rotation matrix around the z axis. The full expression of $\hat{\mathbf{P}}$, $\hat{\mathbf{Q}}$, and $\hat{\mathbf{r}}'$ in terms of Keplerian elements can be found in Chao-Chun (2005). The variables Ω', ω', i', and f' in Equation (7) are, respectively, the right ascension of the ascending node, the argument of the perigee, the inclination and the true anomaly of the perturbing body on its orbit (described with respect to the Earth-centered equatorial reference frame) and $u'=\omega'+f'$. Under the assumption that the parameter δ is small (i.e., the spacecraft is far enough from the perturbing body), Equation (6) can be rewritten as a Taylor series in δ as Kaufman and Dasenbrock (1972):

$$R\left(r,r'\right)=\frac{\mu'}{r'}\sum_{k=2}^{\infty}\delta^k F_k\left(A,B,e,E\right)$$

Note that the summation starts from $k=2$ as the term zero of the series is influent as is a constant, while the term 1 simplifies with the second term of Equation (6). The average operation in eccentric anomaly, passing through the mean anomaly via $dM=(1-e\cos E)\,dE$ can then be performed, assuming that the orbital elements of the spacecraft a, e, i, Ω, and ω are constant over one orbit revolution:

$$\bar{F}_k\left(A,B,e\right)=\frac{1}{2\pi}\int_{-\pi}^{\pi}F_k\left(A,B,e,E\right)\left(1-e\cos E\right)dE$$

to obtain:

$$\bar{R}\left(r,r'\right)=\frac{\mu'}{r'}\sum_{k=2}^{\infty}\delta^k\bar{F}_k\left(A,B,e\right) \quad (8)$$

where the averaged terms $\bar{F}_k\left(A,B,e\right)$ are reported in Kaufman and Dasenbrock (1972) and in **Appendix** in a more compact form. Note that the term 2 of Equation (8) is the one given by Chao-Chun (2005). Equation (8) can be now inserted into the Lagrange equations by computing the partial derivatives with respect to the orbital elements, considering that the dependences of the terms in Equation (8) are: $A\left(\Omega,i,\omega,\Omega',i',\omega'+f'\right)$, $B\left(\Omega,i,\omega,\Omega',i',\omega'+f'\right)$, and $\bar{R}_k\left(A,B,e\right)$ (see **Appendix** for details).

$$\begin{aligned}
\frac{\partial\bar{F}_k}{\partial\Omega}&=\frac{\partial\bar{F}_k}{\partial A}\frac{\partial A}{\partial\Omega}+\frac{\partial\bar{F}_k}{\partial B}\frac{\partial B}{\partial\Omega}\\
\frac{\partial\bar{F}_k}{\partial i}&=\frac{\partial\bar{F}_k}{\partial A}\frac{\partial A}{\partial i}+\frac{\partial\bar{F}_k}{\partial B}\frac{\partial B}{\partial i}\\
\frac{\partial\bar{F}_k}{\partial\omega}&=\frac{\partial\bar{F}_k}{\partial A}\frac{\partial A}{\partial\omega}+\frac{\partial\bar{F}_k}{\partial B}\frac{\partial B}{\partial\omega}\\
\frac{\partial\bar{F}_k}{\partial a}&=\frac{k}{a}\bar{R}_k\\
\frac{\partial\bar{F}_k}{\partial e}&
\end{aligned} \quad (9)$$

The derivatives up to the 8th order of the Taylor series are reported by Kaufman and Dasenbrock (1972); we report them in **Appendix** in a more concise form up to order 6th.

Earth Zonal Harmonic Potential

The disturbing function of the zonal harmonic potential is expressed also in terms of classical orbital elements. The zonal harmonics were modeled up to order 6 considering also the J_2^2 term (Blitzer, 1970; Liu and Alford, 1980). We report here only the term associated with J_2 that is the one most important one for the application considered in this work. However, all the terms were retained in the orbit propagation.

$$\bar{R}_{J_2} = W\frac{na^2}{6}\frac{3\cos^2 i - 1}{\left(1-e^2\right)^{3/2}}$$

where W is the oblateness parameter

$$W = \frac{3}{2}J_2\frac{R_{\text{Earth}}^2}{a^2}n$$

where $J_2 = 1.083 \cdot 10^{-3}$ denotes the second zonal harmonic coefficient and R_{Earth} is the mean radius of the Earth. $n = \sqrt{\mu_{\text{Earth}}/a^3}$ is the orbit angular velocity of the spacecraft on its orbit, with μ_{Earth} the gravitational constant of the Earth.

Model Validation

The averaged dynamical model described in section Orbit Evolution With Single-Averaged Disturbing Potential was validated by comparison with the actual ephemerides of two artificial satellites in highly-elliptical orbit: INTEGRAL and XMM-Newton. The orbit of INTEGRAL was used in Colombo et al. (2014a) and validated against the ephemerides from the NASA-Horizon system. XMM-Newton orbit was propagated in the time span from 1999/12/15 to 2013/01/01 with the initial Keplerian elements on 1999/12/15 at 15:00 as: $a = 67045$ km, $e = 0.7951$, $i = 0.67988$ rad, $\Omega = 4.1192$ rad, $\omega = 0.99259$ rad, true anomaly $f = 3.2299$ rad, and radius of the perigee 13,737 km. **Figure 2** shows the results of the validation with the actual ephemerides form ESA (2013) (blue line). Luni-solar and Earth zonal harmonics perturbations are included in this validation with PlanODyn (red line) (Colombo, 2016). The reference system used is inertial, centered at the Earth, on the Earth equator.

Orbit Evolution With Double-Averaged Disturbing Potential

Under the further assumption that the orbital elements do not change significantly during a full revolution of the perturbing body around the central body (i.e., Earth), the variation of the orbit over time can be approximately described through the disturbing potential double averaged over one orbit evolution of the s/c and over one orbital revolution of the perturbing body (either the Moon or the Sun) around the Earth. The terms of the disturbing potential due to the third body effect in Equation (3) can be substituted by the double-averaged one $\bar{\bar{R}}_{3-\text{Sun}}$ and $\bar{\bar{R}}_{3-\text{Moon}}$:

$$\bar{\bar{R}} = \bar{R}_{\text{zonal}} + \bar{\bar{R}}_{\text{3B-Sun}} + \bar{\bar{R}}_{\text{3B-Moon}} \tag{10}$$

$$\bar{\bar{R}}_{\text{3B}}\left(r, r'\right) = \frac{\mu'}{r'}\sum_{k=2}^{\infty}\delta^k\bar{\bar{F}}_k\left(e, i, \Omega, \omega, i'\right) \tag{11}$$

In this work we decided to express the double-averaged potential with respect to the Keplerian elements described in the Earth's centered equatorial reference system. This will give a more complex expression for the potential in Equation (11), with respect to the one by El'yasberg (1967) and Costa and Prado (2000) but it has the advantage of avoiding the simplification that Moon and Sun orbit on the same plane and facilitating the introduction of the effect of the zonal harmonics.

The terms of the third body potential are obtained starting from the single-averaged terms, performing the averaging operation $\bar{\bar{F}}_k\left(A, B, e\right)$.

$$\bar{\bar{F}}_k\left(e, i, \Delta\Omega, \omega, i'\right) = \frac{1}{2\pi}\int_0^{2\pi}\bar{F}_k\left(A\left(\Omega, i, \omega, \Omega', i', \omega' + f'\right), B\left(\Omega, i, \omega, \Omega', i', \omega' + f'\right), e\right)df'$$

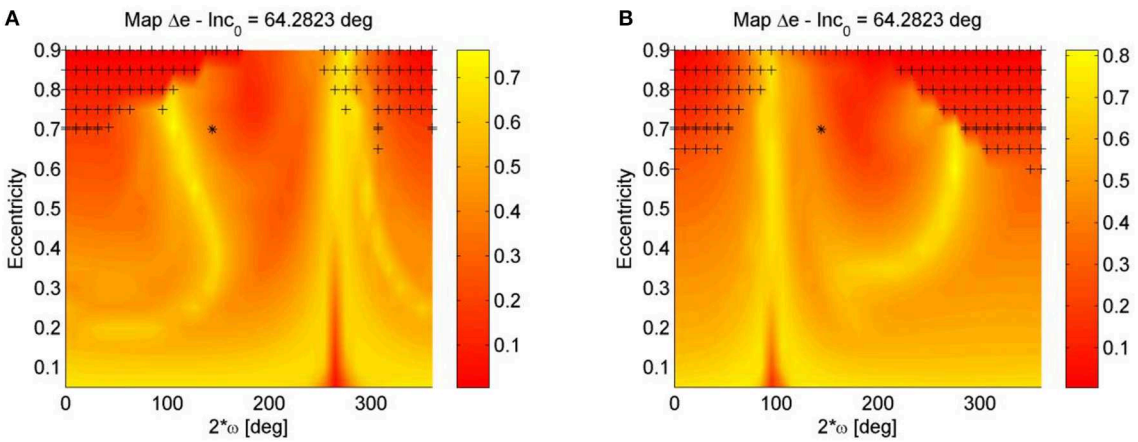

FIGURE 5 | Luni-solar + zonal Δe maps for XMM Newton orbit: **(A)** Forward propagation, and **(B)** backward propagation. The initial inclination and the argument of the perigee are measured with respect to the Moon's plane.

where $\Delta\Omega = \Omega - \Omega'$. The term up to order four of the potential were computed; only the second term $\bar{\bar{F}}_2$ is reported here as $\bar{\bar{F}}_3 = 0$:

$$\begin{aligned}\bar{\bar{F}}_2 = & \frac{1}{128} \cdot \left(\cos\left(2i'\right)\left(6 + 9e^2 + 90e^2\cos\left(2\omega\right)\sin^2 i\right)\right. \\ & + \left(2 + 3e^2 + 15e^2\cos\left(2\omega\right)\right)\left(1 + 6\cos\left(2\Delta\Omega\right)\sin^2 i'\right) \\ & + 3\cos\left(2i\right)\left(\left(6 + 9e^2\right)\cos\left(2i'\right) + \left(-2 - 3e^2 + 5e^2\cos\left(2\omega\right)\right)\right. \\ & \left.\left(-1 + 2\cos\left(2\Delta\Omega\right)\sin^2 i'\right)\right) \\ & 12\left(2 + 3e^2 - 5e^2\cos\left(2\omega\right)\right)\cos\left(2\Delta\Omega\right)\sin\left(2i\right)\sin\left(2i'\right) \\ & + 120e^2\sin i\sin\left(2i'\right)\sin\left(2\omega\right)\sin\left(\Delta\Omega\right) - \\ & \left.120e^2\cos i\sin^2 i'\, sin\left(2\omega\right)\sin\left(2\Delta\Omega\right)\right) \end{aligned} \quad (12)$$

The evolution of the orbit in time can be then computed computing the partial derivatives of Equation (10) and substituting them into the Lagrange form of planetary equations Equations (1).

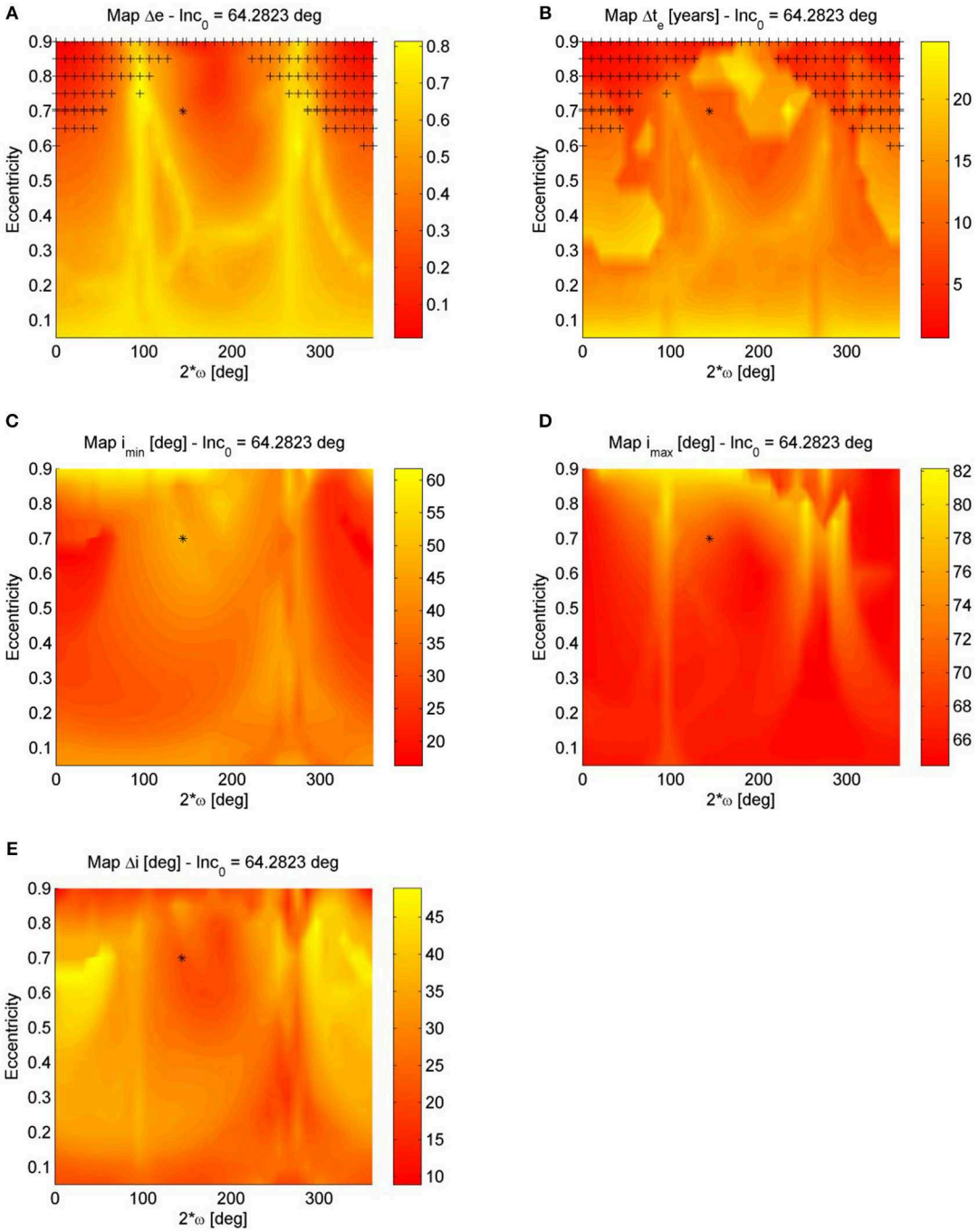

FIGURE 6 | Luni-solar + zonal maps for semi-major axis of XMM Newton orbit a = 67045.39 km: **(A)** Δe map, **(B)** Δt_e map, **(C)** $i_{\min}$ map, **(D)** $i_{\max}$ map, and **(E)** Δi map. The initial inclination and the argument of the perigee are measured with respect to the Moon's plane.

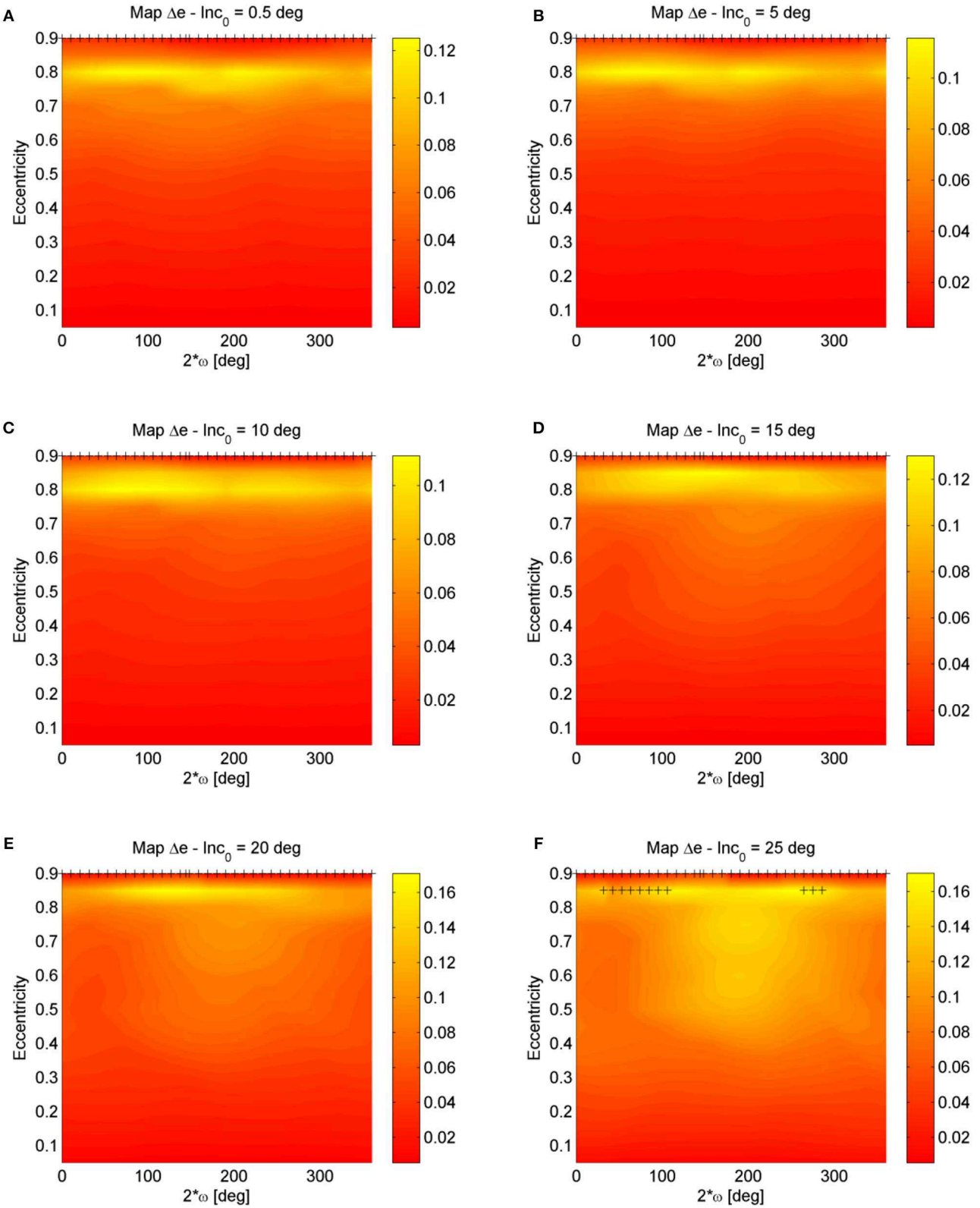

FIGURE 7 | Continued

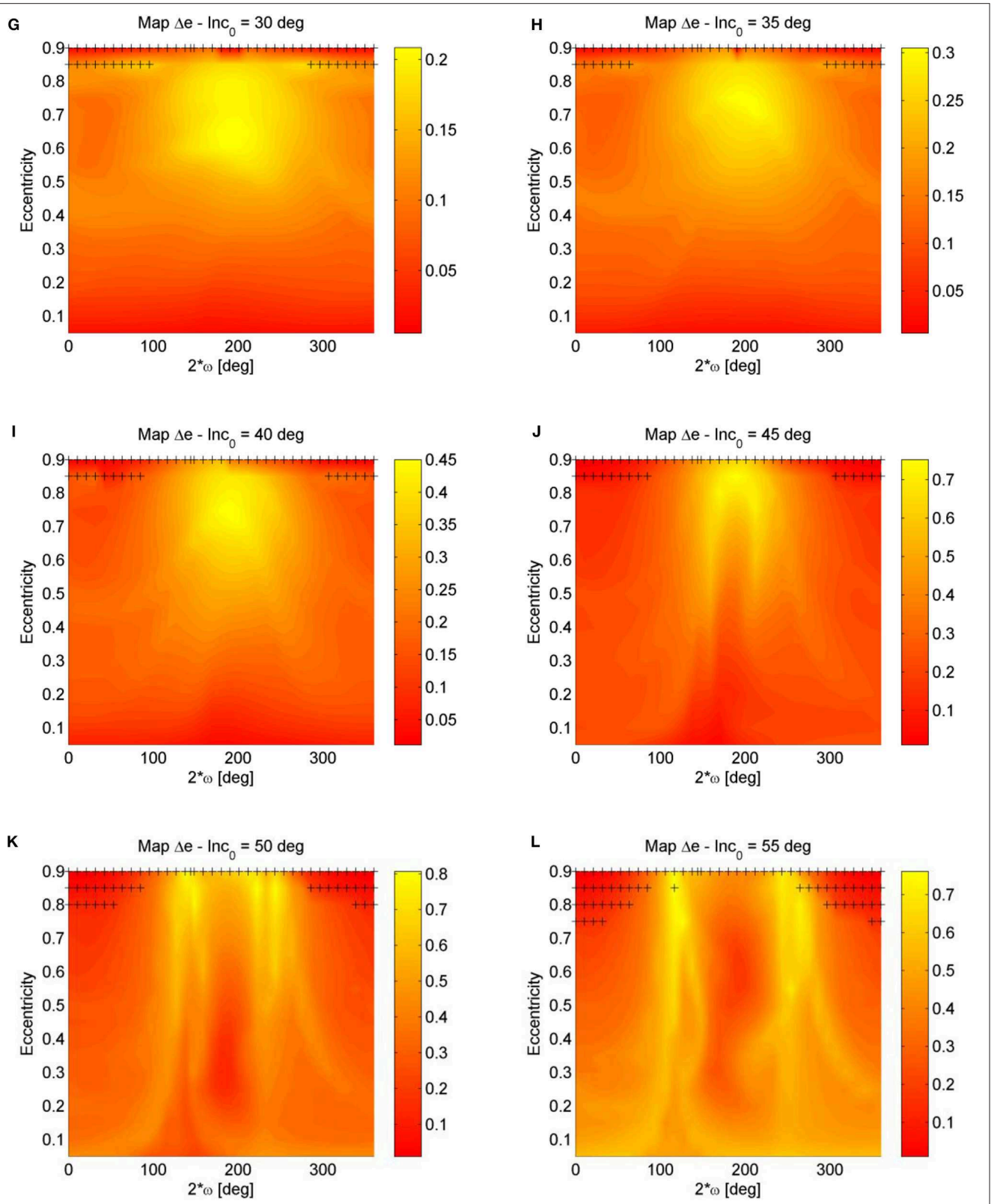

FIGURE 7 | Continued

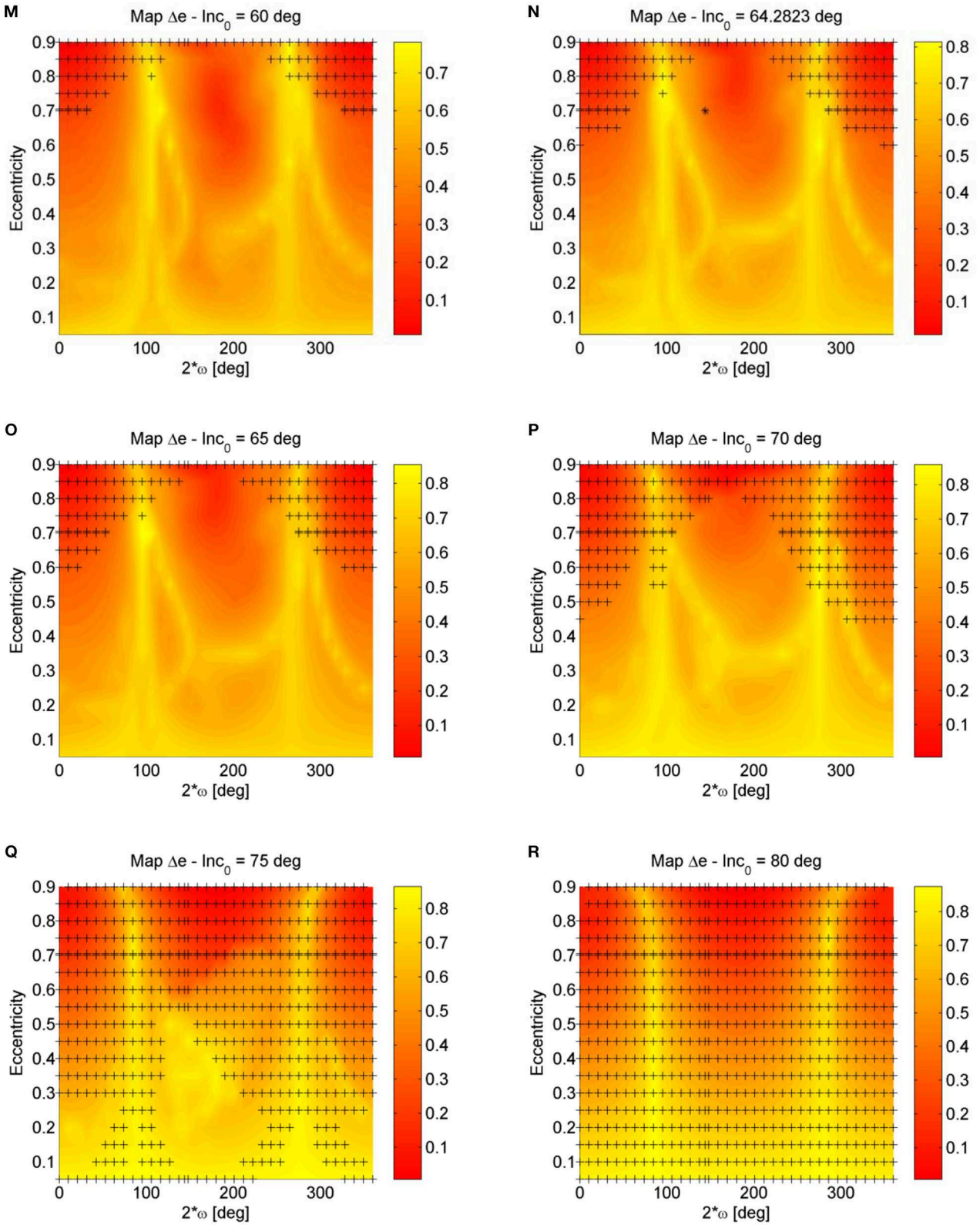

FIGURE 7 | Continued

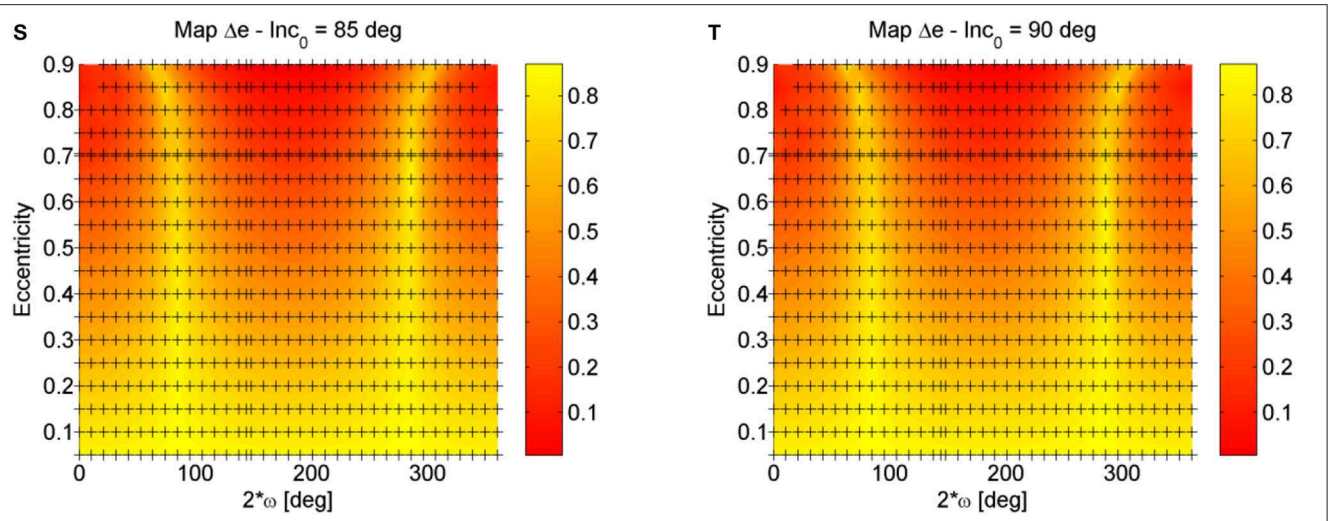

FIGURE 7 | Luni-solar + zonal Δe maps for semi-major axis equal to 67045.39 km (XMM Newton's orbit) for different values of initial inclination with respect to the orbiting plane of the Moon. The initial inclination and the argument of the perigee are measured with respect to the Moon's plane. **(A)** Initial inclination = 0.5 deg. **(B)** Initial inclination = 5 deg. **(C)** Initial inclination = 10 deg. **(D)** Initial inclination = 15 deg. **(E)** Initial inclination = 20 deg. **(F)** Initial inclination = 25 deg. **(G)** Initial inclination = 30 deg. **(H)** Initial inclination = 35 deg. **(I)** Initial inclination = 40 deg. **(J)** Initial inclination = 45 deg. **(K)** Initial inclination = 50 deg. **(L)** Initial inclination = 55 deg. **(M)** Initial inclination = 60 deg. **(N)** Initial inclination = 64.2823 deg. **(O)** Initial inclination = 65 deg. **(P)** Initial inclination = 70 deg. **(Q)** Initial inclination = 75 deg. **(R)** Initial inclination = 80 deg. **(S)** Initial inclination = 85 deg. **(T)** Initial inclination = 90 deg.

Note that, with the same procedure, the double averaged disturbing potential can be also written in the form proposed by El'yasberg (1967) and Costa and Prado (2000). A different reference system needs to be used, which is still centered at the central body (i.e., Earth) but the x-y plane lay on the perturbing body orbital plane, with its x-axis in the direction of the perturbing body on its orbit, the z-axis in the direction of the perturbing body angular momentum, and the y-axis that completes the reference system. The corresponding orbital elements are $\boldsymbol{\alpha}_{3\text{Bsys}} = \left[a_{3\text{Bsys}}\ e_{3\text{Bsys}}\ i_{3\text{Bsys}}\ \Omega_{3\text{Bsys}}\ \omega_{3\text{Bsys}}\ M_{3\text{Bsys}}\right]^T$. It is interesting to note that this rotating reference system is equivalent to the synodic system used in the circular restricted three-body problem.

In this case the eccentricity unit vector $\hat{\mathbf{P}}_{3\text{Bsys}}$, the semilatus rectum unit vector $\hat{\mathbf{Q}}_{3\text{Bsys}}$ and the unit vector to the third body $\hat{\mathbf{r}}'_{3\text{Bsys}}$ have to be expressed with respect to the third body rotating system, through the following composition of rotations

$$\begin{aligned}
\hat{\mathbf{P}}_{3\text{Bsys}} &= \Re_3\left(\Omega_{3\text{Bsys}}\right)\Re_1\left(i_{3\text{Bsys}}\right)\Re_3\left(\omega_{3\text{Bsys}}\right)\cdot\left[1\ 0\ 0\right]^T \\
\hat{\mathbf{R}}_{3\text{Bsys}} &= \Re_3\left(\Omega_{3\text{Bsys}}\right)\Re_1\left(i_{3\text{Bsys}}\right)\Re_3\left(\omega_{3\text{Bsys}}+\pi/2\right)\cdot\left[1\ 0\ 0\right]^T \\
\hat{\mathbf{r}}'_{3\text{Bsys}} &= \Re_3\left(0\right)\Re_1\left(0\right)\Re_3\left(0\right)\cdot\left[1\ 0\ 0\right]^T = \left[1\ 0\ 0\right]^T
\end{aligned} \tag{13}$$

where $\Omega_{3\text{Bsys}} = \Omega_{3\text{Bsys},\,0} - u'$. By using Equations (13), the new expressions of $A_{3\text{Bsys}}$ and $B_{3\text{Bsys}}$ are found as

$$\begin{aligned}
A_{3\text{Bsys}} &= \hat{\mathbf{P}}_{3\text{Bsys}}\cdot\hat{\mathbf{r}}'_{3\text{Bsys}} \\
B_{3\text{Bsys}} &= \hat{\mathbf{Q}}_{3\text{Bsys}}\cdot\hat{\mathbf{r}}'_{3\text{Bsys}}
\end{aligned}$$

that are function of $A_{3\text{Bsys}}\left(u'-\Omega_{3\text{Bsys}}, i_{3\text{Bsys}}, \omega_{3\text{Bsys}}\right)$, $B_{3\text{Bsys}}\left(u'-\Omega_{3\text{Bsys}}, i_{3\text{Bsys}}, \omega_{3\text{Bsys}}\right)$ so that the doubly averaged potential loses the dependence on the right ascension of the ascending node,

$$\begin{aligned}
&\bar{\bar{F}}_{3\text{Bsys},\,k}\left(e_{3\text{Bsys}}, i_{3\text{Bsys}}, \omega_{3\text{Bsys}}\right) \\
&= \frac{1}{2\pi}\int_0^{2\pi}\bar{F}_{3\text{Bsys},\,k}\left(A_{3\text{Bsys}}\left(u'-\Omega_{3\text{Bsys}}, i_{3\text{Bsys}}, \omega_{3\text{Bsys}}\right),\right. \\
&\left. B_{3\text{Bsys}}\left(u'-\Omega_{3\text{Bsys}}, i_{3\text{Bsys}}, \omega_{3\text{Bsys}}\right), e_{3\text{Bsys}}\right)du'.
\end{aligned}$$

So equivalently to Equation (12), we can compute the terms 2 to 4 were we dropped the subscript 3BSys.

$$\bar{\bar{F}}_{3\text{Bsys},\,2} = \frac{1}{32}\left(\left(2+3e^2\right)\left(1+3\cos\left(2i\right)\right)+30e^2\cos\left(2\omega\right)\sin^2 i\right)$$

$$\bar{\bar{F}}_{3\text{Bsys},\,3} = 0$$

$$\begin{aligned}
\bar{\bar{F}}_{3Bsys,\,4} = \frac{9}{32768}&\left(\left(8+40e^2+15e^4\right)\left(9+20\cos\left(2i\right)+35\cos\left(4i\right)\right)\right. \\
&+560e^2\left(2+e^2\right)\left(5+7\cos\left(2i\right)\right)\cos\left(2\omega\right)\sin^2 i \\
&\left.+\ 5880e^4\cos\left(4\omega\right)\sin^4 i\right)
\end{aligned}$$

that are equivalent to the expression in El'yasberg (1967) and Costa and Prado (2000). If the partial derivatives of Equation (11) are inserted into the Lagrange form of planetary equations we get the expression of variation of elements double-averaged over one orbit evolution of the s/c and over one orbital revolution of the perturbing body (either the Moon or the Sun). **Figure 3** compares the evolution of a high-altitude orbit using the single averaged dynamics (red line) and the double averaged dynamics (cyan line) in eccentricity and argument of the perigee with respect to the Moon plane. It is interesting to see the evolution in the phase space of eccentricity and argument of the perigee measured with respect to the Moon orbiting plane as done in Ely (2005) and Colombo et al. (2014a). For the initial conditions in **Figure 3**, the simplified model by

El'yasberg (1967) and Kozai (1962) predicts a pure librational orbit (Ely, 2005) (magenta line) which, in reality, is corrupted by the coupling between Moon and Sun third-body effect and by the effect of J_2 (see the red and cyan lines). The double averaged propagation derived in Equation (12) is used for the Moon and the Sun in Equation (10) for obtaining the orbit propagation represented with the cyan line, while the single averaged propagation described in sections Luni-Solar Averaged Potential and Earth Zonal Harmonic Potential is used for obtaining the orbit propagation represented with the red line. The single and double average propagation are compared against the actual spacecraft ephemerides from the NASA Horizon system in blue. Both the single and the double averaged approach show very good accuracy against the real ephemerides. With

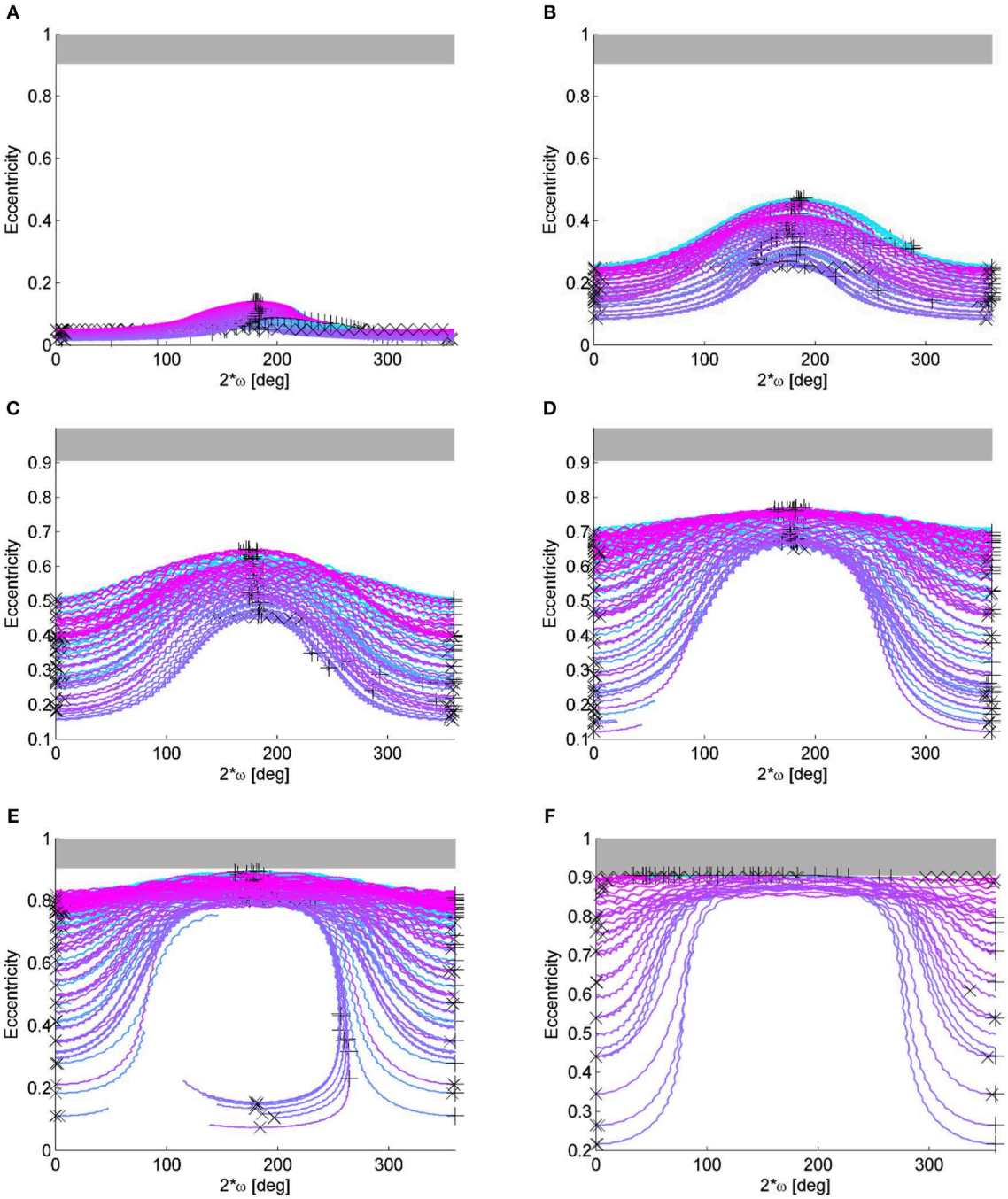

FIGURE 8 | Maps for initial inclination with respect to the Moon's plane of 45° and semi-major axis equal to 67045.39 km. The initial inclination and the argument of the perigee are measured with respect to the Moon's plane. **(A)** Eccentricity-2ω plot for $e_0 = 0.05$. **(B)** Eccentricity-2ω plot for $e_0 = 0.25$. **(C)** Eccentricity-2ω plot for $e_0 = 0.45$. **(D)** Eccentricity-2ω plot for $e_0 = 0.65$. **(E)** Eccentricity-2ω plot for $e_0 = 0.8$. **(F)** Eccentricity-2ω plot for $e_0 = 0.9$.

respect to the pure librational loop predicted by the Lidov-Kozai dynamics, still a quasi-librational behavior can be noted and will be further studied in the next section through propagation via the single-averaged dynamics.

LUNI-SOLAR AND ZONAL HARMONICS MAPS

To the purpose of studying the long term evolution of many initial conditions, a grid was built in the domain of inclination, eccentricity and argument of the perigee. Equally spaced steps in initial eccentricity (19 steps between 0.05 and 0.9), initial inclination (20 steps between 0.5° and 90°) and initial right ascension of the ascending node (36 steps between 0° and 180°) were selected as starting points. Note that, inclination and argument of the perigee are here described with respect to the Moon plane reference system; in other words i is the inclination of the spacecraft orbit with respect to the Moon's orbit plane and ω is the argument of the perigee measured from the direction of the ascending node of the spacecraft's orbit with respect to the Moon's orbit plane. Each initial condition on the grid is propagated over 30 years with the tool PlanODyn (Colombo, 2016) using the single averaged dynamics. As mentioned before, only luni-solar and zonal harmonics perturbations are here taken into account as we want to analyze their interaction. For each initial condition we evaluate the change between the minimum and the maximum eccentricity that the spacecraft will attain during its motion (see **Figure 4**):

$$\Delta e = e_{\max} - e_{\min} \tag{14}$$

with

$$\begin{aligned} e_{\max} &= \max_t e(t) \quad t \in \left[0 \;\; \Delta t_{\text{disposal}} \right] \\ e_{\min} &= \min_t e(t) \quad t \in \left[0 \;\; \Delta t_{\text{disposal}} \right] \end{aligned} \tag{15}$$

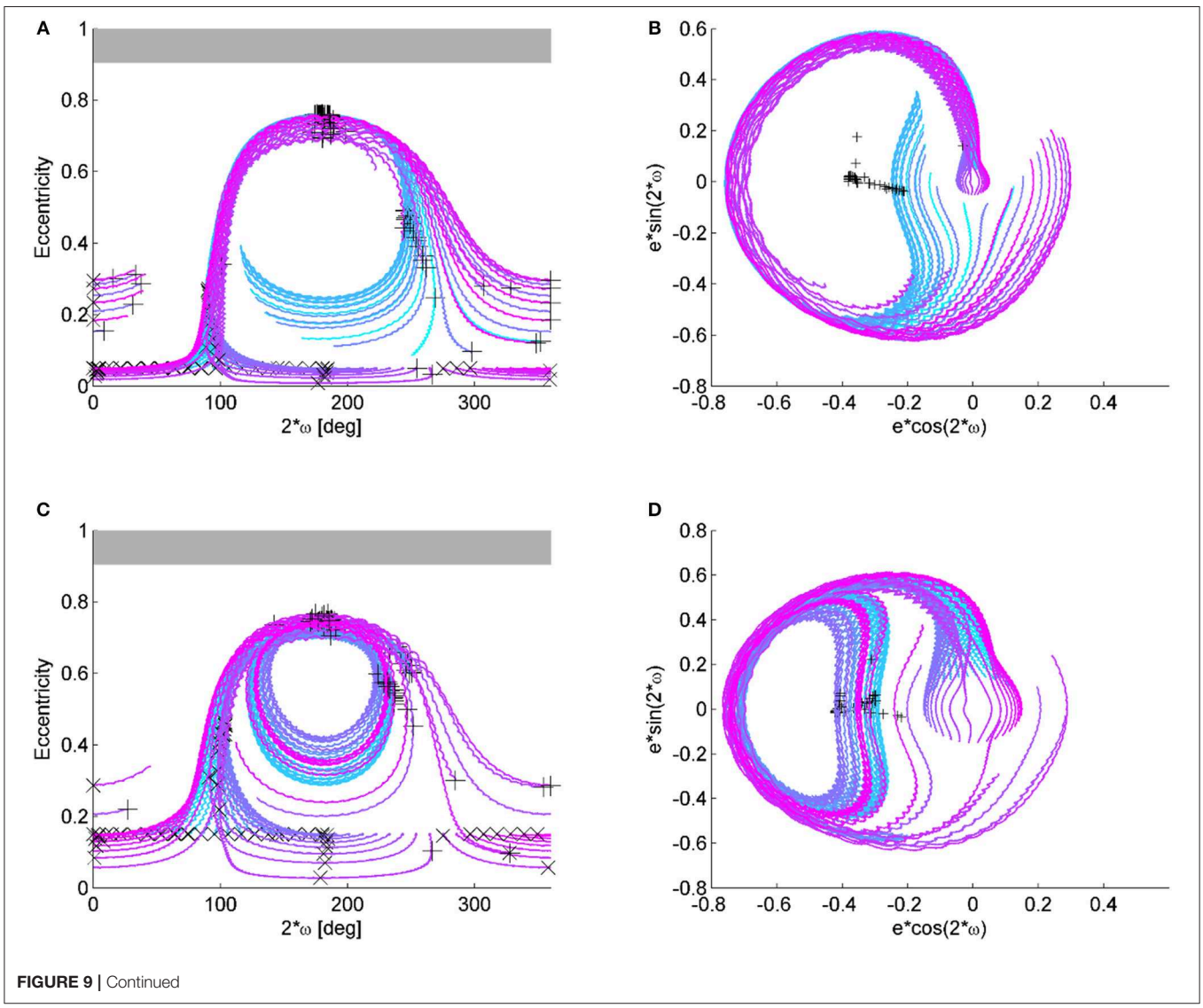

FIGURE 9 | Continued

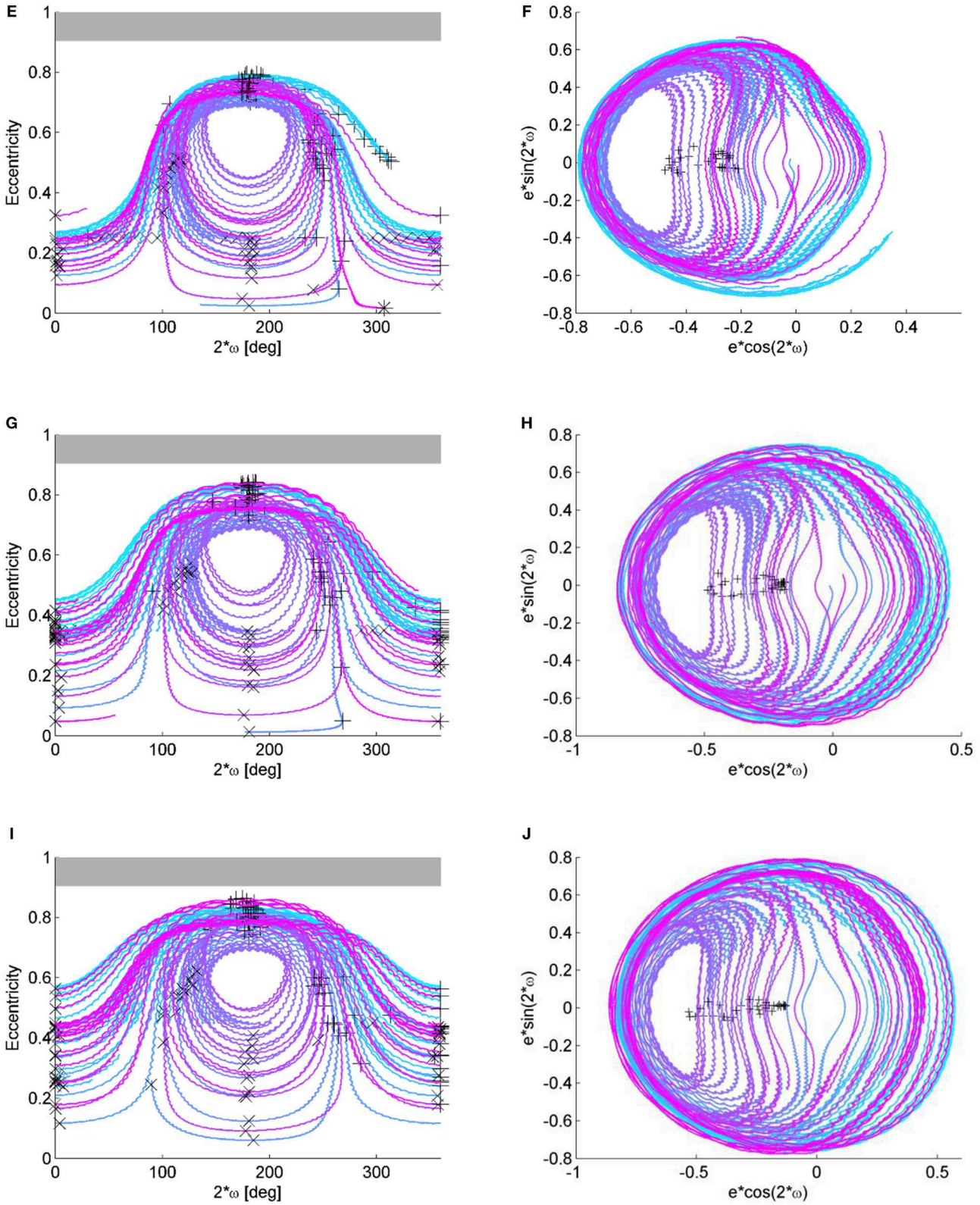

FIGURE 9 | Continued

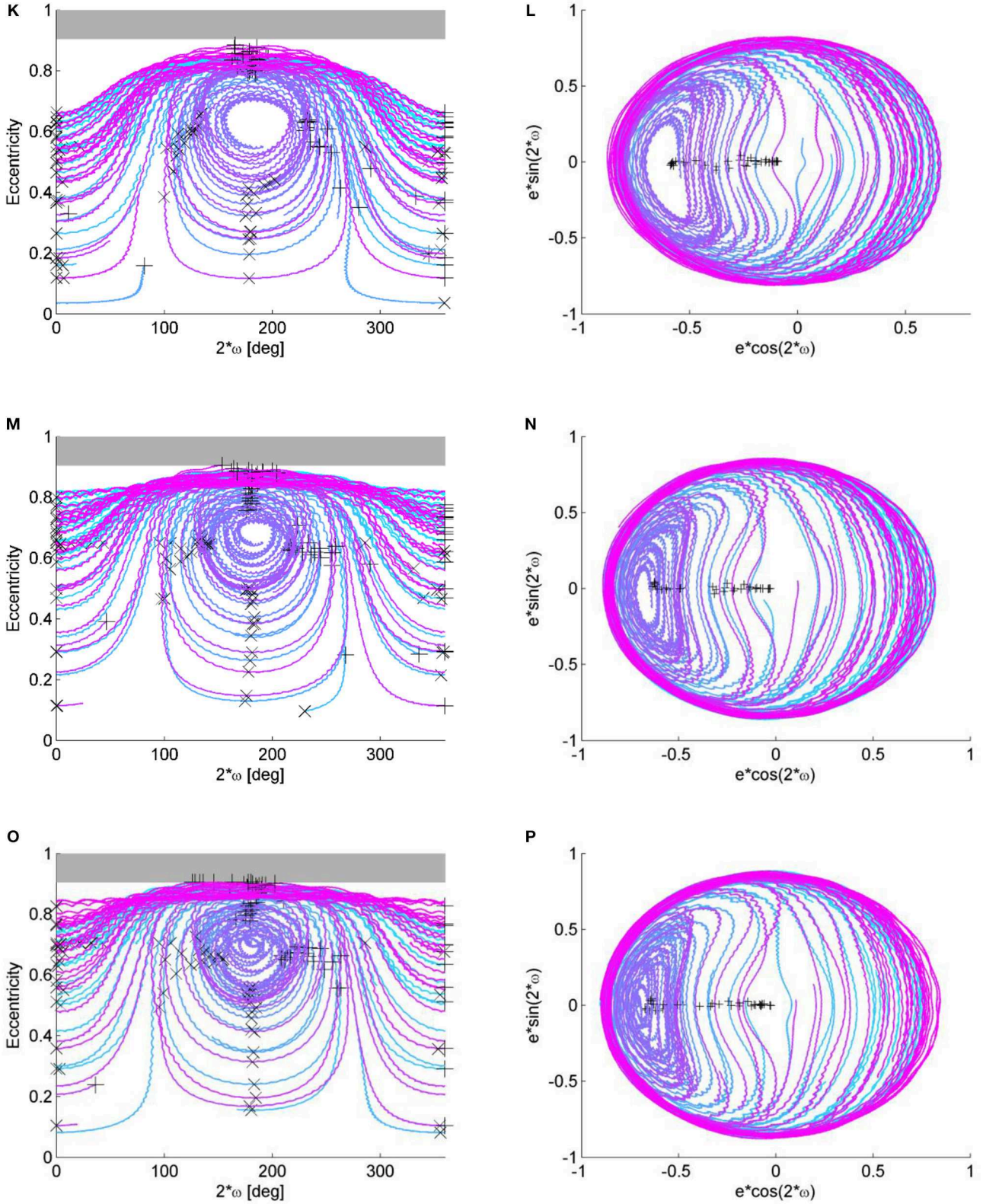

FIGURE 9 | Continued

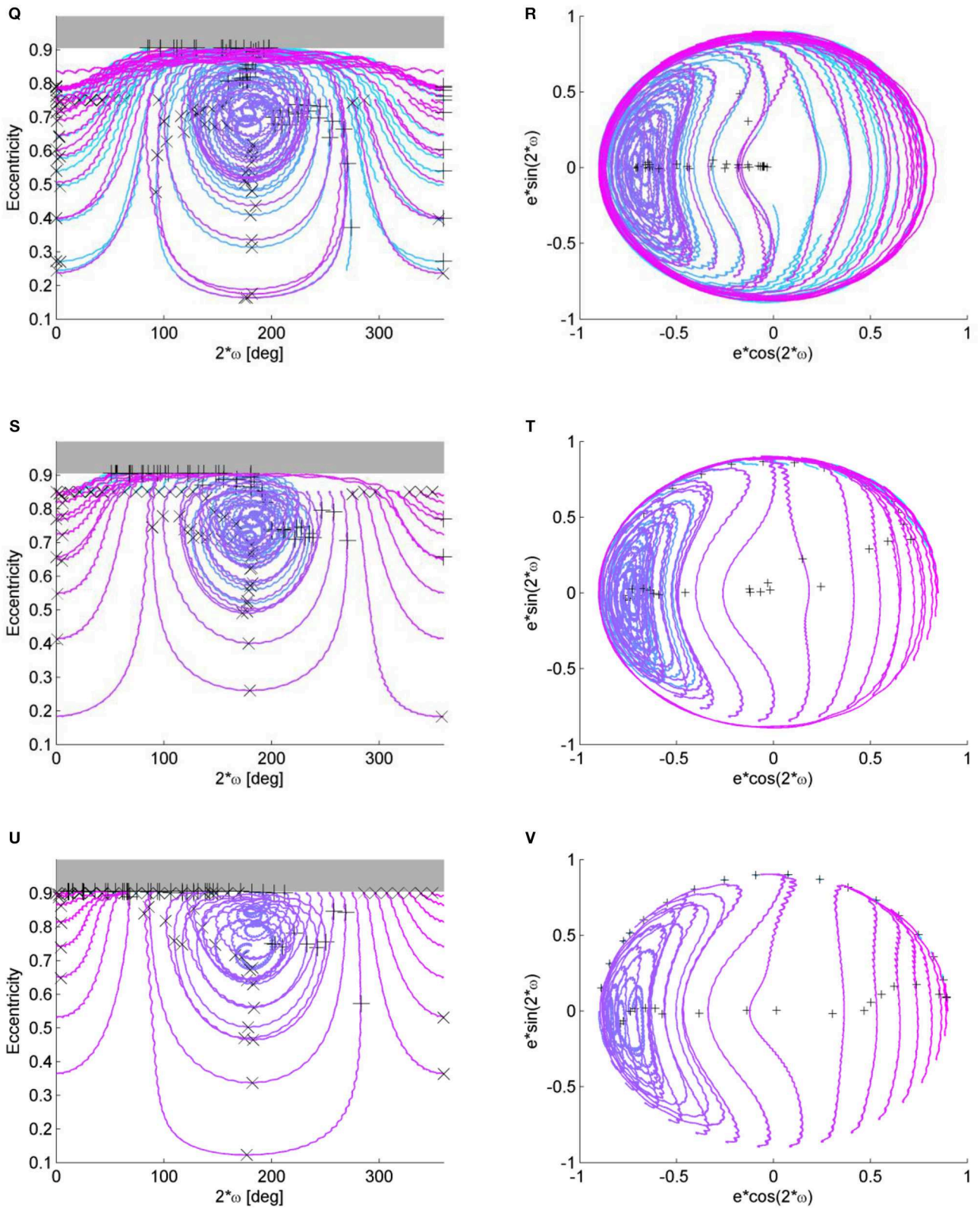

FIGURE 9 | Maps for initial inclination with respect to the Moon's plane of 64.28° and semi-major axis equal to 67045.39 km. The initial inclination and the argument of the perigee are measured with respect to the Moon plane. **(A)** Eccentricity-2ω plot: $e_0 = 0.05$. **(B)** Polar plot: $e_0 = 0.05$. **(C)** Eccentricity-2ω plot: $e_0 = 0.15$. **(D)** *(Continued)*

FIGURE 9 | Polar plot: $e_0 = 0.15$. **(E)** Eccentricity-2ω plot: $e_0 = 0.25$. **(F)** Polar plot: $e_0 = 0.25$. **(G)** Eccentricity-2ω plot: $e_0 = 0.35$. **(H)** Polar plot: $e_0 = 0.35$. **(I)** Eccentricity-2ω plot: $e_0 = 0.45$. **(J)** Polar plot: $e_0 = 0.45$. (K) Eccentricity-2ω plot: $e_0 = 0.55$. **(L)** Polar plot: $e_0 = 0.55$. **(M)** Eccentricity-2ω plot: $e_0 = 0.65$. **(N)** Polar plot: $e_0 = 0.65$. **(O)** Eccentricity-2ω plot: $e_0 = 0.705$. **(P)** Polar plot: $e_0 = 0.705$. **(Q)** Eccentricity-2ω plot: $e_0 = 0.75$. **(R)** Polar plot: $e_0 = 0.75$. **(S)** Eccentricity-2ω plot: $e_0 = 0.85$. **(T)** Polar plot: $e_0 = 0.85$. **(U)** Eccentricity-2ω plot: $e_0 = 0.90$. **(V)** Polar plot: $e_0 = 0.90$.

setting $\Delta t_{\text{disposal}} = 30$ years. As introduced the idea will be then to select limited Δe for graveyard disposal orbits or, at the opposite, maximum Δe orbits can be exploited for disposal through re-entry or for passive orbit transfer by exploiting the effects of perturbations.

Figure 5 represents the result of the forward (a) and backward (b) integration for 30 years using, as initial conditions, the semi-major axis of XMM-Newton orbit, i.e., 67045.39 km, and different values of initial eccentricity and argument of the perigee in the grid, measured in the Moon reference system. The initial condition in terms of inclination and eccentricity corresponding to the one of the XMM-Newton orbit is represented by a star symbol. The maps are colored according to the maximum change of eccentricity $\Delta e = e_{\max} - e_{\min}$ during the 30-year forward or backward propagation, respectively. If, for some initial conditions, the maximum eccentricity reaches the value of the critical eccentricity e_{critical}, corresponding to a perigee of $h_{p,\,\text{re-entry}} = 50$ km

$$e_{\text{critical}} = 1 - \frac{R_E + h_{p,\,\text{re-entry}}}{a}$$

the integration is terminated and the corresponding initial condition is marked with a cross symbol in **Figure 5**. Note that, for those solutions, the actual orbit evolution should be computed considering the effect of aerodynamic drag. This was not done in the current work to limit the computational time, however, we expect that the effect of drag will act as a dumping of the dynamical system, decreasing the amplitude of the librational or rotational loops in the (e, 2ω) phase space and progressively decreasing the semi-major axis, as shown in Colombo and McInnes (2011) for the case of solar radiation pressure, Earth's oblateness and drag. This will be subject of future work.

Now, if we compute the maps considering both a forward and a backward propagation, both for 30 years, the map becomes more symmetric, as no particular choice (in terms of symmetry in the position of the Sun and the Moon) was made for the initial epoch. This is due to the fact that, if in the propagation the eccentricity reaches the maximum value e_{impact} corresponding to a perigee equal to the Earth radius,

$$e_{\text{impact}} = 1 - \frac{R_E}{a}$$

the integration is terminated. Performing, from each starting point in the grid both a forward and a backward integration in time, instead, allows characterizing the dynamics in the phase space (e, 2ω) in terms of reachable conditions. **Figure 6A** shows the forward-backward maps starting from a semi-major axis of 67045.39 km, where now $\Delta e = e_{\max} - e_{\min}$ is computed as

$$e_{\max} = \max_t e\,(t) \qquad t \in \left[-\Delta t_{\text{disposal}} \; +\Delta t_{\text{disposal}} \right]$$
$$e_{\min} = \min_t e\,(t) \qquad t \in \left[-\Delta t_{\text{disposal}} \; +\Delta t_{\text{disposal}} \right]$$

setting $\Delta t_{\text{disposal}} = 30$ years. The map in **Figure 6A** present and island of low eccentricity variation close to the initial condition of XMM Newton's orbit. The condition of quasi-frozen orbit is located around $2\omega_0 = 180$ deg and $e_0 \simeq 0.8$. The solutions around this conditions librate around the limited-eccentricity orbit. Other two islands of small eccentricity are present in this map, one around $2\omega_0 = 180$ deg and $e_0 \simeq 0.2$ and another around $2\omega_0 = 0$ deg and high values of the initial eccentricities. Those solution corresponds to orbits which rotate is terms of ω but have a limited variation in terms of eccentricity. Solutions starting at eccentricity close to zero have the highest variation of eccentricity. This means that for this semi-major axis and inclination, spacecraft on circular orbit can naturally get on an elliptical orbit and eventually reach re-entry.

In order to approximate the half-period of the oscillation in the (e, 2ω) phase space, the time interval between the points when the spacecraft attain the minimum and the maximum eccentricity is computed (as an averaged between the forward and the backward propagation) and shown in **Figure 6B**. From **Figure 6B** it is for example possible to see that the quasi-frozen solution is stable for 30 years. Indeed, due to the oscillation in inclinations, which has longer period, the orbit may encounter some instability is a longer propagation time is chosen as the eccentricity may increase beyond the critical eccentricity [this can be noted for example in the case of the INTEGRAL spacecraft (Colombo et al., 2014a)]. The maximum and minimum inclination attained with respect to the Moon's plane are shown in **Figures 6C, D**, while the variation of inclination is represented in **Figure 6E**. As it can be seen from **Figure 6E** the limited eccentricity conditions do not have a zero variation of the inclination; therefore, the long-term stability over longer time period is not guaranteed and an analysis over longer timeframe is required.

Once the behavior on the (e, 2ω) phase space is understood by looking at the map showing the result of the backward and forward propagation as in **Figure 6A**, it is possible to study the sensitivity to the initial condition in inclination with respect to the Moon's plane. In **Figure 7**, the Δe maps are computed for different starting inclination with respect to the orbiting plane of the Moon to show how the phase space changes depending on the initial inclination. For low inclinations the solutions are all rotational in ω (measured with respect to the Moon's plane) and exhibits a higher variation of eccentricity the more the initial eccentricity is high (**Figures 7A–E**) and for a high initial eccentricity the solutions which exhibits a higher eccentricity variation are characterized by $2\omega_0 = 180$ deg. This behavior is

clearer in **Figures 7F–L**: the solutions initiating from the yellow area of high initial eccentricities and $2\omega_0 = 180$ deg rotate in ω, while quasi-equilibrium solutions exists at high eccentricities and $2\omega_0 \simeq 0$ deg (red island around $2\omega_0 \simeq 0$ deg). This is also visible from **Figure 8** that shows the orbit evolution in the (e, 2ω) phase space for many initial conditions all at starting inclination with respect to the Moon's plane of 45° and semi-major axis equal to 67045.39 km but for different starting ω_0 (color code) and for different initial eccentricity (**Figures 9A,L**).

Going back at the Δe maps in **Figure 7**, a new island appear for inclinations above 45° at low eccentricities and $2\omega_0 \simeq 180$ deg of quasi-equilibrium solutions and librational solutions (**Figure 7L**), while the island at high eccentricities and $2\omega_0 \simeq 0$ deg move up. This is clearly visible from **Figure 9** that shows the orbit evolution in the (e, 2ω) phase space and the polar plots for many initial conditions all at starting inclination with respect to the Moon's plane of 64.28° and semi-major axis equal to 67045.39 km but for different starting ω_0 (color code) and for different initial eccentricity (**Figures 9A**, **L**).

For the semi-major axis considered (67045.39 km) $i_0 = 45$ deg is approximately the critical inclination (Kozai, 1962; Costa and Prado, 2000). Indeed, for inclination higher than the critical values, circular orbits get very elliptic (see yellow path in **Figures 7L–T**). The more the initial inclination with respect to the Moon increases, the more the initial orbit reaches the critical eccentricity for re-entry (cross symbols). Finally, for initial inclinations above $i_0 = 70$ deg, the quasi-equilibrium solutions in correspondence of $2\omega_0 \simeq 180$ deg are in correspondence of $e_0 > e_{\text{critic}}$, therefore not feasible, however, the fast eccentricity solution starting from $e_0 = 0$ still exist. It is important to remember that, even if qualitatively similar, the behavior depends also on the orbit semi-major axis that here is kept constant.

RE-ENTRY OR GRAVEYARD DESIGN

The initial conditions characterized by limited Δe variation identified in **Figures 7L–T** could be selected as graveyard orbits (Ely, 2005), while the high eccentricity variation solutions as initial condition for passive eccentricity increase to target Earth re-entry. It must be stressed that, while a re-entry trajectory will remove completely the spacecraft from the space environment, a graveyard solution will leave the satellite on a long-term stable orbit. In this sense, however, the time within which the orbit stability has been verified becomes an important parameter as the orbit may de-stabilize afterwards (Daquin et al., 2016). On the other side, it must be noted that re-entry need to be carefully designed according to casualty risk constraints on ground (Merz et al., 2015).

This section will exploit the findings from the previous Sections to design the end-of-life disposal for XMM-Newton mission by enhancing the effect of the natural dynamics or luni-solar and J_2 perturbation. The approach for the optimal Δv computation was detailed in Colombo et al. (2014a) where the re-entry of the INTEGRAL spacecraft was designed. The approach is summarized here and extended to the graveyard disposal design. For the disposal a single maneuver is considered, performed during the natural orbit evolution of the spacecraft (computed under the effect of perturbations). The finite variation in orbital elements $\Delta\boldsymbol{\alpha}$ achieved by an impulsive maneuver, is computed through Gauss' planetary equations written in finite-difference form and the new set of orbital elements after the maneuver is propagated with PlanODyn (Colombo, 2016) in single-averaged orbital elements considering luni-solar perturbation and the zonal terms of the Earth gravity potential for the maxim disposal time $\Delta t_{\text{disposal}} = 30$ years. Re-entry transfer orbits are selected that achieve in the propagation time $\Delta t_{\text{disposal}}$ the critical eccentricity e_{critical} as in Colombo et al. (2014a), while for selecting a suitable graveyard disposal, solutions that attain the minimum Δe over the propagation time are selected. A graveyard orbit is designed imposing that after the maneuver, the variation of the eccentricity in time stays limited, that is Δe in Equation (14) is minimized. In order to analyze a wide range of disposal dates, different starting dates for the disposal were selected, whereas, to determine the maneuver magnitude Δv and direction (α and β) and the point on the orbit where the maneuver is performed f, an optimization procedure with genetic algorithm was performed in order to find the optimal set of

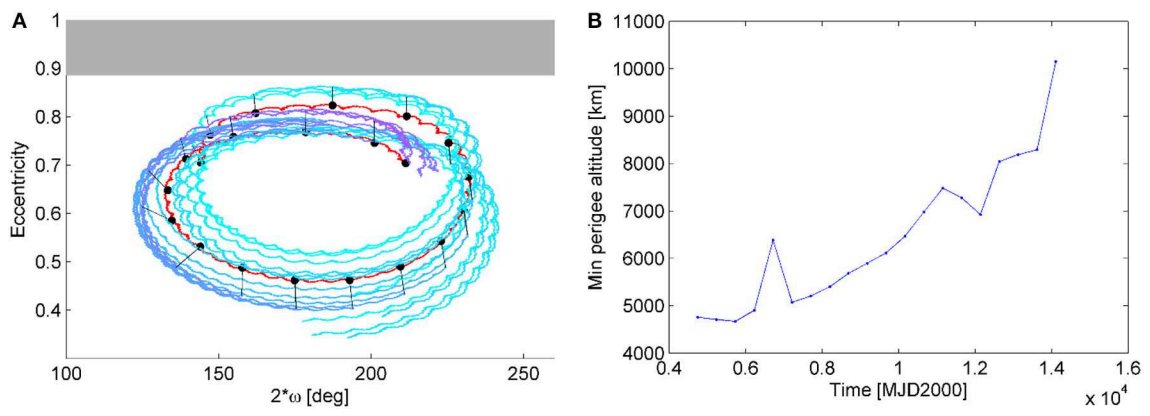

FIGURE 10 | XMM-Newton re-entry disposal. **(A)** Maneuvers in the eccentricity-2ω phase space (black points: starting times analyzed for the re-entry disposal). **(B)** Minimum perigee reached during the orbit long-term evolution for each solution. The initial inclination and the argument of the perigee are measured with respect to the Moon's plane.

parameters $\mathbf{x} = [\Delta v \ \alpha \ \beta \ f]$ that minimizes the cost function $J = \Delta e + w \cdot \Delta v$ where w is a weighting factor set equal to 1,000. Rather than optimizing the timing for the optimal disposal maneuver; it was chosen instead to leave the time for that maneuver as a parameter of a sensitivity analysis; in other words, the insertion to graveyard was optimized for many different starting dates to analyze how the natural evolution of the orbit can be exploited. A maximum magnitude for the Δv is considered based on the available on-board propellant.

XMM-Newton Re-entry Disposal

The time interval considered for the disposal design is from 2013/01/01 to 2035/01/01. The maximum Δv available for the maneuver sequences is estimated to be 40.5 m/s in 2013/01/01 (Colombo et al., 2014a). The re-entry can be considered satisfied when an altitude of 50 km or lower is reached from the Earth's surface. The natural orbit evolution of the spacecraft is shown in **Figure 10** in the $(e, 2\omega)$ phase space. The black points represent the initial conditions (and corresponding starting time) considered for the maneuver of disposal. For each starting point an impulsive maneuver of maximum magnitude equal to two times the available Δv on board on 2013/01/01 (equal to 81.1 m/s) is optimized in direction in order to maximize the following variation of the orbit eccentricity in the available $\Delta t_{\text{disposal}}$. The results of the Δv optimization for each initial starting condition along the natural orbit evolution are reported in **Figure 10** in colored line. Moving toward the external part of the phase space correspond to target the yellow regions in **Figure 7P** (for that map the initial semi-major axis and inclination are the one of the XMM spacecraft). Corresponding to large eccentricity variation. However, as it can be seen from **Figure 10B**, re-entry is not achievable within the considered $\Delta t_{\text{disposal}}$ for the maximum Δv considered (equal to 81.1 m/s) as the minimum perigee reached (among all the possible starting dates) is equal or above 4,700 km (too high for re-entry). This demonstrates that re-entry for XMM-Newton is not a feasible option during this time range as the propellant requirements for such a disposal would be over the actual propellant on-board the spacecraft. **Figure 10A** represents the maneuver in the eccentricity-perigee angle (measured with respect to the Earth-Moon plane) phase space. Future studies for XMM-Newton disposal through re-entry could investigate the possibility to increase the propagation time to verify whether the interaction between Moon and Sun third body perturbation will cause a natural decrease in the perigee. However, it needs to be taken into account that the available Δv on-board the spacecraft decreases with time due to orbit correction.

XMM-Newton Graveyard Disposal

Another disposal option that can be investigated for HEO in case the re-entry option is not feasible, is the option to transfer the spacecraft into a graveyard orbit. The existence of long-term stable orbits can be investigated, where the evolution of the orbital elements due to natural perturbation is limited. Such orbits can be chosen as graveyard orbits. Such orbits are visible in the map in **Figure 7P** (for that map the initial semi-major axis and inclination are the one of the XMM spacecraft) with a red color corresponding to a small variation of eccentricity. Importantly, note that the strategy would ideally aims at reaching the center of libration in the phase space; however, due to the limitation in the maximum available Δv, imposed as an upper bound for the global optimization, a more stable orbit cannot be reached, but only an orbit that is more stable than the nominal one. In other words, optimal solution is to move toward the center of the phase space loop. Also note that, due to the chaotic behavior of the orbit evolution under the effect of luni-solar perturbation, a driving factor is the time period $\Delta t_{\text{graveyard}}$ used for the propagation of the orbit after the maneuver to compute Equations (15) and (14). For this study $\Delta t_{\text{graveyard}}$ was set equal to 30 years, but this number can be easily increased for further work. **Figure 11A** shows the optimal maneuver for a transfer into a graveyard orbit for each starting time analyzed. The maneuver is represented in the phase space of eccentricity, inclination and anomaly of the percenter

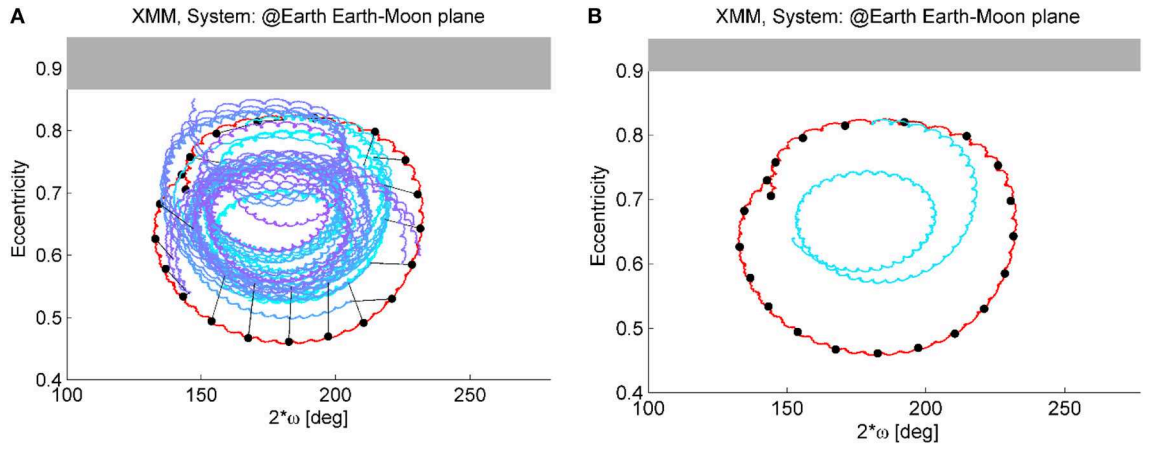

FIGURE 11 | XMM-Newton graveyard disposal. **(A)** Optimal maneuvers in the eccentricity-2ω phase space (black points: starting times analyzed for the re-entry disposal). **(B)** Example of a disposal trajectory (cyan line). The initial inclination and the argument of the perigee are measured with respect to the Moon's plane.

with respect to the Earth-Moon plane. The magnitude of the maneuver is always close to the upper bound of available Δv as is clear that a higher Δv would allow reaching a more stable orbit. However, the new graveyard orbit reduces at least the oscillations in eccentricity, preventing the spacecraft from an uncontrolled re-entry within the 30-year period. As an example, a disposal trajectory, whose maneuver is performed on 20/04/2016, is shown in **Figure 11B**.

CONCLUSION

This article analyzed the effect of luni-solar perturbations and the Earth's oblateness on the stability of highly elliptical orbits. The disturbing potential of the third body perturbation is written in Taylor expansion of the distances to the third body. The potential is firstly averaged over the revolution of the spacecraft around the Earth (mean anomaly) then is averaged again over the revolution of the perturbing body around the Earth. The existence of quasi-frozen, librational and rotational trajectories foreseen by the Kozai's analytical theory are found also when the Sun third body effect and the Earth's oblateness are included in the simulation. Maps are constructed over a wide domain of initial conditions in terms of eccentricity, inclination and argument of the perigee with respect to the Moon's plane. These maps represents the change in eccentricity over a long time space and in general can be used to study the orbit stability properties. These findings are finally used to design the end-of-life disposal for the XMM-Newton spacecraft as graveyard orbit injection or Earth re-entry. In this work, the effect of tesseral harmonics was not taken into account, while this could be important for creating maps in correspondence of lower semi-major axis, for example for Geostationary transfer orbits; the same approach however could be followed.

DATA AVAILABILITY

The datasets generated for this study can be found in the repository at the link www.compass.polimi.it/publications (Colombo, 2018).

AUTHOR CONTRIBUTIONS

CC contributed to the conception and design of the study by writing the PlanODyn code and simulating the maps contained in this paper. She wrote the first draft of the manuscript firstly presented at the 25th AAS/AIAA Space Flight Mechanics Meeting, in Williamsburg (VA) in January 2015.

FUNDING

CC acknowledges the support received by the Marie Curie grant 302270 (SpaceDebECM - Space Debris Evolution, Collision risk, and Mitigation) and the European Research Council (ERC) under the European Union's Horizon 2020 research and innovation programme (grant agreement No 679086 - COMPASS). These two projects brought to the development and completion of this work.

ACKNOWLEDGMENTS

This work was initiated as a follow-up of a study for the European Space Agency named End-Of-Life Disposal Concepts for Lagrange-Point and Highly Elliptical Orbit Missions (Contract No. 4000107624/13/F/MOS). The author would like to acknowledge the team members of the ESA study: F. Letizia, S. Soldini, H. Lewis, E. M. Alessi, A. Rossi, L. Dimare, M. Vasile, M. Vetrisano, Van der Weg W., and M. Landgraf.

REFERENCES

Alessi, E. M., Deleflie, F., Rosengren, A. J., Rossi, A., Valsecchi, G. B., Daquin, J., et al. (2016). A numerical investigation on the eccentricity growth of gnss disposal orbits. *Celest. Mech. Dynam. Astron.* 125, 71–90. doi: 10.1007/s10569-016-9673-4

Alessi, E. M., Schettino, G., Rossi, A., and Valsecchi, G. B. (2018). Natural highways for end-of-life solutions in the leo region. *Celest. Mech. Dynam. Astron.* 130:34. doi: 10.1007/s10569-018-9822-z

Armellin, R., Di Mauro, G., Rasotto, M., Madakashira, H. K., Lara, M., and San-Juan, J. F. (2014). *End-of-Life Disposal Concepts for Lagrange-Points and HEO Missions*. Final Report, ESA/ESOC contract No. 4000107624/13/F/MOS.

Battin, R. H. (1999). *An Introduction to the Mathematics and Methods of Astrodynamics*. Reston: Aiaa Educational Series.

Blitzer, L. (1970). *Handbook of Orbital Perturbations*. Tucson, AZ: University of Arizona.

Cefola, P. J., and Broucke, R. (1975). "On the formulation of the gravitational potential in terms of equinoctial variables," in *13th Aerospace Sciences Meeting* (Pasadena, CA: American Institute of Aeronautics and Astronautics). doi: 10.2514/6.1975-9

Chao-Chun, G. C. (2005). *Applied Orbit Perturbation and Maintenance*. El Segundo, CA.

Colombo, C. (2015). "Long-term evolution of highly-elliptical orbits: luni-solar perturbation effects for stability and re-entry," in *Proceedings of the 25th AAS/AIAA Space Flight Mechanics Meeting* (Williamsburg: AAS-15–395).

Colombo, C. (2016). "Planetary orbital dynamics (Planodyn) suite for long term propagation in perturbed environment,". *Proceedings of the 6th International Conference on Astrodynamics Tools and Techniques (ICATT)* (Darmstadt: ESOC/ESA).

Colombo, C. (2018). *Long-Term Evolution of Highly-Elliptical Orbits: Luni-Solar Perturbation Effects for Stability and Re-Entry. COMPASS*. Grant agreement 679086. Politecnico di Milano. Available online at: www.compass.polimi.it/publications (accessed August 5, 2018).

Colombo, C., and Gkolias, I. (2017). "Analysis of the orbit stability in the geosyncronous region for end-of-life disposal,"in *Proceedings of the 7th European Conference on Space Debris* (Darmstadt: ESA/ESOC).

Colombo, C., Letizia, F., Alessi, E. M., and Landgraf, M. (2014a). "End-of-life earth re-entry for highly elliptical orbits: the integral mission," in *Proceedings of the 24th AAS/AIAA Space Flight Mechanics Meeting* (Santa Fe: AAS 14-325).

Colombo, C., Letizia, F., Soldini, S., Lewis, H., Alessi, E. M., Rossi, A., et al. (2014b). *End-of-Life Disposal Concepts for Lagrange-Point and Highly Elliptical Orbit Missions*. Final Report, ESA/ESOC contract No. 4000107624/13/F/MOS.

Colombo, C., and McInnes, C. (2011). Orbital dynamics of "Smart-Dust" devices with solar radiation pressure and drag. *J. Guid. Control Dyn.* 34, 1613–1631. doi: 10.2514/1.52140

Cook, G. E. (1962). Luni-solar perturbations of the orbit of an earth satellite. *Geophy. J. Int.* 6, 271–291.

Costa, I. V. d., and Prado, A. F. B. d. A. (2000). Orbital evolution of a satellite perturbed by a third body. *Adv. Space Dyn.*

Daquin, J., Rosengren, A. J., Alessi, E. M., Deleflie, F., Valsecchi, G. B., and Rossi, A. (2016). The dynamical structure of the meo region: long-term stability, chaos, and transport. *Celest. Mech. Dynam. Astron.* 124, 335–366. doi: 10.1007/s10569-015-9665-9

Draim, J. E., Inciardi, R., Proulx, R., Cefola, P. J., Carter, D., and Larsen, D. E. (2002), Beyond geo—using elliptical orbit constellations to multiply the space real estate. *Acta Astronaut.* 51, 467–489. doi: 10.1016/s0094-5765(02)00036-x

Ely, T. A. (2005). Stable constellations of frozen elliptical inclined lunar orbits. *J. Astronaut. Sci.* 3, 301–16.

Ely, T. A. (2014). Mean element propagations using numerical averaging. *J. Astron. Sci.* 61, 1–30. doi: 10.1007/s40295-014-0020-2

El'yasberg, P. E. (1967). *Introduction to the Theory of Flight of Artificial Earth Satellites*. (Translated from Russian). NASA.

ESA (2013). *Xmm-Newton Users Handbook*. European Space Agency.

Gkolias, I., and Colombo, C. (2017). "End-of-life disposal of geosynchronous satellites," in *Proceedings of the 68th International Astronautical Congress* (Adelaide: IAC-17-A6.4.3).

Gkolias, I., Daquin, J., Gachet, F., and Rosengren, A. J. (2016). From order to chaos in earth satellite orbits. *Astron. J.* 152:119. doi: 10.3847/0004-6256/152/5/119

Jenkin, A. B., and McVey, J. (2008). "Lifetime reduction for highly inclined, highly eccentric disposal orbits by changing inclination," in *Proceedings of the AIAA/AAS Astrodynamics Specialist Conference and Exhibit* (Hawaii: AIAA/AAS Honolulu).

Katz, B., Dong, S., and Malhotra, R. (2011). Long-term cycling of kozai-lidov cycles: extreme eccentricities and inclinations excited by a distant eccentric perturber. *Phy. Rev. Lett.* 107:181101. doi: 10.1103/PhysRevLett.107.181101

Kaufman, B., and Dasenbrock, R. (1972). *Higher Order Theory for Long-Term Behaviour of Earth and Lunar Orbiters*. NRL Repot 7527. Naval Research Laboratory.

Kozai, Y. (1962). Secular perturbations of asteroids with high inclination and eccentricity. *Astron. J.* 67, 591–598. doi: 10.1086/108790

Krivov, A. V., and Getino, J. (1997). Orbital evolution of high-altitude balloon satellites. *Astron. Astrophys.* 318, 308–314.

Lara, M., San-Juan, J., López, L., and Cefola, P. (2012). On the third-body perturbations of high-altitude orbits. *Celest. Mechan. Dynam. Astron.* 113, 435–452. doi: 10.1007/s10569-012-9433-z

Laskar, J., and Bou,é, G. (2010). Explicit expansion of the three-body disturbing function for arbitrary eccentricities and inclinations. *A&A* 522:A60.

Lidov, M. L. (1962). The evolution of orbits of artificial satellites of planets under the action of gravitational perturbations of external bodies. *Planet. Space Sci.* 9, 719–759. doi: 10.1016/0032-0633(62)90129-0

Liu, J. J. F., and Alford, R. L. (1980). Semianalytic theory for a close-earth artificial satellite. *J. Guid. Control Dyn.* 3, 304–311.

Merz, K., Krag, H., Lemmens, S., Funke, Q., Böttger, S., Sieg, D., et al. (2015). "Orbit aspects of end-of-life disposal from highly eccentric orbits," in *Proceedings of the 25th International Symposium on Space Flight Dynamics ISSFD* (Munich).

Murray, C. D., and Dermott, S. F. (1999). *Solar System Dynamics*. Cambridge University Press. doi: 10.1017/CBO9781139174817

Naoz, S., Farr, W. M., Lithwick, Y., Rasio, F. A., and Teyssandier, J. (2013). Secular dynamics in hierarchical three-body systems. *Month. Notices. R. Astron. Soc.* 431, 2155–2171. doi: 10.1093/mnras/stt302

Rossi, A., Alessi, E. M., Valsecchi, G. B., Lewis, H. G., Colombo, C., Anselmo, L., et al. (2015). *Disposal Strategies Analysis for Meo Orbits*. ESA contract 4000107201/12/F/MOS.

Shapiro, E. B. (1995). Phase plane analysis and observed frozen orbit for the topex/poseidon mission. *Adv. Astron. Sci.* 91, 853–872.

Skoulidou, D. K., Rosengren, A. J., Tsiganis, K., and Voyatzis, G. (2017). "Cartographic study of the meo phase space for passive debris removal," in *7th European Conference on Space Debris* (Darmstadt).

Srongprapa, P. (2015). *Mapping the Effects of Earth's Gravity Field on the Orbit Propagation of Gto Spacecraft a Study within the Context of Passive De-Orbiting through the Use of Perturbations*. Faculty of Engineering and the Environment, University of Southampton, Southampton.

Conflict of Interest Statement: The author declares that the research was conducted in the absence of any commercial or financial relationships that could be construed as a potential conflict of interest.

APPENDIX

Luni-Solar Perturbation Development

The average disturbing potential due to the third body effect can be written as Kaufman and Dasenbrock (1972):

$$\bar{R}\left(r,r'\right)=\frac{\mu'}{r'}\sum_{k=2}^{\infty}\delta^{k}\bar{F}_{k}\left(A,B,e\right) \tag{16}$$

where μ' is the gravitational coefficient of the third body, r' is the spacecraft distance to the third body. The factors of the Taylor expansion can be written as function of the power of the ratio between the orbit semi-major axis and the distance to the third body $\delta = a/r'$ multiplied by the function $\overline{R}_k(A,B,e)$, which is function of the orbit eccentricity and the function A and B (Chao-Chun, 2005) that are here written in terms of A_{Blizer} and B_{Blizer} given by Blitzer (1970) to show the link between them.

$$\begin{aligned}
A &= \cos\omega A_{\text{Blizer}}+\sin\omega A_{\text{Blizer}}\\
B &= -\sin\omega A_{\text{Blizer}}+\cos\omega A_{\text{Blizer}}\\
A_{\text{Blizer}} &= \cos\Delta\Omega\cos u'+\cos i'\sin u'\sin\Delta\Omega\\
B_{\text{Blizer}} &= -\cos i\left(\cos u'\sin\Delta\Omega-\cos i'\cos\Delta\Omega\sin u'\right)\\
&\quad+\sin i\sin i'\sin u'
\end{aligned}$$

The terms $\overline{F}_k(A,B,e)$ in Equation (16) are given by Kaufman and Dasenbrock (1972) and are here reported in a more compact form up to order 6th as:

$$\begin{aligned}
\bar{F}_2\left(A,B,e\right) &= \frac{1}{4}\left(\left(-2+3A^2+3B^2\right)-3\left(1-4A^2+B^2\right)e^2\right)\\
\bar{F}_3\left(A,B,e\right) &= \frac{5}{16}Ae\left(\left(12-15A^2-15B^2\right)+\left(9-20A^2+15B^2\right)e^2\right)\\
\bar{F}_4\left(A,B,e\right) &= \frac{3}{64}\left(\left(8-40A^2+35A^4-40B^2+70A^2B^2+35B^4\right)\right.\\
&\quad+\left(40-410A^2+420A^4+10B^2+350A^2B^2-70B^4\right)e^2\\
&\quad\left.+\left(15-180A^2+280A^4+30B^2-420A^2B^2+35B^4\right)e^4\right)\\
\bar{F}_5\left(A,B,e\right) &= -\frac{21}{128}Ae\left(\left(40-140A^2+105A^4-140B^2\right.\right.\\
&\quad\left.+210A^2B^2+105B^4\right)\left(100-490A^2\right.\\
&\quad\left.+420A^4+70B^2+210A^2B^2-210B^4\right)e^2\\
&\quad+\left(25-140A^2+168A^4+70B^2-420A^2B^2\right.\\
&\quad\left.\left.+105B^4\right)e^4\right)
\end{aligned}$$

$$\begin{aligned}
\bar{F}_6\left(A,B,e\right) &= \frac{1}{256}\left(\left(-80+840A^2-1890A^4+1155A^6\right.\right.\\
&\quad+840B^2-3780A^2B^2+3465A^4B^2-1890B^4\\
&\quad\left.+3465A^2B^4+1155B^6\right)\\
&\quad+\left(-840+16380A^2\right.\\
&\quad-42525A^427720A^6+1260B^2-39690A^2B^2\\
&\quad+51975A^4B^2+2835B^4+20790A^2B^4\\
&\quad\left.-3465B^6+20790A^2B^4-3465B^6\right)e^2\\
&\quad+\left(-1050+23625A^2-75600A^4+55440A^6\right.\\
&\quad-1575B^2+28350A^2B^2-51975A^2B^4\\
&\quad\left.+3465B^6\right)e^4\\
&\quad+\left(-175+4200A^2-15120A^4\right.\\
&\quad+14784A^6-525B^2+15120A^2B^2-55440A^4B^2\\
&\quad\left.\left.-945B^4+27720A^2B^4-1155B^6\right)e^6\right)
\end{aligned}$$

The derivatives of Equation (16) with respect to the orbital elements need to be computed to be inserted into the Lagrange planetary equations Equation (4) as in Equation (9), with

$$\begin{aligned}
\frac{\partial B}{\partial\Omega} &= \cos\omega\left(-\cos u'\sin\Delta\Omega+\cos i'\cos\Delta\Omega\sin u'\right)\\
&\quad-\cos i\sin\omega\left(\cos\Delta\Omega\cos u'+\cos i'\sin\Delta\Omega\sin u'\right)\\
\frac{\partial B}{\partial\Omega} &= \sin\omega\left(\cos u'\sin\Delta\Omega-\cos i'\cos\Delta\Omega\sin u'\right)\\
&\quad-\cos i\cos\omega\left(\cos\Delta\Omega\cos u'+\cos i'\sin\Delta\Omega\sin u'\right)\\
\frac{\partial A}{\partial i} &= C_{\text{Blitzer}}\sin\omega\\
\frac{\partial B}{\partial i} &= C_{\text{Blitzer}}\cos\omega\\
\frac{\partial A}{\partial\omega} &= B\\
\frac{\partial B}{\partial\omega} &= -A
\end{aligned}$$

where (Blitzer, 1970): $C_{\text{Blizer}} = \sin i\left(\cos u'\sin\Delta\Omega-\cos i'\cos\Delta\Omega\sin u'\right)+\cos i\sin i'\sin u'$.

frontiers in Astronomy and Space Sciences

ORIGINAL RESEARCH
published: 22 June 2018
doi: 10.3389/fspas.2018.00020

Periodic Orbits Close to That of the Moon in Hill's Problem

Giovanni B. Valsecchi [1,2]*

[1] IAPS-INAF, Rome, Italy, [2] IFAC-CNR, Sesto Fiorentino, Italy

In the framework of the restricted, circular, 3-dimensional 3-body problem Sun-Earth-Moon, Valsecchi et al. (1993) found a set of 8 periodic orbits, with duration equal to that of the Saros cycle, and differing only for the initial phases, in which the motion of the massless Moon follows closely that of the real Moon. Of these, only 4 are actually independent, the other 4 being obtainable by symmetry about the plane of the ecliptic. In this paper the problem is treated in the framework of the 3-dimensional Hill's problem. It is shown that also in this problem there are 8 periodic orbits of duration equal to that of the Saros cycle, and that in these periodic orbits the motion of the Moon is very close to that of the real Moon. Moreover, as a consequence of the additional symmetry of Hill's problem about the *y*-axis, only 2 of the 8 periodic orbits are independent, the other ones being obtainable by exploiting the symmetries of the problem.

Keywords: moon, lunar orbit, periodic orbits, Hill's problem, restricted 3-body problem

OPEN ACCESS

Edited by:
Josep Masdemont, Universitat Politecnica de Catalunya, Spain

Reviewed by:
Seppo Ilmari Mikkola, University of Turku, Finland
Alain Vienne, Université de Lille, France

***Correspondence:**
Giovanni B. Valsecchi
giovanni@iaps.inaf.it

Specialty section:
This article was submitted to Fundamental Astronomy, a section of the journal Frontiers in Astronomy and Space Sciences

Received: *09 March 2018*
Accepted: *23 May 2018*
Published: *22 June 2018*

Citation:
Valsecchi GB (2018) Periodic Orbits Close to That of the Moon in Hill's Problem. Front. Astron. Space Sci. 5:20. doi: 10.3389/fspas.2018.00020

1. INTRODUCTION

Roy (1973) was apparently the first to notice and discuss the occurrence of near Mirror Configurations in the main lunar prolem. In a system of n gravitating point-masses, a Mirror Configuration (MC; Roy and Ovenden, 1955) occurs when each radius vector from the centre of mass of the system happens to be perpendicular to every velocity vector. The importance of MCs for such systems is due to the following property: if, during its evolution, a system of n gravitating point-masses passes through an MC, then the Mirror Theorem (Roy and Ovenden, 1955) states that the time evolution of the system afterwards is the mirror image of the evolution before the occurrence of the MC; moreover, a corollary of the Mirror Theorem states that, if a system passes through two MCs, then each of its point-masses is on a periodic orbit.

The latter property was exploited, in the framework of the circular, restricted, 3-dimensional 3-body problem (CR3D3BP) Sun-Earth-Moon, to show the existence of periodic orbits with duration equal to that of the Saros (Valsecchi et al., 1993), an eclipse cycle known since more than two millennia, in which the mutual configurations of Sun, Earth and Moon nearly repeat, to considerable accuracy, after 223 synodic months (Roy, 1973; Perozzi et al., 1991).

In this paper, the issue is revisited in the framework of the 3-dimensional Hill's problem (3DHP), proceeding as in Valsecchi et al. (1993), and it is shown that 8 periodic orbits with duration equal to that of the Saros exist also in this case, but only 2 of them are actually independent, while the other ones can be obtained considering the symmetries of the problem.

2. MIRROR CONFIGURATIONS

According to Roy and Ovenden (1955), there are two types of MCs: colinear MCs, in which all the bodies are located along a straight line, with their velocity vectors orthogonal to the straight line, and coplanar MCs, in which all the bodies are located on a plane, with the velocity vectors orthogonal to that plane.

2.1. MCs in the CR3D3BP

In Valsecchi et al. (1993) the two types of MCs are discussed in the framework of the CR3D3BP Sun-Earth-Moon. Given that in this problem the Earth moves on a circular orbit about the Sun, a colinear MC is achieved if the massless Moon is at perigee or apogee, at the ascending or at the descending node of its geocentric orbit, and perfectly aligned with the Sun and the Earth (i.e., in solar or lunar eclipse configuration).

In terms of the geocentric orbital elements of the Moon, these conditions imply that the Moon must be at mean anomaly M equal to either 0° or 180°, argument of mean latitude $\theta = \omega + M$ equal to either 0° or 180°, and difference of mean longitude $\Delta\lambda = \lambda - \lambda'$ between the mean longitude of the Moon λ and that of the Sun λ' again equal to either 0° or 180°.

For a coplanar MC to occur, the constraints on M and $\Delta\lambda$ are the same, while that on the argument of mean latitude becomes θ equal to either 90° or 270°. Given that anyway M must be either 0° or 180°, the constraint on the argument of latitude implies $\omega = 0°$ or $\omega = 180°$ for a colinear MC, and $\omega = 90°$ or $\omega = 270°$ for a coplanar MC.

Table 1 summarizes the situation; in it the MCs are coded as in Valsecchi et al. (1993), with a three-digit code representing ω, M and $\Delta\lambda$ as multiples of 90°. Note that MCs differing by 180° in ω are grouped together in the same row, due to the symmetry of the problem about the plane in which the Sun and the Earth move.

2.2. MCs in the 3DHP

In the 3DHP the possible MCs are again 16, and their coding is exactly the same as in the CR3D3BP. In this case, however, there is an important difference, due to the additional symmetry present in this problem, namely, the one about the y-axis; as a consequence, two MCs differing only because in one of them $\Delta\lambda = 0°$ and in the other $\Delta\lambda = 180°$ are equivalent. Taking this into account, in the case of the 3DHP we rearrange the MCs of **Table 1** as shown in **Table 2**.

TABLE 1 | The 16 possible MC's of the CR3D3BP.

MC	ω	M	$\Delta\lambda$
000:200	0°:180°	0°	0°
002:202	0°:180°	0°	180°
020:220	0°:180°	180°	0°
022:222	0°:180°	180°	180°
100:300	90°:270°	0°	0°
102:302	90°:270°	0°	180°
120:320	90°:270°	180°	0°
122:322	90°:270°	180°	180°

3. THE SAROS CYCLE AND THE ASSOCIATED PERIODIC ORBITS

There is a vast literature concerning lunar cycles (see, e.g., Steves, 1997) and the Saros is perhaps the most interesting one among them. In fact, at variance from most of the other lunar eclipse-predicting cycles, it involves not only the synodic and the nodical months, but also the anomalistic one. Let us consider the mean durations of the synodic ($T_{\Delta\lambda}$), anomalistic (T_M) and nodical month (T_θ), given by:

$$\begin{aligned} T_{\Delta\lambda} &= 29.530\,589 \text{ d} \\ T_M &= 27.554\,551 \text{ d} \\ T_\theta &= 27.212\,220 \text{ d;} \end{aligned}$$

then, one easily sees that:

$$223T_{\Delta\lambda} = 6\,585.32 \simeq 239T_M = 6\,585.54 \simeq 242T_\theta = 6\,585.36.$$

In the rest of this paper, the duration of the Saros will be taken to be that of 223 synodic months, i.e., 6 585.321 347 d.

During a Saros, the argument of perigee ω of the lunar orbit makes 3 full revolutions; this happens because the argument of latitude makes 242 revolutions (the 242 nodical months), and the mean anomaly M makes 239 revolutions (the 239 anomalistic months): the difference is due to the 3 revolutions of ω. If the Moon is started from, say, the MC coded 000, in which $\omega = 0°$, $M = 0°$, $\Delta\lambda = 0°$, after a half Saros each of these angles will have made a half-integer number of revolutions; thus, the MC occurring at that time will be 222, in which $\omega = 180°$, $M = 180°$, $\Delta\lambda = 180°$. In this way it is possible to establish the pairs of MCs that occur during the periodic orbits of duration equal to that of the Saros (Valsecchi et al., 1993).

3.1. Periodic Orbits in the CR3D3BP

As shown in Valsecchi et al. (1993), there exist 8 such periodic orbits in the CR3D3BP, in which the 16 MCs are combined in pairs as discussed above. To find these orbits, Valsecchi et al. (1993) used a 3-dimensional Newton-Raphson root finder and Everhart's integrator RADAU (Everhart, 1985) at 15th order. In these computations, the ratio of the mass of the Earth to that of the Sun was set to

$$m_\oplus = \frac{1}{328\,900.53},$$

TABLE 2 | The 16 possible MC's of the 3DHP.

MC	ω	M	$\Delta\lambda$
000 : 002 : 200 : 202	0° : 0° : 180° : 180°	0°	0° : 180° : 0° : 180°
020 : 022 : 220 : 222	0° : 0° : 180° : 180°	180°	0° : 180° : 0° : 180°
100 : 102 : 300 : 302	90° : 90° : 270° : 270°	0°	0° : 180° : 0° : 180°
120 : 122 : 320 : 322	90° : 90° : 270° : 270°	180°	0° : 180° : 0° : 180°

corresponding to that of the real Earth-Moon system.

The Moon was placed in one of the 8 colinear MCs, say 000, by specifying the appropriate values for ω, M and $\Delta\lambda$ from **Table 1**, assigning tentative values for the starting geocentric orbital elements a, e and i, and then looking for the occurrence of the paired MC (in this case 222) at the end of a numerical integration for half of a Saros. The Newton-Raphson root finder was used to converge to the values of a, e and i that led to the occurrence of the paired MC. In this way, all the 8 periodic orbits were found; they are summarized in **Table 3**.

3.2. Periodic Orbits in the 3DHP

The procedure followed to find the periodic orbits associated to the Saros in Hill's problem has been the same as in Valsecchi et al. (1993), the only difference being in the equations of motion; those used in the present work are the ones of Hill's problem, in the form given in Schmidt (1979):

$$\begin{aligned}\ddot{x} &= -\frac{\mu}{r^3}x + 2n'\dot{y} + 3n'^2x\\ \ddot{y} &= -\frac{\mu}{r^3}y - 2n'\dot{x}\\ \ddot{z} &= -\frac{\mu}{r^3}z - n'^2z,\end{aligned}$$

where:

$$\begin{aligned}k &= 0.017\,202\,098\,95\\ \mu &= k^2 m_\oplus\\ n' &= \frac{k}{\sqrt{1+m_\oplus}}\\ r &= \sqrt{x^2+y^2+z^2}.\end{aligned}$$

In this way, distances are in astronomical units, and time is in days.

The resulting periodic orbits are given in **Table 4**; comparing the values of a, e, i with those of the corresponding MCs in **Table 3**, one sees that the differences are rather small.

The time behaviour of the geocentric orbital elements of the Moon in these periodic orbits is quite close to that of the real Moon, just as found by Valsecchi et al. (1993); a similar comparison is repeated here.

A good approximation to a MC 200 was realized by the real Moon on JD 2 371 846.872 (17.372 October 1781, Valsecchi et al., 1993); according to the JPL ephemeris DE406, the orbit of the Moon had, at that time, $\omega = 179.^\circ0$, $M = 0.^\circ0$ and $\Delta\lambda = 0.^\circ0$.

The four panels of **Figure 1** show the time evolution of, from top to bottom, a, e, i, ω of the real Moon, taken from JPL DE406, in red, and the corresponding quantities for the periodic orbit passing through MCs 200 and 022, in green. The behaviour of a and ω of the periodic orbit match very closely that of the real Moon. For e and i there is a systematic difference, but the short-period terms affecting these two elements appear to be the same as those of the real orbit.

Figure 2 contains the last year of the Saros, and shows that the close matching is preserved for the entire cycle.

4. DISCUSSION

The periodic orbits found in the 3DHP, besides mimicking closely the real lunar orbit, are also very similar to those found in Valsecchi et al. (1993) in the CR3D3BP, as also shown by the closeness of the values of the geocentric orbital elements reported by **Tables 3**, **4**. In fact, the principal lunar short-period terms (Brouwer and Clemence, 1961) are contained in the periodic orbits in both problems:

- the variation, a term depending on $2\Delta\lambda$, an angle that makes 446 revolutions in the periodic orbits associated to the Saros;
- the parallactic inequality, depending on $\Delta\lambda$, that makes 223 revolutions;
- the evection, to which are due a perturbation in e and ω, depending on $2\lambda' - 2\tilde{\omega}$, that makes 32 revolutions, and another perturbation in λ, depending on $\lambda - 2\lambda' + \tilde{\omega}$, that makes 207 revolutions;
- the principal perturbation in latitude, depending on $\lambda - 2\lambda' + \Omega$, that makes 204 revolutions.

On the other hand, these orbits differ substantially from Hill's periodic orbit (Hill, 1878). Hill's periodic orbit lasts for exactly one synodic month, is planar, and in it all the crossings of the x and y-axes take place at right angles.

Actually, using the same periodic-orbit-finder software used to find the orbits of **Table 4**, we can compute Hill's orbit. The MCs in this orbit are of the colinear type (coplanar MCs, in spite of their name, cannot take place if the motion is planar), and

TABLE 3 | The osculating elements a, e and i of the massless Moon, in the periodic orbits associated to the Saros, when at the 16 possible MCs of the CR3D3BP (from Valsecchi et al., 1993).

MC	a (au)	e	i (°)
000 : 200	0.002 580 997 16	0.083 356 670	5.690 814 6
222 : 022	0.002 590 632 07	0.056 488 496	5.688 171 3
002 : 202	0.002 580 820 66	0.083 864 066	5.691 513 5
220 : 020	0.002 590 854 05	0.056 953 569	5.688 726 1
100 : 300	0.002 580 819 14	0.083 936 251	5.365 847 6
322 : 122	0.002 590 433 42	0.057 165 911	5.348 172 9
102 : 302	0.002 580 646 47	0.084 452 672	5.365 595 9
320 : 120	0.002 590 651 20	0.057 640 009	5.347 565 5

TABLE 4 | The osculating elements a, e and i of the Moon, in the periodic orbits associated to the Saros, when at the 16 possible MCs of the 3DHP.

MC	a (au)	e	i (°)
000 : 002 : 200 : 202	0.002 580 906 41	0.083 640 384	5.688 149 3
222 : 220 : 022 : 020	0.002 590 744 66	0.056 751 303	5.685 433 3
100 : 102 : 300 : 302	0.002 580 730 50	0.084 224 104	5.362 866 7
322 : 320 : 122 : 120	0.002 590 544 13	0.057 432 758	5.345 016 3

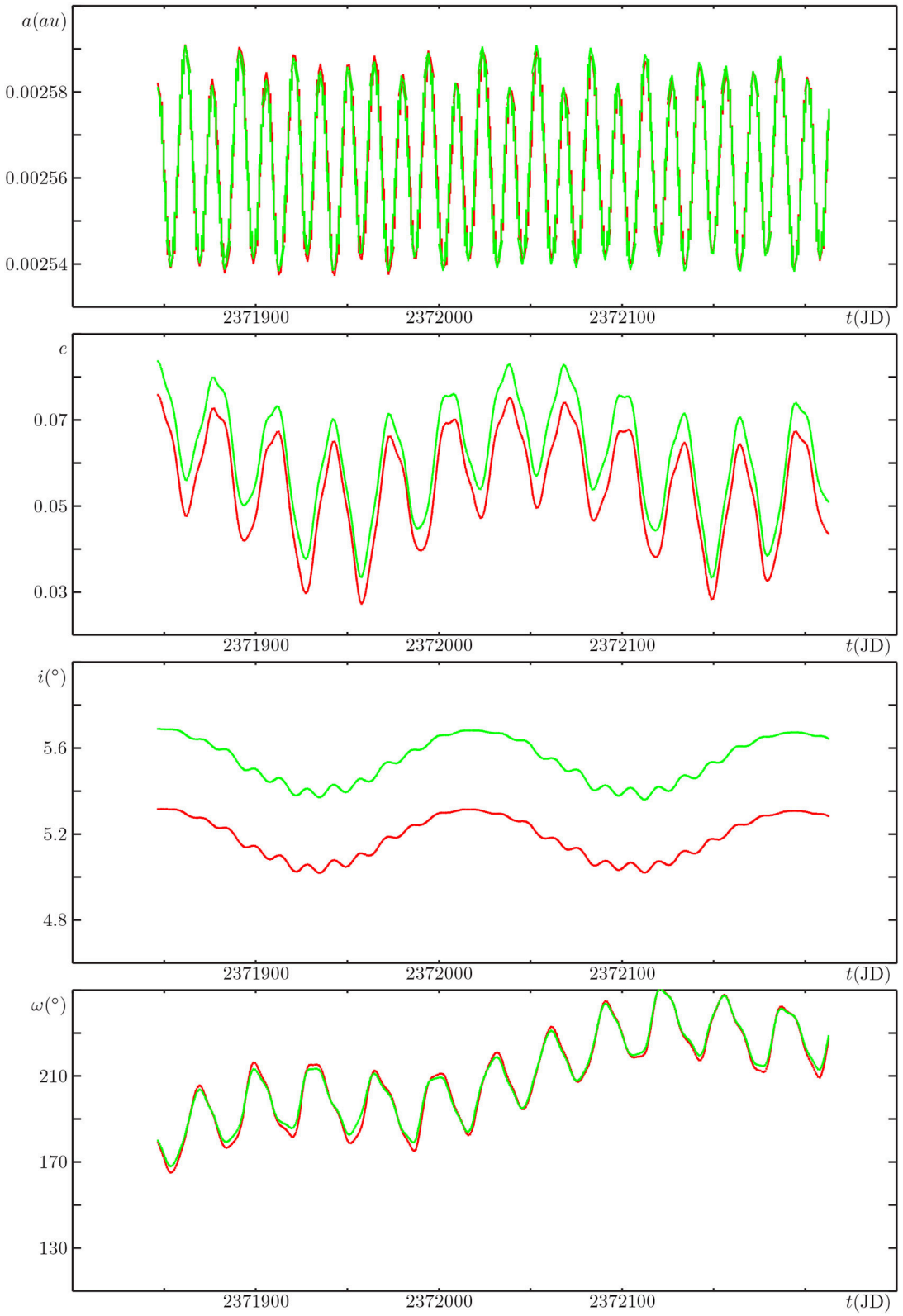

FIGURE 1 | Time evolution of the elements of the Moon taken from JPL DE406 (in red) and for the periodic orbit passing through MCs 200 and 022 (in green); top to bottom: semimajor axis a, eccentricity e, inclination i, argument of perigee ω; the time span covered is one year, starting from 17.372 October 1781.

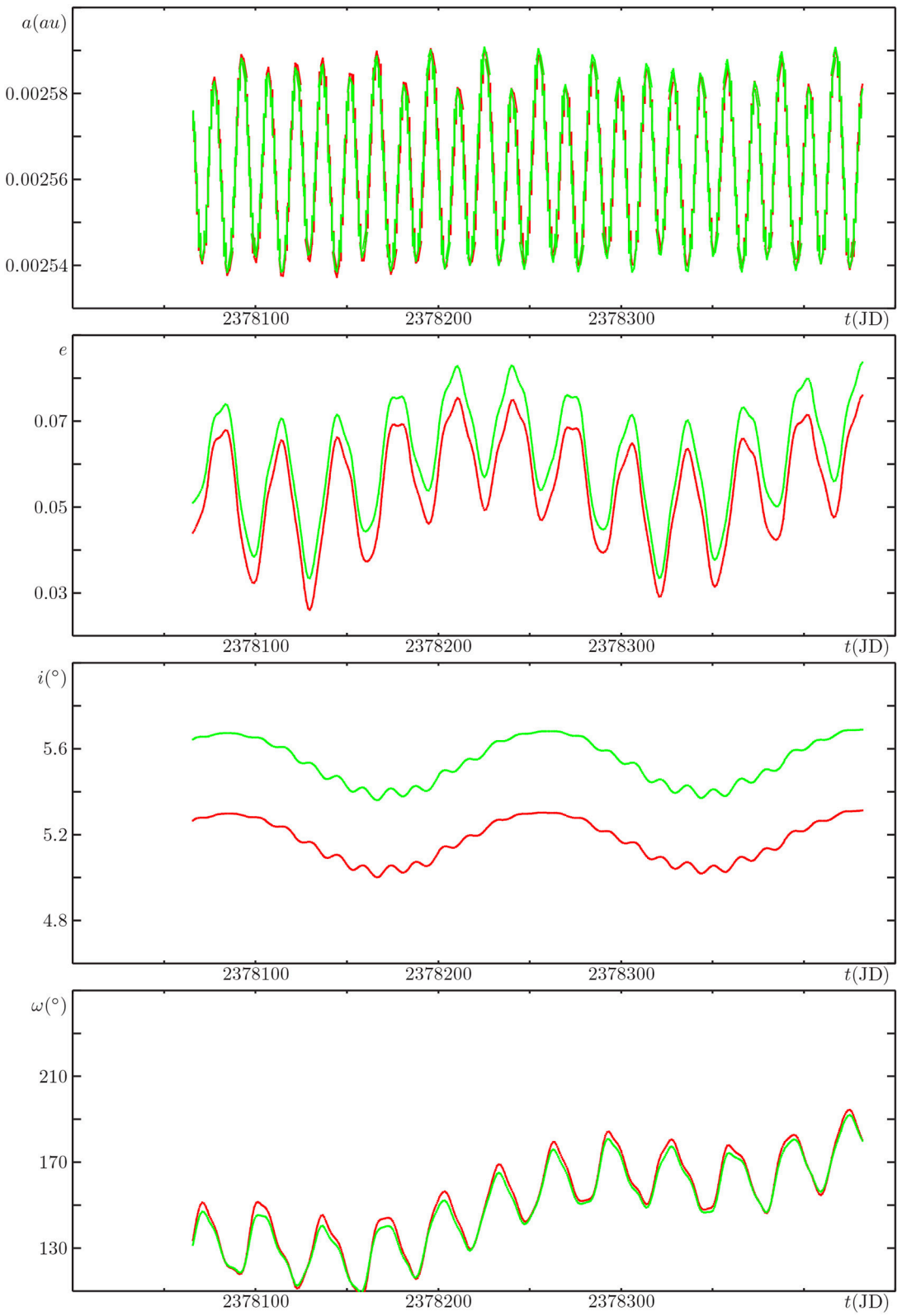

FIGURE 2 | Same as **Figure 1**, but for the time span of one year, ending one Saros later, on 28.693 October 1799.

correspond to the two crossings of the x-axis. At these crossings, the geocentric distance of the Moon has two identical minima, and the orbital elements are:

$$a = 0.002\,586\,071\,80 \text{ au}$$
$$e = 0.013\,517\,273,$$

while at the two crossings of the y-axis, where the geocentric distance has two identical maxima, the orbital elements are:

$$a = 0.002\,540\,020\,84 \text{ au}$$
$$e = 0.018\,894\,762.$$

It is notheworthy that in Hill's orbit there are two perigee passages of the Moon, at the crossings of the x-axis, and two apogee passages, at the crossings of the y-axis; this means that during the single synodic month corresponding to its duration, there are two full anomalistic months. Moreover, the osculating geocentric eccentricity never exceeds 0.02, a value much lower than the mean eccentricity of the real lunar orbit.

Therefore, the time evolution of the elements of the periodic orbits described in this paper follows the behaviour of the osculating geocentric elements of the real Moon much more closely than in the case of Hill's orbit; on the other hand, the latter is succesfully used as intermediate orbit in the Hill-Brown lunar theory (Brown, 1896). Whether these new, longer periodic orbits are suitable for such a task will be the subject of future research.

A natural question to ask is whether periodic orbits similar to those described here do exist, in Hill's problem, for different values of the geocentric distance of the Moon, i.e., for different values of the ratio of the mean motion of Sun and Moon; in Valsecchi et al. (1993) an example of such an orbit of the CR3D3BP was given, corresponding to the probable lunar orbit of the late Precambrian. On the other hand, the Saros-associated periodic orbits in the two problems are so close to each other, as can be seen comparing the numbers in **Tables 3**, **4**, that very likely the same orbits should exist in Hill's problem; also this issue will be the subject of future research.

5. CONCLUSIONS

Building on the results of Valsecchi et al. (1993) for the CR3D3BP, it has been shown that also in Hill's problem it is possible to find 8 periodic orbits of duration one Saros, in which the orbital evolution of the Moon closely resembles that of the real Moon. An important difference from the previous case is that, at variance from the periodic orbits found in the CR3D3BP, in Hill's case only 2 orbits are independent, the others being obtainable by considering the symmetries of the problem.

AUTHOR CONTRIBUTIONS

The author confirms being the sole contributor of this work and approved it for publication.

ACKNOWLEDGMENTS

Fruitful discussions with Ettore Perozzi, Bonnie Steves and the late Archie Roy on the subject of this paper are gratefully acknowledged.

REFERENCES

Brouwer, D., and Clemence, G. M. (1961). *Methods of Celestial Mechanics*. New York, NY: Academic Press.

Brown, E. W. (1896). *An Introductory Treatise on the Lunar Theory*. Cambridge, The University Press.

Everhart, E. (1985). "An efficient integrator that uses Gauss-Radau spacings," in *Dynamics of Comets: Their Origin and Evolution*, eds A. Carusi, and G. B. Valsecchi (Dordrecht: D. Reidel), 185.

Hill, G. W. (1878). Researches in the Lunar Theory. *Am. J. Math.* 1, 5–26, 129–147, 245–260. doi: 10.2307/2369430

Perozzi, E., Roy, A. E., Steves, B. A., and Valsecchi, G. B. (1991). Significant high number commensurabilities in the main lunar problem. I - The Saros as a near-periodicity of the Moon's orbit. *Celest. Mech. Dynam. Astron.* 52:241. doi: 10.1007/BF00048486

Roy, A. E. (1973). The use of the saros in lunar dynamical studies. *Moon* 7:6. doi: 10.1007/BF00578803

Roy, A. E., and Ovenden, M. W. (1955). On the occurrence of commensurable mean motions in the solar system. The mirror theorem. *Mon. Not. R. Astron. Soc.* 115:296. doi: 10.1093/mnras/115.3.296

Schmidt, D. S. (1979). Literal solution for Hill's lunar problem. *Celest. Mech.* 19:279. doi: 10.1007/BF01230219

Steves, B. A. (1997). The cycles of Selene. *Vistas Astron.* 41:543. doi: 10.1016/S0083-6656(98)00004-X

Valsecchi, G. B., Perozzi, E., Roy, A. E., and Steves, B. A. (1993). Periodic orbits close to that of the Moon. *Astron. Astrophys.* 271:308.

Conflict of Interest Statement: The author declares that the research was conducted in the absence of any commercial or financial relationships that could be construed as a potential conflict of interest.

frontiers in Applied Mathematics and Statistics

ORIGINAL RESEARCH
published: 20 July 2018
doi: 10.3389/fams.2018.00032

Two Periodic Models for the Earth-Moon System

Marc Jorba-Cuscó[1]*, *Ariadna Farrés*[2] *and Àngel Jorba*[1]

[1] Departament de Matemàtiques i Informàtica, Universitat de Barcelona, Barcelona, Spain, [2] Goddard Planetary Heliophysics Institute, University of Maryland Baltimore Country, Baltimore, MD, United States

This paper discusses two alternative models to the Restricted Three Body Problem (RTBP) for the motion of a massless particle in the Earth-Moon system. These models are the Bicircular Problem (BCP) and the Quasi-Bicircular Problem (QBCP). While the RTBP is autonomous, the BCP and the QBCP are periodically time dependent due to the inclusion of the Sun's gravitational potential. Each of the two alternative models is suitable for certain regions of the phase space. More concretely, we show that the BCP is more adequate to study the dynamics near the triangular points while the QBCP is more adequate for the dynamics near the collinear points.

Keywords: Restricted Three Body Problem, Bicircular Problem, Quasi-Bicircular Problem, periodic hamiltonian, stroboscopic map, invariant manifolds

OPEN ACCESS

Edited by:
Elisa Maria Alessi,
Consiglio Nazionale Delle Ricerche (CNR), Italy

Reviewed by:
Giuseppe Pucacco,
Università degli Studi di Roma Tor Vergata, Italy
Marco Sansottera,
Università degli Studi di Milano, Italy

***Correspondence:**
Marc Jorba-Cuscó
marc@maia.ub.es

Specialty section:
This article was submitted to Dynamical Systems, a section of the journal Frontiers in Applied Mathematics and Statistics

Received: *03 May 2018*
Accepted: *29 June 2018*
Published: *20 July 2018*

Citation:
Jorba-Cuscó M, Farrés A and Jorba À (2018) Two Periodic Models for the Earth-Moon System. Front. Appl. Math. Stat. 4:32. doi: 10.3389/fams.2018.00032

1. INTRODUCTION

During the last years, the scientific community has increased its interest in the natural motions occurring in the Earth-Moon system. The list of possible applications is vast, for instance: the study of the far side of Moon and the relation with the translunar point L_2; the aim to exploit the cis-lunar space and the convenience of using the invariant structures related to L_1.

We have mentioned a couple which are specifically related to the Lagrangian points but, obviously, the list goes on covering a wide range of interests. Efficient mission designs depend ultimately on the understanding of the natural dynamics. To fulfill this goal, it is advisable to use simplified models. Simple models allow us to understand the underlying mechanisms that lead to interesting phenomena. From the dynamical systems point of view, the comprehension of the invariant structures (and their stability) of simple models has helped to shed light on difficult problems such as the motion of asteroids through the solar system, station keeping of spacecraft and taking advantage on the natural dynamics to design spacecraft missions. Perhaps the most illustrative example for the purpose of this work is the existence of the Trojan asteroids that can be predicted using the effective stability of the triangular points of the Sun-Jupiter Restricted Three Body Problem (RTBP). This example is convenient for the purposes of this work because the existence of objects in the triangular points has a counterpart in the Earth-Moon system: the Kordylewsky clouds. We shall come back to this example during this work (section 4.3)but, for the moment being, we want to stress that the existence of these clouds cannot be established by using the same theoretical mechanisms as the Trojan asteroids [1–3]. In fact, the literature related to the Kordylewsky clouds has been stumbling around the existence or nonexistence of objects in the Earth-Moon triangular points, mostly because of the lack of observations. Therefore, it is convenient to analyze whether a simple model is suitable for the problem we want to study.

The Earth-Moon RTBP is the most used simple model for the motion of a small body in the Earth-Moon system. There is, however, a remarkable number of works that take into account the

presence of Sun's gravitation (see, for instance, [4–8]). Indeed, the most relevant effect ignored by the Earth-Moon RTBP is the gravitational attraction of Sun. In this respect, a simple model to study the dynamics near the Earth-Moon system needs to take into account Solar gravity. The problem has a natural non-autonomous periodic time dependence formulation. An advantage of the periodic models is that they can be handled by means of a stroboscopic map i.e., the map defined by the evaluation of the flow at the period of the vectorfield. This is crucial because, while the complexity of the system increases, the study of maps (even if they are numerically defined) is, in some aspects, more comfortable than the study of flow. In periodic time dependent systems, the simplest invariant objects, the ones the dynamics is organized from, are the periodic orbits with the same period as the vectorfield. These periodic orbits appear as fixed points of the stroboscopic maps and their robustness is assured by the classical Implicit Function Theorem. We would like to remark that, in quasi-periodic models the simplest invariant objects are invariant tori. The computation and study of these objects is more difficult. The discussion in this paragraph vindicates a closer look to periodic models for the Earth-Moon system. We have selected two among the literature, the Bicircular Problem (BCP) and the Quasi-Bicircular Problem (QBCP). Both models include Sun's gravity and can be written as periodic perturbations of the RTBP.

The BCP is a restricted four body problem [9, 10]. There are three primaries and a fourth, massless, test particle. In our case, the three primaries are Earth, Moon and Sun. However, this model has been utilized in other cases [11]. It is assumed that Earth and Moon move as in the RTBP, that is, along a circular orbit around its common center of masses. Let us name C_{EM} this barycenter. Name C_{SEM} the center of masses of the Sun-C_{EM} system. As Moon and Earth move, it is assumed that Sun and C_{EM} move in another circular orbit around C_{SEM}. We refer to Gómez, et al. [12] for a detailed derivation of the equations of motion. The BCP is a periodic perturbation of the RTBP that takes into account the direct gravitational effect of a third primary (in our case, Sun) on the particle. This model captures the non-stable character of the triangular points. Henceforth, it is suitable to use it when studying problems related with these locations (see, for instance, [13, 14]). A remarkable shortcoming of the BCP is its lack of coherence i.e., the motion assumed for the primaries does not verify Newton's laws. Moreover, the BCP has no translunar dynamical structure. This justifies the seek for a more complex model for the study of, at least, the L_2 point.

The QBCP is a version of the four body problem. It is conceived to be a coherent counterpart of the BCP. This model was introduced by C. Simó, and it has been used in several works, see [15–17] and, more recently, [18]. A characteristic of the BCP is the lack of coherence of the bicircular solution assumed for the primaries. However, there exist solutions of the three body problem which are close to bicircular [19]. To build the QBCP it is necessary to compute a quasi-bicircular solution of the three body problem, in this case, for the Earth-Moon-Sun case. There are several ways to do such a thing. In Andreu [15], Andreu and Simó [16], and Andreu [17] the authors build a specific algebraic manipulator and compute directly the Fourier coefficients of the quasi-bicircular solution. In Gabern [20], Gabern and Jorba [21], and Gabern et al. [22] the authors use a continuation scheme to compute the desired solution starting from a solution of the two body problem. After that, a Fourier transform is applied to get the Fourier coefficients of the solution. The QBCP is suitable for the study of the collinear points, especially L_1 and L_2.

With this paper, we aim to provide a general insight about the dynamics of these models for a particle in the Earth-Moon system. We care about (practical) stable motion near the triangular points and, to do so, we use the BCP. We also study invariant manifolds related to the collinear points in the QBCP. We believe that the value of this work is, precisely, giving a wide perspective and help the interested reader to choose a suitable simple model to face a first exploration related to a problem concerning the Earth-Moon system.

The paper is organized as follows: section 2 is devoted to a brief description of the RTBP. We explain how the phase space near the Lagrangian points is organized referencing some remarkable works and mentioning the techniques used to study the problem. In section 3 we give some words on the stroboscopic maps and periodic time-dependent Hamiltonian systems. We also explain how to compute high order unstable manifolds related to fixed points using the parameterization method with single and parallel shooting. Section 4 describes how the BCP can be used to study the motion near the triangular points. The advantage of this model with respect to the RTBP is that it captures the unstable character of the triangular points in the real system. The results presented are mainly devoted to stable motion in an extended vicinity of the triangular points. In section 5 we describe results concerning the QBCP. We focus on the unstable manifolds related to the periodic orbits that replace the collinear points. Finally, section 6 is devoted to conclusions and section 7 to technical details.

2. RESTRICTED THREE BODY PROBLEM

The (Circular) RTBP is a simplified model for the motion of a massless particle under the gravitational attraction of two massive bodies, the so-called primaries [23]. The primaries are assumed to revolve along circular orbits around their common center of masses. It is usual to take units of masses so the sum of the masses of the primaries is equal to one. The units of length are taken so the distance between the primaries is equal to one and the units of time are taken so the period of the revolution of the primaries is equal to 2π. It is also standard to take a rotating frame of reference that fixes the primaries at the horizontal axis. The RTBP is an autonomous Hamiltonian system with three degrees of freedom. The Hamiltonian function writes as:

$$H_{RTBP} = \frac{1}{2}(p_x^2 + p_y^2 + p_z^2) - xp_y + yp_x - \frac{1-\mu}{r_{PE}} + \frac{\mu}{r_{PM}}, \quad (1)$$

where $r_{PE}^2 = (x-\mu)^2 + y^2 + z^2$ and $r_{PM}^2 = (x-\mu+1)^2 + y^2 + z^2$. The parameter μ is called the mass parameter and it is the mass of the smallest primary. In the case of the

Earth-Moon system $\mu \approx 0.012$. It is well known that the RTBP has five equilibrium points (see **Figure 1**). Three of them, the collinear points, are located in the horizontal axis. The other two, the triangular points, are located at the third vertex of an equilateral triangle whose other two vertices are the position of the primaries.

The only integral of motion of the RTBP is its Hamiltonian. In many texts, this integral of motion is presented under a slightly different form as the Jacobi integral. Each surface level of this integral is a five dimensional manifold. If the velocities are set to zero, this defines the so-called Zero Velocity Surface. These surfaces separate the configuration space in different regions. The trajectories of the system cannot cross the boundary between two of these regions. The shape of these regions change with the value of the Jacobi integral. As the Lagrangian equilibrium points are critical points of the Jacobi integral, the topology of these regions change when the energy value crosses the value associated to one of the Lagrangian points (for more details, see [23]).

The three collinear points are of type saddle×center×center. This means that, under generic conditions, a 4-dimensional center manifold emerges from each of these points. These manifolds are tangent to the elliptic eigendirections at the points. There exist, as well, one dimensional stable and unstable directions emerging tangentially to the hyperbolic eigendirections. Moreover:

- By the Lyapunov Center Theorem [24], two families of periodic orbits, the Lyapunov families, emanate from the equilibria. One of the families is born tangent to the (z, p_z) plane so it is called vertical family. The other family is contained in the (x, y, p_x, p_y) plane and it is called horizontal family. One can parametrize each family by the amplitude of the orbits. The horizontal families related to L_1 and L_3 can be continued up to trajectories which collide with Earth. The horizontal family related to L_2 can be followed up to collisions with Moon. The vertical families end up in bifurcating planar orbits [12, 25].
- The Lyapunov families can be regarded as the non-linear continuation of the harmonic oscillator given by each elliptic direction of the linearization around the equilibria. When the amplitude tends to zero, the frequency of the family tends to the normal modes of the equilibria.
- As the frequency varies, the horizontal family undergo a 1:1 resonance and the Halo [12, 26–28] family are originated (by means of a pitchfork bifurcation). Secondary families of Halo-type orbits appear by duplication and triplication of the main family [29, 30].

The center manifold can be computed by means of normal form techniques [31–33], with the parametrization method [34–37] and also numerically [29]. The dynamics restricted to the center manifold can be described by a Hamiltonian with two degrees of freedom. By fixing a level of energy and taking a Poincaré section, one can reduce the problem to the study of a family of area preserving maps. This methodology suffices to observe the phase space during the bifurcation that give rise to the Halo families.

2.1. Motion Near the Triangular Points

The Earth-Moon triangular points of the RTBP are linearly stable [23]. KAM theory can be used to establish the existence of a dense set of Lagrangian invariant tori close enough to the equilibria [38]. This has important consequences on the nonlinear stability of the triangular points. If we restrict ourselves to the planar case, these KAM tori (of dimension two) act as barriers for the dynamics in a fixed level of energy. Therefore, KAM tori enclose stable motion for initial conditions which are close enough to the triangular points. This argument based on KAM theory falls apart in the spatial case. Indeed, Lagrangian tori have, in that case, dimension three and the phase space, for a fixed level of energy, is five dimensional. There is, in general, no way to avoid Arnold diffusion [39]. However, using normal form techniques, it is possible to derive bounds on the diffusion time [40] (these techniques can be extended to the periodic [41] and the quasi-periodic case [42]). These, make us think about regions of practical stability i.e., regions in which the motion is non-stable but initial conditions take a long time, maybe longer than the expected age of the solar system, to escape. These theoretical results are valid for a small region near the triangular points and numerical simulations provide evidences of large regions of practical stability [43].

It is natural to look for other invariant structures that play a remarkable role to define the shape of the (numerically computed) region. In this regard, [43] provides numerical evidence on the role of the center-unstable and center-stable manifolds of the collinear point L_3. These manifolds are of dimension five and act as barriers of the dynamics. Obviously, the motion driven by these manifolds escape from the vicinity of the triangular points at some moment, but, again, the required time to do so can be large.

3. PERIODIC TIME-DEPENDENT HAMILTONIANS AND STROBOSCOPIC MAPS

The alternatives to the RTBP presented in this paper, the BCP and the QBCP are both periodic time dependent Hamiltonian systems that can be seen as perturbations of the RTBP. Because of this periodic time-dependence, the Lagrangian points are no longer equilibria but they are replaced by minimal periodic orbits i.e., periodic orbits with the same period as the perturbation. These periodic orbits are known as the *dynamical equivalents* of the Lagrangian points. The usual tools to study numerically the RTBP are the combination of fixing suitable energy levels and suitable Poincaré sections. We note that, in time dependent models like the BCP and the QBCP the Hamiltonian is no longer preserved. A standard tool to deal with these periodic time-dependent systems is the so called stroboscopic map: Let $\mathcal{U} \subset \mathbb{R}^n$ be an open set, T the period of the vectorfield and $\varphi : [0, T] \times \mathbb{R} \times \mathcal{U} \mapsto \mathbb{R}^n$, where $\varphi(t_0, t, x_0)$ stands for the solution which, at time t_0 lies at x_0 evaluated at time t, the flow of the differential equation. We define the stroboscopic map for $x \in \mathcal{U}$ as $f(x) =$

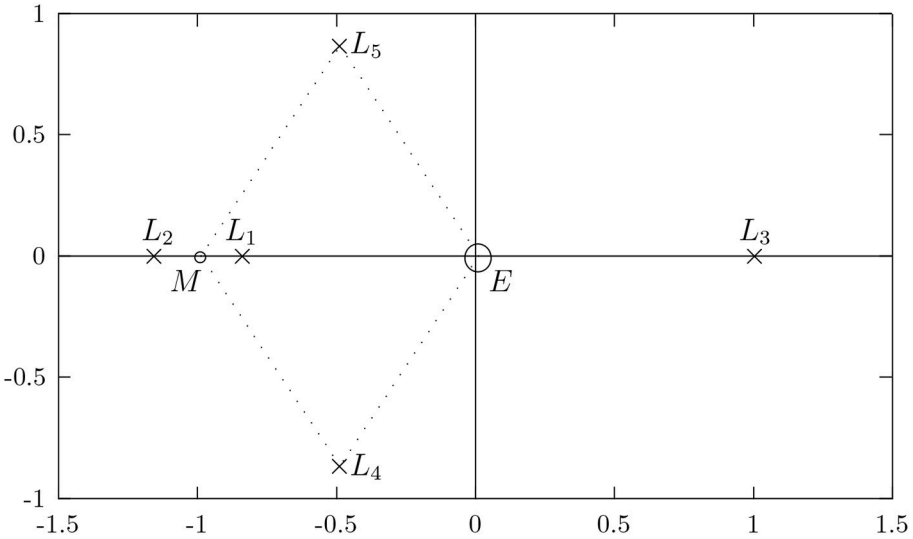

FIGURE 1 | The restricted three body problem.

$\varphi(0, T, x)$. In this work we care about Hamiltonian differential equations. In this case, the stroboscopic map is symplectic.

3.1. Invariant Structures

The simplest invariant objects of the original system are periodic orbits with the same period as the vectorfield. These appear as fixed point of the stroboscopic map. The monodromy matrix associated to these periodic orbits is the differential of the stroboscopic map. The eigenvalues of this matrix determine the linear behavior around the fixed points and, under generic conditions, give some insight about the local non-lineal dynamics. In the symplectic case, under generic conditions, each elliptic direction give rise to a family of invariant curves which can be parametrized by the frequency ([44]). This frequency approaches to the normal mode responsible form the birth of the family at the fixed point. Along the hyperbolic directions, unstable (stable) manifolds depart (arrive) from the fixed points. These invariant objects are crucial to understand the dynamics of the system.

In this paper we focus on the information that can be extracted from the computation of invariant curves and high order approximations of unstable invariant manifolds. While it is quite common, in the literature related astrodynamics, to find discussions on the computation of invariant tori of maps [13, 45, 46] it is not so usual for high order approximations of stable/unstable manifolds.

3.2. High Order Approximation of Unstable Manifolds Using the Parametrization Method

Let $\mathcal{U} \subset \mathbb{R}^n$ be an open set and assume that we are given a map $f : \mathcal{U} \mapsto \mathbb{R}^n$ induced by the evaluation at time T of a flow of some ordinary differential equation (stroboscopic map). The following discussion can be done for any Poincaré map as well. Here we assume that the section is temporal for simplicity of the exposition and because it is the natural section to chose in a periodically perturbed autonomous system. Let us suppose also that $\bar{x} \in \mathcal{U}$ is a fixed point i.e., $f(\bar{x}) = \bar{x}$. Obviously $\bar{x}$ is an initial condition for a T-periodic orbit of the original flow. The linearized normal behavior around the fixed point is given by the eigenvalues of the differential of the map evaluated at the point. Assume spec $Df = \{\lambda, \lambda_2, \ldots, \lambda_n\}$ with $|\lambda| > 1$. Under generic conditions, we know that there exist a 1-dimensional unstable invariant manifold related to the fixed point. That is, there exist an open interval $I \subset \mathbb{R}$ and a map $x : I \mapsto \mathcal{U}$ such that $x(0) = \bar{x}$ and

$$f(x(s)) = x(\lambda s). \tag{2}$$

Equation (2) is known as the invariance equation of the invariant manifold. The parametrization method [47–50] is a powerful tool to, both, prove the existence of the manifold and compute it. The idea is to expand the parameterization of the manifold in Taylor series at $s = 0$ and solve Equation (2) order by order. This makes sense in the case when both the map and the manifold are analytic. This assumption is fulfilled by the applications we are interested in. Hence, the goal is to compute a semi-analytic approximation of a parametrization of the invariant manifold. Let us name

$$x(s) = \sum_{j=0}^{\infty} a_j s^j.$$

We are interested in numerically compute the coefficients a_j for $j = 0, \ldots, d$ for a given degree d. This is achieved by a recurrent scheme in which we solve Equation (2) order by order:

- Order 0 is given by the coordinates of the fixed point.
- Order 1 is given by the eigenvector related to λ.

- For $k > 0$, order $k+1$ is given by the solution of the following linear system:

$$(Df(0) - \lambda^{k+1} I) a_{k+1} = -b_{k+1}.$$

Here, b_{k+1} is the $k+1$-th term of the evaluation of the manifold up to degree k by the map f, that is:

$$f_{\leq k+1}(x_{\leq k}(s)) = \sum_{j=0}^{k} b_j s^j + b_{k+1} s^{k+1},$$

where the subindices $(\cdot)_{\leq k+1}$ denote the truncation of the power expansion of $(\cdot)$ at order $k+1$.

Notice that it is mandatory to have a method to compose power expansions of the manifold with the map itself. Sometimes, when, the map is explicit, one is able to find a suitable recurrence expression to compute the terms of this composition. If a recurrence is not available one can compute higher order terms by automatic differentiation[1]. In the case we are interested, the map is not given explicitly but comes from a numerical integration of a differential equation. Here, the only reasonable strategy seems to use Jet Transport. This technique is based in the idea of, instead of integrating a single point, integrate a function given by its expansion in Taylor series. That is, one transports the jet, the set of derivatives of the function at a given point, up to a given order. It is straightforward to construct an integrator of jets from an integrator of numbers. It is only a matter of replacing the standard floating arithmetic by a polynomial arithmetic [Farrés et al., to appear].

There is another obstacle that can appear when dealing with Poincaré maps: if the orbit is very unstable, the hyperbolic direction may lead to a huge error propagation. This problem can be avoided by using parallel shooting. The idea behind parallel shooting is to enlarge the dimension of the system in order to decrease the time of integration. Let us denote by $\varphi_{t_0}^{t_f}(x)$ the solution of the differential equation with initial condition (t_0, x) evaluated at time t_f. Fix $k \in \mathbb{N}$, the number of sections, and set $h = T/k$. For $i = 0, \ldots k$, we define $\tau_i = ih$. If $m = nk$, we define the function $F : \mathcal{V} \mapsto \mathbb{R}^m$

$$F : \begin{pmatrix} x_1 \\ x_2 \\ \vdots \\ x_k \end{pmatrix} \mapsto \begin{pmatrix} f_k(x_k) \\ f_1(x_1) \\ \vdots \\ f_{k-1}(x_{k-1}) \end{pmatrix}.$$

Here $\mathcal{V} = \mathcal{U}^k$ is an open set of $\mathbb{R}^m$, and, for $x \in \mathcal{U}$, $f_j(x) = \varphi_{\tau_{j-1}}^{\tau_j}(x)$. The differential map DF is given by

$$DF = \begin{pmatrix} 0 & \ldots & \ldots & Df_k \\ Df_1 & \ldots & \ldots & \vdots \\ \vdots & \ldots & \ldots & \vdots \\ 0 & \ldots & Df_{k-1} & 0 \end{pmatrix}.$$

[1]In principle, one could also use numerical differentiation but it is a bad approach in terms of efficiency and accuracy.

For $\bar{x} \in \mathcal{U}$, name $y = (x_1, \ldots, x_k)$ where $x_1 = \bar{x}$ and $x_j = f_j(x_{j-1})$ if $1 < j \leq k$. Then:

1. y is a fixed point of F if and only if $\bar{x}$ is a fixed point of f.
2. The duple $(\zeta, v = (v_1, \ldots, v_k))$, $\zeta \in \mathbb{C}$ and $v_k \in \mathbb{C}^n$ is a pair eigenvalue/eigenvector of $DF(y)$ if and only if (ζ^k, v_1) is a pair eigenvalue/eigenvector of $Df(\bar{x})$.
3. The projection to the first coordinate of the invariant manifold of F related to ζ coincides with the invariant manifold of f related to $\zeta^k = \lambda$.

4. THE BICIRCULAR PROBLEM AND THE TRIANGULAR POINTS

The BCP is a perturbation of the RTBP. It is usual to take the units and the synodic coordinates of the Earth-Moon RTBP (see **Figure 2**). The BCP is not coherent, that is, the trajectories followed by the primaries do not obey Newton's laws. This is not an inconvenient since the model has been shown to be useful to describe the dynamics near the triangular points [51]. As a dynamical system, the BCP is a Hamiltonian system with three and a half degrees of freedom, i.e., a non-autonomous periodically time dependent with three degrees of freedom. The Hamiltonian function, written in the RTBP coordinates and units, is given by

$$H = \frac{1}{2}(p_x^2 + p_y^2 + p_z^2) - x p_y + y p_x - \frac{1-\mu}{r_{PE}} - \frac{\mu}{r_{PM}} - \frac{m_S}{a_S^2}(y \sin\theta - x \cos\theta) - \frac{m_S}{r_{PS}}. \quad (3)$$

Here μ, r_{PE} and r_{PM} denote the same quantities as in (1). Moreover, m_S denotes the mass of Sun, a_S the averaged semi-major axis of Sun, $\theta = \omega_S t$, ω_S is the frequency of Sun in this system of reference, $T_S = \frac{2\pi}{\omega_S}$ is its period and finally, $r_{PS}^2 = (x - a_S \cos\theta)^2 + (y - a_S \sin\theta)^2 + z^2$. Notice that this Hamiltonian can be splitted in two parts:

$$H_{BCP} = H_{RTBP}(X) + H_S(\theta, X).$$

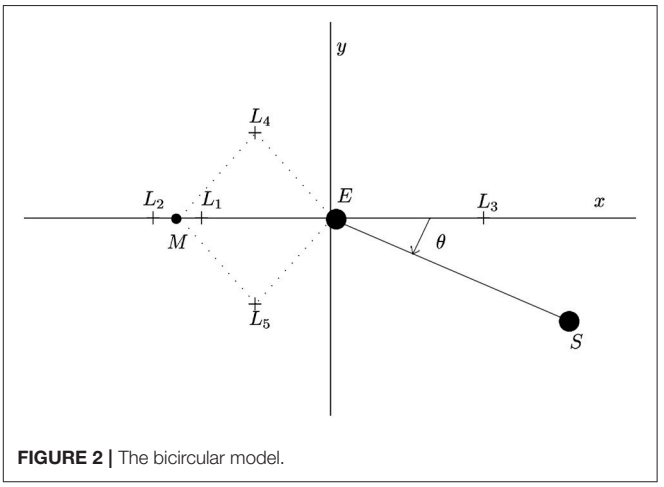

FIGURE 2 | The bicircular model.

The time dependent part contains two terms, the Coriolis effect due to the rotating frame of coordinates and Sun's gravitational potential. The Taylor expansion of the potential starts with

$$\frac{1}{a_S}\left(1+\frac{x\cos\theta - y\sin\theta}{a_S}\right).$$

Therefore, the Hamiltonian, if we truncate the Sun's potential at linear order is written as

$$H_{BCP}^{<2} = H_{RTBP} - \frac{m_S}{a_S}.$$

So, the Coriolis term and the truncated Sun's potential cancel out and the dynamics is the one of the RTBP. This is to say that the contribution due to Sun's potential starts at order two, that is, the BCP is a periodic time dependent perturbation with size $\mathcal{O}(\frac{m_S}{a_S^3}) \approx 0.0056$. Anyhow, it is large enough to produce remarkable changes on the dynamics, especially near the triangular points. In **Figures 3** (left), **6** (left) we display continuations from the RTBP to the BCP. The vertical axis in these plots represent an artificial parameter ε which multiplies the mass of Sun. Therefore, when $\varepsilon = 0$ the model corresponds to the RTBP and, when $\varepsilon = 1$ the model corresponds to the BCP. We shall comment these figures in detail in the next sections.

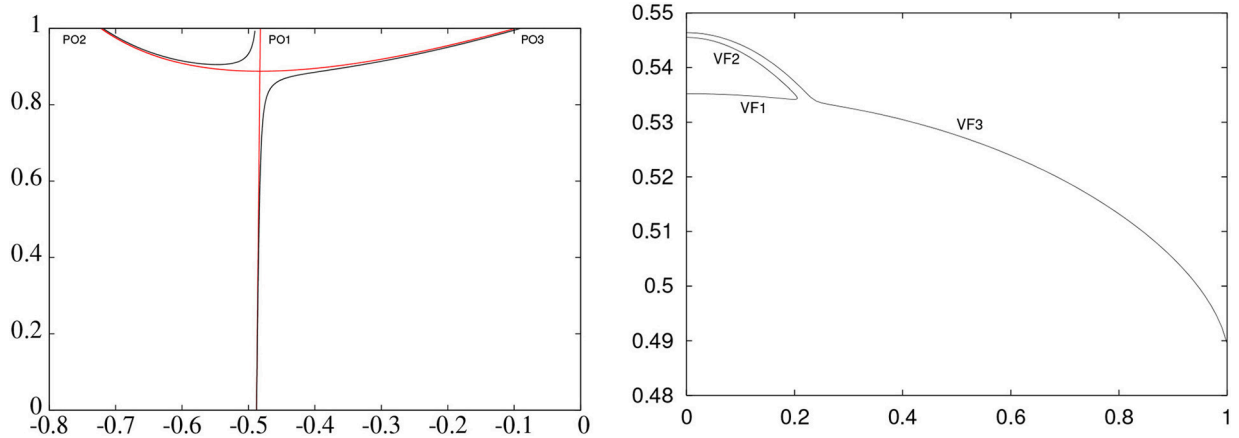

FIGURE 3 | Left: Continuation of L_4 as a periodic orbit with respect to the mass of Sun. Horizontal axis: x. Vertical axis: ε. The black curve stands for the continuation to the BCP. The red curve for the truncated version of the BCP. See text for more details. **Right:** Vertical families of 2*D* tori for the BCP. The horizontal axis is the p_Z coordinate and the vertical axis displays the frequency. See text for more details.

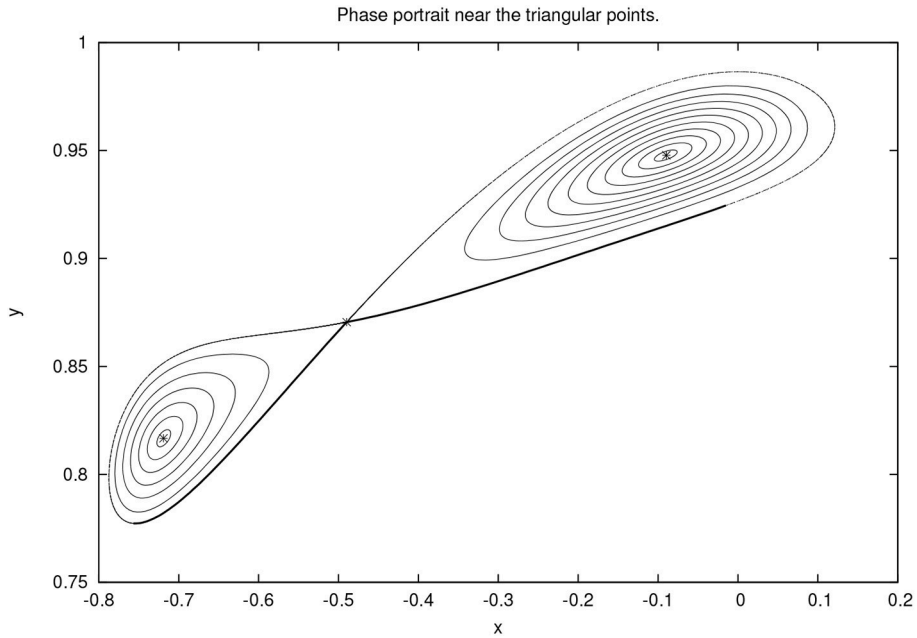

FIGURE 4 | Stroboscopic map near the triangular points: Horizontal axis x. Vertical axis y. See text for more details.

4.1. Dynamical Equivalents of the Triangular Points

First of all let us mention that, due to a symmetry, the dynamics near L_4 is the same as the dynamics near L_5 (in fact, this symmetry maps orbits in the region $y > 0$ to orbits in the region $y < 0$). A feature of the BCP to be stressed is that the region around the geometrically defined triangular points is unstable. The influence of Sun's potential is enough to produce a bifurcation in the periodic orbit that replaces L_4 (i.e., L_5). It is well known [51] that each triangular point is replaced by three periodic orbits with the same period as Sun. One small and unstable (the actual replacement of L_4) and two which are stable. We have named these orbits *PO*1, *PO*2, and *PO*3. See **Figure 3** (left) a continuation diagram from the RTBP to the BCP. The two additional periodic orbits are produced by an imperfect pitchfork bifurcation (i.e., a pitchfork bifurcation broken due to a loss of symmetry).

One may ask which is the model that displays the perfect bifurcation and which is the broken symmetry. To address this question we take a look at the order two of the Taylor expansion of Sun's gravitational potential. We have

$$H_S^2(\theta, x, y, z) = \frac{1}{a_S^3}\left(\frac{3}{2}T(x, y, \theta)^2 - \frac{1}{2}(x^2 + y^2)\right).$$

We have named $T(x, y, \theta) = -x\cos\theta + y\sin\theta$. We would like to stress again that H_S^2 is the first contributing non-autonomous term in the model due to the cancellation produced by the Coriolis acceleration. This term is invariant under the symmetry $(x, y, x, \theta) \mapsto (x, -y, x, -\theta)$. The order three of the expansion is given by:

$$H_S^3 = \frac{1}{a_S}\left(\left(\frac{\rho}{a_S}\right)^3 \frac{\frac{5}{2}T^3 - \frac{3}{2}T}{a_S\rho}\right).$$

Here $\rho^2 = x^2 + y^2$. The polynomial in T is no longer even. This breaks the symmetry and, hence, the pitchfork bifurcation. The non-autonomous model that displays the perfect bifurcation is:

$$H_{BCP}^{\leq 2} = H_{RTBP}(X) + H_S^2(X, \theta).$$

The perfect (non broken) pitchfork bifurcation in **Figure 3** (left, curve in red) shows the continuation diagram from the RTBP to this simplified version of the BCP. Due to the symmetry, periodic orbits *PO*2 and *PO*3 only differ on the phase on the orbit.

4.2. Phase Space of the Stroboscopic Map Near the Triangular Points

The three periodic orbits appear as fixed points of the stroboscopic map. We recall that their linear normal behavior is of type saddle×center×center for *PO*1 and totally elliptic for *PO*2 and *PO*3. There are several ways to justify that, from the elliptic directions of each fixed point, there is a family of invariant curves whose frequency tends to the normal modes of the fixed points [44, 52].

Therefore, we have a family of invariant curves for each elliptic direction, that is, two for *PO*1 (*HF*1 in the horizonal plane and *VF*1 in the vertical direction), three for *PO*2 (*HF*2*F*1 and *HF*2*F*2 are horizontal, and *VF*2 is vertical) and three for *PO*3 (*HF*3*F*1 and *HF*3*F*2 horizontal, and *VF*3 vertical). The remaining eigendirection of *PO*1 is hyperbolic. There exist stable and unstable one-dimensional invariant manifolds associated to these hyperbolic directions. Initial conditions near the triangular points shadow the unstable manifold which wonder some time around the periodic orbits *PO*2 and *PO*3 and finally abandon the vicinity of the triangular points. These manifolds are of special interest if one plans to put or take out objects near L_4 and L_5. The stable and unstable manifolds related to *PO*1 can be computed up to high order directly on the stroboscopic map (section 3.2 and [Farrés et al., to appear]). In **Figure 4** we observe a projection of the phase portrait of the map. The three points displayed with crosses correspond to *PO*1 (in the middle), *PO*2 and *PO*3. It is displayed as well, semianalytical approximations of the stable and unstable invariant manifolds. We have used an approximation of order 64. The width curve are the pieces given by the parameterization. The thin curve correspond to some iterations of these pieces. It can be observed, also, some invariant curves growing from *PO*2 and *PO*3. These invariant curves are totally elliptic near the fixed points.

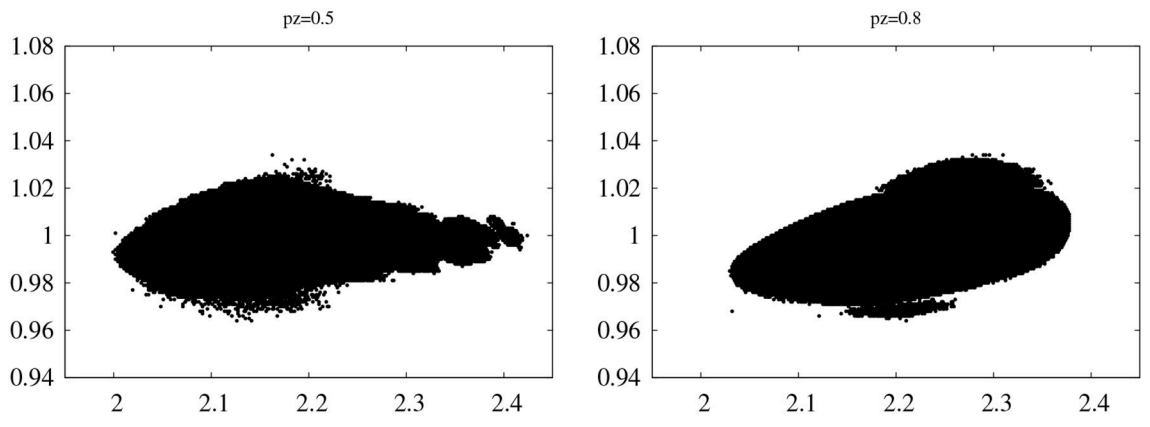

FIGURE 5 | Stability regions with initial conditions on the tori of the *VF*3 identified by $p_z = 0.5$ and $p_z = 0.8$. Horizontal axis: α. Vertical axis r. See text for more details.

4.3. Regions of Effective Stability Near the Triangular Points

As we have observed, the triangular points are replaced by three periodic orbits, one of them unstable. This is the reason why the BCP is an interesting model [12]. Indeed, the unstable manifold of the triangular periodic orbit takes initial conditions away from the vicinity of the triangular points. However, we can pursue on the seek for regions of (effective) stability out of the plane of motion of the primaries. The mechanism that suggest the existence of regions of effective stability is the stickiness of normally elliptic low dimensional invariant tori. See [41, 52]. As we discussed before, there are families of invariant tori emanating from the periodic orbits *PO*2 and *PO*3. These families are elliptic close enough to the fixed points. This results on two small regions of effective stability in the plane of motion of the primaries related to the totally elliptic orbits.

We put our attention on the vertical families (one for each orbit) of invariant tori. In **Figure 3**, Right, we display how these families vary when they grow out of the plane of motion of the primaries. We observe that the three families display a broken pitchfork symmetry, analogous to the one of the periodic orbits. The linear normal behavior of the tori is the same as the periodic orbit near the plane. As a consequence of the pitchfork bifurcation, at some some distance of the plane, the surviving family is totally elliptic. Therefore, the tori are sticky and regions of effective stability are to be expected. We label these families *VF*1, *VF*2 and *VF*3 after the corresponding periodic orbits. The families *VF*1 and *VF*2 are connected, as it happens with *PO*1 and *PO*2. On the other hand *VF*3 reaches high amplitudes in the (z, p_z) plane. It is known that, skipping resonances, the three families have the same stability as the corresponding periodic orbits. Therefore, the tori of *VF*1 have hyperbolic directions while the ones of *VF*2 are normally elliptic (except for small intervals of instability produced by resonances involving internal and normal frequencies). Recall that both families are connected and the change of stability takes place at a turning point. The tori of *VF*3 are normally elliptic up to very high values (again, except for resonances).

Normally elliptic lower dimensional tori induce regions of effective stability. Numerical estimations of the shape and the size of these regions show that, in the case of *VF*2, the regions are small and narrow while in the case of *VF*3 large regions exist for sufficiently high values of the vertical amplitude. In **Figure 5** we show two stability regions out of the horizontal plane. These regions seem to persist in the real model for time spans of 1,000 years [14, 53]. The effect of Solar Radiation Pressure on the effective stability regions of the BCP is discussed in Jorba-Cuscó et al.[54].

Let us explain how **Figure 5** is obtained. Each of the vertical family of invariant tori can be identified by the value of the coordinate p_z when $z = 0$ and $p_z > 0$. Denote by $a(p_z) \in \mathbb{R}^6$ the coordinates of the point that identifies a torus. We have to select a set of initial conditions near $a(p_z)$ and integrate them for a long time span. Let us be more precise on how to select the initial conditions. We use a two dimensional grid, the coordinates z, p_x, p_y and p_z will be fixed by the corresponding values of $a(p_z)$. To adapt to the shape of the regions, we use a polar-like grid, centered at Earth:

$$\begin{cases} x_{ij} = r_i \cos\alpha_j + \mu, & r_i = 1 + ih_r, \\ y_{ij} = r_i \sin\alpha_j, & \alpha_j = 2\pi j h_\alpha, \end{cases}$$

where h_r and h_α are used to control the density of the grid. The computation goes as follows. Take a point of the grid and integrate the vector field 15000 Moon revolutions. At each integration step, we test if there is a collision with Earth or Moon. If there is a collision, or the coordinate y becomes negative, we stop the integration (Recall that we are interested in the points that remain close to L_4). We have used $h_r = 0.001$ and $h_\alpha = 0.0002$. The difference on the sizes of these small quantities is aimed to produce a nearly squared grid.

4.4. A Weakness of the BCP

The translunar point is one of the most interesting locations at the Earth-Moon system. The reason is that L_2 seems suitable to observe the far side at Moon. Taking into account that, a

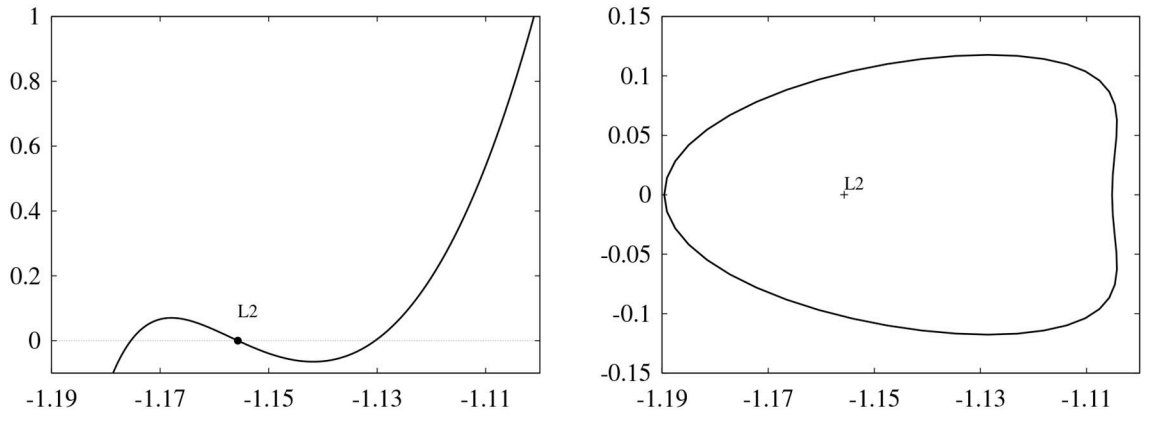

FIGURE 6 | Left: Continuation of L_2 as a periodic orbit with respect to the mass of the Sun. Horizontal axis: x. Vertical axis: ε. See text for more details. **Right:** Periodic orbit near L_2 in the BCP. Horizontal axis: x. Vertical axis: y.

natural criticism to the BCP is that it does not have a dynamical replacement of L_2. In **Figure 6** (left) it is displayed a continuation of L_2 as a periodic orbit from the RTBP to the BCP. The periodic orbits are identified by their coordinates as fixed points of the Stroboscopic map. These orbits have been computed by means of the parallel shooting method. Again, the vertical axis is an additional parameter, ε, multiplying the mass of Sun. The point L_2 is the middle crossing of the characteristic curve with the homotopy level corresponding to the RTBP, at the bottom. The other two points of the RTBP correspond to the same 1:2 resonant planar Lyapunov orbit but with different initial times. We observe that the continuation of L_2 reaches a turning point and it never reaches the homotopy level of the BCP. The result is that the translunar dynamical structure is lost in the BCP. This suggest that a more complex model needs to be used to analyze the natural behavior near the translunar point. The resonant Lyapunov orbit can be continued to the BCP. The result is a large orbit that remains away from the translunar point, see **Figure 6** (right).

5. THE QUASI-BICIRCULAR PROBLEM AND THE COLLINEAR POINTS

The quasi-bicircular solution of the Earth-Moon-Sun system is planar i.e., the three bodies move in the same plane. After the quasi-bicircular solution is computed one can write the equations of motion of the test particle, prescribing the quasi-bicircular solution as motion for the primaries. It is usual to compute the quasi-bicircular solution in the Jacobi frame, however, if one has the purpose of describing the dynamics in the Earth-Moon vicinity, it is suitable to use the frame of coordinates corresponding to the Earth-Moon RTBP. To do so, one has to perform three different transformations. First, one has to use a translation to move the origin from the global barycenter to Earth's and Moon's center of masses. Second, one has to use a rotating (synodic) frame to keep Earth and Moon fixed on the horizontal axis. Third, the unit of length is scaled so the distance between Earth and Moon is equal to one. The units of mass and time which are usually selected in the Earth-Moon RTBP can be imposed already in the Jacobi formulation of the Three Body Problem.

The resulting model is a Hamiltonian system with three and a half degrees of freedom. The Hamiltonian function can be written as

$$H = \frac{1}{2}\alpha_1(p_x^2+p_y^2+p_z^2)+\alpha_2(p_x x+p_y y+p_z z)+\alpha_3(p_x y-p_y x) +\alpha_4 x+\alpha_5 y-\alpha_6\left(\frac{1-\mu}{r_{pe}}+\frac{\mu}{r_{pm}}+\frac{m_S}{r_{ps}}\right), \quad (4)$$

TABLE 2 | Continuation of the low order resonant orbits from the RTBP to the QBCP.

RTBP	RES	BIF	QBCP
012	1 : 2	2	12, 13
014	1 : 1	4	14, 15, 16, 17
018	1 : 1	4	18, 19, 1A, 1B
01C	1 : 3	2	1C, 1D
01E	1 : 3	2	1E, 1F
022	1 : 2	4	22, 23, 24, 25
026	1 : 6	4	26, 27, 28, 29
02A	1 : 2	4	2A, 2B, 2C, 2D
02E	1 : 3	2	2E, 2F
026	1 : 4	2	2G, 2H

The first column contains the label of the orbits corresponding to the RTBP. The second column contains the order of the resonance. The third columns contains number of bifurcating orbits. The fourth column contains the label of the orbits corresponding to the QBCP. See [15] for more details. See text for the color code.

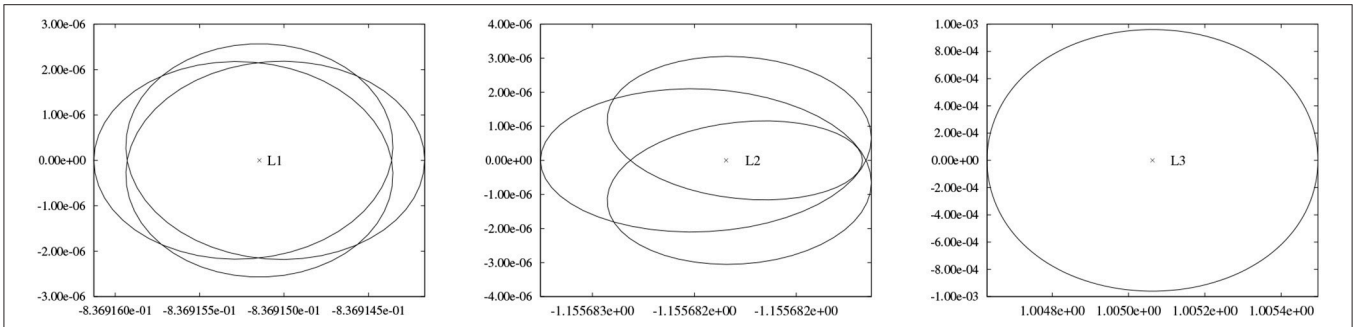

FIGURE 7 | Dynamical equivalents of the collinear points. **Left:** L_1. **Center:** L_2. **Right:** L_3. Horizontal axis: x. Vertical axis: y. See text for more details.

TABLE 1 | Eigenvalues of the three dynamical equivalents of L_1, L_2 and L_3.

	L_1	(real)	(imag)	L_2	(real)	(imag)	L_3	(real)	(imag)
1		460182151.57	0		2397196.84	0		3.370855	0
2		−0.987151	0.159784		0.995818	0.0913562		0.863840	−0.503764
3		−0.963639	0.267205		0.917527	0.3976716		0.841148	0.5408042

We only put three for each orbit. The rest are given by their inverses due to the symplectic character of the stroboscopic map.

where, $r_{pe}^2 = (x-\mu)^2 + y^2 + z^2$, $r_{pm}^2 = (x-\mu+1)^2 + y^2 + z^2$, $r_{ps}^2 = (x-\alpha_7)^2 + (y-\alpha_8)^2 + z^2$, and for $i = 1, \ldots, 8$ $\alpha_i : \mathbb{T} \mapsto \mathbb{R}$ are periodic functions. That is,

$$\alpha_i(\theta) = a_0^i + \sum_{k\geq 0} a_k^i \cos k\theta + \sum_{k\geq 0} b_k^i \sin k\theta. \tag{5}$$

Here, $\theta = \omega_S t$ and ω_S is the frequency of Sun. Moreover, α_i is odd for $i = 1, 3, 4, 6, 7$ and even for $i = 2, 5, 8$. Obviously one can only have a numerical approximation of these functions. In this case, we take advantage on the computations done in [15] and take the same values for the Fourier coefficients of the periodic functions α_i's. To end, and taking into account the properties of the functions α_i's, it is easy to see that the Hamiltonian function (4) has the symmetry $(\theta, x, y, z, \dot{x}, \dot{y}, \dot{z}) \mapsto (-\theta, x, -y, z, -\dot{x}, \dot{y}, -\dot{z})$, $\dot{x} = p_x + y$, $\dot{y} = p_y - x$, $\dot{z} = p_z$.

The meaning of these periodic functions is the following:

1. $(\alpha_7, \alpha_8, 0)$ is the position of Sun in the plane of motion of the primaries.
2. α_1, α_2, α_3 and α_6 capture the fact that the distance between Earth and Moon is not constant.
3. α_4 and α_5 take into account the Coriolis effect due to the rotating frame of reference.

5.1. Dynamical Equivalents of the Collinear Points

In this section we give some words about the minimal periodic orbits that replace the collinear points in the QBCP. In **Figure 7** we display the dynamical equivalents, from left to right, of L_1, L_2 and L_3. We observe that the orbits replacing L_1 and L_2 are small, their maximal distance to the corresponding equilibrium point is of order $\mathcal{O}(10^{-6})$. As the original equilibrium points, the linear normal behavior of these orbits is of type saddle×center×center. In **Table 1** we display the eigenvalues of each orbit. We notice that the unstable direction of L_1 (of order 10^8) and the unstable direction of L_2 (of order 10^6) are large and this implies huge propagation of error near these orbits. On the other hand, the dynamical equivalent of

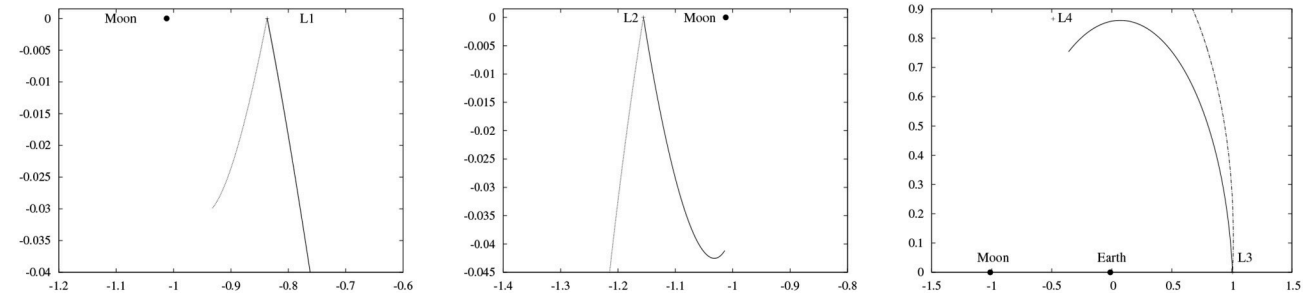

FIGURE 8 | Approximation of order 64 of the stable (dashed) unstable (solid) manifolds of L_1, L_2 and L_3. Horizontal axis x. Vertical y.

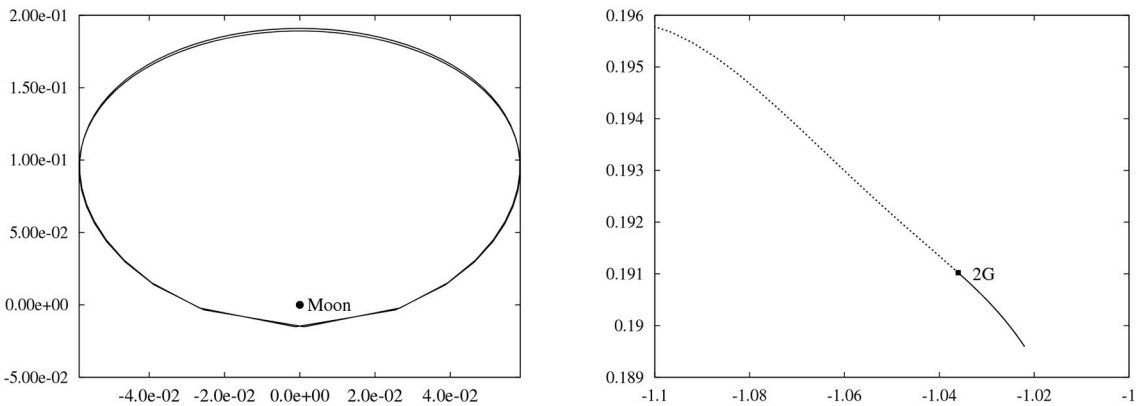

FIGURE 9 | Left: Resonant orbit 2G. **Right:** Approximation of order 64 of the stable (dashed) unstable (solid) manifolds of the ressonant orbit 2G. Horizontal axis y. Vertical z.

TABLE 3 | Values of the parametres used in this paper.

μ	a_S	m_S	ω_S
0.012150581623433623	388.81114302335106	328900.54999999906	0.92519598551829646

L_3 has a very weak unstable direction, at least compared to the other two.

5.2. Resonant Orbits of Low Order

As the QBCP is a T_S-periodic system, the simplest invariant objects are T_S-periodic orbits. We already have mentioned that the equilibrium points are replaced by these periodic orbits of minimal period. Periodic orbits of the RTBP whose frequency is resonant with the one of Sun also persist as T_S-periodic orbits in the QBCP. The Lyapunov and Halo families of periodic orbits related to the equilibrium points L_1 and L_2, are a source for these kind of resonant orbits. In contrast with the families related with L_3, the families of the two first libration points are nourished with low order resonant orbits. A relation of low order resonant periodic orbits of the RTBP can be found in [15]. In [29] the authors show the ranges for the admissible periods for each family. The families related to L_3 are of relatively large period and there are not many periodic orbits whose frequency are in low order rational relation with the frequency of Sun. There is, however, a 1:1 resonant periodic orbit near the end of the vertical family. This orbit is enormous in size and cannot be considered in the vicinity of L_3. In **Table 2** details of the continuations of low order resonant orbits from the RTBP to the QBCP are given: The first column corresponds to resonant periodic orbits of the RTBP. The label in this first column consist in three numbers that encode each orbit. The first is a zero and indicates that the orbit belongs to the RTBP (this is intended to distinguish them from the orbits in the last column corresponding to the QBCP). The second number refers to the libration point related to each orbit (all of them belong to Lyapunov and Halo families related to L_1 and L_2). The third number is just an enumeration. The second column indicates the order of the resonance. We stress that the influence of Sun is relevant enough to produce bifurcating orbits in each of the continuations. The third column shows how many orbits bifurcate from the original ones when they are continued to the QBCP. Finally the last column contains the labels of the resulting orbits in the QBCP. **Table 2** can be found originally in Andreu [15]. We have added the order of the resonance and the color code to indicate the linear normal behavior of each orbit. Labels in blue stand for orbits of type saddle×center×center. Labels in green denote linear character of the kind saddle×saddle×center. Names in cyan denote totally hyperbolic orbits. The color yellow denotes totally elliptic orbits. The continuation for the orbits in red do not reach the homotopy level of the QBCP and, therefore, are not considered.

5.3. High Order Approximation of the Unstable Manifolds of the Collinear Periodic Orbits

This section is devoted to the results of implementing the algorithm explained in section 3.2 to the dynamical equivalents of the collinear points. **Figure 8** shows pieces of the stable (dashed) and unstable (solid) manifolds related to the three

TABLE 4 | Coefficients of the functions α_j, $j = 1, \ldots, 8$, in (5).

α_1		α_2		α_3		α_4	
k	a_k	k	a_k	k	b_k	k	a_k
0	1.001841608924835e+00	0	0.e0	0	9.999999999999983e-01	0	−9.755242327484885e-04
1	5.767517726198399e-04	1	−2.644376028499938e-04	1	5.634125997553694e-04	1	2.154764362707107e+00
2	1.438777025507630e-02	2	−1.328686903400173e-02	2	1.889687440172882e-02	2	3.657484468968697e-04
3	−2.630362974972015e-06	3	9.386093208089751e-06	3	−9.911758802567132e-06	3	3.295673376166588e-03
4	1.176278356118933e-04	4	−1.218509057517414e-04	4	1.568708136031134e-04	4	3.301031400812427e-07
5	−38.068581391005552e-08	5	1.522127598557008e-07	5	−1.707762576173484e-07	5	1.278840687376320e-05
6	9.843249766501285e-07	6	−1.072102664277996e-06	6	1.319613679707437e-06	6	−2.623797952127926e-09
7	−1.172054394418197e-09	7	1.889371261374048e-09	7	−2.136550041985646e-09	7	6.533805514561511e-08
8	8.311905970879588e-09	8	−9.324985038927486e-09	8	1.117168916673893e-08	8	−3.891720707783511e-11
9	−1.408584238695393e-11	9	2.114490981280258e-11	9	−2.387253631031108e-11	9	3.812275838944432e-10
10	7.050713786466840e-11	10	−8.071111743144353e-11	10	9.490879622095902e-11	10	−3.907906049834876e-13
11	−1.494259634910463e-13	11	2.218118050420168e-13	11	−2.462732581558427e-13	11	2.407471187576443e-12
12	5.982418979451232e-13	12	−7.036155161882012e-13	12	8.101067708009743e-13		

α_5		α_6		α_7		α_8	
k	b_k	k	a_k	k	a_k	k	b_k
0	0.e0	0	1.000907457708158e+00	0	−6.314069568006227e-02	0	0.e0
1	−2.192570751040067e+00	1	2.870921750053134e-04	1	3.885638623098048e+02	1	−3.897437256237654e+02
2	−3.337210485472868e-04	2	7.187177998612875e-03	2	1.736910203345558e-01	2	−1.734279166322518e-01
3	−3.295001430200974e-03	3	−2.351183147213254e-06	3	3.382908071669699e+00	3	−3.385696486642120e+00
4	−3.100635053052634e-07	4	4.585758971122060e-05	4	1.574837565380491e-04	4	−1.555886632413398e-04
5	−1.277777336854128e-05	5	−3.848683620107037e-08	5	2.936360489004438e-02	5	−2.937582671967532e-02
6	2.652806405498111e-09	6	3.270677504935666e-07	6	−1.224434550116014e-05	6	1.225851213107933e-05
7	−6.528479245085066e-08	7	−4.406966481041876e-10	7	2.538935434262443e-04	7	−2.539596887692642e-04
8	3.891720707783511e-11	8	2.452600662570259e-09	8	−2.278929040007574e-07	8	2.280029220202363e-07
9	−3.812275838944432e-10	9	−4.542938800673444e-12	9	2.190432706181655e-06	9	−2.190834624429040e-06
10	3.907906049834876e-13	10	1.892348855112616e-11	10	−3.033311961234353e-09	10	3.036109035120856e-09
11	−2.407471187576443e-12	11	−4.178420101480123e-14	11	1.886971545290216e-08	11	−1.887457647579322e-08
		12	1.480048946961583e-13	12	−3.432375106898453e-11	12	3.432375106898453e-11
				13	1.611513703999101e-10	13	−1.631723641506449e-10

Due to the symmetries of the model, each α_j only contains either $\sin$ or $\cos$ terms, so we only list either the a_k or b_k coefficients.

collinear periodic orbits (the other branches can be obtained by symmetry). From left to right: the one related to L_1, the one related to L_2 and the one related to L_3. We would like to remark that these pieces are obtained directly from the evaluation of the approximation (of order 64) of the manifolds. The error is controlled by checking that the contribution of the last term of the approximating polynomial is small. It is also checked that all the points in the pieces verify the invariance equation with high accuracy. We can observe that these approximations already give large excursions far away from the collinear points. Especially in the case of L_3, where the piece of the manifold passes very close to the triangular points. The axes of **Figure 8** show the x and y values. These pieces can be mapped through the stroboscopic map to obtain larger pieces of the manifolds if it is necessary. The point of giving high order approximations of the manifold is that, just a fewer number of iterates are necessary. For the computation of the manifold related to L_3, a simple shooting method has been used. Indeed, the instability associated to this libration orbit is very weak. For the computation of the manifold related to L_2, multiple shooting is required. We have used two sections. For the computation of the manifold related to L_1, the most unstable one, we have used a single shooting strategy but with an extended precision arithmetic of 128 bits. This last approach makes the program far slower but very simple to code. In **Figure 9** (left) we show the resonant orbit $2G$ of **Table 2**. We display also (right) the stable (dashed) and unstable (manifolds).

6. CONCLUSIONS

We have presented two alternatives to the RTBP for the study of the motion of a test particle in the Earth-Moon system. Both models, the BCP and the QBCP, depend periodically on the time. We use the so-called stroboscopic map to study the minimal periodic orbits of the systems and the invariant manifolds related to them.

The BCP is as useful model for the study of the triangular points. The simplicity of the vectorfield is a strong point, especially in problems related to effective stability where massive integrations are mandatory. We have also stressed its weakness: it is not suitable to understand the dynamics around the collinear points. The BCP is useless to describe the vicinity of the translunar point.

We have used the parametrization method to obtain high order approximations of the unstable manifolds related to the minimal periodic orbits that replace the collinear points in the QBCP. This is helpful to design long excursions between the two primaries and the collinear points. The main novelty is that we have computed the manifolds directly on the stroboscopic map. The QBCP is a complicated model with a numerically computed vectorfield. This makes it a bad candidate (in front of the BCP) to be the model used to face the problems involving massive simulations related to the triangular points.

We would like to stress that the BCP should be used to face problems related to the triangular points. Especially if this problems involve large time integrations to seek for regions of practical stability. The QBCP should be used when dealing with problems involving the collinear points.

7. TECHNICAL DETAILS

All the computations appearing in the Figures of this paper, also the ones which appear in the literature, have been performed by the authors. The integrations for the RTBP, the BCP and the QBCP have used a Taylor method with variable order and stepsize. The demanded accuracy for the standard double precision has been 10^{-16}. The computations in multiple accuracy have been done using the library mpfr. The LAPACK library has also been used for some computations related to linear algebra. The rest of the programs have been written by the authors in C and C++ languages from the scratch. **Table 3** and **Table 4** contains the values of the parametres used for the computations.

AUTHOR CONTRIBUTIONS

AF, ÀJ, and MJ-C split, more or less, equally the tasks regarding the computation and writing of the paper.

ACKNOWLEDGMENTS

The authors would like to thank J. Gimeno and N. Miguel for their help. This work has been supported by the Spanish grants MTM2015-67724-P (MINECO/FEDER), MDM-2014-0445 and the Catalan grant 2017 SGR 1374. The project leading to this application has received funding from the European Union's Horizon 2020 research and innovation programme under the Marie Skłodowska-Curie grant agreement No 734557.

REFERENCES

1. Gabern F, Jorba À, Locatelli U. On the construction of the Kolmogorov normal form for the Trojan asteroids. *Nonlinearity* (2005) **18**:1705–34. doi: 10.1088/0951-7715/18/4/017
2. Páez RI, Locatelli U. Trojan dynamics well approximated by a new hamiltonian normal form. *arXiv:1508.00381* (2015)
3. Páez RI, Efthymiopoulus C. Secondary resonances and the boundary of effective stability of trojan motions. *arXiv:1712.08460* (2017)
4. Gómez GG, Jorba À, Masdemont J, Simó C. A quasiperiodic solution as a substitute of l_4 in the Earth-Moon system. In: *Proceedings of the 3rd International Sysmposium on Spacecraft Flight Dynamics*, ESTEC. Noordwijk: ESA Publications Division (1991). p. 35–41.
5. Gómez GG, Jorba À, Masdemont J, Simó C. Quasiperiodic orbits as a substitute of libration points in the solar system. In: Roy, AE editor, *Predictability, Stability and Chaos in N-Body Dynamical Systems*. Plenum Press (1991). p. 433–438.
6. Gómez GG, Jorba À, Masdemont J, Simó C. *Study of Poincaré Maps for Orbits Near Lagrangian Points*. ESOC contract 9711/91/D/IM(SC), final report, European Space Agency (1993). Reprinted as *Dynamics and mission design near libration points. Vol. IV, Advanced methods for triangular points*, volume 5 of World Scientific Monograph Series in Mathematics, (Singapore) 2001.

7. Gómez GG, Llibre J, Martínez R, Simó C. *Dynamics and Mission Design Near Libration Points. Vol. I, Fundamentals: The Case of Collinear Libration Points, Vol. 2, World Scientific Monograph Series in Mathematics*. World Scientific Publishing Co. Inc., (2001).
8. Gómez GG, Llibre J, Martínez R, Simó C. *Station Keeping of Libration Point Orbits*. ESOC contract 5648/83/D/JS(SC), final report, European Space Agency (1985).
9. Huang SS. *Very Restricted Four-Body Problem*. NASA technical note. Washington, DC: National Aeronautics and Space Administration, (1960).
10. Cronin J, Richards PB, Russell, LH. Some periodic solutions of a four-body problem. *Icarus* (1964) **3**:423–8.
11. Barrabés E, Gómez G, Mondelo JM, Ollè M. Pseudo-heteroclinic connections between bicircular restricted four-body problems. *Month Not R Astron Soc.* (2016) **462**:740–50.
12. Gómez G, Jorba À, Masdemont J, Simó C. *Study Refinement of Semi-Analytical Halo Orbit Theory*. ESOC contract 8625/89/D/MD(SC), final report, European Space Agency (1991).
13. Castellà E, Jorba À. On the vertical families of two-dimensional tori near the triangular points of the Bicircular problem. *Celestial Mech.* (2000) **76**:35–54. doi: 10.1023/A:1008321605028
14. Jorba À. A numerical study on the existence of stable motions near the triangular points of the real Earth-Moon system. *Astron. Astrophys.* (2000) **364**:327–38.
15. Andreu MA. *The Quasi-Bicircular Problem*. PhD thesis, University of Barcelona (1998).
16. Andreu MA, Simó C. The quasi-bicircular problem for the Earth-Moon-Sun parameters. (2000). Available online at: http://www.maia.ub.es/dsg/2000/index.html
17. Andreu MA. Dynamics in the center manifold around L_2 in the quasi-bicircular problem. *Celestial Mech.* (2002) **84**:105–33. doi: 10.1023/A:1019979414586
18. Bihan BL, Masdemont JJ, Gómez G, Lizy-Destrez S. Invariant manifolds of a non-autonomous quasi-bicircular problem computed via the parameterization method. *Nonlinearity* (2017) **30**:3040. doi: 10.1088/1361-6544/aa7737
19. Siegel CL, Moser JK. *Lectures on Celestial Mechanics*, Vol. 187 of *Grundlehren der mathematischen Wissenschaften* New York, NY: Springer (1971).
20. Gabern F. *On the Dynamics of the Trojan Asteroids*. Ph.D. thesis, Universitat de Barcelona (2003).
21. Gabern F, Jorba À. A restricted four-body model for the dynamics near the Lagrangian points of the Sun-Jupiter system. *Discrete Contin. Dyn. Syst. Ser. B* (2001) **1**:143–82. doi: 10.3934/dcdsb.2001.1.143
22. Gabern F, Jorba À, Robutel P. On the accuracy of restricted three-body models for the Trojan motion. *Discrete Contin. Dyn. Syst. Ser. B* (2004) **11**:843–54. doi: 10.3934/dcds.2004.11.843
23. Szebehely V. *Theory of Orbits*. Orlando, FL: Academic Press (1967).
24. Meyer KR, Hall GR. *Introduction to Hamiltonian Dynamical Systems and the N-Body Problem*. New York, NY: Springer (1992).
25. Mondelo JM. *Contribution to the study of Fourier methods for quasi-periodic functions and the vicinity of the collinear libration points*. Ph.D. thesis, University of Barcelona (2001).
26. Farquhar RW, Kamel AA. Quasi-periodic orbits about the translunar libration point. *Celest Mech.* (1973) **7**:458–73.
27. Breakwell JV, Brown JV. The 'halo' family of 3-dimensional periodic orbits in the earth-moon restricted 3-body problem. *Celest Mech.* (1979) **20**:389–404.
28. Celletti A, Pucacco G, Stella D. Lissajous and halo orbits in the restricted three-body problem. *J Nonlinear Sci.* (2015) **25**:343–70.
29. Gómez G, Mondelo JM. The dynamics around the collinear equilibrium points of the RTBP. *Phys. D* (2001) **157**:283–321. doi: 10.1016/S0167-2789(01)00312-8
30. Broucke RA. *Periodic Orbits in the Restricted Three-Body Problem With Earth-Moon Masses*. JPL Technical Report. Jet Propulsion Laboratory, California Institute of Technology (1968).
31. Jorba À. A methodology for the numerical computation of normal forms, centre manifolds and first integrals of Hamiltonian systems. *Exp. Math.* (1999) **8**:155–95.
32. Jorba À, Masdemont J. Nonlinear dynamics in an extended neighbourhood of the translunar equilibrium point. In: Simó C. editor. *Hamiltonian Systems With Three or More Degrees of Freedom, NATO Advance Science Series C: Mathematical and Physical Science*, Held in S'Agaró, Kluwer Academic Publishers, Dordrecht (1999). p. 430–434.
33. Jorba À, Masdemont J. Dynamics in the centre manifold of the collinear points of the restricted three body problem. *Phys. D* (1999) **132**:189–213.
34. Haro À, de la Llave R. A parameterization method for the computation of invariant tori and their whiskers in quasiperiodic maps: numerical algorithms. *Discrete Continuous Dyn Syst B* (2006) **6**:1261–300. doi: 10.3934/dcdsb.2006.6.1261
35. Haro À, de la Llave R. A parameterization method for the computation of invariant tori and their whiskers in quasiperiodic maps: numerical implementation and examples. *SIAM J Appl Dyn Syst.* (2005) **6**:142–207. doi: 10.1137/050637327
36. Farrés A, Jorba À. On the high order approximation of the centre manifold for ODEs. *Discrete Contin. Dyn. Syst. Ser. B* (2010) **14**:977–1000. doi: 10.3934/dcdsb.2010.14.977
37. Farrés A, JorbaÀ. Periodic and quasi-periodic motions of a solar sail close to SL_1 in the Earth-Sun system. *Celest Mech.* (2010) **107**:233–253. doi: 10.1007/s10569-010-9268-4
38. Meyer KR, Schmidt DS. The stability of the Lagrange triangular point and a theorem of Arnold. *J. Diff Equat.* (1986) **62**: 222–36.
39. Arnold VI. Instability of dynamical systems with several degrees of freedom. *Soviet Math. Dokl.* (1964) **5**:581–5.
40. Giorgilli A, Delshams A, Fontich E, Galgani L, Simó C. Effective stability for a Hamiltonian system near an elliptic equilibrium point, with an application to the restricted three body problem. *J. Diff Equat.* (1989) **77**:167–98.
41. Jorba À, Villanueva J. Numerical computation of normal forms around some periodic orbits of the restricted three body problem. *Phys. D* (1998) **114**:197–229.
42. Gabern F, Jorba À. Effective computation of the dynamics around a two-dimensional torus of a Hamiltonian system. *J. Nonlinear Sci.* (2005) **15**:159. doi: 10.1007/s00332-005-0663-z
43. Simó C, Sousa-Silva P, Terra M. Practical stability domains near $L_{4,5}$ in the restricted three-body problem: Some preliminary facts. In: Santiago Ibáñez, Jesús S. Pérez del Río, Antonio Pumariño, and J. Ángel Rodríguez, editors, *Progress and Challenges in Dynamical Systems* Berlin; Heidelberg: Springer Berlin Heidelberg (2013). P. 367–382.
44. Jorba À, Villanueva J. On the persistence of lower dimensional invariant tori under quasi-periodic perturbations. *J. Nonlinear Sci.* (1997) **7**:427–73.
45. Jorba À, Ollé M. Invariant curves near Hamiltonian-Hopf bifurcations of four-dimensional symplectic maps. *Nonlinearity* (2004) **17**:691–710. doi: 10.1088/0951-7715/17/2/019
46. Jorba À. Numerical computation of the normal behaviour of invariant curves of n-dimensional maps. *Nonlinearity* (2001) **14**:943–976. doi: 10.1088/0951-7715/14/5/303
47. Cabré X, E. Fontich, and R. de la Llave. The parameterization method for invariant manifolds I: Manifolds associated to non-resonant subspaces. *Indiana Univ. Math. J* (2003) **52**:283–328. doi: 10.1512/iumj.2003.52.2245
48. Cabré X, Fontich E, de la Llave R. The parameterization method for invariant manifolds II: Regularity with respect to parameters. *Ind Univ Math J.* (2003) **52**:329–60.
49. Cabré X, Fontich E, de la Llave R. The parameterization method for invariant manifolds III: Overview and applications. *J Diff Equat.* (2005) **218**:444–515. doi: 10.1016/j.jde.2004.12.003
50. C. Simó. On the analytical and numerical approximation of invariant manifolds. In: Benest D, Froeschlé C editors, *Modern Methods in Celestial Mechanics*. Toulouse: Frontières (1990). p. 285–330.
51. Simó C, Gómez G, Jorba À, Masdemont J. The Bicircular model near the triangular libration points of the RTBP. In: Roy AE, Steves BA editors. *From Newton to Chaos*, New York, NY: Plenum Press. (1995). p. 343–370.

52. Jorba À, Villanueva J. On the normal behaviour of partially elliptic lower dimensional tori of Hamiltonian systems. *Nonlinearity* (1997) **10**:783–822.
53. Hou XY, Xin X, Scheeres DJ, Wang J. Stable motions around triangular libration points in the real earth-moon system. *Month Not R Astron Soc.* (2015) **454**:4172–81. doi: 10.1093/mnras/stv2216
54. Jorba-Cuscó M, Farrés A, Jorba À. A study on the effect of solar radiation pressure on the stability region near the earth-moon triangular points. In: *Proceedings of the 66th International Astronautical Congress*, Jerusalem (2015). p. 12–16.

Conflict of Interest Statement: The authors declare that the research was conducted in the absence of any commercial or financial relationships that could be construed as a potential conflict of interest.

Advantages of publishing in Frontiers

OPEN ACCESS
Articles are free to read for greatest visibility and readership

FAST PUBLICATION
Around 90 days from submission to decision

HIGH QUALITY PEER-REVIEW
Rigorous, collaborative, and constructive peer-review

TRANSPARENT PEER-REVIEW
Editors and reviewers acknowledged by name on published articles

Frontiers
Avenue du Tribunal-Fédéral 34
1005 Lausanne | Switzerland

Visit us: www.frontiersin.org
Contact us: info@frontiersin.org | +41 21 510 17 00

REPRODUCIBILITY OF RESEARCH
Support open data and methods to enhance research reproducibility

DIGITAL PUBLISHING
Articles designed for optimal readership across devices

FOLLOW US
@frontiersin

IMPACT METRICS
Advanced article metrics track visibility across digital media

EXTENSIVE PROMOTION
Marketing and promotion of impactful research

LOOP RESEARCH NETWORK
Our network increases your article's readership